

UNIVERSITY OF OKLAHOMA
GRADUATE COLLEGE

DEVELOPMENT OF HELICOPTER ATTITUDE AXES CONTROLLED HOVER
FLIGHT WITHOUT PILOT ASSISTANCE AND VEHICLE CRASHES

A DISSERTATION
SUBMITTED TO THE GRADUATE FACULTY
in partial fulfillment of the requirements for the
degree of
Doctor of Philosophy

By
MIGUEL SIMON
Norman, Oklahoma
2007

UMI Number: 3261118

Copyright 2007 by
Simon, Miguel

All rights reserved.

UMI[®]

UMI Microform 3261118

Copyright 2007 by ProQuest Information and Learning Company.
All rights reserved. This microform edition is protected against
unauthorized copying under Title 17, United States Code.

ProQuest Information and Learning Company
300 North Zeeb Road
P.O. Box 1346
Ann Arbor, MI 48106-1346

DEVELOPMENT OF HELICOPTER ATTITUDE AXES CONTROLLED HOVER
FLIGHT WITHOUT PILOT ASSISTANCE AND VEHICLE CRASHES

A DISSERTATION APPROVED FOR THE
SCHOOL OF AEROSPACE AND MECHANICAL ENGINEERING

BY

Dr. Harold Stalford

Dr. David Miller

Dr. John Fagan

Dr. Luther White

Dr. Yunjun Xu

*To Elias, Betsy, Oraidia, Miguel P. Simon.
To Mory, Brian and Sophia.*

Acknowledgments

I would like to thank Dr. Harold Stalford, my mentor and advisor, for his many suggestions and constant support during this thesis work. Dr. Stalford taught me how to think as an engineer and how to be an engineer. To Ute Stalford, who has provided her support during the whole of the dissertation, thank you for the cookies!

I am grateful to my parents Oraida and Miguel for their patience, support and *love*. Without them this work would simply not be.

Gloria and Mitch Burrus, your care and your giving is an inspiration to many, specially to Betsy and myself.

To Betsy my dear wife whose unconditional support helped me persevere. And to Betsy's parents, Bob and Lydia Soroosh who *prayed* constantly for both Betsy and myself. To the Church in Oklahoma City, Norman and Ann Arbor for their *love and support* in all spiritual and practical matters. Thank you.

To Elias our son, who is so precious.

To my co-workers at SAIC that allowed me to get away so often to finish my dissertation work. Ron Scott, my supervisor at SAIC, thank you for your mentoring help and support in all matters. John Winger, Charles Lors, Thomas Connolly, Mariano Nadal, Wilfred Smith, Marc Compere, Jarrett Goddel, John Kajs, Gary Willenbring, and so many other collages. Thank you as well, I appreciate your help and encouragement all these time.

Billy Mays and Greg Williams at the AME machine shop for your *any time support*. Thank you. And to the staff at the school of AME, Margaret, Suzi, Vicki, and Lawana. Thank you all for your timely help.

Miguel Simon, Norman, Oklahoma, May, 2007

Table of Contents

Acknowledgments	iv
Table of Contents	v
List of Tables	xiv
List of Figures	xvi
Abstract	xxxix
1 Introduction	1
1.1 Introduction	1
2 Helicopter Research Testbed	12
2.1 Introduction	12
2.2 Helicopter Research Testbed Components	12
2.2.1 Basic Helicopter	14
2.2.1.1 Main Rotor	14
2.2.1.2 Tail Rotor	15
2.2.1.3 Helicopter Engine	16
2.2.1.4 Transmission Gears	17
2.2.1.5 Swashplate and Blade Pitch Angle Control Links	18
2.2.1.6 Digital Electro-Mechanical Actuator and Radio Control Transmitter/Receiver	18
2.2.1.7 Helicopter Component Hardware Interface	20
2.2.2 MotionPak	23
2.2.3 Differential GPS System	23
2.2.4 FreeWave Wireless Data Transceiver	24
2.2.5 Range Sensor	24
2.2.6 Electronic Compass	26
2.2.7 Hall Effect Sensors	26
2.2.8 On-Board Central Processing Units (CPU)	26
2.2.8.1 Primary Mission Planning and Control CPU: Ampro PC104	28
2.2.8.2 Low Level Actuator Command and Sensor Input/Output CPU: Motorola MC68332	28
2.2.9 Rate Table Stand	30
2.2.10 Linear and Directional Test Stand	31

2.2.11	Rotational Dynamics Test Stand	31
3	Helicopter Electro-Mechanical Control Actuators	34
3.1	Introduction	34
3.2	Main Rotor Collective Control Servo	34
3.3	Main Rotor Longitudinal and Lateral Cyclic Control Servo	36
3.4	Tail Rotor Collective Control Servo	39
3.5	Throttle Control Servo	40
3.6	Summary of Control Servo Settings	40
4	Test Stand	42
4.1	Introduction	42
4.2	Test Stand Survey	44
4.3	Test Stand for Helicopter Research	44
4.3.1	Linear and Directional Test Stand	45
4.3.2	Rotational Dynamics Test Stand	47
4.3.3	Rate Table Stand	48
4.4	Conclusions.	48
5	Math Models	50
5.1	Introduction	50
5.2	Models of the Helicopter Components	52
5.2.1	Main Rotor Aerodynamic Actuator Model	52
5.2.1.1	Momentum and Blade Element Theories for the Helicopter	53
5.2.1.2	Main Rotor Blade Equation of Motion	55
5.2.1.3	Tip Path Plane Blade Equations of Motion	56
5.2.1.4	Main Rotor Stabilizer Bar	58
5.2.2	Tail Rotor Aerodynamic Actuator Model	59
5.2.3	Model of Helicopter Engine	60
5.2.4	Models of Remaining Components	61
5.3	Rigid Body Dynamics	61
5.3.1	Simplified Equations of Trim	64
5.3.2	Linear Equations of Motion about Trim	65
5.4	Stability Derivatives	67
6	Helicopter Sensors	68
6.1	Signals and Sensors	68
6.2	Main Rotor Angular Velocity Measurement	68
6.2.1	Main Rotor Angular Velocity Ω Measurement via a Hall Effect Sensors	69
6.3	Fuselage Linear Acceleration and Angular Velocity Measurements	70
6.3.1	MotionPak Sensor Suite Location	70
6.4	Center of Mass Position	77
6.5	Helicopter Body Attitude	78

6.6	Center of Mass Altitude	79
7	Design of the Helicopter Feedback Control Loops	80
7.1	Engine Governor and Main Rotor RPM Control Loop	80
7.2	Yaw Rate and Heading Control Loop	80
7.3	Pitch Rate and Pitch Attitude Control Loop	82
7.4	Roll Rate and Roll Attitude Control Loop	86
7.5	Altitude Control Loop	86
7.6	Baseline Helicopter Feedback Control	88
7.7	Helicopter Position Feedback Control	90
8	Engine Governor and Main Rotor Angular Velocity Experiment	93
8.1	Experiment Setup	93
8.1.1	Open Loop Engine and Main Rotor Dynamics Characterization	93
8.1.2	Modeling of the Open Loop Engine and Main Rotor Dynamics	94
8.1.3	Engine Governor and Main Rotor Angular Velocity Control design and implementation	97
8.2	Testing and Experimental Results of Closed Loop Feedback Control	97
9	Helicopter Aerodynamic Model Experiment	99
9.1	Experiment Setup	99
9.2	Open Loop Main Rotor Torque Characterization	100
9.3	Open Loop Tail Rotor Aerodynamic Characterization	107
9.4	Experimental Results	109
10	Helicopter Yaw Rate and Heading Control Experiment	111
10.1	Experiment Setup	111
10.2	Open Loop Tail Rotor Control Input Characterization	111
10.3	Yaw Rate and Heading Hold Control Design	116
10.4	Experiment Results	116
11	Helicopter Pitch and Roll Attitude Experiments	119
11.1	Experiment Setup	119
11.1.1	Pitch Rate Stability and Pitch Command Track and Hold Experiment	119
11.1.2	Roll Rate Stability and Roll Command Track and Hold Experiment	123
11.1.3	Simultaneous Pitch and Roll Stability Command Track and Hold Experiment while Tracking and Holding Heading Commands	123
12	Helicopter Hardware and Software Integration	129
12.1	OU Helicopter Research Testbed: A Systems Engineering Design Approach	129
12.2	Hardware Interface	131
12.3	Software Interface	134
12.4	Hardware, Software and Systems Integration	135
12.4.1	Embedded Software Generation	136
12.4.2	Hardware and Software Integration	138

12.4.2.1	Hardware Initialization	138
12.4.2.2	Sensor Reading	139
12.4.2.3	Step Embedded Controller	140
12.4.2.4	Update Actuator Commands	140
13	Summary and Conclusions	141
13.1	Summary	141
	Bibliography	148
A	First Principles	163
A.1	Notations	163
A.2	Angular Momentum and Moment of Momentum	165
A.3	Newton’s Law for Moment of Momentum	168
A.4	Newton’s Law for Linear Momentum	168
A.5	Fluid Equations of Change	169
A.5.1	Mass Equations of Change: Conservation of Mass	172
A.5.2	Momentum Equations of Change: Conservation of Momentum	174
A.5.3	Energy Equations of Change: Conservation of Energy	176
B	Helicopter Frames of Reference	179
B.1	Inertial and Earth Reference Frames	179
B.1.1	Heliocentric Reference Frame	179
B.1.2	Geocentric Reference Frame	180
B.1.3	Earth-Centered Reference Frame	180
B.1.4	Earth-Surface Reference Frame	180
B.1.5	Vehicle-Carried Reference Frame	181
B.1.6	Atmosphere-Fixed or Wind Reference Frame	181
B.1.7	Body-Fixed Reference Frame	181
B.1.8	Inertial Reference Frame	181
B.2	Relations between the Body \mathcal{B} and Vehicle \mathcal{V} Reference Frame	184
B.3	Relations between Wind Reference Frame \mathcal{W} and Body Reference Frame \mathcal{B}	188
B.4	Euler Angle Rates	189
B.5	Applied Newton’s Laws	191
B.5.1	Translation Dynamics	191
B.5.2	Position Dynamics	193
B.5.3	Rotational Dynamics	194
B.5.4	Solution and System Simulation	196
B.6	Main Rotor Frame of Reference	196
B.6.1	Hub Plane (HP) Reference Frame	198
B.6.2	Non Feathering Plane (NFP) Reference Frame	199
B.6.3	Tip Path Plane (TPP) Reference Frame	200
B.6.4	Relations Among Main Rotor Frame of Reference	200

C	Helicopter Momentum Theory and Blade Element Theory	202
C.1	Simple Momentum Theory in Hovering Flight	203
C.1.1	Momentum Theory: Vertical Climb	209
C.1.2	Momentum Theory: Vertical Descent	213
C.1.2.1	Windmill Break State ($V_C/v_h \leq -2$)	213
C.1.2.2	Vortex Ring State	216
C.1.2.3	Turbulent Wake State	217
C.1.2.4	Autorotation	217
C.1.3	Momentum Theory: Forward Flight	217
C.1.4	Momentum Theory: Power Consideration in Forward Flight . . .	220
C.1.5	Summary of Results from Momentum Theory	220
C.2	Blade Element Theory	222
C.2.1	Tip-Loss Factor	228
C.3	Combined Blade Element and Momentum Theory	229
C.3.1	Other Effects	233
D	Helicopter Rotor Equations of Motion	234
D.1	Preliminaries and Motivation	234
D.2	Fundamental Rotor Equations of Motion	235
D.2.1	Pure Blade Flap Equations of Motion	241
D.2.1.1	Pure Blade Flap Equilibrium Equations	244
D.2.2	Pure Blade Drag Equations of Motion	248
D.2.2.1	Pure Blade Drag Equilibrium Equations	250
D.2.3	Pure Blade Feathering Equations of Motion	251
D.2.4	Combined Blade Flap and Drag Equations of Motion	254
D.3	Rigid Blade Flapping Equations of Motion	258
D.3.1	Blade Flapping Disturbance at Constant Feather Angle	258
D.3.2	Flapping Motion with Cyclic Feather Angle	260
D.3.3	Flapping Motion with Body Pitch Rate	264
D.3.4	Flapping Motion with Body Roll Rate	271
D.3.5	Flapping Motion with Body Angular Roll and Pitch Rates and Angular Rates of Change	279
D.3.5.1	Flapping Motion with Body Angular Roll and Pitch Rates	283
D.3.5.2	Flapping Motion with Body Roll and Pitch Rates Rate of Change	288
D.3.6	Flapping Motion for Semi-rigid Rotors with Hinge Offset, Hub Pre- cone and Spring Restoring Moment	291
D.3.7	Blade Equation of Motion for Forward Flight Including Body Pitch and Roll Rates	292
D.3.7.1	Thrust and Torque Coefficients in Forward Flight	298
D.3.7.2	Simplified Thrust and Torque Coefficients in Forward Flight	301
D.3.7.3	Blade Equation of Motion for Forward Flight: Non-Constant Blade Flap Coefficients	302

D.3.7.4	Blade Equation of Motion for Forward Flight: Low Frequency Dynamics	304
D.3.7.4.1	Blade Equation of Motion: Low Translational Speed 306	
D.3.7.4.2	Blade Equation of Motion: No-Flapping Hinge Offset and no Hub Precone 307	
D.3.7.4.3	Simplified First Order Tip Path Plane Blade Flapping Equation of Motion 309	
D.3.7.4.4	Blade Equation of Motion: Teetering Blade 310	
D.3.7.5	Blade Equation of Motion for Forward Flight: Constant Blade Flap Coefficients	311
D.4	Summary of Blade Equations of Motion	314
E	Helicopter Rotor Forces and Moments	316
E.1	Aerodynamic Rotor Forces and Moments	316
E.2	Rotor Forces	321
E.2.1	Simplified Rotor Forces	323
E.3	Rotor Hub Moments	325
E.4	Coupled Fuselage-Rotor Forces and Moments	329
F	Helicopter Trim Equations	331
F.1	Small Perturbation Theory and Trim Equations	332
F.1.1	Symmetric Flight Equilibrium Equations	336
F.1.2	Linearized Equations of Motion about a Trim Condition	339
G	Helicopter Stability Derivatives	342
G.1	Main Rotor Stability Derivatives	343
G.1.1	Main Rotor Forward Velocity Stability Derivatives	344
G.1.2	Main Rotor Vertical Velocity Stability Derivatives	347
G.1.2.1	Main Rotor Heave Damping	349
G.1.3	Main Rotor Control Derivatives	350
G.1.4	Main Rotor Blade Flapping Derivatives	353
G.1.5	Main Rotor Force and Moment Derivatives	355
H	Helicopter Model	357
H.1	Helicopter Model	357
H.1.1	Rigid Body Equation of Motion	358
H.1.2	Main Rotor Forces and Moments	361
H.2	Extended Linearized Rigid Body Equations for Motion	365
H.2.1	Flapping Motion for Semi-rigid Rotors with Stabilizer Bar	367

I	Hardware Parameters and Sensor Calibration	371
I.1	Helicopter Parameter Estimation	371
I.1.1	Rotational Inertia	371
I.1.2	Helicopter Testbed Platform Parameters	372
I.2	Sensors and Actuators	376
I.2.1	Systron Donner MotionPak	376
I.2.2	NovAtel Global Positioning System	378
I.2.3	FreeWave Wireless Data Transceiver	381
I.2.4	SHARP GP2D02 Infrared Sensor	382
I.2.5	AccuStar II Dual Axis Clinometer	383
I.2.6	Electronic Compass	384
I.2.7	O.S.61 Helicopter Engine	385
I.2.8	Ultrasound Altimeters	388
I.3	Calibration	389
I.3.1	Helicopter Main Rotor Blade Pitch Angle Calibration	389
I.3.2	Helicopter Main Rotor Cyclic Angle Calibration	390
I.3.3	Helicopter Tail Rotor Collective Angle Calibration	392
I.3.4	OU Helicopter Throttle Fuel Flow Rate Calibration	392
I.3.5	Cantilever Beam Strain Gage Calibration	392
I.4	Helicopter Linear and Directional Test Platform	395
J	Helicopter Engine Controller	398
J.1	Introduction	398
J.2	Main Rotor Characterization Experiment	399
J.2.1	Estimation of Simple Engine-Rotor Dynamics from Experimental Data	404
J.2.1.1	Estimation of Available Power and Main Rotor Torque	405
J.2.1.2	Relationship between Available Power and Main Rotor Torque Required	406
J.2.2	Engine-Carburetor and Coupled Main Rotor Dynamics Open-Loop Modeling Results	409
J.2.3	Synthesis of the Engine Control Law Based on Experimental Data Parameter Estimation	410
J.3	Summary of Main Rotor Characterization Results	416
K	Helicopter Aerodynamic Model Identification	418
K.1	Introduction	418
K.2	Helicopter Thrust Experimental Setup	419
K.3	Helicopter Experimental Setup for Power and Torque Characterization	421
K.3.1	Main Rotor Induced and Profile Power Experiment	421
K.3.2	Tail Rotor Aerodynamic Model Identification Experiment	431

L	Helicopter Stability and Control	433
L.1	Introduction	433
L.2	Experiment: Yaw Stability and Heading Control	434
L.2.1	Trim Tail Rotor Blade Pitch Angle	437
L.2.2	Helicopter Yaw Rate Control Design	438
L.2.3	Helicopter Heading Control Design	443
L.2.4	Helicopter Yaw Rate and Heading Control Synthesis	445
L.2.5	Test Results for Helicopter Yaw Rate and Heading Control	445
L.3	Experiment: Pitch Rate Stability and Pitch Attitude Hold Control	448
L.4	Experiment: Roll Rate Stability and Roll Attitude Hold Control	452
L.5	Experiment: Roll and Pitch Stability with Yaw Rate and Heading Control	457
M	Helicopter Systems Design	459
M.1	Systems Engineering and Integration	459
M.1.1	Systems Engineering Standards	459
M.1.2	Configuration Management Standards and Capability Maturity Models.	460
M.1.3	Systems Engineering Processes	461
M.1.4	Definition of Integrated Product and Processes Development (IPPD)	461
M.1.5	IPPD Case Studies	463
M.2	Application of Integrated Product and Processes Development (IPPD) to the University of Oklahoma Helicopter Research Testbed	463
M.2.1	Voice of the Customer (VOC)	464
M.2.1.1	VOC: Mission Profile Requirements	464
M.2.1.2	VOC: Affinity Diagram	465
M.2.1.3	VOC: Tree Diagram	465
M.2.2	Voice of the Engineer (VOE)	465
M.2.2.1	VOE: Affinity Diagram	467
M.2.2.2	VOE: Tree Diagram	467
M.2.3	Quality Function Deployment (QFD)	467
M.2.3.1	QFD: Functional Deployment Matrix	467
M.2.3.2	QFD: Voice of the Customer Prioritization	471
M.2.3.3	Quality Function Deployment (QFD): Voice of the Customer Benchmark	473
M.2.3.4	QFD: Interaction Matrix for Design Requirements (VOE)	473
M.3	Modular Functional Decomposition	473
M.4	System Architecture	476
N	Nomenclature	479
O	Glossary	480

P Acronyms	482
Index	485

List of Tables

2.1	Basic Helicopter Parameters	12
2.2	Helicopter Research Testbed Components	14
2.3	O.S.61 Helicopter Engine	17
2.4	Engine, Main Rotor and Tail Rotor Gear	17
3.1	Helicopter Electromechanical Control Servos	34
3.2	Helicopter Servos Inputs and Corresponding Actuator Settings	41
4.1	Test Bed	44
5.1	Momentum Theory Applications	54
5.2	Blade Equation of Motion Application	56
5.3	Blade Equation of Motion Application	58
5.4	Other Helicopter Components and their Models	61
6.1	Sensors	68
6.2	Standard Deviation of MotionPak Measured Data.	73
12.1	Hardware Interface to Flight Computers	134
12.2	Hardware Initialization Action	139
B.1	Reference Frames in Flight Mechanics	179
D.1	Summary of Blade Equations of Motion	315
E.1	Moment contribution about the hub	325
I.1	Rotational Inertial Parameters	372

I.2	Helicopter Mass and Inertial Parameters	373
I.3	Helicopter Dimensions	373
I.4	Main Rotor Parameters	373
I.5	Stabilizer Bar Parameters	374
I.6	Tail Rotor	374
I.7	Helicopter Mass (Weight) Parameters	375
I.8	Mechanical and Electrical Specifications	377
I.9	MotionPak Angular Measurements Specifications	377
I.10	MotionPak Linear Measurements Specifications	377
I.11	GPS MiLLennium GPSCard Selected Performance Parameters	378
I.12	FreeWave Selected Technical Specifications	382
I.13	AccuStar II Performance	383
I.14	Honeywell HMR3000 Specifications [72].	386
I.15	Honeywell HMR3000 Physical Characteristics [72].	387
I.16	O.S.61 Helicopter Engine	387
J.1	Engine-Carburetor and Main Rotor Rotational Dynamic Characteristics .	416
J.2	Engine-Carburetor Control Characteristics	417
K.1	Aerodynamic Model Parameters for the Main Rotor	419
K.2	Aerodynamic Model Parameters for the Tail Rotor	431
L.1	Yaw Rate and Heading Control Design	445
M.1	Systems Engineering (SE) Standards	460
M.2	Configuration Management (CM) Standards	460

List of Figures

2.1	Helicopter Research Testbed Mechanical Components.	13
2.2	Main Rotor and Stabilizer Bar Dimensions.	16
2.3	O.S.61 Helicopter Engine	17
2.4	Belt and Transmission Gears between the Engine, Main Rotor and Tail Rotor. In the figure, (1) is the engine gear, (2) is the transmission belt-gear, (3) is an interim gear between the engine and the main rotor, (4) is the main rotor gear with a clutch inside (not visible), (5) is the tail rotor transmission gear. The clutch in the main rotor gear engages when the clutch has sufficient angular velocity of 200 RPM or more.	18
2.5	Helicopter Swashplate and Blade Pitch Control Links. In the figure, (1) is the swashplate that tilts, (2) is the lateral cyclic control link, (3) is the longitudinal control link, (4) is a direct swashplate input to main rotor blade pitch (Bell input), (5) is the stabilizer bar input to main rotor blade pitch (Hiller input).	19
2.6	JR Pro PCM 10S Radio Control (RC) Transmitter.	21
2.7	Electro-Mechanical Digital Servo Devices and their respective Control Tasks. In the figure, (1) is the main rotor collective, (2) is the longitudinal cyclic, (3) is the lateral cyclic, (4) is the rudder or tail rotor collective, and (5) is the throttle servo.	21
2.8	Helicopter Components Hardware Interface. Red lines represent hard connecting links between the servos and the connecting hardware.	22
2.9	Systron Donner MotionPak.	23

2.10	NovAtel GPS Ground Station Receiver, On-Board Card, Antenna, and Reference Station Antenna.	24
2.11	FreeWave Wireless Data Transceiver On-Board Card and Ground Station Unit.	25
2.12	SHARP GP2D02 Infrared Distance Sensor.	25
2.13	Ultrasound Sensors	26
2.14	Electronic Compass Honeywell HMR3000	27
2.15	Main Rotor Gear with Embedded Permanent Magnets	27
2.16	Hall Effect Sensor near the Main Rotor Gear with Embedded Permanent Magnet	28
2.17	Mission Planning and Command CPU: Ampro PC104	29
2.18	Actuator Command and Sensor I/O CPU: Dual Motorola MC68332	29
2.19	Rate Table Stand (RTS).	30
2.20	Helicopter Research Testbed sitting on the instrumented, purposed built Linear and Directional Test Stand (LDTS).	32
2.21	Real-Time Run of the Helicopter on top of the Rotational Dynamic Test Stand (RDTS).	33
3.1	Collective control servo settings with corresponding swashplate deflections and main rotor collective pitch angle θ . Left column corresponds to $\theta = -3$ deg. The middle column corresponds to the idle setting of $\theta = 3$ deg. The right column corresponds to a maximum collective deflection of $\theta = 12$ deg.	35
3.2	Longitudinal control servo settings with corresponding swashplate deflections and main rotor Bell cyclic pitch angle θ_{lon} . The left column corresponds to positive longitudinal cyclic inputs which result in positive pitch attitude or nose up motion. The right column corresponds to negative longitudinal cyclic inputs which result in negative pitch attitude or nose down motion.	37

3.3	Lateral control servo settings with corresponding swashplate deflections and main rotor Bell cyclic roll angle θ_{lat} . Left column corresponds to negative lateral cyclic inputs which result in negative roll attitude or left-wing-up motion. The right column corresponds to positive lateral cyclic inputs which result in positive roll attitude or left-wing-down motion.	38
3.4	Tail Rotor collective settings and corresponding calibration results. The right-most column corresponds to positive tail rotor thrust that compensates for the main rotor torque.	39
3.5	Throttle servo settings. The left column corresponds to a fully opened throttle with 100% air-fuel mixture flow, and the right column corresponds to a fully closed throttle with 0% air-fuel mixture flow.	40
4.1	Side view of the LDTS. Note that in the left picture the altitude stand is at its minimum point. On the right, the attachment plate is at its maximum height of 14 in (0.36 m).	46
4.2	Top view of the LDTS. Note the top-left against the red-stopper, and the top-right against the stopper. The stopper prevented the test helicopter from winding around when performing heading track and hold. The stoppers can be removed to perform 360° yaw rate experiments.	46
4.3	On the left, note the view of the two middle steel plates. On the right, note the Lazy-Suzy attachment.	47
4.4	Rotational Dynamic Test Stand (RDTW). The RDTW can rotate freely about the z-axis for yaw rate and heading track and hold commands. The RDTW can also rotate independently or in combination rotation about the x and y axes for roll and pitch attitude control.	47
4.5	Rate Table Stand (RTS).	48
5.1	Helicopter Research Testbed Mechanical Components.	53
5.2	Closed Loop Control Design Diagram.	60

6.1	MontionPak Sensor Suite Location at front of the Helicopter.	71
6.2	MontionPak Sensor Suite rigidly attached to the fuselage and positioned beneath the engine, close to the vehicle's center of mass.	71
6.3	MotionPak linear accelerations (\dot{u}, \dot{v}) and angular rates (p, q) measure- ments with sensor suite positioned beneath the engine close to the vehicle's center of mass. Data collected during a test run with main rotor angular velocity Ω actively controlled in real-time.	72
6.4	Photo montage of the MontionPak Sensor Suite mounted on vibration isolation pads.	74
6.5	MontionPak Sensor Suite mounted on vibration isolation pads and posi- tioned beneath the helicopter engine.	74
6.6	MontionPak Sensor Suite positioned beneath the engine and mounted on vibration isolation pads.	74
6.7	MotionPak linear accelerations (\dot{u}, \dot{v}) and angular rates (p, q) measure- ments with sensor suite positioned beneath the engine and mounted on vibration isolation pads. Data collected during a test run with roll, pitch and yaw actively controlled in real-time.	75
6.8	MontionPak Sensor Suite distribution for linear acceleration (x, y) and angular rates (p, q) . The dash-dash curves present data taken with the MotionPak rigidly attached to the fuselage, and the solid curves present measured data with the MotionPak mounted on vibration isolation pads.	76
6.9	Differential GPS Experiment at the University of Oklahoma. Portions of differential data loss are the result of positioning the GPS antenna under a tree canopy.	78
7.1	Block diagram for the engine governor and main rotor angular velocity control loop.	81

7.2	Torque Equilibrium about the Center of Mass (CM) along the z-axis. In the figure, Ω is the main rotor angular velocity, Ω_{TR} is the tail rotor angular velocity, Q_E , Q_{MR} , Q_{TR} are the engine available torque, the main rotor torque and the tail rotor torque respectively. In addition, n_{TR} is the main rotor to tail rotor gear ratio, and l_{TR} is the location of the tail rotor hub behind the CM.	82
7.3	Tail Rotor collective pitch angle. In the figure, the tail rotor collective pitch angle (1) generates the least thrust as illustrated in Figure 7.2 on page 82, and the thrust may even be in the opposite direction. The tail rotor collective pitch angle (2) is in the same direction as in Figure 7.2, and provides proper compensation.	83
7.4	Block diagram for yaw rate and heading angle control loop.	84
7.5	Swashplate longitudinal cyclic control input. In the figure, the swashplate position (1) inputs longitudinal cyclic to the main rotor blade pitch angle that will result in a nose-up tilt of the fuselage. The swashplate position (2) inputs longitudinal cyclic to the main rotor blade pitch angle that will result in a nose-down tilt of the fuselage.	84
7.6	Block diagram for longitudinal pitch rate q and pitch attitude θ control loop.	85
7.7	Swashplate lateral cyclic control input. In the figure, the swashplate position (1) inputs lateral cyclic to the main rotor blade pitch angle that will result in a positive roll of the fuselage. The swashplate position (2) inputs lateral cyclic to the main rotor blade pitch angle that will result in negative roll of the fuselage.	87
7.8	Block diagram for lateral roll rate q and roll attitude ϕ control loop. . .	87
7.9	Main Rotor Collective Blade Pitch Angle Input. In the picture, the swashplate is at its lowest position at (1), mid position at (2), and highest position at (3).	88

7.10	Block diagram for the altitude feedback control loop.	89
7.11	Block diagram for longitudinal and lateral feedback control.	91
7.12	Block diagram for position hold and locomotion. Note the nested attitude, altitude and position loops.	92
8.1	Sample Main Rotor Angular Velocity Ω data resulting from varying throttle inputs and Main Rotor Blade Pitch Angle θ set at 8 degrees.	94
8.2	Time to Rise and Time Constant estimates for Engine/Carburetor-Main Rotor dynamic system.	95
8.3	Open Loop Simulation Result for Rotor Angular Velocity Ω	96
8.4	Engine-Carburetor and Main Rotor Dynamics Model.	96
8.5	Closed-Loop Engine-Carburetor, Main Rotor Dynamics Model.	97
8.6	Engine-Carburetor model simulation results compared with real-time data.	98
9.1	Torque Equilibrium about the Center of Mass (CM) along the z-axis. In the figure, Ω is the main rotor angular velocity, Ω_{TR} is the tail rotor angular velocity, Q_E , Q_{MR} , Q_{TR} are the engine available torque, the main rotor torque and the tail rotor torque respectively. In addition, n_{TR} is the main rotor to tail rotor gear ratio, and l_{TR} is the location of the tail rotor hub behind the CM.	101
9.2	Helicopter Research Testbed sitting on the instrumented, purposed-built Linear and Directional Test Stand (LDTS).	102
9.3	Torque Experiment with no Tail Rotor Inputs.	104
9.4	Torque Experiment sample data $\Omega = 1400$ rpm.	105
9.5	Torque Measurements Experiment with free tail rotor inputs.	106
9.6	Effects of Tail Rotor Torque on Bending Beam Load Cell Torque Measurements	108
9.7	Torque Measurements and Computed Torque.	110

10.1 Helicopter on the Rotational Dynamics Test Stand (RDTS) during a real-time yaw rate experiment.	112
10.2 Helicopter on the Linear and Directional Test Stand (LDTS) during a real-time yaw rate experiment.	112
10.3 Real Time Run with Tail Rotor Inputs.	113
10.4 Multiple Real Time Run with Tail Rotor Inputs.	114
10.5 Empirical Tail Rotor Blade Pitch Angle and resulting Equilibrium Torque N_{TR}	115
10.6 Yaw Rate p Feedback Control Law.	116
10.7 Yaw Heading ψ Feedback Control Law.	116
10.8 Block diagram for yaw rate and heading angle control loop.	117
10.9 Real-Time Data with Helicopter Heading Command. Red solid curve is the heading command ψ_C , dark green curve is the yaw rate r measured data. The solid blue curve is the helicopter measured heading ψ , and the magenta curve is the scaled tail rotor blade pitch command δ_{TR} in pulse width units ($\mu\text{sec}/100$). The light green curve is the scaled main rotor angular velocity $\Omega/100$	118
11.1 Real-Time Run of the Helicopter on top of the Rotational Dynamics Test Stand (RDTS).	120
11.2 Block diagram for longitudinal pitch rate q and pitch attitude θ control loop.	121
11.3 Pitch command θ_c tracking with the helicopter on the Rotational Dynamics Test Stand (RDTS). In the figure, the top graph plots the roll p and pitch q rates and the main rotor angular velocity Ω	122
11.4 Block diagram for lateral roll rate q and roll attitude ϕ control loop. . .	124

11.5	Roll command ϕ_c tracking with the helicopter on the Rotational Dynamic Test Stand (RDTS). In the figure, the top graph plots the roll p and pitch q rates and the main rotor angular velocity Ω . Notice the large time constant of the feedback control loop during an experimental stability test.	125
11.6	Block diagram for longitudinal and lateral feedback control.	127
11.7	Simultaneous attitude command tracking and hold for roll ϕ , pitch θ and heading ψ with constant angular velocity Ω . In the figure, the top-most graph presents the heading command tracking and hold, the second graph shows the roll p and pitch rate q during the flight. The third graph down shows the pitch attitude θ holding zero for the first part of the run, and tracking commands for the second part of the run. The same is true for the roll attitude ϕ in the fourth graph.	128
12.1	Simplified system architecture for the University of Oklahoma Helicopter Research Testbed for Autonomous Flight.	130
12.2	Simplified system architecture suitable for Hardware-in-the-Loop real-time tests with the University of Oklahoma Helicopter Research Testbed. . .	130
12.3	Hardware component interface.	132
12.4	Hardware data bus architecture.	133
12.5	Software abstraction for data input/output across the various software components.	135
12.6	Helicopter SIMULINK simulation environment.	136
12.7	Embedded software generation process.	137
12.8	Helicopter top level initialization state diagram.	139
A.1	Differential fluid element volume dv with fluid velocity \vec{V} in region $\mathfrak{R}(t)$ delimited by surface $S(t)$ with surface normal \vec{n} and surface velocity \vec{V}_s	169
A.2	Differential fluid volume dv resulting from surface velocity \vec{V}_s	170

B.1	Earth-Centered Reference Frame and Earth-Surface Reference Frame . . .	182
B.2	Vehicle Body-Fixed Frame \mathcal{B}	185
B.3	Symmetric flight nomenclature and body frame axis. Side view.	186
B.4	Asymmetric flight nomenclature and body frame axis. Top view.	187
B.5	Euler angles and frame rotations. Rear view.	187
B.6	Euler rates tracking.	190
B.7	Inertial Body Dynamics.	191
B.8	Simulation Block Diagram Sketch.	197
B.9	Rotor Reference Frames [11, 92, 119, 124].	199
C.1	Actuator disc concept for rotor in vertical flight (for hover case V_c equals zero)	204
C.2	Variation of induced velocity for climbing rate	211
C.3	Effects of climb speed on induced power	212
C.4	Actuator disc concept for rotor in axial descent	214
C.5	Theoretical and empirical induced velocity profiles	215
C.6	Velocity, angles and parameters associated with a rotor blade element.	223
C.7	Rotor annulus used in local momentum analysis for hovering [53, 92].	229
D.1	Helicopter rotor in forward flight.	234
D.2	Rotor blade nomenclature.	236
D.3	Rotor blade rotating about the flapping hinge.	246
D.4	Rotor blade rotating on a drag (lead/lag) hinge.	250
D.5	Blade Flapping Disturbance at Constant Feather Angle.	259
D.6	Blade Flapping Disturbance at Constant Feather Angle.	260
D.7	Blade Flapping Disturbance due to Body Pitch Rate.	269
D.8	Blade Flapping Disturbance due to Body Roll Rate.	277
D.9	Blade Flapping Disturbance due to Body Roll and Pitch Rates.	284
D.10	Aerodynamic Elements Pertaining to Rotor Forces and Moments.	293

E.1	Rotor Forces and Moments.	318
E.2	Forces and Moments with Blade Flap Angles	324
E.3	Blade force equilibrium	325
F.1	Longitudinal Forces and Moments.	333
F.2	Lateral Forces and Moments.	333
H.1	Main Rotor Stabilizer Teetering Mechanism.	369
H.2	Main Rotor and Stabilizer Bar Cyclic Mechanism.	370
I.1	Systron Donner MotionPak.	376
I.2	NovAtel GPS Ground Station Receiver, On-Board Card, Antenna, and Reference Station Antenna.	379
I.3	Differential GPS measurements with 2.0cm Circle Error Probable (CEP) position accuracy at a location on the University of Oklahoma Campus. .	379
I.4	GPS Reference Antenna on top of the Sarkey Energy Center at the Uni- versity of Oklahoma.	380
I.5	FreeWave Wireless Data Transceiver On-Board Card and Ground Station Unit.	381
I.6	SHARP GP2D02 Infrared Distance Sensor.	382
I.7	Dual Axis Clinometer AccuStar II.	383
I.8	Calibration Curve for the AccuStar II Dual Axis Clinometer.	384
I.9	Electronic Compass Honeywell HMR3000	385
I.10	O.S.61 Helicopter Engine	385
I.11	Ultrasound Sensors	388
I.12	Ultrasound Sensors Location in the Helicopter	388
I.13	Calibration curve for main rotor collective blade pitch θ from collective stick inputs δ_θ	389

I.14	Calibration Curve for longitudinal δ_{lon} and lateral δ_{lat} cyclic main rotor blade stick inputs.	390
I.15	Bell cyclic stick input range for longitudinal δ_{lon} and lateral δ_{lat} main rotor blade pitch angle.	391
I.16	Calibration curve for tail rotor collective pitch angle θ_{TR} . Top graph plots tail rotor servo input pulse-width δ_{TR} (μsec , dashed black curve) along with inclinometer data (deg , blue curve) and best-fit estimation curve (red curve). The bottom graph plots the measured tail rotor angle against the input pulse width. The data shows input hysteresis due to mechanical slop in the linkage.	393
I.17	Calibration Curve for throttle δ_{Th} servo pulse-width command to throttle opening.	394
I.18	Cantilever Beam with strain gages.	394
I.19	Calibration Curve for cantilever beam with strain gages.	395
I.20	Helicopter Test Platform.	396
I.21	Calibration curve for vertical force exerted by the HTF springs.	397
J.1	Sample Main Rotor Angular Velocity Ω data resulting from varying throttle inputs and Main Rotor Blade Pitch Angle θ set at 8 degrees.	400
J.2	Time to Rise and Time Constant estimates for Engine/Carburator-Main Rotor dynamic system.	401
J.3	Time Constant Estimation for Engine/Carburetor-Main Rotor dynamic system.	402
J.4	Main Rotor Dynamics with Fixed Shaft Engine.	404
J.5	Estimated engine power available for required main rotor torque.	406
J.6	Change in Main Rotor Angular Velocity Ω and related throttle inputs δ_{Th} to a Fixed-Shaft Engine.	407

J.7	Engine Torque Control Derivative $\partial Q/\partial w_f$ derived from estimated fuel flow rate.	408
J.8	Engine-Carburetor and Main Rotor Dynamics Model.	408
J.9	Open Loop Simulation Result for Rotor Angular Velocity Ω	409
J.10	Engine governor and main rotor angular velocity closed loop control design block diagram.	412
J.11	Bode and Nyquist diagrams for the open-loop engine governor controller.	413
J.12	Real-Time data for a run of the engine operating in closed loop control	414
J.13	Closed-Loop Engine-Carburetor, Main Rotor Dynamics Model.	414
J.14	Engine-Carburetor model simulation results compared with real-time data.	415
K.1	Thrust Experiment with Helicopter on the HTF with vertical one-DOF enabled.	420
K.2	Measured and Estimated Thrust.	420
K.3	Torque Experiment with Helicopter on the HTF with cantilever beam as a torque measuring device.	422
K.4	Torque Experiment with no Tail Rotor Inputs.	425
K.5	Torque Experiment sample data $\Omega = 1400$ rpm.	426
K.6	Torque Measurements Experiment with free tail rotor inputs.	427
K.7	Torque Measurements with blade pitch angle and angle of attack.	428
K.8	Torque Measurements and Computed Torque.	429
K.9	Engine Torque Map.	430
K.10	Effects of Tail Rotor Torque on Bending Beam Load Cell Torque Measurements	432
L.1	Tail Rotor Hub referenced to the Center of Mass CM	435
L.2	Real Time Run with Tail Rotor Inputs.	438
L.3	Multiple Real Time Run with Tail Rotor Inputs.	439

L.4	Empirical Tail Rotor Blade Pitch Angle and resulting Equilibrium Torque N_{TR}	440
L.5	Yaw Rate p Feedback Control Law.	441
L.6	Yaw Heading ψ Feedback Control Law.	443
L.7	Yaw Heading ψ Feedback Control Law with collapsed inner stability yaw rate loop. In this case, the constant $k_1 = k_r/I_{zz}$. The inner loops are equivalent to the transfer function equation (L.2.11) on page 441.	443
L.8	Frequency plots for the heading compensator loop including inner yaw rate stability loop.	446
L.9	Real-Time Data with Yaw Rate Command. The red solid curve is the yaw rate command r_C , dark green curve is the yaw rate r measured data. The solid blue curve is the helicopter heading ψ , and the magenta curve is the tail rotor blade pitch command δ_{TR} in pulse width (μ second). The light green curve is the scaled main rotor angular velocity $\Omega/100$. The outer loop for Heading performance is disabled.	447
L.10	Real-Time Data with Helicopter Heading Command. Red solid curve is the heading command ψ_C , dark green curve is the yaw rate r measured data. The solid blue curve is the helicopter measured heading ψ , and the magenta curve is the scaled tail rotor blade pitch command δ_{TR} in pulse width (μ second/100). The light green curve is the scaled main rotor angular velocity $\Omega/100$	447
L.11	Real-Time Run of the Helicopter on top of the Rotational Dynamic Test Stand (RDTS).	449
L.12	Pitch Rate and Attitude Perturbation Model for the Helicopter on the Rotational Dynamic Test Stand (RDTS).	450
L.13	Pitch Rate Feedback Control Loop for the Helicopter on the Rotational Dynamic Test Stand (RDTS).	451

L.14	Pitch rate and pitch attitude Feedback Control Loop for the Helicopter on the Rotational Dynamic Test Stand (RDTS).	452
L.15	Pitch command θ_c tracking with the helicopter on the Rotational Dynamic Test Stand (RDTS). In the figure, the top graph plots the roll p and pitch q rates and the main rotor angular velocity Ω	453
L.16	Roll Rate Feedback Control Loop for the Helicopter on the Rotational Dynamic Test Stand (RDTS).	455
L.17	Roll command ϕ_c tracking with the helicopter on the Rotational Dynamic Test Stand (RDTS). In the figure, the top graph plots the roll p and pitch q rates and the main rotor angular velocity Ω . Notice the large time constant of the feedback control loop during an experiment stability test.	456
L.18	Simultaneous attitude command tracking and hold for roll ϕ , pitch θ and heading ψ with constant angular velocity Ω . In the figure, the top-most graph presents the heading command tracking and hold, and the second graph shows the roll p and pitch rate q during the flight. The third graph shows the pitch attitude θ holding zero for the first part of the run, and tracking commands for the second part of the run. The same is true for the roll attitude ϕ in the fourth graph.	458
M.1	Mission profile requirements for the OU autonomous miniature helicopter.	464
M.2	The Affinity Diagram, Voice of the Customer (VOC).	465
M.3	Tree Diagram, Voice of the Customer.	466
M.4	Voice of the Engineer: Affinity Diagram.	468
M.5	Voice of the Engineer: Tree Diagram.	469
M.6	Quality Function Deployment (QFD). Identifying the customer priorities and related engineering activities that will yield the best value to the customer.	470

M.7	Quality Function Deployment matrix for the University of Oklahoma Helicopter Research Testbed.	471
M.8	Voice of the Customer Prioritization. In the graph, the symbol \odot is a strong selling point for the customer. The symbol \bigcirc indicates some selling point for the customer.	472
M.9	Voice of the Customer Benchmarking. In the graph, the <i>VOC Benchmark</i> column follows the following convention: 1 = no compliance (empty circle), 2 = partial compliance, 3 = general compliance, 4 = full compliance, 5 = total compliance (full dark circle).	474
M.10	Interaction Matrix for Design Requirements (VOC). In the figure, a lone horizontal bar indicates a primary correlation, a + sign indicates a possible positive effect among the two design requirements, a double ++ sign indicates a positive effect, a negative – sign indicates a possible negative effect, and a double negative sign -- indicates a negative effect.	475
M.11	First level functional decomposition.	476
M.12	OU Helicopter work breakdown structure. In the figure, the letter <i>P</i> indicates a primary relationship while an empty space indicates a secondary or support relationship.	477
M.13	System Architecture for the University of Oklahoma Helicopter Research Testbed for Autonomous Flight.	478

Abstract

One of the most critical areas in a flight program for unmanned vehicles is getting the feedback controls to the point that the vehicle can achieve stable flight reasonably well so that the best tradeoff between flight performance and stability and the vehicle's flight envelop can be determined and finalized in actual flight conditions. Two basic methods are most often used for this purpose. One is the extreme method of pilot assistance (i.e. remote control) without the use of test stands. In this case, theory, experience, and pilot assistance are used to develop an autonomous feedback controller. That is, a remote pilot on the ground flies the unmanned vehicle high up into the air and flight behavior is observed after the controls on board are switched from remote pilot to autonomous flight. The feedback controller is modified through these observations to achieve stable flight. The second method is pilot assistance with the use of test stands. In this case, theory, experience, pilot assistance, and results from tests on flight stands are used to develop an autonomous feedback controller. In this thesis, we explore the other extreme method of only using test stands results without any pilot assistance to develop an autonomous controller for unmanned vehicles. The main objective is to develop a method for deriving an autonomous flight controller for a miniature scaled model helicopter by only using test stands together with theory and previous experience, all without pilot assistance and without damaging the vehicle.

In this work, we show how to computerize a helicopter to fly attitude axes controlled hover flight without the assistance of a pilot and without ever crashing. We start by developing a helicopter research test bed system including all hardware, software, and means for testing and training the helicopter to fly by computer. We select a Remote Controlled helicopter with a 5 ft. diameter rotor and 2.2 hp engine. We equip the helicopter with a

payload of sensors, computers, navigation and telemetry equipment, and batteries. We develop a differential GPS system with cm accuracy and a ground computerized navigation system for six degrees of freedom (6-DoF) free flight while tracking navigation commands. We design feedback control loops with yet-to-be-determined gains for the five control "knobs" available to a flying radio-controlled (RC) miniature helicopter: engine throttle, main rotor collective pitch, longitudinal cyclic pitch, lateral cyclic pitch, and tail rotor collective pitch.

We develop helicopter flight equations using fundamental dynamics, helicopter momentum theory and blade element theory. The helicopter flight equations include helicopter rotor equations of motions, helicopter rotor forces and moments, helicopter trim equations, helicopter stability derivatives, and a coupled fuselage-rotor helicopter 6-DoF model. The helicopter simulation also includes helicopter engine control equations, a helicopter aerodynamic model, and finally helicopter stability and control equations. The derivation of a set of non-linear equations of motion for the main rotor is a contribution of this thesis work.

We design and build two special test stands for training and testing the helicopter to fly attitude axes controlled hover flight, starting with one axis at a time and progressing to multiple axes. The first test stand is built for teaching and testing controlled flight of elevation and yaw (i.e., directional control). The second test stand is built for teaching and testing any one or combination of the following attitude axes controlled flight: (1) pitch, (2) roll and (3) yaw. The subsequent development of a novel method to decouple, stabilize and teach the helicopter hover flight is a primary contribution of this thesis.

The novel method included the development of a non-linear modeling technique for linearizing the RPM state equation dynamics so that a simple but accurate transfer function is derivable between the "available torque of the engine" and RPM. Specifically, the main rotor and tail rotor torques are modeled accurately with a bias term plus a nonlinear term involving the product of RPM squared times the main rotor blade pitch angle raised to the three-halves power. Application of this non-linear modeling technique

resulted in a simple, representative and accurate transfer function model of the open-loop plant for the entire helicopter system so that all the feedback control laws for autonomous flight purposes could be derived easily using classical control theory. This is one of the contributions of this dissertation work.

After discussing the integration of hardware and software elements of our helicopter research test bed system, we perform a number of experiments and tests using the two specially built test stands. Feedback gains are derived for controlling the following: (1) engine throttle to maintain prescribed main rotor angular speed, (2) main rotor collective pitch to maintain constant elevation, (3) longitudinal cyclic pitch to maintain prescribed pitch angle, (4) lateral cyclic pitch to maintain prescribed roll angle, and (5) yaw axis to maintain prescribed compass direction. Videos are taken of the tests showing that the helicopter has been successfully taught to fly attitude axes controlled hover flight. Next we teach the rotorcraft how to maintain attitude stability and track navigation commands in x, y, z space without ever needing the assistance of a pilot. Furthermore, neither the author nor his advisor knows how to pilot the helicopter, and all the work proceeds without ever crashing the helicopter. To be sure, the training "wheels" of the test stands do save the helicopter many times from crashing until the helicopter learns how to fly attitude axes controlled hover flight, and fly well. The development of the test stand and related processes presented in this thesis work constitute a primary contribution that can be applied to numerous real world projects. Another contribution is the entire integration of the flight program by one single engineer (the author) and no technicians.

Chapter 1

Introduction

1.1 Introduction

The bee hummingbird, measuring about two inches long and weighing about one-half ounce, has incredible flight ability, hovering with absolute precision over flowers as he feeds and darting with rapid flight from one target flower to the next. The hummingbird is nature's highest standard for aerospace engineering to mimic in building an autonomous unmanned aerial vehicle (AUAV) that flies to a target in very tight quarters, hovers in mission as long or as short as is needed, and then darts swiftly back to base. The helicopter is aerospace engineering's greatest marvel in trying to mimic the capability of a hummingbird's exemplary hover and darting flight. Our research herein focuses on teaching a helicopter to fly autonomously, unmanned, without the assistance of a remote pilot, and without crashing the vehicle. The helicopter treated in this work is 25 times longer and 800 times heavier than the bee hummingbird.

Historically, someone teaching a helicopter to fly has met enormous challenges. The history of helicopter flight is well covered in literature in the works of Gregory [60], Boulet [10] and Liberatore [94] (to mention a few). Early helicopter work had to overcome many problems related to mechanics and science [92]. On the scientific side, early work had to overcome the problem of understanding the basic aerodynamics of vertical flight, the need to compensate for rotor torque, and the need to provide proper helicopter stability through individual blade control. On the mechanical side, early work with helicopters

had to deal with structural integrity and weight, engine size, available engine power, and proper means to overcome machine vibrations.

The solutions to these early problems with helicopter flight created a large and vast array of scientific literature that covers all aspects of full size helicopter flight. Therefore, most of the research literature to this present day deals with full-size helicopters. Limited research with model rotors and blades and scale helicopters were important for their use in wind tunnel research as illustrated in the work done in the 1950's by Castles and Gray at Georgia Tech [83, 84].

Early work with miniature helicopters began in the 1960's. One example were the Schlüter *Helicopter Meetings* in Germany in the late 1960's and early 1970's [129]. Their work consisted of small radio-controlled helicopters that varied much from one to the other, mainly because the application of full-scale helicopter principles and know-how did not directly apply or directly scale to miniature helicopters, and early results were more art than science.

Early work with small scale-helicopters for autonomous flight began during the last years of the 1980s and early 1990s. In 1990, the Association for Unmanned Vehicle Systems International (AUVSI) created the International Aerial Robotics Competition on the campus of Georgia Tech. The competition attracted mostly research institutions whose early work used inexpensive radio controlled (RC) helicopters with a rotor radius of 3 to 4 feet (1.0 m) with weight in the range of 10 lb (4.5 Kg). The payload that these helicopters could carry was limited, in contrast to the need for sensors and flight computers required by autonomous helicopter flight [157].

The advent of sensor and flight computer miniaturization, as well as the availability of powerful small engines, were enabling technologies that made rotary wing scaled aerial robots possible. Fifteen years of aerial robotics research work is beginning to produce results such as the work done by Amidi, Mettler and coworkers at Carnage Mellon [3, 50, 107] and Schrage, Johnson, Prasad and coworkers at Georgia Tech [59, 80, 81]. Currently,

there are three national Centers of Excellence (COE) for rotary wing research where a large portion of helicopter research takes place. Each center manages multi-million dollar programs, and each center is charged with advancing the state of the art for rotary wing research.

- Georgia Institute of Technology Center of Excellence for Rotary Wing Aircraft (CERWAT) [117]. This is the largest of the three national centers. The key research areas in this center are aerodynamics, aeroelasticity, structures and materials, and flight controls and mechanics.
- University of Maryland Alfred Gessow Rotorcraft Center of Excellence [116]. The core program involves aerodynamics, dynamics, flight mechanics, CFD, acoustics, transmissions, and composite structures. This center also works with the Army in smart structures.
- Pennsylvania State Rotorcraft Center of Excellence Vertical Lift Research Center [18]. Their work includes unsteady, turbulent, separated flow around helicopter fuselages, tiltrotor aeromechanical stability analysis, experimental and computational instrumentation for rotorcraft, carefree maneuvering control laws for rotorcraft, simulation/control of helicopter shipboard launch/recovery, flight control design for future generation compound rotorcraft, and rotary-wing Unmanned Air Vehicles (UAV).

Modeling of miniature helicopter dynamics has been a great challenge. In the case of scale helicopters, the lower weights and lower inertias make miniature helicopters extremely agile, unstable platforms that are difficult to model. Moreover, the helicopter dynamics and rotor aerodynamics change considerably during hover, climb, descent and cruise flight conditions [13, 82]. This is due to aerodynamic effects on the helicopter body and the various working states of the helicopter rotor [92]. The difference in behavior during the various flight conditions affects the helicopter modeling and control design

[124]. The assistance of a remote pilot has often been used to help overcome some of these modeling challenges, but not without bringing some problems of its own along with it.

It was the experience of the author, before coming to the University of Oklahoma, that the method for flight automation included the use of an experienced remote pilot. Even though remote pilot assistance was present, preliminary helicopter flight occasionally resulted in the destruction of the helicopter, long before any useful research could be done for control law development. In those occasions where research work proceeded, one feedback loop was enabled at a time, and every one hoped for the best. On some occasions the feedback control law would not work as expected, and on other occasions experienced pilots reacted adversely to proper control and aided instability. Most of these failures resulted in a helicopter crash and subsequent loss of flight hardware. Experimental development flight testing had to be put on hold to tend to the mechanical issues of replacing parts and understanding what failed. A fully instrumented aerial robot, which is very expensive and difficult to repair or replace, can only be maintained in such cases by richly funded research programs.

Current research programs for UAV based on a helicopter platform use remote pilots for testing and for obtaining real-time flight data that can be used in system identification and control development research [145]. It is the fast helicopter dynamics and the dominance of the rotor in the vehicle dynamics what makes helicopter flight difficult. In the case of small-scale aerial robot helicopters, the dynamics are very fast due to the low weight and low inertias of the helicopter as well as the rigidity of the main rotor hub assembly. The possibility of crashing a vehicle is eliminated if test stands are used rather than remote pilot-assisted free flight. Therefore, there is an advantage to using test stands to teach a helicopter to fly. The test stands remove the need for the remote pilot. There are no crashes. And, there is no down time for repairs. The training can be carried out by one test engineer. Furthermore, the tests are done without traveling

beyond the lab to remote field locations.

Goal of dissertation: To design and test control laws that will fly a miniature (scale-model) helicopter with controlled attitude axes and track navigational commands without skilled remote pilot inputs and with no loss of hardware at any point.

This thesis approach to attaining the goal of the dissertation is to use test stands instead of the assistance of a pilot. We will now review in the literature the use of test stands in the development of feedback control laws for helicopters.

Many programs use scale helicopters as testbeds for controls research. An instrumented helicopter crash -while testing controls laws in free flight- is very expensive because of the loss of the aircraft testbed and some or all of the sensors and actuators. Many research programs have developed test stand technology as a step to validate the control work. In many cases, validation of the feedback control is all that matters, and the test stands are built indoors for easy access, independence from weather conditions, as part of laboratory setup, and are able to operate within a more controlled environment. The indoors testing of helicopters very frequently necessitates the use of electric motors to avoid the complexities associated with gas engines and exhaust fumes. The simplest test stands are sold for hobby enthusiasts to aid with and build up flying skills for pilots. Some examples of the use of test stands follow.

Weilenmann [156, 155] rigged a scale helicopter linked to a plate through a 3 degree of freedom joint. This upper plate is joined to a ground plate via rods that flex. Prior to takeoff, the rods carry the weight of the helicopter, and at one point, the helicopter carries its own weight and the weight of the plate. The helicopter is powered by a DC motor, and it is free to translate and rotate within certain limits. Weilenmann developed an accurate, non-linear differential equation model of the helicopter from full-scale helicopter theory. Subsequent linearization about the hover flight condition resulted in an 18 state model with a number of parameters that were directly measured, but some were estimated. The effort was successful, but the applicability of the effort to

real systems is limited in that other flight conditions would have generated much more complicated mathematical models.

Bendotti and Morris [7, 109] used a small scale helicopter (35 in rotor) attached to a wrist with three angular degrees of freedom for system identification experiments. The wrist rotates freely in roll, pitch and yaw, but cannot translate in any of the linear directions. The small helicopter is powered by a DC motor, and the sensors are attached to the structure and not the helicopter. The authors ensured that the helicopter remained within the linear range of operation, and superimposed small signal excitations on top of the trim signals. The authors used rigid body dynamics to identify the model which produced a fair match with experimental data.

The Autonomous Helicopter Project headed by Amidi from the Carnegie Mellon University [123] developed a number of testbeds for indoor flight control systems. Their work used incremental test beds that lead to full autonomous flight [2, 3]. The first testbed used an electrical model helicopter mounted on a swiveling arm platform attitude control in yaw, pitch and roll. A second six degree of freedom testbed was used to evaluate various helicopter control schemes. A third indoor testbed used tethered flight that allowed full six-degree of freedom limited motion. A progressive number of experiments led to full autonomous flight. This program has been successfully demonstrated to perform visual-based stability and control, autonomous trajectory following, aerial mapping, and object recognition and manipulation.

Students at Southern Polytechnic State University developed a test stand that tests the helicopter attitude control one axis at a time [17]. A student at The University of Toronto developed a test stand for indoors use that can exercise all three angular axes and one linear motion [95]. Researchers at the University of Toronto also developed a three degrees of freedom testbed for testing formation flying [134].

As we have shown above, test stands have been used previously to teach a helicopter to fly attitude axes in controlled hover flight. We also will use test stand, and will point

out the differences in our novel approach. Indeed, the test stand technology developed in this present work is one of the contributions of the thesis.

The work done in this document uses an entry level small helicopter that weighs 11 lb (5 kg) empty and has a rotor diameter of 4.86 ft (1.48 m). This helicopter is our base platform for autonomous unmanned aerial vehicle research. The helicopter is structurally modified to support the sensor suite necessary for instrumented flight. The key dynamics and aerodynamics of the helicopter need to be simplified to make the problem tractable with the intent of increasing the level of technical difficulty as the stability of the system increases with the design of each control loop. The final control design needs to stabilize the platform in flight to be ready for free flight without aid from a pilot. The method developed to achieve controlled hover flight is a primary contribution of this thesis work.

A brief outline of the work presented in the following chapters follows.

Chapter 2 This chapter describes the components that make up the Helicopter Research Testbed. A description of the basic helicopter gives an understanding of the various components that make up the basic frame with components such as the main rotor, the tail rotor, the engine, and the electro-mechanical servo mechanisms. A general description of how the basic components work attempts to familiarize the reader with the system that will become a UAV.

The sensor suite that instruments the University of Oklahoma Helicopter Research Testbed (OU-HRT) is presented as well. This includes a brief description of the sensors themselves and the signals that the sensors measure. An introduction to the onboard processing unit follows as well as a brief description of the architecture framework with regard to how the processing unit function. Finally, a description of the test equipment utilized throughout the project gives a familiarization with the tools used in the project.

Chapter 3 The helicopter electromechanical actuators introduced in Section 2 on

page 12 in turn control the aerodynamic actuators (the main rotor collective and two cyclic inputs, the tail rotor collective) and the engine throttle. This chapter explains in great detail how the electromechanical actuators affect the throttle and aerodynamic actuators. This information is necessary to understand the open loop helicopter dynamic reaction to pilot inputs.

Chapter 4 This chapter points out the differences between the test stands used in this dissertation and those used in other dissertations. Unlike all other uses of test stands in other research projects, the test stands built for this dissertation are portable, and able to operate indoors and outdoors. Such capability is highly valuable because it enables the use of real flight hardware at all times during the development of the feedback control laws. The test stands are an enabling technology that allows the researchers to teach the helicopter hover flight without using a remote pilot and without crashing the scale helicopter.

Chapter 5 An understanding of the math models that describe the fundamental behavior of the helicopter is very important for the development of the simulation tools and the control laws that follow. First, models for each of the major helicopter components bring to the front of the task at hand the need to understand the underlying physics, dynamics and aerodynamics that influence the behavior of the individual components and the system as a whole. The fundamental theories that describe the helicopter as a flying machine help to identify key signals necessary for the operation of the helicopter and their relation with other signals. A model for the rigid body dynamics provides the framework for the development of simplified equations of motion. Trim models and the corresponding perturbation models allow for the development of linearized dynamics about a trim condition. In the present work, hover is by necessity the trim condition that highlights the relevant dynamics.

Chapter 6 Autonomous flight necessitates the use of a complimentary sensor suite able to cover a wide spectrum of signals. This chapter explores the sensors themselves along with the signals that the sensors measure. Signals and sensors are intrinsically related to the automation process, and therefore this chapter is a preamble to the development of the feedback control laws.

Chapter 7 This chapter explores each of the relevant feedback control loops. Each feedback control loop helps to stabilize the helicopter system, and therefore, each feedback control loop takes away a layer of complexity by automating some part of the helicopter operation. The engine governor and main rotor angular velocity feedback control loop is the first and most important control loop to implement. This feedback control loop takes away the complexities associated with the nonlinearities pertaining to the main rotor angular velocity. In turn, the directional control loop automates the torque changes involved in normal operation of the helicopter. As before, this feedback control loop peels away another layer of non-linearities. Next, the roll and pitch attitude feedback control loop put the final touches on the stability of the helicopter as a platform. From this point onward, the helicopter is ready for stable free flight.

Chapter 8 The main rotor angular velocity is one of the most important parameters that influence the helicopter behavior. The main rotor angular velocity influences rigid body dynamics via gyroscopic moments, and in addition, torque and power needs are directly affected by the main rotor angular velocity. This chapter explores the approach to design an engine governor that maintains a constant angular velocity.

Chapter 9 Once the main rotor angular velocity is stable, a series of experiments help with some simple parameter identification that validate the models obtained from first

principles. A good knowledge of the aerodynamic characteristics of the main and tail rotor is very important at this point. The development of a set of non-linear equations of motion for the main rotor from first principles is a contribution of this thesis work. The results obtained in this chapter constitute the basis for a comprehensive aerodynamic model of the helicopter.

Chapter 10 Yaw rate and heading feedback control loops compensate for the torque needs of the main rotor. The main rotor torque, main rotor blade drag, the engine power available, and the fuselage reaction torque are all intrinsically linked in non-linear ways. Specifically, the main rotor torque and power requirements vary continuously because of cyclic inputs to the rotor blades and other non-linear variations that take place at the rotor. This very important control loop helps to stabilize the helicopter as a whole by peeling away one layer of non-linearities from the overall helicopter platform.

Chapter 11 Once the helicopter operates with constant angular velocity, and once the torque and power needs are automatically compensated with the yaw rate and heading loop, then the helicopter rotor behaves as an aerodynamic actuator. Stabilizing the aerodynamic actuator is difficult but very much feasible. This chapter describes the steps needed to achieve stable hover flight.

Chapter 12 Concepts from System Engineering (SE) help with the development of the overall University of Oklahoma Helicopter Research Testbed (OU-HRT) system architecture. This chapter describes the hardware and software interface, and the hardware and software integration. A description of the embedded code generation method emphasizes the advantages of current graphical simulation tools and the process of embedding auto-generated code into the actual flight computer.

Chapter 13 This final chapter summarizes results from the work effort, achieved goals and contributions of this thesis work. The work effort is considerable and highly difficult because it involves real hardware operating in a real environment where the laws of physics test every mistake. The stated goal of developing a method to teach a miniature helicopter to fly stable hover is accomplished. Finally, the primary contributions of this thesis work are the derivation of a full set of equations of motion for the main rotor, the development of a novel test stand enabling technology that allow for real-time Hardware-in-the-Loop (HWIL) helicopter tests, and the ultimate development of a method to teach a miniature helicopter hover flight with no remote pilot in the loop.

Appendix A through *Appendix G* provide necessary theoretical background. Work in subsequent Appendices derive results from these fundamental principles and applied science. *Appendix H* derives various mathematical tools used in modeling the helicopter in flight. The emphasis is in understanding the underlying physics that allows for the control of the vehicle. *Appendix I* documents the physical characteristics of the helicopter. This Appendix details the systematic approach needed to calibrate and characterize various physical quantities associated with the helicopter airframe, sensors and actuators. *Appendix J* explores the approach to design an engine governor that maintains a constant angular velocity in the presence of disturbances. Feedback linearization mechanization enables the engine governor to operate throughout the allowable flight envelope. *Appendix K* details the approach for parameter identification of various aerodynamic quantities. This work results in the aerodynamic characterization of the helicopter model. *Appendix L* documents the design and synthesis of the feedback control laws for roll, pitch and yaw control. Finally, *Appendix M* illustrates how this thesis work fits into widely accepted system engineering framework currently utilized throughout government, academia and industry.

Chapter 2

Helicopter Research Testbed

2.1 Introduction

Figure 2.1 on the next page shows the basic helicopter frame. A number of attributes that characterize the helicopter are tabulated in Table 2.1, and Appendix I.1.2 on page 372 describes and tabulates the complete set of helicopter parameters.

Table 2.1: Basic Helicopter Parameters

		unit	description
R	0.74	m	rotor radius (<i>diameter</i> $\approx 4.86\text{ ft}$)
Ω	157.1	rad/sec	nominal main rotor angular speed (1500 <i>rpm</i>)
T_{MR}	106.7	N	nominal hover maximum thrust (24 <i>lbf</i>)
R_{TR}	0.13	m	tail rotor radius (<i>diameter</i> $\approx 10.23\text{ in}$)
R_{stab}	0.31	m	stabilizer bar radius (<i>diameter</i> $\approx 12.2\text{ in}$)
M_{heli}	5.21	kg	basic (empty) helicopter mass (11.46 <i>lbf</i>)
M_{fuel}	0.494	kg	fuel mass (1.1 <i>lbf</i>)

2.2 Helicopter Research Testbed Components

The principal component of the University of Oklahoma Helicopter Research Testbed (OU-HRT) is the basic helicopter shown in Figure 2.1 on the next page. The basic helicopter comes equipped with five digital servo mechanisms and a Remote Control (RC) receiver matched to a RC transmitter shown in Figure 2.6 on page 21. This transmitter-receiver combination is the primary means of control for most RC pilots. Table 2.1 indicates that the basic helicopter has an empty mass of 5.21 kg (11.46*lbf*). When fully

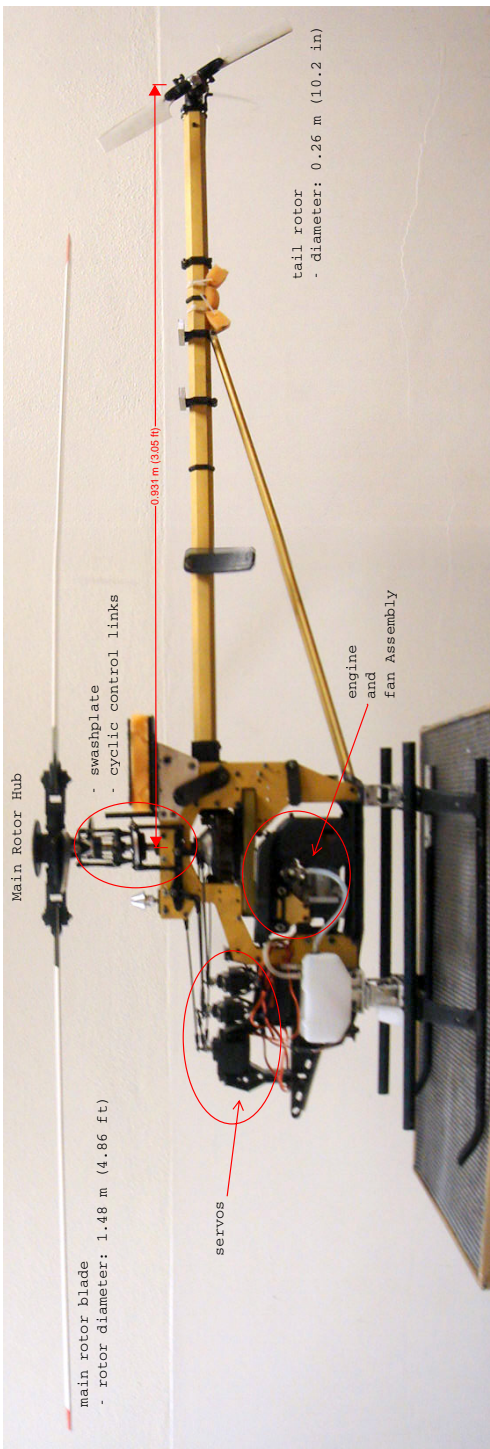


Figure 2.1: Helicopter Research Testbed Mechanical Components.

fueled, the mass of the helicopter increases to $5.7kg$ ($12.6lbf$). The addition of sensors and various test apparatus completes the Helicopter Research Testbed, and Table 2.2 itemizes these additional components.

Table 2.2: Helicopter Research Testbed Components

basic helicopter	
main rotor	lift & locomotion
tail rotor	torque compensator & heading
engine	vehicle power source
RC receiver	primary and back-up link
digital servo-mechanisms	electro-mechanical actuators
motionPak	linear acc, angular rates sensor
GPS	inertial position
FreeWave	primary digital link
ultrasound & infrared altimeters	range to ground
electronic compass	inertial attitude & heading
hall effect sensor	main rotor angular velocity
on Board Computing Processing Units (CPU)	
Ampro PC104	main on-board CPU
Motorola MC68332	actuator input/output CPU
ground station computer	
rate table stand (RTS)	angular rates measurements
linear and directional test stand (LDTS)	lift/altitude, heading
rotational dynamics test stand (RDTS)	roll, pitch, yaw, test stand

2.2.1 Basic Helicopter

The basic helicopter is a self-contained airframe capable of vertical take-off and landing. As such it is a very versatile machine that has been used extensively and successfully in a number of civil and military scenarios.

2.2.1.1 Main Rotor

The main rotor blades are attached to a main shaft that rotates the blades around with a particular angular velocity, and in doing so, the rotating blades interact with the flow. The governing principle responsible for helicopter lift is the change of momentum that the rotating blades impart to a stream tube accelerated through the rotor. As

a reaction to the air change of momentum, the accelerated flow imparts an equal but opposite reaction that keeps the blades, and thus the helicopter, in the air. A penalty for imparting momentum to the airmass passing through the rotor in exchange for lift comes in the form of blade induced and profile drag, helicopter body parasite drag, and the need for torque compensation via a tail rotor or comparable device. The primary control inputs to the helicopter rotor are the rotor angular velocity and the blade pitch angle. Figure 2.2 on the next page shows a top view of the main rotor with the fly-bar or auxiliary rotor that augments both the main rotor blade pitch angle control input and the main rotor damping.

Section C on page 202 explores the details of the Momentum Theory (MT), Blade Element Theory (BET) and combined Blade Element Momentum Theory (BEMT). In turn, Section D on page 234 details the development of the rotating blades equations of motion, and Appendix E on page 316 looks into the rotor forces and moments. Finally, Appendix J on page 398 together with Appendix K on page 418 apply previously developed theory to derive an aerodynamic model for this particular helicopter and a rotor angular velocity controller.

2.2.1.2 Tail Rotor

The tail rotor thrust has three primary functions:

1. compensate for the fuselage reaction torque due to the main rotor dragging the blades through the air.
2. provide lateral trim due to main rotor side forces
3. provide directional control for the helicopter

The tail rotor is an aerodynamic actuator, and control of the tail rotor thrust is done via collective pitch of the tail rotor blades. Since a primary function for the tail rotor is to compensate for torque and forces produced by the main rotor, then the tail rotor

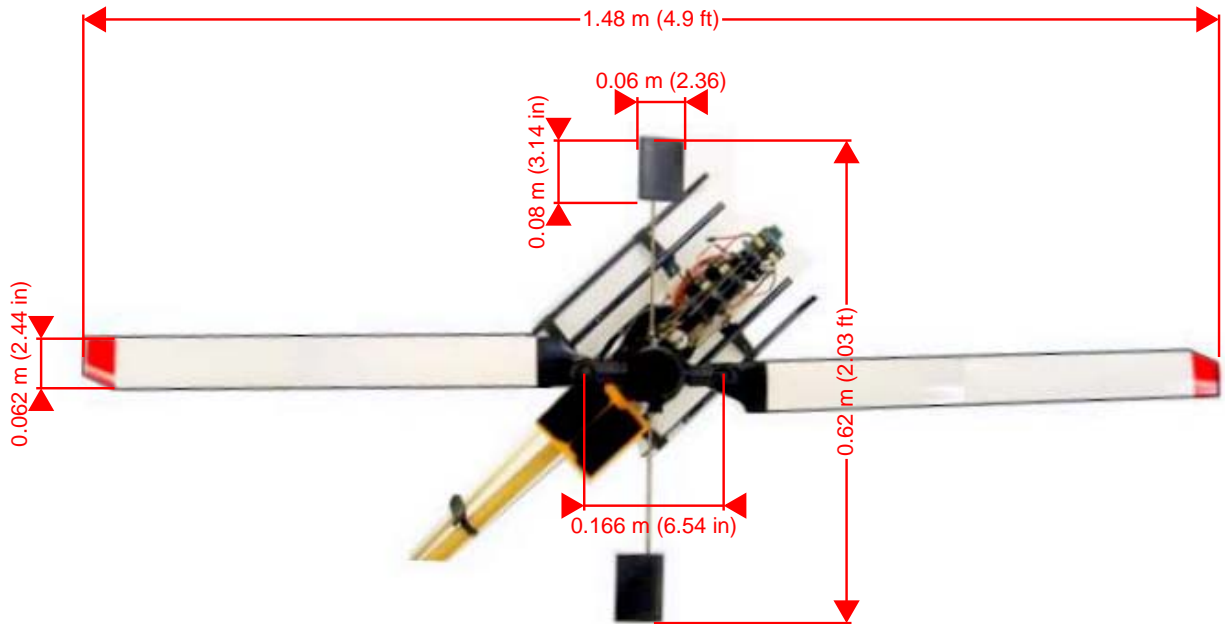


Figure 2.2: Main Rotor and Stabilizer Bar Dimensions.

thrust is a function of the main rotor angular rotation and main rotor blade collective and cyclic pitch angles. The exception arises when the the tail rotor is used for directional control. Appendix K on page 418 results in an aerodynamic model for the tail rotor, and Section L.2 on page 434 in Appendix L generates closed loop directional feedback control laws.

2.2.1.3 Helicopter Engine

Figure 2.3 on the next page shows the engine used for the operation of the research helicopter. Table 2.3 on the following page tabulates the most important parameters pertaining to the engine [37]. The engine maximum power output is about 2.2 horsepower, but its useful output is less than the maximum rated output due to the losses that take place within the various components of the helicopter power transmission.

Table 2.3: O.S.61 Helicopter Engine

RPM	2,000 – 18,000
Output	2.2 hp @ 16,000 rpm
Torque	1.052 Nm @ 10,720 rpm
Weight	600 g



Figure 2.3: O.S.61 Helicopter Engine

2.2.1.4 Transmission Gears

Figure 2.4 on the next page shows the transmission gear implementation for the University of Oklahoma Helicopter Research Testbed. The engine transmits angular motion and torque via a belt gear to an interim main rotor transmission gear. The interim transmission gear drives the main rotor gear via a clutch that engages when the clutch has sufficient angular velocity of approximately 200 RPM or more. The tail rotor transmission gear feeds directly from the main rotor gear at all times. Therefore, when the main rotor rotates so does the tail rotor. Table 2.4 tabulates the gear ratios between the engine and the main rotor, the main rotor and the tail rotor, and the engine and the tail rotor.

Table 2.4: Engine, Main Rotor and Tail Rotor Gear

		description
n_{MR}	9.29	engine to main rotor gear ratio
n_{TR}	4.667	main rotor to tail rotor gear ratio
n_{eTR}	43.4	engine to tail rotor gear ratio

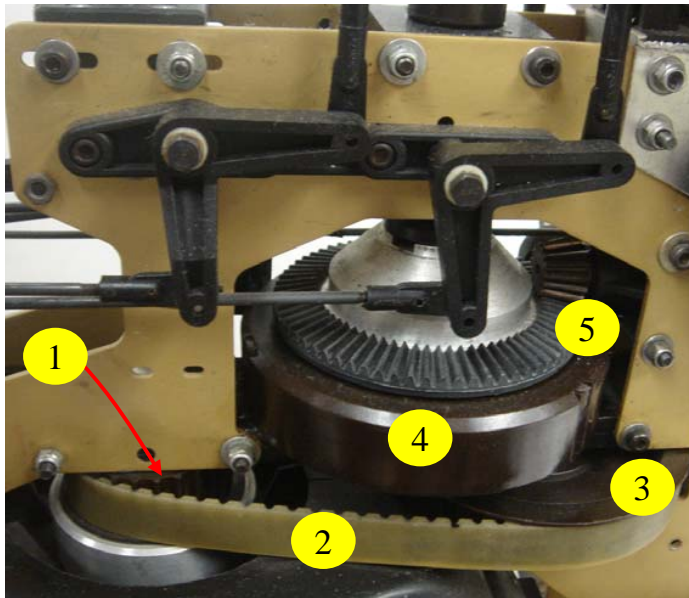


Figure 2.4: Belt and Transmission Gears between the Engine, Main Rotor and Tail Rotor. In the figure, (1) is the engine gear, (2) is the transmission belt-gear, (3) is an interim gear between the engine and the main rotor, (4) is the main rotor gear with a clutch inside (not visible), (5) is the tail rotor transmission gear. The clutch in the main rotor gear engages when the clutch has sufficient angular velocity of 200 RPM or more.

2.2.1.5 Swashplate and Blade Pitch Angle Control Links

Figure 2.5 on the next page shows the swashplate and the main rotor blade pitch angle inputs. The Bell input is a direct swashplate angle input to the main rotor blade. The Hiller input link augments the Bell input with a component that is proportional to the stabilizer bar flapping angle [88, 105]. The main blade pitch angle is therefore a proportional mix of Bell and Hiller inputs, and the mixing mechanism is commonly known as the Bell-Hiller cyclic mixer.

2.2.1.6 Digital Electro-Mechanical Actuator and Radio Control Transmitter/Receiver

Figure 2.6 on page 21 shows a typical Radio Controlled (RC) helicopter transmitter, a receiver, and two digital electro-mechanical actuators commonly known as servos. In a normal flying scenario, a pilot commands the various digital actuators on the helicopter via the transmitter stick and other control settings [73]. The on-board receiver decodes

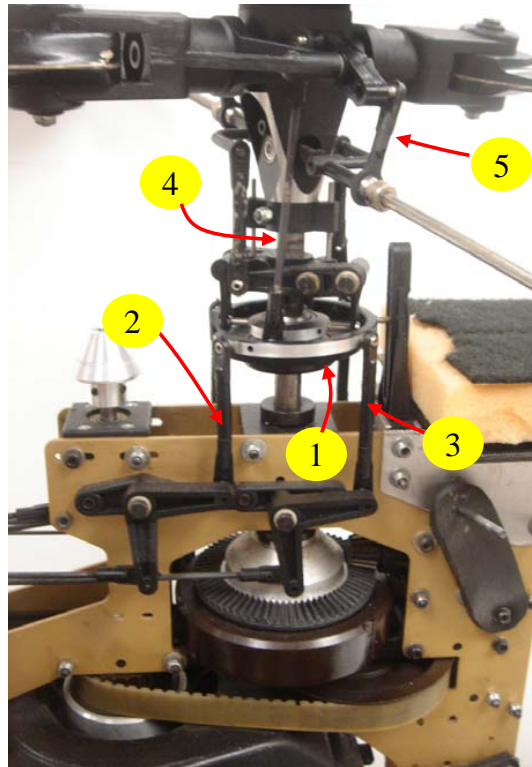


Figure 2.5: Helicopter Swashplate and Blade Pitch Control Links. In the figure, (1) is the swashplate that tilts, (2) is the lateral cyclic control link, (3) is the longitudinal control link, (4) is a direct swashplate input to main rotor blade pitch (Bell input), (5) is the stabilizer bar input to main rotor blade pitch (Hiller input).

the transmitted data from the carrier signal, and makes it available on various channels as pulse-width modulated (PWM) TeleTYpe (TTY) level signals (fast-switching 0-5 volts, 10-30 mA). A main advantage of PWM signals is that the signal remains digital from the receiver's output to the servo's transducers.

Figure 2.7 on the next page shows a picture of the five servos available for helicopter control:

1. main collective (θ_0): controls the main rotor blade pitch angle. This control input is responsible for generating the necessary main rotor blade pitch angle to maintain lift.
2. longitudinal cyclic (θ_{lon}): adds a differential angle to the main rotor collective blade pitch angle. This control input is responsible for longitudinal (forward and backward) locomotion.
3. lateral cyclic (θ_{lat}): adds a differential angle to the main rotor collective blade pitch angle. This control input is responsible for lateral trim (counter tail rotor thrust), and occasionally lateral cyclic inputs that provide sideways locomotion.
4. tail rotor collective (θ_{tr}): controls the tail rotor blade pitch angle. This control input is responsible for generating the necessary trim setting that will compensate the main rotor torque induced by the generation of lift and drag. This control also provides directional control.
5. throttle input (θ_{th}): controls the fuel flow rate into the carburetor as well as the fuel/air mixture that the carburetor provides to the engine.

2.2.1.7 Helicopter Component Hardware Interface

Figure 2.8 on page 22 shows the hardware interface among the various components on the helicopter. The servos connect to the helicopter hardware via adjustable mechanical links



Figure 2.6: JR Pro PCM 10S Radio Control (RC) Transmitter.

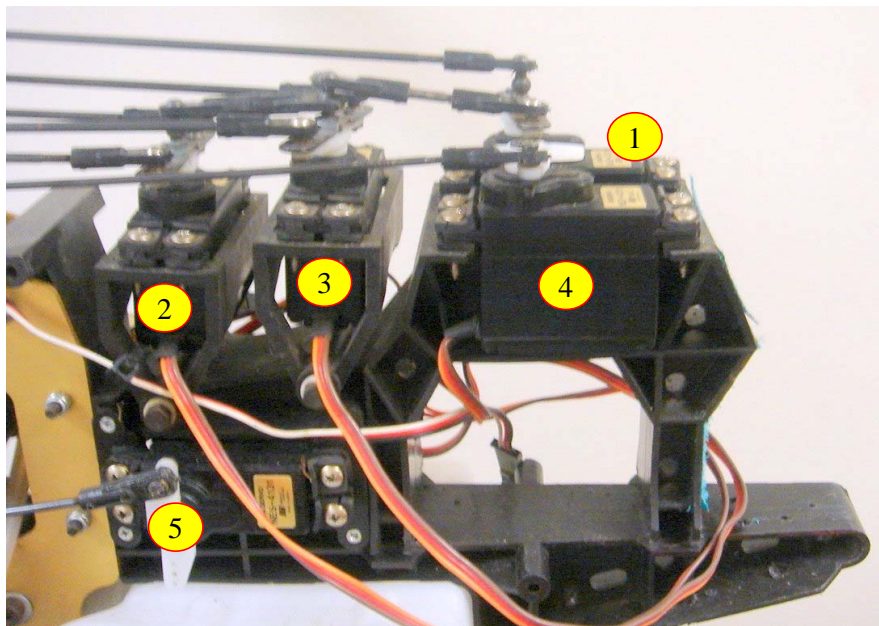


Figure 2.7: Electro-Mechanical Digital Servo Devices and their respective Control Tasks. In the figure, (1) is the main rotor collective, (2) is the longitudinal cyclic, (3) is the lateral cyclic, (4) is the rudder or tail rotor collective, and (5) is the throttle servo.

(shown in Figure 2.7 on the previous page). The main rotor collective and cyclic servos connect to the swashplate via adjustable mechanical links. The same type of adjustable mechanical links connect the throttle servo to the throttle arm on the engine carburetor, and the tail rotor servo to the tail rotor collective link at the tail rotor hub. The engine connects to the main rotor and tail rotor via a belt gear, a gear set and a clutch shown in Figure 2.4 on page 18. The engine shaft motion engages the main rotor gear and shaft via a clutch when the clutch as angular velocity is sufficiently large at 200 RPM or more. The tail rotor is always engaged such that the tail rotor turns when the main rotor does.

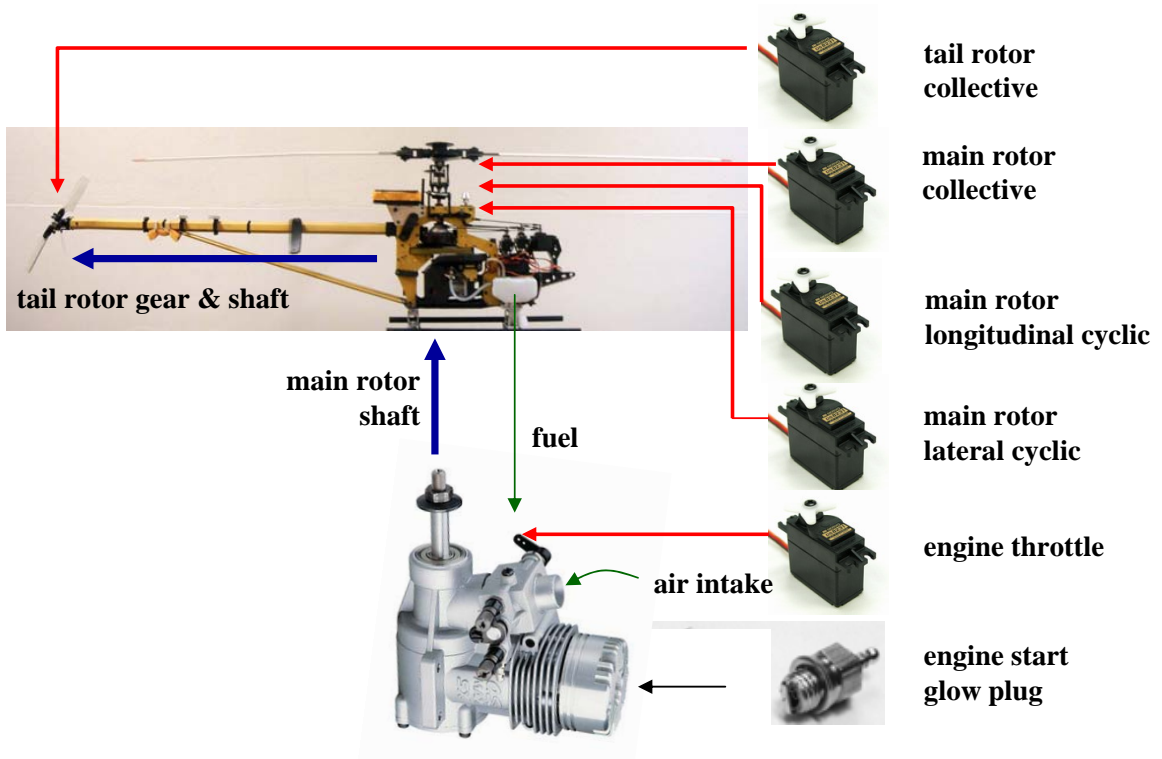


Figure 2.8: Helicopter Components Hardware Interface. Red lines represent hard connecting links between the servos and the connecting hardware.

2.2.2 MotionPak

Figure 2.9 shows a picture of the Systron Donner MotionPak, a six degree of freedom sensor that measures the body inertial acceleration in three orthogonal axes \dot{u} , \dot{v} , \dot{w} , and the three body inertial angular rates roll p , pitch q , and yaw r . Section I.2.1 on page 376 details the most important parameters pertaining to the MotionPak sensor. With a mass of $1.1kg(2.43lb_f)$, this is the heaviest of all on-board equipment.

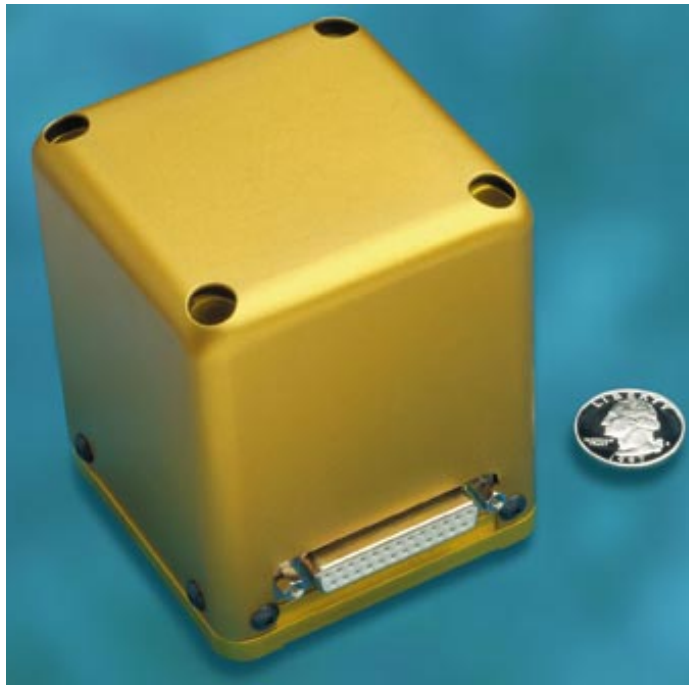


Figure 2.9: Systron Donner MotionPak.

2.2.3 Differential GPS System

The Differential GPS system (DGPS) is based on the ruggedized NovAtel ProPack II technology as the ground reference unit and a stand alone MiLLennium L2 GSPCard as the on-board kinematic and dynamic GPS unit. The MiLLennium L2 GSPCard has an integrated radio frequency (RF) and digital sections capable of receiving and tracking the L1 C/A code, the L1 and L2 carrier phase, and the L2 P-code for up to 12 satellites [63, 76]. Figure 2.10 on the next page shows a ProPack unit along with a stand alone

GPSCard unit with their respective antennas. Section I.2.2 on page 378 contains some additional information regarding this sensor package.



Figure 2.10: NovAtel GPS Ground Station Receiver, On-Board Card, Antenna, and Reference Station Antenna.

2.2.4 FreeWave Wireless Data Transceiver

The FreeWave wireless digital transceiver shown in Figure 2.11 on the next page is a robust and very reliable hardware component. The unit presents a serial port interface to the host computer and to the ground station for seamless serial port communication between the two for up to 20 miles. Section I.2.3 on page 381 presents more details about the FreeWave wireless digital serial port.

2.2.5 Range Sensor

The Helicopter Research Testbed uses two complimentary range transducers for the estimation of distance and altitude. Figure 2.12 on the next page shows the SHARP GP2D02



Figure 2.11: FreeWave Wireless Data Transceiver On-Board Card and Ground Station Unit.

infrared sensor, and Figure 2.13 on the following page shows the ultrasound sensor. The infrared sensor has a range of 10 – 80 cm while the ultrasound sensor has a range of 15 – 120 cm. The infrared sensor is more sensitive for measurements of short range distances, and the ultrasound sensor is more reliable at measuring long range distances. As such, the two sensors complement each other in their operational envelope. The complimentary range information for altitude estimation is useful for automated takeoff and landing maneuvers. Section I.2.4 on page 382 and Section I.2.8 on page 388 provide more detailed information pertaining to the infrared and ultrasound sensors respectively.

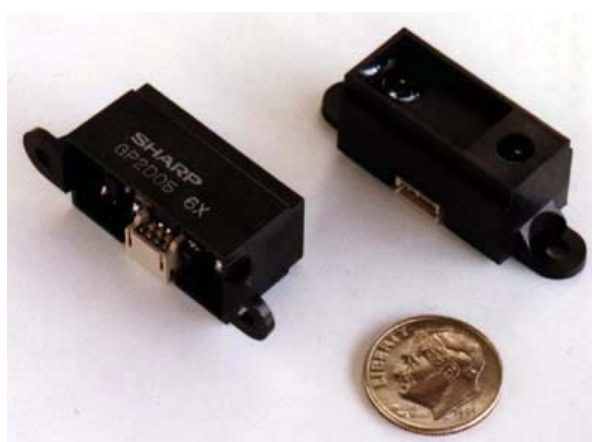


Figure 2.12: SHARP GP2D02 Infrared Distance Sensor.



Figure 2.13: Ultrasound Sensors

2.2.6 Electronic Compass

Section I.2.6 on page 384 details the various characteristics of the Honeywell HMR3000 electronic compass shown in Figure 2.14 on the following page. The HMR3000 measures inertial roll ϕ , pitch θ , and heading ψ . The HMR3000 automatically compensates for pitch and roll attitude in its heading sensor signal.

2.2.7 Hall Effect Sensors

The Helicopter's main rotor gear has three permanent magnets embedded at 120° to each other as shown in Figure 2.15 on the next page. The permanent magnet swoops very closely by a Hall effect sensor embedded in the helicopter's frame as shown in Figure 2.16 on page 28. Each time the magnet is next to the sensor, the sensor activates a pulse that is detected by an on-board computer. The estimation of the main rotor angular velocity follows by counting the time lapse between pulse events. The angular velocity of the main rotor is one of the most important measurements necessary for automatic control of the various aerodynamic and electro-mechanical actuators as indicated in Section 6.2 on page 68.

2.2.8 On-Board Central Processing Units (CPU)

The on-board Central Processing Units (CPU) are responsible for the interface with sensors via the available input/output ports and the implementation of the control laws

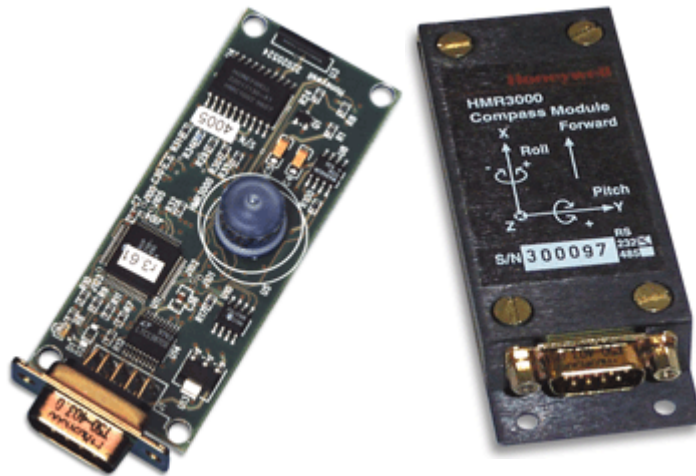


Figure 2.14: Electronic Compass Honeywell HMR3000



Figure 2.15: Main Rotor Gear with Embedded Permanent Magnets



Figure 2.16: Hall Effect Sensor near the Main Rotor Gear with Embedded Permanent Magnet

that stabilize and control the helicopter. There are two primary on-board CPUs

1. principal decision making CPU that plans and controls the mission: Figure 2.17 on the following page
2. secondary CPU that interfaces with the various sensors and actuators: Figure 2.18 on the next page

2.2.8.1 Primary Mission Planning and Control CPU: Ampro PC104

The primary Mission Planning and Control (MPC) CPU in its current instantiation runs on a platform based on the Intel x86 ship at 100 MHz. The MPC runs on the QNX Real-Time Operation System (RTOS) [49, 93, 125].

2.2.8.2 Low Level Actuator Command and Sensor Input/Output CPU: Motorola MC68332

The MC68332 is a highly-integrated 32 bit microcontroller that combines high-performance data manipulation capabilities with powerful peripheral subsystems. This MCU is built

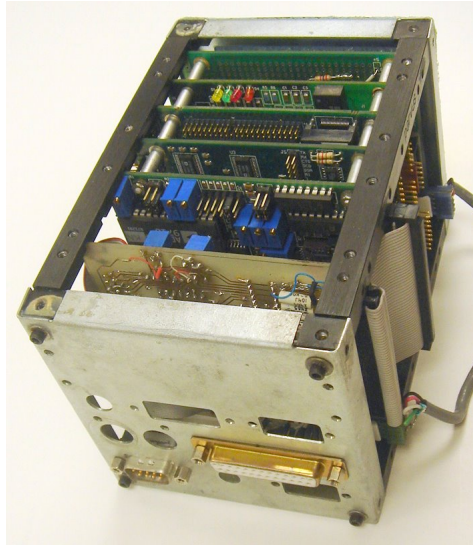


Figure 2.17: Mission Planning and Command CPU: Ampro PC104

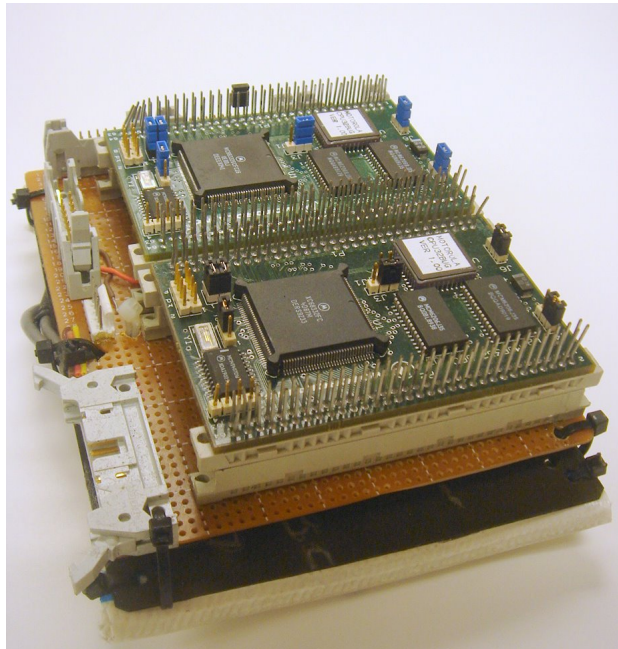


Figure 2.18: Actuator Command and Sensor I/O CPU: Dual Motorola MC68332

up from standard modules that interface through a common intermodule bus (IMB). The MCU incorporates a 32 bit CPU (CPU32), a system integration module (SIM), a Time Processing Unit (TPU), a queued serial module (QSM) and a 2 Kbyte static RAM module with TPU emulation capability (TPURAM) [45, 46].

2.2.9 Rate Table Stand

The Rate Table Stand in Figure 2.19 is a vintage 80's device that rotates at a precise rate. It is useful for testing rate gyros, angular orientation devices, and other transducers that may need periodic triggering events.



Figure 2.19: Rate Table Stand (RTS).

2.2.10 Linear and Directional Test Stand

Figure 2.20 on the next page shows the Linear and Directional Test Stand (LDTS) with the instrumented helicopter on top of the stand. The LDTS is primarily used to aid in the test and design of rotor angular velocity testing (Appendix J), altitude and heave mode testing, and directional control testing (Section L.2 on page 434). Section I.4 on page 395 presents more information related to the LDTS.

2.2.11 Rotational Dynamics Test Stand

Figure 2.21 on page 33 shows the Rotational Dynamics Test Stand (RDTS) with the helicopter during a test run. The RDTS allows free movement about the roll, pitch and yaw axis one at a time or all axes combined.

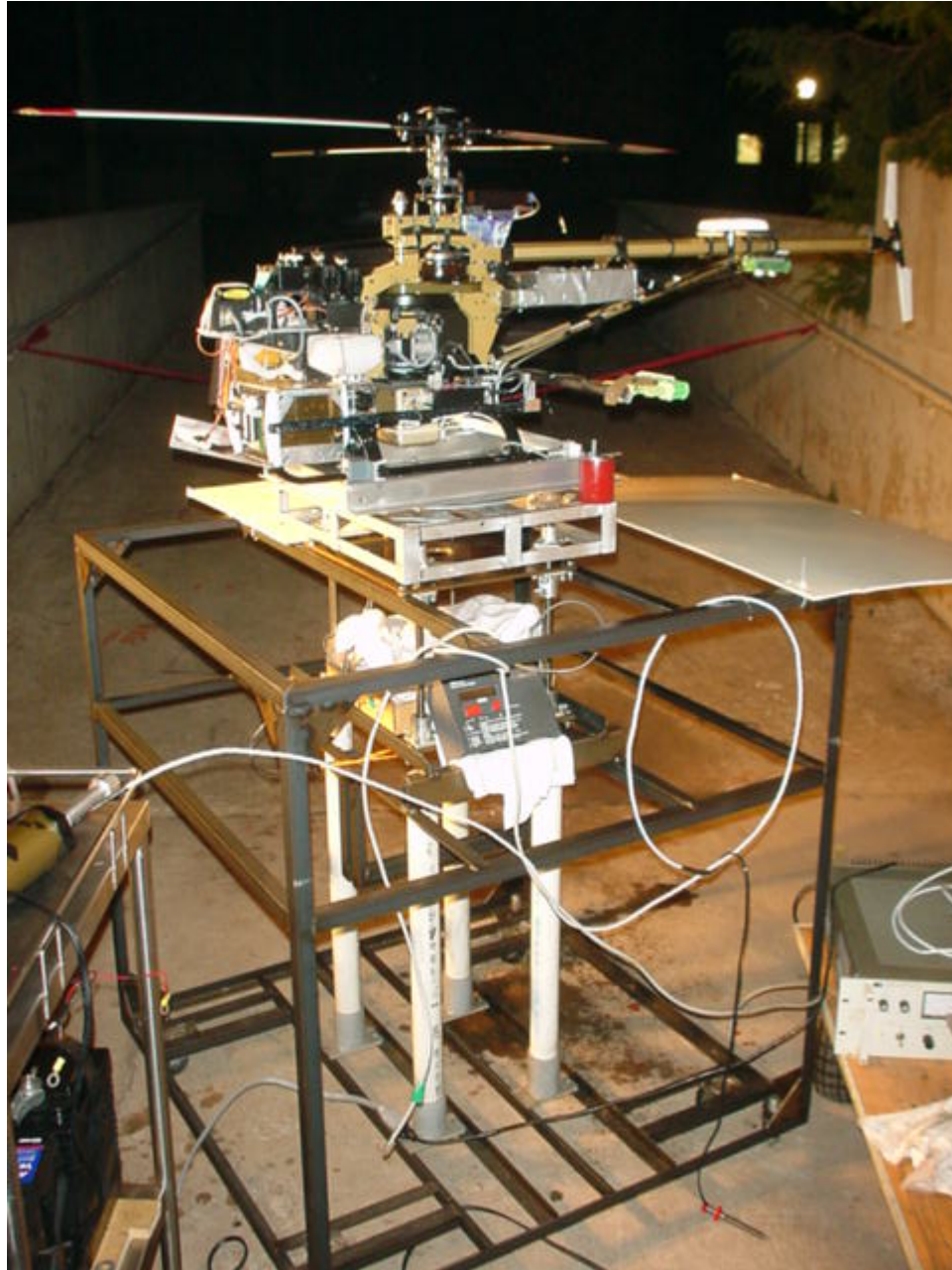


Figure 2.20: Helicopter Research Testbed sitting on the instrumented, purposely built Linear and Directional Test Stand (LDTS).

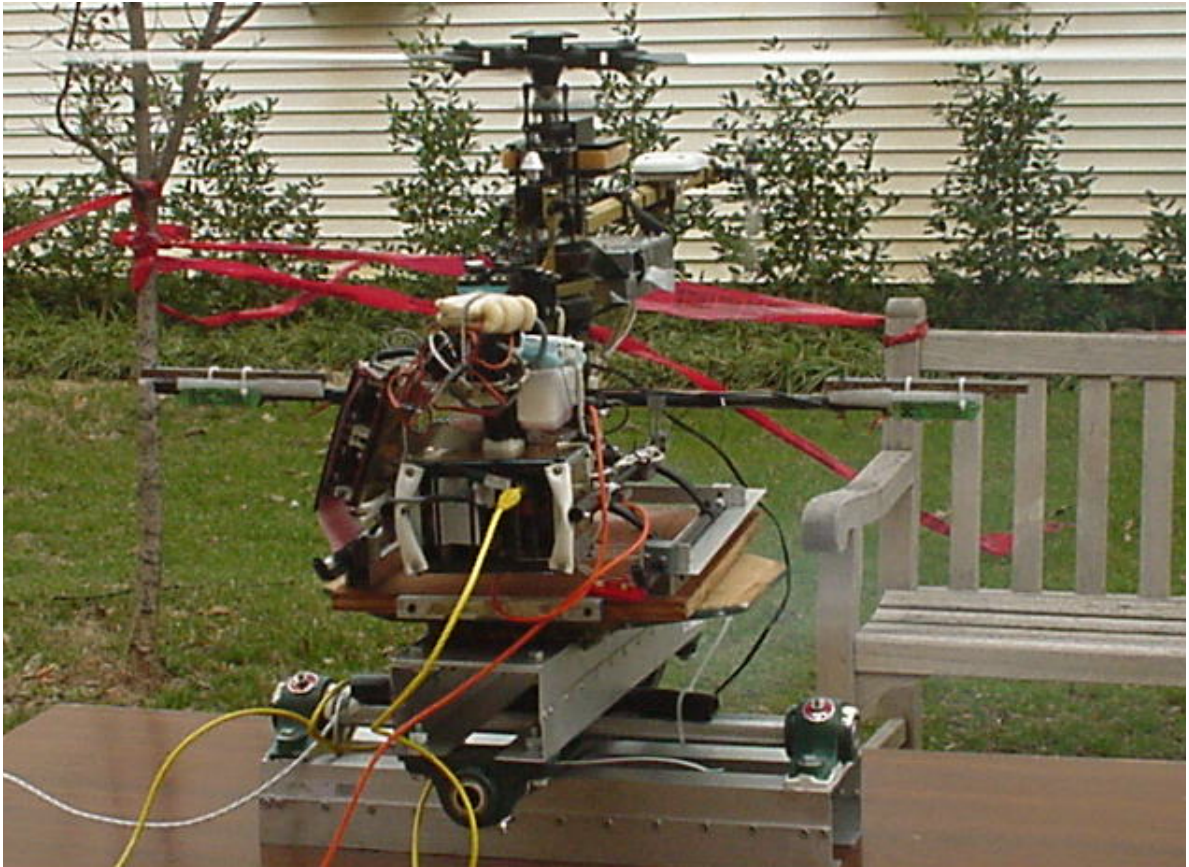


Figure 2.21: Real-Time Run of the Helicopter on top of the Rotational Dynamic Test Stand (RDTS).

Chapter 3

Helicopter Electro-Mechanical Control Actuators

3.1 Introduction

Figure 2.7 on page 21 and Figure 2.8 on page 22 show the five electromechanical control servos available to the model helicopter. This chapter explores the mechanics of each control servomechanism, and its influence in helicopter flight. The servos primary functions are listed below:

Table 3.1: Helicopter Electromechanical Control Servos

		primary function	secondary function
main rotor collective	δ_θ	lift	altitude control
main rotor lon. cyclic	δ_{lon}	lon. stability	lon. locomotion
main rotor lat. cyclic	δ_{lat}	lat. stability	lat. locomotion
tail rotor main collective	δ_{TR}	torque compensation	directional control
throttle	δ_{th}	engine power	

3.2 Main Rotor Collective Control Servo

The main rotor collective control servo transducer uniformly changes the main rotor blade pitch angle θ during a complete blade revolution. That is, the main rotor collective provides the same blade pitch angle at all blade azimuth. The collective servo achieves uniform blade pitch angle input by mechanically raising and lowering the swashplate while maintaining a constant swashplate angle with respect to the x, y plane of the



$$\delta_{\theta} = 1200 \mu\text{sec}$$

$$\theta_0 \approx -3^{\circ}$$

$$\delta_{\theta} = 1500 \mu\text{sec}$$

$$\theta_0 \approx 3^{\circ}$$

$$\delta_{\theta} = 1900 \mu\text{sec}$$

$$\theta_0 \approx 11^{\circ}$$

Figure 3.1: Collective control servo settings with corresponding swashplate deflections and main rotor collective pitch angle θ . Left column corresponds to $\theta = -3$ deg. The middle column corresponds to the idle setting of $\theta = 3$ deg. The right column corresponds to a maximum collective deflection of $\theta = 12$ deg.

helicopter body. The swashplate position determines the main rotor blade pitch angle via mechanical links shown in Figure 3.1 on the previous page.

Section I.3.1 on page 389 details the calibration whereby the main rotor collective servo input δ_θ maps to the main rotor collective pitch θ_0 . Calibration results are plotted in Figure I.13 on page 389. The calibration curve is a direct function of the mechanical links settings which have a direct effect on the main rotor blade pitch angle. The links are set such that the main rotor blade pitch angle $\theta_0 = 3 \text{ deg}$ for a stick input $\delta_\theta = 1500 \mu\text{sec}$.

3.3 Main Rotor Longitudinal and Lateral Cyclic Control Servo

Figure H.2 on page 370 shows the source of longitudinal δ_{lon} and lateral δ_{lat} cyclic inputs to the main rotor blade pitch. Bell cyclic inputs δ_{cyc} result from direct blade pitch contribution from pilot stick, and Hiller cyclic inputs result from the teetering blade angle β_{stab} of the stabilizer bar. Both contributions to cyclic inputs are given by equation (H.2.4) in Section H.2.1 on page 367.

$$\theta_{cyc} = \frac{L_2}{L_4} \delta_{cyc} + \frac{L_1 L_3}{L_4 (L_2 + L_3)} \beta_{stab} \quad (3.3.1)$$

$$\theta_{cyc} = K_{cyc} \delta_{cyc} + K_{stab} \beta_{stab}$$

Figure 3.2 on the following page shows the swashplate settings for the longitudinal cyclic stick inputs. In turn, Figure 3.3 on page 38 shows the swashplate settings for lateral cyclic stick inputs. Section I.3.2 on page 390 details the calibration sequence for the longitudinal and lateral Bell cyclic inputs, and the calibration results are shown in Figure I.14 on page 390 and Figure I.15 on page 391.



$$\delta_{lon} = 1200 \mu\text{sec}$$

$$\theta_{lon} \approx 21^\circ$$

$$\delta_{lon} = 1482 \mu\text{sec}$$

$$\theta_{lon} \approx 0^\circ$$

$$\delta_{lon} = 1800 \mu\text{sec}$$

$$\theta_{lon} \approx -21^\circ$$

Figure 3.2: Longitudinal control servo settings with corresponding swashplate deflections and main rotor Bell cyclic pitch angle θ_{lon} . The left column corresponds to positive longitudinal cyclic inputs which result in positive pitch attitude or nose up motion. The right column corresponds to negative longitudinal cyclic inputs which result in negative pitch attitude or nose down motion.



$$\delta_{lat} = 1200 \mu\text{sec}$$

$$\theta_{lat} \approx -21^\circ$$

$$\delta_{lat} = 1482 \mu\text{sec}$$

$$\theta_{lat} \approx 0^\circ$$

$$\delta_{lat} = 1800 \mu\text{sec}$$

$$\theta_{lat} \approx 21^\circ$$

Figure 3.3: Lateral control servo settings with corresponding swashplate deflections and main rotor Bell cyclic roll angle θ_{lat} . Left column corresponds to negative lateral cyclic inputs which result in negative roll attitude or left-wing-up motion. The right column corresponds to positive lateral cyclic inputs which result in positive roll attitude or left-wing-down motion.

3.4 Tail Rotor Collective Control Servo

The tail rotor blade pitch angle θ_{TR} has a single collective stick input δ_{TR} . Section I.3.3 on page 392 details the calibration results for the tail rotor servo inputs and its mapping to the tail rotor collective pitch angle. Figure 3.4 presents a summary of these calibration results. By convention, positive tail rotor blade angle of attack provides the necessary torque that compensates for the main rotor torque.

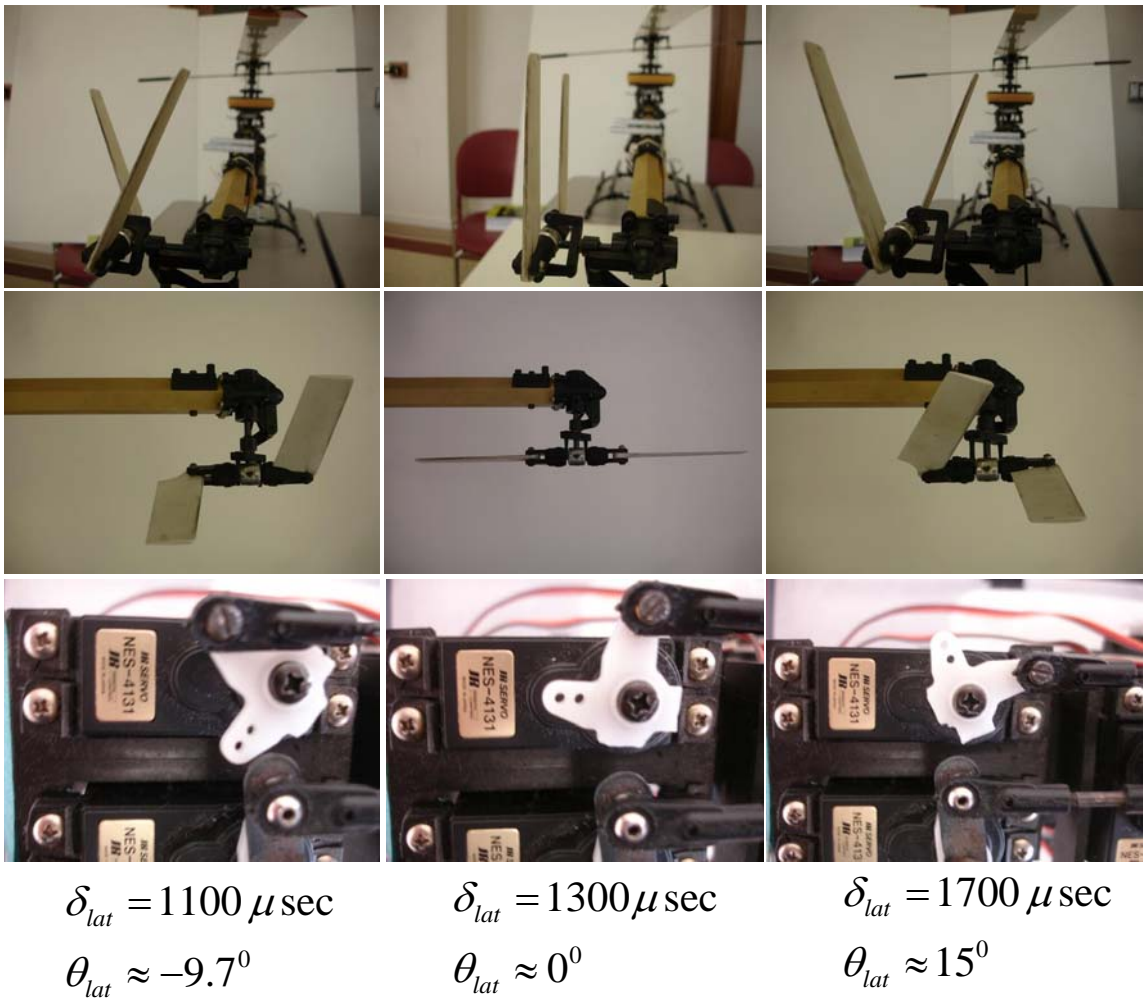


Figure 3.4: Tail Rotor collective settings and corresponding calibration results. The right-most column corresponds to positive tail rotor thrust that compensates for the main rotor torque.

3.5 Throttle Control Servo

Figure 3.5 shows the engine throttle servo settings for the closed and opened servo settings. Figure I.17 on page 394 in Section I.3.4 on page 392 shows the corresponding throttle calibration settings.

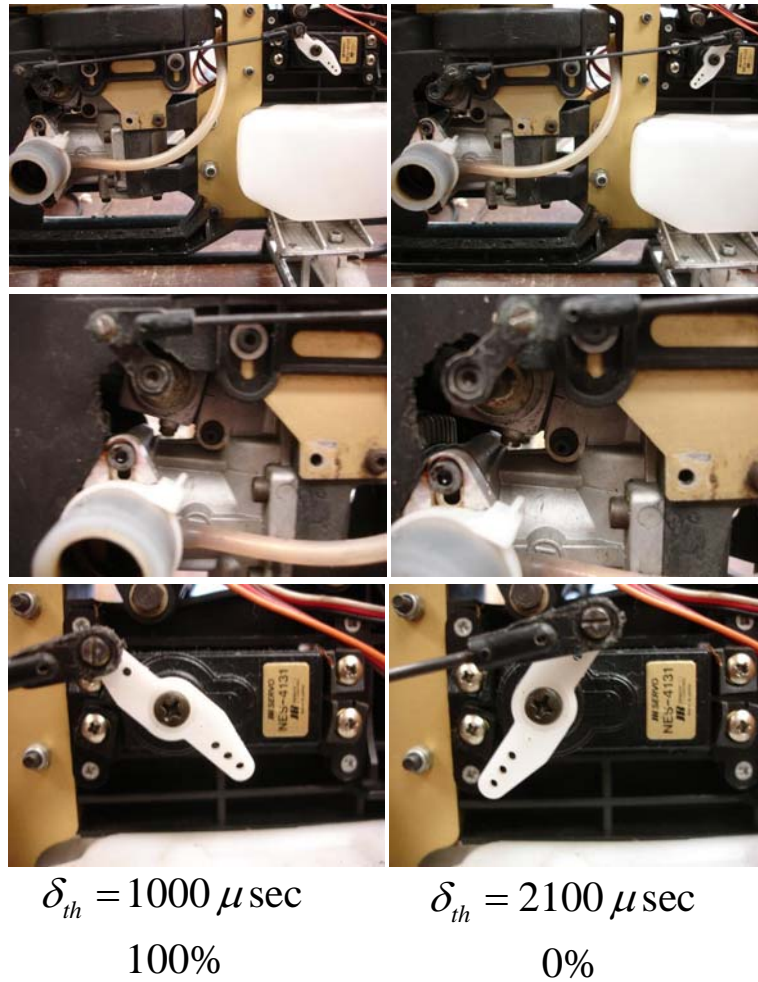


Figure 3.5: Throttle servo settings. The left column corresponds to a fully opened throttle with 100% air-fuel mixture flow, and the right column corresponds to a fully closed throttle with 0% air-fuel mixture flow.

3.6 Summary of Control Servo Settings

Table 3.2 on the following page summarizes the servo control inputs and corresponding aerodynamic actuator settings. In most cases the calibration results are due to direct

measurement of servo input and actuator deflection. The same estimates result from careful consideration of mechanical links and kinematic constraints. Both methods are equivalent, and both methods yield approximate servo input to actuator deflection mapping due to nonlinear effects such as mechanical links bending, loose play in the servo-link attachments, non-linear relations between angular motion and linear motion of several links, and others. The effects of non-linear mapping between servo inputs and actuator deflection are equivalent to and of the same order of magnitude of gusts of wind and other aerodynamic effects.

Table 3.2: Helicopter Servos Inputs and Corresponding Actuator Settings

		$\delta (\cdot deg)$	servo input (μsec)
main rotor collective	δ_θ	-3.0	1200
		3.0	1500
		11.0	1900
main rotor lon. cyclic	δ_{lon}	-21.0	1200
		0.0	1482
		21.0	1800
main rotor lat. cyclic	δ_{lat}	-3.0	1200
		0.0	1482
		21.0	1800
tail rotor main collective	δ_{TR}	-9.7	1100
		0.0	1300
		15.0	1700
throttle	δ_{th}	100.0%	1000
		0.0%	2100

Chapter 4

Test Stand

4.1 Introduction

Many research studies related to miniature helicopter modeling and feedback control development have used or currently use test stands to aid in the development and testing of modeling techniques and related control work. The large number and wide variety of different and ingenious test stand designs that are currently in use are a testimony to the importance that researchers give to avoiding using a human pilot. But perhaps more importantly, test stands used for helicopter research are indeed Hardware-in-the-Loop (HWIL) testbeds that serve as teaching aids. The experience that newly mint researchers obtain from working with real hardware is very valuable. The skills obtained from HWIL experimentation carry over in very useful ways to work duties after the school years are over. Some advantages of using a test stand for miniature helicopter research are listed below.

- helicopters rigged to test stands allow for careful experimentation without the possibility of crashing the helicopter [2].
- instrumented test stands can provide ground truth to sensor data obtained during the testing [7].
- test stands can isolate any number of degrees of freedom, and can operate in one or more axes at the time

- test stands offer an excellent platform for testing hardware and software interaction.
- test stands offer a controlled lab environment immune to weather conditions. This is particularly important for researchers in extreme geographical latitudes during winter time [95].

Equally important are some concerns that must be accounted for when using a test stand.

- the test stand influences the inertias and weight of the experimental vehicle
- aerodynamic interactions between the helicopter and the test stand must be accounted for with care
- mechanical interactions between the helicopter and the test stand must be accounted for with care
- results obtained from the test stand experimentation must account for the test stand effects on the data.
- results obtained from the test stand experimentation must be post processed to yield real physical meaning
- experimental data is not equivalent to real flight data. Results obtained from a test stand may not be suitable for system identification, unless the model explicitly accounts for the influence of the test stand.

This chapter explores various test stand designs and the major characteristics of these designs. Then an overview of the test stand developed for work on this dissertation follows. Finally, the contribution of combining a test stand with real flight hardware is well stated.

4.2 Test Stand Survey

The simplest test stands are used by pilots of Remote Controlled (RC) miniature helicopters. These consist of a helicopter rigged at or near the center of mass to a light rod that allows for six degrees of freedom movement. These stands are a great aid for RC pilots to learn and share knowledge. The main disadvantage relates to the limited weight that these stands can carry. The most involved test stands allow the helicopter six degree of freedom hover motion. In research done at the Autonomous Helicopter Project at Carnegie Mellon [3, 2], the use of different test stands allowed for incremental development of helicopter autonomy. The following is a characterization of key parameters of test stands found in the literature.

Table 4.1: Test Bed

ref.	DOF (lin/ang)	power dc/gas	loc. in/out
[2]	6	dc	in
[17]	1-ang	gas	out
[95]	3-ang, 1-lin+1-ang	dc	in
[155, 156]	6	dc	in
[134]	2-ang, 1-lin	dc	in
[144]	2-lin (x,y),	dc	in

A number of research facilities have indoor test stands for vibration, noise, performance, and aerodynamic studies of blades and fuselage. Examples are the *Active Aeroelasticity and Structures Research Laboratory (A2SRL)* at the University of Michigan and the *Fully Instrumented Helicopter Rotor Test Stand Facility* at Pennsylvania State. These test stands are not generally used for scaled helicopter research.

4.3 Test Stand for Helicopter Research

Three test stands were build to aid with this thesis research. The Linear Directional Test Stand (LDTS), the Rotational Dynamics Test Stand (RDTS), and the Rate Table Stand

(RTS). Each will be discussed in the following sections.

4.3.1 Linear and Directional Test Stand

Figure 4.1 on the next page shows the altitude axis with the attachment platform extended and compressed. When the helicopter generates thrust and lifts, the springs exert less force on the helicopter until a point when the helicopter starts to lift more than its own weight. Figure 4.2 on the following page shows the range of rotation about the z-axis when experimenting with the yaw rate and heading track and hold commands. Figure 4.3 on page 47 shows the middle plates and the Lazy-Suzy arrangement. The LDTS can operate the linear altitude command independent of the yaw rate command. The two degrees of freedom can operate simultaneously as well.

The test stand built for this dissertation is unique in various aspects:

1. portable and easily transportable
2. can be used for indoors or outdoors tests
3. the test stand is robustly built, and it is therefore immune to helicopter forces, moments or vibration environment.
4. the test stand can handle gas or electric helicopters.

To the authors knowledge, there is no single test stand in use anywhere that has the characteristics listed above. Most of the test stands are built for indoors use, but no stand has the versatility and wide range of applications that the LDTS has.



Figure 4.1: Side view of the LDTS. Note that in the left picture the altitude stand is at its minimum point. On the right, the attachment plate is at its maximum height of 14 in (0.36 m).

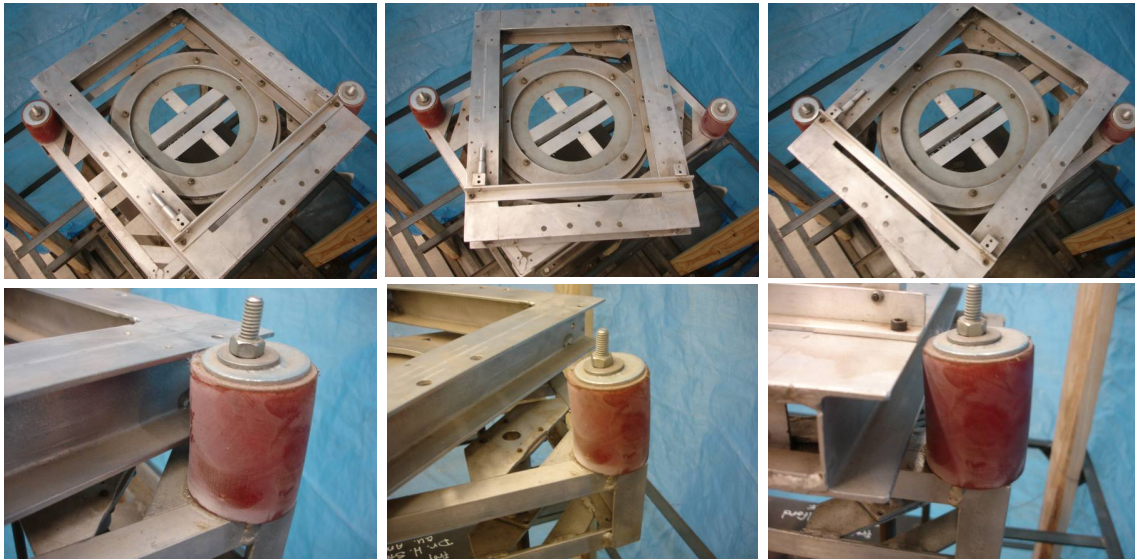


Figure 4.2: Top view of the LDTS. Note the top-left against the red-stopper, and the top-right against the stopper. The stopper prevented the test helicopter from winding around when performing heading track and hold. The stoppers can be removed to perform 360° yaw rate experiments.

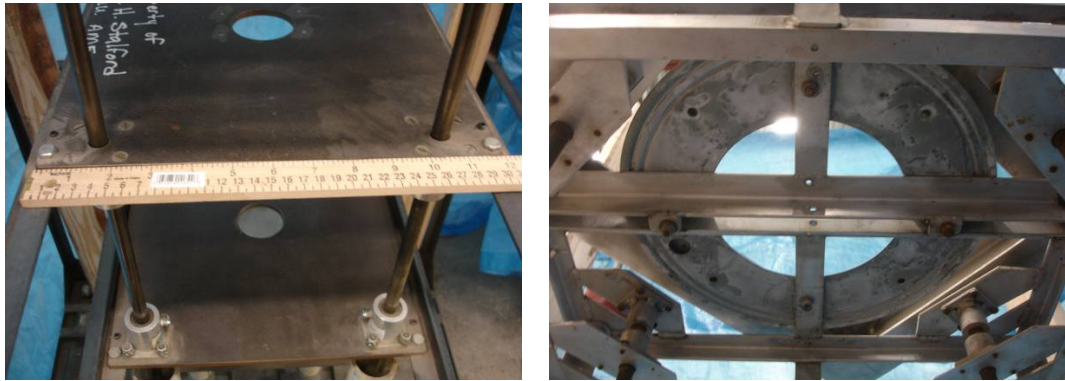


Figure 4.3: On the left, note the view of the two middle steel plates. On the right, note the Lazy-Suzy attachment.

4.3.2 Rotational Dynamics Test Stand

The Rotational Dynamics Test Stand (RDTS) can operate on only one axis, or it can operate in several axes simultaneously in any combination. Figure 4.4 shows various attitude positions for the RDTS. The RDTS is portable, and can perform experiments indoors or outdoors. The RDTS is robustly constructed, and can handle large payloads.

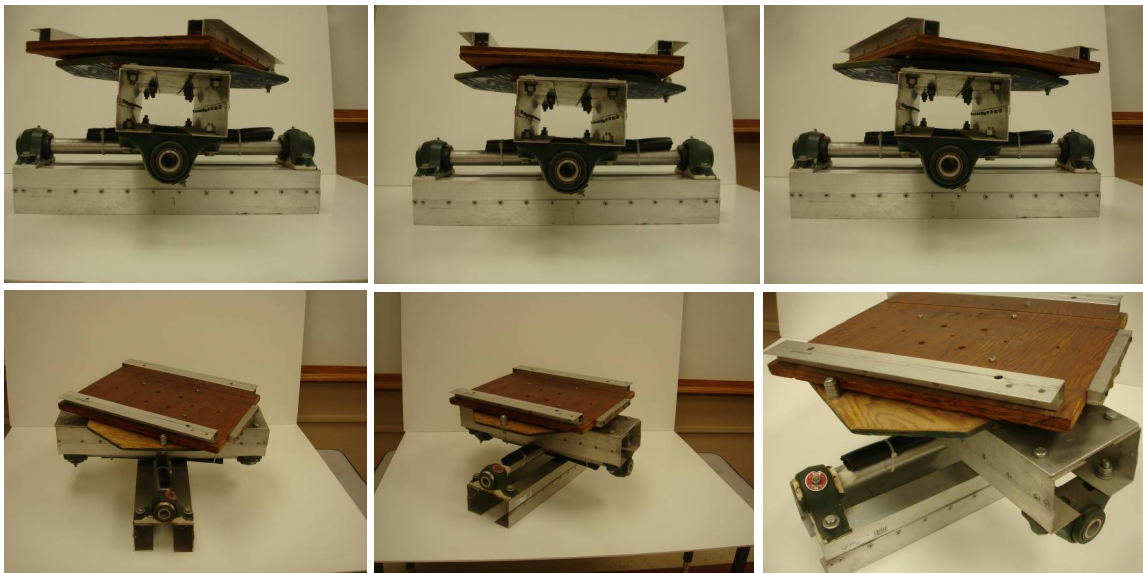


Figure 4.4: Rotational Dynamic Test Stand (RDTW). The RDTS can rotate freely about the z-axis for yaw rate and heading track and hold commands. The RDTS can also rotate independently or in combination rotation about the x and y axes for roll and pitch attitude control.

4.3.3 Rate Table Stand

The Rate Table Stand (RTS) is a 1980's vintage hardware used to test angular rates and angular acceleration components. The RTS has been very useful in this research to test the various sensors available, and to validate models for sensor measurements. Additional use of the RTS was to test yaw rate and heading command track hold experiments on a device with very little friction. Figure 4.5 shows a picture of the venerable rate table stand.



Figure 4.5: Rate Table Stand (RTS).

4.4 Conclusions.

This chapter has shown three test stands, two of which were designed and built by the two members of the helicopter team. The test stands are valuable assets that are

unique among those used in other research efforts. All three test stands, the Linear and Directional Test Stand (LDTS), the Rotational Dynamic Test Stand (RDTS) and the Rate Table Stand (RTS) are robust but portable test stands that can operate equally well in the lab or in an outdoor environment. The LDTS is configurable and able to operate in one or two degrees of freedom. The RDTS is also configurable and can operate in one, two or three degrees of freedom. The RTS is a one degree of freedom device that can rotate at precise rates for testing of angular rates and other measuring sensors. More importantly, all three stands are enabling technologies fundamental to the operation of helicopters with gas engines when outdoors. All these characteristics make the test stands developed for this thesis work and their use one of the primary contributions of this dissertation.

Chapter 5

Math Models

5.1 Introduction

Dynamic modeling of scale helicopters is challenging because the small weight and related inertias of scale helicopters results in higher natural frequencies and faster response of the fuselage-rotor dynamics. Mathematical models for scale helicopters need to capture the high bandwidth inherent in the physics of the vehicle. Two complimentary modeling techniques exists, first principles and system identification, and both are widely used in rotatory aircraft research. First-principle modeling uses the fundamental laws of mechanics and aerodynamics to arrive at a physics-based model [13, 82, 119, 120, 135]. First-principle derived models where the aerodynamics, structures, and controls are modeled explicitly can be daunting, and in general, simplification of these models is necessary and adequate for the design of control laws. First-principle models can be put into mathematical models that can be used in simulation programs [21, 68, 70, 74], but these models require real flight data for their validation.

In contrast, system-identification modeling [97, 89, 147] requires the use of real flight data, and is often used for flight control design because the model is based on real flight data. Often, system identification techniques are used to identify and validate models obtained from first principles. An example of system-identification tools used in rotary aircraft research is the Comprehensive Identification from FrEQUENCY Responses (CIFER) tool developed by the Army/NASA Rotorcraft Division [146].

Modeling related to small-scale helicopter is an active research area [30]. Until very recently, available literature on small helicopters was limited, and the existing literature

for full-scaled helicopters did not apply directly due to scaling factors and operational Reynolds number [92, 104]. Mettler has studied scaling factors between full-sized helicopters and scale-model helicopters, and has extensively researched the area of modeling and system identification [105, 106, 108]. Other existing work has also enriched the literature on small-scale helicopters. [50, 87, 88, 91]

In the recent past, researchers have used system identification methods for modeling of scaled helicopters with some measure of success [7, 16, 109]. Mettler [105] used real flight data from two instrumented helicopters to perform system identification techniques [108] that characterized open loop aircraft dynamics. Mettler developed a general helicopter model that describes key physical effects of helicopter dynamics, and used the real flight data with system identification methods [147] to obtain abstract physical information from the identified model. His system identification model is applicable to other small-scaled aircraft. More recently, Tischler and coworkers have successfully used system identification techniques in a number of UAV programs [145, 147] which include Northrop Grummans Fire Scout vertical takeoff unmanned air vehicle demonstrator; the broad-area unmanned responsive resupply operations UAV based on Kamans twin-rotor K-MAX helicopter; AeroVironments Pathfinder solar-powered stratospheric research aircraft; Yamahas R-50 small-scale helicopter; and the class of small-scale ducted fan vehicles developed separately by Allied Aerospace (formerly Micro Craft) and Honeywell [145].

As previously stated, first-principle modeling is not a substitute for system identification methods, and system identification methods utilize first principle results to understand and analyze the data that is collected from the various experiments. The two complimentary methods have their use for proper problems. Modeling based on first principles is complex and results in a number of equations that describe the physics of the helicopter. In developing equations from first principles, it is important to understand they key aspects that influence helicopter behavior. A number of simplifying assumptions may be relevant, and with an understanding of the underlying physics, a simplified

model may yield results useful for control applications.

This chapter presents results from first principles. Various mathematical models have been derived for the OU helicopter. First, the main helicopter components are identified, and subsequently, respective models are presented. The main rotor and the tail rotor are both represented as aerodynamic actuators. The Momentum Theory, the Blade Element Theory and the combined Blade Element and Momentum Theory are presented along with their fundamental results. Following this, the main rotor blade equation of motion is presented along with the first order Tip Path Plane (TPP) blade equations of motion. The main rotor stabilizer bar is presented as a teetering rotor with modified TPP equations of motion. The tail rotor model is presented as an extension of the main rotor. The helicopter engine is also presented as an actuator, and a closed-feedback control loop is presented. Other components of the helicopter are tabulated with a short note on how these are accounted for in the various models. Following this, the six degree of freedom rigid body equations of motion are presented along with the three inertial position dynamics and three kinematic equations. The trim equations are presented as well as the linear equations of motion about the trim condition.

5.2 Models of the Helicopter Components

Figure 5.1 on the following page illustrates the primary helicopter components and mechanisms. The main rotor is the primary aerodynamic actuator responsible for generating lift and locomotion. The tail rotor provides torque compensation and heading control. The engine converts chemical energy stored in the available fuel into mechanical power necessary to drive the various helicopter components.

5.2.1 Main Rotor Aerodynamic Actuator Model

Section C on page 202 summarizes the theory that allows for the prediction of lift, torque, and the necessary power to generate and maintain lift. Following this, Section H.1.2 on

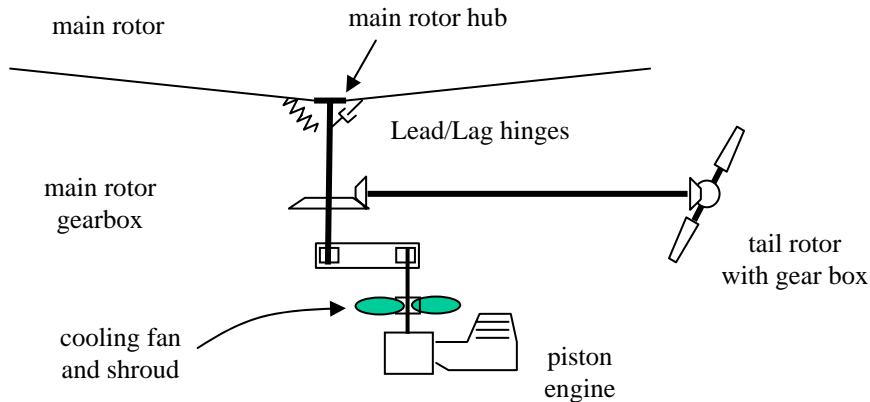


Figure 5.1: Helicopter Research Testbed Mechanical Components.

page 361 explores the main rotor contribution to the forces and moments. The tail rotor is a specialized extension of the same main rotor analysis.

5.2.1.1 Momentum and Blade Element Theories for the Helicopter

Two theories provide the framework for the analysis of the main rotor forces and moments. Momentum Theory (Section C.1 on page 203) applies the conservation laws of aerodynamics to predict basic performance factors of the helicopter. A fundamental assumption in Momentum Theory is the presence of a stream tube through the walls of which there is no fluid flux. The theory breaks down in flight regimes where the upward velocity of the rotor equals the rotor induced velocity (slow descent), when the slip stream expands and recirculating flow exists throughout the rotor (vortex ring state), and when the wake above the rotor becomes turbulent and aperiodic (turbulent wake state) [92, 124]. During axial-symmetric flight (hover, ascent, and high speed descent), the necessary assumptions for momentum theory hold. In these cases, the governing principle is the work done by the rotor on the flowing air. This work results in a sudden increase of flow velocity as the flow passes through the rotor (induced velocity v_i). The change of momentum on the column of air imparts an opposite reaction force (thrust T)

given by equation (C.1.12) on page 206

$$T = 2\rho\pi R^2 v_i^2 \quad (5.2.1)$$

where ρ is the air density, R is the rotor radius and πR^2 is the rotor area. Equation (5.2.1) is a fundamental result from Momentum Theory in the flight regimes in which the theory applies. In hover case, the induced velocity $v_i = v_h$, and the general theoretical results are listed in Table 5.1.

Table 5.1: Momentum Theory Applications

hover	$(V_c = 0, v_h = \sqrt{T/2\rho\pi R^2})$	Section C.1 on page 203
vertical climb	$(V_c/v_h > 0)$	Section C.1.1 on page 209
windmill break state	$(V_c/v_h \leq -2)$	Section C.1.2 on page 213
forward flight	$(v_i \ll V_\infty)$	Section C.1.3 on page 217

Section C.2 on page 222 discusses the Blade Element Theory (BET). The BET estimates the dynamic forces and moments associated with each blade element at a given radius from the rotating axis and at a given position of the blade azimuth. A blade section has a speed that is proportional to the local radius. If the blade section is sufficiently small, conditions across the section are constants [92]. In this way, the drag and thrust of the blade element can be readily computed, and the contributions of all the small blade elements are added to generate the total or net rotor thrust, drag and moment. Thus, a fundamental theoretical result from (BET) for lift is given in equation (C.2.10) on page 226

$$dC_T = \frac{\sigma}{2} C_l r^2 dr \quad (5.2.2)$$

where C_T is the thrust coefficient defined in equation (C.1.17) on page 208, σ is the solidity ratio defined in equation (C.2.11) on page 226, C_l is the section lift coefficient, and $r = y/R$ is the blade section station where y is the distance to the blade section from the rotational axis. This result does not depend on any specific rotor configuration, and applies to all blade platforms.

Section C.3 on page 229 follows on with results from the combined Blade Element and Momentum Theories (BEMT). A primary result from BEMT is given in equation (C.3.7) on page 231

$$dC_T = \frac{1}{2} \sigma a (\theta r^2 - \lambda r) dr$$

$$\lambda(r, \lambda_C) = \sqrt{\left(\frac{\sigma a}{16} - \frac{\lambda_C}{2}\right)^2 + \frac{\sigma a}{8} \theta r} - \left(\frac{\sigma a}{16} - \frac{\lambda_C}{2}\right) \quad (5.2.3)$$

where $r = y/R$ is the blade station as given before, and $\lambda(x, \lambda_C)$ is the inflow ratio as a function of blade station and climb inflow λ_C .

5.2.1.2 Main Rotor Blade Equation of Motion

Appendix D on page 234 derives the main rotor blade equation of motion which results in equation (D.3.117) on page 298.

$$\begin{aligned} \ddot{\beta} + \frac{\gamma}{8} \Omega K_{\dot{\beta}} \dot{\beta} + \Omega^2 \left(\nu^2 + \frac{\gamma}{8} K_{\beta\mu} \right) \beta &= \frac{\gamma}{8} \Omega^2 K_{\theta} \theta - \frac{\gamma}{8} \Omega^2 K_{\lambda} \lambda \\ &+ \frac{\gamma}{8} \Omega^2 K_{pq} \left(\frac{p}{\Omega} \sin \psi + \frac{q}{\Omega} \cos \psi \right) \\ &+ 2\Omega^2 \nu_{\beta}^2 \left(\frac{p}{\Omega} \cos \psi - \frac{q}{\Omega} \sin \psi \right) \\ &+ \nu_{\beta}^2 (\dot{p} \sin \psi + \dot{q} \cos \psi) + \nu_0^2 \beta_P \end{aligned} \quad (5.2.4)$$

Equation (5.2.4) above is the fundamental equation of motion for the main rotor blade as it rotates about the rotor shaft [13, 22, 68]. The equation applies for blades of uniform mass attached to the main rotor via lead/lag and flapping hinges, and includes the effects of the fuselage roll p and pitch q rates and their derivatives. Given the above expression for the Blade Equation of Motion (BEOM), equation (D.3.121) on page 299 and equation (D.3.124) on page 300 are the full expressions for the thrust and torque coefficients respectively. Section D.3.7 on page 292 shows the application of the BEOM to specific flight conditions which are summarized below in Table 5.2 on the next page.

The derivation of the above set of main rotor equations of motion is one of the

Table 5.2: Blade Equation of Motion Application

simplified C_T and C_Q	Section D.3.7.2 on page 301
non-constant blade flap coefficients	Section D.3.7.3 on page 302
low frequency dynamics $\dot{p}, \dot{q} \rightarrow small$	Section D.3.7.4 on page 304
low translational speed $\mu \rightarrow small$	Section D.3.7.4.1 on page 306
no hinge offset $e = 0$, no precone $\beta_p = 0$	Section D.3.7.4.2 on page 307
first order Tip Path Plane BEOM	Section D.3.7.4.3 on page 308
teetering blade BEOM	Section D.3.7.4.4 on page 310
forward flight with constant flap coefficients	Section D.3.7.5 on page 311

contributions of this thesis work. Some researchers and engineers derive main rotor blade equations of motion with physics based arguments such as gyroscopic effects and angular dynamics. While valid, these derivations are difficult to reproduce. Most researchers and engineers make reference to authors that have derived similar equations from hinge force and moment equilibrium equations. While valid and insightful, such derivations do not quite derive the full non-linearities associated with the complexity of a rotating blade. In all cases, most of the linearities can be neglected, and even the remaining equations of motion are burdensome. Many simplifications must be made to arrive to a set of tractable mathematical equations. Even further simplifications may be needed to arrive at the same results obtained from hinge force and moment equilibrium equations. The work presented in this section and related appendices mechanizes the derivation of the blade equation of motion such that a full non-linear equation for a given set of simplifying conditions is readily available. This is one of the contributions of this thesis work.

5.2.1.3 Tip Path Plane Blade Equations of Motion

Section B.6.3 on page 200 defines the Tip Path Plane (TPP). A useful assumption regarding the main rotor blade motion is that the thrust vector is perpendicular to the

TPP [82]. Equation (D.3.156) on page 309 describes the TPP BEOM

$$\begin{aligned}\frac{16}{\gamma\Omega}\dot{\beta}_{1c} &= -\beta_{1c} + \frac{p}{\Omega} - \frac{16}{\gamma}\frac{q}{\Omega} + \frac{8}{\gamma}\frac{K_\beta}{\Omega^2 I_\beta}\beta_{1s} - \theta_{1s} \\ \frac{16}{\gamma\Omega}\dot{\beta}_{1s} &= -\beta_{1s} - \frac{q}{\Omega} - \frac{16}{\gamma}\frac{p}{\Omega} - \frac{8}{\gamma}\frac{K_\beta}{\Omega^2 I_\beta}\beta_{1c} + \theta_{1c}\end{aligned}\tag{5.2.5}$$

where the main rotor time constant τ_{MR} is given by

$$\tau_{MR} = \frac{16}{\gamma\Omega}\tag{5.2.6}$$

The same time constant applies to the longitudinal $\tau_{MR}q$ and lateral $\tau_{MR}p$ flapping produced by the body pitching rate q and rolling rate p respectively

$$\begin{aligned}q\tau_{MR} &= -\frac{16}{\gamma\Omega}q \\ p\tau_{MR} &= -\frac{16}{\gamma\Omega}p\end{aligned}\tag{5.2.7}$$

These terms above are important in that they are a source of rotor damping. The terms $-p/\Omega$ and $-q/\Omega$ are, respectively, the longitudinal and lateral blade flapping produced by aerodynamic cross coupling via the body roll p and pitch q rates. Finally, the term

$$\frac{8}{\gamma}\frac{K_\beta}{\Omega^2 I_\beta}\tag{5.2.8}$$

results from hinge offset and flapping restraint. It is a source of cross-coupling and it is related to the blade natural flapping frequency defined in D.3.101

$$\frac{8}{\gamma}\frac{K_\beta}{I_\beta\Omega^2} = \frac{8}{\gamma}(\nu_\beta^2 - 1 - \varepsilon)\tag{5.2.9}$$

The main rotor aerodynamic forces and moments are described in Appendix E on page 316, and are summarized next in Table 5.3 on the following page.

In the case when $\bar{x}_{CM} \approx 0$, $\bar{y}_{CM} \approx 0$, and the body angular rate of change \dot{p} , \dot{q} are

Table 5.3: Blade Equation of Motion Application

aerodynamic rotor forces and moments	Section E.1 on page 316
rotor forces	Section E.2 on page 321
rotor hub moments	Section E.3 on page 325
coupled rotor forces and moments	Section E.4 on page 329

neglected, the non-dimensional rotor forces and moments are given by equation (E.4.3) on page 329.

$$\begin{aligned}
 C_{xMR} &= \left(\bar{h}C_T + \frac{a\sigma}{16}S_\beta \right) \beta_{1s} + \nu_\beta^2 \frac{a\sigma}{\gamma} \frac{q}{\Omega} \\
 C_{yMR} &= \left(\bar{h}C_T - \frac{a\sigma}{16}S_\beta \right) \beta_{1c} + \nu_\beta^2 \frac{a\sigma}{\gamma} \frac{p}{\Omega}
 \end{aligned}
 \tag{5.2.10}$$

where the stiffness number $S_\beta = 8(\nu^2 - 1)/\gamma$ is given by equation (D.3.19) on page 263, and its value is tabulated in Table I.4 on page 373.

5.2.1.4 Main Rotor Stabilizer Bar

Section H.2.1 on page 367 develops the equations of motion and associated model for the stabilizer bar shown in Figure 2.2 on page 16. The stabilizer bar is a teetering rotor that carries negligible force, but serves the very important dual purpose of augmenting the main rotor cyclic pitch command and increasing the damping moment in the helicopter attitude dynamic [88, 87, 105]. An application of the main rotor blade dynamics in equation (5.2.5) on the preceding page results in the first order Tip Path Plane (TPP) equation of motion for the stabilizer bar in equation (H.2.6) on page 368

$$\begin{aligned}
 \frac{16}{\gamma\Omega} \dot{\beta}_{stab,1c} &= -\beta_{stab,1c} + \frac{p}{\Omega} - \frac{16}{\gamma} \frac{q}{\Omega} - \theta_{stab,1s} \\
 \frac{16}{\gamma\Omega} \dot{\beta}_{stab,1s} &= -\beta_{stab,1s} - \frac{q}{\Omega} - \frac{16}{\gamma} \frac{p}{\Omega} + \theta_{stab,1c}
 \end{aligned}
 \tag{5.2.11}$$

5.2.2 Tail Rotor Aerodynamic Actuator Model

The tail rotor is the primary mechanism for torque compensation for the helicopter in its current configuration. The tail rotor is a two-blade rotor with symmetric airfoils with collective pitch control. Adjustments to the collective tail rotor blade pitch angle generates sufficient thrust to counter the main rotor torque and any side forces that may result from main rotor Tip Path Plane tilt. The tail rotor also provides the means for directional heading control. Appendix L in Section L.2 on page 434 details the design of control laws for automated tail rotor torque compensation.

In full scale helicopters, the tail rotor consumes about 5 – 10% of the main rotor power during normal flight, and as much as 20% during flights at the edge of the flight envelope [92]. For model helicopters, the tail rotor power consumption is about 10 – 20% due to the lower Reynolds number involved which increases the profile drag considerably [105]. During normal flight operations, the trim side force needed to compensate for the main rotor torque is found from equation (F.1.15) on page 338 and augmented in equation (L.2.9) on page 437.

$$Y_{TR} = \left[\frac{Q_{MR} + n_{TR}Q_{TR}}{l_{TR}} \right]_{\dot{r}=r=0} \quad (5.2.12)$$

An equivalent formulation is found directly from the power required to operate the helicopters [92]

$$Y_{TR} \approx T_{TR} = \frac{P_i + P_0 + P_p}{\Omega l_{TR}} \quad (5.2.13)$$

where the term $P_i + P_0 + P_p$ is the total power of the helicopter which can be found from equation (C.2.14) on page 227 with the addition of the tail rotor power and parasite power $\lambda_C C_W$

$$C_P = C_Q = \frac{k}{\sqrt{2}} C_T^{3/2} + \frac{1}{8} \rho C_D + \lambda_C C_W + C_{P_{TR}} \quad (5.2.14)$$

where the term k is an empirical factor that accounts for nonlinear aerodynamic physics such as non-uniform rotor inflow, blade tip losses, nonlinear slip stream and wake effects

on the tail rotor, etc. For the OU research helicopter, the value for $k = 1.2$.

5.2.3 Model of Helicopter Engine

The University of Oklahoma Helicopter Research Testbed (OU-HRT) runs with a 2-cycle engine with a fuel capacity of 0.61 in^3 or 9.9582 cc . Table I.16 on page 387 summarizes the primary characteristics of this engine which has a maximum power output of about 2.2 Hp [8, 37]. The engine has a three needle carburetor that provides fine tune adjustments throughout the operational range.

Section J on page 398 explores in detail the experiments related to the coupled engine and main rotor characterization. Table J.1 on page 416 summarizes the primary components that relate the operation of the engine-carburetor to the helicopter rotational elements. Equation (J.2.19) on page 411 is the main rotor control design shown in Figure J.10.

$$\begin{aligned} k_i &= \frac{\pi^2}{k} \\ k_p &= \frac{\pi\sqrt{2}}{k} - k_\Omega \end{aligned} \tag{5.2.15}$$

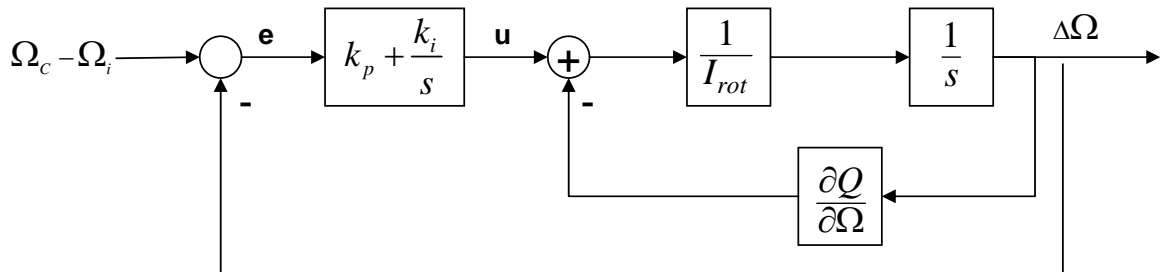


Figure 5.2: Closed Loop Control Design Diagram.

Finally, the continuous time control design and loop transfer function characteristics are summarized in table J.2 on page 417.

5.2.4 Models of Remaining Components

Other components in the helicopter serve useful purposes. Table 5.4 tabulates the most important of these components and how they are accounted for in the various models.

Table 5.4: Other Helicopter Components and their Models

	equation	description
cooling fan	(5.2.14)	induced power factor k
transmission gears	(5.2.14)	induced power factor k
semi-rigid blade		equivalent flapping hinge
drag hinge dynamics	(D.2.41)	model not used

Equation (D.2.41) on page 250 indicates that when the blade only rotates about the drag (or lead/lag) rotation axis ζ with pure lead/lag motion, the blade does not induce any feathering or flapping rotation. Therefore, the main rotor blade drag hinge dynamics are mostly important for high fidelity models and for research concerned with the main rotor overall vibration signature and associated higher order effects on helicopter dynamics [53, 119]. For first order dynamic modeling, the drag hinge dynamics are considered stable with a net zero average effect in the rotor dynamic behavior.

5.3 Rigid Body Dynamics

Section B.5.1 on page 191 derives that translational dynamics which results in the six degrees of freedom (6-DOF) rigid body equation of motion (EOM) given by equation (B.5.6) on page 193. In turn, Section B.5.3 on page 194 derives the rotational dynamics given

by equation (B.5.14) on page 196. The resultant derivations are summarized in equation (H.1.1) on page 359 in Section H.1.1 on page 358.

$$\begin{aligned}
\dot{u} &= rv - qw + x(q^2 + r^2) + y(pq - \dot{r}) + z(pr + \dot{q}) - g \sin \theta + \frac{X}{m} \\
\dot{v} &= pw - ru + y(p^2 + r^2) + z(qr - \dot{p}) + x(pq + \dot{r}) + g \sin \phi \cos \theta + \frac{Y}{m} \\
\dot{w} &= qu - pv + z(p^2 + q^2) + x(pr - \dot{q}) + y(qr + \dot{p}) + g \cos \phi \cos \theta + \frac{Z}{m} \\
\dot{p} &= \frac{L}{I_x} + \frac{I_{yz}}{I_x} (q^2 - r^2) + \frac{I_{zx}}{I_x} (\dot{r} + pq) + \frac{I_{xy}}{I_x} (\dot{q} - rp) + \frac{(I_y - I_z)}{I_x} qr + \frac{{}^B H_x^i}{I_x} \\
\dot{q} &= \frac{M}{I_y} + \frac{I_{zx}}{I_y} (r^2 - p^2) + \frac{I_{xy}}{I_y} (\dot{p} + qr) + \frac{I_{yz}}{I_y} (\dot{r} - pq) + \frac{(I_z - I_x)}{I_y} rp + \frac{{}^B H_y^i}{I_y} \\
\dot{r} &= \frac{N}{I_z} + \frac{I_{xy}}{I_z} (p^2 - q^2) + \frac{I_{yz}}{I_z} (\dot{q} + rp) + \frac{I_{zx}}{I_z} (\dot{p} - qr) + \frac{(I_x - I_y)}{I_z} pq + \frac{{}^B H_z^i}{I_z}
\end{aligned} \tag{5.3.1}$$

where $[X Y Z]^T$ are the total forces acting on the vehicle, $[L M N]^T$ are the total moments acting on the vehicle, and $[{}^B H_x^i {}^B H_y^i {}^B H_z^i]^T$ are the total moment contribution from all rotating parts other than the main rotor and the tail rotor. In the above expressions, the $)_{MR}$ subscript applies to the main rotor, $)_{TR}$ applies to the tail rotor, $)_{HT}$ applies to the horizontal tail, the $)_{VT}$ applies to the vertical tail, $)_F$ applies to the fuselage. The following simplifications apply:

1. the current helicopter configuration does not have a vertical and horizontal tail, and the $)_{HT}$ and $)_{VT}$ components drop.
2. the center of pressure coincides with the vehicle's center of mass, and the fuselage moment contribution $M_F = 0, N_F = 0$ are zero.
3. the rotating engine components contribution to moment is negligible when compared to the main and tail rotor moment contributions.
4. all the rotating moment contributions are accounted for by the main rotor and the tail rotor, and the terms ${}^B H^i$ are zero.
5. take the moments about the center of mass, and the x, y, z components of the

moment arm are zero.

6. the cross inertias are much smaller than the principal inertias, and the cross product moment of inertia can be neglected without loss of accuracy [91].

The resultant 6-DOF EOM are now

$$\begin{aligned}
\dot{u} &= rv - qw + -g \sin \theta + \frac{X_{MR} + X_F}{m} \\
\dot{v} &= pw - ru + g \sin \phi \cos \theta + \frac{Y_{MR} + Y_F + Y_{TR}}{m} \\
\dot{w} &= qu - pv + g \cos \phi \cos \theta + \frac{Z_{MR} + Z_F + Z_{TR}}{m} \\
\dot{p} &= \frac{(I_y - I_z)}{I_x} qr + \frac{L_{MR} + L_{TR}}{I_x} \\
\dot{q} &= \frac{(I_z - I_x)}{I_y} rp + \frac{M_{MR}}{I_y} \\
\dot{r} &= \frac{(I_x - I_y)}{I_z} pq + \frac{N_{MR} + N_{TR}}{I_z}
\end{aligned} \tag{5.3.2}$$

Section B.5.2 on page 193 derives the position dynamics resulting in equation (B.5.8) on page 194, and work in Section B.4 on page 189 yields the kinematic equations equation (B.4.6) on page 190. The two results are again summarized in equation (H.1.6) on page 361

$$\begin{aligned}
\begin{bmatrix} \dot{\phi} \\ \dot{\theta} \\ \dot{\psi} \end{bmatrix} &= \begin{bmatrix} 1 & \sin \phi \tan \theta & \cos \phi \tan \theta \\ 0 & \cos \phi & -\sin \phi \\ 0 & \sin \phi \sec \theta & \cos \phi \sec \theta \end{bmatrix} \begin{bmatrix} p \\ q \\ r \end{bmatrix} \\
\begin{bmatrix} \dot{x}_E \\ \dot{y}_E \\ \dot{z}_E \end{bmatrix} &= \begin{bmatrix} c\theta c\psi & s\phi s\theta c\psi - c\phi s\psi & c\phi s\theta c\psi + s\phi s\psi \\ c\theta s\psi & s\phi s\theta s\psi + c\phi c\psi & c\phi s\theta s\psi - s\phi c\psi \\ -s\theta & s\phi c\theta & c\phi c\theta \end{bmatrix} \begin{bmatrix} u \\ v \\ w \end{bmatrix}
\end{aligned} \tag{5.3.3}$$

5.3.1 Simplified Equations of Trim

Appendix F on page 331 explores the trim equations. Equation (F.1.12) on page 336 presents the most general equation of trim. Derivation of the trim equations use the following considerations where they apply

1. the linear and angular trim velocity vector is constant or equal to zero
2. for symmetric flight, the trim velocities are set to zero
3. small angle approximation apply such that $\sin \theta \approx \theta$ and $\cos \theta \approx 1$
4. the thrust generated by the main rotor T and the helicopter weight $W = mg$ dominate the force related dynamics.
5. small drag terms multiplied by small angles are of much less in magnitude than the thrust T and the weight W

Given the above conditions, then equation (F.1.15) on page 338 present a set of trim equations

$$\begin{aligned}
 0 &= W - T_{MR} \\
 0 &= D + H_{MR} - T_{MR} \theta_F \\
 0 &= Y_{MR} + T_{TR} + Y_F + T_{MR} \phi_F \\
 0 &= M_{yMR} + M_{yF} + W (h \theta_F - x_{CM}) - h D \\
 0 &= M_{xMR} + M_{xF} + W (h \phi_F - y_{CM}) + T_{TR} h_{TR} \\
 0 &= Q_{MR} - Y_{TR} l_{TR}
 \end{aligned} \tag{5.3.4}$$

5.3.2 Linear Equations of Motion about Trim

Section F.1.2 on page 339 derives the linear equations of motion about the trim condition

$$\begin{aligned}
 \dot{u} + q w_0 &= \frac{X}{m} \\
 \dot{v} + r u_0 - p w_0 &= \frac{Y}{m} \\
 \dot{w} - q u_0 &= \frac{Z}{m} \\
 I_x \dot{p} - I_{zx} \dot{r} &= L \\
 I_y \dot{q} &= M \\
 I_z \dot{r} - I_{zx} \dot{q} &= N
 \end{aligned} \tag{5.3.5}$$

The equivalent state space representation of the linear equations of motion is given by Equation (F.1.21) on page 339

$$\dot{x} = Ax + Bu(t) + d(t) \tag{5.3.6}$$

where the state and control vector are given by Equation (F.1.24) on page 340

$$\begin{aligned}
 x &= \begin{bmatrix} u & w & q & \theta & v & p & r & \phi \end{bmatrix}^T \\
 u &= \begin{bmatrix} \theta_0 & \theta_{1s} & \theta_{1c} & \theta_{0TR} \end{bmatrix}^T
 \end{aligned} \tag{5.3.7}$$

The elements of the input control vector u are the main rotor collective, longitudinal and lateral cyclic, and the tail rotor collective input.

The respective longitudinal and lateral stability matrices are

$$\begin{aligned}
 A_{lon} &= \begin{bmatrix} X_u & X_w - q_0 & X_q - w_0 & -g \cos \theta_0 \\ Z_u + q_0 & Z_w & Z_q + u_0 & -g \cos \phi \sin \theta_0 \\ \bar{M}_u & \bar{M}_w & \bar{M}_q & 0 \\ 0 & 0 & \cos \phi_0 & 0 \end{bmatrix} \\
 A_{lat} &= \begin{bmatrix} Y_v & Y_p + w_0 & Y_r - u_0 & g \cos \phi \cos \theta_0 \\ \bar{L}_v & \bar{L}_p + \bar{I}_{pr}q_0 & \bar{L}_r - \bar{I}_p q_0 & 0 \\ \bar{N}_v & \bar{N}_p - \bar{I}_r q_0 & \bar{N}_r - \bar{I}_{pr}q_0 & 0 \\ & 1 & \cos \phi_0 \tan \theta_0 & 0 \end{bmatrix}
 \end{aligned} \tag{5.3.8}$$

The cross-coupling matrices are

$$\begin{aligned}
 A_{12} &= \begin{bmatrix} X_v + r_0 & X_p & X_r + v_0 & 0 \\ Z_v - p_0 & Z_p - v_0 & Z_r & -g \sin \phi \cos \theta_0 \\ \bar{M}_v & \bar{M}_p \cdots & \bar{M}_r \cdots & 0 \\ & -\bar{I}_q r_0 - 2\bar{I}_{zx}p_0 & -\bar{I}_q p_0 + 2\bar{I}_{zx}r_0 & \\ 0 & 0 & -\sin \phi_0 & \bar{K}_\phi \end{bmatrix} \\
 A_{21} &= \begin{bmatrix} Y_u - r_0 & Y_w + p_0 & Y_q & -g \sin \phi \sin \theta_0 \\ \bar{L}_u & \bar{L}_w & \bar{L}_q + \bar{I}_{pr}p_0 - \bar{I}_p r_0 & 0 \\ \bar{N}_u & \bar{N}_w & \bar{N}_q - \bar{I}_r p_0 - \bar{I}_{pr}r_0 & 0 \\ 0 & 0 & \sin \phi_0 \tan \theta_0 & \bar{K}_\theta \end{bmatrix}
 \end{aligned} \tag{5.3.9}$$

The control matrix is given as

$$B = \begin{bmatrix} B_{lon} \\ B_{lat} \end{bmatrix} \tag{5.3.10}$$

where the longitudinal and lateral control matrices are

$$B_{lon} = \begin{bmatrix} X_{\theta_0} & X_{\theta_{1s}} & X_{\theta_{1c}} & X_{\delta_T} \\ Z_{\theta_0} & Z_{\theta_{1s}} & Z_{\theta_{1c}} & Z_{\delta_T} \\ \bar{M}_{\theta_0} & \bar{M}_{\theta_{1s}} & \bar{M}_{\theta_{1c}} & \bar{M}_{\theta_{TR}} \\ 0 & 0 & 0 & 0 \end{bmatrix} \quad B_{lat} = \begin{bmatrix} Y_{\theta_0} & Y_{\theta_{1s}} & Y_{\theta_{1c}} & Y_{\delta_T} \\ \bar{L}_{\theta_0} & \bar{L}_{\theta_{1s}} & \bar{L}_{\theta_{1c}} & \bar{L}_{\delta_T} \\ \bar{N}_{\theta_0} & \bar{N}_{\theta_{1s}} & \bar{N}_{\theta_{1c}} & \bar{N}_{\delta_T} \\ 0 & 0 & 0 & 0 \end{bmatrix} \quad (5.3.11)$$

5.4 Stability Derivatives

Section G on page 342 looks into the stability derivatives that affect the helicopter coupled rotor-fuselage equations of motion.

Chapter 6

Helicopter Sensors

6.1 Signals and Sensors

Table 6.1 summarizes the sensors available to the OU research helicopter.

Table 6.1: Sensors

main rotor angular velocity	Ω	hall effect sensor
body inertial angular rates	p, q, r	pizo-elec rate gyro, MotionPak
angular attitude angles	ϕ, θ, ψ	electronic compass
body inertial linear acceleration	$\dot{u}, \dot{v}, \dot{w}$	pizo-elec accelerometers, MotionPak
inertial position	x, y	differential GPS
altitude above ground	z	ultrasound/infrared transducers
on-board battery voltage	V_{bat}	analog-to-digital transducer
blade pitch angles (static mea.)	θ_{blade}	inclinometer

6.2 Main Rotor Angular Velocity Measurement

The engine, main rotor, tail rotor and transmission angular velocities are related via fixed gears relations. The belt that transmits angular motion from the engine to the main rotor is flexible, and thus the belt drive provides a degree of damping. The remaining set of transmission gears are fixed. Therefore, measurements of the main rotor angular velocity provides an estimate for the angular velocity of all rotating components. Table I.1 on page 372 tabulates various parameters that characterize the rotating components including the overall rotational inertia I_{rot} . Equation (C.1.17) on page 208 indicates that the main rotor angular velocity Ω is a most fundamental parameter due to the large

magnitude of the angular velocity for model helicopters ($\Omega \approx 1500 \text{ rpm}$) and it is being raised to the second or higher power in each of the thrust T , torque Q and power P expressions.

$$T = \rho \pi R^2 (\Omega R)^2 C_T Q = \rho \pi R^2 (\Omega R)^2 R C_Q P = \rho \pi R^2 (\Omega R)^3 C_P \quad (6.2.1)$$

where C_T , C_Q , C_P are the thrust, torque and power coefficients respectively. In turn, the thrust T and the thrust coefficient C_T are necessary to compute the main rotor blade pitch angle to generate the proper lift as indicated in equation (C.2.15) on page 227

$$\theta = \frac{6}{a\rho} C_T + \frac{3}{2} \sqrt{\frac{C_T}{2}} \quad (6.2.2)$$

The torque Q is necessary to compute the tail rotor compensating torque as indicated by the trim equation equation (F.1.15) on page 338

$$0 = Q_{MR} - Y_{TR} l_{TR} \quad (6.2.3)$$

and the overall power P is necessary to compute the engine throttle setting as indicated by equation (L.2.9) on page 437.

$$Y_{TR} = \left[\frac{Q_{MR} + n_{TR} Q_{TR}}{l_{TR}} \right]_{\dot{r}=0} \quad (6.2.4)$$

6.2.1 Main Rotor Angular Velocity Ω Measurement via a Hall Effect Sensors

The Helicopter's main rotor gear has three permanent magnets embedded at 120° of each other as shown in Figure 2.15 on page 27. The permanent magnet swoops very closely by a hall effect sensor embedded in the helicopter's frame as shown in Figure 2.16 on page 28. Each time the magnet is next to the sensor, the sensor activates a pulse that

is detected by an on-board computer. The estimation of the main rotor angular velocity follows directly by counting the time lapse between pulse events.

6.3 Fuselage Linear Acceleration and Angular Velocity Measurements

The Systron Donner *MotionPak* precision sensor suite measures the fuselage linear inertial accelerations and the body inertial angular rates. Both the linear accelerations and the angular rates were calibrated with the use of the rate table shown in Figure 2.19 on page 30.

Section I.2.1 on page 376 on Appendix I details the most important parameters pertaining to the MotionPak sensor.

6.3.1 MotionPak Sensor Suite Location

The actual location of the MotionPak sensor suite is very important. Figure 6.1 on the following page shows the MotionPak rigidly attached to a structure at the nose of the helicopter. This position is far from the engine heat with cooling airflow from the main rotor wake, but the location is not optimal due to excessive vibrations encountered at this location. Figure 6.2 on the next page shows the relocation of the MotionPak sensor suite rigidly attached beneath the engine, closer to the center of mass. A thermal cover over the MotionPak (not shown) deflected the hot air pushed along the sides of the engine by the cooling fan. Figure 6.3 on page 72 presents the MotionPak measurements of the linear accelerations (\dot{u}, \dot{v}) and angular rates (p, q) during a real-time test run when the helicopter is constrained to move only along the z -axis. The acceleration and rates should be nearly zero during this run, but both the measured accelerations and rates vary widely in amplitude rendering the data useless for feedback control or navigation purposes.



Figure 6.1: MontionPak Sensor Suite Location at front of the Helicopter.

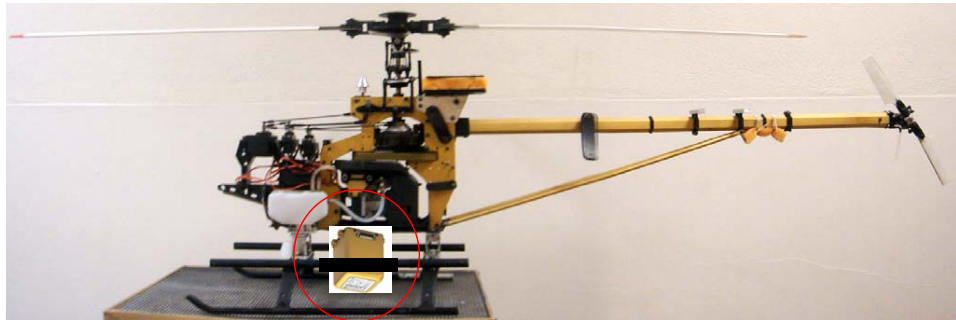


Figure 6.2: MontionPak Sensor Suite rigidly attached to the fuselage and positioned beneath the engine, close to the vehicle's center of mass.

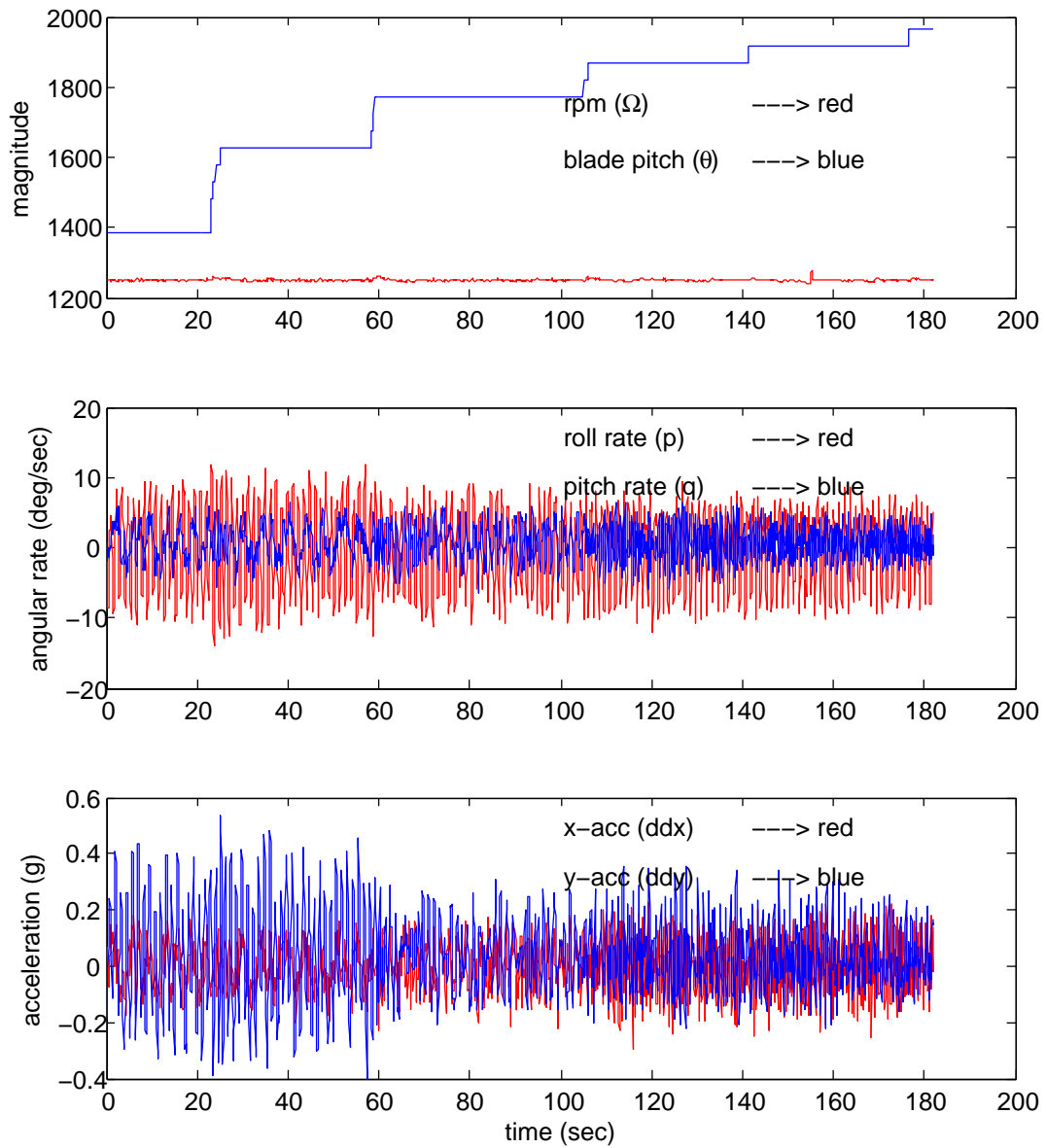


Figure 6.3: MotionPak linear accelerations (\dot{u} , \dot{v}) and angular rates (p , q) measurements with sensor suite positioned beneath the engine close to the vehicle's center of mass. Data collected during a test run with main rotor angular velocity Ω actively controlled in real-time.

Figure 6.4 on the next page shows the MotionPak sensor suite mounted on vibration isolation pads, and Figure 6.5 on the following page is a close-up of the MotionPak as mounted on the helicopter. Figure 6.6 on the next page is a photo montage that shows the MotionPak position in the helicopter relative to the main rotor, tail rotor and engine. Figure 6.7 on page 75 shows data collected during a test run with roll, pitch and yaw actively controlled in real-time. The blue curve on the top graph is the measured heading ψ , the black curve is the command heading ψ_C , the red curve is the yaw rate, the green curve is the measured main rotor angular velocity Ω , the magenta curve is the tail rotor autopilot command, and the dark-green curve is the main rotor blade pitch angle θ command. Figure 6.8 on page 76 shows the Gaussian distribution of the collected data for runs with the MotionPak rigidly attached to the helicopter frame, and for data collected with the MotionPak mounted on the vibration isolation pads. The plots indicate that the data quality is more than one order of magnitude better than data measured prior to mounting the MotionPak on vibration isolation pads. 6.2 tabulates the standard deviation of two data runs. The first data run on the left column was taken with the MotionPak rigidly mounted underneath the engine, and the second data run on the right column was taken with the MotionPak mounted on isolation pads.

Table 6.2: Standard Deviation of MotionPak Measured Data.

Mounting Option \rightarrow	<i>Rigidly-Attached</i>	<i>Isolation-Pads</i>
linear x-axis velocity \dot{u}	0.0887	0.0191
linear x-axis velocity \dot{v}	0.1501	0.0276
roll rate p	5.5546	0.0575
pitch rate q	2.4315	0.0399



Figure 6.4: Photo montage of the MontionPak Sensor Suite mounted on vibration isolation pads.



Figure 6.5: MontionPak Sensor Suite mounted on vibration isolation pads and positioned beneath the helicopter engine.

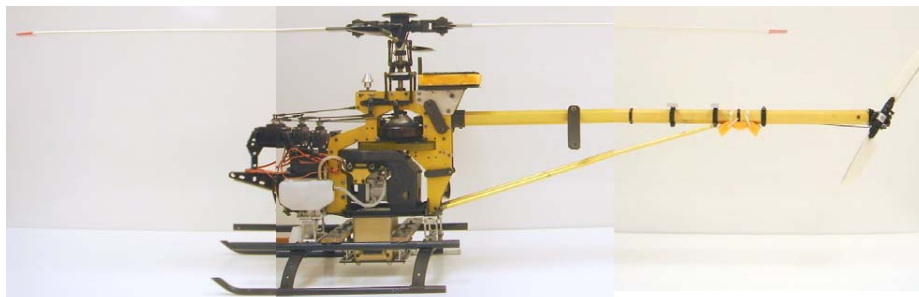


Figure 6.6: MontionPak Sensor Suite positioned beneath the engine and mounted on vibration isolation pads.

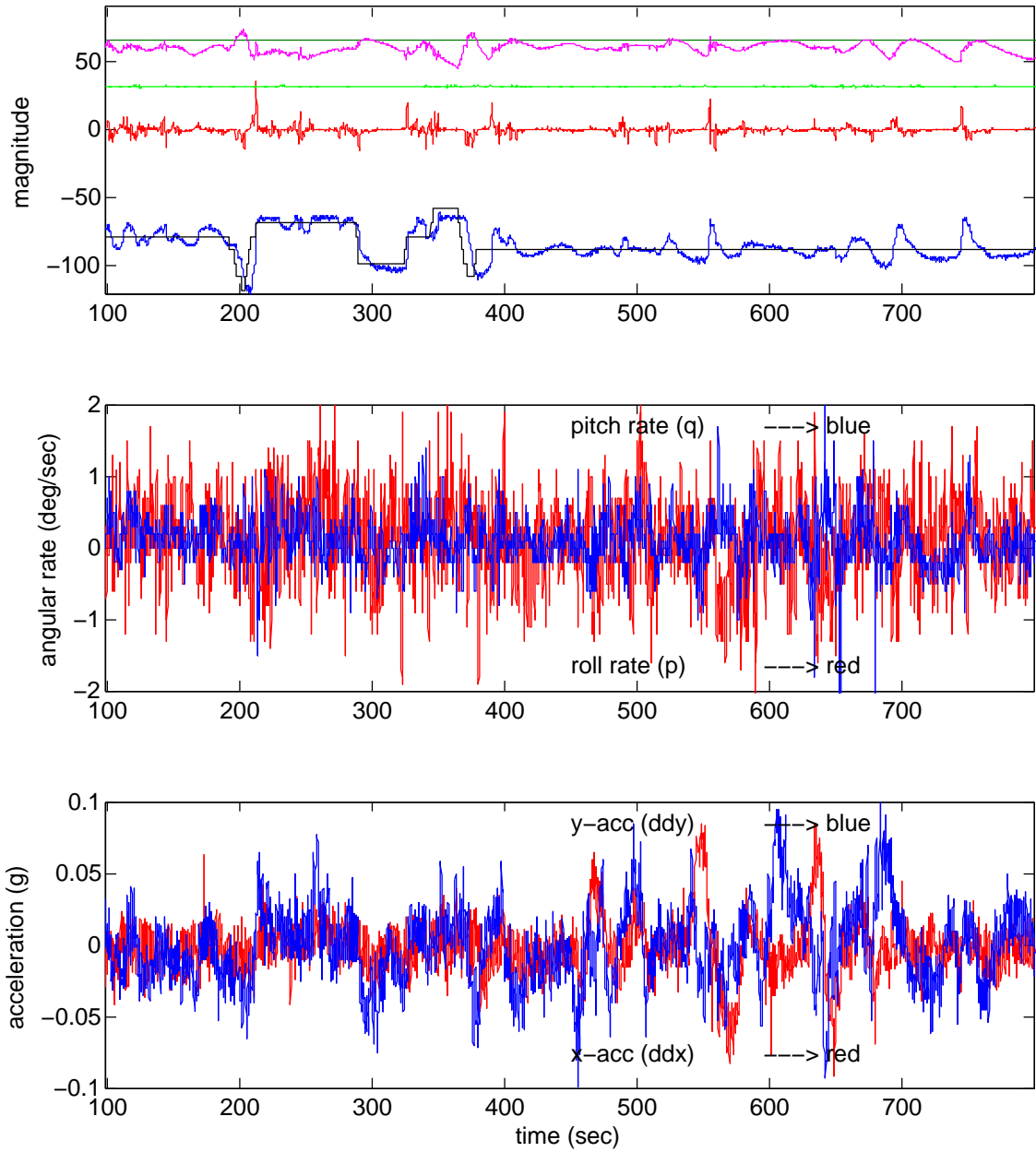


Figure 6.7: MotionPak linear accelerations (\dot{u} , \dot{v}) and angular rates (p , q) measurements with sensor suite positioned beneath the engine and mounted on vibration isolation pads. Data collected during a test run with roll, pitch and yaw actively controlled in real-time.

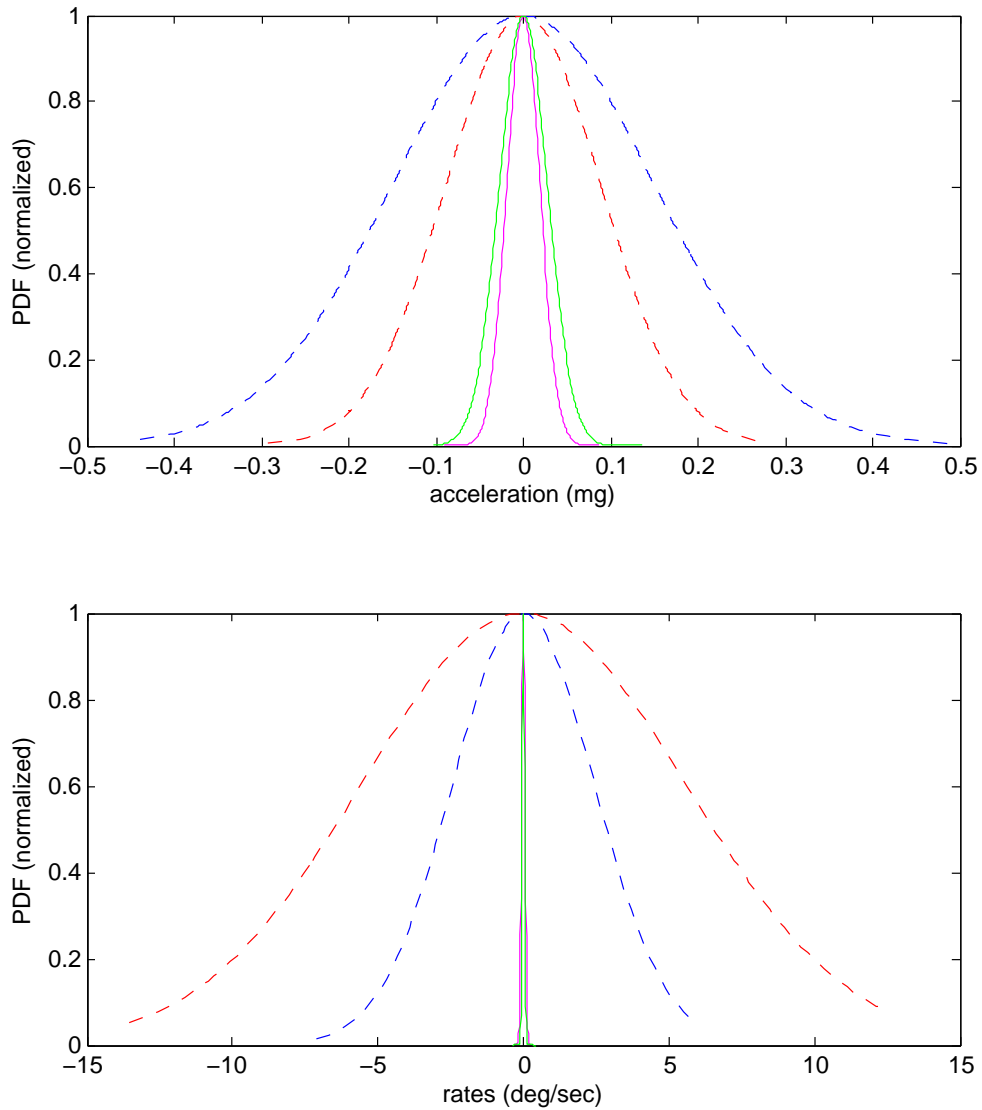


Figure 6.8: MontionPak Sensor Suite distribution for linear acceleration (x, y) and angular rates (p, q). The dash-dash curves present data taken with the MotionPak rigidly attached to the fuselage, and the solid curves present measured data with the MotionPak mounted on vibration isolation pads.

6.4 Center of Mass Position

Position information comes from differential GPS setup that uses the NovAtel ProPack reference station and MiLLennium II RTK2 GPScard as the dynamic GPS engine (Section I.2.2 on page 378). The GPS latitude and longitude are converted to Earth Centered Earth Fixed Coordinate (Section B.1.8 on page 181) system using the WGS-84 ellipsoidal datum and the standard algorithm [].

$$\begin{aligned}X &= (N + h) \cos \phi \cos \lambda \\Y &= (N + h) \cos \phi \sin \lambda \\Z &= [N (1 - e^2) + h] \sin \phi \\N(\phi) &= \frac{a}{\sqrt{1 - e^2 \sin^2 \phi}} \\f &= \frac{a - b}{a} \\e^2 &= 2f - f^2\end{aligned}\tag{6.4.1}$$

and the following holds

- ϕ, λ, h are the geodetic latitude, longitude, and hight above ellipsoid.
- X, Y, Z are the Earth-Centered Earth-Fixed Cartesian Coordinates.
- $N(\phi)$ is the radius of curvature in prime vertical.
- a is the semi-major Earth axis (ellipsoid equatorial radius).
- b is the semi-major Earth axis (ellipsoid polar radius).
- f is the Earth flattening.
- e^2 is the eccentricity squared.

Helicopter flight involves angular dynamics that are inherently faster than the Earth's rotation Ω_E . Therefore a large number of helicopter flight missions neglect the Earth's

rotation and assume a non-rotating earth approximation. In addition, the three dimensional displacements and velocities involved in most helicopter maneuvers do not require taking into account the curvature of the Earth. Therefore it is reasonable to accept a locally flat Earth approximation for helicopter missions of short duration. For any particular mission, the distance traveled is known by computing the differential ECEF coordinates from the current position to the starting position. The differential ECEF coordinates computed on board the helicopter correspond to a particular place on the GPS antenna. Simple geometry transfers this knowledge to the helicopter's center of mass.

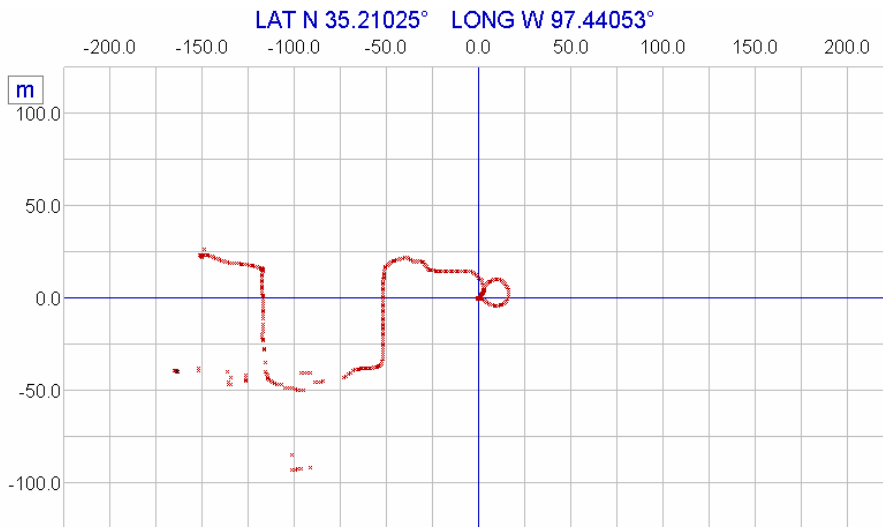


Figure 6.9: Differential GPS Experiment at the University of Oklahoma. Portions of differential data loss are the result of positioning the GPS antenna under a tree canopy.

6.5 Helicopter Body Attitude

Section I.2.6 on page 384 presents the specifications related to the Honeywell HMR3000 electronic compass. The compass gives information at a rate of 10 Hz about the roll ϕ , pitch θ and heading angle ψ attitude of the helicopter. The compass's input stream passes through non-linear filters that keep missed readings from corrupting the data.

6.6 Center of Mass Altitude

Section I.2.8 on page 388 presents data pertaining to the ultrasound transducers used in the helicopter. The helicopter has three ultrasound transducers working in unison in an attempt to provide redundant altitude information and attitude information. The ultrasound interfaces with a host CPU via digital input/output, and the host CPU controls the sensitivity of the various ultrasounds by varying the setting on a digital potentiometer.

Chapter 7

Design of the Helicopter Feedback Control Loops

7.1 Engine Governor and Main Rotor RPM Control Loop

Figure 7.1 on the following page presents a block diagram of the the engine governor and the main rotor angular velocity control loop. A component of the available torque Q_e generated by the engine is utilized to turn the main rotor and to drag the main rotor blades through the air. When an equilibrium point exists, the difference between the available engine torque and the summation of all required torques will be zero $Q_e - \Sigma = 0$, and the angular velocity will remain constant. To ensure that this is the case in all flight conditions, the main rotor angular velocity Ω is subtracted from a reference or command angular velocity Ω_C to generate an error signal equal to the difference $error_\Omega = \Omega_C - \Omega$. The error signal $error_\Omega$ serves as an input to a proportional plus integral (PI) compensator which will output a differential command δ_{th} to the throttle electro-mechanical digital servo. The end result is a control loop that will track a desired main rotor angular velocity Ω .

7.2 Yaw Rate and Heading Control Loop

Figure 7.2 on page 82 shows a graphical representation of the torque equilibrium about the Center of Mass (CM) along the z-axis. The engine generates torque to turn the main and tail rotors and to drag the main and tail rotor blades. Since the engine is attached to

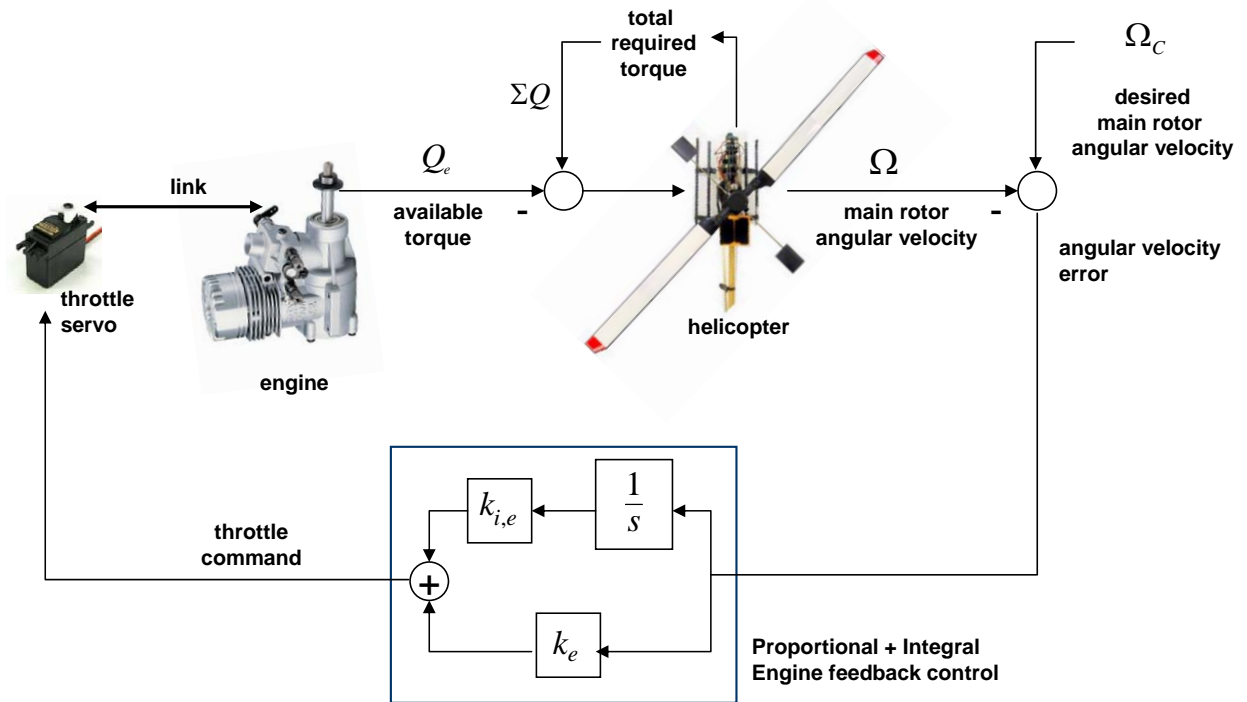


Figure 7.1: Block diagram for the engine governor and main rotor angular velocity control loop.

the fuselage, the fuselage responds with an equal but opposite reaction torque. The tail rotor compensates by generating sufficient thrust T_{TR} such that, when multiplied with the moment arm l_{TR} , the tail-rotor-compensating torque $l_{TR} \cdot T_{TR}$ is equal but opposite to the fuselage torque. Figure 7.3 on page 83 shows two instances of tail rotor collective pitch angle. In the first case (1), the thrust generated by the tail rotor is in the negative y -direction. In the second case (2), the thrust is in the positive y -direction and provides proper compensation.

Figure 7.4 on page 84 presents a block diagram for the yaw rate and heading control loop. The heading measurement ψ is subtracted from the desired heading setting ψ_C , and the heading error $error_\psi$ is the input to the proportional plus integral (PI) heading feedback control compensator. A proportional yaw rate measurement also contributes to the output of the compensator that provides a differential input to the tail rotor collective blade pitch angle command. The loop is designed to track the desired heading and to

reject disturbances at the tail rotor.

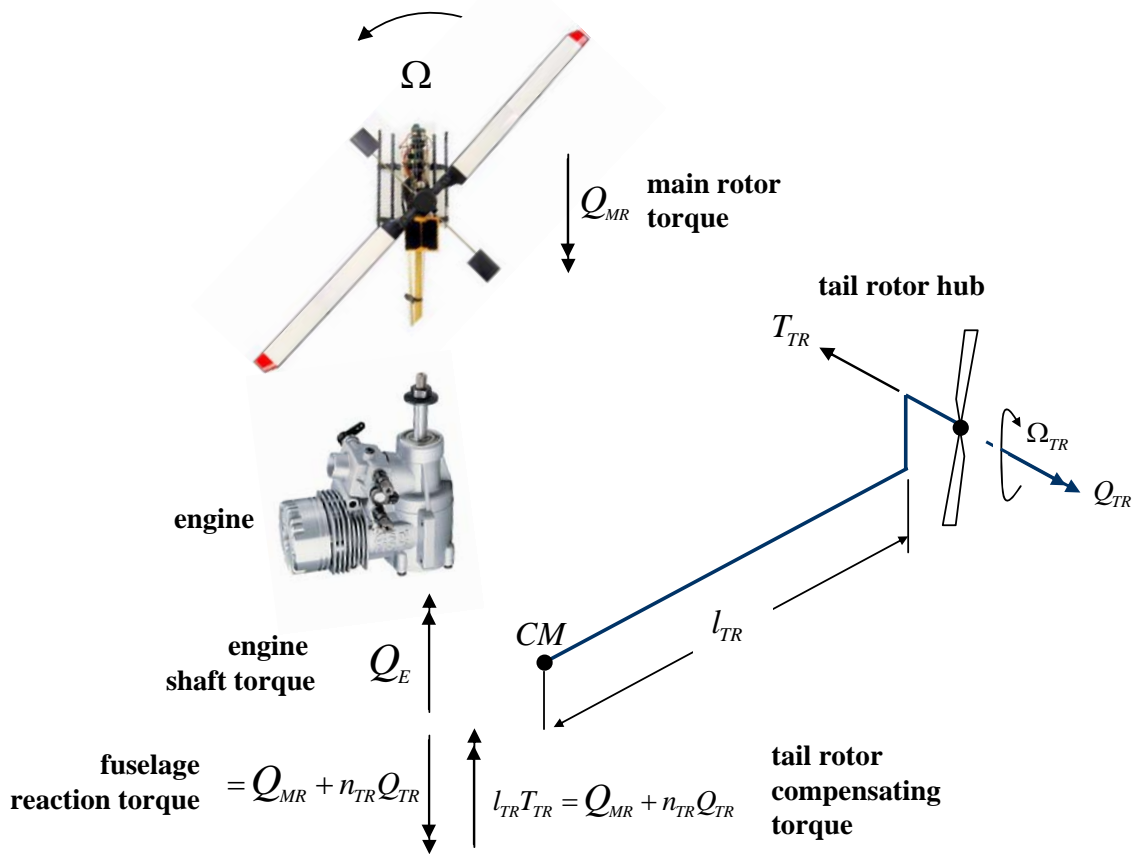


Figure 7.2: Torque Equilibrium about the Center of Mass (CM) along the z-axis. In the figure, Ω is the main rotor angular velocity, Ω_{TR} is the tail rotor angular velocity, Q_E , Q_{MR} , Q_{TR} are the engine available torque, the main rotor torque and the tail rotor torque respectively. In addition, n_{TR} is the main rotor to tail rotor gear ratio, and l_{TR} is the location of the tail rotor hub behind the CM.

7.3 Pitch Rate and Pitch Attitude Control Loop

Figure 7.5 on page 84 shows the swashplate longitudinal inputs δ_{lon} to the main rotor blade pitch angle θ . In the first case (1), the longitudinal cyclic forces the main rotor blade to reach a maximum angle of attack at the 90° blade azimuth station (positive y-axis at the right side of the aircraft). At this azimuth point, the blade experiences the largest thrust, which in turn forces the blade to flap upward. The blade reaches its maximum flapping angle at the nose of the aircraft which has the effect of tilting the Tip

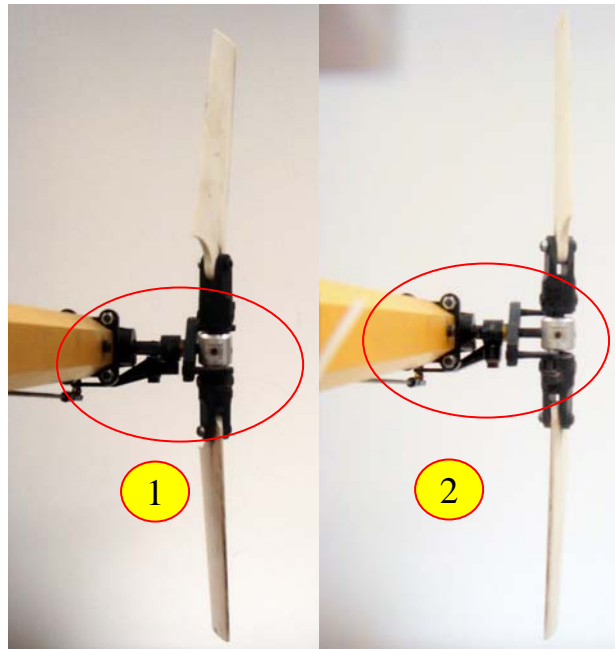


Figure 7.3: Tail Rotor collective pitch angle. In the figure, the tail rotor collective pitch angle (1) generates the least thrust as illustrated in Figure 7.2 on the previous page, and the thrust may even be in the opposite direction. The tail rotor collective pitch angle (2) is in the same direction as in Figure 7.2, and provides proper compensation.

Path Plane (TPP) and the rotor thrust vector rearward. A rearward tilt of the thrust vector causes the nose of the aircraft to pitch up. In the same figure, the swashplate longitudinal input (2) causes the blade to reach its maximum angle of attack at the blade azimuth station of 270° degrees (negative y-axis at the left side of the aircraft). In this case the maximum thrust at this location causes the blade to flap to its most upward angle at the blade azimuth station of 0° degrees. The TPP tilts up at this location and down at the nose of the aircraft, and the thrust vector follows soon thereafter. The result is a nose-down fuselage attitude.

Figure 7.6 on page 85 shows a block diagram in which a pitch attitude error $error_\theta$ is the input to a proportional plus integral compensator. A proportional pitch rate q adds to the output of the PI compensator to generate a differential input to the longitudinal cyclic servo.

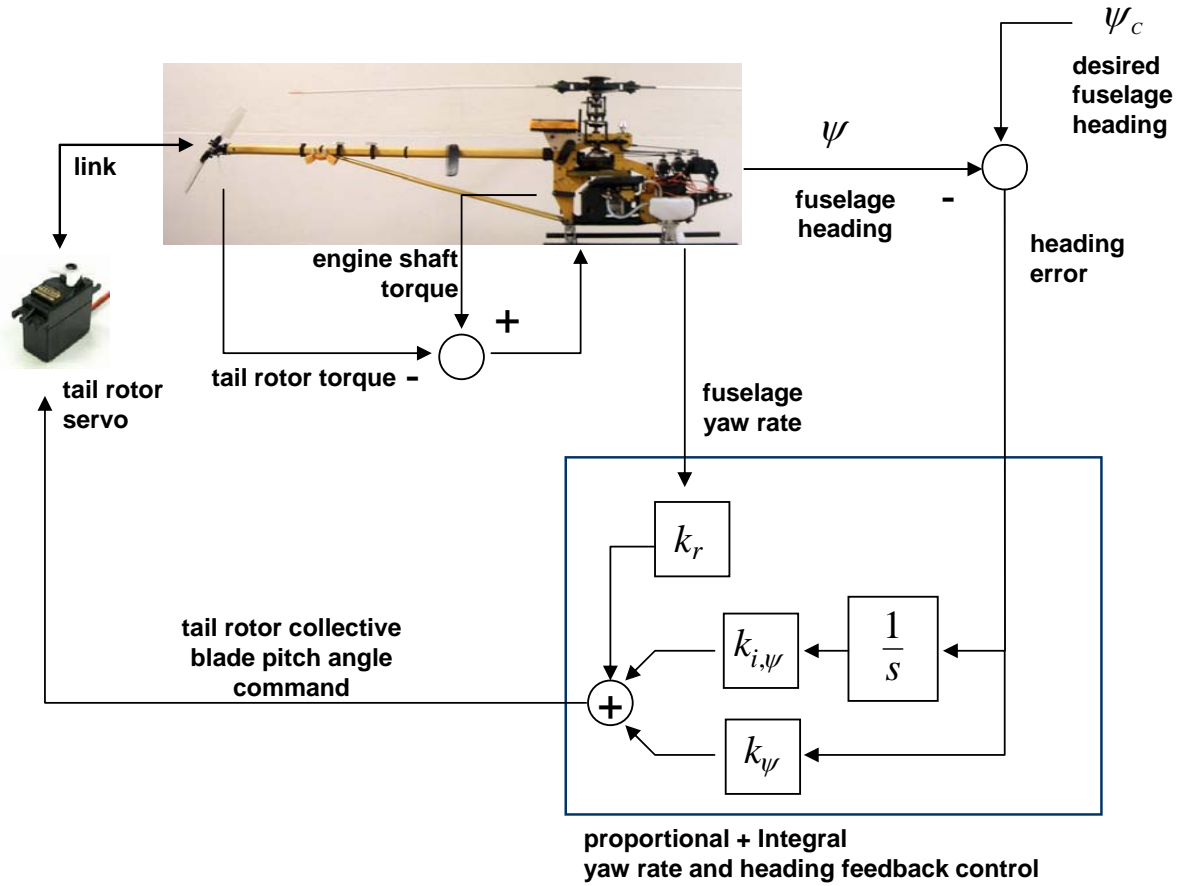


Figure 7.4: Block diagram for yaw rate and heading angle control loop.

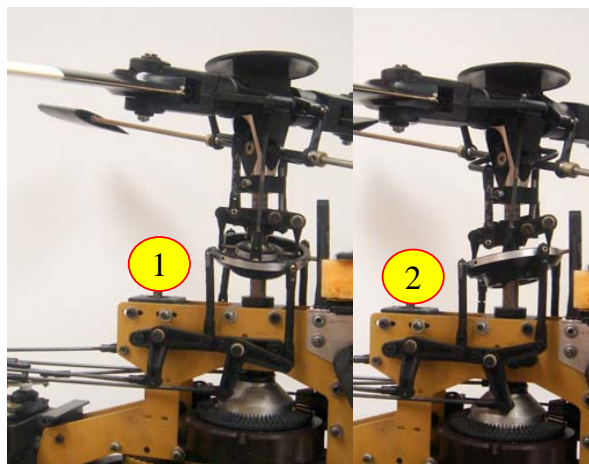


Figure 7.5: Swashplate longitudinal cyclic control input. In the figure, the swashplate position (1) inputs longitudinal cyclic to the main rotor blade pitch angle that will result in a nose-up tilt of the fuselage. The swashplate position (2) inputs longitudinal cyclic to the main rotor blade pitch angle that will result in a nose-down tilt of the fuselage.

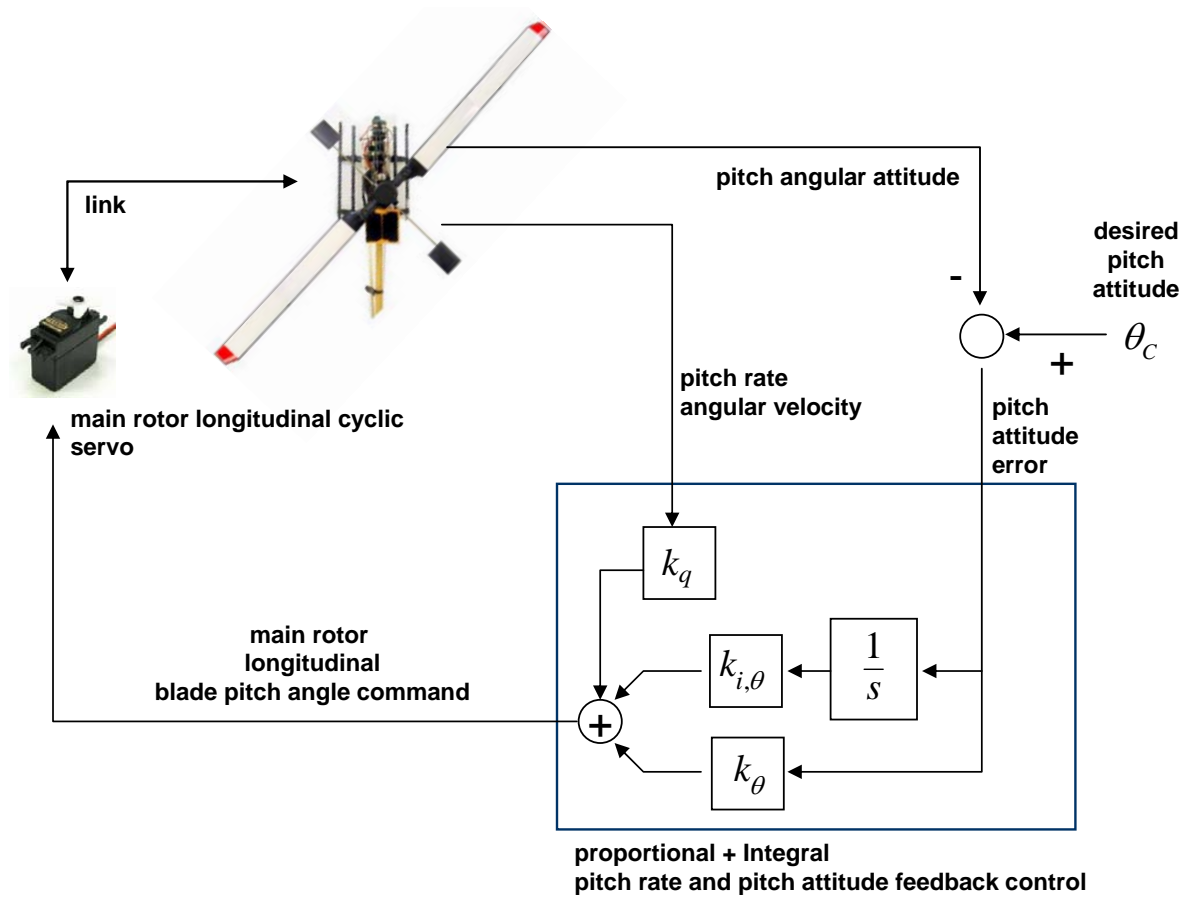


Figure 7.6: Block diagram for longitudinal pitch rate q and pitch attitude θ control loop.

7.4 Roll Rate and Roll Attitude Control Loop

Figure 7.7 on the following page shows the swashplate lateral inputs δ_{lat} to the main rotor blade pitch angle θ . In the first case (1), the lateral cyclic reaches maximum angle of attack at the 180° blade azimuth station (positive x-axis at the nose of the aircraft). At this azimuth point the blade experiences the largest thrust, which in turn forces the blade to flap upward at this location. The blade reaches its maximum flapping angle at the left side of the aircraft which has the effect of tilting the Tip Path Plane (TPP) and the rotor thrust vector to the right. A positive tilt of the thrust vector causes the fuselage to roll to the right. In the same figure, the swashplate longitudinal input (2) causes the blade to reach its maximum angle of attack at the blade azimuth station of 0° degrees (at the rear of the aircraft). In this case the maximum thrust at this location causes the blade to flap to its most upward angle at the blade azimuth station of 90° degrees blade azimuth station (positive y-axis at the right side of the aircraft). The TPP tilts up at this location and down at the left of the aircraft, and the thrust vector follows soon thereafter. The result is a left roll of the fuselage attitude.

Figure 7.8 on the next page shows a block diagram for the lateral roll rate q and roll attitude ϕ feedback loop. A proportional plus integral compensator takes as its input the roll attitude error $error_\phi$, and a proportional component of the roll rate q adds to the compensator output to provide a lateral cyclic δ_{lat} to the lateral cyclic servo.

7.5 Altitude Control Loop

Figure 7.9 on page 88 shows a photo montage of the swashplate with no cyclic inputs, and therefore the swashplate remains horizontal with respect to the x-y plane of the helicopter. In this figure, position (1) corresponds to the lowest position of the swashplate at which the rotor generates negative or downward thrust. In turn, position (2) is a midway position where the rotor generates positive or upward thrust, while the swashplate

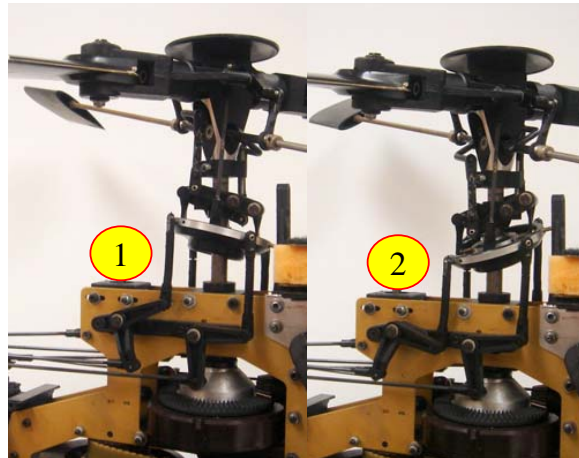


Figure 7.7: Swashplate lateral cyclic control input. In the figure, the swashplate position (1) inputs lateral cyclic to the main rotor blade pitch angle that will result in a positive roll of the fuselage. The swashplate position (2) inputs lateral cyclic to the main rotor blade pitch angle that will result in negative roll of the fuselage.

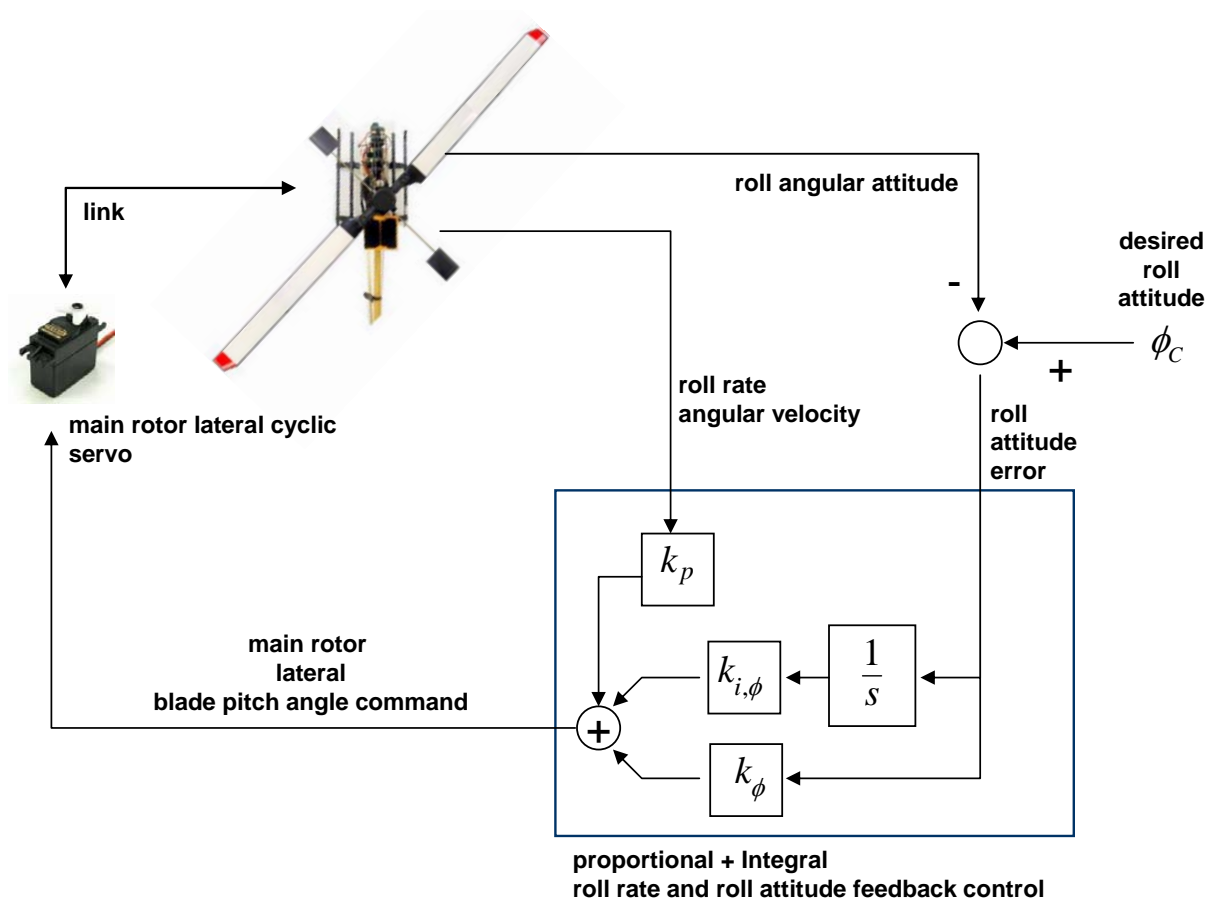


Figure 7.8: Block diagram for lateral roll rate q and roll attitude ϕ control loop.

position (3) is at its highest where the blade pitch angle will be the largest.

Figure 7.10 on the next page shows a block diagram for the baseline altitude h control loop. The vertical velocity w is estimated from the vertical acceleration measurement and the collective blade pitch angle inputs. The proportional portion of the estimated vertical velocity is added to the output of an altitude compensator that takes the altitude error $error_h$ as its input. The output of the compensator provides the differential input to the collective blade pitch angle servo.

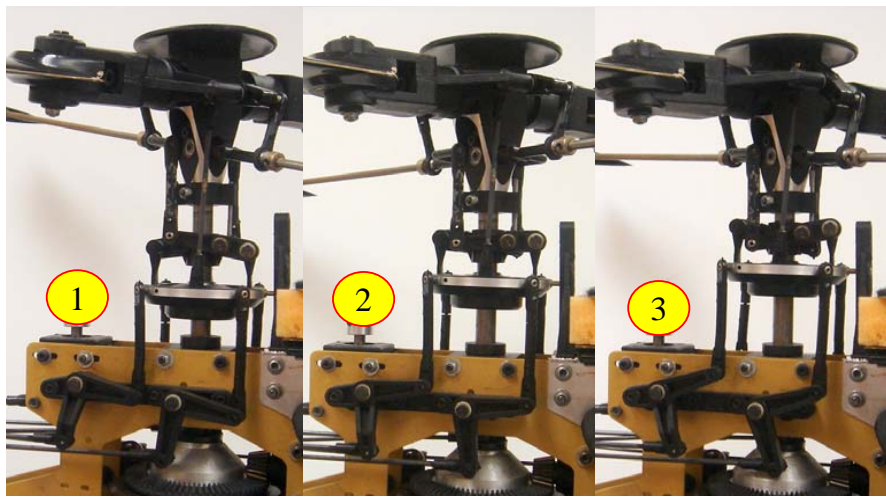


Figure 7.9: Main Rotor Collective Blade Pitch Angle Input. In the picture, the swashplate is at its lowest position at (1), mid position at (2), and highest position at (3).

7.6 Baseline Helicopter Feedback Control

Figure 7.11 on page 91 shows the baseline control design for the research helicopter. The sensor models are ignored in this diagram. The main rotor angular velocity feedback maintains a constant angular velocity Ω and decouples the rest of the control loops from this measurement. The heading feedback control loop automatically compensates for the torque induced when generating thrust. This loop decouples the engine and tail rotor torque from the remainder of the control loops. The roll and pitch rate and attitude loops stabilize the helicopter platform. The altitude hold loop provides the necessary inputs

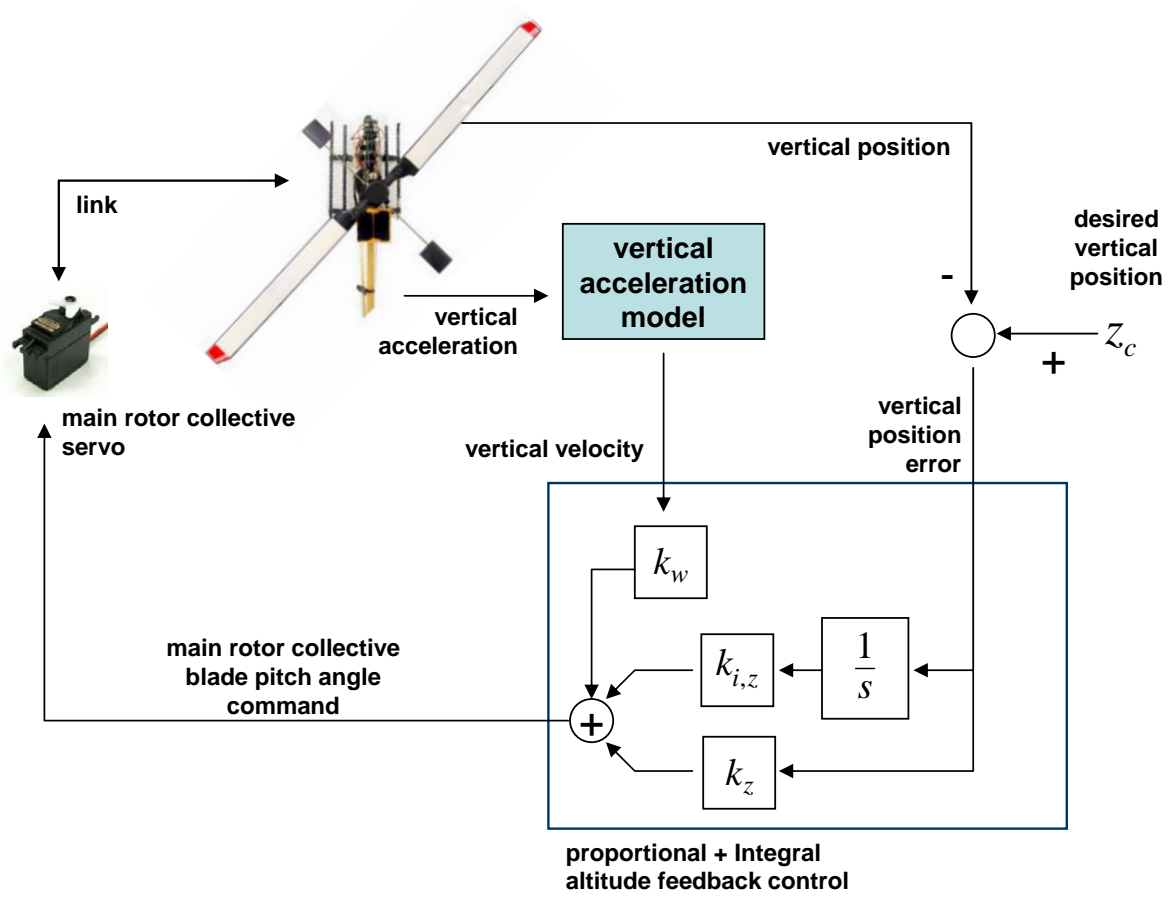


Figure 7.10: Block diagram for the altitude feedback control loop.

to maintain a desired altitude above the ground. At this point, the helicopter is a stable platform with the main rotor that serves as an actuator to provide locomotion at an altitude.

7.7 Helicopter Position Feedback Control

Figure 7.12 on page 92 shows the baseline helicopter feedback control block diagram with augmented controls to provide locomotion and position hold. The control loop is designed for position hold and small displacements. The aircraft will navigate between waypoints and hold altitude and position at the destination point.

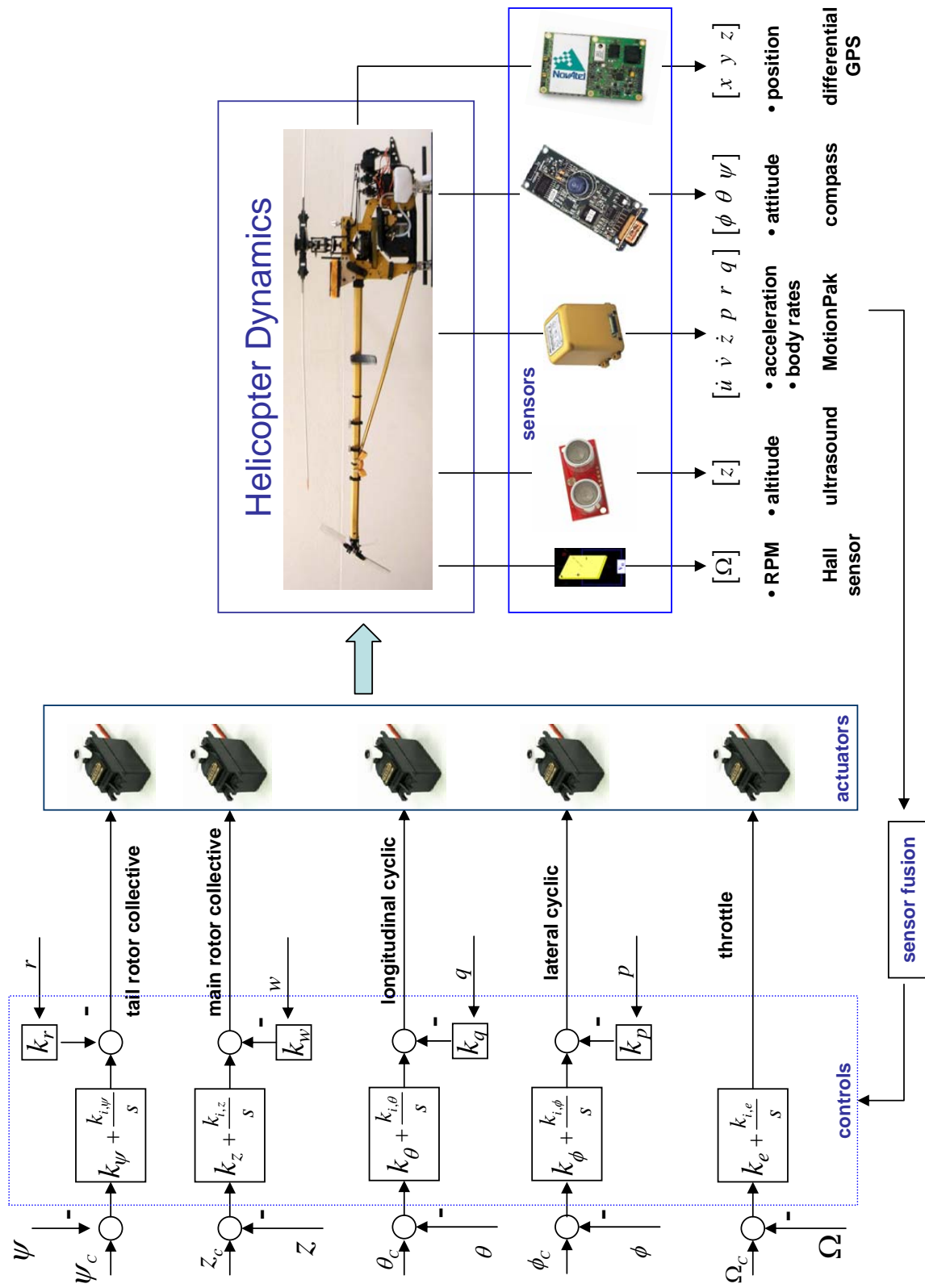


Figure 7.11: Block diagram for longitudinal and lateral feedback control.

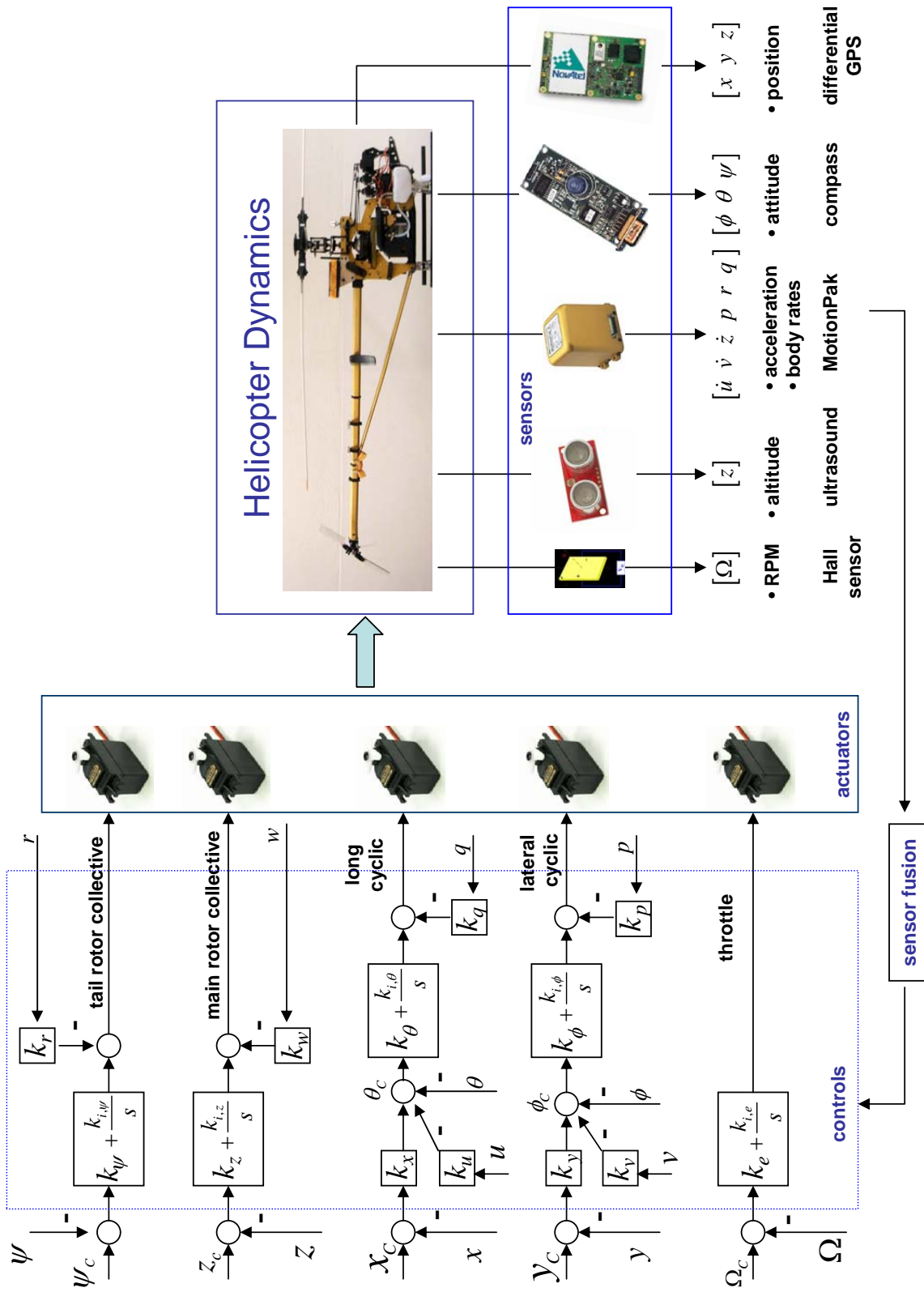


Figure 7.12: Block diagram for position hold and locomotion. Note the nested attitude, altitude and position loops.

Chapter 8

Engine Governor and Main Rotor Angular Velocity Experiment

8.1 Experiment Setup

The Linear and Directional Test Stand (LDTS) is restricted to move in the vertical direction only with a lock on the angular motion about vertical. The tail rotor collective pitch angle is disconnected to allow the tail rotor blades to spin freely to its equilibrium position. This avoids unnecessary stress on the helicopter structure and on the LDTS itself. The experiment consists of four parts

1. open loop engine and main rotor dynamics characterization
2. modeling of the open loop engine and main rotor dynamics
3. engine governor and main rotor angular velocity control design and implementation
4. testing and experimental results of closed loop feedback control

Appendix J on page 398 details the above steps, a summary of which follows.

8.1.1 Open Loop Engine and Main Rotor Dynamics Characterization

Figure 8.1 on the following page plots data characteristic of an open loop real-time test run. The inputs consists of steps in throttle command, and the collected data yields

information related to the engine-main rotor system time constant, rise time, and rotor damping, throttle gain, etc. Figure 8.2 on the next page shows an example of data extraction from open loop data. This work is detailed in Section J.2 on page 399.

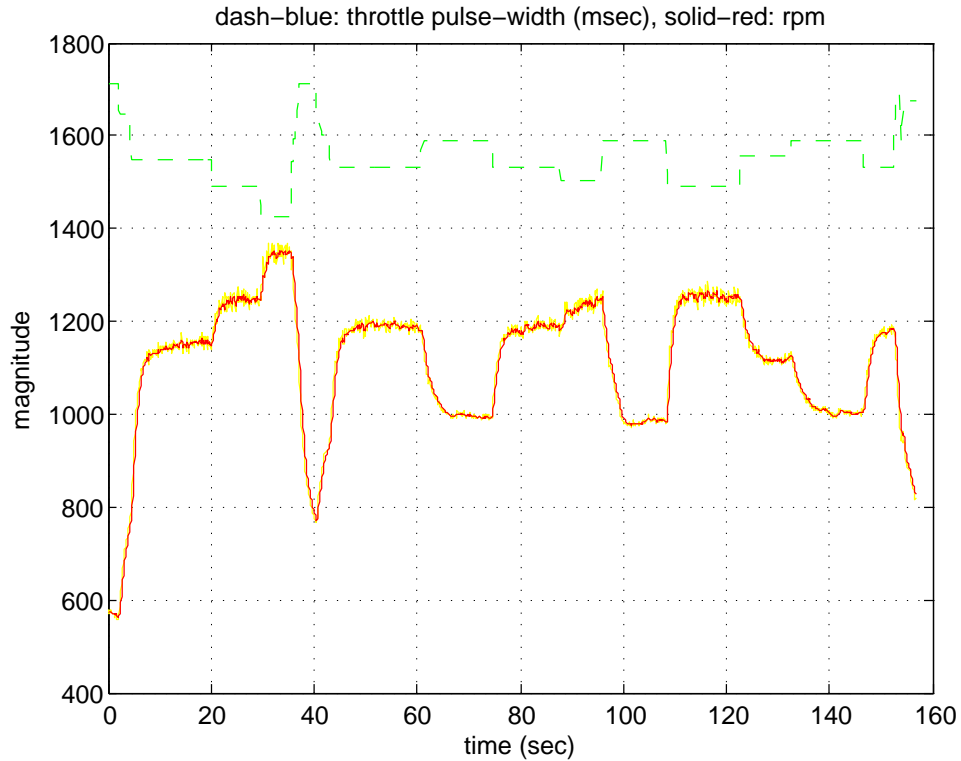


Figure 8.1: Sample Main Rotor Angular Velocity Ω data resulting from varying throttle inputs and Main Rotor Blade Pitch Angle θ set at 8 degrees.

8.1.2 Modeling of the Open Loop Engine and Main Rotor Dynamics

Figure 8.3 on page 96 presents simulation results superimposed on real-time data obtained from open loop commands to the engine-main rotor system. The block diagram in Figure 8.4 on page 96 shows the mathematical simulation model with the previously obtained time constant, rise time, rotor damping and throttle gain. The simulated data follows the collected data closely, with the caveat that the model lacks some drag terms. In contrast, the rise time and the rotor damping are captured very well by the model.

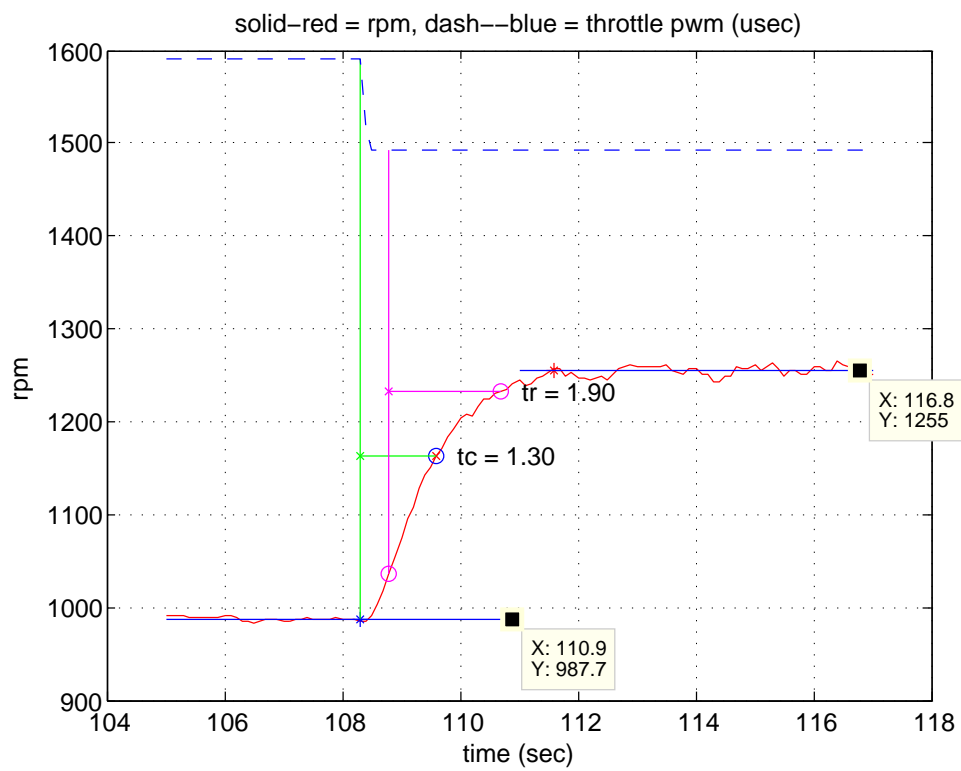


Figure 8.2: Time to Rise and Time Constant estimates for Engine/Carburetor-Main Rotor dynamic system.

This model is therefore suitable for control design. Section J.2.1 on page 404 and Section J.2.2 on page 409 detail the steps taken to arrive at these results.

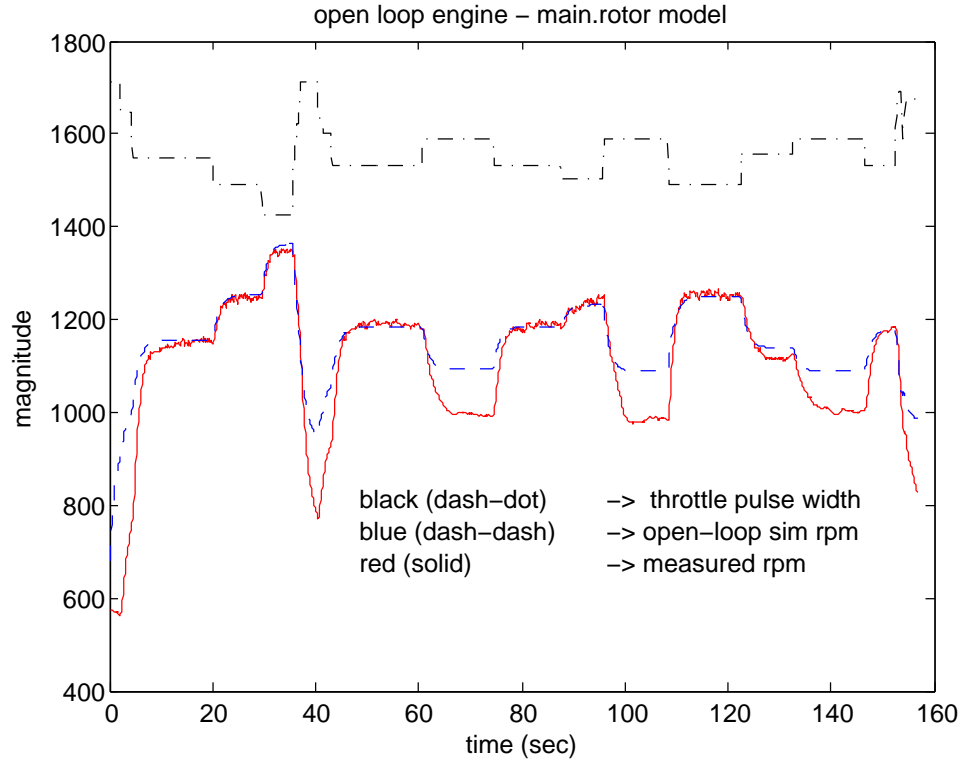


Figure 8.3: Open Loop Simulation Result for Rotor Angular Velocity Ω .

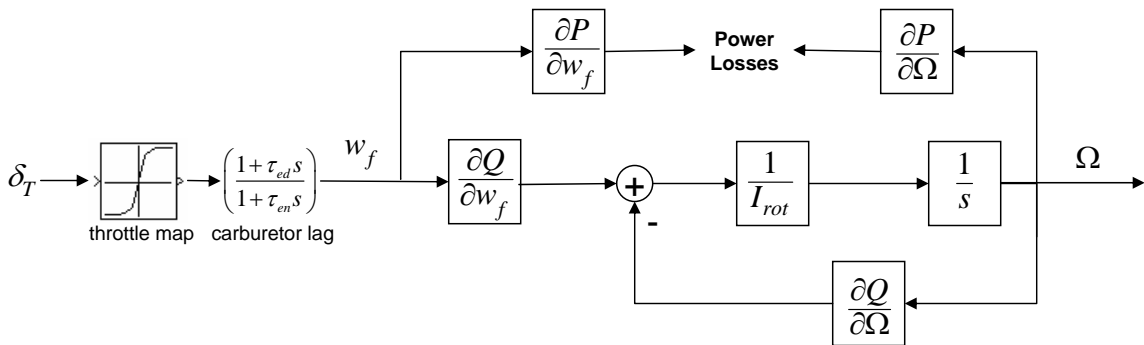


Figure 8.4: Engine-Carburetor and Main Rotor Dynamics Model.

8.1.3 Engine Governor and Main Rotor Angular Velocity Control design and implementation

Once the open model predicts the fundamental dynamics for the system that needs control, the control design can readily take place. This is done in Section J.2.3 on page 410, and Figure 8.5 shows the block diagram for the engine governor and main rotor angular velocity feedback controller.

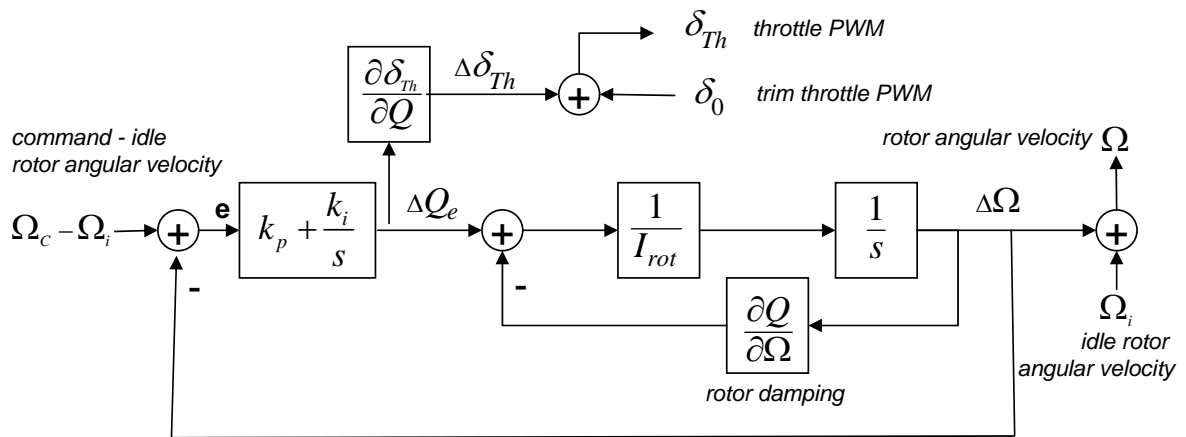


Figure 8.5: Closed-Loop Engine-Carburetor, Main Rotor Dynamics Model.

8.2 Testing and Experimental Results of Closed Loop Feedback Control

Section J.3 on page 416 summarizes the results from the engine governor and main rotor angular velocity experiments. This is the main result of the experiment; the closed loop control on Figure 8.5 is able to maintain constant angular velocity in the presence of disturbances (changing blade pitch angle) with model uncertainties. Figure 8.6 on the next page shows real-time data obtained with the system operating under closed loop feedback. The black curve present open loop changes in the main rotor blade angle of attack, and the red curve is the measured angular velocity during the test flight. The main rotor angular velocity remains constant even when the main rotor blade pitch angle

changes.

Figure 8.6 also plots the simulated data. The simulated data matches the collected data almost exactly, and the throttle command input obtained from simulation matches the actual input very closely. This is a component of the main result for the experiment, that the simulation model for the engine-main rotor system dynamics accurately predicts the real system behavior.

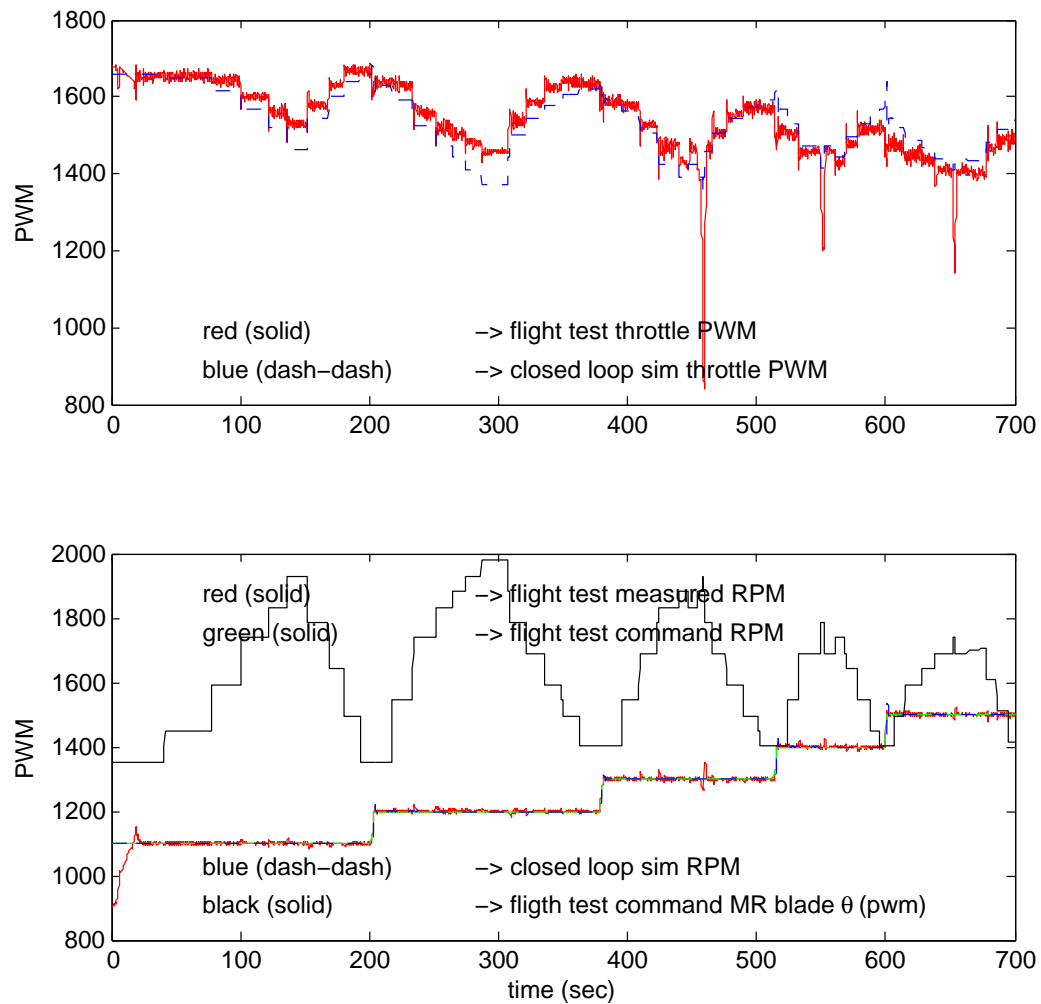


Figure 8.6: Engine-Carburetor model simulation results compared with real-time data.

Chapter 9

Helicopter Aerodynamic Model Experiment

9.1 Experiment Setup

The Linear and Directional Test Stand (LDST) is allowed to move both in the vertical direction and with angular motion about vertical axis. The experiment consists of two parts. The first part disconnects the tail rotor collective blade pitch input to characterize the torque generated by the main rotor induced and profile blade drag. During the second part of the experiment the tail rotor collective pitch angle is active, and inputs to the tail rotor will result in torque generation of the tail rotor thrust times the moment arm. This part of the experiment attempts to characterize the tail rotor thrust and torque. A cantilever beam fitted with strain gages acts as a bending beam load cell used to measure the reaction torque generated by the fuselage as a result of the available engine torque.

Figure 9.1 on page 101 shows the torque equilibrium setup present in this experiment. The engine generates sufficient torque to drag the main and tail rotor blades through the air, and the fuselage reacts with equal and opposite torque. As said previously, the first part of the experiment frees the tail rotor inputs such that the tail rotor blades find an equilibrium position with minimum energy. This minimum energy equilibrium state for the tail rotor corresponds to the torque consumed to overcome profile drag. In contrast, the main rotor generates thrust which induces a component of drag in addition to profile drag. This is the torque that the engine puts on the body, and the torque that the bending beam load cell measures. During the second part of the experiment, the lad

cell beam measures the difference between the reaction force from the fuselage and the torque generated by the tail rotor. This allows for the characterization of the tail rotor torque.

The experiment consists of four parts

1. open loop main rotor torque characterization
2. open loop tail rotor aerodynamic characterization.

Appendix K on page K details this experiment. The main rotor angular velocity remains constant throughout the duration of the experiments. Figure 9.2 on page 102 shows the helicopter on top of the Linear and Directional Test Stand (LDTS).

9.2 Open Loop Main Rotor Torque Characterization

Section K.3.1 on page 421 details the work done during this part of the experiment. Figure 9.3 on page 104 shows data collected during this portion of the experiment. The main rotor angular velocity remains constant for portions of the data run when the collective blade pitch angle is varied to generate thrust. The torque measured by the bending beam load cell measures the reaction torque from the fuselage. It is easy to see that the fuselage reaction torque follows the main rotor collective blade pitch angle; this is due to the torque induced by the generation of thrust (lift on the rotating wings or blades). Figure 9.4 on page 105 shows a portion of the data presented in the previous figure, and the measured average torque for a section of the flight data when the blade pitch angle remained constant. The change of altitude of the helicopter (bottom graph) helps determine the thrust generated by the helicopters as described in Section I.4 on page 395. With the thrust of the main rotor known, the related torque is also known. These values are varied until the aerodynamic model matches the data collected as shown on Figure 9.5 on page 106.

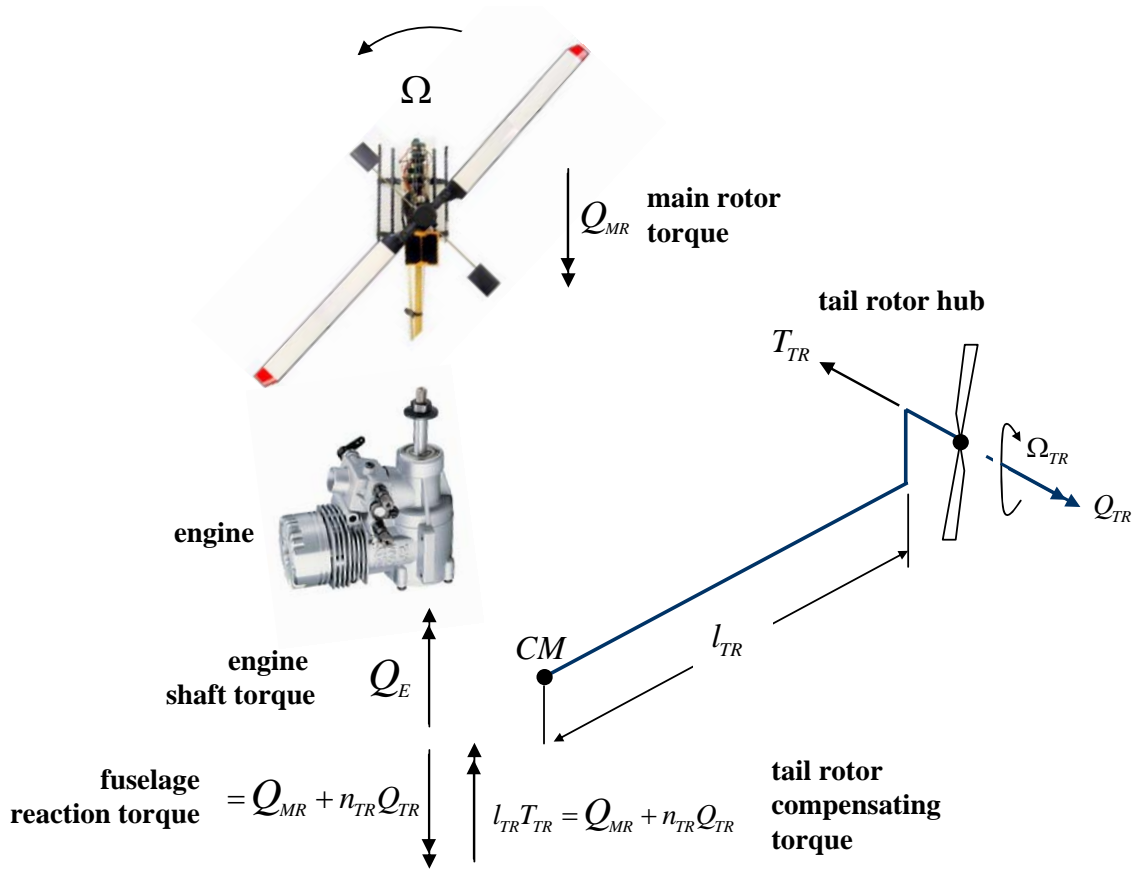


Figure 9.1: Torque Equilibrium about the Center of Mass (CM) along the z-axis. In the figure, Ω is the main rotor angular velocity, Ω_{TR} is the tail rotor angular velocity, Q_E , Q_{MR} , Q_{TR} are the engine available torque, the main rotor torque and the tail rotor torque respectively. In addition, n_{TR} is the main rotor to tail rotor gear ratio, and l_{TR} is the location of the tail rotor hub behind the CM.

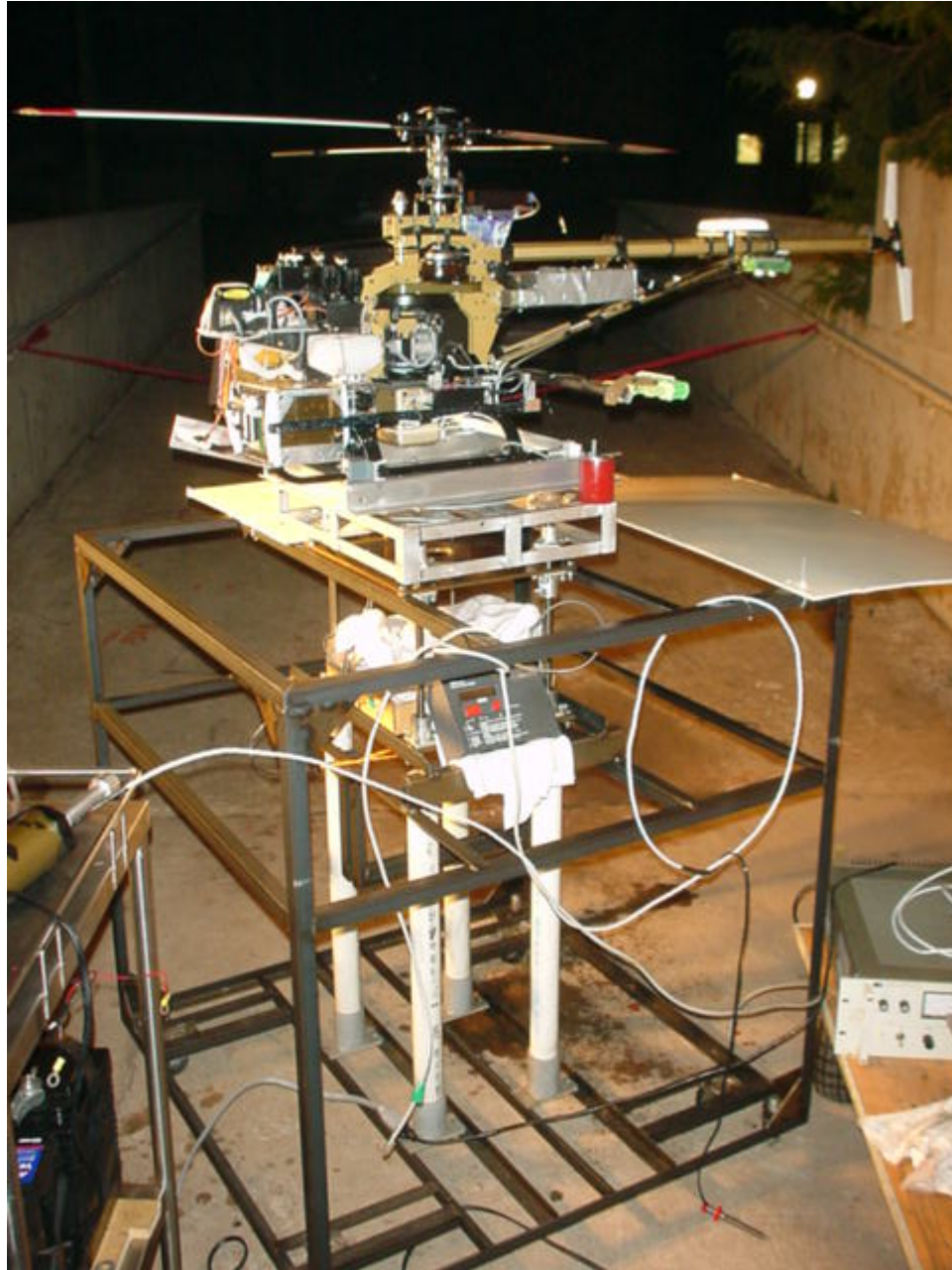


Figure 9.2: Helicopter Research Testbed sitting on the instrumented, purposed-built Linear and Directional Test Stand (LDTS).

A fundamental non-linear model of RPM is derived in Section J.2 on page 399 and proved experimentally in Section K.3.1 on page 421. Figure K.6 on page 427 shows that the compound main rotor and tail rotor torques could be modeled very accurately with a bias term plus a nonlinear term involving the product of RPM squared times the main rotor blade pitch angle raised to the three-halves power. It follows that this model (equation (J.1.3) on page 398) is key to developing a simple, but accurate transfer function model of the open-loop plant for the entire helicopter system which is then used to develop all the feedback control laws for autonomous flight purposes. In particular, the model is used to linearize the state-equation for RPM dynamics and develop a simple but accurate transfer function between the *available torque of the engine* and RPM (equation (J.2.5) on page 403). Consequently, it is of paramount importance, then, that the data in the upper graph in Figure 9.5 on page 106 matches the theory developed in Section J.2 on page 399. This validation of the theory for developing a simple, but accurate transfer function of the open-loop plant (Figure J.9 on page 409) paves the way for developing simple, but robust feedback control laws for autonomous flight of the helicopter. Moreover, the model in equation (J.1.3) on page 398 and experimental data in Figure 9.5 on page 106 are used in a feedback linearization loop that estimates the trim engine torque very accurately for all flight conditions. That is, for a given input RPM and main rotor blade pitch angle θ_{MR} , equation (J.1.3) on page 398 and experimental results in Figure 9.5 on page 106 give a non-linear estimate of the trim throttle setting throughout the helicopter flight envelope. The intrinsic and fundamental importance of this result cannot be overstated. The development of accurate and robust open-loop transfer function for the helicopter main rotor RPM and the development of a torque feedback linearization mechanism valid throughout the allowable flight envelope are key milestones for and two primary contributions of this thesis work.

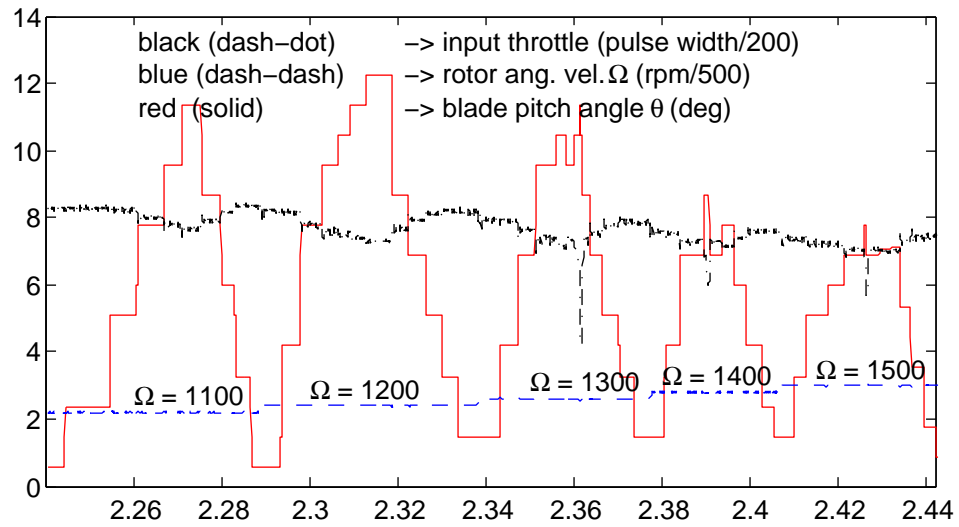
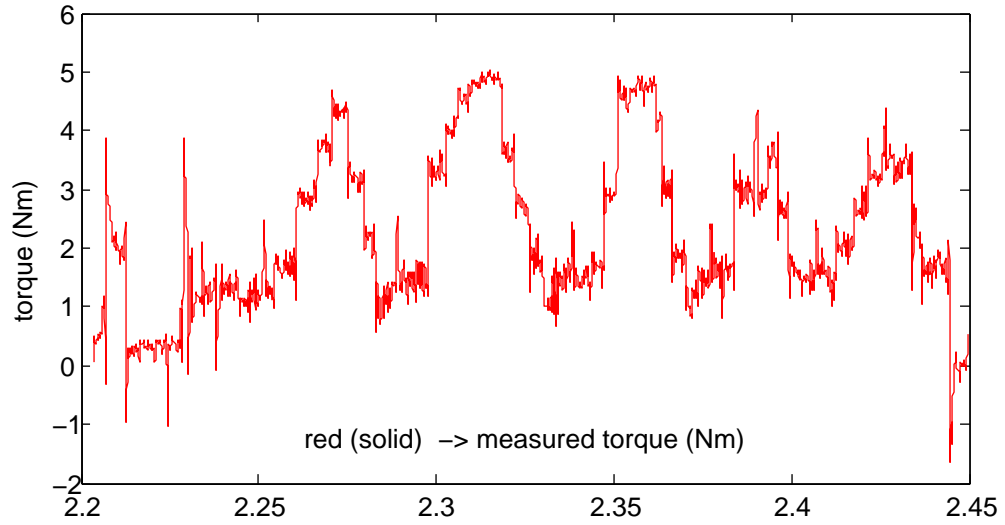


Figure 9.3: Torque Experiment with no Tail Rotor Inputs.

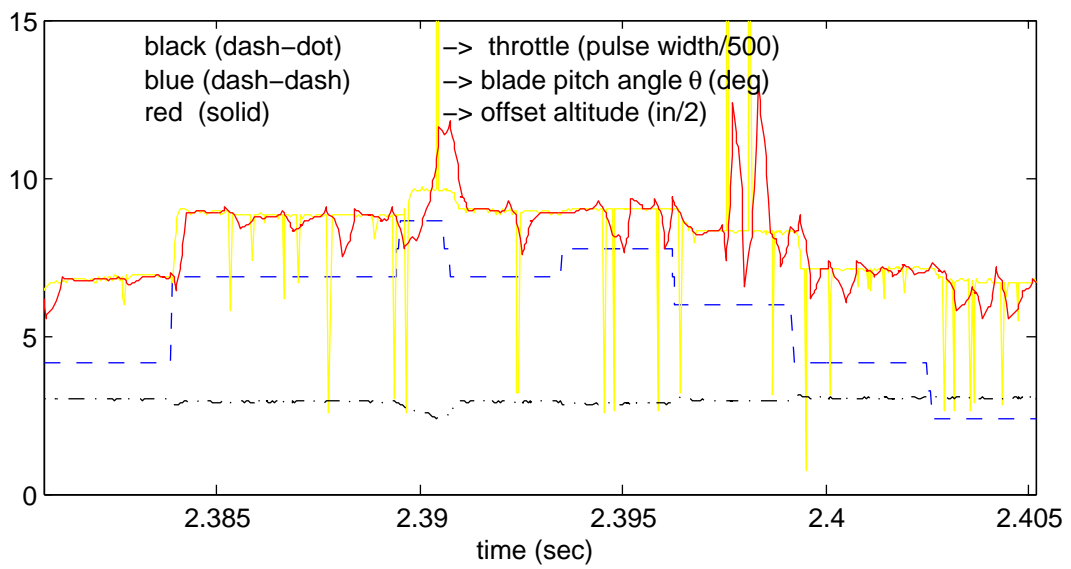
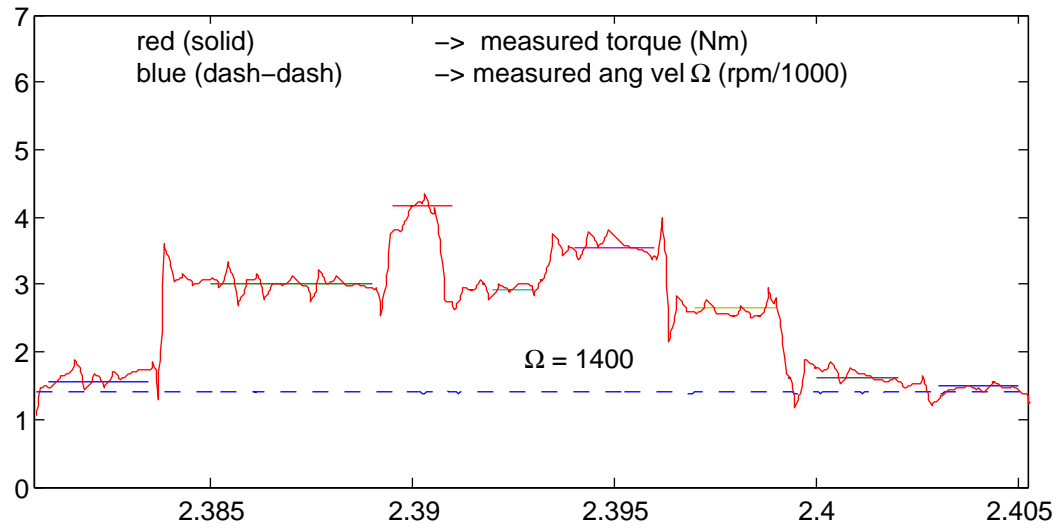


Figure 9.4: Torque Experiment sample data $\Omega = 1400$ rpm.

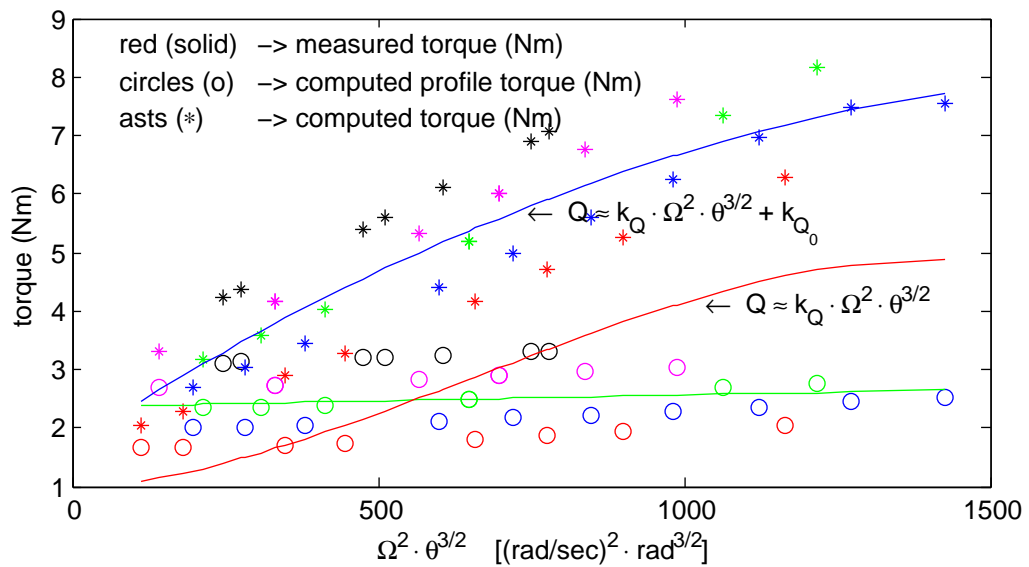
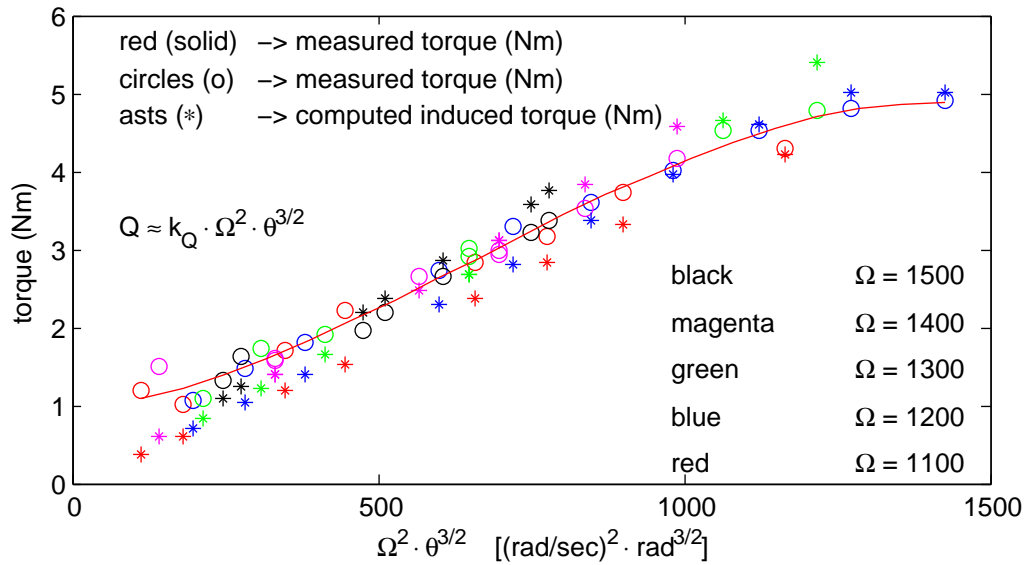


Figure 9.5: Torque Measurements Experiment with free tail rotor inputs.

9.3 Open Loop Tail Rotor Aerodynamic Characterization

Once the main rotor aerodynamic model and related torque characterization is complete, then the tail rotor aerodynamic characterization use these results to arrive at a reasonable model for the tail rotor. The tail rotor is particularly difficult to characterize because of the complex airflow characteristics in which the tail rotor operates. The tail rotor sees flow components from the main rotor wake which is turbulent and highly non-linear, from the angular rotation of the body, and from its own rotatory related aerodynamics. A characterization of the tail rotor will provide the necessary understanding to design closed loop directional control laws. Section K.3.2 on page 431 details the work done in this part of the experiment.

Figure 9.6 on the next page shows a data set from a real-time run in which the tail rotor actively controlled the heading of the helicopter. The bending beam load cell measured the difference between the reaction torque and the compensating tail rotor torque. The tail rotor thrust and compensating torque are isolated from the data by subtracting the component of main rotor torque. The residual torque is the torque generated by the tail rotor thrust times the moment arm from the center of mass to the tail rotor hub. In this figure, the red curve is the experimental measured data with the model-theoretical main rotor torque subtracted from the data. The dark blue curve is the tail rotor thrust times the moment arm. The light blue curve at the top of the graph is the main rotor angular velocity in RPM units, the magenta curve is the tail rotor collective input to the corresponding tail rotor servo. The green curve is the main rotor induced torque. The graph shows that the model-theoretical computed (dark blue curve) tail rotor torque closely matches the torque (red curve) estimated from real-time data measurements.

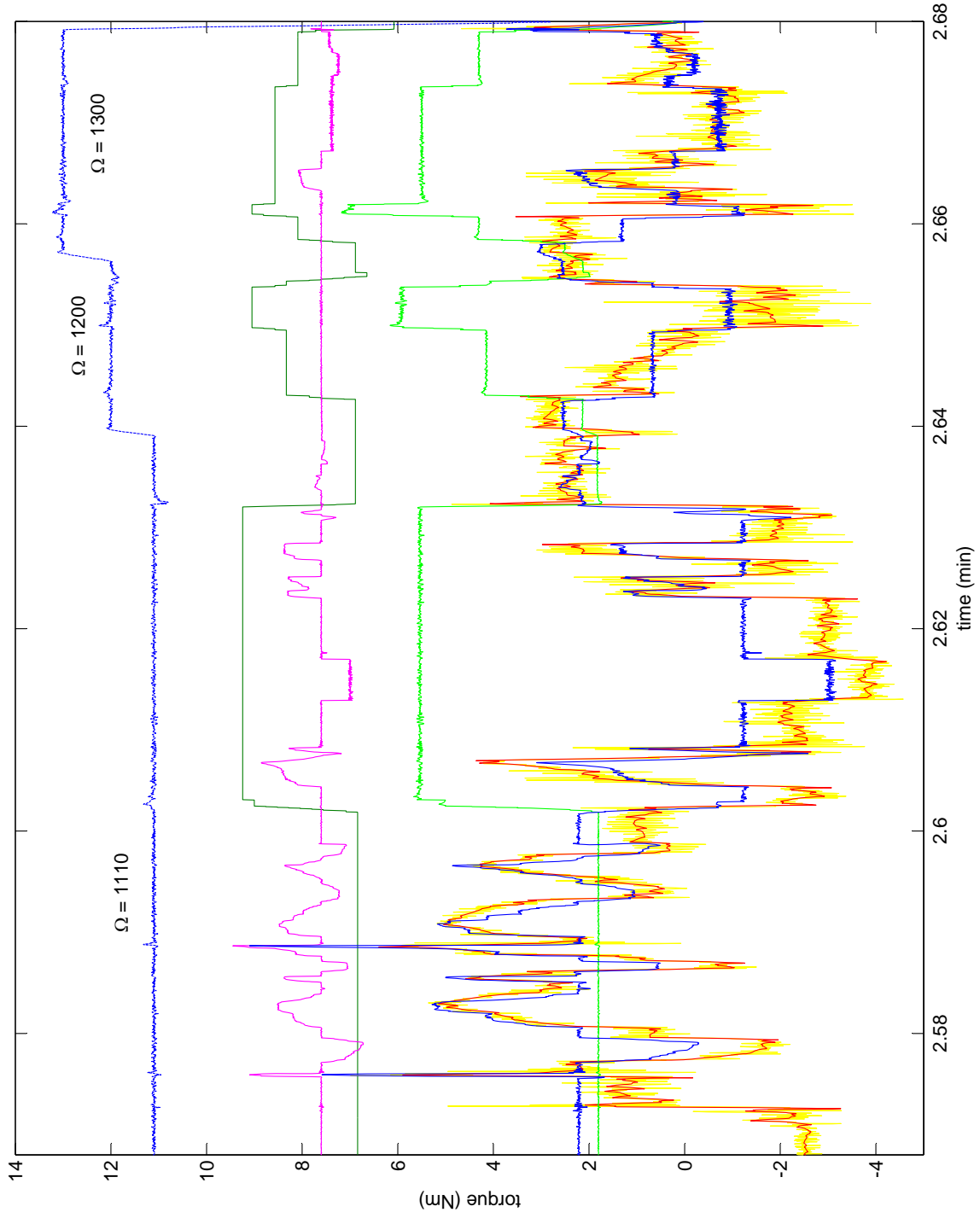


Figure 9.6: Effects of Tail Rotor Torque on Bending Beam Load Cell Torque Measurements

9.4 Experimental Results

The top graph on Figure 9.7 on the following page shows the measured torque (red curve) and the computed torque (black curve). The blue curve is the total computed torque. The difference between the measured torque and the total computed torque amounts to losses in the system and in the experimental setup. The induced torque matches the measured torque very closely. In turn, Figure 9.6 on the previous page shows close agreement between measured data and estimated tail rotor data.

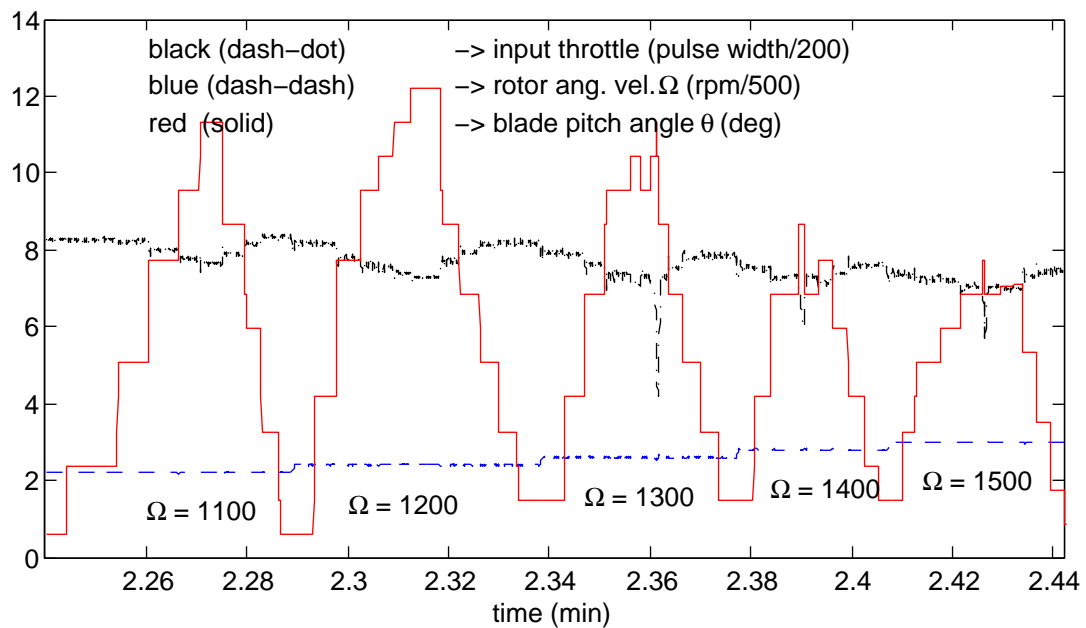
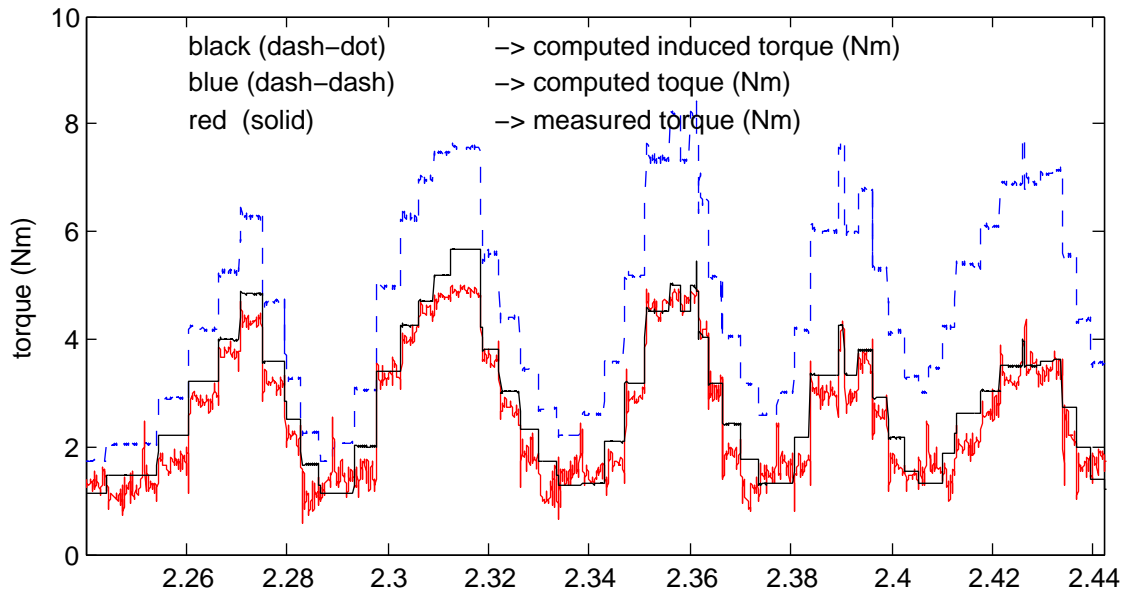


Figure 9.7: Torque Measurements and Computed Torque.

Chapter 10

Helicopter Yaw Rate and Heading Control Experiment

10.1 Experiment Setup

The yaw rate and heading hold experiments were conducted in two steps. During the first part, the yaw rate experiments utilized the Rotational Dynamics Test Stand (RDTS) seen in Figure 10.1 on the following page. The second part of the experiments used the Linear and Directional Test Stand (LDTS) shown in Figure 10.2 on the next page. The following steps followed the development of the experiments

1. open loop tail rotor control input characterization
2. yaw rate control design
3. heading hold control design

Section L.2 on page 434 covers the development of this section in great detail.

10.2 Open Loop Tail Rotor Control Input Characterization

The principal objective in this portion of the experiment is to find the trim settings when the tail rotor operates in open loop. This empirical solution to find the tail rotor trim bypasses a number of difficulties with the tail rotor aerodynamic model, principally



Figure 10.1: Helicopter on the Rotational Dynamics Test Stand (RDTS) during a real-time yaw rate experiment.



Figure 10.2: Helicopter on the Linear and Directional Test Stand (LDTS) during a real-time yaw rate experiment.

as it relates to the tail rotor thrust prediction in the presence of the main rotor wake. Figure 10.3 shows data from a real-time data run with the helicopter operating on the LDTS. The heading of the helicopter is held constant over short periods of time at various flight conditions indicated by the different main rotor angular velocity settings and different settings in the main rotor blade pitch angle. Figure 10.4 on the following page and Figure 10.5 on page 115 plot a collection of data taken during multiple real-time runs, and the empirical trend in both figures show the relationship between the aerodynamic model and the trim condition for the tail rotor. These empirical relations are bounded within errors, and the general trend for tail rotor setting for various flight conditions is sufficient to predict the corresponding tail rotor trim control setting. Section L.2.1 on page 437 covers the details pertaining to this work.

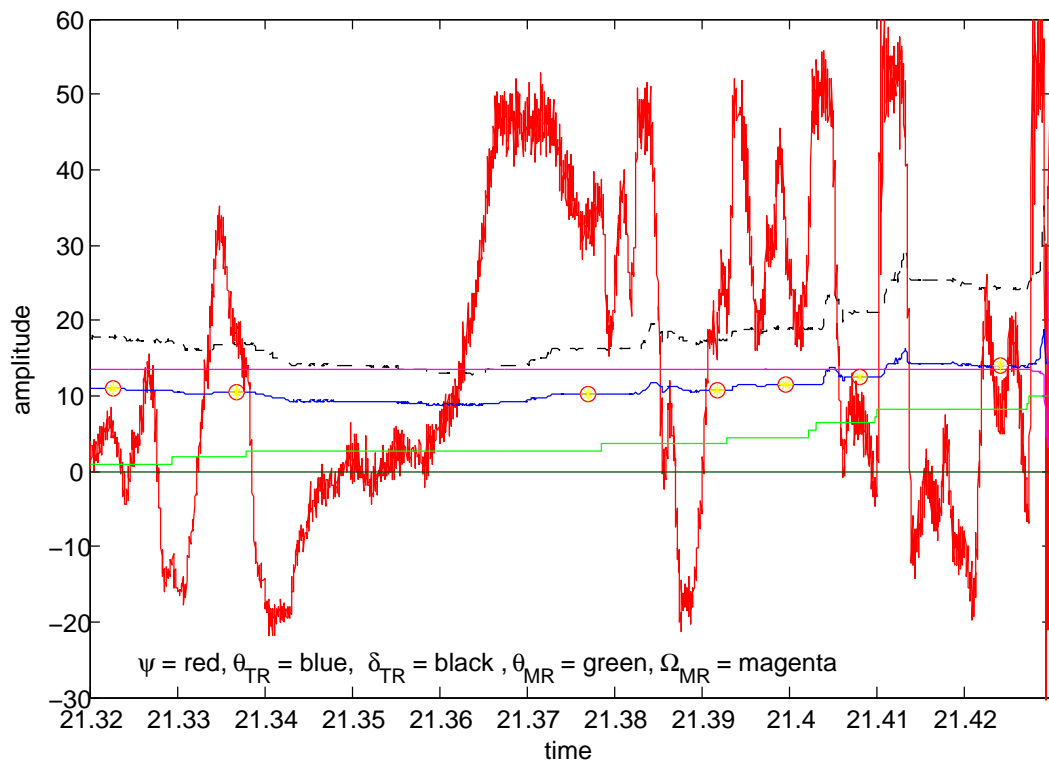


Figure 10.3: Real Time Run with Tail Rotor Inputs.

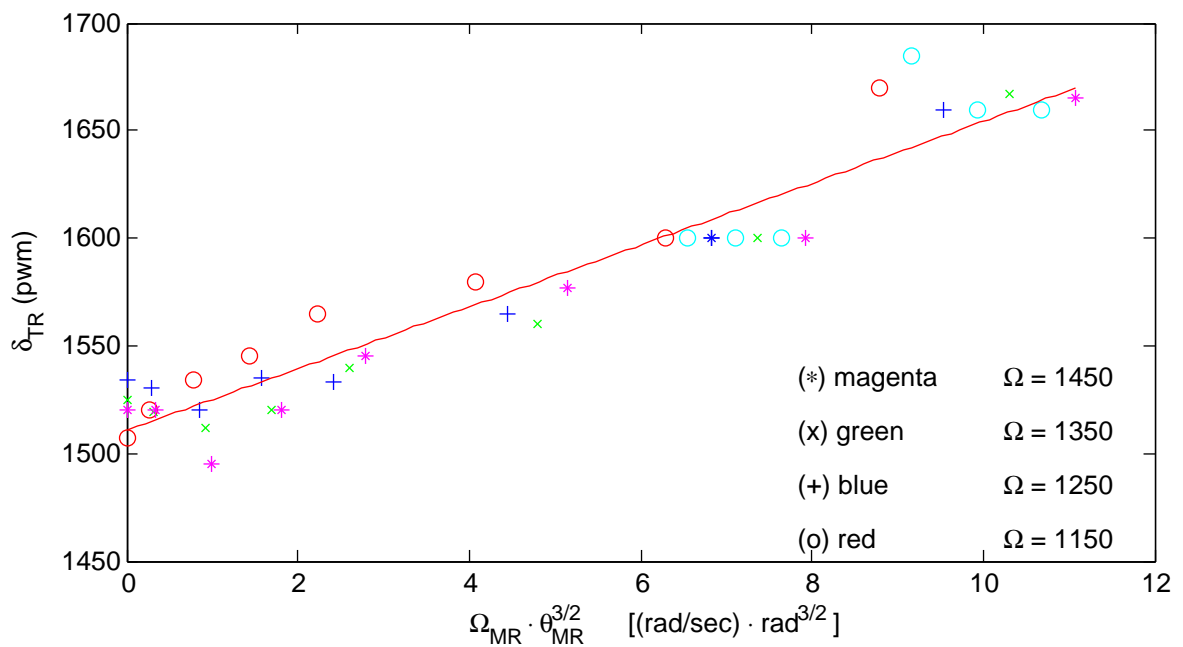
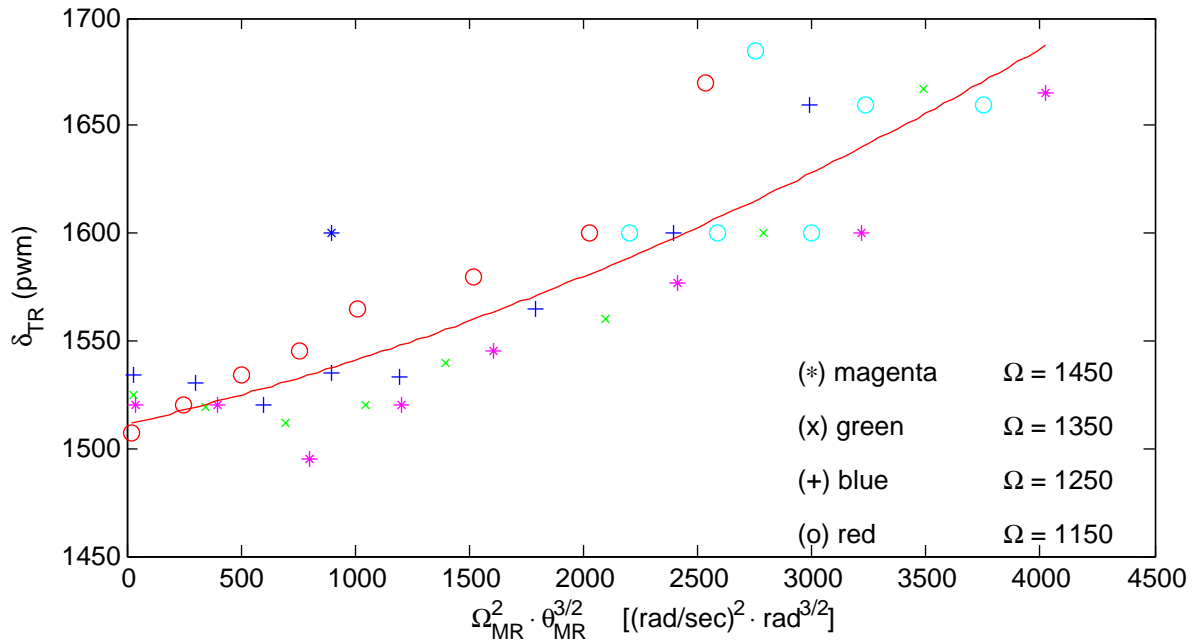


Figure 10.4: Multiple Real Time Run with Tail Rotor Inputs.

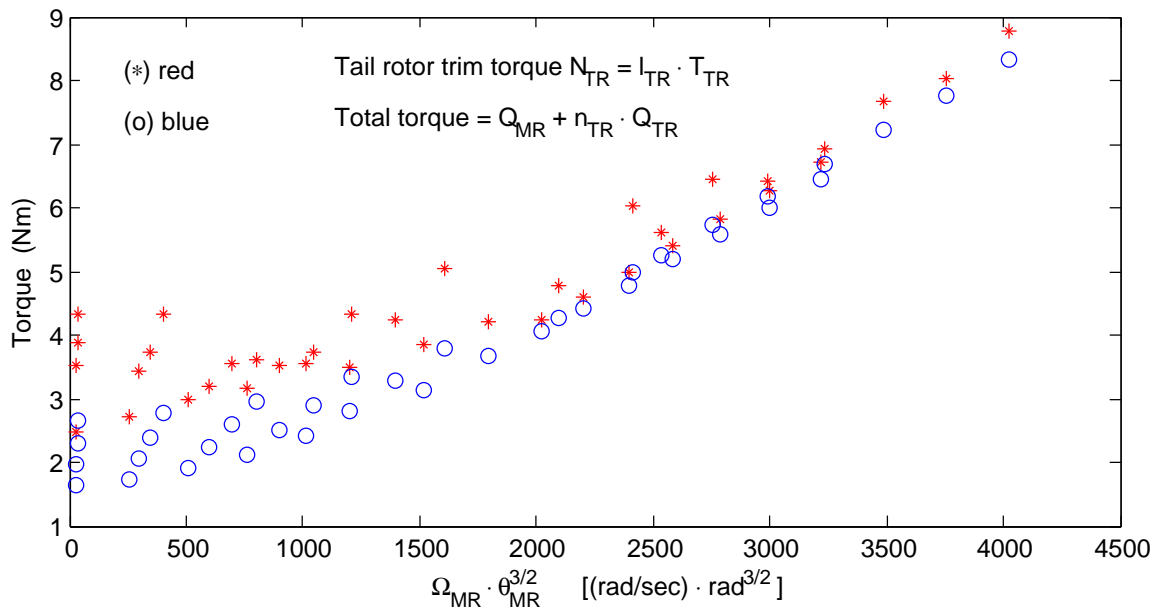
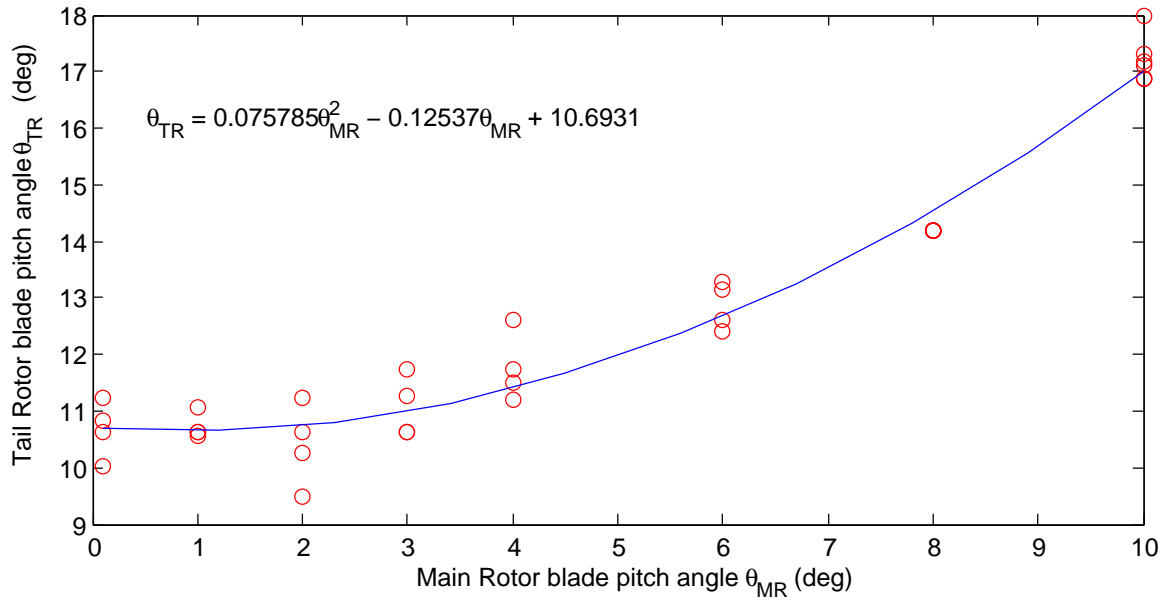


Figure 10.5: Empirical Tail Rotor Blade Pitch Angle and resulting Equilibrium Torque N_{TR} .

10.3 Yaw Rate and Heading Hold Control Design

Figure 10.6 in Section L.2.2 on page 438 shows the model for the yaw rate control design while Figure 10.7 in Section L.2.3 on page 443 shows the overall design for the yaw rate and heading hold control. The present control design leads to the general compensator seen in Figure 10.8 on the next page presented on Section 7.2 on page 80

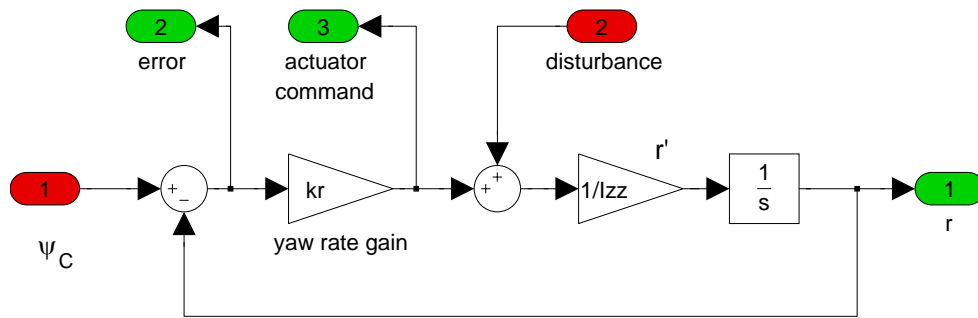


Figure 10.6: Yaw Rate p Feedback Control Law.

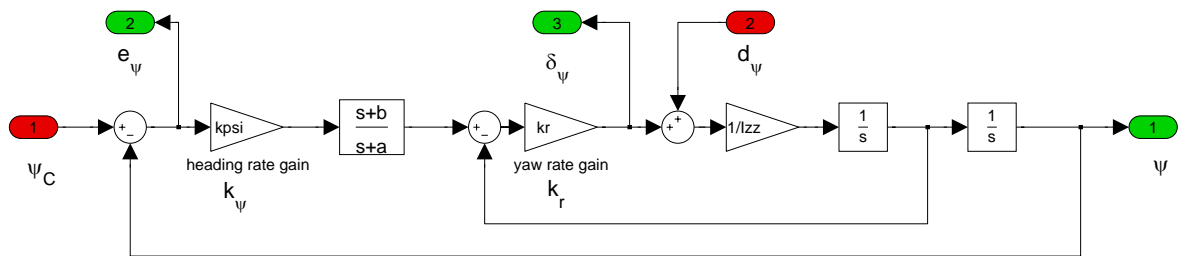


Figure 10.7: Yaw Heading ψ Feedback Control Law.

10.4 Experiment Results

Section L.2.5 on page 445 presents the results for both the yaw rate and heading hold experiments. The heading hold experiment is shown in Figure 10.9 on page 118 for convenience. The heading hold works with adequate performance which can be modified by tuning of the proper control gains.

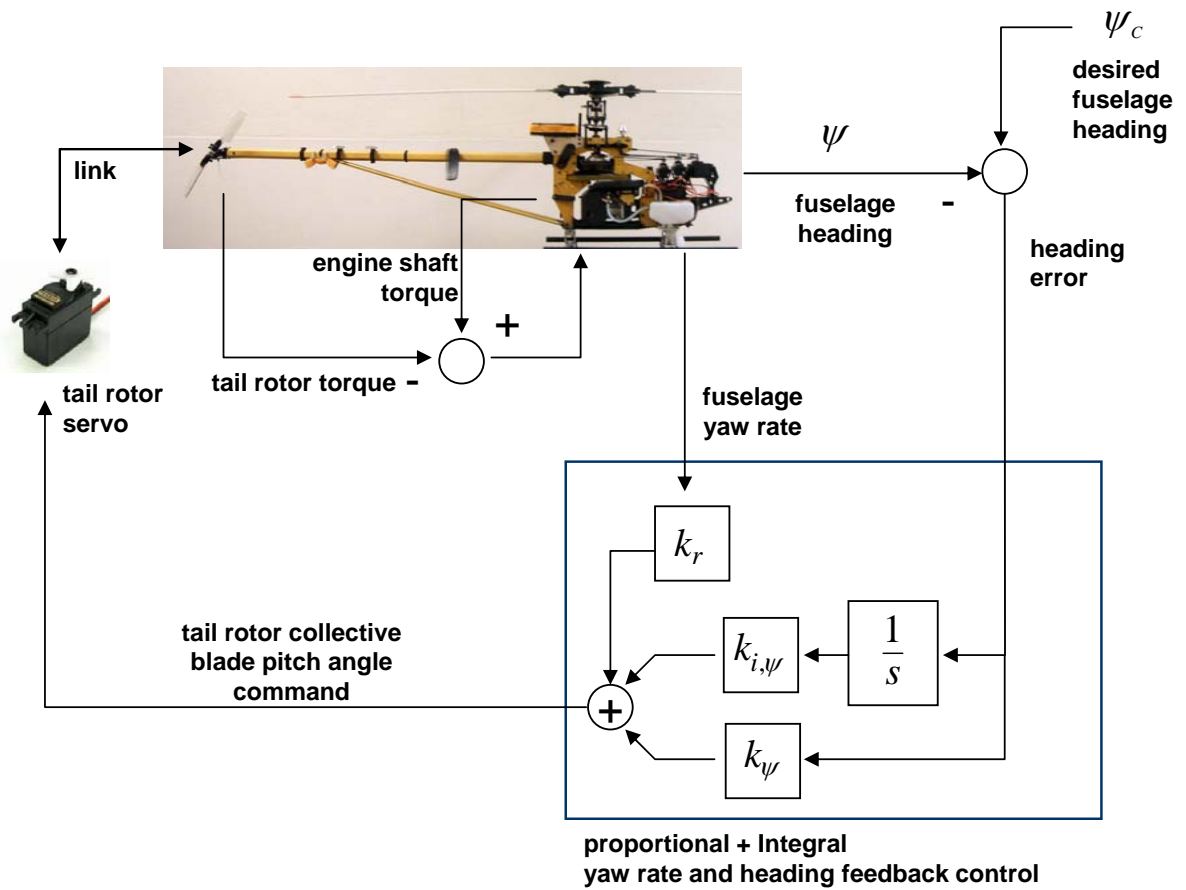


Figure 10.8: Block diagram for yaw rate and heading angle control loop.

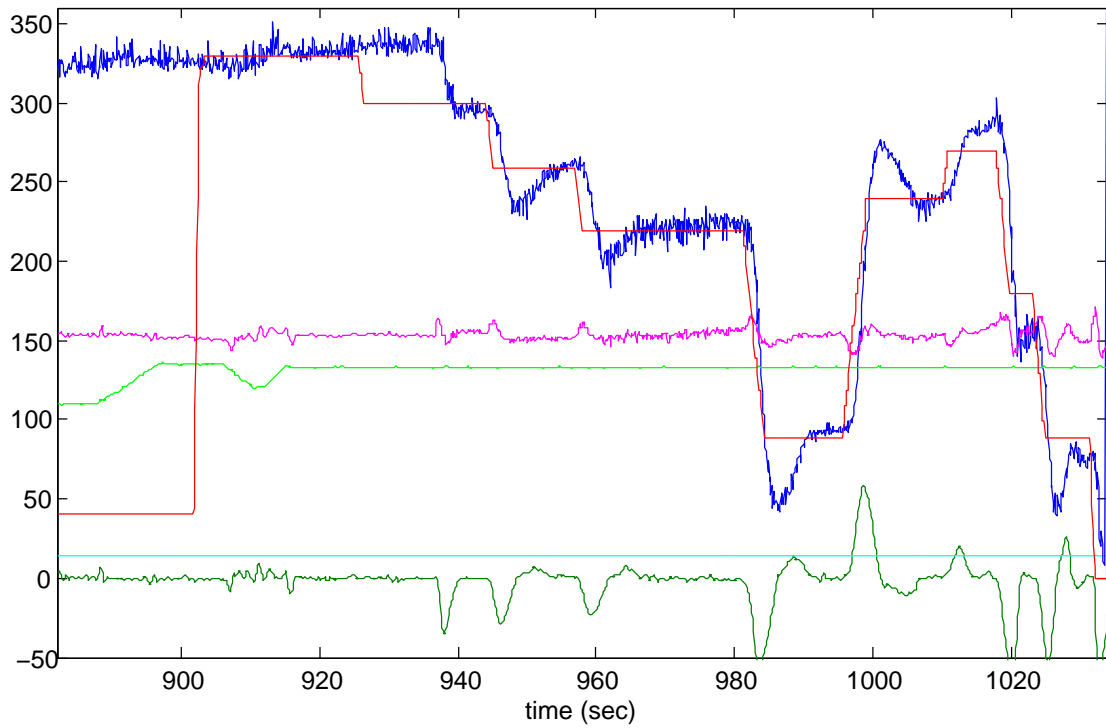


Figure 10.9: Real-Time Data with Helicopter Heading Command. Red solid curve is the heading command ψ_C , dark green curve is the yaw rate r measured data. The solid blue curve is the helicopter measured heading ψ , and the magenta curve is the scaled tail rotor blade pitch command δ_{TR} in pulse width units ($\mu\text{sec}/100$). The light green curve is the scaled main rotor angular velocity $\Omega/100$.

Chapter 11

Helicopter Pitch and Roll Attitude Experiments

11.1 Experiment Setup

The roll θ and pitch ϕ attitude experiments take place on the Rotational Dynamics Test Stand (RDTS) shown in Figure 11.1 on the next page. This test stand can pitch, roll and yaw in all three axis simultaneously or one axes at the time, or with any combination of the three axes. As such, it is particularly useful for the testing of the pitch and roll control loops of the helicopter. The experiments consist of three parts:

1. pitch rate q stability and pitch command θ_c tracking and hold
2. roll rate p stability and roll command ϕ_c tracking and hold
3. pitch and roll stability and command attitude command track while tracking and holding heading commands ψ_c

11.1.1 Pitch Rate Stability and Pitch Command Track and Hold Experiment

Unlike previous experiments, the pitch rate stability and command track and hold experiment does not require special test runs to determine the trim conditions. The control loop is as shown in Figure 11.2 on page 121, and Section L.3 on page 448 presents the derivation of the control laws. In this test run, the main rotor angular velocity Ω and the main rotor blade pitch angle θ_{blade} remain constant. The RDTS is configured such

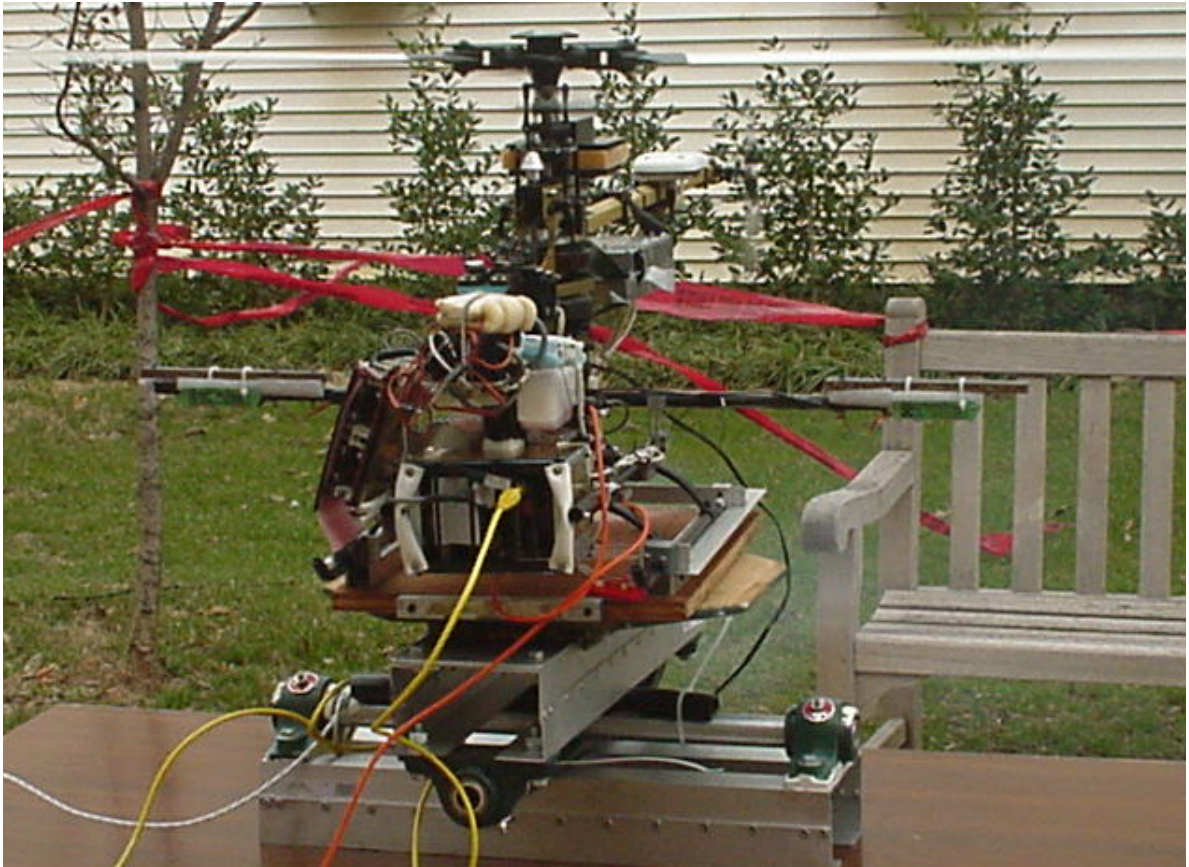


Figure 11.1: Real-Time Run of the Helicopter on top of the Rotational Dynamics Test Stand (RDTS).

that only pitch attitude is possible to minimize damage in case the experiment does not go as planned. Figure 11.3 on the following page presents data from test results. It can be seen that the pitch control loop remains stable while tracking and holding the pitch command. During free flight, the pitch command would not remain constant for an extended period of time, but rather, the pitch command would track commands from a performance locomotion loop as shown in Figure 7.12 on page 92.

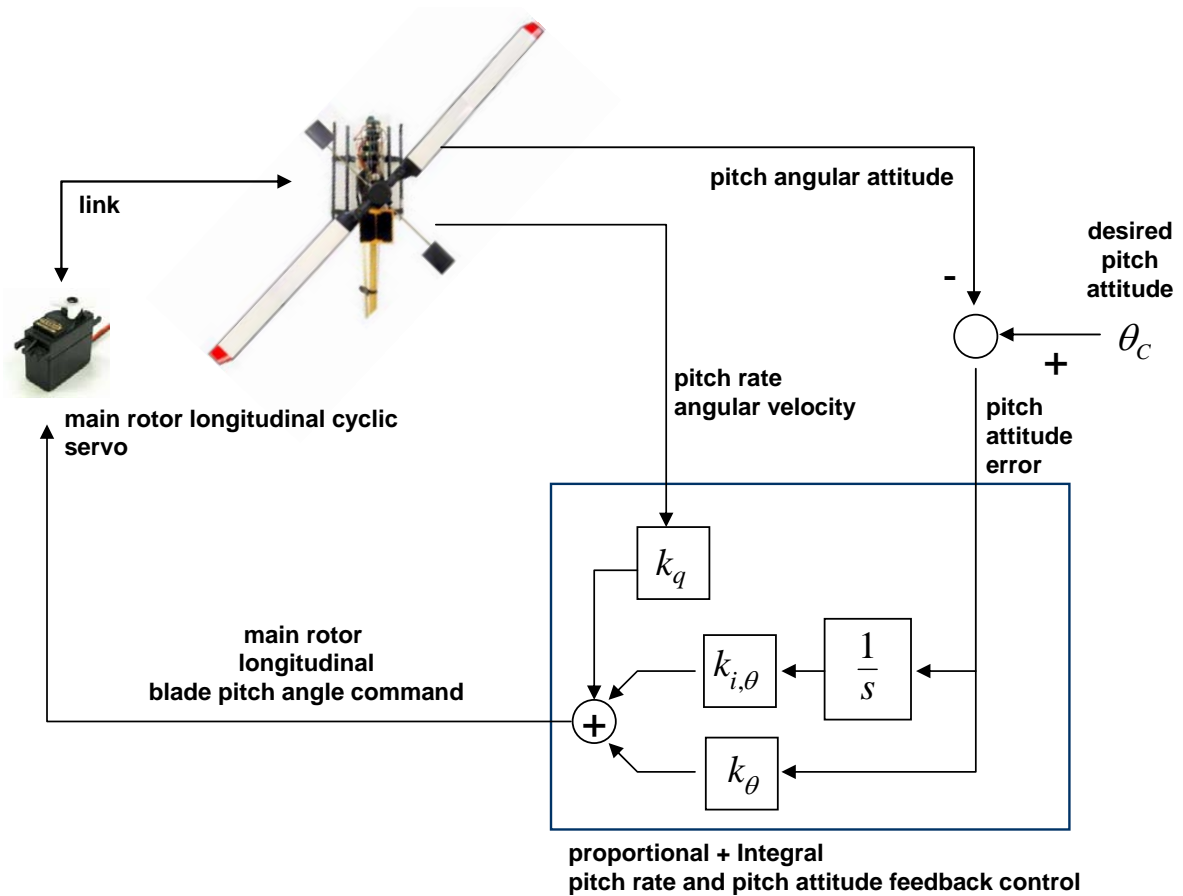


Figure 11.2: Block diagram for longitudinal pitch rate q and pitch attitude θ control loop.

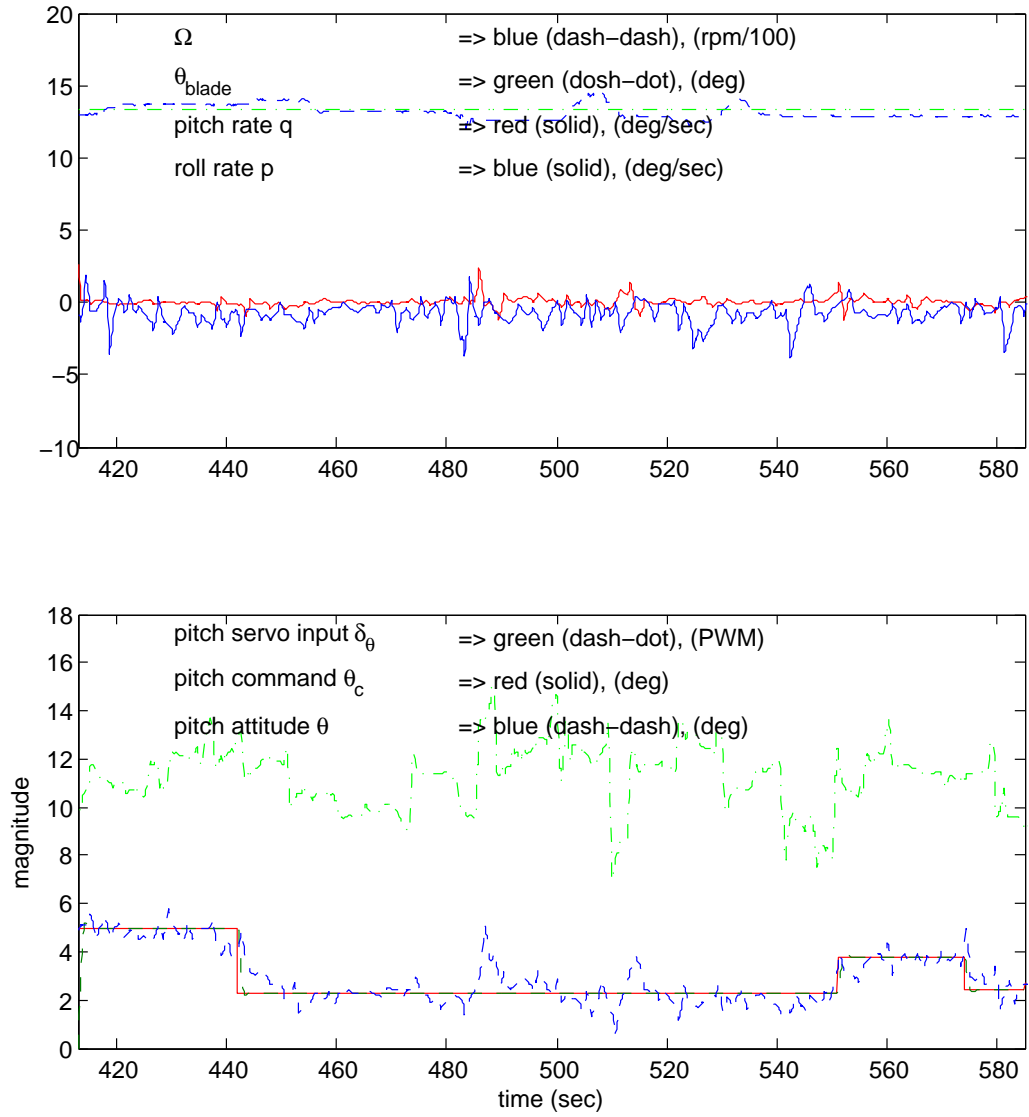


Figure 11.3: Pitch command θ_c tracking with the helicopter on the Rotational Dynamics Test Stand (RDTS). In the figure, the top graph plots the roll p and pitch q rates and the main rotor angular velocity Ω .

11.1.2 Roll Rate Stability and Roll Command Track and Hold Experiment

The roll rate and roll command track and hold control law design is as shown in Figure 11.4 on the following page, and Section L.4 on page 452 presents the derivation of the control laws. Similar to the test run for the pitch control loop, in this test run, the main rotor angular velocity Ω and the main rotor blade pitch angle θ_{blade} remain constant. The RDTS is configured such that only roll attitude is possible to minimize damage in case the experiment does not go as planned. Figure 11.5 on page 125 presents data from test results. It can be seen that the roll control loop remains stable while tracking and holding the roll command ϕ_c . During free flight, the roll command would not remain constant for an extended period of time, but rather, the roll command would track commands from a performance locomotion loop as shown in Figure 7.12 on page 92.

11.1.3 Simultaneous Pitch and Roll Stability Command Track and Hold Experiment while Tracking and Holding Heading Commands

The simultaneous roll and pitch attitude control laws operate as shown in Figure 11.6 on page 127. The control laws are the same as those derived in previous sections. During tests, the main rotor angular velocity Ω and the main rotor blade pitch angle θ_{blade} remain constant. In this case, however, the RDTS is configured to move in all axis. Figure 11.7 on page 128 shows data results from a test run experiment with all axes free. During the first part of the experiment, the pitch and roll loops track and hold a zero attitude command. The loops remain stable during the complete flight even in the presence of hard directional maneuvers. During the second part of the experiment, the heading loop tracks and holds a constant command even when subject to a hard attitude maneuver. All throughout the experiment, the roll rate p and the pitch rate q remain bounded as

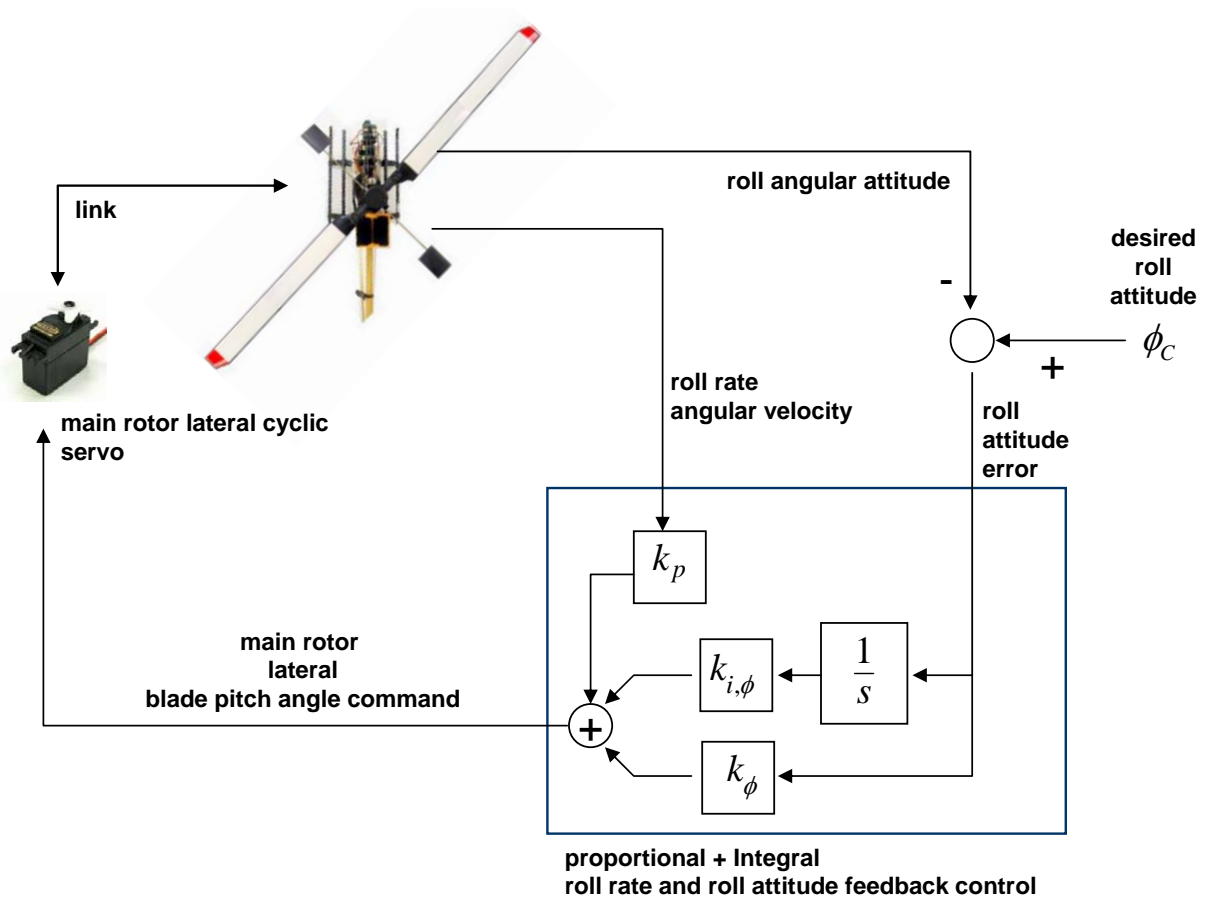


Figure 11.4: Block diagram for lateral roll rate q and roll attitude ϕ control loop.

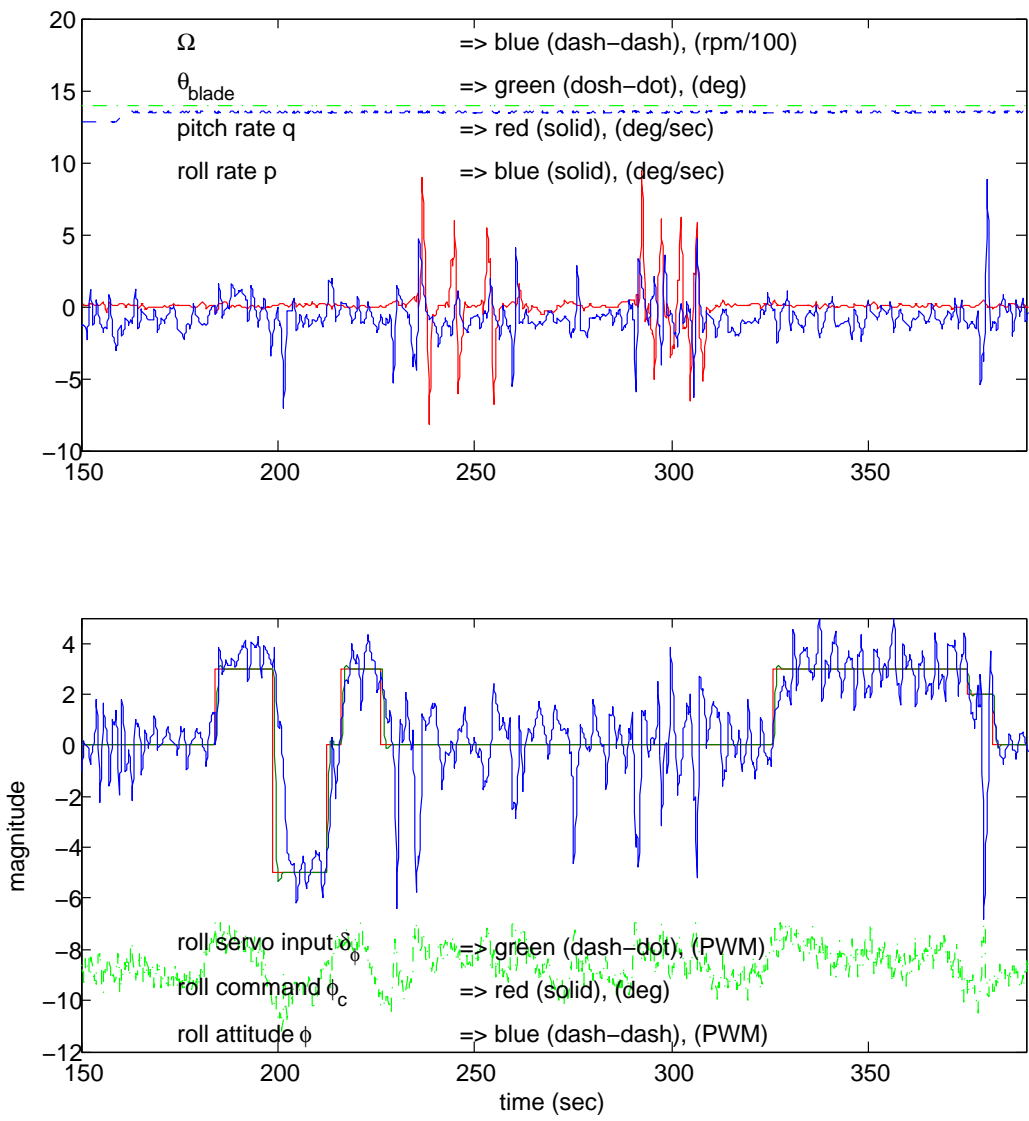


Figure 11.5: Roll command ϕ_c tracking with the helicopter on the Rotational Dynamic Test Stand (RDTS). In the figure, the top graph plots the roll p and pitch q rates and the main rotor angular velocity Ω . Notice the large time constant of the feedback control loop during an experimental stability test.

expected. At this point, the helicopter is a stable platform ready for free flight. Figure 11.7 tells us that the helicopter knows how to maintain attitude stability

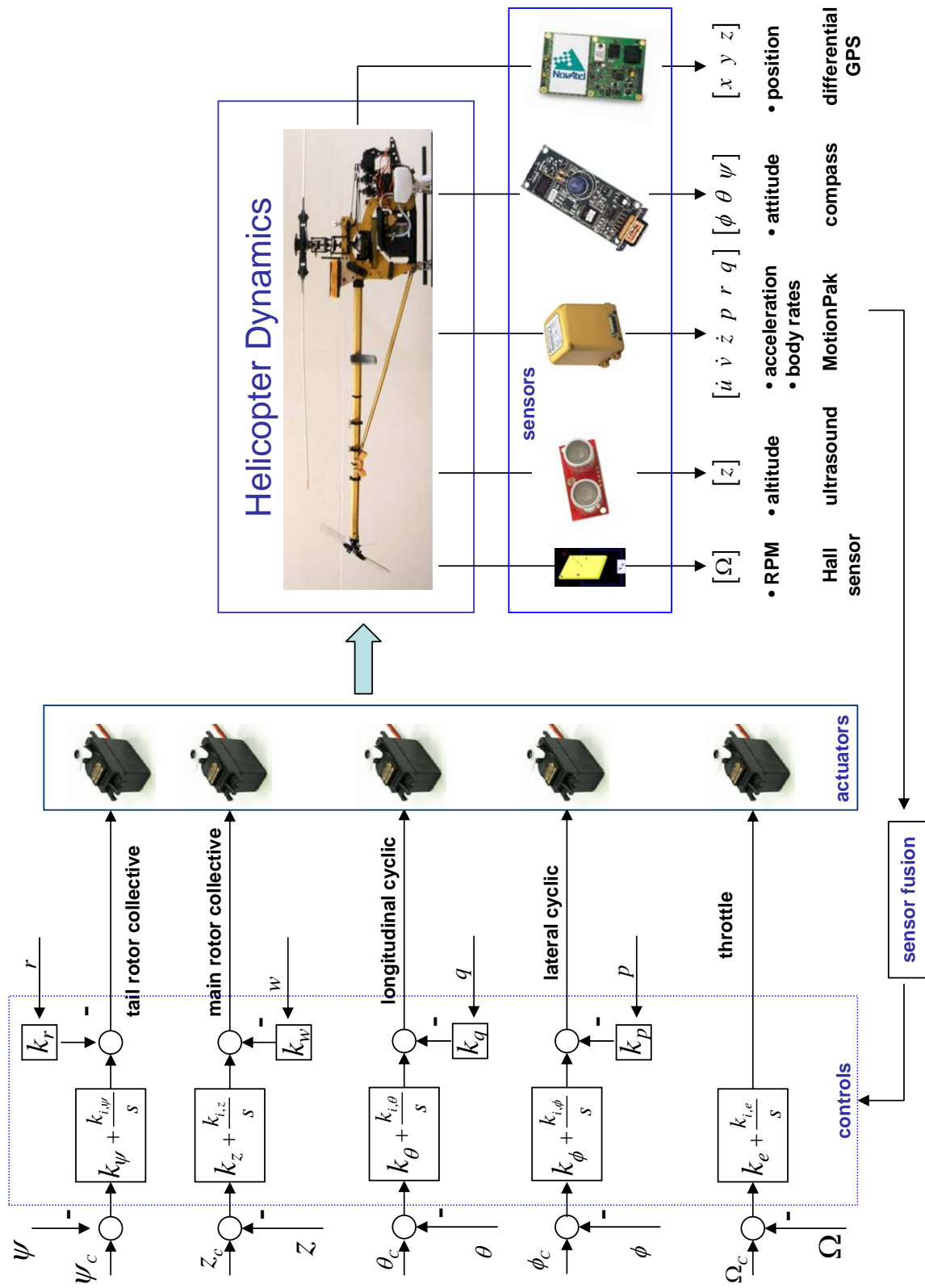


Figure 11.6: Block diagram for longitudinal and lateral feedback control.

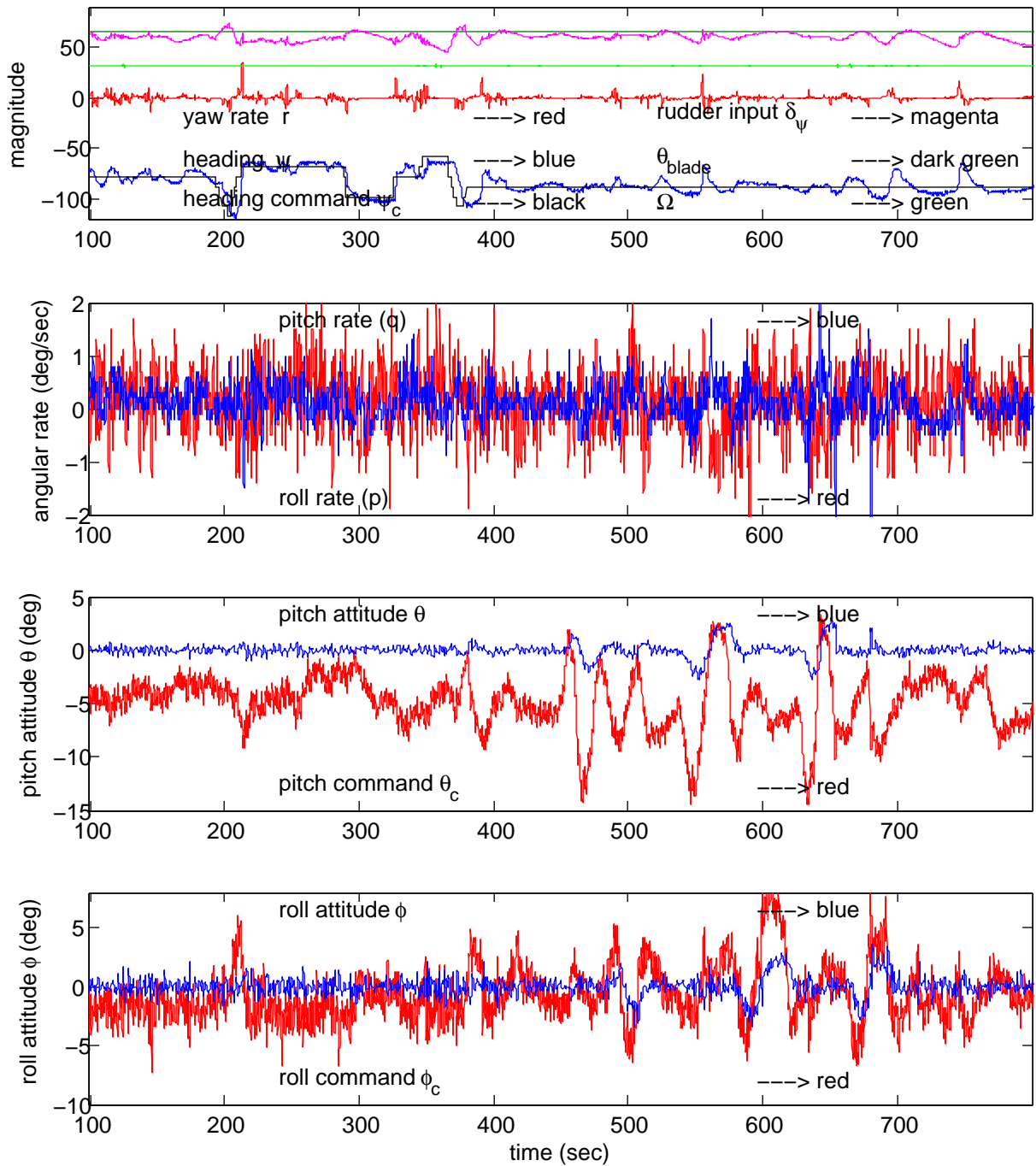


Figure 11.7: Simultaneous attitude command tracking and hold for roll ϕ , pitch θ and heading ψ with constant angular velocity Ω . In the figure, the top-most graph presents the heading command tracking and hold, the second graph shows the roll p and pitch rate q during the flight. The third graph down shows the pitch attitude θ holding zero for the first part of the run, and tracking commands for the second part of the run. The same is true for the roll attitude ϕ in the fourth graph.

Chapter 12

Helicopter Hardware and Software Integration

12.1 OU Helicopter Research Testbed: A Systems Engineering Design Approach

Section M on page 459 details a System Engineering (SE) approach to the design of the University of Oklahoma Helicopter Research Testbed (OU-HRT). The systems requirements originate from the customer or principal stakeholder. Careful consideration of the Voice of the Customer (VOC) through the use of SE tools such as Affinity Diagrams, Tree Diagrams and Quality Function Deployment (QFD) arrives at the need to develop a computer based method for autonomous flight (the process) with a miniature helicopter and the testbed (the product). In this regard, the combined autonomous miniature helicopter and the method for autonomous flight is collectively named the OU Helicopter Research Testbed. Figure M.11 on page 476 illustrates the top level functional decomposition for the OU-HRT, and Figure M.12 on page 477 shows the OU-HRT subsystem decomposition and related work break-down structure. Based on these results from the SE analysis, Figure M.13 on page 478 shows the complete system architecture for the OU-HRT. This system architecture is useful within the context of a much larger project than the present. A simplified system architecture shown in Figure 12.1 on the following page is suitable for initial autonomous flight research. Moreover, Figure 12.2 on the next page illustrates an architecture suitable for Hardware-in-the-Loop (HWIL) work the OU-HRT.

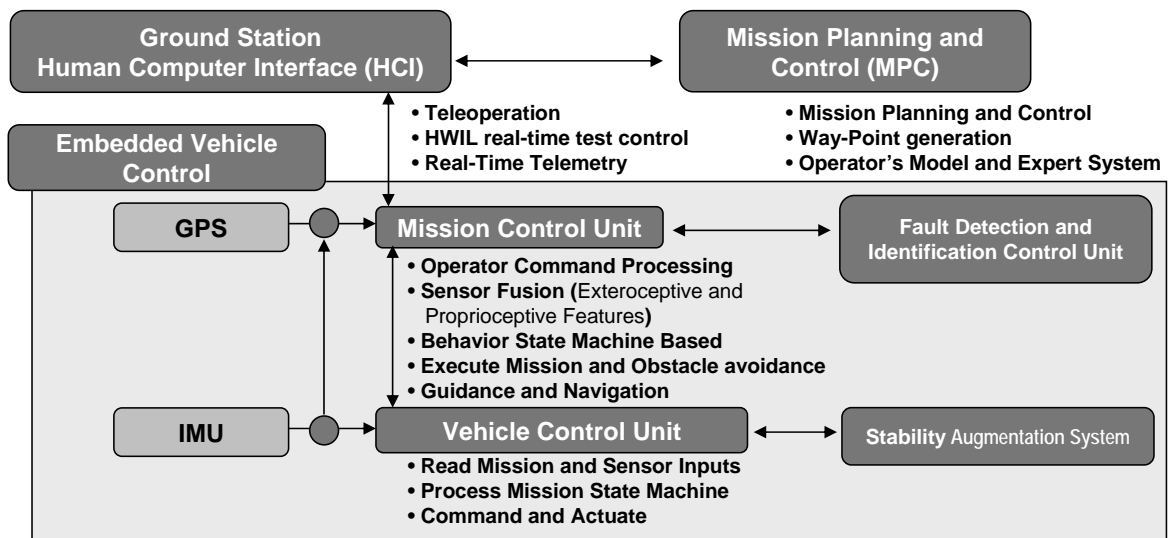


Figure 12.1: Simplified system architecture for the University of Oklahoma Helicopter Research Testbed for Autonomous Flight.

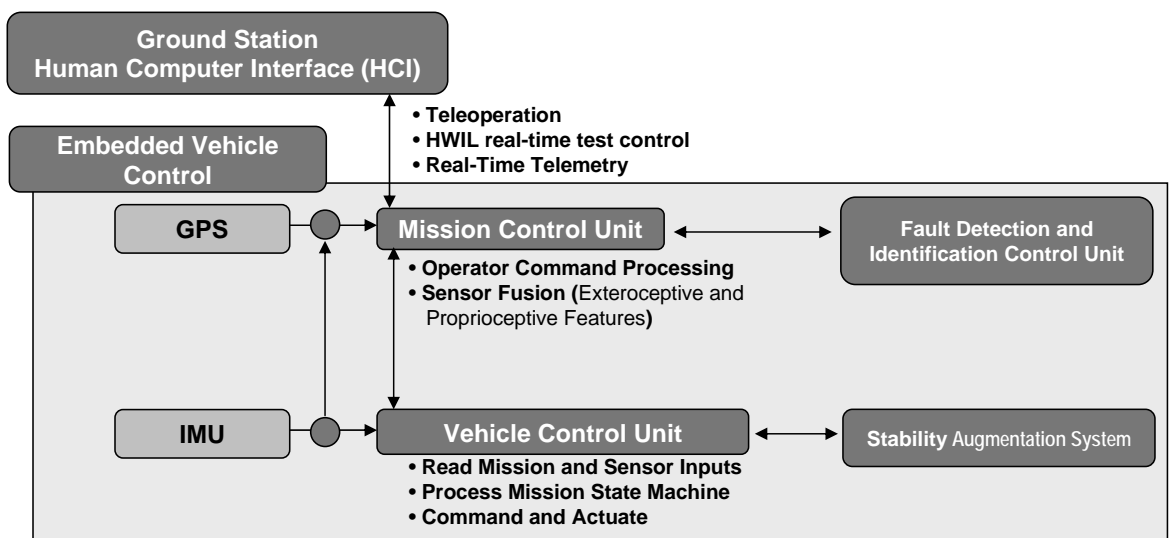


Figure 12.2: Simplified system architecture suitable for Hardware-in-the-Loop real-time tests with the University of Oklahoma Helicopter Research Testbed.

12.2 Hardware Interface

Figure 12.3 on the following page shows the primary hardware interface among the various components of the autonomous helicopter. Two sets of flight computers interface the hardware to the software. A dual MC68332 μC ¹ (Figure 2.18 on page 29) interfaces to the aerodynamic actuators via electromechanical servomechanisms and related mechanical links (Figure 2.5 on page 19, Figure 2.8 on page 22 and other details in Chapter 3 on page 34). The interface to the engine is via a servo and a throttle that controls the air-fuel mixture to the engine, and the engine interface to the rotating main and tail rotor components is via a set of belt-gear and other related gears (Figure 2.4 on page 18). In addition, the dual MC68332 μC interfaces to some sensors via a digital bus.

A second (primary) flight computer in the PC104 form factor (Figure 2.17 on page 29) interfaces to various sensors via analog, digital and serial bus, to the dual MC68332 μC via a serial bus, and to the ground station via serial wireless link. Figure 12.4 on page 133 shows the data bus interface among the various hardware components, and Table 12.1 on page 134 itemizes the bus interface for the same hardware components.

¹ μC = microcontroller

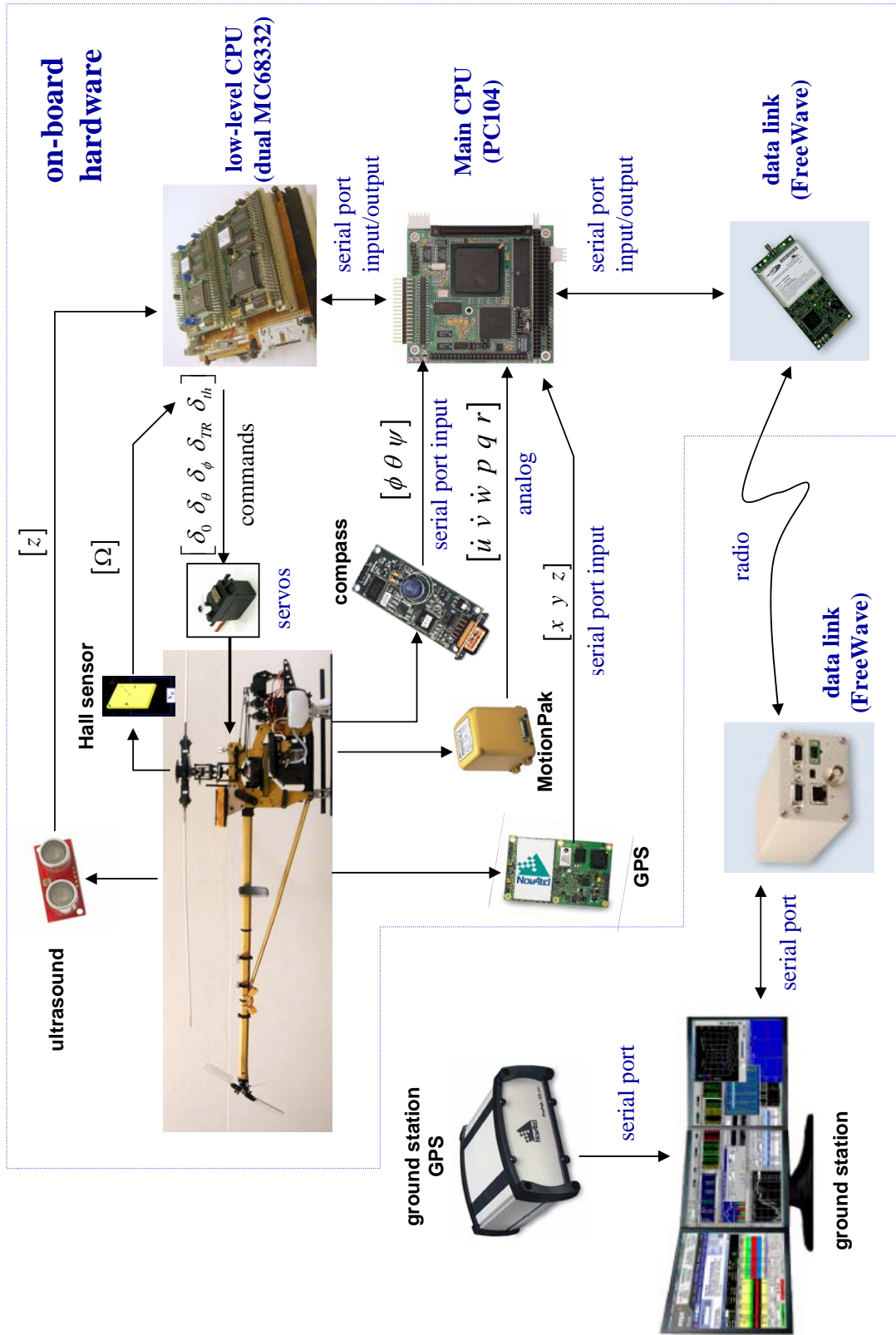


Figure 12.3: Hardware component interface.

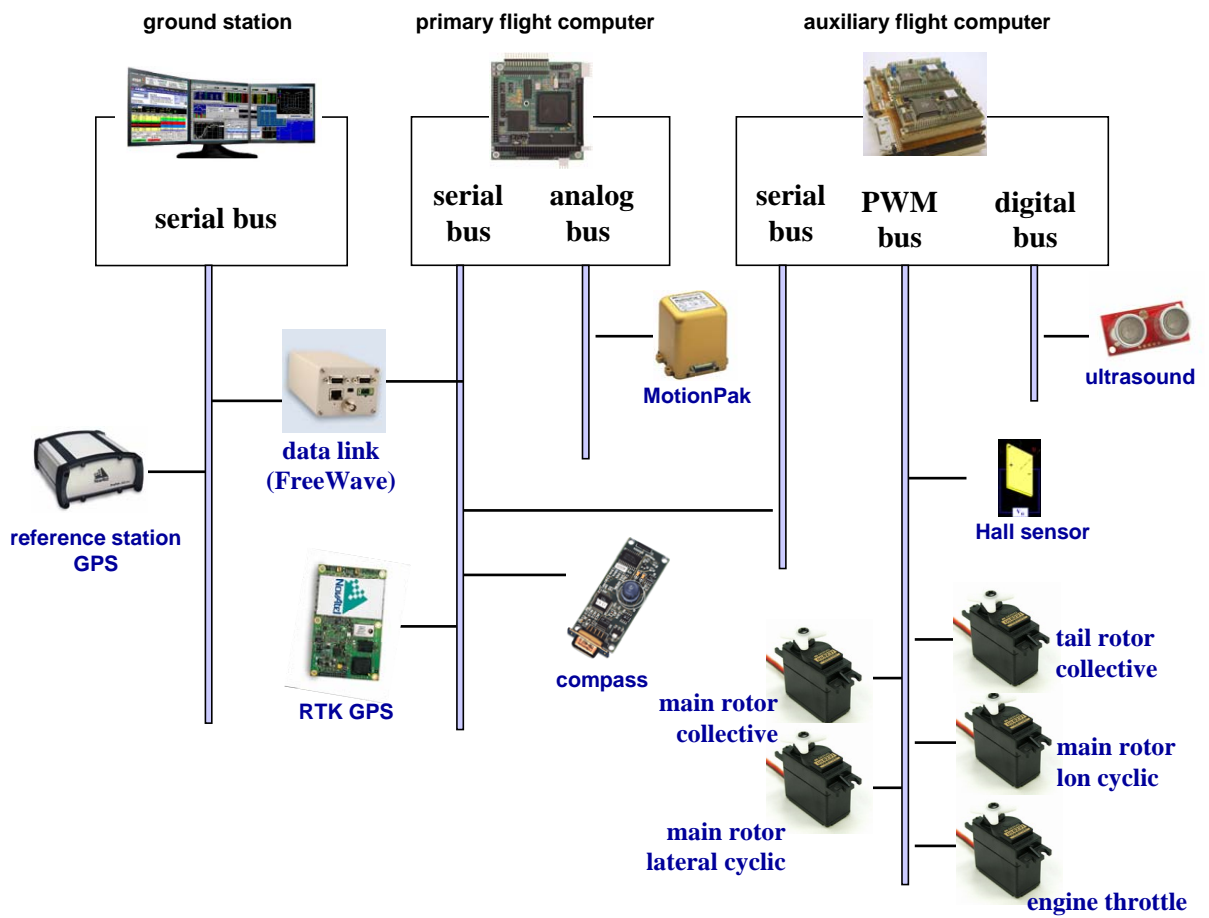


Figure 12.4: Hardware data bus architecture.

Table 12.1: Hardware Interface to Flight Computers

	bus interface	component
dual MC68332 μC	digital	ultrasound sensor (z)
	PWM ^a	Hall sensor (Ω)
	PWM	servo inputs ($\delta_0, \delta_\phi, \delta_\theta, \delta_{TR}, \delta_{th}$)
	serial	main CPU (PC104)
main CPU (PC104)	serial	compass (ϕ, θ, ψ)
	serial	GPS (x, y, z)
	analog	MotionPak ($\dot{u}, \dot{v}, \dot{w}, p, q, r$)
	serial	dual MC68332 μC
	serial	wireless link to ground

^a PWM = digital pulse-width modulation

12.3 Software Interface

Figure 12.5 on the following page shows a UML² sequence diagram [9, 35, 128] with the primary helicopter software components. The ground station provides the human interface to the rest of the system. A wireless link provides a data path between the ground station and the free flying helicopter. The flight code that executes on the primary flight computer performs three main tasks: (1) gather sensor and ground station command information, (2) perform data fusion and step the control software, and (3) send actuator commands to the hardware actuators. The helicopter dynamics and the environment actions are themselves software components during simulation runs.

²UML = Unified Modeling Language

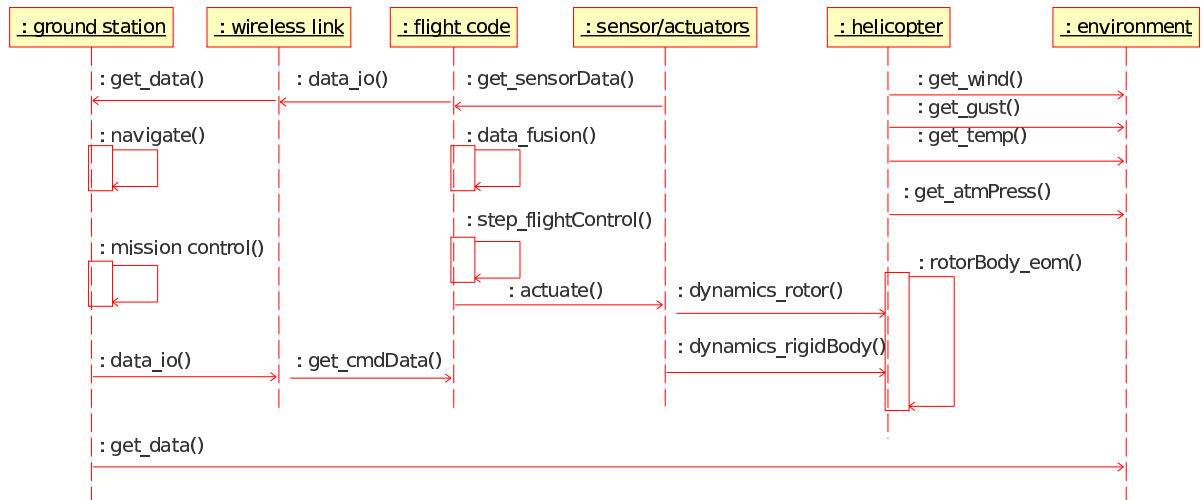


Figure 12.5: Software abstraction for data input/output across the various software components.

12.4 Hardware, Software and Systems Integration

Figure 12.3 on page 132 shows the basic layout of the helicopter system. The various onboard hardware sensors are itemized in Table 6.1 on page 68 and in Table 12.1 on the previous page. Figure 12.4 on page 133 shows the hardware bus architecture used for data collection and data transfer, and Figure 12.5 shows the primary software components that glue together the control code with the various sensors and hardware actuators shown in Figure 2.8 on page 22.

Figure 12.6 on the next page shows the top level simulation diagram for the helicopter SIMULINK [101] simulation and control environment. The simulation block implements a physics-based aerodynamic model of the helicopter’s main rotor, tail rotor, and the helicopter rigid body six degrees-of-freedom (6DoF) equations of motions (EOM). The control block, which operates in the primary flight control computer shown in Figure 12.3 on page 132, implements the helicopter flight controls and the guidance and navigation scheme. The control block implements all the signals and integrates the various feedback control loops (Figure 7.12 on page 92) and the bus management control logic (Figure 12.4 on page 133) into a single control module [136].

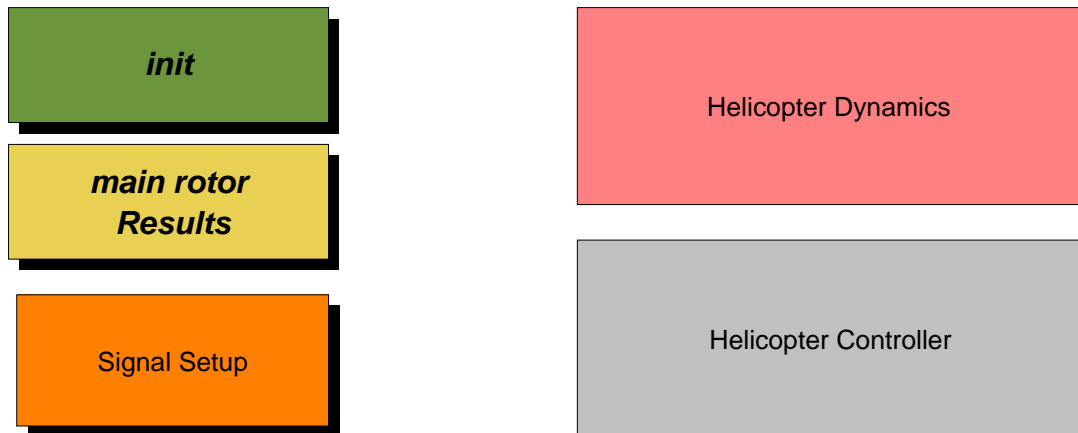


Figure 12.6: Helicopter SIMULINK simulation environment.

12.4.1 Embedded Software Generation

The simulation environment shown in Figure 12.6 is implemented in SIMULINK [101]. This is a pictorial or diagram based simulation language that provides two major advantages. The first advantage is that pictorial diagrams make complex information management and processing easier to understand and communicate. The second advantage is that SIMULINK allows for automated code generation via the Real Time Workshop (RTW) software suite. Once the diagrams have been debugged in simulation, the RTW automated code generation tool exports error free C/C++ code that is easily integrated within the helicopter embedded software architecture. The code that is used in simulation is exactly the same code that is used in implementing the real-time embedded flight code [136]. Figure 12.7 on the following page shows the process for embedding the control code in the working hardware with the following steps:

1. design and test the control code in the SIMULINK simulation environment
2. generate automated C/C++ code from SIMULINK via the RTW tools.
3. interface the embedded control code with the real-time operating system (RTOS) in a middleware (wrapper) code.
4. run the executable code within the real-time hardware-in-the-loop (HIL) environment.

12.4.2 Hardware and Software Integration

The hardware and software integration takes place in the middleware or wrapper code. The middleware code connects the various software components with the hardware via input/output interface to sensors and actuators. The nature of the interface is dictated by the hardware itself and can be digital, analog, serial or other related standards such as CAN or 1553 standard interface. The abstract top-most middleware embedded code takes the form in Listing 12.1 on page 138.

```
main ()
{
    init ();
    while( true )
    {
        read_sensors ();
        step_control_code ();
        update_actuators ();
    }
}
```

Listing 12.1: Embedded runtime hardware/software integration code

The initialization code contained within the `init ()` method contains the necessary commands that set the hardware to a known initial state. Subsequent to this, an infinite loop reads the sensor outputs, steps the embedded control code that generate the proper actuator commands, and sends those new updated commands to the hardware actuators.

12.4.2.1 Hardware Initialization

The hardware initialization process is of paramount importance. The initial system state defines a known starting point that define initial stabilization, guidance and navigation

control inputs. Table 12.2 defines initialization actions for the various hardware components, and Figure 12.8 illustrates the top-most level for the initialization state diagram.

Table 12.2: Hardware Initialization Action

hardware component	signal	initialization action
hall effect sensor	Ω	initialize software filter
pizo-elec rate gyro, MotionPak	p, q, r	bias reading initialize software filter
electronic compass	ϕ, θ, ψ	bias reading initialize software filter
pizo-elec accelerometers, MotionPak	$\dot{u}, \dot{v}, \dot{w}$	bias reading initialize software filter
differential GPS	x, y	establish differential link read initial position
ultrasound/infrared transducers	z	initialize software filter
analog to digital transducer	V_{bat}	initiate reading
electro-mechanical servos	PWM	initiate to neutral settings (see Table 3.2 on page 41)
ground station		init comm. with helicopter ground commands ready

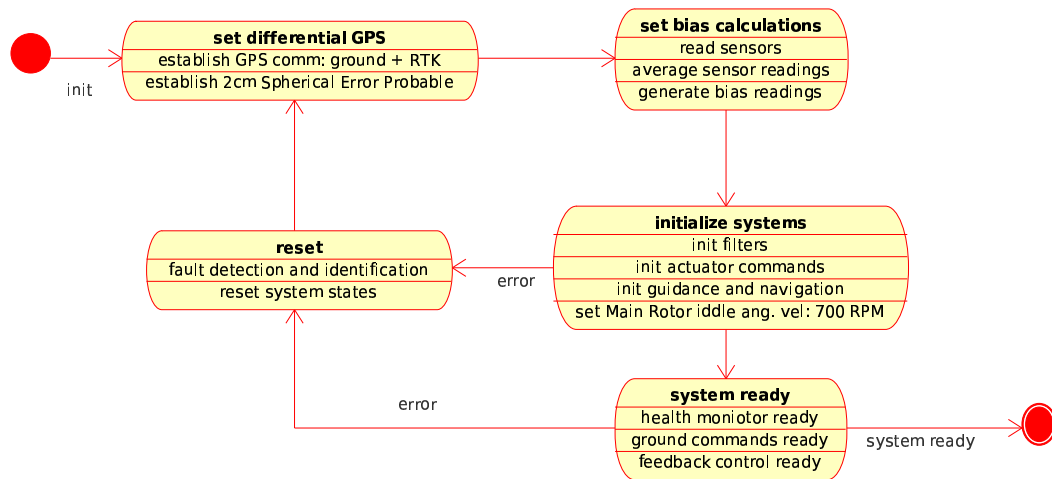


Figure 12.8: Helicopter top level initialization state diagram.

12.4.2.2 Sensor Reading

Table 6.1 on page 68 summarizes the signals available to the various sensors. In turn, Table 12.1 on page 134 summarizes the hardware interface to the sensors themselves.

Figure 12.3 on page 132 and Figure 12.4 on page 133 illustrate the hardware interface between the sensors and the flight computers. The sensor information is recorded asynchronously from the respective sensors and stored in a universally available data bus. The data bus information is available to all software engines (i.e. the embedded control executing in the main and secondary flight control computers and the ground station software) at every control step. The sensor data record is obtained by low level drivers which update the data bus at proper intervals. There is no direct control of the low level input drivers from any of the supervisory control loops. This ensures modularity between the system specific low level drivers and the more general supervisory control schemes running in the distributed flight and control computers.

12.4.2.3 Step Embedded Controller

The embedded controller step takes place at 50 Hz which is the update rate for the actuator pulse with modulation signals. The embedded control code is contained within the SIMULINK *Helicopter Control* in Figure 12.6 on page 136. This embedded control is designed, simulated and tested within the SIMULINK environment, and auto generated into C/C++ code via the *Real Time Workshop* (RTW) SIMULINK tools. Figure 7.12 on page 92 illustrates the general control design for the stability augmentation control (SAC) scheme implemented in the control step. Guidance and Navigation (G & N) commands are executed at a higher level that feed position commands to the embedded SAC controller.

12.4.2.4 Update Actuator Commands

The embedded controller generates a new set of actuator commands that are directly fed to the five basic helicopter actuators (Figure 2.7 on page 21 and Figure 2.8 on page 22).

Chapter 13

Summary and Conclusions

13.1 Summary

The work accomplished in this dissertation included building an entire experimental flight program from scratch that encompassed (a) the instrumentation of a miniature helicopter (4.86 ft. main rotor diameter, 11.5 lbs. empty weight) with 6DOF accelerators and gyros, telemetry, differential GPS system, compass, on-board computer, hall effect sensor, (b) design and fabrication of test stands for testing flight controls, (c) development of dynamics/aerodynamics models of main rotor, tail rotor, and main rotor stabilizer bar, helicopter engine, and rigid body frame, (d) design and development of feedback control for engine governor, main rotor RPM control, heading and yaw rate control, pitch and pitch rate control, roll and roll rate control, (e) running numerous real-time hardware-in-the-loop experiments with helicopter on test stands to test flight behavior, (f) on-board software integration of sensors, actuators, telemetry, controls, and models, (g) development of ground station interaction with helicopter, and (h) understanding how main rotor longitudinal and lateral cyclic control works.

The hardware sensors installed aboard the helicopter included the Systron Donner MotionPak (6DOF inertial system), NovaAtel ProPack II (Differential GPS), SHARP GP2D02 infrared and Ultrasound sensors (short range and altitude), Honeywell HMR3000 electronic compass (direction), and Hall effect sensor (main rotor RPM). The performance specifications for these sensors are detailed in Appendix I. Five servos were installed to

provide control inputs to main collective (lift control), tail rotor collective (heading control), throttle input (RPM control of main rotor), longitudinal cyclic (pitch control), and lateral cyclic (roll control).

The Ampro PC104 (Intel x86 chip at 100 MHz) which runs on the QNX Real-Time Operating System and the Dual Motorola MC68332 were selected as the two on-board CPU systems for carrying out all mission planning, sensor, telemetry and control functions. The PC104 is a 32bit microcontroller with 32 DIO, 32 TPU channels, and QSPI communication between it and the MC68332. It served as the primary flight computer and handled the FreeWave data link, the RTK GPS, compass sensor, and MotionPak as well as communications between its serial bus and the serial bus of the auxiliary flight computer (i.e., the dual MC68332). The two MC68332 microcontrollers are 32bit in which one is the master and the other is the slave. The master does the ground station i/o, handles the direct RC-safety link to the five actuators, and produces the five servo inputs through its PWM bus as well as sensor i/o from the Hall sensors through its PWM bus. The slave communicates with the PC104, handles GPS i/o, and handles sensor i/o from the ultrasound sensor through its digital bus. The software packages used to program the CPUs with embedded C/C++ code were MATLAB, SIMULINK, Real-Time Workshop, QNX RTOS.

Two novel test stands were designed and fabricated so that the instrumented helicopter could be placed on them for experimental testing of feedback control behavior. These were build from scratch. The first one is a linear and directional test stand (LDTS) for testing elevation, yaw, and heading commands. The second one is a rotational and dynamics test stand (RDTS) for testing pitch, pitch rate, roll, and roll rate commands. These two test stands were designed and built so that the RDTS stand could be mounted easily on top of the LDTS test stand making a combined LRDTTS stand. The combined LRDTTS stand is a test stand for testing all the above in any combination as desired: elevation, yaw, heading, pitch, pitch rate, roll, and roll rate commands. Finally, we made

use of a third test stand - the rate-table test stand (RTS) for calibrating the compass and MotionPak sensors as well as calibrating for horizontal position, ranging position, and angular motion about axes of rotation. The calibration of all sensors and hardware parameters (e.g., inertias) are presented in detail in Appendix I.

Next, the fundamental helicopter aerodynamic theory was fully developed for our specific application to the helicopter system under study. Momentum theory and Blade element theory were combined to provide the theory for blade element-momentum theory (BEMT) and documented in Appendix C. This was used to develop the blade equations of motion in Appendix D which in turn was used to develop the rotor force and moment equations in Appendix E. The rigid body dynamics equations of motion were used to provide the trim equations about a flight conditions (Appendix F) and helicopter stability derivatives (Appendix G) and these were used together with the rotor forces and moments equations (Appendix E) in deriving the coupled rotor-fuselage equations of motion (Appendix H). These in turned were used together with the trim equations (Appendix F) to develop the final set of linear rotor-fuselage equations of motion (Appendix H) for the Helicopter model.

The open-loop dynamics model for helicopter engine and main rotor RPM control was derived in Appendix J using the combined Blade Element and Momentum and Theory (BEMT) of Appendix C, taking into account the coupled dynamics of the carburetor, engine, main rotor and blade systems. Experimental data from test stand runs were used to estimate parameters of our theoretical model and, therefore, estimate accurately available power and main rotor torque. The non-linear throttle command input mapping to fuel rate was obtained using this method. A very important development was made at this step. We showed that main rotor and tail rotor torques could be modeled very accurately with a bias term plus a nonlinear term involving the product of RPM squared times the main rotor angle-of-attack raised to the three-halves power. This model was then used to linearize the state-equation for RMP dynamics and develop a simple but

accurate transfer function between the "available torque of the engine" and RPM. This transfer function was then used to develop a simple, but accurate transfer function model of the open-loop plant for the entire helicopter system which was then used to develop all the feedback control laws for autonomous flight purposes. Classical control methods (e.g., Nyquist diagrams, Bode plots, pole placement, gain and phase margins) were used to derive the feedback controller for controlling the main rotor RPM and achieve 60 degrees phase margin and infinite gain margin. An engine-carburator model was used to perform simulation of the closed loop systems. The simulation results compared well with the real-time data; see Figure J.14. Reliable control of the main rotor RPM is very fundamental for subsequent control and performance work since this control loop decouples the engine and the main rotor RPM from the remainder of the helicopter dynamics. Consequently, the RPM could be taken as a constant in the development of the other feedback controllers.

Combined Blade Element and Momentum theory was used to derive theoretical models for main and tail rotor aerodynamics of the helicopter. The parameters of these theoretical models were fine tuned using experimental data from runs on the test stands. The identification results for these helicopter aerodynamic models are described in Appendix K. The governing equations for yaw and heading angular motion were then obtained by implanting these identified models into the rigid body equations of motion that had been derived in Appendix B. Applying the appropriate trim conditions for the hover case (Appendix F), the open loop plant dynamics are derived for the yaw and heading control loops in Appendix L in Section L.2. Using the open loop plant and classical control, a yaw rate feedback controller was designed. After its implementation into the helicopter's CPU, test stand runs were made. The experiments on the test stands demonstrated accurate tracking of heading commands as well as holding a prescribed heading. Simulations were also conducted. The simulation results were shown to agree well with the real-time flight data obtained from the test stand experiments, Figures L.9 and L.10. This closed

loop decoupled another layer of non-linear dynamics from the overall helicopter equations of motion. That is, the heading feedback control loop automatically compensates for the torque and power changes due to the main rotor and tail rotor aerodynamics.

With RPM and heading loops well stabilized and with the helicopter tracking RPM and heading commands accurately, we focused next on the pitch axis. Main rotor longitudinal cyclic blade flapping theory (Appendix D) and the rigid body equations of motion (Appendix E) together with the extended linearized equations of motion (Appendix H) were used to derive a theoretical model for the open loop plant for the pitch axis, Section L.3 in Appendix L. Parameters of the model were fine tuned using experimental flight data from test stand runs. The application classical control techniques generated a closed loop system that provides adequate performance and disturbance rejection and is illustrated in Figure L.15. Again, simulation runs were conducted and the results compared well with real-time flight data gathered on the test stand, Figure L.15.

Next, we focused on the roll axis. The process for developing feedback control for the roll axis was similar to that used for the pitch axis except that lateral cyclic was used instead of longitudinal cyclic. That development was documented on Section L.4 of Appendix L. The application of classical control techniques generated a closed loop system that provides adequate performance and disturbance rejection and is illustrated in Figure L.17. Again, simulation runs were conducted and the results compared well with real-time flight data gathered on the test stand, Figure L.17. Coupled pitch and roll axis behavior is shown in Figure L.18 and demonstrates that the feedback controllers for the pitch and roll axes track commands very well in the presence of disturbances.

The experimental results that came from the test stands proved invaluable in developing stability and tracking capability for the helicopter to track RPM, heading, yaw rate, pitch, pitch rate, roll, and roll rate commands in the presence of disturbances. This was achieved with the execution of all the real-time hardware-in-the-loop (HWIL) experimental testing on the test stands. The Real-time HWIL testing on the test stands proved

valuable in every aspect of our work since such HWIL tests utilized actual flight hardware to characterize the dynamic and aerodynamic behavior of the helicopter. The feedback control law development in this dissertation demonstrates that helicopter stability and its capability to track commands are completely achievable by using only test stands and actual flight hardware in HWIL, all without pilot assistance and without crashing the vehicle

Appendix M describes a modern system engineering approach to the design of the overall helicopter system. Furthermore, Chapter 12 details the steps taken to integrate all hardware and software. The hardware interface or hardware data bus architecture between the various sensors and actuators and the flight computers were described in Figure 12.4. Next, the integration of the relevant embedded software with the actual hardware had to follow a specific process for proper system initialization and subsequent operation. This process was described in Figure 12.5. Part of the embedded software was auto generated from SIMULINK using the control laws that had been developed earlier and that had been validated against the various models obtained from actual flight data. This step was of great importance because the auto code generation process implemented in this way, using only proven and validated software without any further (hand-coded) human intervention, minimizes the possibility of human errors.

The hardware and software integration also included the development and integration of the ground station with the flight hardware and flight software. The ground station provided the flight vehicle with reference GPS information needed for differential GPS. In addition, the ground station provided a proper engineering graphical user interface (GUI) that enabled a necessary human-computer interface (HCI). The ground station, therefore, was both a vital link and enabling technology that made the real-time HWIL testing possible as well as a highly desirable data collection link.

In summary, the method developed in this thesis work consisted of at least four fundamental steps. The first step was to achieve an in-depth understanding of how

the complete overall system works. This step started with gaining a theoretical and fundamental understanding of how the rotor aerodynamics interacted with the fuselage and how that affected the control of the vehicle. Understanding this interaction indicated how to decouple a highly non-linear system via feedback linearization techniques. That is, the RPM feedback loop had to be closed first so that RPM could be treated very much like a constant for the rest of the feedback loops. Next, it was beneficial to compensate the tail rotor torque for tracking heading commands before proceeding to the pitch and roll attitude axes. As a result, the feedback controllers for the pitch and roll attitude axes could be easily derived using classical control techniques.

Second, the integration of the relevant sensor suite hardware with embedded software necessitated an understanding of system engineering techniques that enabled the encapsulation of a complex problem (generation of embedded real-time code) to be easily abstracted as part of the system characterization, simulation and validation work. Third, the design of relevant real-time HWIL tests that are needed for proper system identification, subsequent development of feedback controllers, and performance testing served as a tool of great value to the engineer, since flight hardware is an essential part of the package that is needed to fully characterize any real system. Fourth, the application of control theory in the development of feedback controllers follows naturally and with relative ease once the other steps have been done correctly.

In conclusion, the main contribution of this work is laying out every detail of what is required to design and execute successfully a helicopter hover mode flight program based on using only test stands without the assistance of a pilot and without ever crashing the vehicle. The main point is that every unmanned helicopter flight program could implement this method for flying autonomously in the neighborhood of the hover mode before ever bringing in pilot assistance to do gain scheduled flight across an extended flight envelop.

Bibliography

- [1] T. S. Alderete. Simulation aero model implementation. Technical Report NASA Ref. Pub. 1373, DOT/FAA/CT-94/83., NASA Ames Aviation Systems Division, NASA Ames Research Center, Moffet Field, CA, 1995.
- [2] O. Amidi. *An Autonomous Vision-Guided Helicopter*. PhD thesis, Robotics Institute, Carnegie Mellon University, Pittsburgh, PA, 1996.
- [3] O. Amidi, T. Kanade, and R. Miller. Vision-based autonomous helicopter research at carnegie mellon robotics institute. Technical Report NACA TN 2474, US Army and Troop Command, Aviation Research and Development Center, St. Louis, MS, October 1996.
- [4] Electronic Industries Association. *ANSI/EIA-632-1998, EIA Standard - Processes for Engineering a System*. Arlington, VA, 1999.
- [5] Electronic Industries Association. *EIA/IS-731.1, Systems Engineering Capability Model*. Arlington, VA, 1999.
- [6] A. Azuma and K. Kawachi. Local momentum theory and its application to the rotary wing. In *AIAA Fluid and Plasma Dynamics Conference*, 1975.
- [7] P. Bendotti and J. C. Morris. Robust hover control for a model helicopter. *Proceedings of the American Control Conference*, June, 1995.
- [8] M. Billinton. O.s. engines .61 sx-h wc product review. *R/C Rotary Modeler*, 1998.
- [9] G. Booch, J. Rumbaugh, and I. Jacobson. *The Unified Modeling Language User Guide*. Addison-Wesley, New Jersey, second edition, 2005.
- [10] J. Boulet. *History of the helicopter: as told by its pioneers, 1907-1956*. Editions France-Empire, Paris, first edition, 1984.

- [11] A. R. S. Bramwell. *Helicopter Dynamics*. Edward Arnold, London, second edition, 1976.
- [12] A. R. S. Bramwell. Response characteristics of the gyro-controlled lockheed rotor system. *The City University, Research Memorandum Aero 69/4*, April, 1969.
- [13] A. R. S. Bramwell, George Done, and David Balmford. *Bramwell's Helicopter Dynamics*. AIAA, Butterworth-Heinemann, Reston, VA, second edition, 2001.
- [14] J. T. Brewer, D. N. Mavris, and D. P. Schrage. Implementation of Georgia Tech's concurrent engineering methodology to a high speed civil transport (HSCT). *AIAA 5th Symposium on Multidisciplinary Analysis and Optimization*, Sept, 1994.
- [15] P. Brotherhood and W. Stewart. An experimental investigation of the flow through a helicopter rotor in forward flight. *ARC R & M 2734*, 1949.
- [16] P. D. Bruce, J. E. F. Silva, and M. G. Kellett. Maximum likelihood identification of a rotary-wing rpv simulation model from flight-test data. *AIAA Atmospheric Flight Mechanics Conference and Exhibit*, Aug, 1998.
- [17] W. L. Burleson, J. G. Hudak, K. Keller, and J. F. Sweigart. Southern Polytechnic State University autonomous remote reconnaissance system. *Proceedings AUVS 2002*, 2002.
- [18] Penn State Rotorcraft Center. Penn State Rotorcraft Center of Excellence/Vertical Lift Research Center. <http://www.engr.psu.edu/rcoe/>, 2006.
- [19] C. Chen and J. V. R. Prasad. A simplified inflow model of a helicopter rotor in forward descent. In *43rd AIAA Aerospace Sciences Meeting and Exhibit*, 2005.
- [20] C. Chen and J. V. R. Prasad. Theoretical investigations of a helicopter rotor in steep descent. In *AIAA Modeling and Simulation Technologies Conference and Exhibit*, 2005.
- [21] R. T. Chen. A simplified rotor system mathematical model for piloted flight dynamics simulation. Technical Report NASA TR 78575, Ames Research Center, Moffet Field, CA, June 1979.

- [22] R. T. Chen. Effects of primary rotor parameters on flapping dynamics. Technical Report NASA TP 1431, Ames Research Center, Moffet Field, CA, January 1980.
- [23] R. T. Chen and W. S. Hindson. Influence of the dynamic inflow on the helicopter vertical response. Technical Report NASA TM 88327, Ames Research Center, Moffet Field, CA, June 1986.
- [24] M. B. Chrissis, M. Konrad, and S. Shrum. *CMMI. Guidelines for Process Integration and Product Improvement*. Addison-Wesley, Reading, MA, first edition, 2003.
- [25] R. P. Coleman, A. M. Feingold, and C. W. Stempin. Evaluation of the induced-velocity field of an idealized helicopter rotor. Technical Report NACA ARR L5E10, Langley Aeronautical Laboratory, Langley Field, VA, June 1945.
- [26] U. S. Army Materiel Command. *Engineering Design Handbook, Helicopter Engineering, Part One, Preliminary Design. AMCP 706-201*. U.S. Army, Alexandria, VA, 1974.
- [27] A. K. Cooke and Eric W.H. Fitzpatrick. *Helicopter Test and Evaluation*. AIAA, Reston, VA, first edition, 2002.
- [28] SHARP Corporation. *GP2D02, Compact, High Sensitive Distance Measuring Sensor*. USA, December 1999.
- [29] SHARP Corporation. *Application Note: Distance Measuring Sensors*. USA, February 2003.
- [30] D. Cvetkovic, I. Kostic, C. Mitrovic, and A. Bengin. Mathematical models of helicopter flight dynamics. In *40th AIAA Aerospace Sciences Meeting & Exhibit*, 2002.
- [31] J. J. D’Azzo and C. H. Houpis. *Feedback Control System Analysis and Synthesis*. McGraw-Hill, New York, first edition, 1966.
- [32] C. W. de Silva. *Vibration and Shock Handbook*. CRC Press, Taylor & Francis Group, Boca Raton, FL, second edition, 2005.

- [33] Systron Donner Inertial Division. *Digital Compass Module HMR3000*. Concord, CA, December 1998.
- [34] Systron Donner Inertial Division. Motionpak: Multi-axis inertial sensing system, 2006.
- [35] B. P. Douglas. *Real Time UML*. Addison-Wesley, Boston, MA, third edition, 2004.
- [36] J. M. Drees. A theory of airflow through rotors and its application to some helicopter problems. *Journal Helicopter Association*, 1949.
- [37] O. S. Engines. *O.S. ENGINES .61 SX-H WC Operator's Manual*, 1994.
- [38] L. Thornhill et. all. Design of an agile unmanned combat vehicle: A product of the darpa ugcvc program. *Unmanned ground vehicle technology. Conference No5.*, 5083(4):358–370, April, 2003.
- [39] B. Etkin. *Dynamics of Atmospheric Flight*. John Wiley and Sons, New York, second edition, 1972.
- [40] B. Etkin. *Dynamics of Flight, Stability and Control*. John Wiley and Sons, New York, second edition, 1982.
- [41] R. I. Faulconbridge and M. J. Ryan. *Managing Complex Technical Projects: A Systems Engineering Approach*. Artech House Inc., Norwood, MA, first edition, 2003.
- [42] National Center for Advanced Technologies (NCAT). Overall perspective of ippd workshop. <http://www.ncat.com/ippdper.html>, 2007.
- [43] European Cooperation for Space Standardization. *ECSS-E-10A, Space Engineering-System Engineering*. Noordwijk, the Netherlands, 1996.
- [44] G. F. Franklin, J. D. Powell, and A. Emami-Naeini. *Feedback Control of Dynamic Systems*. Prentice Hall, New York, fifth edition, 2006.
- [45] Inc. Freescale Semiconductor. *MC68332 Technical Summary. 32-Bit Modular Microcontroller*. Austin, TX, December 2005.

- [46] Inc. Freescale Semiconductor. Mc68332: 32 bit microcontroller. <http://www.freescale.com/>, 2006. MC68332TS/D Rev. 2.
- [47] Inc FreeWave Technologies. *FreeWave Wireless Data Transceiver. User Manual*. Boulder, CO, December 1996.
- [48] Inc FreeWave Technologies. Freewave model information. <http://www.freewave.com/products/>, 2006.
- [49] S. Furr. What is real time and why do I need it? <http://www.qnx.com>, 2002. White Paper.
- [50] V. Gavrilets, B. Mettler, and E. Feron. Dynamic model for a miniature aerobatic helicopter. *MIT-LIDS report, no. LIDS-P-2580*, page all, 2003.
- [51] A. Gessow. Review of information on induced flow of a lifting rotor. *NACA-TN-3238*, page all, 1948.
- [52] A. Gessow. Effect of rotor-blade twist and plan-form taper on helicopter hovering performance. *NACA-TN-1542*, page all, 1954.
- [53] A. Gessow and G. C. Myers Jr. *Aerodynamics of the Helicopter*. College Park Press, New York, first edition, 1952. reprinted in 1985.
- [54] H. Glauert. The analysis of experimental results in the windmill brake and vortex ring states of an airscrew. Technical Report ARC R & M 1026, February 1926.
- [55] H. Glauert. A general theory of the autogyro. Technical Report ARC R & M 1111, November 1926.
- [56] H. Glauert. Airplane propellers. Vol. 4, Div. L in *Aerodynamic Theory*, edited by Durand W.F., Dover ed. 1943, 1928.
- [57] H. Glauert. On a horizontal flight of a helicopter. ARC R & M 1157, 1928.
- [58] L. Goldstein. On the vortex theory of screw propellers. *Proc. of the Royal Soc., Series A* 123, p. 440, 1929.

- [59] M. A. Gordon, D. P. Schrage, and K. Kuck. The Autonomous Scout Rotorcraft Testbed (ASRT) - a U.S. Army IPPD pilot project. In *Vertical Lift Aircraft Design Conference*, 1995.
- [60] H. F. Gregory. *Anything a horse can do: the story of the helicopter*. Reynal & Hitchcock, New York, first edition, 1944.
- [61] F. B. Gustafson and A. Gessow. Effect of rotor tip speed on helicopter rotor performance and maximum forward speed. *NACA ARP No. L6A16*, page all, 1946.
- [62] C. D. Hall. Spacecraft attitude dynamics and control. World.Wide.Web, 2002. <http://www.aoe.vt.edu/~chall/courses/aoe4140/>.
- [63] C. D. Hall. Novatel. <http://www.novatel.com/index.htm>, 2006.
- [64] C. M. Harris and A. G. Pierson. *Harris' Shock and Vibration Handbook*. McGRAW-HILL, New York, fifth edition, 2002.
- [65] F. D. Harris. Articulated rotor blade flapping motion at low advance ratio. *Journal of The American Helicopter Society*, page 41, 1972.
- [66] R. K. Heffley. A compilation and analysis of helicopter handling qualities data. volume ii. Technical Report NASA CR 9344, Systems Technology, Inc, Mountain View, CA, December 1979.
- [67] R. K. Heffley and W. F. Jewell. Aircraft handling qualities data. Technical Report NASA CR 2144, Systems Technology, Inc, Mountain View, CA, December 1972.
- [68] R. K. Heffley and M. A. Mnich. Minimum-complexity helicopter simulation math model. Technical Report NASA USAAVSCOM TR 87-A-7, Manudyne Systems, Inc, Los Altos, CA, July 1987.
- [69] H. H. Heyson and S. Katsoff. Induced velocities near a lifting rotor with nonuniform disk loading. Technical Report NACA TR 1319, Langley Aeronautical Laboratory, Langley Field, VA, December 1957.

- [70] K. B. Hilbert. A mathematical model of the uh-60. Technical Report NASA-TM-85890, Sikorsky Aircraft, Moffet Field, CA, December 1984.
- [71] J. Holt. *UML for Systems Engineering: Watching the Wheels*. IEE, United Kingdom, second edition, 2004.
- [72] Honeywell. *Digital Compass Module HMR3000*. Plymouth, MN, December 1999.
- [73] Inc Horizon Hobby Distributors. *JR PCM10x User Manual. Helicopter Version*. Champaign, IL, December 1999.
- [74] J. J. Howlet. Uh-60a black hawk engineering simulation program: Volume i - mathematical model. Technical Report NASA-CR-166309, Sikorsky Aircraft, Stratford, Conn, December 1981.
- [75] NovAtel Inc. *MiLLennium GPSCard, Guide to Installation & Operation*. Alberta, Ca, May 1997.
- [76] NovAtel Inc. *GPS+ Reference Manual*. Alberta, Ca, May 2006.
- [77] Carnegie Mellon University Software Engineering Institute. *The Capability Maturity Model: Guidelines for Improving the Software Process*. Addison-Wesley, Reading, MA, first edition, 1999.
- [78] Carnegie Mellon University Software Engineering Institute. *CMU/SEI-2002-TR-011, Capability Maturity Model Integration (CMMI), Version 1.1 Continuous Representation*. Pittsburgh, PA, 2002.
- [79] Carnegie Mellon University Software Engineering Institute. *CMU/SEI-2002-TR-012, Capability Maturity Model Integration (CMMI), Version 1.1 Staged Representation*. Pittsburgh, PA, 2002.
- [80] E. Johnson and D. Schrage. The Georgia Tech unmanned aerial research vehicle: GTMax. *AIAA Guidance, Navigation, and Control Conference and Exhibit*, 2003.
- [81] E. Johnson, D. Schrage, J. Prasad, and G. Vachtsevanos. UAV flight test programs at Georgia Tech. *AIAA 3rd "Unmanned Unlimited" Technical Conference, Workshop and Exhibit*, 2004.

- [82] W. Johnson. *Helicopter Theory*. Princeton University Press, New Jersey, first edition, 1980. reprinted in 1985.
- [83] A. Walter Castles Jr. and A Robin B. Gray. Empirical relation between induced velocity, thrust, and rate of descent of a helicopter rotor as determined by wind-tunnel tests on four model rotors. Technical Report NACA TN 2474, Georgia Institute of Technology, Atlanta, GA, October 1951.
- [84] A. Walter Castles Jr. and J. H. De Leeuw. The normal component of the induced velocity in the vicinity of a lifting rotor and some examples of its application. Technical Report NACA TR 1184, Georgia Institute of Technology, Atlanta, GA, October 1954.
- [85] T. R. Kane and D. A. Levinson. *Dynamics, Theory and Applications*. McGraw-Hill, New York, first edition, 1985.
- [86] T. Kasse. *Practical Insight Into CMMI*. Artech House, Norwood, MA, first edition, 2004.
- [87] S. K. Kim and D. M. Tilbury. Mathematical modeling and experimental identification of a model helicopter. In *AIAA Modeling and Simulation Technologies Conference & Exhibit, Collection of Technical Papers*, 1998.
- [88] S. K. Kim and D. M. Tilbury. Mathematical modeling and experimental identification of an unmanned helicopter robot with flybar dynamics. *J. Robot. Syst.*, 21(3):95–116, 2004.
- [89] V. Klein and E. A. Morelli. *Aircraft System Identification. Theory and Practice*. AIAA, Blacksburg, VA, 2006.
- [90] M. Knight and R. A. Hefner. Static thrust of the lifting airscrew. Technical Report NASA TN 626, Georgia Institute of Technology, Atlanta, GA, December 1937.
- [91] K. Kondak, C. Deeg, G. Hommel, M. Musial, and V. Remuss. Mechanical model and control of an autonomous small size helicopter with a stiff main rotor. *Intelligent Robots and Systems, 2004. (IROS 2004). Proceedings. 2004 IEEE/RSJ International Conference on*, 3:2469–2474, 2004.

- [92] J. G. Leishman. *Principles of Helicopter Aerodynamics*. Cambridge University Press, Cambridge, UK, second edition, 2006.
- [93] P. Leroux. Microkernel RTOSs simplify software testability. <http://www.qnx.com>, 2002. White Paper.
- [94] E. K. Liberatore. *Helicopters before Helicopters*. Krieger Publishing, Malabar, FL, 1998.
- [95] Charles Lidstone. The gimballed helicopter testbed: Design, build and validation. Master's thesis, Department of Electrical and Computer Engineering University of Toronto, Toronto, CA, 2003.
- [96] P. W. Linkins. *Elements of Engineering Mechanics*. McGraw-Hill, New York, 1973.
- [97] L. Ljung. *System Identification*. Prentice-Hall, New York, 1987.
- [98] C. N. H. Lock, H. Bateman, and H. C. H. Townsend. An extension of the vortex theory of airscrew with applications to airscrews of small pitch and including experimental results. ARC R & M 1014, 1925.
- [99] K. W. Mangler and H. B. Squire. The induced velocity field of a rotor. Technical Report ARC R & M 2642, London, UK, May 1950.
- [100] MapleSoft. Maple. <http://www.maplesoft.com/applications/>, 2007.
- [101] Mathworks. Mathworks matlab and simulink. <http://www.mathworks.com>, 2007.
- [102] R. E. McFarland75. A standard kinematic model for flight simulation at NASA-AMES. Technical Report NASA CR 2497, Computer Sciences Corporation, Mountain View, CA, January 1975.
- [103] D. McRuer, I. Ashkenas, and D. Graham. *Aircraft Dynamics and Automatic Control*. Princeton University Press, New York, first edition, 1973.
- [104] B. Mettler, C. Denver, and E. Feron. Scaling effects and dynamic characteristics of miniature rotorcraft. *Journal of Guidance, Control, and Dynamics* 2004, 27, June, 2004.

- [105] Bernard Mettler. *Identification Modeling and Characteristics of a Miniature Rotorcraft*. Kluwer Academic Publishers, Boston, MA, first edition, 2003.
- [106] Bernard Mettler, M. B. Tischler, and Takeo Kanade. System identification of small-size unmanned helicopter dynamics. In *American Helicopter Society 55th Forum*, 1999.
- [107] Bernard Mettler, M. B. Tischler, and Takeo Kanade. Attitude control optimization for a small-scale unmanned helicopter. In *AIAA Guidance, Navigation and Control Conference*, 2000.
- [108] Bernard Mettler, Mark Tischler, and Takeo Kanade. System identification of a model-scale helicopter. Technical Report CMU-RI-TR-00-03, Robotics Institute, Carnegie Mellon University, Pittsburgh, PA, January 2000.
- [109] J. C. Morris, , M. van Nieuwstadt, and P. Bendotti. Identification and control of a model helicopter in hover. *Proceedings of the American Control Conference*, June, 1994.
- [110] Alexander A. Nikolsky. *Helicopter Analysis*. John Wiley & Sons, New York, first edition, 1951.
- [111] N. S. Nise. *Control Systems Engineering*. John Wiley & Sons, New York, fourth edition, 2004.
- [112] U. S. Department of Defense. *DoD Integrated Product and Process Development Handbook*. Washington, D.C, 1998.
- [113] U. S. Department of Defense. *MIL-HDBK-61A(SE), Military Handbook - Configuration Management Guidance*. Washington, D.C, 2001.
- [114] U.S. Department of Defense. *Military Standard - Configuration Management*. Washington, D.C., 1992.
- [115] U.S. Department of Defense. *MIL-STD-499B, Military Standard - Systems Engineering - Draft*. Washington, D.C., 1994.

- [116] University of Maryland. University of Maryland Alfred Gessow Rotorcraft Center of Excellence (AGRC). <http://www.enaе.umd.edu/AGRC/>, 2006.
- [117] Georgia Institute of Technology. Georgia Institute of Technology Center of Excellence for Rotary Wing Aircraft Technology (CERWAT). <http://www.ae.gatech.edu/labs/windtunl/expaero/coehome.html>, 2006.
- [118] K. Ogata. *Modern Control Engineering*. Prentice Hall, New Jersey, second edition, 1990.
- [119] Gareth D. Padfield. *Helicopter Flight Dynamics: The Theory and Application of Flying Qualities and Simulation Modeling*. AIAA, London, first edition, 1996. reprinted in 1985.
- [120] P. R. Payne. *Helicopter Dynamics and Aerodynamics*. Pitman & Sons, London, first edition, 1959. reprinted in 1985.
- [121] M. G. Perhinschi and J. V. R. Prasad. A simulation model of an autonomous helicopter. In *RPVs/UAVs International Conference, 13th, Conference Papers*, pages 36.1–36.13, 1998.
- [122] Andrea Prencipe, Andrew Davies, and Mike Hobday (eds). *The Business of Systems Integration*. Oxford University Press, Oxford, first edition, 2004.
- [123] Carnegie Mellon Autonomous Helicopter Project. Carnegie Mellon Autonomous Helicopter Project. <http://www.cs.cmu.edu/afs/cs/project/chopper/www/>, 2007.
- [124] R. W. Prouty. *Helicopter Performance, Stability and Control*. Krieger Publishing Co., New York, first edition, 1986. reprinted in 2002.
- [125] QSSL. QNX product portfolio. <http://www.qnx.com>, 2007.
- [126] Wolfram Research. Mathematica. <http://www.wolfram.com/>, 2007.
- [127] J. B. ReVelle. *Quality Essentials. A Reference Guide from A to Z*. Quality Press, Milwaukee, WI, 2004.
- [128] J. Rumbaugh, I. Jacobson, and G. Booch. *The Unified Modeling Language Manual*. Addison-Wesley, New Jersey, second edition, 2005.

- [129] D. Schlüter. *Radio Controlled Helicopter Manual (Hubschrauber Ferngesteuert)*. Aurgus Books, Exeter, England, 1992.
- [130] D. Schrage, K. Taggart, and D. DeLaurentis. IPPD concept development process for Future Combat System. *9th AIAA/ISSMO Symposium on Multidisciplinary Analysis and Optimization*, Sept., 2002.
- [131] D. P. Schrage. Autonomous scout rotorcraft testbed (asrt) final report. Technical Report NASA Ref. Pub. 1373, DOT/FAA/CT-94/83., Georgia Tech, Georgia Tech, Atlanta, GA, July 24, 1997.
- [132] E. Seckel. *Stability and Control of Airplanes and Helicopters*. Academic Press Inc., New York, first edition, 1964.
- [133] J. Seddon and S. Newman. *Basic Helicopter Aerodynamics*. AIAA, Reston, VA, second edition, 2001.
- [134] J. Shan and H. H. T. Liu. Development of an experimental testbed for multiple vehicles formation flight control. *Proceedings of the 2005 IEEE Conference on Control Applications*, 2006.
- [135] J. Shapiro. *Principles of Helicopter Engineering*. Temple PRes Limited, London, England, 1955.
- [136] M. Simon, M. Compere, T Connolly, C. Lors, W. Smith, and M. Brudnak. Hybrid electric power and energy laboratory hardware-in-the-loop and vehicle model implementation. page all, April, 2006. SAE International 2006 World Congress.
- [137] G. J. Sissingh. Response characteristics of the gyro-controlled Lockheed rotor system. *Proceedings of the 23rd Annual Forum of the AHS*, May, 1967.
- [138] IEEE Computer Society. *IEEE-STD-1220, IEEE Standard for Application and Management of the Systems Engineering Process*. New York, 1998.
- [139] B. Springsteen, E. K. Bailey, S. H. Nash, and J. P. Woolsey. Integrated product and process development case study: Development of the f/a-18e/f. *Institute for Defense Analysis, IDA Document D-2228*, page all, 1999.

- [140] J. Stack, F. X. Caradonna, and O. Savas. Flow visualizations and extended thrust time histories of rotor vortex wakes in descent. *American Helicopter Society*, page all, 2004. 4th Decennial Specialist's Conference on Aeromechanics.
- [141] Robert F. Stengel. *Flight Dynamics*. Princeton University Press, New Jersey, first edition, 2004.
- [142] W. Z. Stepniewski and C. N. Keys. *Rotatory-Wing Aerodynamics*. Dover, New York, first edition, 1984.
- [143] B. L. Stevens and F. L. Lewis. *Aircraft Control and Simulation*. John Wiley & Sons, Inc., New York, second edition, 2003.
- [144] O. Tanner and H. P. Geeringt. Two-degree-of-freedom robust controller for an autonomous helicopter. *Proceedings of the American Control Conference, Denver, CO*, June, 2003.
- [145] C. R. Theodore, M. B. Tischler, and J. D. Colbourne. Rapid frequency-domain modeling methods for unmanned aerial vehicle flight control applications. *Journal of Aircraft*, 41(4), July-August, 2004.
- [146] M. B. Tischler and M. G. Cauffman. Frequency-response method for rotorcraft system identification: Flight applications to bo-105 coupled rotor/fuselage dynamics. *Journal of the American Helicopter Society*, pages 3–37, 1992.
- [147] M. B. Tischler and R. K. Remple. *Aircraft and Rotorcraft System Identification*. AIAA, Blacksburg, VA, 2006.
- [148] C. Tomashofski and M. B. Tischler. Flight test identification of sh-2g dynamics in support of digital flight control system development. In *55th Annual Forum of The American Helicopter Society*, 1999.
- [149] Carnegie Mellon University. *SECMM-95-01, Systems Engineering Capability Maturity Model, Version 1.1*. Pittsburgh, PA, 1995.
- [150] G. Vachtsevanos, W. Kim, S. Al-Hasan, F. Rufus, and M. Simon. Autonomous vehicles: From flight control to mission planning using fuzzy logic techniques. *The*

- 1997 13 th International Conference on Digital Signal Processing, 2:977–981, July, 1997.
- [151] George J. Vachtsevanos, Wonoh Kim, Sami A. Al-Hasan, Freeman Rufus Jr., Miguel Simon, Daniel P. Schrage, and J. V. R. Prasad. Mission planning and flight control: Meeting the challenge with intelligent techniques. *JACIII*, 1(1):62–70, 1997.
- [152] D. A. Vallado. *Fundamentals of Astrodynamics and Applications*. McGraw-Hill, New York, 1997.
- [153] U. S. Secretary of Defense W. Perry. Memorandum, use of Integrated Product and Process Development and Integrated Product Teams in DoD acquisition. <http://www.ntsc.navy.mil/resources/library/acqguide/secdef.htm>, 1995.
- [154] J. Watkinson. *The Art of the Helicopter*. Elsevier Butterworth-Heinemann, Oxford, UK, first edition, 2004.
- [155] M. F. Weilenmann, U. Christen, and H. P. Geering. Robust helicopter position control at hover. *Proceedings of the American Control Conference*, 17(4):729–736, Baltimore, 1994.
- [156] M. F. Weilenmann and H. P. Geering. A test bench for rotorcraft hover control. *AIAA Journal of Guidance, Control, and Dynamics*, 17(4):729–736, October, 1994.
- [157] Wikipedia. International Aerial Robotics Competition. http://wikipedia.org/wiki/International_Aerial_Robotics_Competition, 2006.
- [158] R. I. Winner. Integrated product/process development in the new attack submarine program. *OUSD(A & T)*, page all, 2000.
- [159] M. I. Young. A simplified theory of hingeless rotors with application to tandem rotors. *Proceedings of the 18th Annual National Forum of the AHS*, May, 1962.
- [160] J. Zhao, J. V. R. Prasad, and D. Peters. Simplified dynamic wake distortion model for helicopter transitional flight. In *AIAA Atmospheric Flight Mechanics Conference and Exhibit*, 2003.

- [161] Peter H. Zipfel. *Modeling and Simulation of Aerospace Vehicle Dynamics*. AIAA, Reston, VA, first edition, 2000.

Appendix A

First Principles

A.1 Notations

A summary of kinematics definitions follows [85]. In general the angular velocity ${}^A\vec{\omega}^B$ of body \mathcal{B} in \mathcal{A} is given by:

$${}^A\vec{\omega}^B = \vec{b}_1 \frac{{}^A d\vec{b}_2}{dt} \bullet \vec{b}_3 + \vec{b}_2 \frac{{}^A d\vec{b}_3}{dt} \bullet \vec{b}_1 + \vec{b}_3 \frac{{}^A d\vec{b}_1}{dt} \bullet \vec{b}_2 \quad (\text{A.1.1})$$

and also:

$${}^A\vec{\omega}^B = {}^A\vec{\omega}^X + {}^X\vec{\omega}^{N_1} + \dots + {}^{N_{n-1}}\vec{\omega}^Z + {}^N\vec{\omega}^B \quad (\text{A.1.2})$$

where n is the number of auxiliary frames. The angular acceleration of \mathcal{B} in \mathcal{A} is such that:

$${}^A\vec{\alpha}^B = \frac{{}^A d{}^A\vec{\omega}^B}{dt} = \frac{{}^B d{}^A\vec{\omega}^B}{dt} \quad (\text{A.1.3})$$

Given that \vec{n} is a vector fixed in body \mathcal{B} , then:

$$\frac{{}^A d\vec{n}}{dt} = {}^A\vec{\omega}^B \times \vec{n} \quad (\text{A.1.4})$$

If \vec{n} is any vector, its time derivative in both frames \mathcal{A} and \mathcal{B} are related as:

$$\frac{{}^A d\vec{n}}{dt} = \frac{{}^B d\vec{n}}{dt} + {}^A\vec{\omega}^B \times \vec{n} \quad (\text{A.1.5})$$

where ${}^A\vec{\omega}^B$ is the angular velocity of \mathcal{B} in \mathcal{A} . Let vector \vec{p} be a vector from a fixed point O in \mathcal{A} to any other point moving in reference frame \mathcal{A} , then the velocity ${}^A\vec{v}_p$ and

acceleration ${}^{\mathcal{A}}\vec{a}_p$ of \vec{p} in \mathcal{A} are given by:

$$\begin{aligned} {}^{\mathcal{A}}\vec{v}_p &= \frac{{}^{\mathcal{A}}d\vec{p}}{dt} \\ {}^{\mathcal{A}}\vec{a}_p &= \frac{{}^{\mathcal{A}}d{}^{\mathcal{A}}\vec{v}_p}{dt} \end{aligned} \quad (\text{A.1.6})$$

Let P and Q be two points fixed on a rigid body \mathcal{B} with angular velocity ${}^{\mathcal{A}}\vec{\omega}^{\mathcal{B}}$ in \mathcal{A} , and also let \vec{r} be the position vector from Q to P. Then the velocity ${}^{\mathcal{A}}\vec{v}_p$ and acceleration ${}^{\mathcal{A}}\vec{a}_p$ of P in \mathcal{A} , and the velocity ${}^{\mathcal{A}}\vec{v}_q$ and acceleration ${}^{\mathcal{A}}\vec{a}_q$ of Q in \mathcal{A} follow the following relation [85]:

$$\begin{aligned} {}^{\mathcal{A}}\vec{v}_p &= \frac{{}^{\mathcal{A}}d\vec{p}}{dt} & {}^{\mathcal{A}}\vec{a}_p &= \frac{{}^{\mathcal{A}}d{}^{\mathcal{A}}\vec{v}_p}{dt} \\ &= \frac{{}^{\mathcal{A}}d(\vec{q} + \vec{r})}{dt} & &= \frac{{}^{\mathcal{A}}d{}^{\mathcal{A}}\vec{v}_q}{dt} + \frac{{}^{\mathcal{A}}d{}^{\mathcal{A}}\vec{\omega}^{\mathcal{B}}}{dt} \times \vec{r} + {}^{\mathcal{A}}\vec{\omega}^{\mathcal{B}} \times \frac{{}^{\mathcal{A}}d\vec{r}}{dt} \\ &= {}^{\mathcal{A}}\vec{v}_q + {}^{\mathcal{A}}\vec{\omega}^{\mathcal{B}} \times \vec{r} & &= {}^{\mathcal{A}}\vec{a}_q + {}^{\mathcal{A}}\vec{\alpha}^{\mathcal{B}} \times \vec{r} + {}^{\mathcal{A}}\vec{\omega}^{\mathcal{B}} \times ({}^{\mathcal{A}}\vec{\omega}^{\mathcal{B}} \times \vec{r}) \end{aligned} \quad (\text{A.1.7})$$

Let point P be moving in the rigid body \mathcal{B} , while the body \mathcal{B} is itself moving within the reference frame \mathcal{A} , then the velocity ${}^{\mathcal{A}}\vec{v}_p$ of P in \mathcal{A} and the acceleration ${}^{\mathcal{A}}\vec{a}_p$ of P in \mathcal{A} are given by [85]:

$$\begin{aligned} {}^{\mathcal{A}}\vec{v}_p &= {}^{\mathcal{A}}\vec{v}_{\hat{P}} + {}^{\mathcal{B}}\vec{v}_p \\ {}^{\mathcal{A}}\vec{a}_p &= {}^{\mathcal{A}}\vec{a}_{\hat{P}} + {}^{\mathcal{B}}\vec{a}_p + 2{}^{\mathcal{A}}\vec{\omega}^{\mathcal{B}} \times {}^{\mathcal{B}}\vec{v}_p \end{aligned} \quad (\text{A.1.8})$$

where ${}^{\mathcal{A}}\vec{v}_{\hat{P}}$ is the velocity in \mathcal{A} of point \hat{P} of \mathcal{B} that coincides with P at the same instant under consideration, and ${}^{\mathcal{B}}\vec{v}_p$ is the velocity of P in \mathcal{B} . Similarly, the term ${}^{\mathcal{A}}\vec{a}_{\hat{P}}$ is the acceleration of \hat{P} in \mathcal{A} , ${}^{\mathcal{B}}\vec{a}_p$ is the acceleration of P in \mathcal{B} , and $2{}^{\mathcal{A}}\vec{\omega}^{\mathcal{B}} \times {}^{\mathcal{B}}\vec{v}_p$ is the Coriolis acceleration experienced by point P moving in frame \mathcal{B} .

A.2 Angular Momentum and Moment of Momentum

The following originates from a variety of sources, mainly [39, 62, 96, 103].

Let ${}^o\vec{r}_{dm}$ be the position vector from point O to a differential mass element dm in body \mathcal{B} , and let ${}^{\mathcal{I}}\vec{v}_{dm}$ be the velocity of the mass element dm in the inertial frame \mathcal{I} . The moment of momentum \vec{H}^o of a rigid body \mathcal{B} about a point O is defined as:

$$\vec{H}^o = \int_{\mathcal{B}} {}^o\vec{r}_{dm} \times {}^{\mathcal{I}}\vec{v}_{dm} dm \quad (\text{A.2.1})$$

where quantity ${}^{\mathcal{I}}\vec{v}_{dm} dm$ is the momentum of the differential mass element dm , the quantity ${}^o\vec{r}_{dm}$ is the moment arm, and the cross product ${}^o\vec{r}_{dm} \times {}^{\mathcal{I}}\vec{v}_{dm} dm$ is the moment of that momentum about point O in body \mathcal{B} .

Using equation A.1.7 we have that the velocity ${}^{\mathcal{I}}\vec{v}_{dm}$ is given by

$${}^{\mathcal{I}}\vec{v}_{dm} = {}^{\mathcal{I}}\vec{v}_o + {}^{\mathcal{I}}\vec{\omega}^{\mathcal{B}} \times {}^o\vec{r}_{dm} \quad (\text{A.2.2})$$

and equation A.2.1 becomes:

$$\begin{aligned} \vec{H}^o &= \int_{\mathcal{B}} {}^o\vec{r}_{dm} \times \left[{}^{\mathcal{I}}\vec{v}_o + {}^{\mathcal{I}}\vec{\omega}^{\mathcal{B}} \times {}^o\vec{r}_{dm} \right] dm \\ &= \int_{\mathcal{B}} \left[{}^o\vec{r}_{dm} \times {}^{\mathcal{I}}\vec{v}_o \right] dm + \int_{\mathcal{B}} \left[{}^o\vec{r}_{dm} \times \left({}^{\mathcal{I}}\vec{\omega}^{\mathcal{B}} \times {}^o\vec{r}_{dm} \right) \right] dm \end{aligned} \quad (\text{A.2.3})$$

Next we use the triple product identity to get:

$$\vec{a} \times (\vec{b} \times \vec{c}) = \vec{b}(\vec{a} \cdot \vec{c}) - \vec{c}(\vec{a} \cdot \vec{b}) = \vec{b}\vec{a} \cdot \vec{c} - \vec{c}\vec{a} \cdot \vec{b} \quad (\text{A.2.4})$$

and reverse the order of dot products to get:

$$\begin{aligned} {}_o\vec{r}_{dm} \times \left({}^I\vec{\omega}^{\mathcal{B}} \times {}_o\vec{r}_{dm} \right) &= {}^I\vec{\omega}^{\mathcal{B}} {}_o\vec{r}_{dm} \cdot {}_o\vec{r}_{dm} - {}_o\vec{r}_{dm} {}^I\vec{\omega}^{\mathcal{B}} \cdot {}_o\vec{r}_{dm} \\ &= {}_o\vec{r}_{dm} \cdot {}_o\vec{r}_{dm} {}^I\vec{\omega}^{\mathcal{B}} - {}_o\vec{r}_{dm} {}_o\vec{r}_{dm} \cdot {}^I\vec{\omega}^{\mathcal{B}} \end{aligned} \quad (\text{A.2.5})$$

We now use identity tensor operator such that:

$$\vec{\mathcal{I}} \cdot \vec{n} = \vec{n} \cdot \vec{\mathcal{I}} = \vec{n}$$

then

$${}_o\vec{r}_{dm} \cdot {}_o\vec{r}_{dm} {}^I\vec{\omega}^{\mathcal{B}} = {}_o\vec{r}_{dm} \cdot {}_o\vec{r}_{dm} \vec{\mathcal{I}} \cdot {}^I\vec{\omega}^{\mathcal{B}} = {}_o r_{dm}^2 \vec{\mathcal{I}} \cdot {}^I\vec{\omega}^{\mathcal{B}} \quad (\text{A.2.6})$$

using A.2.5 and A.2.6 then equation A.2.3 becomes:

$$\vec{H}^o = \int_{\mathcal{B}} \left[{}_o\vec{r}_{dm} \times {}^I\vec{v}_o \right] dm + \int_{\mathcal{B}} \left[{}_o r_{dm}^2 \vec{\mathcal{I}} \cdot {}^I\vec{\omega}^{\mathcal{B}} - {}_o\vec{r}_{dm} {}_o\vec{r}_{dm} \cdot {}^I\vec{\omega}^{\mathcal{B}} \right] dm \quad (\text{A.2.7})$$

In the above equation A.2.7, both terms ${}^I\vec{v}_o$ and ${}^I\vec{\omega}^{\mathcal{B}}$ are constant with respect to the variable of integration, and can therefore come outside the integral such that:

$$\vec{H}^o = \int_{\mathcal{B}} {}_o\vec{r}_{dm} dm \times {}^I\vec{v}_o + \int_{\mathcal{B}} \left[{}_o r_{dm}^2 \vec{\mathcal{I}} - {}_o\vec{r}_{dm} {}_o\vec{r}_{dm} \right] dm \cdot {}^I\vec{\omega}^{\mathcal{B}} \quad (\text{A.2.8})$$

the term

$$\vec{C}^o = \int_{\mathcal{B}} {}_o\vec{r}_{dm} dm \quad (\text{A.2.9})$$

is the first moment of inertia about point O in body \mathcal{B} , and the term

$$\vec{I}^o = \int_{\mathcal{B}} \left[{}_o r_{dm}^2 \vec{\mathcal{I}} - {}_o\vec{r}_{dm} {}_o\vec{r}_{dm} \right] dm \quad (\text{A.2.10})$$

is the second moment of inertia about point O. Equation A.2.8 becomes

$$\vec{H}^o = \vec{C}^o \times {}^I\vec{v}_o + \vec{I}^o \cdot {}^I\vec{\omega}^{\mathcal{B}} \quad (\text{A.2.11})$$

In the case when the point O is the center of mass of body \mathcal{B} , then the first moment of inertia \vec{C}^o becomes zero (no distance ${}^o\vec{r}_{dm}$). In this case the moment of momentum about the center of mass (CM) of body \mathcal{B} becomes:

$$\vec{H}^{CM} = \vec{I}^{CM} \cdot \mathcal{I}\vec{\omega}^{\mathcal{B}} \quad (\text{A.2.12})$$

In turn, the angular momentum \vec{h}^o about point O of a rigid body \mathcal{B} is defined as:

$$\vec{h}^o = \int_{\mathcal{B}} {}^o\vec{r}_{dm} \times {}^o\dot{\vec{r}}_{dm} dm \quad (\text{A.2.13})$$

Note that in the above equation A.2.13 the term ${}^o\dot{\vec{r}}_{dm} dm$ is not the momentum of the differential element dm . Making use of equation A.1.5 we have that

$${}^o\dot{\vec{r}}_{dm} = \frac{\mathcal{I}d_o\vec{r}_{dm}}{dt} = \frac{\mathcal{B}d_o\vec{r}_{dm}}{dt} + \mathcal{I}\vec{\omega}^{\mathcal{B}} \times {}^o\vec{r}_{dm} \quad (\text{A.2.14})$$

but

$$\frac{\mathcal{B}d_o\vec{r}_{dm}}{dt} = \vec{0} \quad (\text{A.2.15})$$

since ${}^o\vec{r}_{dm}$ is fixed in body \mathcal{B} . Substituting the above in equation A.2.13 we have:

$$\vec{h}^o = \int_{\mathcal{B}} {}^o\vec{r}_{dm} \times \left(\mathcal{I}\vec{\omega}^{\mathcal{B}} \times {}^o\vec{r}_{dm} \right) dm \quad (\text{A.2.16})$$

Following the preceding development, equation A.2.16 above becomes:

$$\vec{h}^o = \vec{I}^o \cdot \mathcal{I}\vec{\omega}^{\mathcal{B}} \quad (\text{A.2.17})$$

It is worthwhile to notice that the moment of momentum \vec{H}^o and the moment of inertia \vec{h}^o are equal only when point O coincides with the center of mass of body \mathcal{B} . Both quantities are not equal in all other cases.

A.3 Newton's Law for Moment of Momentum

An application of Newton's 2nd Law tells us that the sum of all moments \vec{G}^o about point O in body \mathcal{B} equals the rate of change of moment of Momentum $\dot{\vec{H}}^o$ about that point such that:

$$\vec{G}^o = \dot{\vec{H}}^o \quad (\text{A.3.1})$$

Since both the first moment of inertia \vec{C}^o and the second moment of inertia \vec{I}^o are constant in the body frame, we have that

$$\dot{\vec{H}}^o = \vec{C}^o \times \mathcal{I}\dot{\vec{v}}_o + \vec{I}^o \cdot \mathcal{I}\dot{\vec{\omega}}^{\mathcal{B}} + \mathcal{I}\vec{\omega}^{\mathcal{B}} \times \left(\vec{I}^o \cdot \mathcal{I}\vec{\omega}^{\mathcal{B}} \right) \quad (\text{A.3.2})$$

Noticing that $\mathcal{I}\dot{\vec{v}}^o = \mathcal{I}\vec{a}_o$ and rearranging the above equation we have:

$$\vec{G}^o - \vec{C}^o \times \mathcal{I}\vec{a}_o = \vec{I}^o \cdot \mathcal{I}\dot{\vec{\omega}}^{\mathcal{B}} + \mathcal{I}\vec{\omega}^{\mathcal{B}} \times \left(\vec{I}^o \cdot \mathcal{I}\vec{\omega}^{\mathcal{B}} \right) = \dot{\vec{h}}^o \quad (\text{A.3.3})$$

Again, when point O coincides with the center of mass of body \mathcal{B} , then the first moment of inertia becomes zero ($\vec{C}^o = \vec{0}$) and:

$$\vec{G}^{CM} = \dot{\vec{h}}^{CM} \quad (\text{A.3.4})$$

A.4 Newton's Law for Linear Momentum

Derivations of Newton's laws are seen in references [39].

Let m be the mass of a rigid body with center of mass velocity \vec{v}_{CM} , then the rate of change of linear momentum $m\vec{v}$ is given by:

$$\int \vec{F} = \frac{dm\vec{v}}{dt} \quad (\text{A.4.1})$$

In the case when all internal forces occur in equal and opposite vector tuples, then the internal forces cancel. In this case the term $\int \vec{F}$ equals the resultant of all the external forces acting on the system.

A.5 Fluid Equations of Change

Figure A.1 illustrates a fluid region \mathcal{R} at times t and $t + \Delta t$. Let $Q = Q(\vec{r}, t)$ be a property of a fluid volume dv at position \vec{r} and time t , the general integral of the fluid property for a region $\mathcal{R}(t)$ and its derivative are

$$\begin{aligned}
 I(t) &= \iiint_{\mathcal{R}(t)} Q(\vec{r}, t) dv \\
 \frac{dI(t)}{dt} &= \lim_{\Delta t \rightarrow 0} \frac{I(t + \Delta t) - I(t)}{\Delta t} \\
 \frac{dI(t)}{dt} &= \lim_{\Delta t \rightarrow 0} \left[\iiint_{\mathcal{R}(t + \Delta t)} Q(\vec{r}, t + \Delta t) dv - \iiint_{\mathcal{R}(t)} Q(\vec{r}, t) dv \right] \frac{1}{\Delta t}
 \end{aligned} \tag{A.5.1}$$

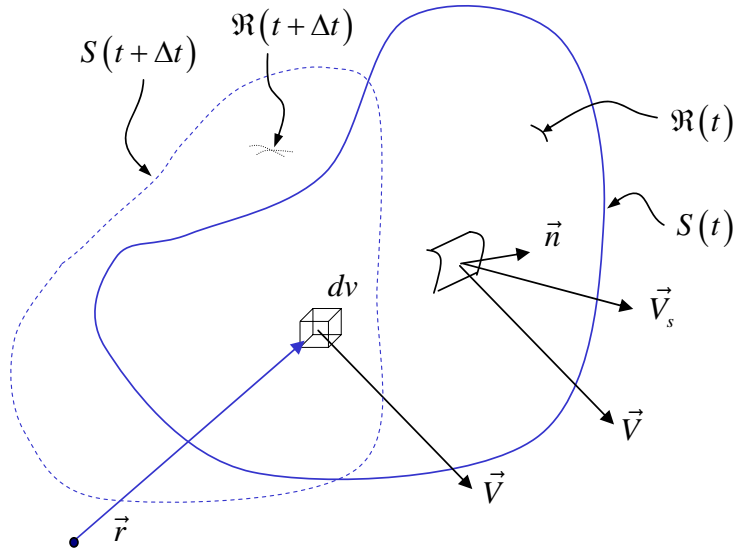


Figure A.1: Differential fluid element volume dv with fluid velocity \vec{V} in region $\mathcal{R}(t)$ delimited by surface $S(t)$ with surface normal \vec{n} and surface velocity \vec{V}_s .

Figure A.2 on the next page illustrates equation (A.5.2) on the following page graphically. Region $\mathcal{R}(t + \Delta t)$ result from $Q(\vec{r}, t + \Delta t) dv$ changes over the original region $\mathcal{R}(t)$ and volumetric changes $Q(\vec{r}, t + \Delta t) \vec{V}_S \cdot \vec{n} \Delta t$ over the differential surface $dS(t)$ where $dv = \Delta S \vec{V}_S \cdot \vec{n} \Delta t$.

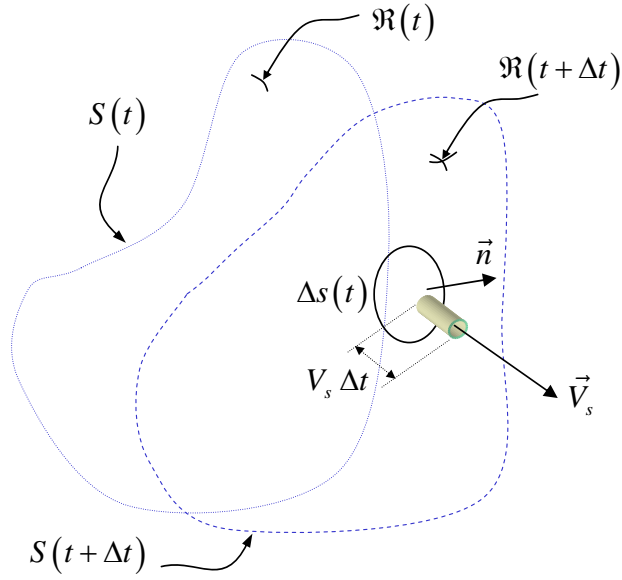


Figure A.2: Differential fluid volume dv resulting from surface velocity \vec{V}_s .

$$\begin{aligned}
 \iiint_{\mathcal{R}(t+\Delta t)} Q(\vec{r}, t + \Delta t) dv &= \iiint_{\mathcal{R}(t)} Q(\vec{r}, t + \Delta t) dv \\
 &+ \iint_{S(t)} \left(Q(\vec{r}, t + \Delta t) \vec{V}_s \cdot \vec{n} \Delta t \right) dS + O(\Delta t^2)
 \end{aligned} \tag{A.5.2}$$

Substituting equation (A.5.2) into (A.5.1) yields

$$\begin{aligned}
 \frac{dI(t)}{dt} &= \lim_{\Delta t \rightarrow 0} \left[\iiint_{\mathcal{R}(t)} Q(\vec{r}, t + \Delta t) dv - Q(\vec{r}, t) dv \right] \frac{1}{\Delta t} \\
 &+ \left[\iint_{S(t)} \left(Q(\vec{r}, t + \Delta t) \vec{V}_s \cdot \vec{n} \Delta t \right) dS \right] \frac{1}{\Delta t} + O(\Delta t^2)
 \end{aligned} \tag{A.5.3}$$

After taking the limit, the above expression gives Leibniz rule of integral differentiation:

$$\begin{aligned} \frac{d}{dt} \iiint_{\mathcal{R}(t)} Q(\vec{r}, t) dv &= \iiint_{\mathcal{R}(t)} \frac{\partial}{\partial t} Q(\vec{r}, t) dv \\ &+ \oiint_{\mathcal{S}(t)} \left(Q(\vec{r}, t) \vec{V}_S \cdot \vec{n} \right) d\mathcal{S} \end{aligned} \quad (\text{A.5.4})$$

Equation (A.5.4) is a general expression for an open finite region $\mathcal{R}(t)$ that does not have knowledge of any physical concept. A specialization of the above equation takes place when the surface is attached to the material such that

$$\vec{V}_S = \vec{V}(\vec{r}, t), \quad \frac{d}{dt} \rightarrow \frac{D}{Dt} \quad (\text{A.5.5})$$

In this case the general derivative operator d/dt becomes the material or substantial derivative operator D/Dt . Application to equation (A.5.4) yields

$$\frac{D}{Dt} \iiint_{\mathcal{R}(t)} Q(\vec{r}, t) dv = \iiint_{\mathcal{R}(t)} \frac{\partial}{\partial t} Q(\vec{r}, t) dv + \oiint_{\mathcal{S}(t)} \left(Q(\vec{r}, t) \vec{V}(\vec{r}, t) \cdot \vec{n} \right) d\mathcal{S} \quad (\text{A.5.6})$$

Equation (A.5.6) is the Reynold's Transport Theorem for closed or material regions. Next, taking the difference of the open region and the closed region gives

$$\frac{d}{dt} \iiint_{\mathcal{R}(t)} Q(\vec{r}, t) dv = \frac{D}{Dt} \iiint_{\mathcal{R}(t)} Q(\vec{r}, t) dv - \oiint_{\mathcal{S}(t)} \left(Q(\vec{r}, t) (\vec{V} - \vec{V}_S) \cdot \vec{n} \right) d\mathcal{S} \quad (\text{A.5.7})$$

Equation (A.5.7) says that the rate of change of an open region equals the rate of change of a closed region minus the velocity of fluid relative to the material surface.

A.5.1 Mass Equations of Change: Conservation of Mass

Let $Q(\vec{r}, t) = 1$, and let $\rho(\vec{r}, t)$ be the mass density per unit volume. In this case, the mass of region \mathcal{R} is given by

$$\iiint_{\mathcal{R}(t)} \rho Q(\vec{r}, t) dv = \iiint_{\mathcal{R}(t)} \rho(\vec{r}, t) dv \quad , \quad \rho(\vec{r}, t) = \text{mass per unit volume} \quad (\text{A.5.8})$$

Application of equation (A.5.7) on the preceding page gives

$$\frac{d}{dt} \iiint_{\mathcal{R}(t)} \rho(\vec{r}, t) dv = \frac{D}{Dt} \iiint_{\mathcal{R}(t)} \rho(\vec{r}, t) dv - \oint\!\!\!\oint_{\mathcal{S}(t)} \left(\rho(\vec{r}, t) (\vec{V} - \vec{V}_S) \cdot \vec{n} \right) d\mathcal{S} \quad (\text{A.5.9})$$

but by definition of ρ as the mass density per unit volume,

$$\frac{D}{Dt} \iiint_{\mathcal{R}(t)} \rho(\vec{r}, t) dv = 0 \quad (\text{A.5.10})$$

then

$$\frac{d}{dt} \iiint_{\mathcal{R}(t)} \rho(\vec{r}, t) dv = - \oint\!\!\!\oint_{\mathcal{S}(t)} \left(\rho(\vec{r}, t) (\vec{V} - \vec{V}_S) \cdot \vec{n} \right) d\mathcal{S} \quad (\text{A.5.11})$$

Equation (A.5.11) is the expression for conservation of mass for an open region where the density ρ can be discontinue. The term on the left is the time rate of change of mass in the region \mathcal{R} , and the term on the right is the net outflow of mass from region \mathcal{R} . Applying equation (A.5.10) to the Reynold's Transport Theorem in equation (A.5.6) on the previous page gives

$$0 = \iiint_{\mathcal{R}(t)} \frac{\partial}{\partial t} \rho(\vec{r}, t) dv + \oint\!\!\!\oint_{\mathcal{S}(t)} \rho(\vec{r}, t) \vec{V}(\vec{r}, t) \cdot \vec{n} d\mathcal{S} \quad (\text{A.5.12})$$

Equation (A.5.12) is the expression for conservation of mass when ρ is continuous and belongs to the same material. Applying the divergence theorem

$$\iiint_{\mathcal{R}(t)} \text{div} \vec{A} dv = \oint\!\!\!\oint_{\mathcal{S}(t)} \vec{A} \cdot \vec{n} d\mathcal{S} \quad (\text{A.5.13})$$

to the right most portion of equation (A.5.12) on the previous page gives

$$\begin{aligned} \iiint_{\mathcal{R}(t)} \text{div}(\rho \vec{V}) dv &= \oiint_{\mathcal{S}(t)} \rho \vec{V} \cdot \vec{n} d\mathcal{S} \\ \text{div}(\rho \vec{V}) &= \lim_{\Delta v \rightarrow 0} \frac{1}{\Delta v} \oiint_{\mathcal{S}(t)} \rho \vec{V} \cdot \vec{n} d\mathcal{S} \end{aligned} \quad (\text{A.5.14})$$

Equation (A.5.14) gives the divergence theorem physical meaning in that $\text{div}(\rho \vec{V})$ equals the net outflow from region \mathcal{R} as the region shrinks to a point. Application of the divergence theorem to equation (A.5.12) on the previous page gives

$$0 = \iiint_{\mathcal{R}(t)} \left[\frac{\partial \rho}{\partial t} + \text{div}(\rho \vec{V}) \right] dv \quad (\text{A.5.15})$$

For an arbitrary region , the integrand in (A.5.15) must be zero

$$0 = \frac{\partial \rho}{\partial t} + \text{div}(\rho \vec{V}) \quad (\text{A.5.16})$$

Equation (A.5.16) is the continuity equation, a conservative form for a point expression for continuous mass conservation that holds at every point in the flow. The term $\rho \vec{V}$ is the mass flux or flow of mass per unit time per unit area. For steady flow $\partial \rho / \partial t = 0$ and

$$\text{div}(\rho \vec{V}) = 0 \quad (\text{A.5.17})$$

Equation (A.5.17) is the continuity equation for steady flow. Expanding the term $\text{div}(\rho \vec{V})$ as

$$\text{div}(\rho \vec{V}) = \rho \text{div} \vec{V} + \vec{V} \cdot \nabla \rho$$

and substituting in equation (A.5.16)

$$\begin{aligned} 0 &= \frac{\partial \rho}{\partial t} + \vec{V} \cdot \nabla \rho + \rho \text{div} \vec{V} \\ 0 &= \frac{D\rho}{Dt} + \rho \text{div} \vec{V} \end{aligned} \quad (\text{A.5.18})$$

where $D\rho/Dt = \partial\rho/\partial t + \vec{V} \cdot \nabla\rho$ is the material or substantial derivative. Equation (A.5.18) on the previous page is the non-conservative or particle form of the continuity equation. For incompressible flows

$$\begin{aligned} \text{div}\vec{V} = 0 &= \lim_{\Delta v \rightarrow 0} \frac{1}{\Delta v} \oint_{S(t)} \vec{V} \cdot \vec{n} dS \\ \frac{D\rho}{Dt} &= 0 \end{aligned} \tag{A.5.19}$$

Equation (A.5.19) says that the density per unit volume ρ is constant or the density of a fluid particle is constant but different particles in the fluid might have different densities.

A.5.2 Momentum Equations of Change: Conservation of Momentum

Let $Q(\vec{r}, t) = \vec{V}(\vec{r}, t)$, then mass flux vector $\rho\vec{V}$ represents the transport of mass through space per unit time per unit area. For a fixed mass system, the time rate of change of momentum equals the sum of the forces acting on the region \mathcal{R}

$$\begin{aligned} \frac{D}{Dt} \iiint_{\mathcal{R}(t)} \rho\vec{V} dv &= \sum (\text{forces acting on region}) \\ &= \iiint_{\mathcal{R}(t)} \rho\vec{f} dv - \oint_{S(t)} p\vec{n} dS + \oint_{S(t)} \vec{n} \cdot \bar{\tau} dS \end{aligned} \tag{A.5.20}$$

where $\bar{\tau}$ is the viscous stress tensor. Substituting equation (A.5.20) into equation (A.5.7) on page 171 gives

$$\begin{aligned} \frac{d}{dt} \iiint_{\mathcal{R}(t)} \rho\vec{V} dv &= \iiint_{\mathcal{R}(t)} \rho\vec{f} dv - \oint_{S(t)} p\vec{n} dS + \oint_{S(t)} \vec{n} \cdot \bar{\tau} dS \\ &\quad - \oint_{S(t)} \left(\rho\vec{V} (\vec{V} - \vec{V}_S) \cdot \vec{n} \right) dS \end{aligned} \tag{A.5.21}$$

where the right most term in the above equation represents the outflow of momentum. Equation (A.5.21) on the previous page is the most general form of the equation of change

for angular momentum for region \mathcal{R} . It says that the time rate of change of momentum of an open region equals the time rate of change of momentum of a closed region minus the outflow of momentum from the region. Application of the gradient and divergence theorems to the Reynold's transport theorem in equation (A.5.6) on page 171 and to equation (A.5.20) on the previous page to a flow in a continuous region \mathcal{R} gives

$$\begin{aligned}
\frac{D}{Dt} \iiint_{\mathcal{R}(t)} \rho \vec{V} dv &= \iiint_{\mathcal{R}(t)} \rho \vec{f} dv - \iiint_{\mathcal{R}(t)} \text{grad}(p) dv + \iiint_{\mathcal{R}(t)} \text{div}(\bar{\tau}) dv \\
&= \iiint_{\mathcal{R}(t)} \left[\rho \vec{f} - \text{grad}(p) + \text{div}(\bar{\tau}) \right] dv \\
&= \iiint_{\mathcal{R}(t)} \left[\frac{\partial}{\partial t} \rho \vec{V} + \text{div}(\rho \vec{V} \vec{V}) \right] dv
\end{aligned} \tag{A.5.22}$$

The integrand in the above equation must vanish for an arbitrary region \mathcal{R} , then

$$\frac{\partial}{\partial t} \rho \vec{V} + \text{div}(\rho \vec{V} \vec{V}) = \rho \vec{f} - \text{grad}(p) + \text{div}(\bar{\tau}) \tag{A.5.23}$$

Equation (A.5.23) above is a differential equation for the conservative form of the time rate of change of momentum. The term $\rho \vec{V} \vec{V}$ is the momentum flux tensor such that

$$\text{div}(\rho \vec{V} \vec{V}) = (\text{div} \rho \vec{V}) \vec{V} + \rho \vec{V} \cdot \nabla \vec{V} \tag{A.5.24}$$

Substitution of equation (A.5.24) into (A.5.23) and expanding gives

$$\rho \frac{\partial}{\partial t} \vec{V} + \left[\frac{\partial \rho}{\partial t} + \text{div} \rho \vec{V} \right] \vec{V} + \rho \vec{V} \cdot \nabla \vec{V} = \rho \vec{f} - \text{grad}(p) + \text{div}(\bar{\tau}) \tag{A.5.25}$$

where $\partial \rho / \partial t + \text{div} \rho \vec{V} = 0$ by virtue of the continuity equation (A.5.16) on page 173. In addition,

$$\rho \frac{\partial \vec{V}}{\partial t} = \rho \frac{\partial}{\partial t} \vec{V} + \rho \vec{V} \cdot \nabla \vec{V}$$

and therefore equation (A.5.25) on the previous page becomes

$$\rho \frac{\partial \vec{V}}{\partial t} = \rho \vec{f} - \text{grad}(p) + \text{div}(\bar{\bar{\tau}}) \quad (\text{A.5.26})$$

Equation (A.5.26) is the particle equation for continuous flow.

A.5.3 Energy Equations of Change: Conservation of Energy

The internal energy of a differential fluid volume dv with mass ρdv is given by $(\rho dv) e$ where e is the internal energy per unit mass. The kinetic energy of the fluid volume is $(\rho dv) V^2/2$. The total internal and kinetic energy of a fluid particle is therefore

$$\rho dv \left(e + \frac{V^2}{2} \right)$$

For a continuous region \mathcal{R} , the first law of thermodynamics says that the time rate of change of internal plus kinetic energy following a closed region equals the rate of work done by the forces action on the system plus the rate of heat going into the system from the surroundings. Mathematically

$$\frac{D}{Dt} \iiint_{R(t)} \rho \left(e + \frac{V^2}{2} \right) dv = \iiint_{R(t)} \rho \vec{f} \cdot \vec{V} dv + \oiint_{S(t)} \vec{n} \cdot \bar{\bar{\sigma}} \cdot \vec{V} dS - \oiint_{S(t)} \vec{q} \cdot \vec{n} dS \quad (\text{A.5.27})$$

where $\bar{\bar{\sigma}}$ is the surface stress tensor. The term

$$\iiint_{R(t)} \rho \vec{f} \cdot \vec{V} dv$$

is the total amount of work done by body forces. In turn, the term

$$\oiint_{S(t)} \vec{n} \cdot \bar{\bar{\sigma}} \cdot \vec{V} dS$$

is the total work done by surface stresses. The term

$$- \oint_{S(t)} \vec{q} \cdot \vec{n} dS$$

is the energy out of the system as indicated by the negative sign. The term

$$\frac{D}{Dt} \iiint_{\mathcal{R}(t)} \rho \left(e + \frac{V^2}{2} \right) dv$$

is the time rate of change of energy in a fixed-mass system or closed system. In this case

$$\begin{aligned} \frac{D}{Dt} \iiint_{\mathcal{R}(t)} \rho \left(e + \frac{V^2}{2} \right) dv &= \iiint_{\mathcal{R}(t)} \frac{D}{Dt} \rho \left(e + \frac{V^2}{2} \right) dv \\ &= \iiint_{\mathcal{R}(t)} \left[\frac{D(\rho dv)}{Dt} \left(e + \frac{V^2}{2} \right) + \rho \frac{D}{Dt} \left(e + \frac{V^2}{2} \right) dv \right] \\ &= \iiint_{\mathcal{R}(t)} \rho \frac{D}{Dt} \left(e + \frac{V^2}{2} \right) dv \end{aligned} \quad (\text{A.5.28})$$

since $D(\rho dv)/Dt$ is invariant for a fluid particle. Applying the divergence theorem to equation (A.5.27) on the previous page gives

$$0 = \iiint_{\mathcal{R}(t)} \left[\rho \frac{D}{Dt} \left(e + \frac{V^2}{2} \right) - \left(\rho \vec{f} \cdot \vec{V} \operatorname{div} (\vec{\bar{\sigma}} \cdot \vec{V}) - \operatorname{div} \vec{q} \right) \right] dv \quad (\text{A.5.29})$$

Since the region \mathcal{R} is arbitrary, the above equation is true for any region, and the integrand must be equal to zero. The resulting equation

$$\rho \frac{D}{Dt} \left(e + \frac{V^2}{2} \right) = \rho \vec{f} \cdot \vec{V} + \operatorname{div} (\vec{\bar{\sigma}} \cdot \vec{V}) - \operatorname{div} \vec{q} \quad (\text{A.5.30})$$

is the equation of change of energy for a continuous medium since the equation does not specify the stress for solid or fluid or the material to which it applies. This is the governing equation commonly known as the conservation of energy. For a fluid, the stress

tensor $\bar{\sigma}$ takes the form

$$\bar{\sigma} = -p\bar{I} + \bar{\tau}$$

where \bar{I} is the hydrodynamic unit tensor. Substituting into equation (A.5.30) on the preceding page yields

$$\rho \frac{D}{Dt} \left(e + \frac{V^2}{2} \right) = \rho \vec{f} \cdot \vec{V} - \text{div} (p\vec{V}) + \text{div} (\bar{\tau} \cdot \vec{V}) - \text{div} \vec{q} \quad (\text{A.5.31})$$

Equation (A.5.31) is the conservation of energy equation for a fluid mass in a continuous region \mathcal{R} .

Appendix B

Helicopter Frames of Reference

B.1 Inertial and Earth Reference Frames

A *first order tensor* satisfies the transformation law [161]

$${}^{\mathcal{B}}\vec{x} = {}^{\mathcal{B}}T^{\mathcal{A}} {}^{\mathcal{A}}\vec{x} \quad (\text{B.1.1})$$

where the vector \vec{x} describes the position of a point in space with respect to a reference frame \mathcal{A} or \mathcal{B} respectively. The transformation ${}^{\mathcal{B}}T^{\mathcal{A}}$ contains the mechanism necessary to transform the description of the point from one reference frame \mathcal{A} to another reference frame \mathcal{B} . Seven reference frames are of particular importance for flight mechanics [40, 161], and these are summarized in Table B.1.

Table B.1: Reference Frames in Flight Mechanics

Heliocentric:	important for interplanetary travel
Geocentric:	considers the rotation of the Earth, important for orbital trajectories.
Earth-Centered	origin at the Earth's center, considers Earth rotation, important for orbital flight
Earth-Surface:	centered at a local horizontal plane, reference frame for atmospheric flight
Vehicle-Carried:	origin attached to the vehicle.
Atmosphere-Fixed:	relevant for aerodynamic velocity and forces
Body frame:	relevant for the position and orientation of a vehicle

B.1.1 Heliocentric Reference Frame

The Heliocentric frame \mathcal{H} is located at the center of the Sun with its orientation defined such that its \vec{h}_1 axis points toward the *Autumnal Equinox* on the plane of the ecliptic,

the \vec{h}_2 axis points toward the *Winter Solstice* on the same ecliptic plane, and the \vec{h}_3 axis completes a right-handed orthonormal set perpendicular to the ecliptic plane. The Heliocentric plane is of importance for interplanetary travel[161].

B.1.2 Geocentric Reference Frame

The Geocentric \mathcal{G} reference frame is located one astronomical unit from the center of the Sun, and its orientation is given by the base vector $[\vec{x}_{EC}, \vec{y}_{EC}, \vec{z}_{EC}]$. The vector \vec{g}_{i1} is oriented toward the *vernal equinox*, the \vec{g}_{i3} vector is oriented with the Earth's rotational axis, and the vector \vec{g}_{i2} completes the orthonormal right-handed vector. Notice that for this frame to be truly an inertial frame, then the frame must define its position and orientation with respect to a particular epoch [161]. Such a frame has been defined by astronomers as the J2000 System [152].

B.1.3 Earth-Centered Reference Frame

The Earth-Centered frame \mathcal{E}_C is collocated with the Geocentric reference frame with its origin at the Earth center, and is defined by the base vectors $[\vec{x}_{EC}, \vec{y}_{EC}, \vec{z}_{EC}]$. The Earth-Centered Frame is similar to the Geocentric reference frame \mathcal{G} except that the \mathcal{E}_C frame has its \vec{x}_{EC} vector aligned with the *equatorial* vernal equinox. The orientation of the \mathcal{E}_C frame differs over long periods of time with respect to the orientation of \mathcal{G} and J2000 systems. The \mathcal{E}_C frame is commonly used in Earth orbital flight since the duration of these orbital flights are short with regard to the drift rate of its defining axis.

B.1.4 Earth-Surface Reference Frame

The Earth-surface \mathcal{E} frame is located on the surface of the Earth, and its most important characteristic is that it neglects the rotation ${}^{\mathcal{I}}\vec{\omega}^{\mathcal{E}}$ of the Earth. The base vectors $[\vec{x}_E, \vec{y}_E, \vec{z}_E]$ describe the orientation of this frame such that \vec{z}_E is directed toward the center of the Earth, \vec{x}_E is directed toward the north, and \vec{y}_E completes the right-handed orthonormal tuple [40].

B.1.5 Vehicle-Carried Reference Frame

The vehicle carried frame \mathcal{V} frame is attached to and is located at the center of mass CM belonging to a vehicle. The base vectors $[\vec{v}_1, \vec{v}_2, \vec{v}_3]$ are oriented such that the \vec{v}_3 axis is directed toward the center of the Earth along the gravity vector \vec{g} . The \vec{v}_1 axis is oriented toward the north, and its \vec{v}_2 axis completes the right-handed orthonormal tuple. The reference frame \mathcal{V} is parallel to the reference frame \mathcal{E} when the travel time or distance is short.

B.1.6 Atmosphere-Fixed or Wind Reference Frame

The Atmosphere-fixed reference frame \mathcal{A} is located relative to \mathcal{E} through a distance related to the average wind velocity ${}^{\mathcal{E}}\vec{w}$ in \mathcal{E} . Let the vehicle velocity relative to the atmosphere be ${}^{\mathcal{A}}\vec{v}$, then the vehicle velocity relative to \mathcal{E} is given by

$${}^{\mathcal{E}}\vec{v} = {}^{\mathcal{E}}\vec{w} + {}^{\mathcal{A}}\vec{v} \quad (\text{B.1.2})$$

B.1.7 Body-Fixed Reference Frame

The Body-Fixed reference frame \mathcal{B} is located at the center of mass CM of the vehicle. The orientation of this reference frame is such that the \vec{b}_3 axis is oriented downward, the \vec{b}_1 axis is oriented toward the nose of the vehicle, and the \vec{b}_2 completes the orthonormal right-handed set of axes. In this frame, the velocity components relative to a suitably defined inertial reference frame are given by $[u, v, w]$ and the corresponding inertial angular velocity is given by the $[p, q, r]$ vector [39, 119].

B.1.8 Inertial Reference Frame

Consider a stationary or not moving coordinate system or inertial reference frame \mathcal{I} in which Newton's laws are valid for mass (m) particle motion such that

1. \vec{f} = sum of all external forces acting on a particle
2. \vec{a} = particle's acceleration relative to \mathcal{I}
3. then $\vec{f} = m\vec{a}$

The angular rotation of the Earth in an inertial frame is a superposition of several angular rotations:

1. rotation on Earth's axis,
2. rotation of Earth's axis in its orbit around the Sun,
3. additional motion of the solar system and galaxy.

Space and hypervelocity flights need to account for all three angular motions, but atmospheric flight is mostly concerned with Earth's rotation about its axis when the flight time is significant with respect to both distance and time. Local (less than 15° of Earth radii) and relatively slow moving helicopter flight (such as hover flight with zero wind) considers the Earth's axis as an inertial frame fixed in space [39]. In this case, Earth's sidereal angular velocity Ω_E is constant with respect to inertial frame. The inertial angular velocity of the Earth expressed in Earth Fixed frame \mathcal{E}_C is

$$\mathcal{I}_{\vec{\omega}}^{\mathcal{E}_C} = \begin{pmatrix} 0 \\ 0 \\ \Omega_E \end{pmatrix} \quad (\text{B.1.3})$$

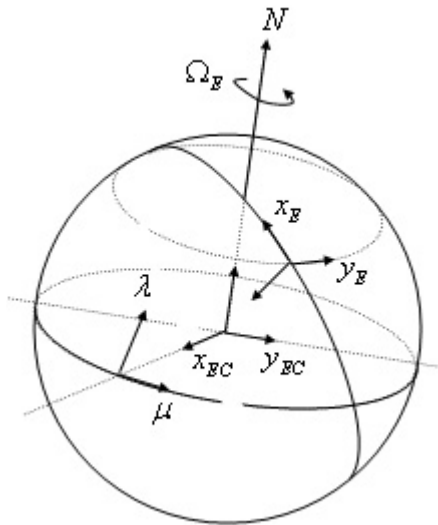


Figure B.1: Earth-Centered Reference Frame and Earth-Surface Reference Frame

In turn, the Earth's inertial angular velocity expressed in Earth Surface frame \mathcal{E} is

$$\begin{aligned}
&= {}^{\mathcal{E}}T_2^{\mathcal{E}c}(\lambda_E)\Omega_E \\
{}^{\mathcal{I}}\vec{\omega}^{\mathcal{E}} &= \begin{bmatrix} \sin \lambda_E & \cos \lambda_E \\ & 1 \\ \cos \lambda_E & -\sin \lambda_E \end{bmatrix} \begin{bmatrix} 0 \\ 0 \\ \Omega_E \end{bmatrix} = \begin{bmatrix} \cos \lambda_E \\ 0 \\ -\sin \lambda_E \end{bmatrix} \Omega_E \quad (\text{B.1.4})
\end{aligned}$$

where (λ_E, μ_E) are the latitude and longitude of a reference point o_E in the Earth frame \mathcal{E} (see Figure B.1 on the preceding page).

The inertial angular velocity ${}^{\mathcal{I}}\vec{\omega}^{\mathcal{V}}$ of the vehicle frame \mathcal{V} is

$${}^{\mathcal{I}}\vec{\omega}^{\mathcal{V}} = {}^{\mathcal{I}}\vec{\omega}^{\mathcal{E}c} + {}^{\mathcal{E}c}\vec{\omega}^{\mathcal{V}} \quad (\text{B.1.5})$$

where the inertial velocity ${}^{\mathcal{I}}\vec{\omega}^{\mathcal{E}c}$ of the Earth Centered frame in terms of the vehicle frame \mathcal{V} is

$$\begin{aligned}
&= {}^{\mathcal{V}}T_2^{\mathcal{E}c}(\lambda)\Omega_E \\
{}^{\mathcal{I}}\vec{\omega}_V^{\mathcal{E}c} &= \begin{bmatrix} \sin \lambda & \cos \lambda \\ & 1 \\ \cos \lambda & -\sin \lambda \end{bmatrix} \begin{bmatrix} 0 \\ 0 \\ \Omega_E \end{bmatrix} = \begin{bmatrix} \cos \lambda \\ 0 \\ -\sin \lambda \end{bmatrix} \Omega_E \quad (\text{B.1.6})
\end{aligned}$$

and the angular velocity ${}^{\mathcal{E}c}\vec{\omega}^{\mathcal{V}}$ of the vehicle frame \mathcal{V} relative to the Earth Centered frame $\mathcal{E}c$ takes the form

$$\begin{aligned}
&= -\dot{\lambda}\vec{v}_2 + \dot{\mu}\vec{z}_{EC} \\
{}^{\mathcal{E}c}\vec{\omega}^{\mathcal{V}} &= \begin{bmatrix} 0 \\ -\dot{\lambda} \\ 0 \end{bmatrix} + \begin{bmatrix} \sin \lambda & \cos \lambda \\ & 1 \\ \cos \lambda & -\sin \lambda \end{bmatrix} \begin{bmatrix} 0 \\ 0 \\ \dot{\mu} \end{bmatrix} = \begin{bmatrix} \dot{\mu} \cos \lambda \\ -\dot{\lambda} \\ -\dot{\mu} \sin \lambda \end{bmatrix} \quad (\text{B.1.7})
\end{aligned}$$

Substituting equations (B.1.6) and (B.1.7) into equation (B.1.5) gives the angular velocity of the vehicle frame \mathcal{V} expressed in the \mathcal{V} reference frame

$${}^{\mathcal{V}}\vec{\omega} = \begin{bmatrix} (\Omega_E + \dot{\mu}) \cos \lambda \\ -\dot{\lambda} \\ -(\Omega_E + \dot{\mu}) \sin \lambda \end{bmatrix} \quad (\text{B.1.8})$$

Helicopter flight involves angular dynamics that is inherently faster than the Earth's rotation Ω_E . Whence a large number of helicopter flight missions neglect the Earth's rotation and assume a non-rotating earth approximation. In addition, the three dimensional displacements and velocities involved in most helicopter maneuvers do not require taking into account the curvature of the Earth. Whence it is reasonable to accept a locally flat Earth approximation for helicopter missions of short duration. Heretofore, the development of the equations of motion (EOM) are based on the following two fundamental assumptions:

1. Local Flat Earth
2. Non-rotating Earth

B.2 Relations between the Body \mathcal{B} and Vehicle \mathcal{V} Reference Frame

Figure B.2 on the next page illustrates the body-fixed reference frame \mathcal{B} with body axis $[x, y, z]^T$, inertial body velocity $[u, v, w]^T$, inertial body angular velocity $[p, q, r]^T$, and corresponding inertial aerodynamic and propulsive forces $[XYZ]^T$ and inertial moments $[LMN]^T$. The angular attitude of the helicopter is most commonly specified by a set of angular rotations about three independent directions. The standard rotation sequence used in flight mechanics consists of a yaw ψ rotation about the v_3 axis of the vehicle frame \mathcal{V} (equation (B.2.1)), a subsequent pitch θ rotation about the new y-axis (equation (B.2.2)), and a final roll ϕ rotation about the intermediary x-axis (equation (B.2.3))

[39, 119, 141].

$${}^x T_3^y(\psi) = \begin{pmatrix} \cos \psi & \sin \psi & \\ -\sin \psi & \cos \psi & \\ & & 1 \end{pmatrix} \quad (\text{B.2.1})$$

$${}^z T_2^x(\theta) = \begin{pmatrix} \cos \theta & -\sin \theta & \\ & 1 & \\ \sin \theta & \cos \theta & \end{pmatrix} \quad (\text{B.2.2})$$

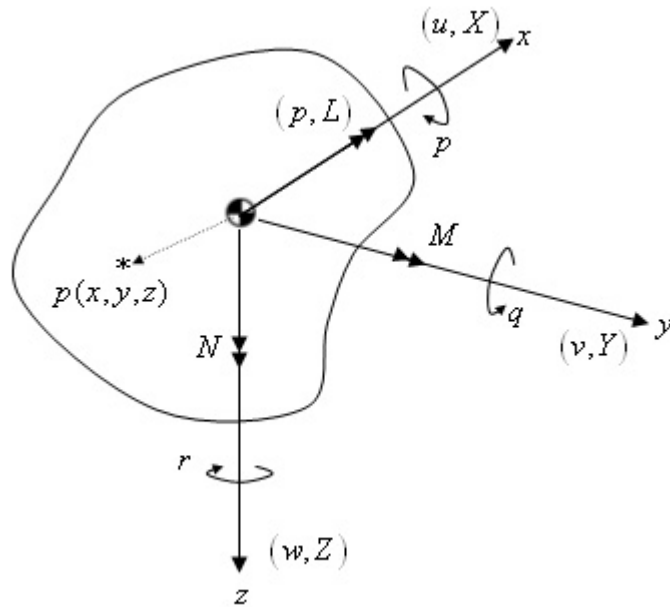


Figure B.2: Vehicle Body-Fixed Frame \mathcal{B}

$${}^B T_1^Z(\phi) = \begin{pmatrix} 1 & & \\ & \cos \phi & \sin \phi \\ & -\sin \phi & \cos \phi \end{pmatrix} \quad (\text{B.2.3})$$

where the frames \mathcal{X} and \mathcal{Z} in the above equation are intermediary frames. The

resultant transformation ${}^{\mathcal{B}}T^{\mathcal{V}}$ from Vehicle Frame \mathcal{V} to body frame \mathcal{B} is therefore

$$\begin{aligned}
 &= {}^{\mathcal{B}}T_1^{\mathcal{Z}}(\phi) {}^{\mathcal{Z}}T_2^{\mathcal{X}}(\theta) {}^{\mathcal{X}}T_3^{\mathcal{V}}(\psi) \\
 {}^{\mathcal{B}}T^{\mathcal{V}} &= \begin{bmatrix} c\theta c\psi & c\theta s\psi & -s\theta \\ s\phi s\theta c\psi - c\phi s\psi & s\phi s\theta s\psi + c\phi c\psi & s\phi c\theta \\ c\phi s\theta c\psi + s\phi s\psi & c\phi s\theta s\psi - s\phi c\psi & c\phi c\theta \end{bmatrix} \quad (\text{B.2.4})
 \end{aligned}$$

where $c(\cdot) = \cos(\cdot)$, $s(\cdot) = \sin(\cdot)$. The transformation ${}^{\mathcal{B}}T^{\mathcal{V}}$ is orthonormal such that

$$[{}^{\mathcal{B}}T^{\mathcal{V}}]^T = [{}^{\mathcal{B}}T^{\mathcal{V}}]^{-1} \Leftrightarrow {}^{\mathcal{V}}T^{\mathcal{B}} = [{}^{\mathcal{B}}T^{\mathcal{V}}]^T \quad (\text{B.2.5})$$

Figure B.3, Figure B.4 on the next page and Figure B.5 on the following page show the standard nomenclature for helicopter flight with a view from the side, top and rear respectively.

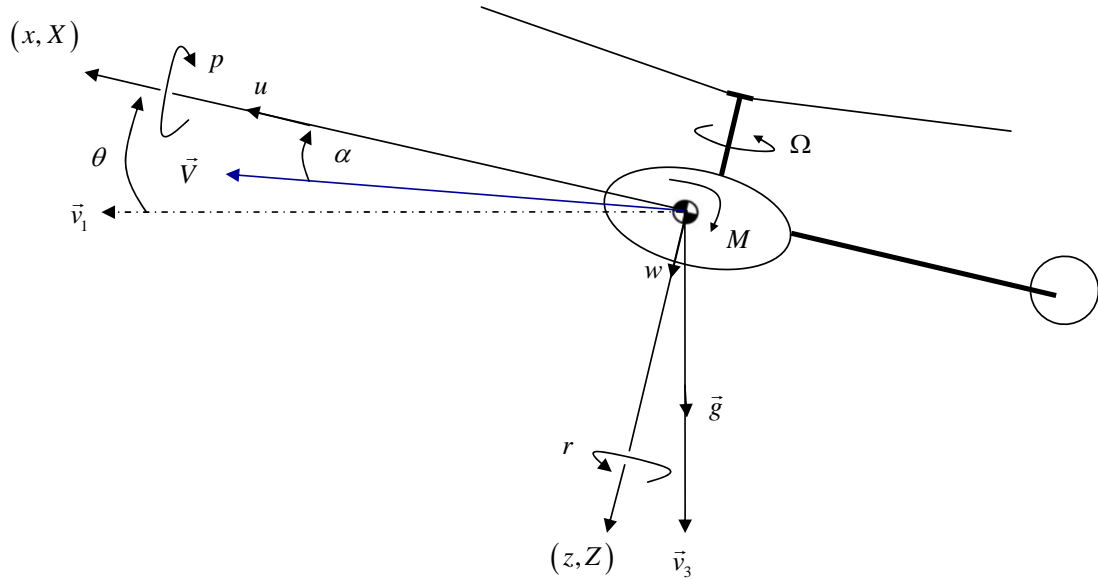


Figure B.3: Symmetric flight nomenclature and body frame axis. Side view.

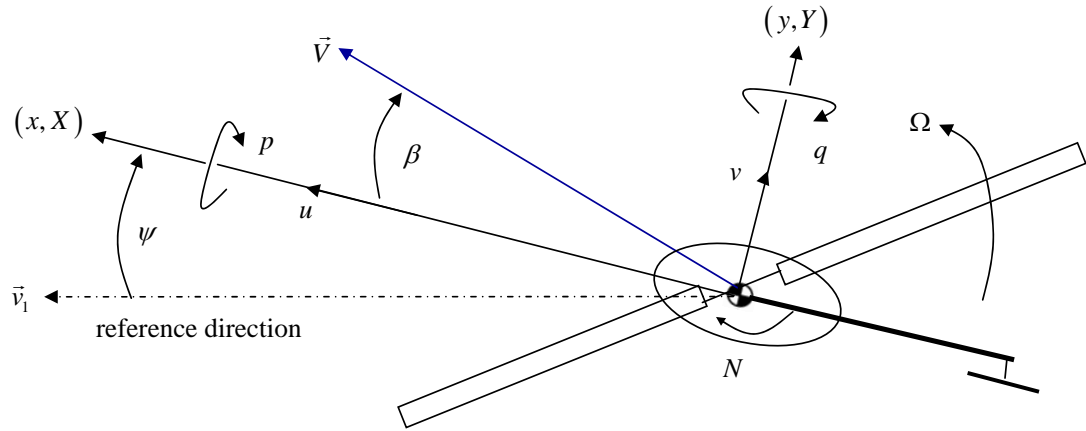


Figure B.4: Asymmetric flight nomenclature and body frame axis. Top view.

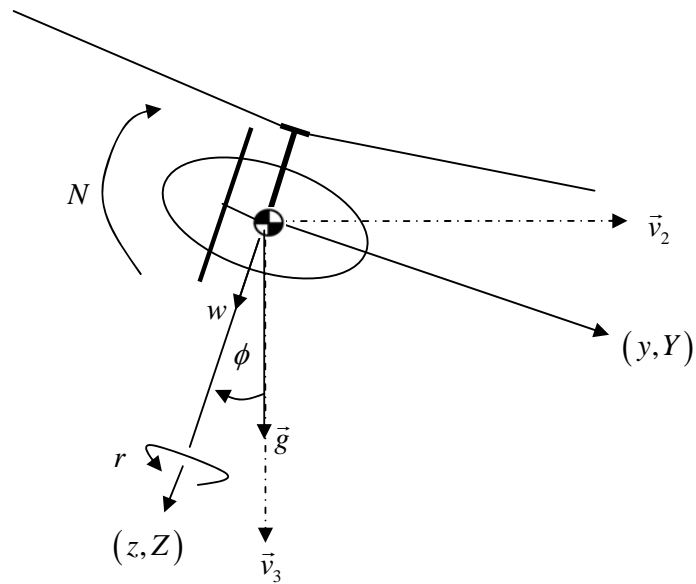


Figure B.5: Euler angles and frame rotations. Rear view.

B.3 Relations between Wind Reference Frame \mathcal{W} and Body Reference Frame \mathcal{B}

The wind reference frame \mathcal{W} is aligned with the free stream velocity vector. The aircraft aerodynamic forces and moments are related to the velocity vector, and therefore, the wind reference frame is of great significance in forward flight. The *sideslip angle* β (see Figure B.4 on the previous page) and the *angle of attack* α (see Figure B.3 on page 186) relate the orientation of the wind reference frame \mathcal{W} to the body reference frame \mathcal{B} . From Figure B.4 on the previous page and Figure B.3 on page 186 it follows

$$\begin{aligned} \begin{bmatrix} u \\ v \\ w \end{bmatrix} &= \begin{bmatrix} V \cos \alpha \sin \beta \\ V \sin \beta \\ V \sin \alpha \cos \beta \end{bmatrix} \\ \begin{bmatrix} V \\ \beta \\ \alpha \end{bmatrix} &= \begin{bmatrix} (u^2 + v^2 + w^2)^{1/2} \\ \sin^{-1}(u/V) \\ \tan^{-1}(w/u) \end{bmatrix} \end{aligned} \quad (\text{B.3.1})$$

To align the vehicle with the relative wind, the aircraft performs a left-handed rotation ${}^{\mathcal{X}}T_3^{\mathcal{W}}(-\beta)$ through sideslip angle β , and a right-handed rotation ${}^{\mathcal{B}}T_3^{\mathcal{X}}(\alpha)$ through angle of attack α such that

$$\begin{aligned} &= {}^{\mathcal{B}}T_3^{\mathcal{X}}(\alpha) {}^{\mathcal{X}}T_3^{\mathcal{W}}(-\beta) \\ &= \begin{bmatrix} \cos \alpha & -\sin \alpha & \\ & 1 & \\ \sin \alpha & \cos \alpha & \end{bmatrix} \begin{bmatrix} \cos \beta & -\sin \beta & \\ \sin \beta & \cos \beta & \\ & & 1 \end{bmatrix} \\ {}^{\mathcal{B}}T^{\mathcal{W}} &= \begin{bmatrix} c\alpha c\beta & -c\alpha s\beta & -s\alpha \\ s\beta & c\beta & \\ s\alpha c\beta & -s\alpha s\beta & c\alpha \end{bmatrix} \end{aligned} \quad (\text{B.3.2})$$

B.4 Euler Angle Rates

Rate gyros physically mounted in the body of the helicopter measure the absolute inertial body rates ${}^{\mathcal{I}}\vec{\omega}^{\mathcal{B}} = [p, q, r]^T$. The angular velocity of the body frame \mathcal{B} is

$${}^{\mathcal{I}}\vec{\omega}^{\mathcal{B}} = {}^{\mathcal{I}}\vec{\omega}^{\mathcal{V}} + {}^{\mathcal{V}}\vec{\omega}^{\mathcal{B}} \quad (\text{B.4.1})$$

where ${}^{\mathcal{I}}\vec{\omega}^{\mathcal{V}}$ is given by equation (B.1.8) and ${}^{\mathcal{V}}\vec{\omega}^{\mathcal{B}} = [P, Q, R]^T$ is the angular velocity of the body frame \mathcal{B} relative to the angular velocity of the vehicle carried frame \mathcal{V} such that

$${}^{\mathcal{I}}\vec{\omega}^{\mathcal{B}} - {}^{\mathcal{I}}\vec{\omega}^{\mathcal{V}} = \begin{bmatrix} P \\ Q \\ R \end{bmatrix} = \begin{bmatrix} p \\ q \\ r \end{bmatrix} - {}^{\mathcal{B}}T^{\mathcal{V}} \begin{bmatrix} ({}^{\mathcal{I}}\omega^{\mathcal{E}} + \dot{\mu}) \cos(\lambda) \\ -\dot{\lambda} \\ ({}^{\mathcal{I}}\omega^{\mathcal{E}} + \dot{\mu}) \sin(\lambda) \end{bmatrix} \quad (\text{B.4.2})$$

Integration of the absolute inertial angular rates $[p, q, r]^T$ has no useful physical meaning since the body rates are expressed in body axes. For the inertial rates measured in the body frame to be useful, they must be related to the Euler angles $[\phi, \theta, \psi]^T$ used in determining the body frame orientation in equation (B.2.4) [39, 119, 141]. The inertial Euler rates expressed in body axes are related to the inertial body angular velocity as:

$$\begin{aligned} \begin{bmatrix} P \\ Q \\ R \end{bmatrix} &= \begin{bmatrix} \dot{\phi} \\ 0 \\ 0 \end{bmatrix} + {}^{\mathcal{B}}T_1^{\mathcal{Z}}(\phi) \begin{bmatrix} 0 \\ \dot{\theta} \\ 0 \end{bmatrix} + {}^{\mathcal{B}}T_1^{\mathcal{Z}}(\phi) {}^{\mathcal{Z}}T_2^{\mathcal{X}}(\theta) \begin{bmatrix} 0 \\ 0 \\ \dot{\psi} \end{bmatrix} \\ &= \begin{bmatrix} 1 & 0 & -s\theta \\ 0 & c\phi & s\phi c\theta \\ 0 & -s\phi & c\phi c\theta \end{bmatrix} \begin{bmatrix} \dot{\phi} \\ \dot{\theta} \\ \dot{\psi} \end{bmatrix} \end{aligned} \quad (\text{B.4.3})$$

Inverting equation (B.4.3) gives an expression for the Euler rates in terms of the relative rates $[PQR]^T$

$$\begin{bmatrix} \dot{\phi} \\ \dot{\theta} \\ \dot{\psi} \end{bmatrix} = \begin{bmatrix} 1 & \sin\phi \tan\theta & \cos\phi \tan\theta \\ & \cos\phi & -\sin\phi \\ & \sin\phi \sec\theta & \cos\phi \sec\theta \end{bmatrix} \begin{bmatrix} P \\ Q \\ R \end{bmatrix} \quad (\text{B.4.4})$$

Using the flat non-rotating Earth assumption on page 184, the expression for ${}^{\mathcal{I}}\vec{\omega}^{\mathcal{V}}$ vanishes such that equation (B.4.2) becomes

$${}^{\mathcal{I}}\vec{\omega}^{\mathcal{B}} - {}^{\mathcal{I}}\vec{\omega}^{\mathcal{V}} = \begin{bmatrix} P \\ Q \\ R \end{bmatrix} = \begin{bmatrix} p \\ q \\ r \end{bmatrix} \quad (\text{B.4.5})$$

and the Euler rates in equation (B.4.4) are found by the following differential equations

$$\begin{bmatrix} \dot{\phi} \\ \dot{\theta} \\ \dot{\psi} \end{bmatrix} = \begin{bmatrix} 1 & \sin \phi \tan \theta & \cos \phi \tan \theta \\ 0 & \cos \phi & -\sin \phi \\ 0 & \sin \phi \sec \theta & \cos \phi \sec \theta \end{bmatrix} \begin{bmatrix} p \\ q \\ r \end{bmatrix} \quad (\text{B.4.6})$$

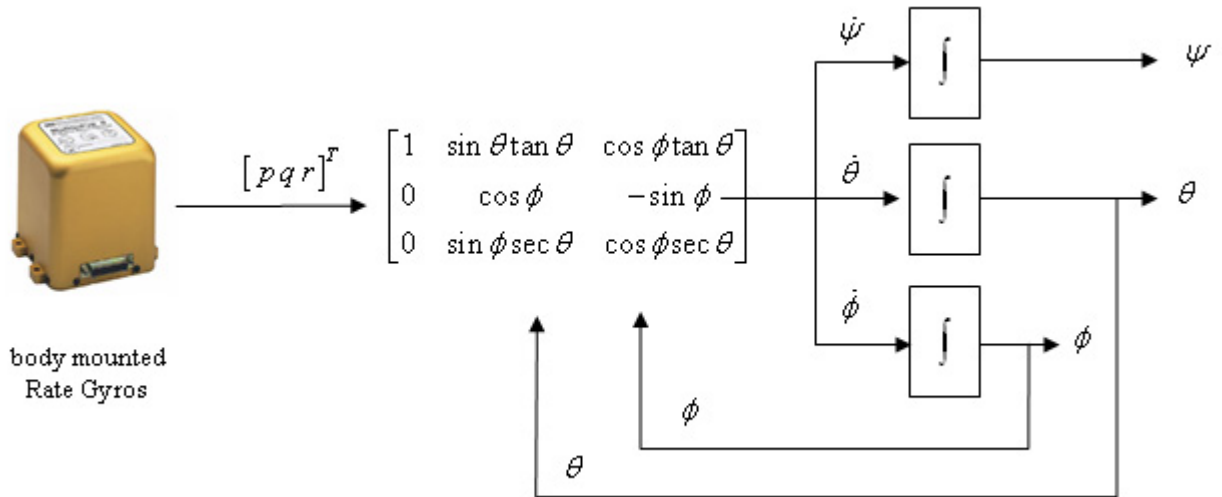


Figure B.6: Euler rates tracking.

The above equation (B.4.6) involves transcendental differential equations for the Euler angles. This implies that in general, the above equation does not have a closed form solution, and a solution may have to use numerical methods. The diagram in Figure B.6 illustrates an algorithm that keeps track of the body frame \mathcal{B} attitude using Euler rates and sensor information from the body fixed mounted gyros.

B.5 Applied Newton's Laws

The goal of this section is to develop a basic set of non-linear equations of motion that describe the kinematics and dynamics that relate to the motion of a six degree of freedom rigid body in atmospheric flight. Standard representation for kinematic equations can be found in reports and papers by McFarland [102], Alderete [1], Heffley and Jewell [67]. Etkin [39] covers a wide range of topics related to atmospheric flight and flight mechanics including the derivation of equation of motion for atmospheric flight. Other literature such as Padfield [119], Seckel [132], Stevens and Lewis [143] and Stengel [141] are sources for detailed flight mechanics derivations. Zipfel [161] covers the topic of flight mechanics from a tensor transformation-invariant perspective. The linear form of Newton's Second Law is given by equation (A.4.1) on page 168, and the angular form of Newton's Laws are given by equation (A.3.1) on page 168. Newton's law is applied to the force and moment resolved into body axes, taking Coriolis and gravity forces into consideration.

B.5.1 Translation Dynamics

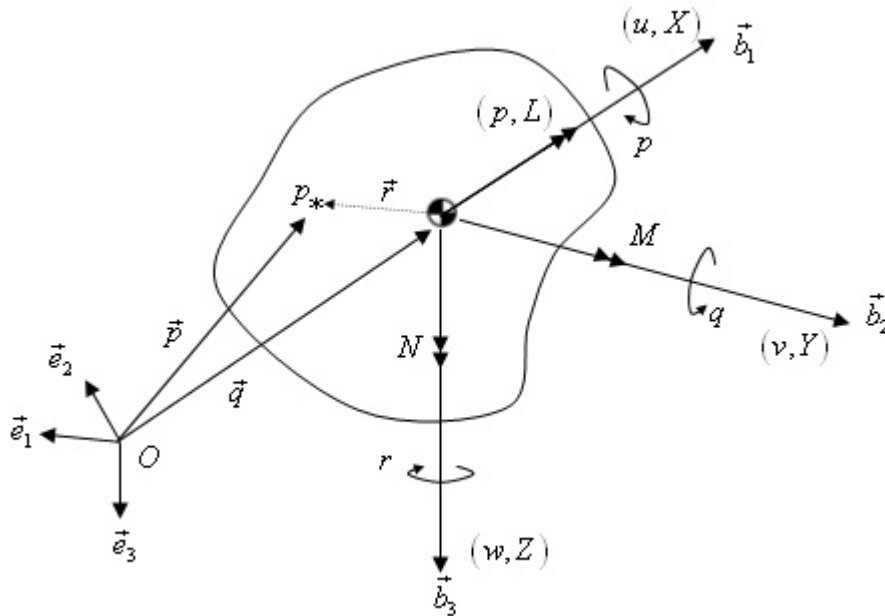


Figure B.7: Inertial Body Dynamics.

Consider the Earth Centered \mathcal{E}_C frame an inertial frame. Further assume a flat, non-rotating Earth (section §B.1.8 page 184) such that the Earth fixed \mathcal{E} frame of reference is also an inertial frame. Let point O in Figure B.7 on the preceding page be a reference point in \mathcal{E} , the vector \vec{q} be a vector from O to the center of mass of body \mathcal{B} , and the vector \vec{p} be a vector from O to an arbitrary point p in \mathcal{B} . Let \vec{r} be the vector from the body's center of mass q to the arbitrary point p . Then the following holds [85] :

$$\begin{aligned}
\vec{p} &= \vec{q} + \vec{r} \\
\frac{{}^I d\vec{p}}{dt} &= \frac{{}^I d\vec{q}}{dt} + \frac{{}^I d\vec{r}}{dt} \\
{}^I \vec{v}_p &= {}^I \vec{v}_q + {}^I \vec{\omega}^{\mathcal{B}} \times \vec{r} \\
\frac{{}^I d{}^I \vec{v}_p}{dt} &= \frac{{}^I d{}^I \vec{v}_q}{dt} + \frac{{}^I d{}^I \vec{\omega}^{\mathcal{B}}}{dt} \times \vec{r} + {}^I \vec{\omega}^{\mathcal{B}} \times \frac{{}^I d\vec{r}}{dt} \\
&= \frac{{}^B d{}^B \vec{v}_q}{dt} + {}^I \vec{\omega}^{\mathcal{B}} \times {}^B \vec{v}_q + {}^I \vec{\alpha}^{\mathcal{B}} \times \vec{r} + {}^I \vec{\omega}^{\mathcal{B}} \times ({}^I \vec{\omega}^{\mathcal{B}} \times \vec{r}) \\
{}^I \vec{a}_p &= {}^B \vec{a}_q + {}^I \vec{\omega}^{\mathcal{B}} \times {}^B \vec{v}_q + {}^I \vec{\alpha}^{\mathcal{B}} \times \vec{r} + {}^I \vec{\omega}^{\mathcal{B}} \times ({}^I \vec{\omega}^{\mathcal{B}} \times \vec{r})
\end{aligned} \tag{B.5.1}$$

where $\vec{r} = [x \ y \ z]^T$, ${}^I \vec{v}_q = {}^\mathcal{E} T^{\mathcal{B}} [u \ v \ w]^T$, ${}^I \vec{\omega}^{\mathcal{B}} = [p \ q \ r]^T$ are expressed in terms of the body frame \mathcal{B} span vector $[\vec{b}_1, \vec{b}_2, \vec{b}_3]^T$. Expansion of the inertial acceleration ${}^I \vec{a}_p$ gives

$${}^I \vec{a}_p = \begin{bmatrix} \dot{u} \\ \dot{v} \\ \dot{w} \end{bmatrix} + \begin{bmatrix} qw - rv \\ ru - pw \\ pv + qu \end{bmatrix} - \begin{bmatrix} x(q^2 + r^2) + y(pq - \dot{r}) + z(pr + \dot{q}) \\ y(p^2 + r^2) + z(qr - \dot{p}) + x(pq + \dot{r}) \\ z(p^2 + q^2) + x(pr - \dot{q}) + y(qr + \dot{p}) \end{bmatrix} \tag{B.5.2}$$

In the case when point p coincides with the center of mass then the vector $\vec{r} = 0$. In this case the above equation (B.5.2) reduces to

$${}^I \vec{a}_p = \begin{bmatrix} \dot{u} \\ \dot{v} \\ \dot{w} \end{bmatrix} + \begin{bmatrix} qw - rv \\ ru - pw \\ pv + qu \end{bmatrix} \tag{B.5.3}$$

Let Newton's Second Law be valid in the Earth fixed \mathcal{E} inertial frame and expressed

in the body frame takes the form:

$$\mathcal{I}\vec{F}_{c\mathcal{M}} = \frac{d(m\mathcal{I}\vec{v}_{c\mathcal{M}})}{dt} \quad (\text{B.5.4})$$

where the vector $\mathcal{I}\vec{F}_{c\mathcal{M}}$ is the sum of inertial forces external to body \mathcal{B}

$$\mathcal{I}\vec{F}_{c\mathcal{M}} = \begin{bmatrix} X \\ Y \\ Z \end{bmatrix} + {}^{\mathcal{B}}T^{\mathcal{V}} \begin{bmatrix} 0 \\ 0 \\ g \end{bmatrix} \quad (\text{B.5.5})$$

The above equation (B.5.5) is expressed in body frame \mathcal{B} axis where the gravitational force is ${}^{\mathcal{B}}T^{\mathcal{V}} [0 \ 0 \ g]^T$, and the aerodynamic and propulsive forces are lumped into $[XYZ]^T$. Substituting equations (B.5.3) and (B.5.5) in equation (B.5.4) and expanding yields the translation dynamic equations:

$$\begin{aligned} \dot{u} &= rv - qw + \frac{X}{m} - g \sin \theta \\ \dot{v} &= pw - ru + \frac{Y}{m} + g \cos \theta \sin \phi \\ \dot{w} &= qu - pv + \frac{Z}{m} + g \cos \theta \cos \phi \end{aligned} \quad (\text{B.5.6})$$

The forces $[X \ Y \ Z]^T$ originate from various components in the helicopter such as the main rotor, the tail rotor, the fuselage, the horizontal and vertical tail, and others. These forces are mostly aerodynamic in nature, but other dynamic effects also contribute, for example, gyroscopic and Coriolis effects in the case of the main rotor rotating blades.

B.5.2 Position Dynamics

Consider the case when the Earth Fixed \mathcal{E} frame is the inertial frame, then the time derivative of vector \vec{q} in equation (B.5.1) and Figure B.7 on page 191 is

$$\frac{I d\vec{q}}{dt} = \mathcal{I}\vec{v}_q = \mathcal{E}T^{\mathcal{B}}\mathcal{B}\vec{v}_q \quad (\text{B.5.7})$$

where ${}^{\mathcal{B}}\vec{v}_q = [u \ v \ w]^T$, $\mathcal{E}T^{\mathcal{B}} = [{}^{\mathcal{B}}T^{\mathcal{E}}]^T$ and ${}^{\mathcal{B}}T^{\mathcal{E}} = {}^{\mathcal{B}}T^{\mathcal{V}}$ is given by equation (B.2.4). The position of the vehicle in the inertial frame $\mathcal{I} = \mathcal{E}$ for a flat, non rotating Earth expressed in Earth Fixed Frame \mathcal{E} is

$$\begin{bmatrix} \dot{x}_E \\ \dot{y}_E \\ \dot{z}_E \end{bmatrix} = \begin{bmatrix} c\theta c\psi & s\phi s\theta c\psi - c\phi s\psi & c\phi s\theta c\psi + s\phi s\psi \\ c\theta s\psi & s\phi s\theta s\psi + c\phi c\psi & c\phi s\theta s\psi - s\phi c\psi \\ -s\theta & s\phi c\theta & c\phi c\theta \end{bmatrix} \begin{bmatrix} u \\ v \\ w \end{bmatrix} \quad (\text{B.5.8})$$

B.5.3 Rotational Dynamics

Section A on page 163 describes the rotational dynamics for a rigid body. The total moment about the body center of mass \vec{G}_{cM} and associated angular momentum \vec{h}_{cM} are given by:

$$\vec{G}_{cM} = \begin{bmatrix} L \\ M \\ N \end{bmatrix} \quad (\text{B.5.9})$$

$${}^{\mathcal{B}}\vec{h}_{cM} = {}^{\mathcal{B}}I^{\mathcal{I}}\vec{\omega}^{\mathcal{B}} + \sum_i {}^{\mathcal{B}}\vec{h}_i$$

The moments $[L \ M \ N]^T$ originate from various components in the helicopter such as the main rotor, the tail rotor, the fuselage, the horizontal and vertical tail, and others. These moments are mostly aerodynamic in nature, but other dynamic effects also contribute, for example, gyroscopic moments. Equation (A.3.4) describes the rotational equations of motion. Presently (A.3.4) takes the form

$$\begin{aligned} &= \frac{{}^{\mathcal{I}}d{}^{\mathcal{B}}\vec{h}_{cM}}{dt} \\ &= \frac{{}^{\mathcal{B}}d{}^{\mathcal{B}}\vec{h}_{cM}}{dt} + \mathcal{I}\vec{\omega}^{\mathcal{B}} \times {}^{\mathcal{B}}\vec{h}_{cM} + \sum_i {}^{\mathcal{B}}\vec{h}_i + \sum_i \mathcal{I}\vec{\omega}^{\mathcal{B}} \times {}^{\mathcal{B}}\vec{h}_i \end{aligned} \quad (\text{B.5.10})$$

$$\vec{G}_{cM} = {}^{\mathcal{B}}I * \mathcal{I}\vec{\alpha}^{\mathcal{B}} + \mathcal{I}\vec{\omega}^{\mathcal{B}} \times {}^{\mathcal{B}}\vec{h}_{cM} + \sum_i {}^{\mathcal{B}}\vec{h}_i + \sum_i \mathcal{I}\vec{\omega}^{\mathcal{B}} \times {}^{\mathcal{B}}\vec{h}_i$$

where the term

$$\frac{{}^{\mathcal{B}}d{}^{\mathcal{B}}I}{dt} = 0 \quad (\text{B.5.11})$$

since the body inertia does not change in the body axis. Also, the terms $\sum_i {}^{\mathcal{B}}\vec{h}_i + \sum_i \mathcal{I}\vec{\omega}^{\mathcal{B}} \times {}^{\mathcal{B}}\vec{h}_i$ relate to the angular momentum of individual rotor components [39]. The inertia tensor is given by

$${}^{\mathcal{B}}I = \begin{bmatrix} I_x & -I_{xy} & -I_{zx} \\ -I_{xy} & I_y & -I_{yz} \\ -I_{zx} & -I_{yz} & I_z \end{bmatrix} \quad (\text{B.5.12})$$

For an xz plane of symmetry the above term becomes:

$${}^{\mathcal{B}}I = \begin{bmatrix} I_x & 0 & -I_{zx} \\ 0 & I_y & 0 \\ -I_{zx} & 0 & I_z \end{bmatrix} \quad (\text{B.5.13})$$

The standard helicopter does not have a plane of symmetry because of the tail rotor and the main rotor rotation. But the assumption of a plane of symmetry is still useful for first order approximations since symmetry simplifies the set of equations. Let the helicopter be a rigid body with rotor terms and a plane of symmetry, then expanding

equation (B.5.10) results in [39, 40, 103]:

$$\begin{aligned}
\dot{p} &= \frac{L}{I_x} + \frac{I_{yz}}{I_x}(q^2 - r^2) + \frac{I_{zx}}{I_x}(\dot{r} + pq) + \frac{I_{xy}}{I_x}(\dot{q} + rp) + \frac{(I_y - I_z)}{I_x}qr \\
&\quad + \frac{1}{I_x} \left[\sum_i \mathcal{B} \dot{h}_x^i + r \sum_i \mathcal{B} h_y^i - q \sum_i \mathcal{B} h_z^i \right] \\
\dot{q} &= \frac{M}{I_y} + \frac{I_{zx}}{I_y}(r^2 - p^2) + \frac{I_{xy}}{I_y}(\dot{p} + qr) + \frac{I_{yz}}{I_y}(\dot{r} + pq) + \frac{(I_z - I_x)}{I_y}rp \\
&\quad + \frac{1}{I_y} \left[\sum_i \mathcal{B} \dot{h}_y^i + p \sum_i \mathcal{B} h_z^i - r \sum_i \mathcal{B} h_x^i \right] \\
\dot{r} &= \frac{N}{I_z} + \frac{I_{xy}}{I_z}(p^2 - q^2) + \frac{I_{yz}}{I_z}(\dot{q} + rp) + \frac{I_{zx}}{I_z}(\dot{p} + qr) + \frac{(I_x - I_y)}{I_z}pq \\
&\quad + \frac{1}{I_z} \left[\sum_i \mathcal{B} \dot{h}_z^i + q \sum_i \mathcal{B} h_x^i - p \sum_i \mathcal{B} h_y^i \right]
\end{aligned} \tag{B.5.14}$$

B.5.4 Solution and System Simulation

Equations (B.4.6), (B.5.6), (B.5.8) and (B.5.14) form a set of 12 ODE's. Six of these equations are dynamic in nature, and the six remaining equations come from kinematic considerations. The state vector is given by:

$$\tilde{\mathbf{x}} = \left[u \quad v \quad w \quad p \quad q \quad r \quad \phi \quad \theta \quad \psi \quad x_E \quad y_E \quad z_E \right]^T \tag{B.5.15}$$

The forces and moments are created by the aerodynamics, gyroscopic, Coriolis forces and other effects. Some of the components that contribute to the forces and moments are the main and tail rotors, the fuselage, the vertical tail and horizontal stabilizer, and other components. Figure B.8 on the next page shows a sketch for a simulation block diagram that accounts for linear and angular dynamics.

B.6 Main Rotor Frame of Reference

Bramwell [11], Leishman [92], Padfield [119], and Prouty [124] each give descriptions of the various reference frames used in the analysis of rotor dynamics. Four natural rotor reference frames are most commonly used in the dynamic analysis of rotors, and

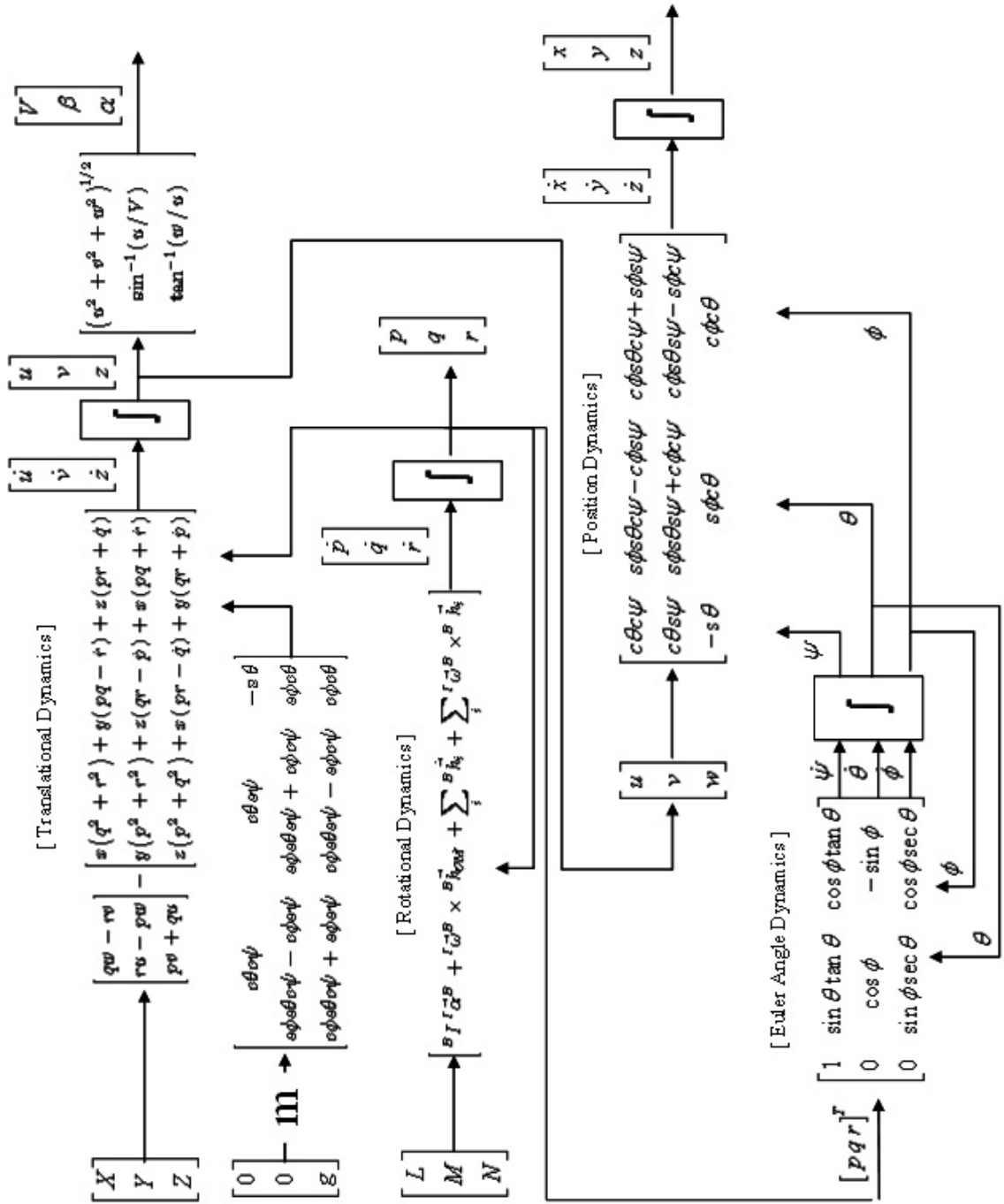


Figure B.8: Simulation Block Diagram Sketch.

no one reference is unique [92]. Rather, the selection of one frame over another is a matter of choice and convenience. The most frequently used rotor coordinate systems are [11, 92, 119, 124]:

1. Hub Plane (HP): The HP is also known as shaft plane axis. In this reference system, the rotor hub (a physical part of the helicopter) is perpendicular to the rotor shaft, and it is oriented with respect to the body axis system. Both flapping and feathering take place in this plane, and therefore the HP is significantly less convenient for the calculation of forces and moments. However, such forces and moments defined in this plane can be easily resolved along the body axis, and consequently the HP is generally used for blade dynamic analysis.
2. Non Feathering Plane (NFP): The NFP is also known as the control plane. No variations in cyclic pitch take place in this reference plane, but the blade flap angle varies cyclically. Performance analysis uses this plane.
3. Tip Path Plane (TPP): The TPP is also known as the Disc Axis. For a rotor with no hinge offset, the blade tips describe the boundary of this plane. In this plane there is no first harmonic flapping. When there is a finite hinge offset, then there is both feathering and flapping in this plane, but the flapping is negligible for small hinge offsets.
4. Control Plane (CP): The CP is also known as the swashplate plane. This plane is aligned to the cyclic pitch. In the absence of mechanical cross coupling between flapping and feathering, the control plane is the same as the NFP. Coupling between flapping and feathering is present when the blade is free to move about the drag hinge via Coriolis effects, and when the flapping and drag hinges are deliberately inclined to induce such coupling [120].

When coupling between blade flapping and feathering exists, the control plane lies between the NFP and TPP.

B.6.1 Hub Plane (HP) Reference Frame

$$\begin{aligned}\theta &= \theta_0 - \theta_{1c} \cos \psi - \theta_{1s} \sin \psi \\ \beta &= \beta_0 - \beta_{1c} \cos \psi - \beta_{1s} \sin \psi\end{aligned}\tag{B.6.1}$$

1. X -axis runs along fuselage symmetry plane and is normal to Z .
2. Y -axis is perpendicular to fuselage symmetry plane and perpendicular to Z .
3. Z axis is normal to shaft.
4. Less convenient to work in this plane, but more useful due to its orientation with respect to the body axis system.

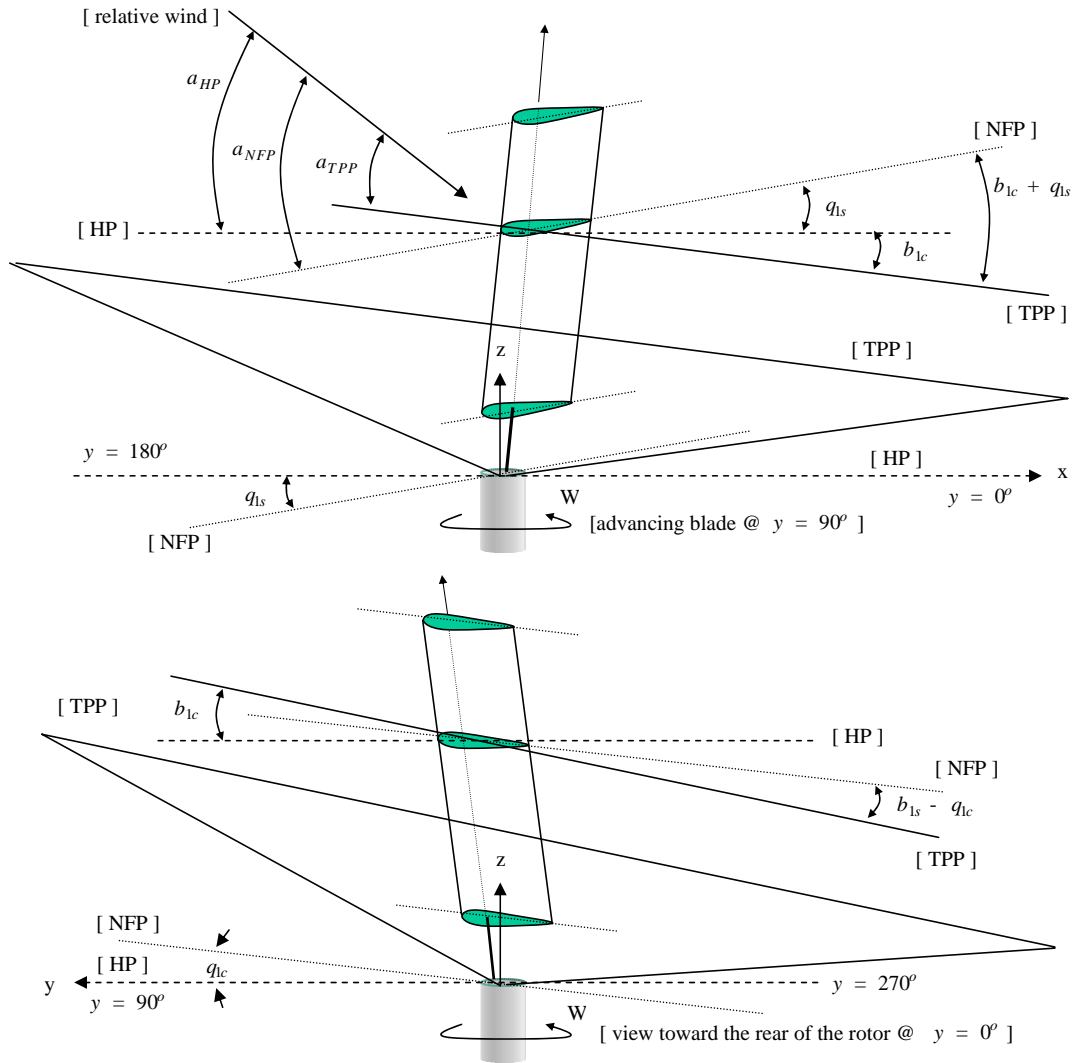


Figure B.9: Rotor Reference Frames [11, 92, 119, 124].

B.6.2 Non Feathering Plane (NFP) Reference Frame

1. Collective control moves the blades in pitch by the same amount.
2. Cyclic control tilts the swash-plate.

$$\begin{aligned}
[\theta]_{NFP} &= [\theta_0]_{NFP} \\
[\beta]_{NFP} &= [\beta_0]_{NFP} - [\beta_{1c}]_{NFP} \cos \psi - [\beta_{1s}]_{NFP} \sin \psi
\end{aligned}
\tag{B.6.2}$$

B.6.3 Tip Path Plane (TPP) Reference Frame

1. This plane is defined by two straight lines.
 - The first connects the blade tips at azimuth angle $\psi = 0$ and $\psi = 180$ deg.
 - The second connects the blade tips at azimuth angle $\psi = 90$ and $\psi = 270$ deg.
2. The rotor thrust is roughly perpendicular to this plane. Whence, this plane is commonly used in aerodynamic analysis.
3. When the flapping hinges are offset, flapping occurs in this plane. However, for small hinge offset, the assumption of no blade flapping is valid.
4. In general, analysis in this plane sets flapping to zero.

$$\begin{aligned}
[\theta]_{TPP} &= [\theta_0]_{TPP} - [\theta_{1c}]_{TPP} \cos \psi - [\theta_{1s}]_{TPP} \sin \psi \\
[\beta]_{TPP} &= [\beta_0]_{TPP}
\end{aligned}
\tag{B.6.3}$$

B.6.4 Relations Among Main Rotor Frame of Reference

The amount of blade feathering and flapping depends on the rotor reference frame. For a teetering type rotor, the amount of blade pitch in the TPP is equivalent to the amount of flapping in the NFP. For other types of rotors, the feathering and flapping relations between the TPP and NFP still hold [92]. The feathering/flap equivalence is illustrated in Figure B.9 on the preceding page from where the following holds [11, 92, 119, 124]

$$\begin{aligned}
\beta_{1c} + \theta_{1s} &= \text{constant} = [\beta_{1c}]_{NFP} = [\theta_{1s}]_{TPP} \\
\beta_{1s} - \theta_{1c} &= \text{constant} = [\beta_{1s}]_{NFP} = [\theta_{1c}]_{TPP} \\
[\alpha]_{TPP} &= [\alpha]_{NFP} - (\beta_{1c} + \theta_{1s}) \\
[\alpha]_{TPP} &= \alpha_h - \beta_{1c} \\
[\alpha]_{NFP} &= \alpha_h + \theta_{1s}
\end{aligned}
\tag{B.6.4}$$

In the above equations α_s is the angle of attack pertaining to the hub plane. In general, if the swash-plate is tilted, then the blade chord remains parallel to the swashplate. As the blade rotates, then feathering takes place in the Hub Plane perpendicular to the shaft. The swashplate defines the plane of no feathering, and the axis of no feathering passes through the hub and is perpendicular to the swashplate plane.

Appendix C

Helicopter Momentum Theory and Blade Element Theory

Helicopters operate in a number of flight regimes that include hover, vertical, and forward flight, and also perform maneuvers which combine elements from the aforementioned and more basic flight conditions. Hover flight involves upward or downward vertical flow through the rotor, and as such hover is of axial type. In contrast, forward flight introduces a component of the free stream velocity which adds a cyclic element to the rotational blade velocity. Therefore, the flow distribution that the blade encounters in forward flight as it rotates around its rotational axis varies with blade azimuth and results in asymmetric flow through the rotor. Whence, in forward flight regime, the free stream velocity combines with varying blade pitch angle and blade flapping to produce non-linear induced inflow through the rotor. In turn, the rotor inflow affects the blade angle of attack and the resulting blade lift distribution, rotor thrust and power consumption.

References [26, 27, 53, 82, 92, 124, 133, 154] treat the subject of helicopter rotor aerodynamics to great depth. This appendix compiles the basic theory and mathematical models of rotor aerodynamics, and summarizes the main results derived from Momentum Theory and Blade Element Theory. These two theories combined explain the fundamental physics involved in helicopter flight mechanics:

1. Simple Momentum Theory:

- Based on an actuator disk concept.
- Provides basic relationships for induced velocity and power required to produce thrust
- Theory is adequate for hover and vertical flight.

- Theory does not dwell in the mechanisms that allow the helicopter to produce thrust.

2. Blade Element Theory:

- Provides a framework for the analysis of the physical mechanisms that keep the helicopter in the air.

C.1 Simple Momentum Theory in Hovering Flight

Hover flight consists of axisymmetrical, mostly uniform flow through the main rotor. The flow through a rotor also contains complicated vortice patterns which result from concentration of aerodynamic forces at the blade tips due to the existence of high dynamic pressure at that location. The mathematics that involve modeling of vortice in rotor aerodynamics is an important active research topic since vortice analysis helps predict rotor flow effects with greater accuracy [92]. These more elaborate analysis tools are necessary for helicopter and rotor design studies as well as for maneuver flight performance prediction of main rotor thrust, torque and overall power consumption. Momentum Theory is a simpler mathematical approach to the analysis of hovering flight that results in first order prediction of helicopter performance.

Figure C.1 on the next page illustrates a control volume of air used for analysis of a helicopter in hover flight [92]. This control volume surrounds the rotor and the air stream with surface area S and unit vector $d\vec{S}$, and includes the free stream velocity V_c and wake velocity $V_c + w$ such that

$$\oiint_S \rho \vec{V} \cdot d\vec{S} = 0 \quad (\text{C.1.1})$$

where ρ is the local fluid density and \vec{V} is the local fluid velocity. The above equation governs the mechanics of conservation of fluid mass (Section A.5.1 on page 172), and it says that the mass flow entering the control volume must equal the mass flow that exits the same control volume. With the reasonable assumptions that the streamlined flow within the rotor wake does not mix with flow outside the wake, and that the flow

through the rotor behaves in a quasi-steady manner, then the mass flow rate \dot{m} remains constant throughout the stream tube that includes the rotor wake. In this case the mass flow rate \dot{m} of air within the wake is given by

$$\dot{m} = \iint_{\textcircled{4}} \rho \vec{V} \cdot d\vec{S} = \iint_{\textcircled{3}} \rho \vec{V} \cdot d\vec{S} \quad (\text{C.1.2})$$

With the added assumption that the stream tube is one-dimensional and incompressible, then equation (C.1.2) becomes a one dimensional equation with the form

$$\dot{m} = \rho A_{\infty} w = \rho A_{\text{station}_2} v_i = \rho A v_i \quad (\text{C.1.3})$$

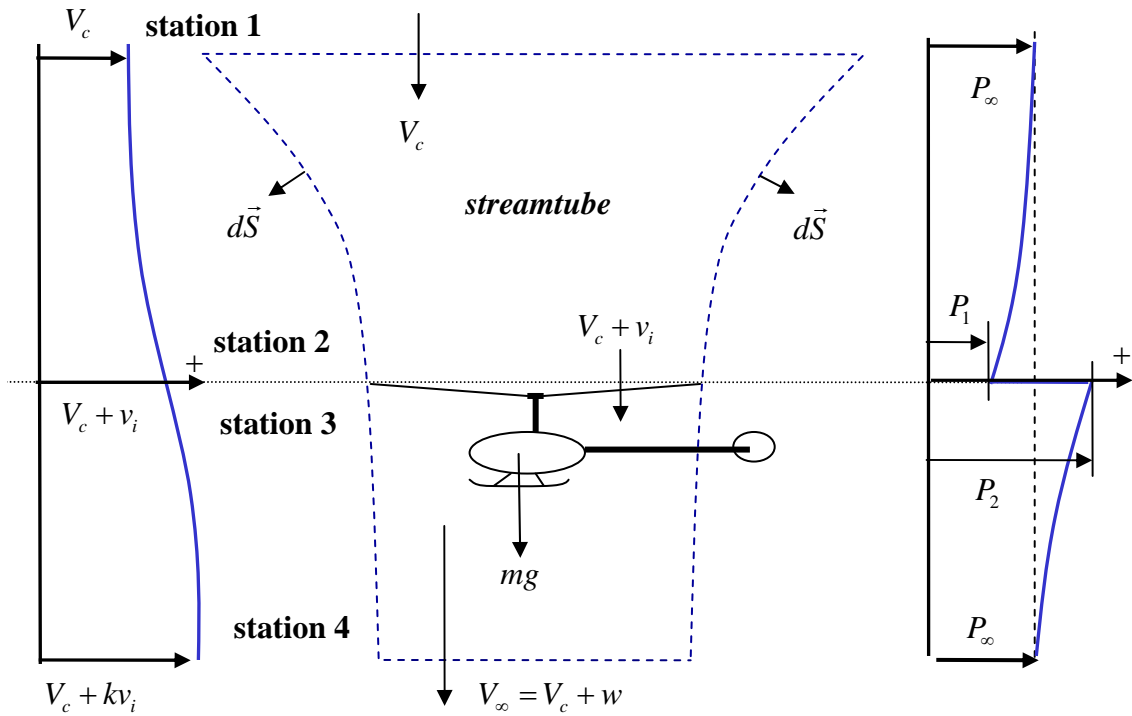


Figure C.1: Actuator disc concept for rotor in vertical flight (for hover case V_c equals zero)

The force exerted on the control volume shown in Figure C.1 equals the rate of change of momentum of the air mass flowing through S . This mechanics takes the form

(Section A.5.2 on page 174):

$$\vec{F} = \oint_S p d\vec{S} + \oint_S (\rho \vec{V} \cdot d\vec{S}) \vec{V} \quad (\text{C.1.4})$$

where the net pressure force on the fluid inside the control volume is zero [56, 92].

$$\oint_S p d\vec{S} = 0 \quad (\text{C.1.5})$$

In a hovering helicopter, the main rotor blades form a disk that behaves as an actuator; that is, the rotor imparts energy to the air mass by accelerating air downwards over the rotor or actuator disk region. The rotor therefore imparts the force \vec{F} in equation (C.1.4) above. By virtue of Newton's third law, the air flow exerts an equal and opposite force (or thrust \vec{T}) on the rotor. The quasi-steady, one-dimensional, incompressible flow assumptions simplify the above equation to the form

$$\vec{F} = \vec{T} = \iint_{\mathbb{Q}_4} \rho (\vec{V} \cdot d\vec{S}) \vec{V} - \iint_{\mathbb{Q}_1} \rho (\vec{V} \cdot d\vec{S}) \vec{V} \quad (\text{C.1.6})$$

Equation (C.1.6) is the net change of momentum between station 1 and station 4 in Figure C.1 on the previous page. In hover flight however, the velocity far above the rotor is zero such that

$$\iint_{\mathbb{Q}_1} \rho (\vec{V} \cdot d\vec{S}) \vec{V} = 0$$

and therefore

$$\vec{T} = \iint_{\mathbb{Q}_4} \rho (\vec{V} \cdot d\vec{S}) \vec{V} = \dot{m} w \quad (\text{C.1.7})$$

The rotor or actuator disk imparts energy to the airflow passing through the rotor with the effect of increasing the flow's kinetic energy. This mechanism in which work W done on the system per unit time (or power consumed by the rotor) is conserved takes the form (Section A.5.3 on page 176):

$$W = \oint_S \frac{1}{2} (\rho \vec{V} \cdot d\vec{S}) \vec{V}^2 \quad (\text{C.1.8})$$

With the quasi-steady, one-dimensional, incompressible flow assumptions, the work done

by the rotor per unit time W , or equivalently, the power P consumed by the rotor is

$$P = W = T v_i = \oint_{\mathbb{Q}_4} \frac{1}{2} (\rho \vec{V} \cdot d\vec{S}) \vec{V}^2 - \oint_{\mathbb{Q}_1} \frac{1}{2} (\rho \vec{V} \cdot d\vec{S}) \vec{V}^2 \quad (\text{C.1.9})$$

In hover flight, the free stream velocity far above is at rest with respect to the rotor, in this case the term

$$\oint_{\mathbb{Q}_1} \frac{1}{2} (\rho \vec{V} \cdot d\vec{S}) \vec{V}^2 = 0$$

and equation (C.1.9) becomes

$$T v_i = \oint_{\mathbb{Q}_4} \frac{1}{2} (\rho \vec{V} \cdot d\vec{S}) \vec{V}^2 = \frac{1}{2} \dot{m} w^2 \quad (\text{C.1.10})$$

Substituting equation (C.1.6) into the above equation (C.1.10) yields

$$w = 2 v_i \quad (\text{C.1.11})$$

Rearranging equations (C.1.3), (C.1.6) and (C.1.11) gives

$$\begin{aligned} T &= \dot{m} w = (\rho A v_i) (2 v_i) = 2 \rho A v_i^2 \\ v_h &= \sqrt{\frac{1}{2} \frac{T}{\rho A}} = \sqrt{\frac{DL}{2\rho}} \end{aligned} \quad (\text{C.1.12})$$

In the above equation v_h is the hover induced velocity, and $DL = T/A$ is the disk loading ratio. The above equation (C.1.12) along with equation (C.1.9) gives the ideal power that is required to hover as

$$P = T v_i = (2 \rho A v_i^2) v_i = 2 \rho A v_i^3 = \frac{T^{3/2}}{\sqrt{2 \rho A}} \quad (\text{C.1.13})$$

Equation (C.1.13) assumes that the air flow behaves as a quasi-steady, one dimensional fluid, and does not take into consideration viscous effects or non-linear flow patterns such as blade tip vortices. The above equation does indicate that for a helicopter to hover at minimum power for a given thrust (or aircraft weight) it is necessary to keep

the induced velocity of the rotor at a minimum, with a large mass flow through the disk. Both conditions for minimum power require a large rotor disk area, and as such, the main rotor disk area is a major design feature for helicopters.

The above development and results from momentum theory consider the main rotor as an actuator disk. The above basic laws of physics say that when the actuator disk imparts energy to the airflow passing through the rotor, this actuation changes the momentum of the air mass, and the resulting reaction force keeps the helicopter in the air. Basic assumptions regarding momentum theory and helicopter rotor are [53, 154]:

1. An infinite number of blades forms an actuator disk or rotor.
2. Across this actuator disk there is a sudden increase of pressure.
3. To satisfy conditions far above or below the actuator disk, the pressure gradient must be decreasing except at the actuator disk.
4. No thrust loss at the blade tips.
5. Vortices generated at blade tips are not directly accounted for.
6. Viscosity effects are not directly accounted for.
7. Velocity across the actuator disk is continuous.
8. Clearly defined stream tube above and below the disc.
9. Air flow is constrained to the stream tube and does not mix with the outside air
10. Rotor disk does not disturb the air outside the stream tube.
11. The actuator disk does not impart flow rotation.

The governing principle is the work done on the column of air by the actuator disk or rotor. The rotor imparts velocity (kinetic energy) to a column of air downwards through the rotor plane. As the air accelerates toward the actuator disk with continuously increasing velocity, the pressure falls and the air tube contracts to conserve the air mass and energy. At the instant when the air passes through the actuator disk, the flow energy increases with a resultant increment in flow velocity known as induced velocity v_i . This

change of momentum of the air column in turn produces a reaction force or upward thrust. Limitations of the simple momentum theory are that the theory only accounts for losses that originate from producing thrust (induced drag), neglects viscosity and blade tip losses in the form of vortices, and considers the profile drag to be zero.

Quasi-steady assumptions on the flow imply that the continuity of mass flow ((C.1.3)) in the stream tube imparts the condition that the velocity is continuous through the disc. One-dimensional flow assumptions allow for the application of the Bernoulli's equation to streamlines of the flow above and below the disc respectively such that

$$P_\infty + \frac{1}{2}\rho V_c^2 = P_1 + \frac{1}{2}\rho (V_c + v_i)^2 \quad (\text{C.1.14})$$

$$P_2 + \frac{1}{2}\rho (V_c + v_i)^2 = P_\infty + \frac{1}{2}\rho (V_c + w)^2 \quad (\text{C.1.15})$$

The disk loading T/A equals the pressure jump across the disk. Subtracting (C.1.14) from (C.1.15) gives

$$\frac{T}{A} = (P_2 - P_1) = \frac{1}{2}\rho (2V_c + w) w \quad (\text{C.1.16})$$

As expected, manipulations of the above equation (C.1.16) yields equation (C.1.12) again.

Define non-dimensional coefficients pertaining to thrust, power and induced velocity (for the hover case when $V_c = 0$):

$$\begin{aligned} \text{thrust coefficient: } C_T &\equiv \frac{T}{\rho A (\Omega R)^2} \\ \text{pressure and torque coefficients: } C_P &\equiv \frac{P}{\rho A (\Omega R)^3} = \frac{Q}{\rho A R (\Omega R)^2} \equiv C_Q \\ \text{normalized induced velocity: } \lambda_i &\equiv \frac{V_c + v_i}{\Omega R} \end{aligned} \quad (\text{C.1.17})$$

where Ω is the angular velocity of the rotor and R is the rotor radius. Substituting equation (C.1.17) into equation (C.1.12) yields ($V_c = 0$, *hover case*):

$$\lambda_i = \frac{1}{\Omega R} \sqrt{\frac{T}{2\rho A}} = \frac{1}{\Omega R} \sqrt{\frac{DL}{2\rho}} = \sqrt{\frac{T}{2\rho A (\Omega R)^2}} = \sqrt{\frac{C_T}{2}} \quad (\text{C.1.18})$$

where the term T/A is the disk loading (DL). Also

$$C_{P_i} = \frac{T v_i}{\rho A (\Omega R)^3} = \frac{T}{\rho A (\Omega R)^2} \frac{v_i}{\Omega R} = C_T \lambda_i = C_T \sqrt{\frac{C_T}{2}} = \frac{C_T^{3/2}}{\sqrt{2}} \quad (\text{C.1.19})$$

Equations (C.1.18) and (C.1.19) are direct results of the application of momentum theory for hover case when climb velocity is zero. These results are mainly used to obtain first order performance values.

C.1.1 Momentum Theory: Vertical Climb

In vertical climb the fluid can be considered quasi-steady and one-dimensional since the flow properties are uniformly distributed at each cross section and vary only in the axial dimension [92]. Referring back to Figure C.1 on page 204 and equation (C.1.2)

$$\begin{aligned} \dot{m} &= \iint_{\textcircled{4}} \rho \vec{V} \cdot d\vec{S} = \iint_{\textcircled{3}} \rho \vec{V} \cdot d\vec{S} \\ &= \rho A_{\textcircled{4}} (V_c + w) = \rho A (V_c + v_i) \end{aligned} \quad (\text{C.1.20})$$

In turn, the momentum equation (C.1.6) becomes

$$\begin{aligned} &= \iint_{\textcircled{4}} \rho (\vec{V} \cdot d\vec{S}) \vec{V} - \iint_{\textcircled{1}} \rho (\vec{V} \cdot d\vec{S}) \vec{V} \\ \vec{T} &= \dot{m} (V_c + w) - \dot{m} V_c = \dot{m} w \end{aligned} \quad (\text{C.1.21})$$

The work equation yields

$$\begin{aligned} &= \iint_{\textcircled{4}} \frac{1}{2} (\rho \vec{V} \cdot d\vec{S}) \vec{V}^2 - \iint_{\textcircled{1}} \frac{1}{2} (\rho \vec{V} \cdot d\vec{S}) \vec{V}^2 \\ T (V_c + v_i) &= \frac{1}{2} \dot{m} (V_c + w)^2 - \frac{1}{2} \dot{m} V_c^2 = \frac{1}{2} \dot{m} w (2V_c + w) \end{aligned} \quad (\text{C.1.22})$$

Equations (C.1.21) and (C.1.22) combined yield $w = 2v_i$ as in equation (C.1.11). Using equations (C.1.20) through (C.1.22) results in

$$T = 2\rho A (V_c + v_i) v_i \quad (\text{C.1.23})$$

Given that thrust in hover is the same as the thrust in un-accelerated climb gives

$$T = 2\rho A v_h^2 = 2\rho A (V_c + v_i) v_i \quad (\text{C.1.24})$$

where v_h is the hover induced velocity for the same thrust T in both hover and un-accelerated cases. Then

$$\begin{aligned} v_h^2 &= (V_c + v_i) v_i \\ 0 &= \frac{v_i^2}{v_h^2} + \frac{v_i V_c}{v_h^2} - 1 \end{aligned} \quad (\text{C.1.25})$$

solving for v_i/v_h

$$\frac{v_i}{v_h} = -\frac{V_c}{2v_h} \pm \sqrt{\left(\left[\frac{V_c}{2v_h}\right]^2 + 1\right)} \quad (\text{C.1.26})$$

The ratio v_i/v_h must be positive for a real flow, and therefore the only valid solution is the one with the positive sign for the squared root [92]

$$\frac{v_i}{v_h} = -\frac{V_c}{2v_h} + \sqrt{\left(\left[\frac{V_c}{2v_h}\right]^2 + 1\right)} \quad (\text{C.1.27})$$

There are two special cases:

$$\frac{v_i}{v_h} \simeq -\frac{V_c}{2v_h} + \frac{V_c}{2v_h} \approx 0 \quad \text{given} \left(1 \ll \frac{V_c}{2v_h}\right) \quad (\text{C.1.28})$$

$$\frac{v_i}{v_h} \simeq -\frac{V_c}{2v_h} + 1 \Rightarrow v_i \approx v_h - \frac{V_c}{2} \quad \text{given} \left(\frac{V_c}{2v_h} \ll 1\right) \quad (\text{C.1.29})$$

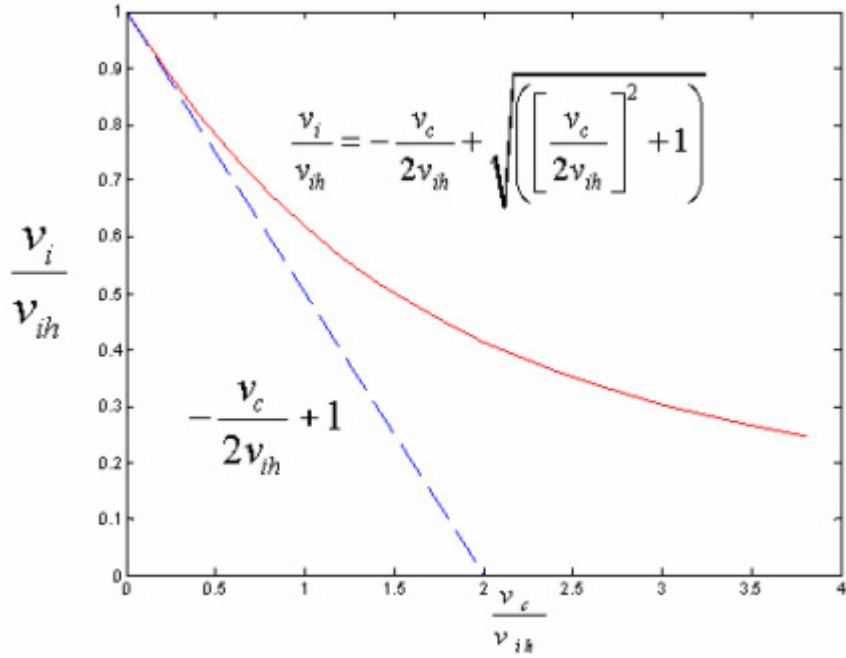


Figure C.2: Variation of induced velocity for climbing rate

Equation (C.1.28) shows that the induced velocity decreases asymptotically towards zero as the climb velocity v_c increases. In turn, equation (C.1.29) says that for a low climb rate, then the induced velocity behaves as a linear function of the climb rate. Figure C.2 below shows the behavior of functions (C.1.28) and (C.1.29). Notice that the climb solution described by equation (C.1.27) is only valid for flight conditions for which the climb velocity is greater than or equal to zero. All other flight conditions violate the flow model used thus far, and the results are therefore not valid.

The required power to climb is related to the rate of change of kinetic energy in the stream tube.

$$\begin{aligned}
 P_i &= \frac{\Delta \text{energy}}{\Delta \text{time}} = \frac{1}{2} \dot{m} [(V_C^2 + V_\infty^2) - V_C^2] \\
 &= \frac{1}{2} \rho A (V_C + v_i) (V_\infty^2 + 2v_c V_\infty)
 \end{aligned}
 \tag{C.1.30}$$

and using equation (C.1.24) yields

$$P_i = 2\rho A (v_i + V_C) v_i (v_i + V_C) = T (v_i + V_C)
 \tag{C.1.31}$$

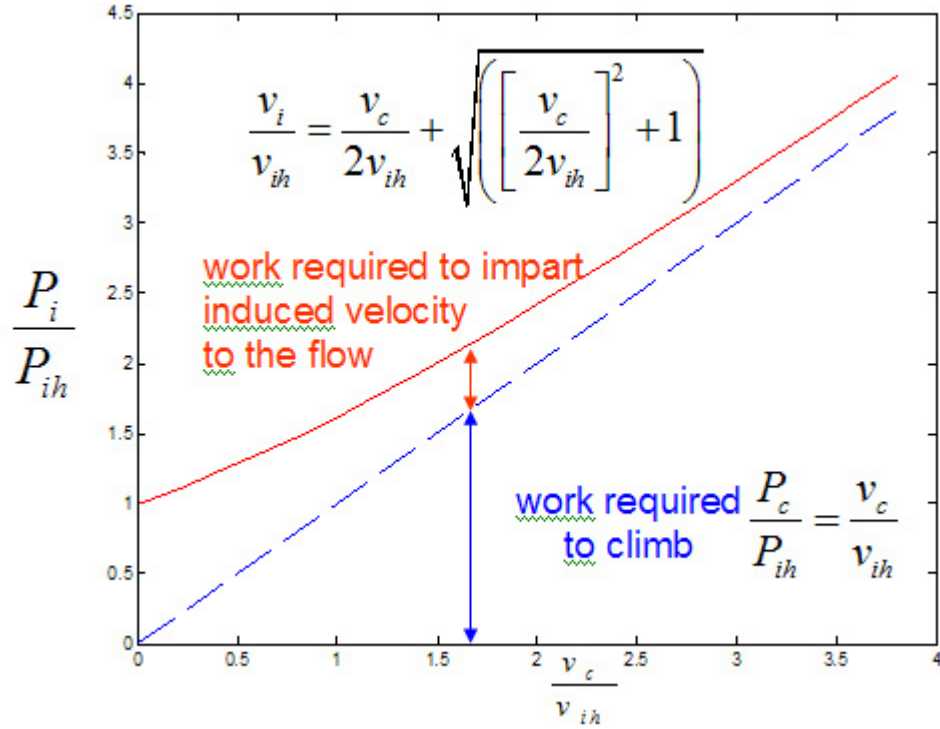


Figure C.3: Effects of climb speed on induced power

It is convenient to see how the hover induced power relates to the climb induced power. Combining equations (C.1.13), (C.1.27) and (C.1.31) gives

$$\begin{aligned} \frac{P_i}{P_h} &= \frac{T(V_C + v_i)}{Tv_h} = \frac{V_C}{v_h} + \frac{v_i}{v_h} \\ &= \frac{V_C}{2v_h} + \sqrt{\left(\frac{V_C}{2v_h}\right)^2 + 1} \end{aligned} \quad (\text{C.1.32})$$

The above equation (C.1.32) (see Figure C.3) says that the induced power increases as the climb speed itself increases. Equations (C.1.27) and (C.1.28) show that at very high speeds of climb, the induced velocity approaches zero and the induced power also approaches zero. In this case, equation (C.1.32) becomes

$$\begin{aligned} \frac{P_i}{P_h} &\approx \frac{V_C}{2v_h} + 1 \Rightarrow P_i \approx P_h + \frac{V_C}{2v_h} P_h \\ &\approx P_h + \frac{Tv_h V_C}{2v_h} \\ &= P_h + \frac{Tv_c}{2} \quad \text{given} \left(1 \ll \frac{V_C}{2v_h}\right) \end{aligned} \quad (\text{C.1.33})$$

C.1.2 Momentum Theory: Vertical Descent

In vertical descent the climb velocity is less than zero ($V_C < 0$, V_C is positive in the downward direction), and the axial flow through the rotor disk is such that the slipstream and rotor vortex are above the rotor. During some descend states the flow pattern is not well defined or recirculating in a non-linear fashion, there is no clearly defined slipstream, and therefore there is no well defined control volume. Under these circumstances, momentum theory is not applicable. Four different descend states are of interest [92, 124]:

1. windmill brake
2. low descend rate
3. vortex ring state
4. autorotation

C.1.2.1 Windmill Break State ($V_C/v_h \leq -2$)

In this case, the rate of descent is large, the flow is smooth, and the slip stream exists. The flow goes up through the rotor, and due to the induced velocity, the velocity decreases as the flow approaches the rotor. This results in the slip stream expanding above the rotor. In the Windmill brake state, power is transferred from air to rotor, and simple momentum theory is applicable once again [124]. Figure C.4 shows the axial descent flow model along with the control volume used to develop results from momentum theory [92]. This flow model works as long as the the slipstream remains well defined. The sign convention for V_C indicates that the flow well below the rotor has magnitude $|V_C|$, at the rotor disk the flow velocity has magnitude $|V_C| - v_i$, and the flow well above the rotor has magnitude $|V_C| - w$. During this type of descent the net flow within the slipstream above the rotor is less than V_C and, as previously said, the flow above the rotor expands. The mass flow rate \dot{m} is constant within the stream tube:

$$\begin{aligned}\dot{m} &= \iint_{@_4} \rho \vec{V} \cdot d\vec{S} = \iint_{@_3} \rho \vec{V} \cdot d\vec{S} \\ &= \rho A_{@_4} (V_c + w) = \rho A (V_c + v_i)\end{aligned}\tag{C.1.34}$$

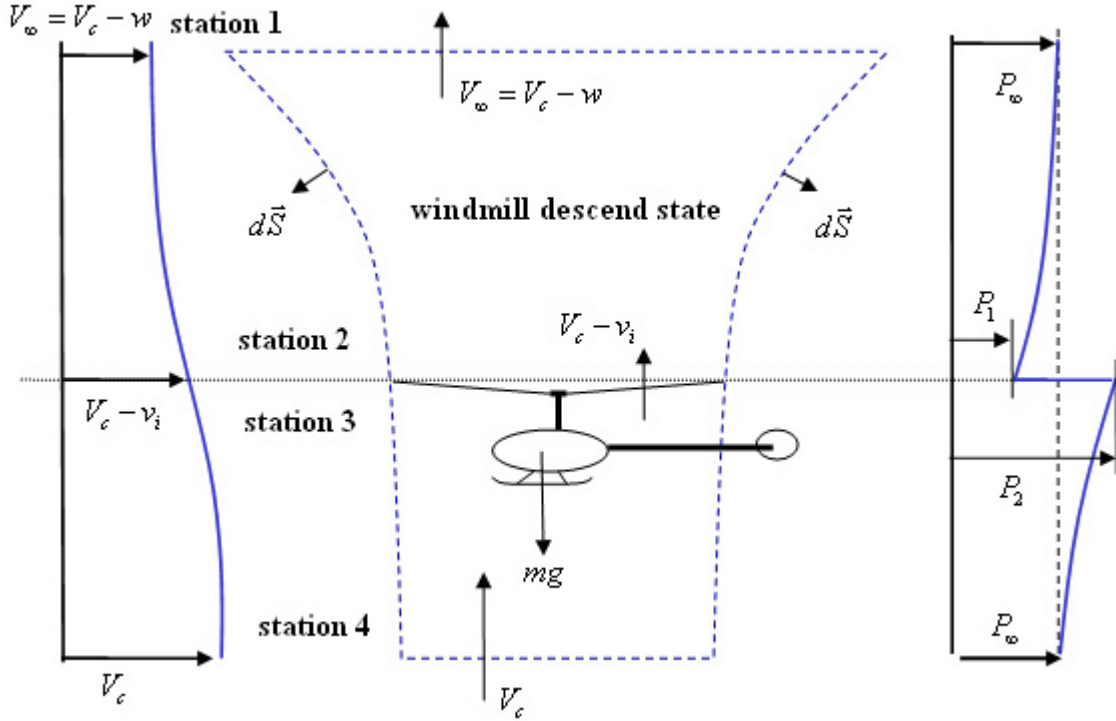


Figure C.4: Actuator disc concept for rotor in axial descent

In this case, the momentum equation (C.1.6) becomes

$$\begin{aligned}
 &= - \iint_{\textcircled{4}} \rho (\vec{V} \cdot d\vec{S}) \vec{V} + \iint_{\textcircled{1}} \rho (\vec{V} \cdot d\vec{S}) \vec{V} \\
 \vec{T} &= -\dot{m} (V_c + w) - (-\dot{m})V_c = -\dot{m}w
 \end{aligned} \tag{C.1.35}$$

where the flow rate \dot{m} is negative during descent. The corresponding work equation is

$$\begin{aligned}
 &= \iint_{\textcircled{4}} \frac{1}{2} (\rho \vec{V} \cdot d\vec{S}) \vec{V}^2 - \iint_{\textcircled{1}} \frac{1}{2} (\rho \vec{V} \cdot d\vec{S}) \vec{V}^2 \\
 T (V_c + v_i) &= \frac{1}{2} \dot{m} V_c^2 - \frac{1}{2} \dot{m} (V_c + w)^2 = -\frac{1}{2} \dot{m} w (2V_c + w)
 \end{aligned} \tag{C.1.36}$$

The negative work indicates that the flow does work on the rotor, or conversely, equation (C.1.36) above says that the rotor extracts power from the flow. Thusly, when the descend speed $V_c/v_h \leq -2$, then the descend region is known as the *windmill break state*. Equations (C.1.35) and (C.1.36) yield the usual result $w = 2v_i$. Following a development

similar to that of section §C.1.1 gives

$$T = 2\rho A(-V_C - v_i) v_i = -2\rho A(V_C + v_i) v_i \quad (\text{C.1.37})$$

Similar steps leading to equation (C.1.27) result in

$$\begin{aligned} v_h^2 &= -(V_C + v_i) v_i \\ \frac{v_i^2}{v_h^2} + \frac{v_i V_C}{v_h^2} + 1 &= 0 \end{aligned} \quad (\text{C.1.38})$$

solving for v_i/v_h

$$\frac{v_i}{v_h} = -\frac{V_C}{2v_h} \pm \sqrt{\left(\left[\frac{V_C}{2v_h}\right]^2 - 1\right)} \quad (\text{C.1.39})$$

In this case the only physically possible solution is the one for which $V_C/v_h \leq 0$, then

$$\frac{v_i}{v_h} = -\frac{V_C}{2v_h} - \sqrt{\left(\left[\frac{V_C}{2v_h}\right]^2 - 1\right)} \quad (\text{C.1.40})$$

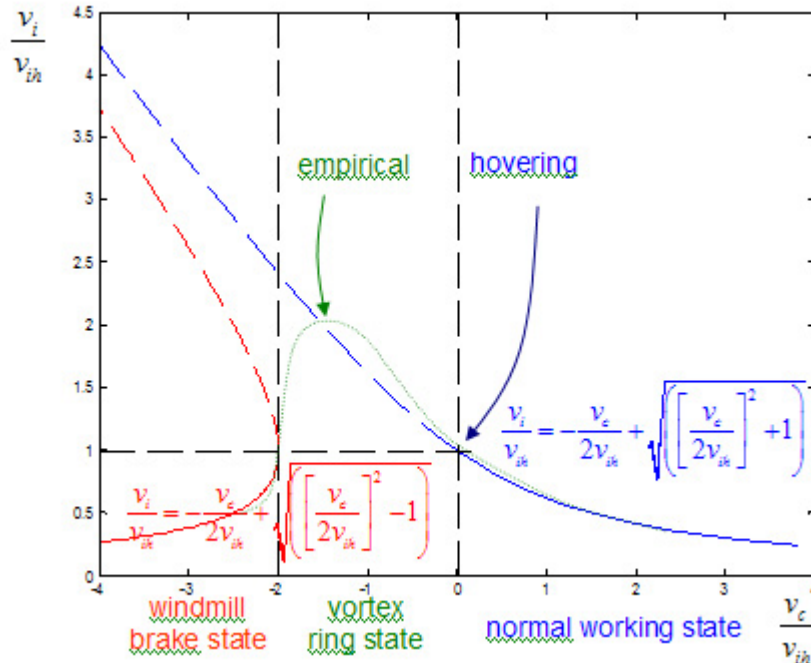


Figure C.5: Theoretical and empirical induced velocity profiles

Figure C.5 on the preceding page shows the theoretical and empirical induced velocity curves for the axial climb (normal working state) and large descend rates (windmill break state). As previously noticed in equations (C.1.27) and (C.1.40), the results from momentum theory only work in the normal working state and the windmill break state. Dashed curves indicate when the momentum theory does not work. Moreover, the Figure C.5 on the previous page shows the variation of the induced velocity with vertical flight. Notice that in the vortex ring state, the induced velocity increases to as much as twice the induced velocity during hover. Equation (C.1.40) indicates that when $V_c/2v_h \ll 1$ then the model generates an invalid solution. There is one special case:

$$\frac{v_i}{v_h} \simeq -\frac{V_c}{2v_h} - \frac{V_c}{2v_h} \approx -\frac{V_c}{v_h} \quad \text{given} \quad \left(1 \ll \frac{V_c}{2v_h}\right) \quad (\text{C.1.41})$$

Equation (C.1.41) along with Figure C.5 on the preceding page show that the induced velocity asymptotically decreases to zero as the descend velocity increases to large values.

C.1.2.2 Vortex Ring State

In the case of low descend rate, the flow is dominated by the induced velocity. The upward velocity of the rotor is close to or equal in magnitude to the induced velocity. In this mode the tip vortex filaments are closer to the plane of the rotor and move radially outward away from the rotor [92]. As a consequence, the expansion of the slipstream is very large, and there is recirculating flow in the rotor [83, 124]. As mentioned before, both the expansion of the slip stream and the recirculating flow invalidate the assumptions necessary for momentum theory, and therefore the momentum theory does not work. The momentum theory also breaks down when the upward velocity equals the induced velocity with a zero net velocity through the rotor which results in no thrust. In real life, the rotor still is able to develop thrust in these circumstances. The vortex ring state is an unsteady state which causes erratic fluctuations in lift such that the helicopter is subject to severe vibrations as well as pitch and roll attitude changes with some loss of rotor control [92, 124]. When the tail rotor experiences a state similar to the vortex ring state (when flying sideways and hovering in a cross wind), the helicopter may experience loss of directional control. A healthy research in the subject is on-going as seen in Chen

[19]. For a more in-depth treatment on the subject matter, references [92] present a good modern and actualized exposition of this and other working states.

C.1.2.3 Turbulent Wake State

In this state (with higher descent rates) of air flow through the rotor, the wake above the rotor becomes more turbulent and aperiodic than during the vortex ring state [92].

C.1.2.4 Autorotation

If the collective pitch of the main rotor is set such that the helicopter begins to fall, the inflow through the rotor reverses and the rotor takes momentum from the air. The source of energy is the potential energy lost due to the falling machine, the change of momentum causes the blades to rotate, and the blade rotation at a suitable angle of attack produces sufficient thrust to slow the rate of descent of the machine. [124]. This condition takes place at a point when $P/P_h = 0$ for a given V_C/v_h and thrust. The topic of autorotation is covered to a great level of detail by the literature, especially references [92, 124].

C.1.3 Momentum Theory: Forward Flight

A helicopter in forward flight develops a well defined slip stream which allows for a control volume necessary to apply momentum theory. As previously stated, momentum theory allows for development of first order performance estimation of forward flight with useful insight into the physics of forward flight [124]. A simple derivation of momentum theory results to forward flight can be found in [92]. The original development for application of momentum theory to forward flight was done by Glauert [54, 57] and referenced by Leishman [92].

Application of the mass flow rate equation (see equation (C.1.1)) gives

$$\begin{aligned} &= \rho A \sqrt{(V_\infty \cos \alpha)^2 + (V_\infty \sin \alpha + v_i)^2} \\ \dot{m} &= \rho A \sqrt{V_\infty^2 + 2v_i V_\infty \sin \alpha + v_i^2} \end{aligned} \tag{C.1.42}$$

Momentum exchange (see equation (C.1.4)) between the flow through the rotor and the

rotor takes the form:

$$\begin{aligned}
 &= \dot{m} (V_\infty \sin \alpha + w) - \dot{m} (V_\infty \sin \alpha) \\
 T &= \dot{m} w
 \end{aligned} \tag{C.1.43}$$

Energy exchange between the rotor and the flow (see equation (C.1.9)) yields an expression for power as

$$\begin{aligned}
 P = T (V_\infty \sin \alpha + v_i) &= \frac{1}{2} \dot{m} (V_\infty \sin \alpha + w)^2 - \frac{1}{2} \dot{m} V_\infty^2 \sin^2 \alpha \\
 &= \frac{1}{2} \dot{m} (2wV_\infty \sin \alpha + w^2)
 \end{aligned} \tag{C.1.44}$$

where $T * V_\infty \sin \alpha$ is the required power for climb and propulsion, and Tv_i is the power required for lift. Equations (C.1.43) and (C.1.44) yield $w = 2v_i$. Whence from equations (C.1.42) and (C.1.43)

$$\begin{aligned}
 T = 2\dot{m}v_i &= 2\rho Av_i \sqrt{(V_\infty \cos \alpha)^2 + (V_\infty \sin \alpha + v_i)^2} \\
 &= 2\rho Av_i \sqrt{V_\infty^2 + 2v_i V_\infty \sin \alpha + v_i^2}
 \end{aligned} \tag{C.1.45}$$

In the case when $V_\infty = 0$, then equation (C.1.45) reduces to the hover case in equation (C.1.12). In forward flight when $v_i \ll V_\infty$, equation (C.1.45) becomes equal to the lift of an elliptically loaded wing [55, 92] as

$$T = 2\rho A v_i V_\infty \tag{C.1.46}$$

Using hover results from equation (C.1.12) and the above equation (C.1.45) gives

$$\begin{aligned}
 2\rho A v_h^2 &= 2\rho A v_i \sqrt{(V_\infty \cos \alpha)^2 + (V_\infty \sin \alpha + v_i)^2} \\
 v_i &= \frac{v_h^2}{\sqrt{(V_\infty \cos \alpha)^2 + (V_\infty \sin \alpha + v_i)^2}}
 \end{aligned} \tag{C.1.47}$$

Define *tip speed ratio* or *advance ratio* μ as

$$\mu = \frac{V_\infty \cos \alpha}{\Omega R} \quad (\text{C.1.48})$$

For forward flight, the normalized inflow velocity or *inflow ratio* λ is

$$\lambda = \frac{V_\infty \sin \alpha + v_i}{\Omega R} = \mu \tan \alpha + \lambda_i \quad (\text{C.1.49})$$

were $\lambda_i = (V_C + v_i)/(\Omega R)$ is given by equation (C.1.17). Rearranging equation (C.1.47) such that

$$v_i = \frac{v_h^2}{\sqrt{(V_\infty \cos \alpha)^2 + (V_\infty \sin \alpha + v_i)^2}} \frac{(\Omega R)^2}{(\Omega R)^2}$$

becomes

$$\lambda_i = \frac{\lambda_h^2}{\sqrt{\mu^2 + \lambda^2}} \quad (\text{C.1.50})$$

In equation (C.1.18) $\lambda_h = \sqrt{C_T/2}$ and equation (C.1.50) is now

$$\lambda_i = \frac{C_T}{2\sqrt{\mu^2 + \lambda^2}} \quad (\text{C.1.51})$$

Substituting (C.1.51) in equation (C.1.49) gives

$$\lambda = \mu \tan \alpha + \frac{C_T}{2\sqrt{\mu^2 + \lambda^2}} \quad (\text{C.1.52})$$

which in general requires numerical procedures to solve for the inflow λ . Equation (C.1.52) can only be applied when the momentum theory itself is valid. Small upward or descent axial flow contributes a small normal component of the velocity that passes through the rotor. As seen in section §C.1.2.2, when this axial flow component is such that $-2v_i \leq V_\infty \sin \alpha \leq 0$, then the flow direction through the rotor can be in two directions and there is no well defined slipstream. Under these conditions results from momentum theory are not valid.

C.1.4 Momentum Theory: Power Consideration in Forward Flight

Equation (C.1.44) gives an expression for the propulsive and lift power estimates (viscous effects are not accounted for in this expression). With regard to the power necessary to hover $P_h = T v_i$ given by equation (C.1.13), equation (C.1.44) becomes [92]:

$$\begin{aligned} &= \frac{P}{T v_h} = \frac{T (V_\infty \sin \alpha + v_i)}{T v_h} = \frac{V_\infty \sin \alpha + v_i}{v_h} \\ \frac{P}{P_h} &= \frac{\lambda}{\lambda_h} = \frac{\mu}{\lambda_h} \tan \alpha + \frac{\lambda_h}{\sqrt{\mu^2 + \lambda^2}} \end{aligned} \quad (\text{C.1.53})$$

In straight and level flight, the equilibrium of forces are such that

$$\begin{aligned} T \cos \alpha &= W \\ T \sin \alpha &= D \cos \alpha \approx D \\ \tan \alpha &\approx \frac{D}{T} = \frac{\text{drag}}{\text{lift}} \end{aligned} \quad (\text{C.1.54})$$

Equation (C.1.53) is now

$$\frac{P}{P_h} = \frac{\mu}{\lambda_h} \frac{D}{T} + \frac{\lambda_h}{\sqrt{\mu^2 + \lambda^2}} \quad (\text{C.1.55})$$

In the case when there is climb or descent, equation (C.1.53) becomes

$$\frac{P}{P_h} = \lambda_c \cos \alpha + \frac{\mu}{\lambda_h} \tan \alpha + \frac{\lambda_h}{\sqrt{\mu^2 + \lambda^2}} \quad (\text{C.1.56})$$

where λ_c is the climb velocity ratio.

C.1.5 Summary of Results from Momentum Theory

Momentum theory captures first order rotor performance characteristics while in hovering, climbing, large descent rate axial flight and forward flight. As such, momentum theory gives insight into some of the factors that influence basic helicopter performance. Among the most important contributions of momentum theory are [92, 124, 140]:

1. provides means for quantification of first order rotor performance (thrust and power) in hover, forward and axial (climb and decent) flight.
2. insight into the importance of inflow velocity through the rotor.
3. shows importance of disk loading as a parameter that influences rotor performance
4. physical insight into the relation between low disk loading and hover performance
5. allows for empirical modifications to momentum theory to account for viscous and other non-linear effects
6. momentum theory is intrinsically simple to develop and apply

Momentum theory does not, however, capture viscous effects such as profile drag, and dynamic effects such as blade tip vortex and wake flow field dynamics. An example of momentum theory shortcomings are the vortex effects on power. Momentum theory fails to account for the effect of the flow conditions due to one blade following the next as the rotor rotates. The net result of this particular nonlinear effect is a change in the rotor upwash velocities that for small climb rates, the required power to climb is somewhat less than the required power to hover. Some additional issues associated with simple momentum theory are:

1. ignores profile drag losses
2. ignores performance of rotor wake vortex
3. provides no information regarding blade load distribution
4. no insights on how to design rotor blades to produce a given performance (thrust and related power)
5. does not deal with development of thrust in the individual blade elements
6. analysis breaks down in the vortex-ring state

Blade element theory and combined momentum and blade element theory address many of the above shortcomings.

C.2 Blade Element Theory

Leishman [92] provides an excellent historical perspective and a straight forward development on the subject of Blade Element Theory (BET). Prouty [124] gives a complete exposition on BET and its application to rotor design, performance and control. Reference [26] explores a preliminary engineering approach that uses BET in the design of helicopter rotors. This appendix summarizes the main results from the blade element theory compiled from the previous citations.

Blade Element Theory (BET) estimates the dynamic forces and moments associated with each blade element at a given radius from the rotating axis and at a given position of the blade azimuth. A blade section has a speed that is proportional to the local radius. If the blade section is sufficiently small, conditions across the section are constants. In this way, drag and thrust of the blade element can be readily computed, and the contributions of all the small blade elements are added to generate the total or net rotor thrust, drag and moment. Blade element theory has the following characteristics:

1. accounts for profile drag losses
2. gives insight into conditions at the rotor and in the wake
3. deals with thrust in the individual blade elements

The following are reasonable assumptions that can be made with blade element theory [26, 92, 124]

1. the radial (out-of-plane) velocity U_P and the tangential (in-plane) velocity U_T are such that $U_P \ll U_T \Rightarrow U = \sqrt{U_T^2 + U_P^2} \approx U_T$.
2. $U_P \ll U_T$ is not valid at the root, but forces close to the root are small.
3. considers each blade element independently from other elements
4. thrust and torque result from integration of the individual contributions of each element along the rotor radius
5. blade is rigid due to large centrifugal forces

6. induced flow angle ϕ is small such that
 $\phi \rightarrow \text{small} \Rightarrow \sin \phi \approx \phi, \cos \phi \approx 1 \rightarrow \tan^{-1}(U_P/U_T) \approx U_P/U_T$
7. blade incidence angle θ is small such that $\sin \theta \approx \theta, \cos \theta \approx 1$
8. L/D is large. That is, drag is one order of magnitude less than the lift such that
 $dD \sin \phi \approx dD\phi \ll dL \Rightarrow dD\phi \rightarrow \text{negligible}$
9. when appropriate, BET necessitates the use of vortex theory to assess the inflow at the root and tip of the blades.

For a given blade element, the incremental lift and drag are given by

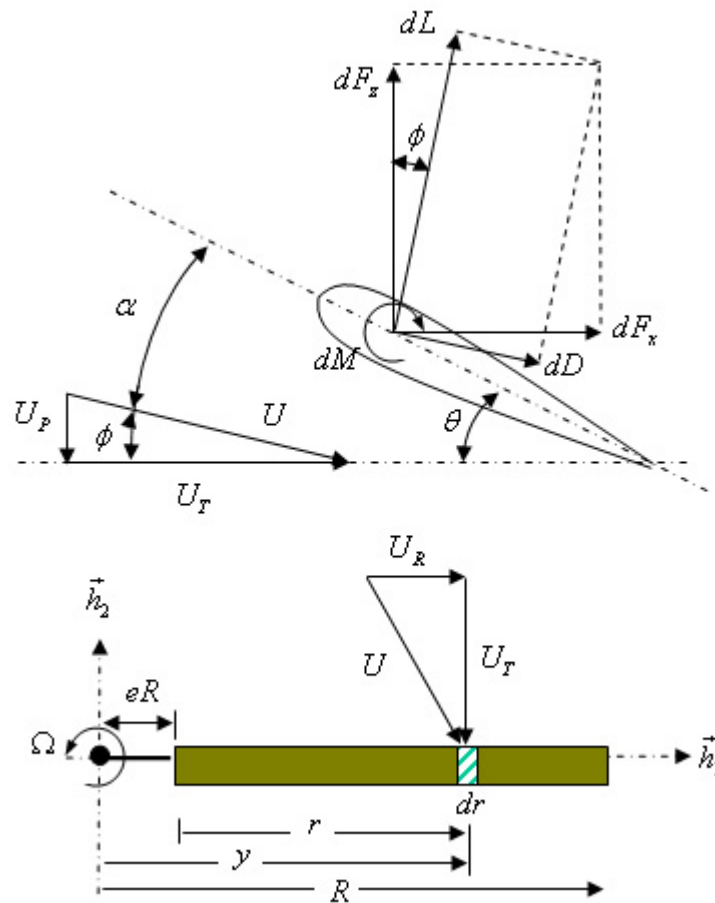


Figure C.6: Velocity, angles and parameters associated with a rotor blade element.

$$\begin{aligned}
dL &= q_\infty C_l S = \frac{1}{2} \rho U^2 C_l c dr \\
&= \frac{1}{2} \rho [(\Omega y)^2 + (v_i + V_c)^2] C_l [c dy] \\
dD &= q_\infty C_d S = \frac{1}{2} \rho U^2 C_d c dy \\
&= \frac{1}{2} \rho [(\Omega y)^2 + (v_i + V_c)^2] C_d [c dy]
\end{aligned} \tag{C.2.1}$$

where c is the local blade section chord, S is the blade section unit area, C_l, C_d are the lift and drag coefficients. Also, since $y = eR + r = R(e + x)$, then $dy = dr = Rdx$. The effective local angle of attack α is a function of the blade pitch angle θ (i.e. the angle between the chordline and the disk plane or disk of rotor angular motion) and the local inflow angle ϕ (i.e. the angle between the effective velocity U and the disk plane), and it is given by

$$\alpha = \theta - \phi = \theta - \tan^{-1} \frac{U_P}{U_T} \approx \theta - \frac{U_P}{U_T} \tag{C.2.2}$$

where ($x = r/R$)

$$\begin{aligned}
U_P &= V_C + v_i \\
U_T &= \Omega y = \Omega R (e + x) \\
\phi &= \tan^{-1} \frac{v_i + V_c}{\Omega y} \approx \frac{v_i + V_c}{\Omega y} = \frac{U_P}{U_T} \\
U^2 &= (v_i + V_c)^2 + \Omega^2 y^2 = (v_i + V_c)^2 + (\Omega R)^2 (e + x)^2
\end{aligned} \tag{C.2.3}$$

The inflow ratio in equation (C.1.17) on page 208 now takes the form

$$\lambda = \frac{V_C + v_i}{\Omega R} \left(\frac{\Omega y}{\Omega y} \right) = \frac{V_C + v_i}{\Omega y} \left(\frac{y}{R} \right) = \frac{U_P}{U_T} (e + x) = \phi(e + x) \tag{C.2.4}$$

For small angles

$$\begin{aligned}
&= C_{l_\alpha} (\alpha - \alpha_0) = C_{l_\alpha} (\theta - \alpha_0 - \phi) \\
&= C_{l_\alpha} \left(\theta - \alpha_0 - \tan^{-1} \frac{U_P}{U_T} \right) \approx C_{l_\alpha} \left(\theta - \alpha_0 - \frac{U_P}{U_T} \right) \\
C_l &= C_{l_\alpha} \left(\theta - \alpha_0 - \frac{v_i + V_c}{\Omega y} \right) \\
C_d &= c_D = f(\alpha, \Omega)
\end{aligned} \tag{C.2.5}$$

where C_{l_α} is the two-dimensional lift-curve-slope of the airfoil section, and α_0 is the zero-lift angle of attack. For incompressible flow, C_{l_α} is a function of Reynolds and local Mach numbers, but a constant average value for C_{l_α} will not result in significant error [92]. In this case let $a = C_{l_\alpha}$, and substituting back in (C.2.1)

$$\begin{aligned}
dL &= \frac{1}{2} \rho a c [(\Omega y)^2 + (v_i + V_c)^2] \left(\theta - \alpha_0 - \frac{v_i + V_c}{\Omega y} \right) dy \\
dD &= \frac{1}{2} \rho c [(\Omega y)^2 + (v_i + V_c)^2] c_D dy
\end{aligned} \tag{C.2.6}$$

in the case when $(v_i + V_c)^2 \ll (\Omega R)^2$, and when $\alpha_0 = 0$ for a symmetric airfoil, then

$$\begin{aligned}
dL &= \frac{1}{2} \rho a c (\Omega y)^2 \left(\theta - \frac{v_i + V_c}{\Omega y} \right) dy \\
dD &= \frac{1}{2} \rho c (\Omega y)^2 c_D dy
\end{aligned} \tag{C.2.7}$$

where the term $\theta - \alpha_0 - (v_i + V_c)/(\Omega y)$ is the effective angle of attack given by equation (C.2.2). From Figure C.6 on page 223, for a number of blades b , the thrust, torque and power are given by:

$$\begin{aligned}
dT &= b (dL \cos \phi - dD \sin \phi) \\
dQ &= b y (dL \sin \phi + dD \cos \phi) \\
dP &= \Omega dQ = b (dL \sin \phi + dD \cos \phi) \Omega y
\end{aligned} \tag{C.2.8}$$

Using the set of assumptions in page 222, equation (C.2.8) becomes ($y\phi = R\lambda$):

$$\begin{aligned}
dT &\approx b dL \\
dQ &\approx y b (\phi dL + dD) = y (\phi dT + b dD) = \frac{(v_i + V_c)}{\Omega} dT + b y dD \\
dP &= \Omega dQ \approx b (\phi dL + dD) \Omega y = (\phi dT + b dD) \Omega y \\
&\approx (v_i + V_c) dT + b \Omega y dD
\end{aligned} \tag{C.2.9}$$

Equation (C.1.17) on page 208 defines the Thrust, Torque and Power coefficients. In terms of the expression for dL in equation (C.2.1) on page 224 and for dT in equation (C.2.9), along with the aforementioned definition for the thrust coefficient C_T , the incremental thrust coefficient takes the form

$$\begin{aligned}
&= \frac{bdL}{\rho\pi R^2 (\Omega R)^2} = \frac{b\rho U_T^2 C_l [cdy]}{2\rho\pi R^2 (\Omega R)^2} = \frac{1}{2} \left[\frac{bc}{\pi R} \right] \left[\frac{\Omega y}{\Omega R} \right]^2 d \left(\frac{y}{R} \right) \\
dC_T &= \frac{\sigma}{2} C_l r^2 dr
\end{aligned} \tag{C.2.10}$$

where σ is the blade solidity σ is defined as the ratio of the total blade area to the rotor disc area

$$\sigma = \frac{\text{blade area}}{\text{disk area}} = \frac{bcR}{\pi R^2} = \frac{bc}{\pi R} \tag{C.2.11}$$

Equation (C.2.10) is a fundamental result from Blade Element Theory [92]. This result does not depend on any specific rotor configuration, and applies to all blade platforms. Continuing with the integration of the above set of equations (C.2.9) along the rotor blade gives

$$\begin{aligned}
T &= \frac{1}{2} \rho abc (\Omega R)^2 \left(\frac{1}{3} \theta R - \frac{1}{2} \frac{v_i + V_c}{\Omega} \right) = \frac{1}{2} \rho a \sigma A (\Omega R)^2 \left(\frac{1}{3} \theta - \frac{1}{2} \lambda \right) \\
D &= \frac{1}{6} \rho bc R (\Omega R)^2 C_D = \frac{1}{6} \rho \sigma A (\Omega R)^2 C_D \\
Q &= \frac{(v_i + V_c)}{\Omega} T + \frac{1}{8} \rho bc (\Omega R)^2 R^2 C_D = \lambda R T + \frac{1}{8} \rho \sigma A R (\Omega R)^2 C_D \\
P &= (v_i + V_c) T + \frac{1}{8} \rho bc (\Omega R)^3 R C_D = \lambda \Omega R T + \frac{1}{8} \rho \sigma A (\Omega R)^3 C_D
\end{aligned} \tag{C.2.12}$$

where $\lambda_i = (V_c + v_i)/(\Omega R)$ is given by equation (C.1.17) on page 208 and revisited in equation (C.2.4) on page 224 and the rotor disk area is given by $A = \pi R^2$. In terms of the results in equation (C.2.12) then

$$\begin{aligned} C_T &= \frac{a\sigma}{2} \left(\frac{1}{3}\theta - \frac{1}{2}\lambda \right) \\ C_P = C_Q &= \frac{a\sigma}{2} \lambda \left(\frac{1}{3}\theta - \frac{1}{2}\lambda \right) + \frac{1}{8}\sigma C_D = \lambda C_T + \frac{1}{8}\sigma C_D \end{aligned} \quad (\text{C.2.13})$$

Using results from simple momentum theory in equation (C.1.18), then equation (C.2.13) above becomes

$$\begin{aligned} C_T &= \frac{a\sigma}{2} \left(\frac{\theta}{3} - \frac{1}{2}\sqrt{\frac{C_T}{2}} \right) \\ C_P = C_Q &= \frac{C_T^{3/2}}{\sqrt{2}} + \frac{1}{8}\rho C_D \end{aligned} \quad (\text{C.2.14})$$

where the thrust coefficient C_T results from an iterative solution of the above equation. Solving for pitch angle θ

$$\theta = \frac{6}{a\rho} C_T + \frac{3}{2}\sqrt{\frac{C_T}{2}} \quad (\text{C.2.15})$$

In the above equation, the term $6C_T/(a\rho)$ is the blade pitch angle required to generate thrust, and the term $3/2\sqrt{C_T/2}$ is the blade pitch necessary to compensate for the induced flow. The above equations are valid for rotors with uniform inflow velocity λ across the rotor, for a constant rotor lift-curve-slope C_{l_α} , and for a symmetric airfoil with no tip loss. Other additional non-ideal and non-linear effects such as flow and thrust at the blade root and tip vortex shading may be accounted for by introducing a first order induced power loss factor k in the C_p , C_Q equation such that

$$C_P = C_Q = \frac{k}{\sqrt{2}} C_T^{3/2} + \frac{1}{8}\rho C_D \quad (\text{C.2.16})$$

where the factor k is approximately equal to 1.2 to 1.5 [13, 92].

C.2.1 Tip-Loss Factor

The BET allows for the blade tip to generate finite thrust which is physically unrealistic [92]. Leishman points out that original work by Gessow [52] and Gessow and Myers [53], and work by Payne [120], Johnson [82] account for the blade tip not to carry thrust by introducing the concept of effective blade radius $R_e = BR$ where $B \approx 0.95 - 0.97$. Integration of the thrust equation (C.2.9) from 0 to B results in

$$C_T = \frac{a\sigma}{2} B^2 \left(\frac{1}{3} \theta B - \frac{1}{2} \lambda \right) \quad (\text{C.2.17})$$

The above effective rotor blade radius concept in equation (C.2.17) indicates that the $R - R_e$ portion of the blade does not contribute to thrust generation. A more appropriate interpretation by Bramwell [11] and Leishman [92] considers an increment of the induced flow for a given thrust such that equation (C.1.12) would become

$$v_h = \sqrt{\frac{T}{2\rho(AB^2)}} = \frac{1}{B} \sqrt{\frac{T}{2\rho A}} \quad (\text{C.2.18})$$

where the effective rotor area $A_e = AB^2 = \pi(RB)^2$. In this case integration of equations (C.2.9) result in

$$\begin{aligned} C_T &= \frac{a\sigma}{2} \left(\frac{1}{3} \theta - \frac{1}{2} \frac{\lambda}{B} \right) \\ C_P = C_Q &= \frac{a\sigma}{2} \frac{\lambda}{B} \left(\frac{1}{3} \theta - \frac{1}{2} \frac{\lambda}{B} \right) + \frac{1}{8} \sigma C_D \end{aligned} \quad (\text{C.2.19})$$

The above equation (C.2.19) says that for a given thrust, the induced flow will be higher for results from BET than the induced flow obtained from simple momentum theory. Similarly, the induced power increases in results from BET as those obtained from momentum theory.

C.3 Combined Blade Element and Momentum Theory

Combined Blade Element Momentum Theory (BEMT) uses Blade Element and Momentum theory principles to find the inflow distribution as function of blade element. This method was first explored by Gustafson & Gessow [61] and Gessow [51] for hovering rotors. The main reference for this section is given by Leishman [92] which explores the subject from a modern vantage point. Figure C.7 shows a rotor disk annulus at a distance r from the rotating axis and with differential area $dA = 2\pi r dr$. Simple momentum theory gives the thrust given by this annulus, and from BET we re-use the assumption that one rotor annuli does not have an impact on the neighbor sections.

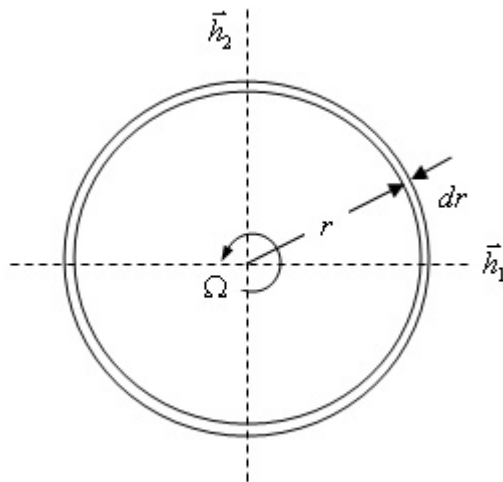


Figure C.7: Rotor annulus used in local momentum analysis for hovering [53, 92].

The differential mass flow $d\dot{m}$ through the rotor annulus, the resulting differential thrust dC_T generated by the rotor annulus, and the differential induced power coefficient

dC_{P_i} are

$$\begin{aligned}
d\dot{m} &= \rho (V_C - v_i) dA = 2\pi\rho (V_C - v_i) r dr \\
dT &= 2\rho (V_C - v_i) v_i dA = 4\pi\rho (V_C - v_i) v_i r dr \\
dC_T &= \frac{dT}{\rho (\pi R^2) (\Omega R)^2} = 4 \frac{(V_C - v_i)}{\Omega R} \left(\frac{v_i}{\Omega R} \right) \left(\frac{r}{R} \right) d \left(\frac{r}{R} \right) = 4\lambda\lambda_i r dr \\
dC_T &= 4\lambda (\lambda - \lambda_C) x dx \\
dC_{P_i} &= \lambda dC_T = 4\lambda^2 (\lambda - \lambda_C) x dx
\end{aligned} \tag{C.3.1}$$

where $\lambda_C = V_C/(\Omega R)$, $\lambda_i = v_i/(\Omega R) \Rightarrow \lambda_i = \lambda - \lambda_C$ and $x = r/R$. For the hovering case $\lambda_C = 0$ and the differential thrust coefficient C_T and induced power coefficient are

$$\begin{aligned}
dC_T &= 4\lambda^2 x dx \\
dC_{P_i} &= \lambda dC_T = 4\lambda^3 x dx
\end{aligned} \tag{C.3.2}$$

Following the development in [92], the inflow λ can be expressed as a function of blade station $x = r/R$ such that

$$\lambda(x) = \lambda_{tip} x^n \quad \forall n \geq 0 \tag{C.3.3}$$

Substituting equation (C.3.3) in (C.3.2) and integrating gives

$$\begin{aligned}
C_T &= 4 \int_0^1 \lambda^2 x dx = 4\lambda_{tip}^2 \int_0^1 x^{2n+1} dx = 4 \frac{1}{2n+2} \lambda_{tip}^2 \\
C_{P_i} &= 4 \int_0^1 \lambda^3 x dx = 4\lambda_{tip}^3 \int_0^1 x^{3n+1} dx = 4 \frac{1}{3n+2} \lambda_{tip}^3
\end{aligned} \tag{C.3.4}$$

Solving for λ_{tip} in the above expression for C_T and substituting back in the expression for C_{P_i}

$$\begin{aligned}
\lambda_{tip} &= \sqrt{n+1} \sqrt{\frac{C_T}{2}} \\
C_{P_i} &= \frac{2(n+2)^{3/2} C_T^{3/2}}{3n+2 \sqrt{2}} = k \frac{C_T^{3/2}}{\sqrt{2}} \Rightarrow k = \frac{2(n+2)^{3/2}}{3n+2}
\end{aligned} \tag{C.3.5}$$

When the flow through the rotor is uniform $n = 0 \rightarrow k = 1$. When $n > 0 \rightarrow k > 1$ and the flow becomes less ideal and more biased toward the blade tip [92]. A related approach equates results from BET and momentum theory. From equations (C.2.7) and (C.2.9)

$$\begin{aligned} &= \frac{(dT \approx bdL)}{\rho(\pi R^2)(\Omega R)^2} = \frac{1}{2} \frac{\rho abc (\Omega r)^2 (\theta - \lambda (R/r))}{\rho(\pi R^2)(\Omega R)^2} dr \\ dC_T &= \frac{1}{2} \rho a (\theta x^2 - \lambda x) dx \end{aligned} \quad (\text{C.3.6})$$

where as before $a = C_{l_\alpha}$ and $x = r/R$. Equating the above expression for the incremental thrust coefficient dC_T to the momentum result in equation (C.3.1) gives

$$\begin{aligned} dC_T &= \frac{1}{2} \sigma a (\theta x^2 - \lambda x) dx = 4\lambda (\lambda - \lambda_C) x dx \\ &\Rightarrow \frac{1}{8} \sigma a \theta x - \frac{1}{8} \sigma a \lambda = \lambda^2 - \lambda_C \lambda \\ &\Rightarrow \lambda^2 + \left(\frac{1}{8} \sigma a - \lambda_C \right) \lambda - \frac{1}{8} \sigma a \theta x = 0 \end{aligned} \quad (\text{C.3.7})$$

$$\lambda(x, \lambda_C) = \sqrt{\left(\frac{\sigma a}{16} - \frac{\lambda_C}{2} \right)^2 + \frac{\sigma a}{8} \theta x} - \left(\frac{\sigma a}{16} - \frac{\lambda_C}{2} \right)$$

For the hover case when $\lambda_C = 0$ then

$$\begin{aligned} &= \sqrt{\left(\frac{1}{16} \sigma a \right)^2 + \frac{1}{8} \sigma a \theta x} - \frac{1}{16} \sigma a \\ \lambda(x) &= \frac{1}{16} \sigma a \left[\sqrt{1 + 32 \frac{\theta}{\sigma a} x} - 1 \right] \end{aligned} \quad (\text{C.3.8})$$

Equations (C.3.7) and (C.3.8) provide the means to compute the inflow distribution as a function of blade station $x = r/R$ and for a given airfoil and blade pitch θ . Once λ is known, then integration of equations (C.3.2) across the rotor disk gives the total thrust

and induced power as [90, 92]

$$\begin{aligned} C_T &= 4 \int_0^1 \lambda^2 x dx \\ C_{P_i} &= 4 \int_0^1 \lambda^3 x dx \end{aligned} \tag{C.3.9}$$

The profile power comes from equations (C.2.7) and (C.2.9) as

$$\begin{aligned} &= \frac{(dP_o \approx b\Omega r dD)}{\rho(\pi R^2)(\Omega R)^3} = \frac{1}{2} \frac{\rho b c \Omega r (\Omega r)^2 c_D}{\rho(\pi R^2)(\Omega R)^3} dr \\ dC_{P_o} &= \frac{1}{2} \sigma c_D x^3 dx \end{aligned} \tag{C.3.10}$$

The airfoil section drag coefficient can be approximated as

$$\begin{aligned} &= d_2 \alpha^2 + d_1 \alpha + c_{d_0} \\ c_D &= d_2 \left(\theta - \frac{\lambda}{x} \right)^2 + d_1 \left(\theta - \frac{\lambda}{x} \right) + c_{d_0} \end{aligned} \tag{C.3.11}$$

where the section angle of attack α is given by equation (C.2.2) together with equation (C.2.4). Substituting the above into equation (C.3.11) and integrating gives

$$\begin{aligned} &= \frac{1}{2} \sigma \int_0^1 c_D x^3 dx = \int_0^1 \left[d_2 \left(\theta - \frac{\lambda}{x} \right)^2 + d_1 \left(\theta - \frac{\lambda}{x} \right) + c_{d_0} \right] x^3 dx \\ C_{P_0} &= \frac{1}{2} \sigma \int_0^1 [d_2 (\theta x - \lambda)^2 x + d_1 (\theta x - \lambda) x^2 + c_{d_0} x^3] dx \end{aligned} \tag{C.3.12}$$

The above equation is for an untwisted blade. In the case when the induced velocity λ is not a function of blade station, then

$$\begin{aligned} C_{P_i} &= 2\lambda^3 \\ C_{P_0} &= \frac{\sigma}{2} \left[\frac{1}{4} (d_2 \theta^2 + d_1 \theta + c_{d_0}) - \frac{1}{3} (2d_2 \theta + d_1) \lambda + \frac{1}{2} d_2 \lambda^2 \right] \end{aligned} \tag{C.3.13}$$

C.3.1 Other Effects

Blade Element Theory accounts for profile drag as a driving force that requires torque to be included in the equations. Other effects include:

1. blade twist
2. variations in induced velocity
3. inflow variations
4. three dimensional flow effects
5. vortex flow effects
6. tip loss and non-uniform flow
7. compressibility effects
8. ground effects

Johnson [82], Prouty [124], Padfield [119], Leishman [92], and other authors cover the various aspects of non-linear aerodynamic effects on helicopter flight, rotor-fuselage interaction, vorticity effects, etc.

Appendix D

Helicopter Rotor Equations of Motion

D.1 Preliminaries and Motivation

Figure D.1 shows that while in forward flight, the helicopter's advancing blade of the rotor encounters a higher free stream velocity ($V_{tip} = R\Omega + V_\infty$) than the retreating blade ($V_{tip} = R\Omega - V_\infty$). A direct consequence is that the dynamic pressure on the rotating wing varies both radially and azimuthally. This creates an asymmetric lift in the rotor which will induce a significant rolling moment.

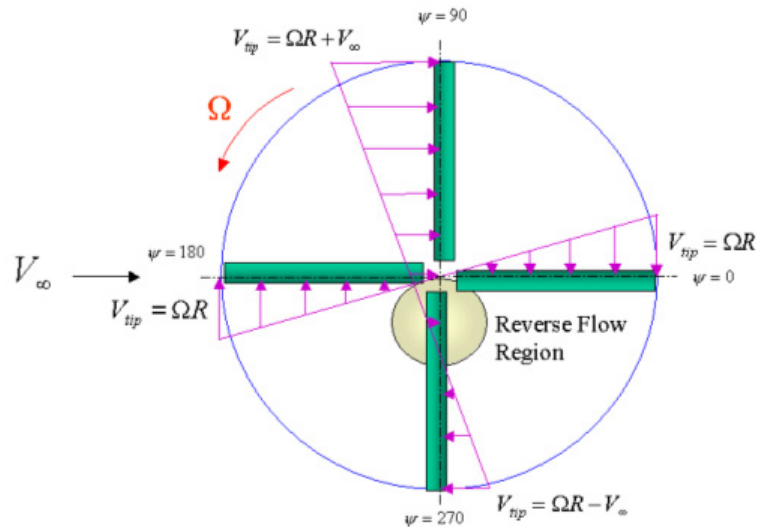


Figure D.1: Helicopter rotor in forward flight.

Commonly, the following standard and equivalent solutions counter the asymmetric lift and resulting rolling moment:

1. blades hinged at the root: lift transfers to the shaft, but no moment is transmitted to the hub. Hub tilting achieves the desired thrust vector.

2. blades rigidly attached: cyclic feathering of the blades decreases the pitch in the advancing blade, and increases the pitch in the retreating blade. Lift is equalized, and no rolling moment results.
3. lead-lag hinges: mitigate the forces and stresses created by Coriolis effect. This motion turns out not to have significant aerodynamic effect, and in most cases it is ignored.

The main difference in the above methods resides in the reference axis. Also, rotors with hinges have the hinges located with a small offset from the root. It is then important to study both the effects of blade hinges and feathering with regard to helicopter stability and control as well as performance.

D.2 Fundamental Rotor Equations of Motion

The hub reference frame \mathcal{H} shown in Figure D.2 on the next page rotates along with the blades with angular velocity $\pi/30 \Omega(\text{rpm}) = \omega(\text{rad})$. In this case every point at a distance r from the hub axis of rotation experiences an acceleration $-(\omega^2 \times r)\vec{h}_1$. As the blade rotates, its mass appears to be located at a distance ρ called the center of gyration. This inward or centripetal (latin: center seeking) force accelerates the blade into a circular path. Moreover, when the blade flaps up or down, the blade center of mass moves toward or away from the axis of rotation. When the blade flaps in the upward direction, its center of mass moves closer to the axis of rotation which causes the blade to accelerate to conserve angular momentum. That is, as the blade flaps upwardly, it will also accelerate with corresponding forward motion in the off-plane direction[154].

where

R = rotor radius

eR = hinge offset

ω = rotor angular velocity

β = blade flap angle

$\tilde{\mathbf{a}}_0$ = acceleration of blade hinge origin at distance eR from the rotor shaft

$\tilde{\mathbf{H}}$ = rotor central angular momentum

$\tilde{\mathbf{G}}$ = rotor total moments

$\tilde{\mathbf{r}}_g$ = position vector from blade hinge to blade c.g.

M_b = rotor blade mass

I = rotor inertia dyad

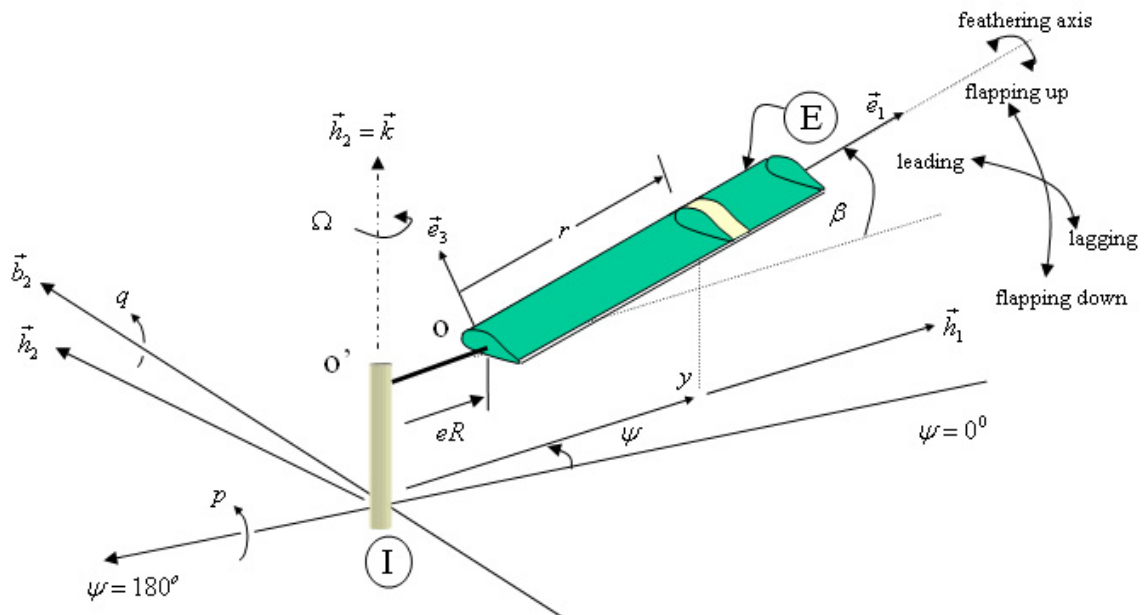


Figure D.2: Rotor blade nomenclature.

The transformation from the rotating hub reference frame \mathcal{H} to the body frame \mathcal{B}

through azimuth angle ψ is:

$${}^{\mathcal{B}}T_3^{\mathcal{H}}(\psi) = \begin{bmatrix} b_1 \\ b_2 \\ b_3 \end{bmatrix} = \begin{bmatrix} -\cos \psi & \sin \psi & \\ \sin \psi & \cos \psi & \\ & & -1 \end{bmatrix} \begin{bmatrix} h_1 \\ h_2 \\ h_3 \end{bmatrix} \quad (\text{D.2.1})$$

where azimuth blade angle ψ is measured from the retreating blade. The transformation between the rotating hub frame \mathcal{H} and the drag frame \mathcal{D} (in the blade lead/lag direction) about the drag hinge through an angle ζ is:

$${}^{\mathcal{D}}T_3^{\mathcal{H}}(\zeta) = \begin{bmatrix} d_1 \\ d_2 \\ d_3 \end{bmatrix} = \begin{bmatrix} \cos \zeta & \sin \zeta & \\ -\sin \zeta & \cos \zeta & \\ & & 1 \end{bmatrix} \begin{bmatrix} h_1 \\ h_2 \\ h_3 \end{bmatrix} \quad (\text{D.2.2})$$

The transformation between the drag frame \mathcal{D} and the blade flap \mathcal{F} about the blade flap hinge through the angle β is:

$${}^{\mathcal{F}}T_2^{\mathcal{D}}(\beta) = \begin{bmatrix} f_1 \\ f_2 \\ f_3 \end{bmatrix} = \begin{bmatrix} \cos \beta & \sin \beta & \\ & 1 & \\ -\sin \beta & \cos \beta & \end{bmatrix} \begin{bmatrix} d_1 \\ d_2 \\ d_3 \end{bmatrix} \quad (\text{D.2.3})$$

Finally, the transformation between the blade flap frame \mathcal{F} and the blade frame \mathcal{E} through the feathering or blade pitch angle θ is:

$${}^{\mathcal{E}}T_1^{\mathcal{F}}(\theta) = \begin{bmatrix} e_1 \\ e_2 \\ e_3 \end{bmatrix} = \begin{bmatrix} 1 & & \\ & \cos \theta & \sin \theta \\ & -\sin \theta & \cos \theta \end{bmatrix} \begin{bmatrix} f_1 \\ f_2 \\ f_3 \end{bmatrix} \quad (\text{D.2.4})$$

The governing equation of motion of rotor blades as they rotate around the rotor axis is

given by equation (A.3.3), and it is reproduced below for convenience.

$$\vec{G}^o - \vec{C}^o \times {}^I\vec{a}_o = \vec{I}^o \cdot \dot{{}^I\vec{\omega}}^\mathcal{E} + {}^I\vec{\omega}^\mathcal{E} \times \left(\vec{I}^o \cdot {}^I\vec{\omega}^\mathcal{E} \right) = \dot{\vec{h}}^o \quad (\text{D.2.5})$$

In the above equation, the term \vec{G}^o represents the resultant aerodynamic blade moments and takes the form:

$$\vec{G}^o = \begin{bmatrix} L \\ M \\ N \end{bmatrix} = \begin{bmatrix} \text{feathering moment} \\ \text{flapping moment} \\ \text{drag (lead/lag) moment} \end{bmatrix} \quad (\text{D.2.6})$$

Moreover, for a blade of uniform mass, the first moment of inertia term \vec{C}^o in equation (D.2.5) takes the form:

$$\begin{aligned} \vec{C}^o &= \int_{\mathcal{B}} {}_o\vec{r}_{dm} dm = \int_0^{(1-e)R} m r dr \vec{e}_1 \\ &= m R^2 \frac{(1-e)^2}{2} \vec{e}_1 \\ &= M_{blade} r_{CM} R \vec{e}_1 \end{aligned} \quad (\text{D.2.7})$$

where the reference point o is the flapping hinge axis, the mass of the blade is $M_{blade} = mR(1-e)$, and the blade center of mass is $Rr_{CM} = R(1-e)/2$ as measured from the flapping hinge axis. Note that $Rx_{CM} = R(r_{CM} + e)$ is the distance to the blade center of mass as measured from the rotational axis. Also, the acceleration term ${}^I\vec{a}_o$ takes the form (see Figure D.2 on page 236)

$${}^I\vec{a}_o = {}^I\vec{a}_{o'} + {}^I\tilde{\omega}^\mathcal{H} \times ({}^I\tilde{\omega}^\mathcal{H} \times {}_o\tilde{\mathbf{r}}_o) + {}^I\tilde{\alpha}^\mathcal{H} \times {}_o\tilde{\mathbf{r}}_o \quad (\text{D.2.8})$$

where ${}^I\vec{a}_{o'} = 0$ when the helicopter itself does not accelerate. In the most general case, the rotor blade angular velocity ${}^I\vec{\omega}^\mathcal{E}$ takes the form:

$${}^I\vec{\omega}^\mathcal{E} = {}^I\vec{\omega}^\mathcal{B} + {}^B\vec{\omega}^\mathcal{H} + {}^H\vec{\omega}^\mathcal{D} + {}^D\vec{\omega}^\mathcal{F} + {}^F\vec{\omega}^\mathcal{E} \quad (\text{D.2.9})$$

and:

\mathcal{I} = inertial reference frame

\mathcal{B} = helicopter body reference frame

\mathcal{H} = rotating hub reference frame

\mathcal{D} = drag or lead/lag reference frame

\mathcal{F} = flap reference frame

\mathcal{E} = blade reference frame

The rotor hub angular velocity is,

$$\begin{aligned} &= {}^{\mathcal{I}}\vec{\omega}^{\mathcal{B}} + {}^{\mathcal{B}}\vec{\omega}^{\mathcal{H}} \\ {}^{\mathcal{I}}\vec{\omega}^{\mathcal{H}} &= p\vec{b}_1 + q\vec{b}_2 + \Omega\vec{h}_3 \end{aligned} \quad (\text{D.2.10})$$

where ($r = 0$). In terms of the rotor hub frame \mathcal{H}

$$\begin{aligned} &= {}^{\mathcal{H}}T_1^{\mathcal{B}}(\psi) \left[p\vec{b}_1 + q\vec{b}_2 \right] + \Omega\vec{h}_3 \\ {}^{\mathcal{I}}\vec{\omega}^{\mathcal{H}} &= \begin{bmatrix} -\cos\psi & \sin\psi & & \\ \sin\psi & \cos\psi & & \\ & & & 1 \end{bmatrix} \begin{bmatrix} p \\ q \\ 0 \end{bmatrix} + \begin{bmatrix} 0 \\ 0 \\ \Omega \end{bmatrix} = \begin{bmatrix} -p\cos\psi + q\sin\psi \\ p\sin\psi + q\cos\psi \\ \Omega \end{bmatrix} \end{aligned} \quad (\text{D.2.11})$$

The main rotor hub angular acceleration ${}^{\mathcal{I}}\vec{\alpha}^{\mathcal{H}}$ is ($\dot{\psi} = \Omega, \dot{\Omega} = 0$) expressed in terms of hub frame \mathcal{H} follows

$${}^{\mathcal{I}}\vec{\alpha}^{\mathcal{H}} = \begin{bmatrix} \Omega(p\sin\psi + q\cos\psi) - (\dot{p}\cos\psi - \dot{q}\sin\psi) \\ \Omega(p\cos\psi - q\sin\psi) + (\dot{p}\sin\psi + \dot{q}\cos\psi) \\ 0 \end{bmatrix} \quad (\text{D.2.12})$$

Provided the helicopter body is not accelerating (${}^{\mathcal{I}}\vec{a}_o = 0$), and substituting equations

(D.2.11), (D.2.12) in equation (D.2.8), ${}^{\mathcal{I}}\vec{a}_o$ becomes

$$\begin{aligned}
&= {}^{\mathcal{I}}\tilde{\omega}^{\mathcal{H}} \times ({}^{\mathcal{I}}\tilde{\omega}^{\mathcal{H}} \times {}_o\tilde{\mathbf{r}}_o) + {}^{\mathcal{I}}\tilde{\alpha}^{\mathcal{H}} \times {}_o\tilde{\mathbf{r}}_o \\
&= \begin{bmatrix} -p \cos \psi + q \sin \psi \\ p \sin \psi + q \cos \psi \\ \Omega \end{bmatrix} \times \left(\begin{bmatrix} -p \cos \psi + q \sin \psi \\ p \sin \psi + q \cos \psi \\ \Omega \end{bmatrix} \times \begin{bmatrix} eR \\ 0 \\ 0 \end{bmatrix} \right) \\
&\quad + \begin{bmatrix} \Omega (p \sin \psi + q \cos \psi) - (\dot{p} \cos \psi - \dot{q} \sin \psi) \\ \Omega (p \cos \psi - q \sin \psi) + (\dot{p} \sin \psi + \dot{q} \cos \psi) \\ 0 \end{bmatrix} \times \begin{bmatrix} eR \\ 0 \\ 0 \end{bmatrix} \\
{}^{\mathcal{I}}\vec{a}_o &= -eR \begin{bmatrix} \Omega^2 + (p \sin \psi + q \cos \psi)^2 \\ (p \sin \psi + q \cos \psi)(p \cos \psi - q \sin \psi) \\ 2\Omega (p \cos \psi - q \sin \psi) + \dot{p} \sin \psi + \dot{q} \cos \psi \end{bmatrix}
\end{aligned} \tag{D.2.13}$$

where the above equation (D.2.13) is given in terms of the hub frame \mathcal{H} . In the particular case when the body rates are zero ($p = 0, q = 0$), and when the rotor angular velocity is constant ($\dot{\Omega} = 0$), then ${}^{\mathcal{I}}\tilde{\alpha}^{\mathcal{H}} = 0$. In this case equation (D.2.8) becomes,

$$\begin{aligned}
{}^{\mathcal{I}}\vec{a}_o &= {}^{\mathcal{I}}\tilde{\omega}^{\mathcal{H}} \times ({}^{\mathcal{I}}\tilde{\omega}^{\mathcal{H}} \times {}_o\tilde{\mathbf{r}}_o) \\
&= \begin{bmatrix} 0 \\ 0 \\ \Omega \end{bmatrix} \times \begin{bmatrix} 0 & eR \\ 0 & 0 \\ \Omega & 0 \end{bmatrix} = \begin{bmatrix} -\Omega^2 eR \\ 0 \\ 0 \end{bmatrix}
\end{aligned} \tag{D.2.14}$$

where ${}_o\tilde{\mathbf{r}}_o = eR \vec{h}_1$. Moreover, with no loss of generality, the second moment of inertia \vec{I}^o can take the form of a thin actuator disk such that

$$\vec{I}^o = \begin{bmatrix} I_a & & \\ & I_b & \\ & & I_c \end{bmatrix} \tag{D.2.15}$$

where for a thin disk $I_c = I_a + I_b$ and $I_a = I_b$.

D.2.1 Pure Blade Flap Equations of Motion

Pure blade flap motion analysis begins by restricting the blade to up and down motion only (an unrealistic assumption in practice, but useful for the present analysis). In this case, ${}^{\mathcal{I}}\vec{\omega}^{\mathcal{E}}$ in equation (D.2.9) takes the form

$${}^{\mathcal{I}}\vec{\omega}^{\mathcal{E}} = {}^{\mathcal{I}}\vec{\omega}^{\mathcal{B}} + {}^{\mathcal{B}}\vec{\omega}^{\mathcal{H}} + {}^{\mathcal{H}}\vec{\omega}^{\mathcal{E}} \quad (\text{D.2.16})$$

where for the case when the helicopter is in stable hover ($q = 0, \dot{q} = 0, r = 0$)

$${}^{\mathcal{I}}\vec{\omega}^{\mathcal{E}} = \vec{0} + \Omega \vec{h}_3 - \dot{\beta} \vec{e}_2 \quad (\text{D.2.17})$$

or in terms of the blade frame \mathcal{E}

$$\begin{aligned} {}^{\mathcal{I}}\vec{\omega}^{\mathcal{E}} &= \vec{0} + {}^{\mathcal{E}}T_2^{\mathcal{H}}(\beta) \left[\Omega \vec{h}_3 \right] - \dot{\beta} \vec{e}_2 \\ &= \begin{bmatrix} \cos \beta & \sin \beta \\ & 1 \\ -\sin \beta & \cos \beta \end{bmatrix} \begin{bmatrix} 0 \\ 0 \\ \Omega \end{bmatrix} - \begin{bmatrix} 0 \\ \dot{\beta} \\ 0 \end{bmatrix} \\ &= \begin{bmatrix} \Omega \sin \beta \\ -\dot{\beta} \\ \Omega \cos \beta \end{bmatrix} \end{aligned} \quad (\text{D.2.18})$$

the term ${}^{\mathcal{I}}\dot{\vec{\omega}}^{\mathcal{E}}$ is therefore (*for* $\dot{\Omega} = 0$)

$${}^{\mathcal{I}}\dot{\vec{\omega}}^{\mathcal{E}} = \begin{bmatrix} \Omega \dot{\beta} \cos \beta \\ -\ddot{\beta} \\ -\Omega \dot{\beta} \sin \beta \end{bmatrix} \quad (\text{D.2.19})$$

Similarly, expressing the terms in equation (D.2.14) in terms of frame \mathcal{E} gives

$$\begin{aligned} {}^{\mathcal{I}}\vec{a}_o = {}^{\mathcal{E}}T_2^{\mathcal{H}}(\beta) \begin{bmatrix} -\Omega^2 eR \\ 0 \\ 0 \end{bmatrix} &= \begin{bmatrix} \cos \beta & \sin \beta \\ & 1 \\ -\sin \beta & \cos \beta \end{bmatrix} \begin{bmatrix} -\Omega^2 eR \\ 0 \\ 0 \end{bmatrix} \\ &= \begin{bmatrix} -\Omega^2 eR \cos \beta \\ 0 \\ \Omega^2 eR \sin \beta \end{bmatrix} \end{aligned} \quad (\text{D.2.20})$$

Substituting the various terms in equation (D.2.5) from equations (D.2.6), (D.2.7), (D.2.14), (D.2.15), (D.2.18), (D.2.19), (D.2.20) gives (expressed in terms of frame \mathcal{E}):

$$\begin{aligned} \begin{bmatrix} L \\ M \\ N \end{bmatrix} &= \begin{bmatrix} M_{blade} r_{CM} R \\ 0 \\ 0 \end{bmatrix} \times \begin{bmatrix} -\Omega^2 eR \cos \beta \\ 0 \\ \Omega^2 eR \sin \beta \end{bmatrix} \\ &+ \begin{bmatrix} I_a \\ I_b \\ I_c \end{bmatrix} \cdot \begin{bmatrix} \Omega \dot{\beta} \cos \beta \\ -\ddot{\beta} \\ -\Omega \dot{\beta} \sin \beta \end{bmatrix} \\ &+ \begin{bmatrix} \Omega \sin \beta \\ -\dot{\beta} \\ \Omega \cos \beta \end{bmatrix} \times \left(\begin{bmatrix} I_a \\ I_b \\ I_c \end{bmatrix} \cdot \begin{bmatrix} \Omega \sin \beta \\ -\dot{\beta} \\ \Omega \cos \beta \end{bmatrix} \right) \end{aligned} \quad (\text{D.2.21})$$

which results in

$$\begin{aligned}
\begin{bmatrix} L \\ -M \\ -N \end{bmatrix} &= \begin{bmatrix} 0 \\ M_{blade} r_{CM} e \Omega^2 R^2 \sin \beta + I_b \left(\Omega^2 \cos \beta \sin \beta + \ddot{\beta} \right) \\ 2I_b \Omega \dot{\beta} \sin \beta \end{bmatrix} \\
&= \begin{bmatrix} \text{feathering moment} \\ M_a = \text{aerodynamic moment} \\ \text{drag moment} \end{bmatrix}
\end{aligned} \tag{D.2.22}$$

In the above equation (D.2.22) the term $M_{blade} r_{CM} e \Omega^2 R^2 \sin \beta$ is the first moment of inertia effect about the flap hinge. This contribution arises from both (1) the center of mass being at a distance $r_{CM}R$ from the flapping hinge, and (2) the hinge itself being a distance eR from the rotation axis and experiencing an acceleration $-\Omega^2 e R \vec{h}_1$ as a consequence. The term $I_b \ddot{\beta}$ is the inertial moment about the flapping hinge, and the term $I_b \Omega^2 \cos \beta \sin \beta$ is the centrifugal moment acting on the same hinge. The term $-M = M_a$ is the resultant aerodynamic moment. By convention, a positive aerodynamic moment causes the blade to flap upwardly, but such a moment equals a negative total moment about the blade flapping hinge. Equation (D.2.22) indicates that when the blade flaps upward there is no resultant feathering moment, but there is a resultant reward moment of magnitude $2I_b \Omega \dot{\beta} \sin \beta$. In the absence of this restoring moment, an upward blade flap induces a blade forward motion in the plane of rotation. This resultant in-plane Coriolis moment arises from conservation of angular momentum [92, 154]. As the blade flaps upward, the blade center of mass moves closer to the rotation axis, and the energy stored in the rotating blade induces a forward motion on the blade to keep the total momentum constant. The presence of a drag (i.e. lead/lag) hinge allows the blade to move in the plane of rotation to relieve the induced in-plane Coriolis moment [27, 92, 154]. For small angles β , the governing equation for blade flapping in equation (D.2.22) takes the form

$$\ddot{\beta} + \Omega^2 \left(1 + \frac{e r_{CM} M_{blade} R^2}{I_b} \right) \beta = \frac{M_{aero}}{I_b} \tag{D.2.23}$$

Equation (D.2.23) above is the fundamental equation of motion for blade flapping. For the equilibrium condition when $\ddot{\beta} = \dot{\beta} = 0$, equation (D.2.23) reduces to

$$\begin{aligned}\frac{-M}{I_b} &= \Omega^2 \left(1 + \frac{M_{blade} r_{CM} e R^2}{I_b} \right) \beta \\ \frac{M_{aero}}{I_b} &= \Omega^2 (1 + \varepsilon) \beta\end{aligned}\tag{D.2.24}$$

where the term ε

$$\begin{aligned}\varepsilon &= \frac{M_{blade} r_{CM} e R^2}{I_b} = \frac{\text{static moment}}{\text{inertial moment}} \\ \nu^2 &= 1 + \varepsilon\end{aligned}\tag{D.2.25}$$

is the ratio of the moment due to the mass of the blade and the inertial moment due to the blade flapping motion itself. The term ν^2 is the nondimensional blade flap frequency. The blade flapping equation (D.2.23) assumes small flap angle and is due to aerodynamic and inertial moments. Assumptions needed to arrive at this equation include a thin blade with uniform mass distribution, or equivalently, a rotor modeled as a thin disk. In addition, the blade center of mass is aligned with the blade axis and passes through the flap hinge. These are reasonable assumptions which result in a representative blade flapping equation. In turn, the aerodynamic term M_{aero}/I_b depends on a specific flight condition (i.e. hover vs. forward flight) and other dynamic terms such as body acceleration and body pitch and roll rates. The effects of the aerodynamic term M_{aero}/I_b will be expanded in coming sections.

D.2.1.1 Pure Blade Flap Equilibrium Equations

Figure D.3 on page 246 below shows the distribution of forces acting on a flapping blade in equilibrium. In this case $\ddot{\beta} = 0$, and for a blade with constant mass the centrifugal

force F_{CF} takes the form

$$\begin{aligned}
F_{CF} &= \int_0^{(1-e)R} \Omega^2 (r \cos \beta + eR) (m \, dr) \\
&= \Omega^2 \cos \beta \int_0^{(1-e)R} m r \, dr + \Omega^2 eR \int_0^{(1-e)R} m \, dr \\
&= \Omega^2 m \left[\cos \beta \frac{(1-e)^2}{2} R^2 + eR(1-e)R \right] \\
&= M_{blade} x_{CM} \Omega^2 R
\end{aligned} \tag{D.2.26}$$

where the small angle assumption gives $\cos \beta \approx 1$. Also $R x_{CM} = R(1+e)/2$ is the distance to the blade center of mass when measured from the axis of rotation, and $M_{blade} = mR(1-e)$ is the blade mass. Equivalently

$$\begin{aligned}
F_{CF} &= \int_{eR}^R (\Omega^2 y) (m \, dy) = \Omega^2 m R^2 \frac{1}{2} (1-e^2) \\
&= \Omega^2 m R^2 \frac{1}{2} (1-e)(1+e) \\
&= M_{blade} x_{CM} \Omega^2 R
\end{aligned} \tag{D.2.27}$$

Equations (D.2.26) and (D.2.27) yield the same result since

$$\begin{aligned}
r \cos \beta = (y - eR) &\iff y = (r \cos \beta + eR) \\
r = 0 &y = eR \\
r = (1-e)R &y = R \\
&dy = dr
\end{aligned} \tag{D.2.28}$$

Notice that when the flap hinge offset $e = 0$, then the centrifugal force reduces to $F_{CF} = \frac{1}{2} M_{blade} \Omega^2 R$.

The centrifugal moment M_{CF} about the hinge equals the component of the centrifugal

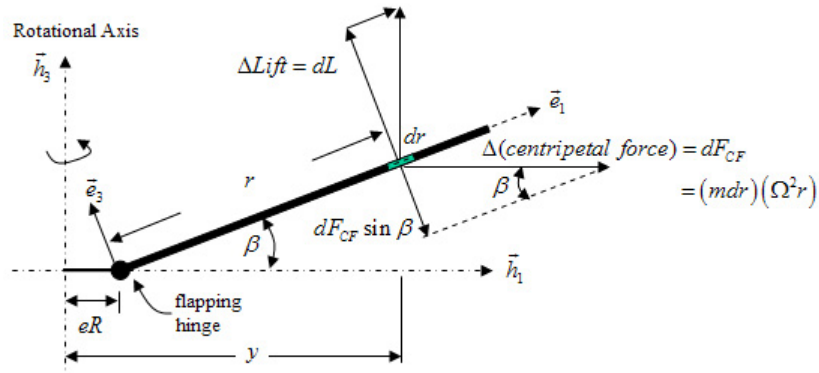


Figure D.3: Rotor blade rotating about the flapping hinge.

force $(m dy)(y \Omega^2 \sin \beta)$ acting at a distance r from the flap hinge.

$$\begin{aligned}
 M_{CF} &= \int_0^{(1-e)R} [(r + eR) \Omega^2 \sin \beta] r (m dr) \\
 &= \Omega^2 \sin \beta \int_0^{(1-e)R} m (r^2 + r eR) dr \\
 &= \Omega^2 m \sin \beta \left[\frac{1}{3} (1-e)^3 R^3 + \frac{1}{2} (1-e)^2 R^2 eR \right] \\
 &= \Omega^2 \sin \beta \left[\frac{1}{3} M_{blade} (1-e)^2 R^2 + \frac{1}{2} M_{blade} (1-e) eR^2 \right] \\
 &= \Omega^2 \sin \beta [I_b + M_{blade} r_{CM} eR^2]
 \end{aligned} \tag{D.2.29}$$

where $R r_{CM} = R (x_{CM} - e) = R (1 - e)/2$ is the distance to the point of action of the centrifugal force (i.e. center of mass of the blade) as measured from the flapping hinge (note that $x_{CM} = (1 + e)/2$ is the distance to the blade center of mass as measured from the rotational axis). Also, the mass of the blade is $M_{blade} = mR(1 - e)$. In like manner,

using equation (D.2.28), recast equation (D.2.29) as

$$\begin{aligned}
M_{CF} &= \int_{eR}^R [(\Omega^2 y) \sin \beta] (y - eR) (m dy) \\
&= \Omega^2 \sin \beta \int_{eR}^R m y (y - eR) dy \\
&= \Omega^2 \sin \beta \int_{eR}^R m [y^2 - yeR - yeR + yeR - (eR)^2 + (eR)^2] dy \\
&= \Omega^2 \sin \beta \left[\int_{eR}^R m (y - eR)^2 dy + eR \int_{eR}^R m (y - eR) dy \right] \\
&= \Omega^2 \sin \beta \left[I_b + eRm(1 - e)R^2 \frac{1}{2}(1 - e) \right] \\
&= \Omega^2 \sin \beta [I_b + M_{blade} r_{CM} e R^2]
\end{aligned} \tag{D.2.30}$$

The above equations (D.2.29) and (D.2.30) yield the same answer as expected. The aerodynamic moment M_{aero} acts in the opposite direction to the centrifugal moment such that for small angles

$$\frac{-M}{I_b} = \frac{M_{aero}}{I_b} = \Omega^2 \beta \left(1 + \frac{M_{blade} r_{CM} e R^2}{I_b} \right) \tag{D.2.31}$$

As expected, equation (D.2.31) yields the same result obtained in equation (D.2.24) when the equilibrium condition $\ddot{\beta} = \dot{\beta} = 0$ holds. Moreover, assuming that β is a small angle, and solving for β in equation (D.2.31) gives

$$\beta_0 = \frac{M_a}{\nu_\beta^2 \Omega^2 I_b} \tag{D.2.32}$$

where ν_β^2 is the non-dimensional natural frequency of the flapping rotor such that

$$\begin{aligned}
&= 1 + \frac{M_{blade} r_{CM} e R^2}{I_b} \\
\left(\frac{\omega_n}{\Omega} \right)^2 &= \nu_\beta^2 = 1 + \varepsilon
\end{aligned} \tag{D.2.33}$$

and $\varepsilon = M_{blade} r_{CM} e R^2 / I_b$ as given in equation (D.2.25) which together with equation (D.2.29) yields

$$\varepsilon = \frac{3}{2} \frac{e}{(1-e)} \approx \frac{3}{2} e \quad (\text{D.2.34})$$

Equation (D.2.32) indicates that the rotor coning angle β_0 decreases with increasing blade rigidity and angular velocity Ω .

D.2.2 Pure Blade Drag Equations of Motion

This time we restrict the blade to lead/lag motion about the drag hinge. In this case, ${}^{\mathcal{I}}\vec{\omega}^{\mathcal{D}}$ in equation (D.2.9) takes the form

$${}^{\mathcal{I}}\vec{\omega}^{\mathcal{D}} = {}^{\mathcal{I}}\vec{\omega}^{\mathcal{B}} + {}^{\mathcal{B}}\vec{\omega}^{\mathcal{H}} + {}^{\mathcal{H}}\vec{\omega}^{\mathcal{D}} \quad (\text{D.2.35})$$

where for the case when the helicopter is in stable hover ($q = 0, \dot{q} = 0, r = 0$)

$${}^{\mathcal{I}}\vec{\omega}^{\mathcal{D}} = \vec{0} + \Omega \vec{h}_3 + \dot{\zeta} \vec{d}_3 \quad (\text{D.2.36})$$

or in terms of the blade frame \mathcal{D}

$$\begin{aligned} {}^{\mathcal{I}}\vec{\omega}^{\mathcal{D}} &= \vec{0} + {}^{\mathcal{D}}T_3^{\mathcal{H}}(\zeta) \left[\Omega \vec{h}_3 \right] + \dot{\zeta} \vec{d}_3 \\ &= \begin{bmatrix} \cos \zeta & \sin \zeta & & \\ -\sin \zeta & \cos \zeta & & \\ & & & 1 \end{bmatrix} \begin{bmatrix} 0 \\ 0 \\ \Omega \end{bmatrix} + \begin{bmatrix} 0 \\ 0 \\ \dot{\zeta} \end{bmatrix} \\ &= \begin{bmatrix} 0 \\ 0 \\ \Omega + \dot{\zeta} \end{bmatrix} \end{aligned} \quad (\text{D.2.37})$$

the term ${}^{\mathcal{I}}\dot{\vec{\omega}}^{\mathcal{D}}$ is therefore (for $\dot{\Omega} = 0$)

$${}^{\mathcal{I}}\dot{\vec{\omega}}^{\mathcal{D}} = \begin{bmatrix} 0 \\ 0 \\ \ddot{\zeta} \end{bmatrix} \quad (\text{D.2.38})$$

Similarly, expressing the terms in equation (D.2.14) in terms of frame \mathcal{D} gives

$$\begin{aligned} {}^{\mathcal{I}}\vec{a}_o = {}^{\mathcal{D}}T_3^{\mathcal{H}}(\zeta) \begin{bmatrix} -\Omega^2 eR \\ 0 \\ 0 \end{bmatrix} &= \begin{bmatrix} \cos \zeta & \sin \zeta \\ -\sin \zeta & \cos \zeta \\ & & 1 \end{bmatrix} \begin{bmatrix} -\Omega^2 eR \\ 0 \\ 0 \end{bmatrix} \\ &= \begin{bmatrix} -\Omega^2 eR \cos \zeta \\ \Omega^2 eR \sin \zeta \\ 0 \end{bmatrix} \end{aligned} \quad (\text{D.2.39})$$

Substituting the various terms in equation (D.2.5) from equations (D.2.6), (D.2.7), (D.2.14), (D.2.15), (D.2.37), (D.2.38), (D.2.39) gives (expressed in terms of frame \mathcal{D}):

$$\begin{aligned} \begin{bmatrix} L \\ M \\ N \end{bmatrix} &= \begin{bmatrix} M_{blade} r_{CM} R \\ 0 \\ 0 \end{bmatrix} \times \begin{bmatrix} -\Omega^2 eR \cos \zeta \\ \Omega^2 eR \sin \zeta \\ 0 \end{bmatrix} \\ &+ \begin{bmatrix} I_a \\ I_b \\ I_c \end{bmatrix} \cdot \begin{bmatrix} 0 \\ 0 \\ \ddot{\zeta} \end{bmatrix} \\ &+ \begin{bmatrix} 0 \\ 0 \\ \Omega + \dot{\zeta} \end{bmatrix} \times \left(\begin{bmatrix} I_a \\ I_b \\ I_c \end{bmatrix} \cdot \begin{bmatrix} 0 \\ 0 \\ \Omega + \dot{\zeta} \end{bmatrix} \right) \end{aligned} \quad (\text{D.2.40})$$

which results in

$$\begin{aligned}
 \begin{bmatrix} L \\ M \\ N \end{bmatrix} &= \begin{bmatrix} 0 \\ 0 \\ M_{blade} r_{CM} e \Omega^2 R^2 \sin \zeta + I_c \ddot{\zeta} \end{bmatrix} \\
 &= \begin{bmatrix} \text{feathering moment} \\ M_a = \text{aerodynamic moment} \\ \text{drag moment} \end{bmatrix}
 \end{aligned} \tag{D.2.41}$$

Equation (D.2.41) indicates that when the blade only rotates about the drag rotation axis ζ with pure lead/lag motion, the blade does not induce any feathering or flapping rotation.

D.2.2.1 Pure Blade Drag Equilibrium Equations

Figure D.4 shows a rotor blade in pure drag motion about the drag (lead/lag) hinge. At each position on the blade we have [92]:

$$\frac{\tan(\xi)}{\tan(\zeta)} = \frac{y - eR}{y}$$

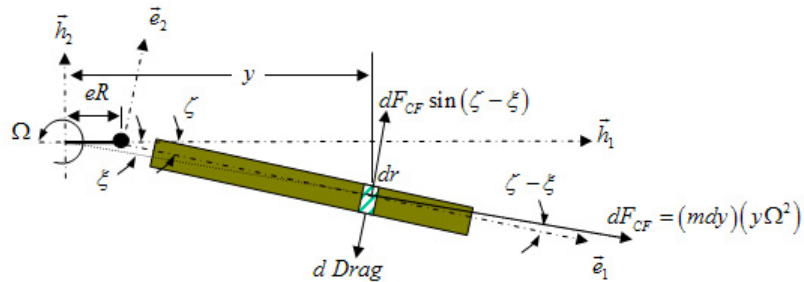


Figure D.4: Rotor blade rotating on a drag (lead/lag) hinge.

from where (using small angle approximation):

$$(\zeta - \xi) = \frac{eR}{y} \tag{D.2.42}$$

The centrifugal force of mass mdy and acceleration $y\Omega^2$ is

$$F_{CF} = \int_{eR}^R (y\Omega^2) (\zeta - \xi) (mdy) \quad (\text{D.2.43})$$

where $(y\Omega^2) (\zeta - \xi)$ is the component of the acceleration perpendicular to the blade. This force acts at a distance $y - eR$ from the drag hinge. Thus the centrifugal moment takes the form:

$$\begin{aligned} M_\zeta &= \int_{eR}^R (y\Omega^2) (\zeta - \xi)(y - eR) (mdy) = eR\Omega^2\zeta \int_{eR}^R m(y - eR) dy \\ &= eR\Omega^2\zeta m \left[\frac{1}{2}(R^2 - e^2 R^2) - eR(R - eR) \right] \\ &= eR\Omega^2\zeta mR^2 \left[\frac{1}{2}(1 - e)(1 + e) - e(1 - e) \right] \\ &= M_{blade} e\Omega^2 R^2 \zeta \frac{1}{2}(1 - e) \\ &= M_{blade} r_{CM} e\Omega^2 R^2 \zeta \end{aligned} \quad (\text{D.2.44})$$

where blade mass is $M_{blade} = mR(1 - e)$ and the distance from the drag hinge to the blade center of mass is $r_{CM}R = \frac{1}{2}(1 - e)R$. Equation (D.2.44) must equal the aerodynamic moment N such that

$$N = M_{blade} r_{CM} e\Omega^2 R^2 \sin \zeta \quad (\text{D.2.45})$$

Equation (D.2.45) gives the same result as in equation (D.2.41) when the equilibrium condition $\ddot{\zeta} = 0$ holds.

D.2.3 Pure Blade Feathering Equations of Motion

Feathering motion takes place about the blade axis through the blade angle θ . Effects of feathering motion are evident when flapping and drag motion are restricted to zero. In this case, ${}^{\mathcal{I}}\vec{\omega}^{\mathcal{E}}$ in equation (D.2.9) takes the form

$${}^{\mathcal{I}}\vec{\omega}^{\mathcal{E}} = {}^{\mathcal{I}}\vec{\omega}^{\mathcal{B}} + {}^{\mathcal{B}}\vec{\omega}^{\mathcal{H}} + {}^{\mathcal{H}}\vec{\omega}^{\mathcal{E}} \quad (\text{D.2.46})$$

where for the case when the helicopter is in stable hover ($q = 0, \dot{q} = 0, r = 0$)

$${}^{\mathcal{I}}\vec{\omega}^{\mathcal{E}} = \vec{0} + \Omega \vec{h}_3 + \dot{\theta} \vec{e}_1 \quad (\text{D.2.47})$$

or in terms of the blade frame \mathcal{D}

$$\begin{aligned} {}^{\mathcal{I}}\vec{\omega}^{\mathcal{E}} &= \vec{0} + {}^{\mathcal{E}}T_1^{\mathcal{H}}(\theta) \left[\Omega \vec{h}_3 \right] + \dot{\theta} \vec{e}_1 \\ &= \begin{bmatrix} 1 & & & \\ & \cos \theta & \sin \theta & \\ & -\sin \theta & \cos \theta & \\ & & & \Omega \end{bmatrix} \begin{bmatrix} 0 \\ 0 \\ \Omega \end{bmatrix} + \begin{bmatrix} \dot{\theta} \\ 0 \\ 0 \end{bmatrix} \\ &= \begin{bmatrix} \dot{\theta} \\ \Omega \sin \theta \\ \Omega \cos \theta \end{bmatrix} \end{aligned} \quad (\text{D.2.48})$$

the term ${}^{\mathcal{I}}\dot{\vec{\omega}}^{\mathcal{D}}$ is therefore (*for* $\dot{\Omega} = 0$)

$${}^{\mathcal{I}}\dot{\vec{\omega}}^{\mathcal{D}} = \begin{bmatrix} \ddot{\theta} \\ \dot{\theta} \Omega \cos \theta \\ -\dot{\theta} \Omega \sin \theta \end{bmatrix} \quad (\text{D.2.49})$$

Similarly, expressing the terms in equation (D.2.14) in terms of frame \mathcal{D} gives

$$\begin{aligned} {}^{\mathcal{I}}\vec{a}_o &= {}^{\mathcal{E}}T_1^{\mathcal{H}}(\theta) \begin{bmatrix} -\Omega^2 eR \\ 0 \\ 0 \end{bmatrix} = \begin{bmatrix} 1 & & & \\ & \cos \theta & \sin \theta & \\ & -\sin \theta & \cos \theta & \\ & & & \Omega \end{bmatrix} \begin{bmatrix} -\Omega^2 eR \\ 0 \\ 0 \end{bmatrix} \\ &= \begin{bmatrix} -\Omega^2 eR \\ 0 \\ 0 \end{bmatrix} \end{aligned} \quad (\text{D.2.50})$$

Substituting the various terms in equation (D.2.5) from equations (D.2.6), (D.2.7), (D.2.14), (D.2.15), (D.2.37), (D.2.38), (D.2.39) gives (expressed in terms of frame \mathcal{E}):

$$\begin{aligned}
 \begin{bmatrix} L \\ M \\ N \end{bmatrix} &= \begin{bmatrix} M_{blade} r_{CM} R \\ 0 \\ 0 \end{bmatrix} \times \begin{bmatrix} -\Omega^2 e R \\ 0 \\ 0 \end{bmatrix} \\
 &+ \begin{bmatrix} I_a \\ I_b \\ I_c \end{bmatrix} \cdot \begin{bmatrix} \ddot{\theta} \\ \dot{\theta} \Omega \cos \theta \\ -\dot{\theta} \Omega \sin \theta \end{bmatrix} \\
 &+ \begin{bmatrix} \dot{\theta} \\ \Omega \sin \theta \\ \Omega \cos \theta \end{bmatrix} \times \left(\begin{bmatrix} I_a \\ I_b \\ I_c \end{bmatrix} \cdot \begin{bmatrix} \dot{\theta} \\ \Omega \sin \theta \\ \Omega \cos \theta \end{bmatrix} \right)
 \end{aligned} \tag{D.2.51}$$

which results in

$$\begin{aligned}
 \begin{bmatrix} L \\ M \\ N \end{bmatrix} &= \begin{bmatrix} I_a \ddot{\theta} + I_a \Omega^2 \sin \theta \cos \theta \\ 0 \\ -2I_a \Omega \dot{\theta} \sin \theta \end{bmatrix} \\
 &= \begin{bmatrix} \textit{feathering moment} \\ M_a = \textit{aerodynamic moment} \\ \textit{drag moment} \end{bmatrix}
 \end{aligned} \tag{D.2.52}$$

Equation (D.2.52) says that pure feathering blade motion induces a small dragging moment on the blade. This drag moment is usually very small.

D.2.4 Combined Blade Flap and Drag Equations of Motion

This time we restrict the blade to lead/lag motion about the drag hinge. In this case, ${}^{\mathcal{I}}\vec{\omega}^{\mathcal{D}}$ in equation (D.2.9) takes the form

$${}^{\mathcal{I}}\vec{\omega}^{\mathcal{D}} = {}^{\mathcal{I}}\vec{\omega}^{\mathcal{B}} + {}^{\mathcal{B}}\vec{\omega}^{\mathcal{H}} + {}^{\mathcal{H}}\vec{\omega}^{\mathcal{D}} + {}^{\mathcal{D}}\vec{\omega}^{\mathcal{E}} \quad (\text{D.2.53})$$

where for the case when the helicopter is in stable hover ($p = 0, q = 0, r = 0$)

$${}^{\mathcal{I}}\vec{\omega}^{\mathcal{D}} = \vec{0} + \Omega \vec{h}_3 + \dot{\zeta} \vec{d}_3 - \dot{\beta} \vec{e}_2 \quad (\text{D.2.54})$$

or in terms of the blade frame \mathcal{E}

$$\begin{aligned} {}^{\mathcal{I}}\vec{\omega}^{\mathcal{D}} &= \vec{0} + {}^{\varepsilon}T_2^{\mathcal{D}}(\beta) {}^{\mathcal{D}}T_3^{\mathcal{H}}(\zeta) \left[\Omega \vec{h}_3 \right] + {}^{\varepsilon}T_2^{\mathcal{D}}(\beta) \dot{\zeta} \vec{d}_3 - \dot{\beta} \vec{e}_2 \\ &= \begin{bmatrix} \cos \beta \cos \zeta & \cos \beta \sin \zeta & \sin \beta \\ -\sin \zeta & \cos \zeta & 0 \\ -\cos \zeta \sin \beta & -\sin \beta \sin \zeta & \cos \beta \end{bmatrix} \begin{bmatrix} 0 \\ 0 \\ \Omega \end{bmatrix} \\ &\quad + \begin{bmatrix} \cos \beta & \sin \beta \\ & 1 \\ -\sin \beta & \cos \beta \end{bmatrix} \begin{bmatrix} 0 \\ 0 \\ \dot{\zeta} \end{bmatrix} - \begin{bmatrix} 0 \\ \dot{\beta} \\ 0 \end{bmatrix} \\ &= \begin{bmatrix} \Omega \sin \beta + \dot{\zeta} \sin \beta \\ -\dot{\beta} \\ \Omega \cos \beta + \dot{\zeta} \cos \beta \end{bmatrix} \end{aligned} \quad (\text{D.2.55})$$

the term ${}^{\mathcal{I}}\dot{\vec{\omega}}^{\mathcal{D}}$ is therefore (for $\dot{\Omega} = 0$)

$${}^{\mathcal{I}}\dot{\vec{\omega}}^{\mathcal{D}} = \begin{bmatrix} \Omega \dot{\beta} \cos \beta + \dot{\beta} \dot{\zeta} \cos \beta + \ddot{\zeta} \sin \beta \\ -\ddot{\beta} \\ -\Omega \dot{\beta} \sin \beta - \dot{\zeta} \dot{\beta} \sin \beta + \ddot{\zeta} \cos \beta \end{bmatrix} \quad (\text{D.2.56})$$

Similarly, expressing the terms in equation (D.2.14) in terms of frame \mathcal{E} gives

$$\begin{aligned}
{}^{\mathcal{I}}\vec{a}_o &= {}^{\mathcal{E}}T_2^{\mathcal{D}}(\beta)^{\mathcal{D}}T_3^{\mathcal{H}}(\zeta) \begin{bmatrix} -\Omega^2 eR \\ 0 \\ 0 \end{bmatrix} \\
&= \begin{bmatrix} \cos \beta \cos \zeta & \cos \beta \sin \zeta & \sin \beta \\ -\sin \zeta & \cos \zeta & 0 \\ -\cos \zeta \sin \beta & -\sin \beta \sin \zeta & \cos \beta \end{bmatrix} \begin{bmatrix} -\Omega^2 eR \\ 0 \\ 0 \end{bmatrix} \\
&= \begin{bmatrix} -eR\Omega^2 \cos \beta \cos \zeta \\ eR\Omega^2 \sin \zeta \\ eR\Omega^2 \sin \beta \cos \zeta \end{bmatrix}
\end{aligned} \tag{D.2.57}$$

Substituting the various terms in equation (D.2.5) from equations (D.2.6), (D.2.7), (D.2.14), (D.2.15), (D.2.37), (D.2.38), (D.2.39) gives (expressed in terms of frame \mathcal{E}):

$$\begin{aligned}
\begin{bmatrix} L \\ M \\ N \end{bmatrix} &= \begin{bmatrix} M_{blade} r_{CM} R \\ 0 \\ 0 \end{bmatrix} \times \begin{bmatrix} -eR\Omega^2 \cos \beta \cos \zeta \\ eR\Omega^2 \sin \zeta \\ eR\Omega^2 \sin \beta \cos \zeta \end{bmatrix} \\
&+ \begin{bmatrix} I_a \\ I_b \\ I_c \end{bmatrix} \cdot \begin{bmatrix} \Omega \dot{\beta} \cos \beta + \dot{\beta} \dot{\zeta} \cos \beta + \ddot{\zeta} \sin \beta \\ -\ddot{\beta} \\ -\Omega \dot{\beta} \sin \beta - \dot{\zeta} \dot{\beta} \sin \beta + \ddot{\zeta} \cos \beta \end{bmatrix} \\
&+ \begin{bmatrix} \Omega \sin \beta + \dot{\zeta} \sin \beta \\ -\dot{\beta} \\ \Omega \cos \beta + \dot{\zeta} \cos \beta \end{bmatrix} \times \left(\begin{bmatrix} I_a \\ I_b \\ I_c \end{bmatrix} \cdot \begin{bmatrix} \Omega \sin \beta + \dot{\zeta} \sin \beta \\ -\dot{\beta} \\ \Omega \cos \beta + \dot{\zeta} \cos \beta \end{bmatrix} \right)
\end{aligned} \tag{D.2.58}$$

which results in

$$\begin{aligned}
\begin{bmatrix} L \\ M \\ N \end{bmatrix} &= \begin{bmatrix} 0 \\ -e r_{CM} M_{blade} \Omega^2 R^2 \sin \beta \cos \zeta \\ e r_{CM} M_{blade} \Omega^2 R^2 \sin \zeta \end{bmatrix} \\
&+ \begin{bmatrix} I_a \ddot{\zeta} \sin \beta \\ -I_b \left(\Omega^2 + 2\Omega \dot{\zeta} + \dot{\zeta}^2 \right) \cos \beta \sin \beta - I_b \ddot{\beta} \\ -2I_b \dot{\beta} \sin \beta \left(\Omega + \dot{\zeta} \right) + (I_a + I_b) \ddot{\zeta} \cos \beta \end{bmatrix} \\
&= \begin{bmatrix} \textit{feathering moment} \\ -M_a = \textit{aerodynamic moment} \\ \textit{drag moment} \end{bmatrix}
\end{aligned} \tag{D.2.59}$$

Assuming small angles and letting the higher order terms go to zero we have:

$$\begin{aligned}
\begin{bmatrix} L \\ M \\ N \end{bmatrix} &= \begin{bmatrix} I_a \beta \ddot{\zeta} \\ -I_b \ddot{\beta} - e r_{CM} M_{blade} \Omega^2 R^2 \beta - I_b \Omega^2 \beta - 2I_b \Omega \dot{\zeta} \beta \\ e r_{CM} M_{blade} \Omega^2 R^2 \zeta - 2I_b \Omega \beta \dot{\beta} + I_c \ddot{\zeta} \end{bmatrix} \\
&= \begin{bmatrix} \textit{feathering moment} \\ -M_a = \textit{aerodynamic moment} \\ \textit{drag moment} \end{bmatrix}
\end{aligned} \tag{D.2.60}$$

were the moment of inertia of a thin rotor disk is given by equation (D.2.15) and $I_c = I_a + I_b$. The flap and drag blade equations are coupled by the Coriolis moments terms $2I_b \Omega \beta \dot{\zeta}$ and $2I_b \Omega \beta \dot{\beta}$. This coupling is induced by the change of the radial distance to the blade center of mass which results when the blade bends, flaps and/or drags about the respective flapping and dragging hinges [27, 92, 154]. The coupled blade flap equation of motion in equation (D.2.60) can be rewritten as

$$M_a = -M = I_b \left[\ddot{\beta} + \left(1 + \frac{e r_{CM} M_{blade} R^2}{I_b} \right) \Omega^2 \beta + 2\Omega \dot{\zeta} \beta \right] \tag{D.2.61}$$

The term $\nu_\beta^2 = 1 + (e r_{CM} M_{blade} R^2)/I_b$ is the non dimensional flap frequency in terms of the rotational frequency Ω [92]. This is the same term present in equations (D.2.29) and (D.2.30). Also

$$\begin{aligned}\nu_\beta^2 &= 1 + \frac{\frac{1}{2} M_{blade}(1-e)eR^2}{\frac{1}{3} M_{blade}(1-e)^2 R^2} \\ \nu_\beta &= \sqrt{1 + \frac{3e}{2(1-e)}} \approx \sqrt{1 + \frac{3}{2}e}\end{aligned}\tag{D.2.62}$$

where $r_{CM} = \frac{1}{2}(1-e)$ as before and ν_β is the undamped natural frequency of the uncoupled flapping blade. Equation (D.2.61) now takes the form

$$\frac{M_a}{I_b} = \ddot{\beta} + \nu_\beta^2 \Omega^2 \beta + 2\Omega \dot{\zeta} \beta\tag{D.2.63}$$

In like manner, the coupled drag equation of motion in equation (D.2.60) is

$$N = I_c \left[\ddot{\zeta} + \frac{e r_{CM} M_{blade} R^2}{I_c} \Omega^2 \zeta \right] - I_c \Omega \beta \dot{\beta}\tag{D.2.64}$$

where the term $\nu_\zeta^2 = (e r_{CM} M_{blade} R^2)/I_c$ is the non-dimensional drag frequency in terms of the rotation frequency Ω , and $I_c \approx 2I_b$. In this case, for an individual blade

$$\begin{aligned}\nu_\zeta^2 &= \frac{\frac{1}{2} M_{blade}(1-e)eR^2}{\frac{1}{3} M_{blade}(1-e)^2 R^2} \\ \nu_\zeta &= \sqrt{\frac{3e}{2(1-e)}} \approx \sqrt{\frac{3}{2}e}\end{aligned}\tag{D.2.65}$$

Rewrite equation (D.2.64) as

$$\frac{N}{I_c} = \ddot{\zeta} + \nu_\zeta^2 \Omega^2 \zeta - \Omega \beta \dot{\beta}\tag{D.2.66}$$

D.3 Rigid Blade Flapping Equations of Motion

Equation (D.2.60) shows that the induced Coriolis moment is the only coupling mechanism for a flapping and dragging blade. Equation (D.2.52) shows that pure blade feathering does not induced flapping, and the blade feathering induced drag moment is sufficiently small that it can be ignored . Whence the following two assumptions hold [27]:

- blade drag (lead/lag) motion induced by blade feathering does not affect the blade flap dynamics significantly (see equations (D.2.41), (D.2.52) and (D.2.60))
- blade feathering motion does not create significant feedback that can affect the blade flap motion (see equation (D.2.52))

D.3.1 Blade Flapping Disturbance at Constant Feather Angle

Figure D.5 on the next page shows a rotor at steady hover with $\dot{\Omega} = 0, q = 0, p = 0$ and no body accelerations. In this case the blade flapping with angular velocity $\dot{\beta}$ about the flap hinge induces a down velocity $r\dot{\beta}$ such that [27]:

$$\begin{aligned}
 \Delta\alpha &\approx \tan \Delta\alpha \approx \frac{-r\dot{\beta}}{\Omega(eR+r)} \\
 \delta L &= -\frac{1}{2}ca\rho\Omega^2(eR+r)^2 \frac{r\dot{\beta}}{\Omega(eR+r)}\delta r \\
 &= -\frac{1}{2}ca\rho\Omega(eR+r)r\dot{\beta}\delta r \\
 M_{aero} &= \int_0^{(1-e)R} r dL \\
 &= -\frac{1}{2}ca\rho\Omega\dot{\beta} \int_0^{(1-e)R} (eR+r)r^2 dr \\
 &= -\frac{1}{8}ca\rho\Omega\dot{\beta}R^4(1-e)^3\left(1+\frac{e}{3}\right) \\
 \frac{M_{aero}}{I_{blade}} &= -\frac{\gamma}{8}\Omega\dot{\beta}(1-e)^3\left(1+\frac{e}{3}\right)
 \end{aligned} \tag{D.3.1}$$

where δL is the blade element lift which results from the flapping motion disturbance,

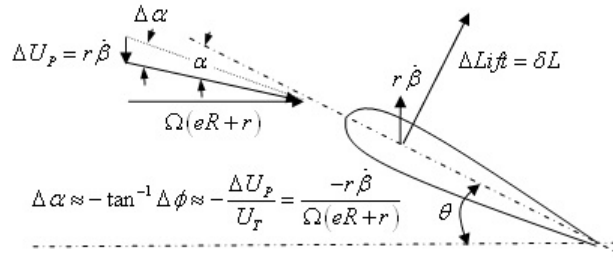


Figure D.5: Blade Flapping Disturbance at Constant Feather Angle.

M_{aero} is the resultant aerodynamic moment, and γ is Lock's inertial number defined as

$$\gamma = \frac{c_a \rho R^4}{I_{blade}} = \frac{\text{aerodynamic term}}{\text{inertial term}} \quad (\text{D.3.2})$$

The non-dimensional Lock's number or mass factor represents the mass constant of the blade [53]. The aerodynamic moment coefficient about the flapping hinge n is

$$n = (1 - e)^3 \left(1 + \frac{e}{3}\right) \quad (\text{D.3.3})$$

Substituting (D.3.1) and Lock's number γ into equation (D.2.23) yields

$$\ddot{\beta} + \frac{\gamma}{8} \Omega (1 - e)^3 \left(1 + \frac{e}{3}\right) \dot{\beta} + \nu_\beta^2 \Omega^2 \beta = 0 \quad (\text{D.3.4})$$

or in terms of Lock's number and the aerodynamic moment coefficient about the flapping hinge n

$$\ddot{\beta} + \frac{n\gamma}{8} \Omega \dot{\beta} + \nu_\beta^2 \Omega^2 \beta = 0 \quad (\text{D.3.5})$$

Equation (D.3.5) is a second order differential equation with natural frequency ω_n and damping ratio ζ given by

$$\begin{aligned} \left(\frac{\omega_n}{\Omega}\right)^2 &= \nu_\beta^2 \\ 2\omega_n \zeta &= \frac{\gamma}{8} \Omega (1 - e)^3 \left(1 + \frac{e}{3}\right) \\ \zeta &= \frac{\gamma (1 - e)^3 (1 + e/3)}{16\nu_\beta} = \frac{n\gamma}{16\nu_\beta} \end{aligned} \quad (\text{D.3.6})$$

where n is as given in equation (D.3.3). When the hinge offset $e = 0$, then $\nu_\beta = 0$, $\omega_n = \Omega$

and the system is in resonance. In this case feathering input drives flapping with a phase shift of 90° .

D.3.2 Flapping Motion with Cyclic Feather Angle

Figure D.6 shows that the angle of attack $\alpha = (\theta - \phi)$ and $U_T = (eR + R)\Omega$. The resultant lift is given by [27]

$$\begin{aligned}\delta L &= \frac{1}{2}ca\rho U_T^2 (\theta - \phi) \delta r \\ &\approx \frac{1}{2}ca\rho U_T^2 \left(\theta - \frac{U_P}{U_T} \right) \delta r \\ &\approx \frac{1}{2}ca\rho\theta \Omega^2 (eR + r)^2 \delta r\end{aligned}\tag{D.3.7}$$

where

$$\begin{aligned}\phi &= \tan^{-1} \frac{U_P}{U_T} \approx \frac{U_P}{U_T} \\ U_P \ll U_T &\Rightarrow \frac{U_P}{U_T} \ll 1 \Rightarrow U_T^2 \left(\theta - \frac{U_P}{U_T} \right) \approx U_T^2 \theta = \theta \Omega^2 (eR + r)^2\end{aligned}$$

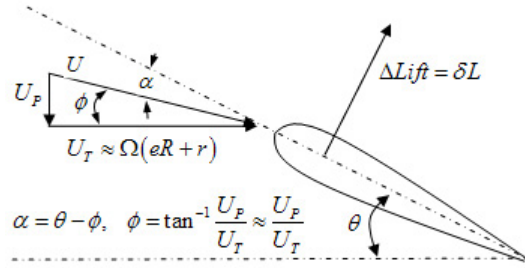


Figure D.6: Blade Flapping Disturbance at Constant Feather Angle.

The blade feathering angle with respect to the hub axis takes the form:

$$\theta = \theta_0 - \theta_{1c} \cos \psi - \theta_{1s} \sin \psi\tag{D.3.8}$$

where θ_0 corresponds to collective blade pitch input, and (θ_c, θ_s) correspond to lateral and longitudinal cyclic input respectively. From the pilot's perspective, the lateral cyclic pitch input θ_c produces a rolling rate and lateral attitude changes while the longitudinal cyclic input θ_s produces pitch rate and attitude motion. The sign convention in equation (D.3.8)

produces steady state blade flapping angles that are consistent with the body attitude sign convention in Figure D.1 on page 234. The pilot longitudinal δ_{lon} and lateral δ_{lat} stick inputs correspond to the blade cyclic inputs via a direct gear transformation such that

$$\begin{aligned}\theta_{1c} &= K_{lat}\delta_{lat} \\ \theta_{1s} &= K_{lon}\delta_{lon}\end{aligned}\tag{D.3.9}$$

The resultant aerodynamic moment M_{aero} is

$$\begin{aligned}M_{aero} &= \int_0^{(1-e)R} r dL \\ &\approx \frac{1}{2}ca\rho\Omega^2 (\theta_0 - \theta_c \cos \psi - \theta_s \sin \psi) \int_0^{(1-e)R} (eR + r)^2 r dr \\ &= \frac{1}{2}ca\rho\Omega^2 (\theta_0 - \theta_c \cos \psi - \theta_s \sin \psi) R^4 \frac{(1-e)^2}{4} \left[1 + \frac{2}{3}e + \frac{1}{3}e^2 \right] \\ \frac{M_{aero}}{I_{blade}} &= \frac{\gamma}{8}\Omega^2 (\theta_0 - \theta_c \cos \psi - \theta_s \sin \psi) (1-e)^2 \left[1 + \frac{2}{3}e + \frac{1}{3}e^2 \right]\end{aligned}\tag{D.3.10}$$

The total flapping moment is given by adding the results from equation (D.3.1) and equation (D.3.10) above

$$\begin{aligned}\frac{M_{aero}}{I_{blade}} &= \frac{\gamma}{8}\Omega^2 (\theta_0 - \theta_c \cos \psi - \theta_s \sin \psi) (1-e)^2 \left[1 + \frac{2}{3}e + \frac{1}{3}e^2 \right] \\ &\quad - \frac{n\gamma}{8}\Omega\dot{\beta}\end{aligned}\tag{D.3.11}$$

Substituting (D.3.11) into equation (D.2.23) yields

$$\begin{aligned}\ddot{\beta} + \frac{n\gamma}{8}\Omega\dot{\beta} + \nu_\beta^2\Omega^2\beta &= \\ \frac{\gamma}{8}\Omega^2 (\theta_0 - \theta_c \cos \psi - \theta_s \sin \psi) (1-e)^2 \left[1 + \frac{2}{3}e + \frac{1}{3}e^2 \right]\end{aligned}\tag{D.3.12}$$

The above blade flapping equation (D.3.12) includes the effects of constant and cyclic blade pitch. Considering the periodic nature of the cyclic input with respect to blade

azimuth angle ψ , the change of variable $\psi = \Omega t$ results in

$$\begin{aligned}\psi &= \Omega t \\ \dot{\beta} &= \frac{d\beta}{dt} = \frac{d\beta}{d\psi} \frac{d\psi}{dt} = \Omega \frac{d\beta}{d\psi} \\ \ddot{\beta} &= \frac{d^2\beta}{dt^2} = \Omega^2 \frac{d^2\beta}{d\psi^2}\end{aligned}\tag{D.3.13}$$

Application of (D.3.13) to equation (D.3.12) gives

$$\frac{d^2\beta}{d\psi^2} + \frac{n\gamma}{8} \frac{d\beta}{d\psi} + \nu_\beta^2 \beta = \frac{\gamma}{8} \bar{e}_\theta (\theta_0 - \theta_{1c} \cos \psi - \theta_{1s} \sin \psi)\tag{D.3.14}$$

where \bar{e}_θ takes the form

$$\bar{e}_\theta = (1 - e)^2 \left[1 + \frac{2}{3}e + \frac{1}{3}e^2 \right]\tag{D.3.15}$$

The first harmonic steady state periodic solution for a blade flapping angle, as the blade completes one revolution is given by

$$\begin{aligned}\beta &= \beta_0 - \beta_{1c} \cos \psi - \beta_{1s} \sin \psi \\ \frac{d\beta}{d\psi} &= \beta_{1c} \sin \psi - \beta_{1s} \cos \psi \\ \frac{d^2\beta}{d\psi^2} &= \beta_{1c} \cos \psi - \beta_{1s} \sin \psi\end{aligned}\tag{D.3.16}$$

Substituting (D.3.16) into (D.3.14) gives

$$\begin{aligned}\beta_{1c} \cos \psi + \beta_{1s} \sin \psi + \frac{n\gamma}{8} (\beta_{1c} \sin \psi - \beta_{1s} \cos \psi) \\ + \nu_\beta^2 (\beta_0 - \beta_{1c} \cos \psi - \beta_{1s} \sin \psi) \\ = \frac{\gamma}{8} \bar{e}_\theta (\theta_0 - \theta_{1c} \cos \psi - \theta_{1s} \sin \psi)\end{aligned}\tag{D.3.17}$$

Harmonic balancing of the constant and periodic terms on both sides of the above equation results in the following relations

$$\begin{aligned}\nu_\beta^2 \beta_0 &= \frac{\gamma}{8} \bar{e}_\theta \theta_0 \\ S_\beta \beta_{1s} - n \beta_{1c} &= \bar{e}_\theta \theta_{1s} \\ S_\beta \beta_{1c} + n \beta_{1s} &= \bar{e}_\theta \theta_{1c}\end{aligned}\tag{D.3.18}$$

Define the stiffness number S_β

$$S_\beta = \frac{8(\nu^2 - 1)}{\gamma}\tag{D.3.19}$$

The stiffness number S_β provides a measure of the ratio of the hub stiffness to aerodynamic moment [119, p. 35]. Rearranging the above expression (D.3.18) takes the form

$$\begin{aligned}\beta_0 &= \frac{\gamma}{8} \frac{\bar{e}_\theta}{\nu_\beta^2} \theta_0 \\ (n^2 + S_\beta^2) \beta_{1c} &= \bar{e}_\theta (S_\beta \theta_{1c} - n \theta_{1s}) \\ (n^2 + S_\beta^2) \beta_{1s} &= \bar{e}_\theta (n \theta_{1c} + S_\beta \theta_{1s})\end{aligned}\tag{D.3.20}$$

In the case of zero hinge offset ($e = 0 \Rightarrow \nu_\beta^2 = 1, S_\beta = 0$), equation (D.3.20) reduces to

$$\begin{aligned}\beta_0 &= \frac{\gamma}{8} \theta_0 \\ \beta_{1c} &= -\theta_{1s} \\ \beta_{1s} &= \theta_{1c}\end{aligned}\tag{D.3.21}$$

Substituting (D.3.21) in (D.3.16) gives the flap response in terms of cyclic inputs

$$\begin{aligned}&= \beta_0 - \beta_{1c} \cos \psi - \beta_{1s} \sin \psi \\ &= \beta_0 + \theta_{1s} \cos \psi - \theta_{1c} \sin \psi \\ \beta &= \beta_0 - \theta_{1c} \cos \left(\psi - \frac{\pi}{2} \right) - \theta_{1s} \sin \left(\psi - \frac{\pi}{2} \right)\end{aligned}\tag{D.3.22}$$

Equations (D.3.21) and (D.3.22) say that for the case of zero hinge offset and the absence

of any blade restraining mechanism, the blade flap lags the aerodynamic blade pitch input by 90° . This is the behavior of a resonant system excited at its natural frequency, which in this case equals Ω , the angular velocity of the main rotor. When the hinge offset is finite or a blade restraining mechanism exists, then the system is no longer in resonance, in which case equation (D.3.20) describes the relation between the blade aerodynamic pitch input and ensuing blade flap [92, 119].

D.3.3 Flapping Motion with Body Pitch Rate

In this case, the rotor hub angular velocity ${}^{\mathcal{I}}\vec{\omega}^{\mathcal{H}}$ takes the form

$$\begin{aligned} {}^{\mathcal{I}}\vec{\omega}^{\mathcal{H}} &= {}^{\mathcal{I}}\vec{\omega}^{\mathcal{A}} + {}^{\mathcal{A}}\vec{\omega}^{\mathcal{H}} \\ &= q\vec{a}_2 + \Omega\vec{h}_3 \end{aligned} \tag{D.3.23}$$

where ($p = 0, r = 0$). In terms of the rotor hub frame \mathcal{H}

$$\begin{aligned} &= {}^{\mathcal{H}}T_1^{\mathcal{A}}(\psi)q\vec{a}_2 + \Omega\vec{h}_3 \\ {}^{\mathcal{I}}\vec{\omega}^{\mathcal{H}} &= \begin{bmatrix} \cos \psi & \sin \psi & & \\ -\sin \psi & \cos \psi & & \\ & & & 1 \end{bmatrix} \begin{bmatrix} 0 \\ q \\ 0 \end{bmatrix} + \begin{bmatrix} 0 \\ 0 \\ \Omega \end{bmatrix} = \begin{bmatrix} q \sin \psi \\ q \cos \psi \\ \Omega \end{bmatrix} \end{aligned} \tag{D.3.24}$$

Whence the main rotor hub angular acceleration ${}^{\mathcal{I}}\vec{\alpha}^{\mathcal{H}}$ is ($\Omega = \dot{\psi}$)

$${}^{\mathcal{I}}\vec{\alpha}^{\mathcal{H}} = \begin{bmatrix} \Omega q \cos \psi \\ -\Omega q \sin \psi \\ 0 \end{bmatrix} \tag{D.3.25}$$

Reusing equation (D.2.8), ${}^{\mathcal{I}}\vec{a}_o$ becomes

$$\begin{aligned}
&= {}^{\mathcal{I}}\tilde{\omega}^{\mathcal{H}} \times ({}^{\mathcal{I}}\tilde{\omega}^{\mathcal{H}} \times {}_o\tilde{\mathbf{r}}_o) + {}^{\mathcal{I}}\tilde{\alpha}^{\mathcal{H}} \times {}_o\tilde{\mathbf{r}}_o \\
&= \begin{bmatrix} q \sin \psi \\ q \cos \psi \\ \Omega \end{bmatrix} \times \left(\begin{bmatrix} q \sin \psi \\ q \cos \psi \\ \Omega \end{bmatrix} \times \begin{bmatrix} eR \\ 0 \\ 0 \end{bmatrix} \right) \\
&\quad + \begin{bmatrix} \Omega q \cos \psi \\ -\Omega q \sin \psi \\ 0 \end{bmatrix} \times \begin{bmatrix} eR \\ 0 \\ 0 \end{bmatrix} \\
{}^{\mathcal{I}}\vec{a}_o &= \begin{bmatrix} -eR\Omega^2 - eRq^2 \cos^2 \psi \\ eRq^2 \sin \psi \cos \psi \\ 2eR\Omega q \sin \psi \end{bmatrix}
\end{aligned} \tag{D.3.26}$$

Equation (D.3.26) above expresses the inertial acceleration of a point coincident with the flapping hinge in terms of the Hub frame axis. In terms of the blade frame \mathcal{E} we have

$$\begin{aligned}
&= {}^{\mathcal{E}}T_2^{\mathcal{H}}(\beta) [{}^{\mathcal{I}}\vec{a}_o]^{\mathcal{H}} \\
&= \begin{bmatrix} \cos \beta & \sin \beta \\ & 1 \\ -\sin \beta & \cos \beta \end{bmatrix} \begin{bmatrix} -eR\Omega^2 - eRq^2 \cos^2 \psi \\ eRq^2 \sin \psi \cos \psi \\ 2eR\Omega q \sin \psi \end{bmatrix} \\
[{}^{\mathcal{I}}\vec{a}_o]^{\mathcal{E}} &= \begin{bmatrix} -(eR\Omega^2 + eRq^2 \cos^2 \psi) \cos \beta + 2eR\Omega q \sin \psi \sin \beta \\ eRq^2 \sin \psi \cos \psi \\ (eR\Omega^2 + eRq^2 \cos^2 \psi) \sin \beta + 2eR\Omega q \sin \psi \cos \beta \end{bmatrix}
\end{aligned} \tag{D.3.27}$$

Using equations (D.2.6) and (D.3.27), the term $\vec{C}^o \times {}^I \vec{a}_o$ in equation (D.2.5) takes the form

$$\begin{aligned}
&= \begin{bmatrix} M_{blade} r_{CM} R \\ 0 \\ 0 \end{bmatrix} \times \\
&\quad \begin{bmatrix} -(eR\Omega^2 + eq^2 R \cos^2 \psi) \cos \beta + 2eqR\Omega \sin \psi \sin \beta \\ eq^2 R \sin \psi \cos \psi \\ (eR\Omega^2 + eq^2 R \cos^2 \psi) \sin \beta + 2eqR\Omega \sin \psi \cos \beta \end{bmatrix} \quad (D.3.28) \\
\vec{C}^o \times {}^I \vec{a}_o &\approx M_{blade} r_{CM} R^2 \\
&\quad \begin{bmatrix} 0 \\ -(e\Omega^2 + eq^2 \cos^2 \psi) \sin \beta - 2eq\Omega \sin \psi \cos \beta \\ eq^2 \sin \psi \cos \psi \end{bmatrix}
\end{aligned}$$

Using small angle assumptions and neglecting higher order terms ($eq^2 \approx 0$, $q^2 \sin \beta \approx 0$), equation (D.3.28) becomes

$$\vec{C}^o \times {}^I \vec{a}_o \approx M_{blade} r_{CM} R^2 \begin{bmatrix} 0 \\ -e\Omega^2 \beta - 2e\Omega q \sin \psi \\ 0 \end{bmatrix} \quad (D.3.29)$$

The inertial angular velocity of the blade frame \mathcal{E} expressed in terms of frame \mathcal{E} is

$$\begin{aligned}
&= {}^\mathcal{E} T_2^{\mathcal{H}}(\beta) \left[{}^{\mathcal{H}} T_1^{\mathcal{A}}(\psi) q \vec{a}_2 + \Omega \vec{h}_3 \right] - \dot{\beta} \vec{e}_2 \\
{}^I \vec{\omega}^{\mathcal{E}} &= \begin{bmatrix} \Omega \sin \beta + q \sin \psi \cos \beta \\ q \cos \psi - \dot{\beta} \\ \Omega \cos \beta - q \sin \psi \sin \beta \end{bmatrix} \quad (D.3.30)
\end{aligned}$$

and the corresponding inertial angular acceleration ${}^{\mathcal{I}}\vec{\alpha}^{\mathcal{E}}$ takes the form

$${}^{\mathcal{I}}\vec{\alpha}^{\mathcal{E}} = \begin{bmatrix} \Omega q \cos \psi \cos \beta + (\Omega \cos \beta - q \sin \psi \sin \beta) \dot{\beta} \\ -\Omega q \sin \psi - \ddot{\beta} \\ -\Omega q \cos \psi \sin \beta - (\Omega \sin \beta + q \sin \psi \cos \beta) \dot{\beta} \end{bmatrix} \quad (\text{D.3.31})$$

The term $\vec{I}^o \cdot \dot{{}^{\mathcal{I}}\vec{\omega}}^{\mathcal{E}} + {}^{\mathcal{I}}\vec{\omega}^{\mathcal{E}} \times \left(\vec{I}^o \cdot {}^{\mathcal{I}}\vec{\omega}^{\mathcal{E}} \right)$ in equation (D.2.5) takes the form

$$\begin{aligned} \vec{I}^o \cdot \dot{{}^{\mathcal{I}}\vec{\omega}}^{\mathcal{E}} + {}^{\mathcal{I}}\vec{\omega}^{\mathcal{E}} \times \left(\vec{I}^o \cdot {}^{\mathcal{I}}\vec{\omega}^{\mathcal{E}} \right) &= \\ & \begin{bmatrix} I_a \Omega q \cos \psi \cos \beta + I_a (\Omega \cos \beta - q \sin \psi \sin \beta) \dot{\beta} \\ -I_b \Omega q \sin \psi - I_b \ddot{\beta} \\ -I_c \Omega q \cos \psi \sin \beta - I_c (\Omega \sin \beta + q \sin \psi \cos \beta) \dot{\beta} \end{bmatrix} \\ & + \begin{bmatrix} \Omega \sin \beta + q \sin \psi \cos \beta \\ q \cos \psi - \dot{\beta} \\ \Omega \cos \beta - q \sin \psi \sin \beta \end{bmatrix} \times \begin{bmatrix} I_a (\Omega \sin \beta + q \sin \psi \cos \beta) \\ I_b (q \cos \psi - \dot{\beta}) \\ I_c (\Omega \cos \beta - q \sin \psi \sin \beta) \end{bmatrix} \\ & = \begin{bmatrix} I_a (2\Omega \cos \beta - q \sin \psi \sin \beta) q \cos \psi \\ -I_b (2\Omega q \sin \psi \cos \beta + (\Omega^2 - q^2 \sin^2 \psi) \sin \beta) \cos \beta - I_b \ddot{\beta} \\ -I_c \Omega q \cos \psi \sin \beta - I_c (\Omega \sin \beta + q \sin \psi \cos \beta) \dot{\beta} \end{bmatrix} \end{aligned} \quad (\text{D.3.32})$$

where ${}^{\mathcal{I}}\vec{\alpha}^{\mathcal{E}} = \dot{{}^{\mathcal{I}}\vec{\omega}}^{\mathcal{E}}$. Using small angle assumptions and neglecting higher order terms ($q^2 \sin \beta \rightarrow \text{small}$, $\beta \dot{\beta} \rightarrow \text{small}$), equation (D.3.32) becomes

$$\vec{I}^o \cdot \dot{{}^{\mathcal{I}}\vec{\omega}}^{\mathcal{E}} + {}^{\mathcal{I}}\vec{\omega}^{\mathcal{E}} \times \left(\vec{I}^o \cdot {}^{\mathcal{I}}\vec{\omega}^{\mathcal{E}} \right) \approx \begin{bmatrix} 2I_a \Omega q \cos \psi \\ -2I_b \Omega q \sin \psi - I_b \Omega^2 \beta - I_b \ddot{\beta} \\ -I_c \Omega \beta q \cos \psi - I_c \dot{\beta} q \sin \psi \end{bmatrix} \quad (\text{D.3.33})$$

Equations (D.3.29) and (D.3.33) give

$$\begin{aligned}
\begin{bmatrix} L \\ -M \\ N \end{bmatrix} &= M_{blade} r_{CM} e R^2 \begin{bmatrix} 0 \\ \Omega^2 \beta + 2\Omega q \sin \psi \\ 0 \end{bmatrix} \\
&+ \begin{bmatrix} 2I_a \Omega q \cos \psi \\ 2I_b \Omega q \sin \psi + I_b \Omega^2 \beta + I_b \ddot{\beta} \\ -I_c \Omega \beta q \cos \psi - I_c \dot{\beta} q \sin \psi \end{bmatrix} \\
&= \begin{bmatrix} \text{gyroscopic} + \text{feathering moment} \\ \text{gyroscopic} + (M_a = \text{aerodynamic}) \text{ moment} \\ \text{drag moment} \end{bmatrix}
\end{aligned} \tag{D.3.34}$$

Equation (D.3.34) says that a steady pitch rate induces both blade pitch and drag moments. The induced drag moment is relieved by the drag (lead/lag) blade hinge, and the induced blade pitch moment is sufficiently small and can be ignored. The resultant blade flapping equation takes the form

$$\ddot{\beta} + \Omega^2 \nu_\beta^2 \beta + 2\Omega q \nu_\beta^2 \sin \psi = \frac{M_{aero}}{I_b} \tag{D.3.35}$$

where ν_β^2 is the non dimensional flap frequency previously defined in equation (D.2.62) such that

$$\begin{aligned}
r_{CM} &= \frac{1-e}{2} \\
I_{blade} &= \int_0^{(1-e)R} m r^2 dr = \frac{m}{3} R^3 (1-e)^3 = \frac{M_{blade}}{3} (1-e)^2 R^2 \\
\varepsilon &= \frac{M_{blade} r_{CM} e R^2}{I_b} = \frac{3e}{2(1-e)} = \frac{\text{static moment}}{\text{inertial moment}} \\
\nu_\beta^2 &= 1 + \varepsilon
\end{aligned} \tag{D.3.36}$$

Figure D.7 on the following page shows the perturbation to the angle of attack $\Delta\alpha$ due to a combination of flapping rate $r\dot{\beta}$ and pitch rate $rq \cos \psi$. The corresponding

Expanding the periodic terms

$$\begin{aligned}
& (\beta_{1c} \cos \psi + \beta_{1s} \sin \psi) + \frac{n\gamma}{8} (\beta_{1c} \sin \psi - \beta_{1s} \cos \psi) \\
& + \nu_\beta^2 (\beta_0 - \beta_{1c} \cos \psi - \beta_{1s} \sin \psi) \\
& = \frac{n\gamma}{8} \frac{q}{\Omega} \cos \psi - 2\nu_\beta^2 \frac{q}{\Omega} \sin \psi
\end{aligned} \tag{D.3.40}$$

Harmonic balancing of the periodic steady-state solution (D.3.16) to the above equation (D.3.39) gives

$$\begin{aligned}
n\beta_{1c} - S_\beta \beta_{1s} &= -\nu_\beta^2 \frac{16}{\gamma} \frac{q}{\Omega} \\
S_\beta \beta_{1c} + n\beta_{1s} &= -n \frac{q}{\Omega}
\end{aligned} \tag{D.3.41}$$

where the rotor stiffness number $S_\beta = 8(\nu^2 - 1)/\gamma$ is given by equation (D.3.19) on page 263. Solving for β_{c1}, β_{s1} results in the following set of equations

$$\begin{aligned}
(n^2 + S_\beta^2) \beta_{1c} &= -n \left(S_\beta + \frac{16}{\gamma} \nu_\beta^2 \right) \frac{q}{\Omega} \\
(n^2 + S_\beta^2) \beta_{1s} &= - \left(n^2 - \frac{16}{\gamma} \nu_\beta^2 S_\beta \right) \frac{q}{\Omega}
\end{aligned} \tag{D.3.42}$$

For the case of zero hinge offset ($e = 0, \varepsilon = 0$), the above equations become

$$\begin{aligned}
\beta_{1c} &= -\frac{16}{\gamma} \frac{q}{\Omega} \\
\beta_{1s} &= -\frac{q}{\Omega}
\end{aligned} \tag{D.3.43}$$

Equations (D.3.42) and (D.3.43) indicate that a non zero steady pitch rate induces lateral cross-coupling flapping which result on a rotor tilt to port (down at station $\psi = 270^\circ$) regardless of whether the blade has a flap hinge offset. In addition, a positive steady body pitch (body nose-up) results on downward blade flapping and corresponding nose-down rotor tilt at blade azimuth station $\psi = 180^\circ$. Such rotor tilt produces a moment that opposes the original nose-up moment of the vehicle. This behavior is a source of stable longitudinal aerodynamic dampening response of the rotor to body pitch rate [27, 92].

The longitudinal flapping damping factor

$$-\beta_{1c} \frac{\Omega}{q} = \frac{16}{\gamma} \propto \frac{\text{inertia or rotor}}{\text{aerodynamic forces}} \quad (\text{D.3.44})$$

is inversely proportional to the Lock's number. Equivalently, the longitudinal flapping damping factor is directly proportional to the inertia of the rotor due to gyroscopic effects and inversely proportional to the aerodynamic forces generated by the rotor. The interaction of inertial and aerodynamic effects with the hinge offset is an important factor to consider for the design of rotor control laws which may depend on flight conditions such as flight altitude. For example, at high altitude, the rotor inertial response due to gyroscopic effects will tend to be greater due to the diminishing relative effect of aerodynamic forces at altitude [27].

D.3.4 Flapping Motion with Body Roll Rate

A development similar to the one presented in the previous section follows. In this case however, the rotor hub angular velocity ${}^{\mathcal{I}}\vec{\omega}^{\mathcal{H}}$ is given by

$$\begin{aligned} {}^{\mathcal{I}}\vec{\omega}^{\mathcal{H}} &= {}^{\mathcal{I}}\vec{\omega}^{\mathcal{A}} + {}^{\mathcal{A}}\vec{\omega}^{\mathcal{H}} \\ &= -p\vec{a}_1 + \Omega\vec{h}_3 \end{aligned} \quad (\text{D.3.45})$$

where ($q = 0, r = 0$). In terms of the rotor hub frame \mathcal{H}

$$\begin{aligned} &= {}^{\mathcal{H}}T_1^{\mathcal{A}}(\psi) - p\vec{a}_1 + \Omega\vec{h}_3 \\ {}^{\mathcal{I}}\vec{\omega}^{\mathcal{H}} &= \begin{bmatrix} \cos \psi & \sin \psi & \\ -\sin \psi & \cos \psi & \\ & & 1 \end{bmatrix} \begin{bmatrix} -p \\ 0 \\ 0 \end{bmatrix} + \begin{bmatrix} 0 \\ 0 \\ \Omega \end{bmatrix} = \begin{bmatrix} -p \cos \psi \\ p \sin \psi \\ \Omega \end{bmatrix} \end{aligned} \quad (\text{D.3.46})$$

Whence the main rotor hub angular acceleration ${}^{\mathcal{I}}\vec{\alpha}^{\mathcal{H}}$ is ($\Omega = \dot{\psi}$)

$${}^{\mathcal{I}}\vec{\alpha}^{\mathcal{H}} = \begin{bmatrix} \Omega p \sin \psi \\ \Omega p \cos \psi \\ 0 \end{bmatrix} \quad (\text{D.3.47})$$

Reusing equation (D.2.8), ${}^{\mathcal{I}}\vec{a}_o$ becomes

$$\begin{aligned} &= {}^{\mathcal{I}}\vec{\omega}^{\mathcal{H}} \times ({}^{\mathcal{I}}\vec{\omega}^{\mathcal{H}} \times {}_o\tilde{\mathbf{r}}_o) + {}^{\mathcal{I}}\vec{\alpha}^{\mathcal{H}} \times {}_o\tilde{\mathbf{r}}_o \\ &= \begin{bmatrix} -p \cos \psi \\ p \sin \psi \\ \Omega \end{bmatrix} \times \left(\begin{bmatrix} -p \cos \psi \\ p \sin \psi \\ \Omega \end{bmatrix} \times \begin{bmatrix} eR \\ 0 \\ 0 \end{bmatrix} \right) \\ &\quad + \begin{bmatrix} \Omega p \sin \psi \\ \Omega p \cos \psi \\ 0 \end{bmatrix} \times \begin{bmatrix} eR \\ 0 \\ 0 \end{bmatrix} \\ {}^{\mathcal{I}}\vec{a}_o &= \begin{bmatrix} -eR\Omega^2 - eRp^2 \sin^2 \psi \\ -eRp^2 \cos \psi \sin \psi \\ -2eR\Omega p \cos \psi \end{bmatrix} \end{aligned} \quad (\text{D.3.48})$$

Equation (D.3.48) above expresses the inertial acceleration of a point coincident with the flapping hinge in terms of the Hub frame axis. In terms of the blade frame \mathcal{E} we have

$$\begin{aligned}
&= {}^{\mathcal{E}}T_2^{\mathcal{H}}(\beta) [{}^{\mathcal{I}}\vec{a}_o]^{\mathcal{H}} \\
&= \begin{bmatrix} \cos \beta & \sin \beta \\ & 1 \\ -\sin \beta & \cos \beta \end{bmatrix} \begin{bmatrix} -eR\Omega^2 - eRp^2 \sin^2 \psi \\ -eRp^2 \cos \psi \sin \psi \\ -2eR\Omega p \cos \psi \end{bmatrix} \\
[{}^{\mathcal{I}}\vec{a}_o]^{\mathcal{E}} &= \begin{bmatrix} -(eR\Omega^2 + eRp^2 \sin^2 \psi) \cos \beta - 2eR\Omega p \cos \psi \sin \beta \\ -eRp^2 \sin \psi \cos \psi \\ (eR\Omega^2 + eRp^2 \sin^2 \psi) \sin \beta - 2eR\Omega p \cos \psi \cos \beta \end{bmatrix}
\end{aligned} \tag{D.3.49}$$

Using equations (D.2.6) and (D.3.49), the term $\vec{C}^o \times {}^{\mathcal{I}}\vec{a}_o$ in equation (D.2.5) takes the form

$$\begin{aligned}
&= \begin{bmatrix} M_{blade} r_{CM} R \\ 0 \\ 0 \end{bmatrix} \times \\
&\begin{bmatrix} -(eR\Omega^2 + eRp^2 \sin^2 \psi) \cos \beta - 2eR\Omega p \cos \psi \sin \beta \\ -eRp^2 \sin \psi \cos \psi \\ (eR\Omega^2 + eRp^2 \sin^2 \psi) \sin \beta - 2eR\Omega p \cos \psi \cos \beta \end{bmatrix} \\
\vec{C}^o \times {}^{\mathcal{I}}\vec{a}_o &\approx M_{blade} r_{CM} eR^2 \\
&\begin{bmatrix} 0 \\ -(\Omega^2 + p^2 \sin^2 \psi) \sin \beta + 2\Omega p \cos \psi \cos \beta \\ -p^2 \sin \psi \cos \psi \end{bmatrix}
\end{aligned} \tag{D.3.50}$$

Using small angle assumptions and neglecting higher order terms ($eq^2 \approx 0$, $q^2 \sin \beta \approx 0$), equation (D.3.28) becomes

$$\vec{C}^o \times {}^{\mathcal{I}}\vec{a}_o \approx M_{blade} r_{CM} eR^2 \begin{bmatrix} 0 \\ -\Omega^2 \beta + 2\Omega p \cos \psi \\ 0 \end{bmatrix} \quad (\text{D.3.51})$$

The inertial angular velocity of the blade frame \mathcal{E} expressed in terms of frame \mathcal{E} is

$$\begin{aligned} &= {}^{\mathcal{E}}T_2^{\mathcal{H}}(\beta) \left[{}^{\mathcal{H}}T_1^{\mathcal{A}}(\psi)(-p)\vec{a}_1 + \Omega\vec{h}_3 \right] - \dot{\beta}\vec{e}_2 \\ {}^{\mathcal{I}}\vec{\omega}^{\mathcal{E}} &= \begin{bmatrix} \Omega \sin \beta - p \cos \psi \cos \beta \\ p \sin \psi - \dot{\beta} \\ \Omega \cos \beta + p \cos \psi \sin \beta \end{bmatrix} \end{aligned} \quad (\text{D.3.52})$$

and the corresponding inertial angular acceleration ${}^{\mathcal{I}}\vec{\alpha}^{\mathcal{E}}$ takes the form

$${}^{\mathcal{I}}\vec{\alpha}^{\mathcal{E}} = \begin{bmatrix} \Omega p \sin \psi \cos \beta + (\Omega \cos \beta + p \cos \psi \sin \beta) \dot{\beta} \\ \Omega p \cos \psi - \ddot{\beta} \\ -\Omega p \sin \psi \sin \beta - (\Omega \sin \beta - p \cos \psi \cos \beta) \dot{\beta} \end{bmatrix} \quad (\text{D.3.53})$$

The term $\vec{I}^o \cdot \mathcal{I}\dot{\vec{\omega}}^\mathcal{E} + \mathcal{I}\vec{\omega}^\mathcal{E} \times \left(\vec{I}^o \cdot \mathcal{I}\vec{\omega}^\mathcal{E} \right)$ in equation (D.2.5) takes the form

$$\begin{aligned}
& \vec{I}^o \cdot \mathcal{I}\dot{\vec{\omega}}^\mathcal{E} + \mathcal{I}\vec{\omega}^\mathcal{E} \times \left(\vec{I}^o \cdot \mathcal{I}\vec{\omega}^\mathcal{E} \right) = \\
& \begin{bmatrix} I_a \Omega p \sin \psi \cos \beta + I_a (\Omega \cos \beta + p \cos \psi \sin \beta) \dot{\beta} \\ I_b \Omega p \cos \psi - I_b \ddot{\beta} \\ -I_c \Omega p \sin \psi \sin \beta - I_c (\Omega \sin \beta - p \cos \psi \cos \beta) \dot{\beta} \end{bmatrix} \\
& + \begin{bmatrix} \Omega \sin \beta - p \cos \psi \cos \beta \\ p \sin \psi - \dot{\beta} \\ \Omega \cos \beta + p \cos \psi \sin \beta \end{bmatrix} \times \begin{bmatrix} I_a (\Omega \sin \beta - p \cos \psi \cos \beta) \\ I_b (p \sin \psi - \dot{\beta}) \\ I_c (\Omega \cos \beta + p \cos \psi \sin \beta) \end{bmatrix} \quad (\text{D.3.54}) \\
& = \begin{bmatrix} I_a (2\Omega \cos \beta + p \cos \psi \sin \beta) p \sin \psi \\ I_b (2\Omega p \cos \psi \cos \beta - (\Omega^2 - p^2 \cos^2 \psi) \sin \beta) \cos \beta - I_b \ddot{\beta} \\ -I_c \Omega p \sin \psi \sin \beta - I_c (\Omega \sin \beta - p \cos \psi \cos \beta) \dot{\beta} \end{bmatrix}
\end{aligned}$$

where $\mathcal{I}\vec{\alpha}^\mathcal{E} = \mathcal{I}\dot{\vec{\omega}}^\mathcal{E}$. Using small angle assumptions and neglecting higher order terms ($p^2 \sin \beta \rightarrow \text{small}$, $\beta \dot{\beta} \rightarrow \text{small}$), equation (D.3.54) becomes

$$\vec{I}^o \cdot \mathcal{I}\dot{\vec{\omega}}^\mathcal{E} + \mathcal{I}\vec{\omega}^\mathcal{E} \times \left(\vec{I}^o \cdot \mathcal{I}\vec{\omega}^\mathcal{E} \right) \approx \begin{bmatrix} 2I_a \Omega p \sin \psi \\ 2I_b \Omega p \cos \psi - I_b \Omega^2 \beta - I_b \ddot{\beta} \\ -I_c \Omega \beta p \sin \psi + I_c \dot{\beta} p \cos \psi \end{bmatrix} \quad (\text{D.3.55})$$

Equations (D.3.51) and (D.3.55) give

$$\begin{aligned}
\begin{bmatrix} L \\ -M \\ N \end{bmatrix} &= M_{blade} r_{CM} e R^2 \begin{bmatrix} 0 \\ \Omega^2 \beta - 2\Omega p \cos \psi \\ 0 \end{bmatrix} \\
&+ \begin{bmatrix} 2I_a \Omega p \sin \psi \\ -2I_b \Omega p \cos \psi + I_b \Omega^2 \beta + I_b \ddot{\beta} \\ -I_c \Omega \beta p \sin \psi + I_c \dot{\beta} p \cos \psi \end{bmatrix} \\
&= \begin{bmatrix} \text{gyroscopic} + \text{feathering moment} \\ \text{gyroscopic} + (M_a = \text{aerodynamic}) \text{ moment} \\ \text{drag moment} \end{bmatrix}
\end{aligned} \tag{D.3.56}$$

Equation (D.3.56) says that a steady pitch rate induces both blade pitch and drag moments. The induced drag moment is relieved by the drag (lead/lag) blade hinge, and the induced blade pitch moment is sufficiently small and can be ignored. The resultant blade flapping equation takes the form

$$\ddot{\beta} + \Omega^2 \nu_\beta^2 \beta - 2\Omega \nu_\beta^2 p \cos \psi = \frac{M_{aero}}{I_b} \tag{D.3.57}$$

where ν_β^2 is the non dimensional flap frequency previously defined in equation (D.2.62) such that

$$\begin{aligned}
r_{CM} &= \frac{1-e}{2} \\
I_{blade} &= \int_0^{(1-e)R} m r^2 dr = \frac{m}{3} R^3 (1-e)^3 = \frac{M_{blade}}{3} (1-e)^2 R^2 \\
\varepsilon &= \frac{M_{blade} r_{CM} e R^2}{I_b} = \frac{3e}{2(1-e)} = \frac{\text{static moment}}{\text{inertial moment}} \\
\nu_\beta^2 &= 1 + \varepsilon
\end{aligned} \tag{D.3.58}$$

Figure D.7 on page 269 shows the perturbation to the angle of attack $\Delta\alpha$ due to a combination of flapping rate $r\dot{\beta}$ and roll rate $rp\sin\psi$. The corresponding differential lift

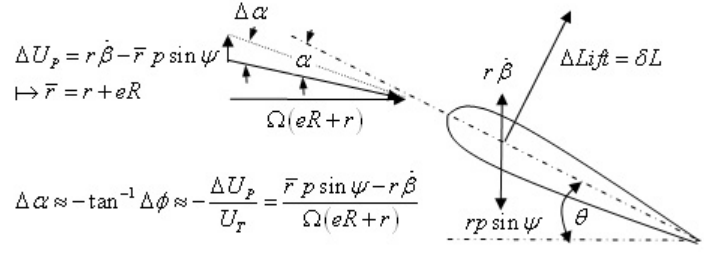


Figure D.8: Blade Flapping Disturbance due to Body Roll Rate.

δL and resultant aerodynamic moment M_{aero} are respectively

$$\begin{aligned}
 \Delta U_P &= r\dot{\beta} - (r + eR)p \cos \psi \\
 \Delta \alpha &= -\tan^{-1} \Delta \phi \approx -\Delta \phi = -\frac{\Delta U_P}{U_T} = \frac{(r + eR)p \cos \psi - r\dot{\beta}}{\Omega(eR + r)} \\
 \delta L &= \frac{1}{2}\rho V_T^2 s C_L \approx \frac{1}{2}\rho \Omega^2 (r + eR)^2 (c\delta r) \left(a \frac{(r + eR)p \cos \psi - r\dot{\beta}}{\Omega(eR + r)} \right) \\
 &= \frac{1}{2}\rho ac \Omega (r + eR) \left((r + eR)p \sin \psi - r\dot{\beta} \right) \delta r \\
 &\approx \frac{1}{2}\rho ac \Omega (r + eR) \left(p \sin \psi - \dot{\beta} \right) r \delta r \\
 M_{aero} &= \int_0^{(1-e)R} r dL = \frac{1}{2}\rho ac \Omega (p \sin \psi - \dot{\beta}) \int_0^{(1-e)R} r^2 (r + eR) dr \\
 &= \frac{1}{8}\rho ac \Omega R^4 (p \sin \psi - \dot{\beta}) (1 - e)^3 \left(1 + \frac{1}{3}e \right) \\
 \frac{M_{aero}}{I_b} &= \frac{\gamma}{8}\Omega (p \sin \psi - \dot{\beta}) (1 - e)^3 \left(1 + \frac{1}{3}e \right) = \frac{n\gamma}{8}\Omega (p \sin \psi - \dot{\beta})
 \end{aligned} \tag{D.3.59}$$

where $e^2 \rightarrow \text{small}$, $r eR \ll r^2$, and $n = (1 - e)^3 (1 + e/3)$. Equating equations (D.3.57) and (D.3.59) yields

$$\ddot{\beta} + \frac{n\gamma}{8}\Omega \dot{\beta} + \Omega^2 \nu_\beta^2 \beta = \frac{n\gamma}{8}\Omega p \sin \psi + 2\Omega \nu_\beta^2 p \cos \psi \tag{D.3.60}$$

Applying the change of variables in (D.3.13), equation (D.3.60) becomes

$$\frac{d^2 \beta}{d\psi^2} + \frac{n\gamma}{8} \frac{d\beta}{d\psi} + \nu_\beta^2 \beta = \frac{n\gamma}{8} \frac{p}{\Omega} \sin \psi + 2\nu_\beta^2 \frac{p}{\Omega} \cos \psi \tag{D.3.61}$$

Expanding the periodic terms

$$\begin{aligned}
& (\beta_{1c} \cos \psi + \beta_{1s} \sin \psi) + \frac{n\gamma}{8} (\beta_{1c} \sin \psi - \beta_{1s} \cos \psi) \\
& + \nu_\beta^2 (\beta_0 - \beta_{1c} \cos \psi - \beta_{1s} \sin \psi) \quad (\text{D.3.62}) \\
& = \frac{n\gamma}{8} \frac{p}{\Omega} \sin \psi + 2\nu_\beta^2 \frac{p}{\Omega} \cos \psi
\end{aligned}$$

Harmonic balancing of the periodic steady-state solution (D.3.16) to the above equation (D.3.61) gives

$$\begin{aligned}
n\beta_{1c} - S_\beta \beta_{1s} &= n \frac{p}{\Omega} \\
S_\beta \beta_{1c} + n\beta_{1s} &= -\nu_\beta^2 \frac{16}{\gamma} \frac{p}{\Omega}
\end{aligned} \quad (\text{D.3.63})$$

Solving for β_{1c}, β_{1s} results in the following set of equations

$$\begin{aligned}
(n^2 + S_\beta^2) \beta_{1c} &= - \left(n^2 - \frac{16}{\gamma} \nu_\beta^2 S_\beta \right) \frac{p}{\Omega} \\
(n^2 + S_\beta^2) \beta_{1s} &= n \left(S_\beta - \frac{16}{\gamma} \nu_\beta^2 \right) \frac{p}{\Omega}
\end{aligned} \quad (\text{D.3.64})$$

where $\bar{n} = n\gamma/8$. For the case of zero hinge offset ($e = 0, \varepsilon = 0$), the above equations become

$$\begin{aligned}
\beta_{1c} &= \frac{p}{\Omega} \\
\beta_{1s} &= -\frac{16}{\gamma} \frac{p}{\Omega}
\end{aligned} \quad (\text{D.3.65})$$

Equations (D.3.64) and (D.3.65) indicate that a non zero steady starboard roll rate induces longitudinal cross-coupling flapping which result in a rotor tilt to the rear (down at blade azimuth station $\psi = 0^0$) regardless of whether the blade has a flap hinge offset. In addition, a positive steady body roll results in blade flapping which corresponds to port rotor tilt (down at blade azimuth station $\psi = 270^0$). Such rotor tilt produces a moment that opposes the original rolling moment of the vehicle. This behavior is a source of stable lateral aerodynamic dampening response of the rotor to body roll rate

[27, 92]. The lateral flapping damping factor

$$-\beta_{1s} \frac{\Omega}{p} = \frac{16}{\gamma} \propto \frac{\text{inertia or rotor}}{\text{aerodynamic forces}} \quad (\text{D.3.66})$$

is inversely proportional to the Lock's number. Equivalently, the lateral flapping damping factor is directly proportional to the inertia of the rotor due to gyroscopic effects and inversely proportional to the aerodynamic forces generated by the rotor. The interaction of inertial and aerodynamic effects with the hinge offset is an important factor to consider for the design of rotor control laws which may depend on flight conditions such as flight altitude. For example, at high altitude, the rotor inertial response due to gyroscopic effects will tend to be greater due to the diminishing relative effect of aerodynamics forces at altitude [27].

D.3.5 Flapping Motion with Body Angular Roll and Pitch Rates and Angular Rates of Change

The rotor hub angular velocity ${}^{\mathcal{I}}\vec{\omega}^{\mathcal{H}}$, corresponding angular acceleration, and resulting flapping hinge acceleration are given by equations (D.2.11), (D.2.12) and (D.2.13) respectively in terms of the rotor hub frame \mathcal{H} where $(\dot{\psi} = \Omega, \dot{\Omega} = 0)$

$${}^{\mathcal{I}}\vec{\omega}^{\mathcal{H}} = \begin{bmatrix} -p \cos \psi + q \sin \psi \\ p \sin \psi + q \cos \psi \\ \Omega \end{bmatrix} \quad (\text{D.3.67})$$

$${}^{\mathcal{I}}\vec{\alpha}^{\mathcal{H}} = \begin{bmatrix} \Omega (p \sin \psi + q \cos \psi) - (\dot{p} \cos \psi - \dot{q} \sin \psi) \\ \Omega (p \cos \psi - q \sin \psi) + (\dot{p} \sin \psi + \dot{q} \cos \psi) \\ 0 \end{bmatrix} \quad (\text{D.3.68})$$

$${}^{\mathcal{I}}\vec{a}_o = -eR \begin{bmatrix} \Omega^2 + (p \sin \psi + q \cos \psi)^2 \\ (p \sin \psi + q \cos \psi) (p \cos \psi - q \sin \psi) \\ 2\Omega (p \cos \psi - q \sin \psi) + \dot{p} \sin \psi + \dot{q} \cos \psi \end{bmatrix} \quad (\text{D.3.69})$$

Equation (D.3.69) above expresses the inertial acceleration of a point coincident with the flapping hinge in terms of the hub frame axis \mathcal{H} . Equation (D.3.69) can be written in terms of the blade frame \mathcal{E} as

$$\begin{aligned}
&= {}^\mathcal{E}T_2^{\mathcal{H}}(\beta) [{}^{\mathcal{I}}\vec{a}_o]^{\mathcal{H}} \\
&= -eR \begin{bmatrix} \cos \beta & \sin \beta \\ & 1 \\ -\sin \beta & \cos \beta \end{bmatrix} \\
&\quad \begin{bmatrix} \Omega^2 + (p \sin \psi + q \cos \psi)^2 \\ (p \sin \psi + q \cos \psi)(p \cos \psi - q \sin \psi) \\ 2\Omega(p \cos \psi - q \sin \psi) + \dot{p} \sin \psi + \dot{q} \cos \psi \end{bmatrix} \\
[{}^{\mathcal{I}}\vec{a}_o]^{\mathcal{E}} &= \begin{bmatrix} [2\Omega(p \cos \psi - q \sin \psi) + \dot{p} \sin \psi + \dot{q} \cos \psi] \sin \beta + \dots \\ [\Omega^2 + (p \sin \psi + q \cos \psi)^2] \cos \beta \\ (p \sin \psi + q \cos \psi)(p \cos \psi - q \sin \psi) \\ [2\Omega(p \cos \psi - q \sin \psi) + \dot{p} \sin \psi + \dot{q} \cos \psi] \cos \beta - \dots \\ [\Omega^2 + (p \sin \psi + q \cos \psi)^2] \sin \beta \end{bmatrix}
\end{aligned} \tag{D.3.70}$$

Using equations (D.2.7) and (D.3.70), the term $\vec{C}^o \times {}^{\mathcal{I}}\vec{a}_o$ in equation (D.2.5) takes the form

$$\begin{aligned}
&= \begin{bmatrix} M_{blade} r_{CM} R + eR \cos \beta \\ 0 \\ -eR \sin \beta \end{bmatrix} \times [{}^{\mathcal{I}}\vec{a}_o]^{\mathcal{E}} \\
\vec{C}^o \times {}^{\mathcal{I}}\vec{a}_o &\approx -M_{blade} r_{CM} eR^2 \dots \\
&\quad \begin{bmatrix} 0 \\ \Omega^2 \beta - 2\Omega(p \cos \psi - q \sin \psi) - (\dot{p} \sin \psi + \dot{q} \cos \psi) \\ 0 \end{bmatrix}
\end{aligned} \tag{D.3.71}$$

where equation (D.3.71) includes small angle assumptions and drop of higher order terms of the form ($p^2 \rightarrow 0$, $q^2 \rightarrow 0$, $pq \rightarrow 0$, $eq^2 \rightarrow 0$, $q^2 \sin \beta \rightarrow 0$, etc). The inertial angular velocity of the blade frame \mathcal{E} expressed in terms of frame \mathcal{E} is

$$\begin{aligned} &= {}^{\mathcal{E}}T_2^{\mathcal{H}}(\beta) \left[{}^{\mathcal{H}}T_1^{\mathcal{A}}(\psi) (-p\vec{a}_1 + q\vec{a}_2) + \Omega\vec{h}_3 \right] - \dot{\beta}\vec{e}_2 \\ \mathcal{I}\vec{\omega}^{\mathcal{E}} &= \begin{bmatrix} \Omega \sin \beta - (p \cos \psi - q \sin \psi) \cos \beta \\ p \sin \psi + q \cos \psi - \dot{\beta} \\ \Omega \cos \beta + (p \cos \psi - q \sin \psi) \sin \beta \end{bmatrix} \end{aligned} \quad (\text{D.3.72})$$

and the corresponding inertial angular acceleration $\mathcal{I}\vec{\alpha}^{\mathcal{E}}$ takes the form

$$\mathcal{I}\vec{\alpha}^{\mathcal{E}} = \begin{bmatrix} \Omega (p \sin \psi + q \cos \psi) - (\dot{p} \cos \psi - \dot{q} \sin \psi) + \dots \\ \Omega \dot{\beta} + (p \cos \psi - q \sin \psi) \beta \dot{\beta} \\ \Omega (p \cos \psi - q \sin \psi) + (\dot{p} \sin \psi + \dot{q} \cos \psi) - \ddot{\beta} \\ -\Omega (p \sin \psi + q \cos \psi) \beta + (\dot{p} \cos \psi - \dot{q} \sin \psi) \beta - \dots \\ \Omega \beta \dot{\beta} + (p \cos \psi - q \sin \psi) \dot{\beta} \end{bmatrix} \quad (\text{D.3.73})$$

Equation (D.3.73) includes the usual small angle and higher order neglect simplifications. The term $\vec{I}^o \cdot \mathcal{I}\dot{\vec{\omega}}^{\mathcal{E}} + \mathcal{I}\vec{\omega}^{\mathcal{E}} \times (\vec{I}^o \cdot \mathcal{I}\vec{\omega}^{\mathcal{E}})$ from equation (D.2.5) takes the form

$$\begin{aligned} &\vec{I}^o \cdot \mathcal{I}\vec{\alpha}^{\mathcal{E}} + \mathcal{I}\vec{\omega}^{\mathcal{E}} \times (\vec{I}^o \cdot \mathcal{I}\vec{\omega}^{\mathcal{E}}) = \\ &\begin{bmatrix} 2I_a \Omega (p \sin \psi + q \cos \psi) - I_a (\dot{p} \cos \psi - \dot{q} \sin \psi) \\ I_b \left[2\Omega (p \cos \psi - q \sin \psi) + (\dot{p} \sin \psi + \dot{q} \cos \psi) - \Omega^2 \beta - \ddot{\beta} \right] \\ I_c \left[(p \cos \psi - q \sin \psi) \dot{\beta} - \Omega (p \sin \psi + q \cos \psi) \beta + \dot{p} \cos \psi - \dot{q} \sin \psi \right] \end{bmatrix} \end{aligned} \quad (\text{D.3.74})$$

where equation (D.3.74) results from applying small angle assumptions and neglecting higher order terms ($p^2 \rightarrow 0$, $q^2 \rightarrow 0$, $pq \rightarrow 0$, $p^2 \sin \beta \rightarrow \text{small}$, $\beta \dot{\beta} \rightarrow \text{small}$). Next,

substituting equations (D.3.71) and (D.3.74) in equation (D.2.5) give

$$\begin{aligned}
 & \begin{bmatrix} L \\ -M \\ N \end{bmatrix} = M_{blade} r_{CM} e R^2 \dots \\
 & \begin{bmatrix} 0 \\ \Omega^2 \beta - 2\Omega (p \cos \psi - q \sin \psi) - (\dot{p} \sin \psi + \dot{q} \cos \psi) \\ 0 \end{bmatrix} + \dots \\
 & \begin{bmatrix} 2I_a \Omega (p \sin \psi + q \cos \psi) - I_a (\dot{p} \cos \psi - \dot{q} \sin \psi) \\ I_b [\ddot{\beta} + \Omega^2 \beta - 2\Omega (p \cos \psi - q \sin \psi) - (\dot{p} \sin \psi + \dot{q} \cos \psi)] \\ I_c [(p \cos \psi - q \sin \psi) \dot{\beta} - \Omega (p \sin \psi + q \cos \psi) \beta + \dot{p} \cos \psi - \dot{q} \sin \psi] \end{bmatrix} \\
 & = \begin{bmatrix} \textit{gyroscopic + feathering moment} \\ M_a = \textit{aerodynamic moment} \\ \textit{drag moment} \end{bmatrix}
 \end{aligned} \tag{D.3.75}$$

D.3.5.1 Flapping Motion with Body Angular Roll and Pitch Rates

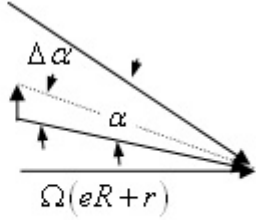
When the angular rate of change $\dot{p} = 0, \dot{q} = 0$, equation (D.3.75) becomes

$$\begin{aligned}
 & \begin{bmatrix} L \\ -M \\ N \end{bmatrix} = M_{blade} r_{CM} e R^2 \dots \\
 & \begin{bmatrix} 0 \\ \Omega^2 \beta - 2\Omega (p \cos \psi - q \sin \psi) \\ 0 \end{bmatrix} + \dots \\
 & \begin{bmatrix} 2I_a \Omega (p \sin \psi + q \cos \psi) \\ I_b \left[\ddot{\beta} + \Omega^2 \beta - 2\Omega (p \cos \psi - q \sin \psi) \right] \\ -I_c \left[(p \cos \psi - q \sin \psi) \dot{\beta} - \Omega (p \sin \psi + q \cos \psi) \beta \right] \end{bmatrix} \\
 & = \begin{bmatrix} \text{gyroscopic} + \text{feathering moment} \\ \text{gyroscopic} + (M_a = \text{aerodynamic}) \text{ moment} \\ \text{drag moment} \end{bmatrix}
 \end{aligned} \tag{D.3.76}$$

Equation (D.3.76) says that a steady pitch rate induces both blade pitch and drag moments. The induced drag moment is relieved by the drag (lead/lag) blade hinge, and the induced blade pitch moment is sufficiently small and can be ignored. The resultant blade flapping equation takes the form

$$\ddot{\beta} + \Omega^2 \nu_\beta^2 \beta - 2\Omega \nu_\beta^2 (p \cos \psi - q \sin \psi) = \frac{M_{aero}}{I_b} \tag{D.3.77}$$

where ν_β^2 is the non-dimensional flap frequency previously defined in equation (D.2.62) on page 257 such that

$$\begin{aligned} \Delta U_p &= r\dot{\beta} - \\ &\bar{r}(p \sin \psi + q \cos \psi) \\ \mapsto \bar{r} &= r + eR \end{aligned}$$


$$\Delta \alpha \approx -\tan^{-1} \Delta \phi \approx -\frac{\Delta U_p}{U_r} = \frac{\bar{r}(p \sin \psi + q \cos \psi) - r\dot{\beta}}{\Omega(eR + r)}$$

Figure D.9: Blade Flapping Disturbance due to Body Roll and Pitch Rates.

$$\begin{aligned} r_{CM} &= \frac{1-e}{2} \\ I_{blade} &= \int_0^{(1-e)R} mr^2 dr = \frac{m}{3} R^3 (1-e)^3 = \frac{M_{blade}}{3} (1-e)^2 R^2 \\ \varepsilon &= \frac{M_{blade} r_{CM} e R^2}{I_b} = \frac{3e}{2(1-e)} = \frac{\text{static moment}}{\text{inertial moment}} \\ \nu_\beta^2 &= 1 + \varepsilon \end{aligned} \tag{D.3.78}$$

Figure D.7 on page 269 shows the perturbation to the angle of attack $\Delta\alpha$ due to a combination of flapping rate $r\dot{\beta}$ and roll rate $rp \sin \psi$. The corresponding differential lift

δL and resultant aerodynamic moment M_{aero} are respectively

$$\begin{aligned}
\Delta U_P &= r\dot{\beta} - (r + eR)(p \cos \psi + q \cos \psi) \\
\Delta \alpha &= -\tan^{-1} \Delta \phi \\
&\approx -\Delta \phi = -\frac{\Delta U_P}{U_T} = \frac{(r + eR)(p \cos \psi + q \cos \psi) - r\dot{\beta}}{\Omega(eR + r)} \\
\delta L &= \frac{1}{2}\rho V_T^2 s C_L \approx \frac{1}{2}\rho \Omega^2 (r + eR)^2 (c\delta r) a \Delta \alpha \\
&\approx \frac{1}{2}\rho ac \Omega (r + eR) (p \sin \psi + q \cos \psi - \dot{\beta}) r \delta r \\
M_{aero} &= \int_0^{(1-e)R} r dL \\
&= \frac{1}{2}\rho ac \Omega (p \sin \psi + q \cos \psi - \dot{\beta}) \int_0^{(1-e)R} r^2 (r + eR) dr \\
&= \frac{1}{8}\rho ac \Omega R^4 (p \sin \psi + q \cos \psi - \dot{\beta}) (1 - e)^3 \left(1 + \frac{1}{3}e\right) \\
\frac{M_{aero}}{I_b} &= \frac{\gamma}{8}\Omega (p \sin \psi + q \cos \psi - \dot{\beta}) (1 - e)^3 \left(1 + \frac{1}{3}e\right) \\
&= \frac{n\gamma}{8}\Omega (p \sin \psi + q \cos \psi - \dot{\beta})
\end{aligned} \tag{D.3.79}$$

where $e^2 \rightarrow \text{small}$, $r eR \ll r^2$, and $n = (1 - e)^3 (1 + e/3)$. Equating equations (D.3.77) and (D.3.79) yield

$$\ddot{\beta} + \frac{n\gamma}{8}\Omega \dot{\beta} + \Omega^2 \nu_\beta^2 \beta = \frac{n\gamma}{8}\Omega (p \sin \psi + q \cos \psi) + 2\Omega \nu_\beta^2 (p \cos \psi - q \sin \psi) \tag{D.3.80}$$

In the case when there is no blade offset $e = 0$, $\varepsilon = 0$, $\nu_\beta = 1$, the above expression takes the form

$$\ddot{\beta} + \frac{\gamma}{8}\Omega \dot{\beta} + \Omega^2 \beta = \frac{\gamma}{8}\Omega (p \sin \psi + q \cos \psi) + 2\Omega (p \cos \psi - q \sin \psi) \tag{D.3.81}$$

Equation (D.3.80) above applies for slender, uniform mass blades that form a thin disk when they rotate, for small flapping angles β , and for hover case undergoing pitch and roll angular rates. Also we assume that the blade center of mass does pass through the

axis along the flap hinge. The term

$$\ddot{\beta} + \Omega^2 \nu_{\beta}^2 \beta$$

is the contribution due to inertial forces and moments about the hinge which include the static moment due to the mass of the blade and the inertial moment due to the blade flapping motion itself. The term ε is in essence a ratio of these two moments as shown in equation (D.3.78). The term

$$\frac{n\gamma}{8} \Omega \dot{\beta}$$

is caused by the blade flapping and the effect that this flapping has on the angle of attack that the blade sees as it rotates around the rotor shaft. This term adds damping to the flapping motion of the blade; whence, a major role played by aerodynamic terms is to add damping to the rotor system [119, p. 34][124]. The term

$$\frac{n\gamma}{8} \Omega (p \sin \psi + q \cos \psi)$$

corresponds to pitch and roll rate contributions due to aerodynamics effects and the term

$$2\Omega \nu_{\beta}^2 (p \cos \psi - q \sin \psi)$$

corresponds to contributions due to gyroscopic effects. For a scaled-model helicopter the flapping undamped natural frequency is approximately that of the rotorspeed at $\Omega \approx 157$ rad/sec (1500 rpm), and the damping ratio is approximated by $\gamma/8$. The time to settle within 5 % of the steady state value would be $-8 \ln(0.05)/\gamma \Omega \approx 0.05$ seconds for a Lock number $\gamma \approx 3$. At a rotorspeed of 157 rad/sec this corresponds to about one revolution. Then the blade flapping needs about one revolution of blade rotation in about 0.05 seconds to settle. Based on this approximate calculation, the forcing term dynamics (on the right hand of equation (D.3.80)) of the body pitch and roll are much slower than the blade flapping dynamics, and therefore, the rotor behaves as a quasi-steady actuator [119]. Also, the above equation says that body pitch and roll rates will force blade flapping via aerodynamic and gyroscopic effects. Applying the change of variables

in (D.3.13), equation (D.3.80) becomes

$$\frac{d^2\beta}{d\psi^2} + \frac{n\gamma}{8} \frac{d\beta}{d\psi} + \nu_\beta^2 \beta = \frac{p}{\Omega} \left(\frac{n\gamma}{8} \sin \psi + 2\nu_\beta^2 \cos \psi \right) + \frac{q}{\Omega} \left(\frac{n\gamma}{8} \cos \psi - 2\nu_\beta^2 \sin \psi \right) \quad (\text{D.3.82})$$

Expanding the periodic terms

$$\begin{aligned} & (\beta_{1c} \cos \psi + \beta_{1s} \sin \psi) + \frac{n\gamma}{8} (\beta_{1c} \sin \psi - \beta_{1s} \cos \psi) \\ & \quad + \nu_\beta^2 (\beta_0 - \beta_{1c} \cos \psi - \beta_{1s} \sin \psi) \\ & = \frac{p}{\Omega} \left(\frac{n\gamma}{8} \sin \psi + 2\nu_\beta^2 \cos \psi \right) + \\ & \quad \frac{q}{\Omega} \left(\frac{n\gamma}{8} \cos \psi - 2\nu_\beta^2 \sin \psi \right) \end{aligned} \quad (\text{D.3.83})$$

Harmonic balancing of the periodic steady-state solution (D.3.16) to the above equation (D.3.82) gives

$$\begin{aligned} n\beta_{1c} - S_\beta \beta_{1s} &= n \frac{p}{\Omega} - \nu_\beta^2 \frac{16}{\gamma} \frac{q}{\Omega} \\ S_\beta \beta_{1c} + n\beta_{1s} &= -\nu_\beta^2 \frac{16}{\gamma} \frac{p}{\Omega} - n \frac{q}{\Omega} \end{aligned} \quad (\text{D.3.84})$$

Solving for β_{1c}, β_{1s} results in the following set of equations

$$\begin{aligned} (n^2 + S_\beta^2) \beta_{1c} &= - \left(n^2 - \frac{16}{\gamma} \nu_\beta^2 S_\beta \right) \frac{p}{\Omega} - n \left(S_\beta + \frac{16}{\gamma} \nu_\beta^2 \right) \frac{q}{\Omega} \\ (n^2 + S_\beta^2) \beta_{1s} &= n \left(S_\beta - \frac{16}{\gamma} \nu_\beta^2 \right) \frac{p}{\Omega} - \left(n^2 - \frac{16}{\gamma} \nu_\beta^2 S_\beta \right) \frac{q}{\Omega} \end{aligned} \quad (\text{D.3.85})$$

For the case of zero hinge offset ($e = 0, \varepsilon = 0$, without loss of generality), the above equations become

$$\begin{aligned} \beta_{1c} &= \frac{p}{\Omega} - \frac{16}{\gamma} \frac{q}{\Omega} \\ \beta_{1s} &= -\frac{16}{\gamma} \frac{p}{\Omega} - \frac{q}{\Omega} \end{aligned} \quad (\text{D.3.86})$$

The above results in (D.3.85) and (D.3.86) are consistent with results in equations (D.3.42) and (D.3.64). As expected, non zero roll and pitch rates induce respective

longitudinal and lateral cross-coupling flapping which result in a rotor tilt to the rear (p/Ω) and to port (q/Ω) directions due to aerodynamic effects. This happens regardless of whether the blade has a flap hinge offset. In addition, gyroscopic effects work such that a positive steady body roll results in rotor tilt to port ($16p/\gamma/\Omega$), and a positive steady pitch rate results in a nose-down rotor tilt ($16q/\gamma/\Omega$). These rotor tilt produce a moments that opposes the original rolling moments of the vehicle, and are therefore sources of stable aerodynamic dampening response of the rotor to body rates [27, 92]. The rotor roll and pitch damping factors

$$\begin{aligned} -\beta_{1c} \frac{\Omega}{q} &= \frac{16}{\gamma} \propto \frac{\text{inertia or rotor}}{\text{aerodynamic forces}} \\ -\beta_{1s} \frac{\Omega}{p} &= \frac{16}{\gamma} \propto \frac{\text{inertia or rotor}}{\text{aerodynamic forces}} \end{aligned} \quad (\text{D.3.87})$$

are inversely proportional to the Lock's number. These are directly proportional to the inertia of the rotor due to gyroscopic effects and inversely proportional to the aerodynamic forces generated by the rotor. The interaction of inertial and aerodynamic effects with the hinge offset is an important factor to consider for the design of rotor control laws which may depend on flight conditions such as flight altitude. For example, at high altitude, the rotor inertial response due to gyroscopic effects will tend to be greater due to the diminishing relative effect of aerodynamics forces at altitude [27].

D.3.5.2 Flapping Motion with Body Roll and Pitch Rates Rate of Change

Equation (D.3.75) gives the contribution of pitch and roll angular rate of change

$$\begin{bmatrix} I_a (\dot{p} \cos \psi - \dot{q} \sin \psi) \\ - (M_{blade} r_{CM} eR^2 + I_b) (\dot{p} \sin \psi + \dot{q} \cos \psi) \\ -I_c (\dot{p} \cos \psi - \dot{q} \sin \psi) \end{bmatrix} \quad (\text{D.3.88})$$

which augment equation (D.3.80) such that

$$\begin{aligned}
\ddot{\beta} + n\frac{\gamma}{8}\Omega\dot{\beta} + \Omega^2\nu_\beta^2\beta &= n\frac{\gamma}{8}\Omega(p\sin\psi + q\cos\psi) \\
&+ 2\Omega\nu_\beta^2(p\cos\psi - q\sin\psi) \\
&+ \nu_\beta^2(\dot{p}\sin\psi + \dot{q}\cos\psi)
\end{aligned} \tag{D.3.89}$$

Applying the change of variables in (D.3.13) equation (D.3.89) becomes

$$\begin{aligned}
\frac{d^2\beta}{d\psi^2} + n\frac{\gamma}{8}\frac{d\beta}{d\psi} + \nu_\beta^2\beta &= \frac{p}{\Omega}\left(n\frac{\gamma}{8}\sin\psi + 2\nu_\beta^2\cos\psi\right) \\
&+ \frac{q}{\Omega}\left(n\frac{\gamma}{8}\cos\psi - 2\nu_\beta^2\sin\psi\right) \\
&+ \frac{\nu_\beta^2}{\Omega}\left(\frac{dp}{d\psi}\sin\psi + \frac{dq}{d\psi}\cos\psi\right)
\end{aligned} \tag{D.3.90}$$

Let the following expression for $\beta(\psi)$ be a solution to (D.3.90) above with non-constant coefficients as function of blade azimuth angle ψ

$$\beta(\psi) = \beta_0(\psi) - \beta_{1c}(\psi)\cos\psi - \beta_{1s}(\psi)\sin\psi \tag{D.3.91}$$

such that

$$\begin{aligned}
\frac{\partial\beta(\psi)}{\partial\psi} &= \frac{\partial\beta_0}{\partial\psi} - \frac{\partial\beta_{1c}}{\partial\psi}\cos\psi - \frac{\partial\beta_{1s}}{\partial\psi}\sin\psi + \beta_{1c}\sin\psi - \beta_{1s}\cos\psi \\
\frac{\partial^2\beta(\psi)}{\partial\psi^2} &= \frac{\partial^2\beta_0}{\partial\psi^2} - \frac{\partial^2\beta_{1c}}{\partial\psi^2}\cos\psi - \frac{\partial^2\beta_{1s}}{\partial\psi^2}\sin\psi \\
&+ 2\frac{\partial\beta_{1c}}{\partial\psi}\sin\psi - 2\frac{\partial\beta_{1s}}{\partial\psi}\cos\psi + \beta_{1c}\cos\psi + \beta_{1s}\sin\psi
\end{aligned} \tag{D.3.92}$$

Substituting (D.3.92) into (D.3.90), and performing harmonic balancing of the periodic solution gives

$$\begin{aligned}
\frac{\partial^2 \beta_0}{\partial \psi^2} + n \frac{\gamma}{8} \frac{\partial \beta_0}{\partial \psi} + \nu_\beta^2 \beta_0(\psi) &= 0 \\
\frac{\partial^2 \beta_{1c}}{\partial \psi^2} + 2 \frac{\partial \beta_{1s}}{\partial \psi} + n \frac{\gamma}{8} \left(\frac{\partial \beta_{1c}}{\partial \psi} + \beta_{1s} \right) + (\nu_\beta^2 - 1) \beta_{1c} \\
&= -2\Omega^2 \nu_\beta^2 \frac{p}{\Omega} - n \frac{\gamma}{8} \Omega^2 \frac{q}{\Omega} - \frac{\nu_\beta^2}{\Omega} \frac{\partial q(\psi)}{\partial \psi} \\
\frac{\partial^2 \beta_{1s}}{\partial \psi^2} - 2 \frac{\partial \beta_{1c}}{\partial \psi} + n \frac{\gamma}{8} \left(\frac{\partial \beta_{1s}}{\partial \psi} - \beta_{1c} \right) + (\nu_\beta^2 - 1) \beta_{1s} \\
&= -n \frac{\gamma}{8} \Omega^2 \frac{p}{\Omega} + 2\Omega^2 \nu_\beta^2 \frac{q}{\Omega} - \frac{\nu_\beta^2}{\Omega} \frac{\partial p(\psi)}{\partial \psi}
\end{aligned} \tag{D.3.93}$$

With no loss of generality, let the hinge offset be zero ($e = 0$), the roll rate $p = 0$ and the pitch rate p be sinusoidally varying

$$\begin{aligned}
p &= 0 \\
q(\psi) &= q_0 \sin \nu \psi \rightarrow \frac{\partial q}{\partial \psi} = q_0 \nu \cos \nu \psi
\end{aligned}$$

The resulting coupled equation is now

$$\begin{aligned}
\frac{\partial^2 \beta_{1c}}{\partial \psi^2} + 2 \frac{\partial \beta_{1s}}{\partial \psi} + \frac{\gamma}{8} \left(\frac{\partial \beta_{1c}}{\partial \psi} + \beta_{1s} \right) &= -\frac{\gamma}{8} \frac{q_0}{\Omega} \sin \nu \psi - \nu \frac{q_0}{\Omega} \cos \nu \psi \\
\frac{\partial^2 \beta_{1s}}{\partial \psi^2} - 2 \frac{\partial \beta_{1c}}{\partial \psi} + \frac{\gamma}{8} \left(\frac{\partial \beta_{1s}}{\partial \psi} - \beta_{1c} \right) &= 2 \frac{q_0}{\Omega} \sin \nu \psi
\end{aligned} \tag{D.3.94}$$

An approximate solution for β_{1c} and β_{1s} is:

$$\begin{aligned}
\beta_{1c} &= -\frac{16}{\gamma} \frac{q}{\Omega} + \left[\left(\frac{16}{\gamma} \right)^2 - 1 \right] \frac{1}{\Omega} \frac{dq}{d\psi} \\
\beta_{1s} &= -\frac{q}{\Omega} + \frac{24}{\gamma} \frac{1}{\Omega} \frac{dq}{d\psi}
\end{aligned} \tag{D.3.95}$$

Typical values for longitudinal and lateral oscillation of the helicopter body are in the range of 10 seconds as compared to a rotor frequency $\Omega = 1500$ rpm for a model helicopter (and 240 rpm for a conventional helicopter). In all cases, the ratio $1/\Omega dq/d\psi$ is much

less than one and of the order 0.025 such that the terms involving $1/\Omega dq/d\psi$ can be discarded [119, p. 35]. The results would again be those given in the case of steady pitch and roll rates in equation (D.3.86). When the helicopter encounters transient states, the longitudinal and lateral blade flapping is proportional to the pitch and roll rates, and the rotor behaves as if the transient instantaneous values were the steady values instead. This rotor behavior is known in literature as *quasi-steady* behavior [124]. Under quasi-steady assumption, the rotor behaves such that a sequence of steady state values adequately describes continuously changing motion.

D.3.6 Flapping Motion for Semi-rigid Rotors with Hinge Offset, Hub Precone and Spring Restoring Moment

The blade flapping contribution of a hub precone $\beta - \beta_P$, and spring restoring moment K_β proportional to the blade flap angle is given by

$$K_\beta (\beta - \beta_P) \tag{D.3.96}$$

The fundamental equation of motion for blade flapping is given by equation (D.2.23)

$$\ddot{\beta} + \Omega^2 \left(1 + \frac{e r_{CM} M_{blade} R^2}{I_b} \right) \beta = \frac{M_{aero}}{I_b} \tag{D.3.97}$$

where ε in equation (D.2.25) is

$$\varepsilon = \frac{M_{blade} r_{CM} e R^2}{I_b} = \frac{\text{static moment}}{\text{inertial moment}} \tag{D.3.98}$$

Substituting the restoring spring and hub precone in (D.3.96) into (D.3.97)

$$\begin{aligned} \ddot{\beta} + \Omega^2 (1 + \varepsilon) \beta + \frac{K_\beta}{I_\beta} (\beta - \beta_P) &= \frac{M_{aero}}{I_\beta} \\ \ddot{\beta} + \Omega^2 \left(1 + \varepsilon + \frac{K_\beta}{\Omega^2 I_\beta} \right) \beta &= \frac{M_{aero}}{I_\beta} + \frac{K_\beta}{I_\beta} \beta_P \\ \frac{\partial^2 \beta}{\partial \psi^2} + \nu^2 \beta &= \frac{M_{aero}}{\Omega^2 I_\beta} + \nu_0^2 \beta_P \end{aligned} \tag{D.3.99}$$

where the nondimensional rotating flap frequency ν^2 and the non-rotating, nondimensional blade flap frequency ν_0 take the form

$$\begin{aligned}\nu^2 &= 1 + \varepsilon + \frac{K_\beta}{\Omega^2 I_\beta} \\ \nu_0^2 &= \frac{K_\beta}{\Omega^2 I_\beta}\end{aligned}\tag{D.3.100}$$

The term Ω in the ν_0^2 expression is the nominal rotor angular velocity. Also, the coefficient of the β term relates to the blade natural flapping frequency such that [105, 119, 124]

$$\nu^2 = 1 + \varepsilon + \frac{K_\beta}{I_\beta \Omega^2} = \frac{\omega_\beta^2}{\Omega^2}\tag{D.3.101}$$

D.3.7 Blade Equation of Motion for Forward Flight Including Body Pitch and Roll Rates

Figure D.10 on the next page and Figure E.1 on page 318 show the rotor and blade conditions in forward flight. During forward flight, the following takes place :

1. the air loads have higher harmonic content (imposes safety limit on forward motion)
2. the advancing blade encounters higher dynamic pressure which may cause shock waves. Cyclic feathering flapping and/or cyclic feathering alleviates this effect.
3. the retreating blade encounters low dynamic pressure. Flap down or increased angle of attack alleviates this effect, but stall may occur.
4. all of the above works to decrease total lift as forward speed increases. Lift will impose a limit on forward speed.

To find the rotor forces and moments during forward flight, the velocities at a blade section airfoil determine the angle of attack seen by the blade section. In general, the angle of attack that the rotor blade sees depends on

1. pilot collective and cyclic pitch input
2. blade twist (if any)
3. free stream advance ratio μ and rotor inflow ratio λ
4. blade flapping

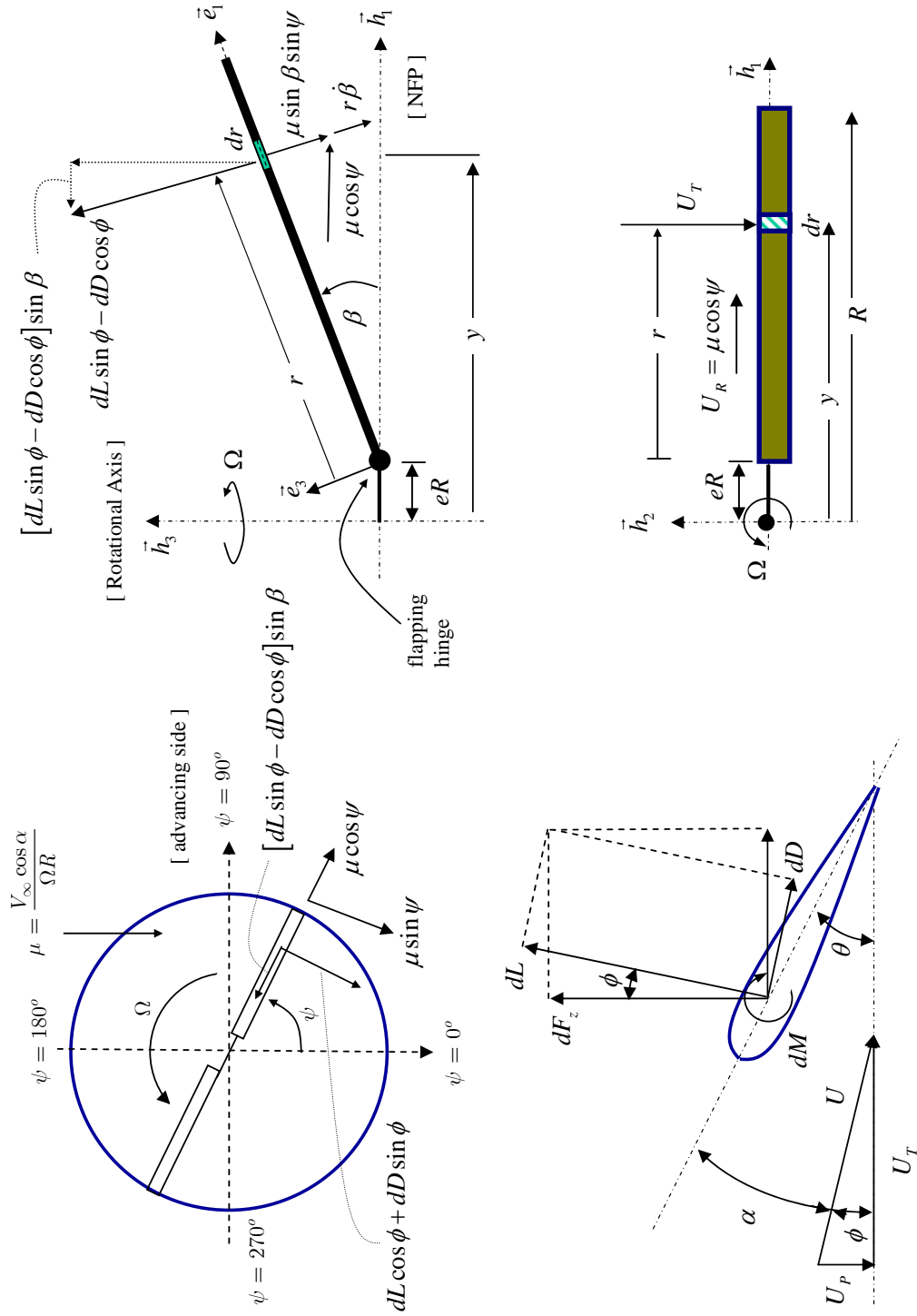


Figure D.10: Aerodynamic Elements Pertaining to Rotor Forces and Moments.

5. anhedral and dihedral effects due to rotor conning
6. body pitch and roll

Following traditional methods for helicopter aerodynamics [82, 92, 105], the collective and cyclic pilot inputs are given by equation (D.3.8) on page 260, and the blade flap angle β is given by equation (D.3.16) on page 262

$$\begin{aligned}\beta &= \beta_0 - \beta_{1c} \cos \psi - \beta_{1s} \sin \psi \\ \theta &= \theta_0 - \theta_{1c} \cos \psi - \theta_{1s} \sin \psi\end{aligned}\tag{D.3.102}$$

The free stream advance ratio μ and rotor inflow ratio λ are given by equation (B.6.4) and subsequently by equation (E.1.1) above.

$$\begin{aligned}\mu &= \frac{V \cos \alpha}{\Omega R} \\ \lambda &= \frac{v_i + V \sin \alpha}{\Omega R} = \mu \tan \alpha + \lambda_i\end{aligned}\tag{D.3.103}$$

At any blade azimuth angle ψ , the anhedral and dihedral effect due to blade flapping and consequent rotor conning is the component of the free stream radial velocity normal to the blade at a flap angle β

$$\begin{aligned}\text{anhedral/dihedral effect} &= \frac{V_\infty \cos \alpha \sin \beta \cos \psi}{\Omega R} \\ &= \mu \cos \psi \sin \beta \approx \beta \mu \cos \psi\end{aligned}\tag{D.3.104}$$

As the blade section airfoil flaps up and down, the airfoil experiences a downwash equal in magnitude and opposite in direction to the blade angular velocity about the flapping hinge

$$\text{blade flapping effect} = r \frac{d\beta}{dt} = r\dot{\beta}\tag{D.3.105}$$

The steady state body pitch and roll also contribute to the U_p component of the blade velocity

$$\text{steady body pitch and roll effect} = (eR + r)(p \sin \psi + q \cos \psi)\tag{D.3.106}$$

Referring to Figure D.10 on page 293, the total velocity encountered by the blade section airfoil in forward flight is then

$$\begin{aligned}
u_T &= \frac{U_T}{\Omega R} = (x + e) + \mu \sin \psi \\
u_P &= \frac{U_P}{\Omega R} = \lambda + x \frac{\dot{\beta}}{\Omega} + \mu \beta \cos \psi - (e + x) \left(\frac{p}{\Omega} \sin \psi + \frac{q}{\Omega} \cos \psi \right) \\
&\approx \lambda + x \frac{\dot{\beta}}{\Omega} + \beta \mu \cos \psi - x \left(\frac{p}{\Omega} \sin \psi + \frac{q}{\Omega} \cos \psi \right) \\
u_r &= \frac{U_R}{\Omega R} = \mu \cos \psi
\end{aligned} \tag{D.3.107}$$

where $x = r/R$, $ep \rightarrow$ small, $eq \rightarrow$ small and eR is the blade flap hinge offset. Also

$$\begin{aligned}
u_T^2 &= (x + e)^2 + \mu^2 \sin^2 \psi \\
u_T (x + e) \left(\frac{p}{\Omega} \sin \psi + \frac{q}{\Omega} \cos \psi \right) \\
&= -(e + x) \left[(x + e) + \mu \sin \psi \left(\frac{p}{\Omega} \sin \psi + \frac{q}{\Omega} \cos \psi \right) \right] \\
&\approx -x (x + e + \mu \sin \psi) \left(\frac{p}{\Omega} \sin \psi + \frac{q}{\Omega} \cos \psi \right)
\end{aligned} \tag{D.3.108}$$

$$u_T \beta \mu \cos \psi = \beta \mu \cos \psi (x + e + \mu \sin \psi)$$

$$u_T x \frac{\dot{\beta}}{\Omega} = x (x + e + \mu \sin \psi) \frac{\dot{\beta}}{\Omega}$$

$$u_T \lambda = \lambda (x + e + \mu \sin \psi)$$

The blade aerodynamic moment about the flapping hinge takes the form

$$\begin{aligned}
M_{aero} &= \int_0^{(1-e)R} r dL \\
&= \frac{1}{2} \rho a c (\Omega R)^2 R^2 \int_0^{(1-e)} (e + x) [\theta u_T^2 - u_T u_P] dx \\
\frac{M_{aero}}{I_\beta} &= \frac{1}{2} \frac{\rho a c (\Omega R)^2 R^2}{I_\beta} \int_0^{(1-e)} (e + x) [\theta u_T^2 - u_T u_P] dx \\
&= \frac{\gamma}{2} \Omega^2 \int_0^{(1-e)} (e + x) [\theta u_T^2 - u_T u_P] dx
\end{aligned} \tag{D.3.109}$$

where I_β is the blade moment of inertia about the flapping hinge and the Lock number γ in equation (D.3.2) is

$$\gamma = \frac{\rho a c R^4}{I_\beta}$$

Substitution of (D.3.108) into the above equation (D.3.109) and integrating

$$\begin{aligned} \frac{8 M_{aero}}{\gamma I_\beta \Omega^2} &= (e-1)^2 \left(1 + \frac{(e+2)}{3} (e+2\mu \sin \psi) \right) \left(\frac{p}{\Omega} \sin \psi + \frac{q}{\Omega} \cos \psi \right) \\ &\quad - (1-e)^3 \left(1 + \frac{e}{3} + \frac{4}{3} \mu \sin \psi \right) \frac{\dot{\beta}}{\Omega} \\ &\quad - (e-1)^2 \left(\frac{2}{3} (e+2) + 2\mu \sin \psi \right) (\beta \mu \cos \psi + \lambda) \\ &\quad + (e-1)^2 \left(1 + \frac{(e+2)}{3} (e+4\mu \sin \psi) + \mu^2 [1 + \cos 2\psi] \right) \theta \end{aligned} \quad (D.3.110)$$

For the case when the flap hinge offset $e = 0$ the above expression becomes

$$\begin{aligned} \frac{8 M_{aero}}{\gamma I_\beta \Omega^2} &= \left(1 + \frac{4}{3} \mu \sin \psi \right) \left(\frac{p}{\Omega} \sin \psi + \frac{q}{\Omega} \cos \psi \right) \\ &\quad - \left(1 + \frac{4}{3} \mu \sin \psi \right) \frac{\dot{\beta}}{\Omega} - \left(\frac{4}{3} + 2\mu \sin \psi \right) (\beta \mu \cos \psi + \lambda) \\ &\quad + \left(1 + \frac{8}{3} \mu \sin \psi + \mu^2 [1 + \cos 2\psi] \right) \theta \end{aligned} \quad (D.3.111)$$

Moreover, if in addition the advance ratio $\mu = 0$ then

$$\frac{8 M_{aero}}{\gamma I_\beta \Omega^2} = \theta - \frac{\dot{\beta}}{\Omega} - \frac{4}{3} \lambda + \left(\frac{p}{\Omega} \sin \psi + \frac{q}{\Omega} \cos \psi \right) \quad (D.3.112)$$

Rearranging the terms in the the general expression (D.3.110) above

$$\frac{8 M_{aero}}{\gamma I_\beta \Omega^2} = K_\theta \theta - K_\lambda \lambda - K_\beta \frac{\dot{\beta}}{\Omega} - K_{\beta\mu} \beta + K_{pq} \left(\frac{p}{\Omega} \sin \psi + \frac{q}{\Omega} \cos \psi \right) \quad (D.3.113)$$

where the following non-constant terms are functions of blade azimuth angle ψ

$$\begin{aligned}
K_{pq} &= (e - 1)^2 \left(1 + \frac{(e + 2)}{3} (e + 2\mu \sin \psi) \right) \\
K_\lambda &= (e - 1)^2 \left(\frac{2}{3} (e + 2) + 2\mu \sin \psi \right) \\
K_{\beta\mu} &= (e - 1)^2 \left(\frac{2}{3} (e + 2) \mu \cos \psi + \mu^2 \sin 2\psi \right) \\
K_{\dot{\beta}} &= (1 - e)^3 \left(1 + \frac{e}{3} + \frac{4}{3} \mu \sin \psi \right) \\
K_\theta &= (e - 1)^2 \left(1 + \frac{(e + 2)}{3} (e + 4\mu \sin \psi) + 2\mu^2 \sin^2 \psi \right)
\end{aligned} \tag{D.3.114}$$

The blade flapping equation of motion with flap hinge offset, hub precone, blade restoring spring, and body pitch and roll rates and pitch/roll rates of change in forward flight is given by equation (D.3.75) and equation (D.3.77) on page 283, and equation (D.3.99) on page 291

$$\begin{aligned}
\ddot{\beta} + \Omega^2 \nu^2 \beta &= \frac{M_a}{I_\beta} + 2\Omega \nu_\beta^2 (p \cos \psi - q \sin \psi) \\
&+ \nu_\beta^2 (\dot{p} \sin \psi + \dot{q} \cos \psi) + \nu_0^2 \beta_P
\end{aligned} \tag{D.3.115}$$

where as before in equations (D.2.25) and (D.3.100)

$$\begin{aligned}
\varepsilon &= \frac{M_{blade} r_{CM} e R^2}{I_b} = \frac{\text{static moment}}{\text{inertial moment}} \\
\nu_\beta^2 &= 1 + \varepsilon \\
\nu^2 &= 1 + \varepsilon + \frac{K_\beta}{I_\beta \Omega^2} \\
\nu_0^2 &= \frac{K_\beta}{I_\beta \Omega^2}
\end{aligned} \tag{D.3.116}$$

Substituting equation (D.3.113) into (D.3.115) and rearranging yields the following expression

$$\begin{aligned}
\ddot{\beta} + \frac{\gamma}{8}\Omega K_{\dot{\beta}}\dot{\beta} + \Omega^2 \left(\nu^2 + \frac{\gamma}{8}K_{\beta\mu} \right) \beta &= \frac{\gamma}{8}\Omega^2 K_{\theta}\theta - \frac{\gamma}{8}\Omega^2 K_{\lambda}\lambda \\
&+ \frac{\gamma}{8}\Omega^2 K_{pq} \left(\frac{p}{\Omega} \sin \psi + \frac{q}{\Omega} \cos \psi \right) \\
&+ 2\Omega^2 \nu_{\beta}^2 \left(\frac{p}{\Omega} \cos \psi - \frac{q}{\Omega} \sin \psi \right) \\
&+ \nu_{\beta}^2 (\dot{p} \sin \psi + \dot{q} \cos \psi) + \nu_0^2 \beta_P
\end{aligned} \tag{D.3.117}$$

Equation (D.3.117) is the fundamental equation of blade flapping [13, 22, 68] since it defines the stability of the blade flapping dynamics. Exact analytical solutions are not possible and numerical methods must be used.

D.3.7.1 Thrust and Torque Coefficients in Forward Flight

From Blade Element Theory (BET) in Section C.2 on page 222, the differential thrust and torque coefficients are given by equation (C.2.9) on page 226

$$\begin{aligned}
dL &= q_{\infty} s C_l = \frac{1}{2} \rho U^2 [c dy] C_l \\
&= \frac{1}{2} \rho U^2 [c dy] a \left(\theta - \frac{U_P}{U_T} \right) \\
dD &= q_{\infty} s C_d = \frac{1}{2} \rho U^2 [c dy] C_d
\end{aligned} \tag{D.3.118}$$

$$dT \approx bdL$$

$$dQ \approx by (dL\phi + dD) = [bdL] [\phi y] + bydD = R\lambda dT + bydD$$

where $R\lambda = \phi y$. Using the following integration formulas

$$\begin{aligned}\int_0^{2\pi} \sin \psi d\psi &= \int_0^{2\pi} \cos \psi d\psi = \int_0^{2\pi} \sin^2 \psi \cos \psi d\psi = 0 \\ \int_0^{2\pi} \sin \psi \cos \psi d\psi &= 0 \\ \int_0^{2\pi} \sin^2 \psi d\psi &= \int_0^{2\pi} \cos^2 \psi d\psi = \pi\end{aligned}\tag{D.3.119}$$

Integration over the length of the blade and through one revolution gives the thrust coefficient C_T

$$\begin{aligned}T &\approx \frac{1}{2} \rho abc (\Omega R)^2 R \frac{1}{2\pi} \int_0^{2\pi} \int_0^{1-e} [\theta u_T^2 - u_T u_P] dx d\psi \\ C_T &= \frac{T}{\rho (\Omega R)^2 \pi R^2} = \frac{1}{2} \frac{\rho abc (\Omega R)^2 R}{\rho (\Omega R)^2 \pi R^2} \frac{1}{2\pi} \int_0^{2\pi} \int_0^{1-e} [\theta u_T^2 - u_T u_P] dx d\psi \\ &= \frac{a\sigma}{2} \frac{1}{2\pi} \int_0^{2\pi} \int_0^{1-e} [\theta u_T^2 - u_T u_P] dx d\psi\end{aligned}\tag{D.3.120}$$

Given the velocity expressions in equation (D.3.107) on page 295, the thrust coefficient is then

$$\begin{aligned}\frac{2C_T}{\sigma a} &= \left(\frac{(1-e^3)}{3} + \frac{(1-e)}{2} \mu^2 \right) \theta_0 + \frac{(e^2-1)}{2} \lambda \\ &\quad + \left((e^2-1) \theta_{1s} + (1-e) e \beta_{1c} + \frac{(1-e^2)}{2} \frac{p}{\Omega} \right) \frac{\mu}{2}\end{aligned}\tag{D.3.121}$$

For the case when the hinge offset is zero $e = 0$, then

$$C_T = \frac{\sigma a}{2} \left[\left(\frac{1}{3} + \frac{1}{2} \mu^2 \right) \theta_0 + \left(\frac{1}{2} \frac{p}{\Omega} - \theta_{1s} \right) \frac{\mu}{2} - \frac{\lambda}{2} \right]\tag{D.3.122}$$

The corresponding torque coefficient C_Q is

$$C_Q = \frac{Q}{\rho(\Omega R)^2(\pi R^2)R} = \frac{\sigma a}{2} \frac{1}{2\pi} \int_0^{2\pi} \int_0^{1-e} (e+x) \left[u_T u_P - u_P^2 + \frac{C_d}{a} u_T^2 \right] dx d\psi \quad (\text{D.3.123})$$

After integration the torque coefficient becomes

$$\begin{aligned} \frac{2C_Q}{\sigma a} &= \frac{C_D}{4a} (1 + \mu^2) + \frac{\lambda}{4} \left(\frac{4}{3} \theta_0 + (2\beta_{1c} - \theta_{1s}) \mu \right) - \frac{\lambda^2}{2} \\ &\quad + \frac{\mu^2}{16} (\beta_{1s} \theta_{1c} + \beta_{1c} \theta_{1s} - 4\beta_0^2 - 3\beta_{1c}^2 - \beta_{1s}^2) \\ &\quad + \frac{\mu}{6} \left(2\frac{q}{\Omega} \beta_0 - \frac{p}{\Omega} \theta_0 + \beta_0 (2\beta_{1s} - \theta_{1c}) \right) - \frac{1}{8} (\beta_{1c}^2 + \beta_{1s}^2) \\ &\quad + \frac{\theta_{1s}}{8} \left(\frac{p}{\Omega} - \beta_{1c} \right) + \frac{\theta_{1c}}{8} \left(\frac{q}{\Omega} + \beta_{1s} \right) \\ &\quad + \frac{1}{4} \left(\frac{p}{\Omega} \beta_{1c} - \frac{q}{\Omega} \beta_{1s} \right) - \frac{1}{8} \left(\frac{p^2}{\Omega^2} + \frac{q^2}{\Omega^2} \right) \\ &\quad + \frac{e}{12} (\dots) + \frac{e^2}{16} (\dots) + \frac{e^3}{12} (\dots) + \frac{e^4}{24} (\dots) \end{aligned} \quad (\text{D.3.124})$$

For the case when the hinge offset is zero ($e = 0$), the above becomes

$$\begin{aligned} \frac{2C_Q}{\sigma a} &= \frac{C_D}{4a} (1 + \mu^2) + \frac{\lambda}{4} \left(\frac{4}{3} \theta_0 + (2\beta_{1c} - \theta_{1s}) \mu \right) - \frac{\lambda^2}{2} \\ &\quad + \frac{\mu^2}{16} (\beta_{1s} \theta_{1c} + \beta_{1c} \theta_{1s} - 4\beta_0^2 - 3\beta_{1c}^2 - \beta_{1s}^2) \\ &\quad + \frac{\mu}{6} \left(2\frac{q}{\Omega} \beta_0 - \frac{p}{\Omega} \theta_0 + \beta_0 (2\beta_{1s} - \theta_{1c}) \right) - \frac{1}{8} (\beta_{1c}^2 + \beta_{1s}^2) \\ &\quad + \frac{\theta_{1s}}{8} \left(\frac{p}{\Omega} - \beta_{1c} \right) + \frac{\theta_{1c}}{8} \left(\frac{q}{\Omega} + \beta_{1s} \right) \\ &\quad + \frac{1}{4} \left(\frac{p}{\Omega} \beta_{1c} - \frac{q}{\Omega} \beta_{1s} \right) - \frac{1}{8} \left(\frac{p^2}{\Omega^2} + \frac{q^2}{\Omega^2} \right) \end{aligned} \quad (\text{D.3.125})$$

For the case of steady symmetric flight the body rates (p, q) are small and can be neglected resulting in the following

$$\begin{aligned} \frac{2C_Q}{\sigma a} &= \frac{C_D}{4a} (1 + \mu^2) + \frac{\lambda}{4} \left(\frac{4}{3}\theta_0 + (2\beta_{1c} - \theta_{1s})\mu \right) - \frac{\lambda^2}{2} - \frac{1}{8} (\beta_{1c}^2 + \beta_{1s}^2) \\ &+ \frac{\mu^2}{16} (\beta_{1s}\theta_{1c} + \beta_{1c}\theta_{1s} - 4\beta_0^2 - 3\beta_{1c}^2 - \beta_{1s}^2) + \frac{\mu}{6} (\beta_0 (2\beta_{1s} - \theta_{1c})) \\ &+ \frac{1}{8} (\theta_{1c}\beta_{1s} - \theta_{1s}\beta_{1c}) \end{aligned} \quad (\text{D.3.126})$$

Neglecting squared terms and products of small flapping angle with cyclic inputs yields

$$C_Q = \frac{\sigma a}{2} \left[\frac{C_D}{4a} (1 + \mu^2) + \frac{\lambda}{4} \left(\frac{4}{3}\theta_0 + (2\beta_{1c} - \theta_{1s})\mu \right) - \frac{\lambda^2}{2} \right] \quad (\text{D.3.127})$$

An approximation to the latest expression uses equation (D.3.118) on page 298 to arrive at a simpler form for the torque coefficient

$$\begin{aligned} &= \lambda C_T + \frac{\sigma C_d}{2} \frac{1}{2\pi} \int_0^{2\pi} \int_0^{1-e} (e+x) u_T^2 dx d\psi \\ C_Q &= \lambda C_T + \frac{\sigma C_d}{8} (1 + \mu^2) \end{aligned} \quad (\text{D.3.128})$$

D.3.7.2 Simplified Thrust and Torque Coefficients in Forward Flight

Substituting equation (D.3.107) on page 295 for u_T, u_P while neglecting fast dynamic contributions of the flapping blade $\dot{\beta}$ and body angular rates ($p, q \rightarrow$ small) such that

$$\begin{aligned} u_T &\approx (e+x) + \mu \sin \psi \\ u_P &\approx \frac{V \sin \alpha + v_i}{\Omega R} = \mu \tan \alpha + \lambda_i = \lambda \end{aligned}$$

Integrating first with respect to azimuth blade angle ψ results in

$$\begin{aligned}
&= \frac{1}{2} a \sigma \int_0^{1-e} \left[\theta \left((x+e)^2 + \frac{\mu^2}{2} \right) - (x+e) \lambda \right] dx \\
C_T &= \frac{a \sigma}{2} \left[\frac{\theta}{3} (1-e) \left((e+1)^2 - e + \frac{3}{2} \mu^2 \right) - \frac{(e^2-1)}{2} \lambda \right] \\
C_Q &= \lambda C_T + \frac{\sigma C_d}{2} \int_0^{1-e} \left((e+x)^2 + \frac{\mu^2}{2} \right) (e+x) dx \\
&= \lambda C_T - \frac{C_d}{8} (e-1)(e+1)(1+e^2+\mu^2)
\end{aligned} \tag{D.3.129}$$

For the case where there is no flapping hinge ($e = 0$)

$$\begin{aligned}
C_T &= \frac{a \sigma}{2} \left[\frac{\theta}{3} \left(1 + \frac{3}{2} \mu^2 \right) - \frac{\lambda}{2} \right] \\
C_Q &= \frac{a \sigma}{2} \left[\frac{\lambda \theta}{3} \left(1 + \frac{3}{2} \mu^2 \right) - \frac{\lambda^2}{2} + \frac{C_d}{4a} (1 + \mu^2) \right] \\
&= \lambda C_T + \frac{\sigma C_d}{8} (1 + \mu^2)
\end{aligned} \tag{D.3.130}$$

D.3.7.3 Blade Equation of Motion for Forward Flight: Non-Constant Blade Flap Coefficients

Using the transformation equation (D.3.13) on page 262, the flapping equation (D.3.117) on page 298 becomes

$$\begin{aligned}
\beta'' + \frac{\gamma}{8} K_{\dot{\beta}} \beta' + \left(\nu^2 + \frac{\gamma}{8} K_{\beta\mu} \right) \beta &= \frac{\gamma}{8} K_{\theta} \theta - \frac{\gamma}{8} K_{\lambda} \lambda \\
&+ \frac{\gamma}{8} K_{pq} \left(\frac{p}{\Omega} \sin \psi + \frac{q}{\Omega} \cos \psi \right) + 2\nu_{\beta}^2 \left(\frac{p}{\Omega} \cos \psi - \frac{q}{\Omega} \sin \psi \right) \\
&+ \nu_{\beta}^2 \left(\frac{\dot{p}}{\Omega^2} \sin \psi + \frac{\dot{q}}{\Omega^2} \cos \psi \right) + \nu_0^2 \beta_P
\end{aligned} \tag{D.3.131}$$

Assume that the following expression for $\beta(\psi)$ is a solution to (D.3.131) above, and the expression for θ represent the blade pitch input

$$\begin{aligned}
\theta &= \theta_0 - \theta_{1c} \cos \psi - \theta_{1s} \sin \psi \\
\beta(\psi) &= \beta_0(\psi) - \beta_{1c}(\psi) \cos \psi - \beta_{1s}(\psi) \sin \psi
\end{aligned} \tag{D.3.132}$$

such that

$$\begin{aligned}
\frac{\partial \beta(\psi)}{\partial \psi} &= \frac{\partial \beta_0}{\partial \psi} - \frac{\partial \beta_{1c}}{\partial \psi} \cos \psi - \frac{\partial \beta_{1s}}{\partial \psi} \sin \psi + \beta_{1c} \sin \psi - \beta_{1s} \cos \psi \\
\frac{\partial^2 \beta(\psi)}{\partial \psi^2} &= \frac{\partial^2 \beta_0}{\partial \psi^2} - \frac{\partial^2 \beta_{1c}}{\partial \psi^2} \cos \psi - \frac{\partial^2 \beta_{1s}}{\partial \psi^2} \sin \psi \\
&\quad + 2 \frac{\partial \beta_{1c}}{\partial \psi} \sin \psi - 2 \frac{\partial \beta_{1s}}{\partial \psi} \cos \psi + \beta_{1c} \cos \psi + \beta_{1s} \sin \psi
\end{aligned} \tag{D.3.133}$$

Substituting expression (D.3.133) into (D.3.131), expanding the periodic terms, and performing harmonic balancing with first harmonic terms gives [22]

$$[A] \beta'' + [D] \beta' + [K] \beta = [F(\theta, \omega, \lambda)] \tag{D.3.134}$$

where $\beta' = \partial \beta / \partial \psi$

$$\begin{aligned}
\beta &= \begin{bmatrix} \beta_0 & \beta_{1c} & \beta_{1s} \end{bmatrix}^T \\
\theta &= \begin{bmatrix} \theta_0 & \theta_{1c} & \theta_{1s} \end{bmatrix}^T \\
\omega &= \begin{bmatrix} p & q & \dot{p} & \dot{q} \end{bmatrix}^T
\end{aligned} \tag{D.3.135}$$

The matrix $[A]$, the damping matrix $[D]$ and the stiffness matrix $[K]$ are

$$\begin{aligned}
A &= \begin{bmatrix} 8/\gamma & & \\ & 8/\gamma & \\ & & 8/\gamma \end{bmatrix} \\
D &= \begin{bmatrix} -x^3 n_4 & & -2x^3 \mu/3 \\ & -x^3 n_4 & 16/\gamma \\ 4x^3 \mu/3 & -16/\gamma & -x^3 n_4 \end{bmatrix} \\
K &= \begin{bmatrix} 8\nu^2/\gamma & -x^2 e \mu & & \\ -n_3 \mu/2 & S_\beta & & -n_1 + x^2 \mu^2/2 \\ & & n_1 + x^2 \mu^2/2 & \\ & & & S_\beta \end{bmatrix}
\end{aligned} \tag{D.3.136}$$

The components of the forcing function $[F] = [C]\theta + [R]\omega + [O]$ take the form

$$\begin{aligned}
 C &= \begin{bmatrix} n_2 + x^2\mu^2 & 0 & -2n_3\mu \\ 0 & n_2 + x^2\mu^2/2 & 0 \\ -4n_3\mu & 0 & n_2 + 3x^2\mu^2 \end{bmatrix} \\
 R &= \begin{bmatrix} n_3\mu/\Omega & & & \\ -16\nu_\beta^2/\gamma\Omega & -(1 - 4e/3)/\Omega & & -8\nu_\beta^2/\gamma\Omega^2 \\ -(1 - 4e/3)/\Omega & 16\nu_\beta^2/\gamma\Omega & & -8\nu_\beta^2/\gamma\Omega^2 \\ & & & \end{bmatrix} \quad (D.3.137) \\
 O &= \begin{bmatrix} -2n_3 \\ 2x^2\mu \end{bmatrix} \lambda + \begin{bmatrix} 8\nu_0^2\beta_P/\gamma \end{bmatrix}
 \end{aligned}$$

and the rotor stiffness number $S_\beta = 8(\nu^2 - 1)/\gamma$ is defined by equation (D.3.19) on page 263. Also the following convenient definitions apply

$$\begin{aligned}
 x &= (e - 1) \\
 n_1 &= (e - 1)^2 \left(\frac{2e}{3} + \frac{e^2}{3} - 1 \right) \quad n_2 = (e - 1)^2 \left(1 + \frac{2e}{3} + \frac{e^2}{3} \right) \\
 n_3 &= \frac{2}{3} - e + \frac{e^3}{3} \quad n_4 = \left(1 + \frac{e}{3} \right)
 \end{aligned} \quad (D.3.138)$$

D.3.7.4 Blade Equation of Motion for Forward Flight: Low Frequency Dynamics

Following results from section §D.3.5.2, equation (D.3.95), terms involving the rate of change of roll $\dot{p}/\Omega \rightarrow$ small and pitch $\dot{q}/\Omega \rightarrow$ small are discarded such that equation

(D.3.131) becomes

$$\begin{aligned}
\beta'' + \frac{\gamma}{8} K_{\dot{\beta}} \beta' + \left(\nu^2 + \frac{\gamma}{8} K_{\beta\mu} \right) \beta &= \frac{1}{8} \gamma K_{\theta} \theta - \frac{1}{8} \gamma K_{\lambda} \lambda \\
&+ \frac{1}{8} \gamma K_{pq} \left(\frac{p}{\Omega} \sin \psi + \frac{q}{\Omega} \cos \psi \right) \\
&+ 2\nu_{\beta}^2 \left(\frac{p}{\Omega} \cos \psi - \frac{q}{\Omega} \sin \psi \right) \\
&+ \nu_0^2 \beta_P
\end{aligned} \tag{D.3.139}$$

In this case, the $[R]$ matrix of the forcing function in equation (D.3.134) on page 303 becomes

$$\bar{R} = \begin{bmatrix} n_3 \mu / \Omega & 0 \\ -16\nu_{\beta}^2 / \gamma \Omega & -(1 - 4e/3) / \Omega \\ -(1 - 4e/3) / \Omega & 16\nu_{\beta}^2 / \gamma \Omega \end{bmatrix} \tag{D.3.140}$$

Since the rotor dynamics are much faster than the body dynamics [22, 68, 105], further simplification discards the blade dynamic second order terms β'' . Moreover, inasmuch as the following assumption within terms in the damping matrix $[D]$ hold

$$\begin{aligned}
(1 - e)^3 (1 + e/3) &< 16/\gamma \\
(1 - e)^3 4\mu/3 &< 16/\gamma
\end{aligned} \tag{D.3.141}$$

then the cross coupling terms and the conning mode can be discarded from the longitudinal and lateral flapping dynamics resulting in the following simplified expression

$$\begin{aligned}
&\begin{bmatrix} 0 & 16/\gamma \Omega \\ 16/\gamma \Omega & 0 \end{bmatrix} \begin{bmatrix} \dot{\beta}_{1c} \\ \dot{\beta}_{1s} \end{bmatrix} + \begin{bmatrix} S_{\beta} & -(n_1 - x^2 \mu^2 / 2) \\ -n_1 - x^2 \mu^2 / 2 & -S_{\beta} \end{bmatrix} \begin{bmatrix} \beta_{1c} \\ \beta_{1s} \end{bmatrix} \\
&= \begin{bmatrix} n_2 + x^2 \mu^2 / 2 & 0 \\ 0 & -(n_2 + x^2 \mu^2) \end{bmatrix} \begin{bmatrix} \theta_{1c} \\ \theta_{1s} \end{bmatrix} \\
&+ \begin{bmatrix} -16\nu_{\beta}^2 / \gamma \Omega & -(1 - 4e/3) / \Omega \\ (1 - 4e/3) / \Omega & -16\nu_{\beta}^2 / \gamma \Omega \end{bmatrix} \begin{bmatrix} p \\ q \end{bmatrix} + \begin{bmatrix} 0 \\ -2x^2 \mu \lambda \end{bmatrix}
\end{aligned} \tag{D.3.142}$$

where x, n_1, n_2 are defined in Equation (D.3.138) on page 304. In the time domain the above expression takes the form

$$[D] \dot{\beta}/\Omega + [K] \beta = [F(\theta, \omega, \lambda)] \quad (\text{D.3.143})$$

In an expanded form

$$\begin{aligned} \frac{16}{\gamma\Omega} \dot{\beta}_{1c} - \left(n_1 + x^2 \frac{\mu^2}{2} \right) \beta_{1c} - S_\beta \beta_{1s} \\ = - (n_2 + x^2 \mu^2) \theta_{1s} + \left(1 - \frac{4e}{3} \right) \frac{p}{\Omega} - \nu_\beta^2 \frac{16}{\gamma} \frac{q}{\Omega} - 2x^2 \mu \lambda \\ \frac{16}{\gamma\Omega} \dot{\beta}_{1s} - \left(n_1 - x^2 \frac{\mu^2}{2} \right) \beta_{1s} + S_\beta \beta_{1c} \\ = \left(n_2 + x^2 \frac{\mu^2}{2} \right) \theta_{1c} - \nu_\beta^2 \frac{16}{\gamma} \frac{p}{\Omega} - \left(1 - \frac{4e}{3} \right) \frac{q}{\Omega} \end{aligned} \quad (\text{D.3.144})$$

Equation (D.3.144) describes the Tip Path Plane (TPP) first order blade flapping dynamics.

D.3.7.4.1 Blade Equation of Motion: Low Translational Speed

In this case the advance ratio $\mu \rightarrow$ small, the rotor inflow ratio $\lambda \approx \lambda_i$ and equation (D.3.139) takes the form

$$\begin{aligned} \beta'' + \frac{\gamma}{8} \bar{K}_{\dot{\beta}} \beta' + \nu^2 \beta &= \frac{\gamma}{8} \bar{K}_\theta \theta - \frac{\gamma}{8} \bar{K}_\lambda \lambda_i \\ &+ \frac{\gamma}{8} \bar{K}_{pq} \left(\frac{p}{\Omega} \sin \psi + \frac{q}{\Omega} \cos \psi \right) \\ &+ \nu_\beta^2 \left(\frac{p}{\Omega} \cos \psi - \frac{q}{\Omega} \sin \psi \right) + \nu_0^2 \beta_P \end{aligned} \quad (\text{D.3.145})$$

where the constant coefficients are defined as

$$\begin{aligned} \bar{K}_{pq} = \bar{K}_\theta = n_2 &= (e-1)^2 \left(1 + \frac{2}{3}e + \frac{e^2}{3} \right) \\ \bar{K}_{\dot{\beta}} &= (1-e)^3 \left(1 + \frac{1}{3}e \right) \\ \bar{K}_\lambda &= (e-1)^2 \left(\frac{4}{3} + \frac{2}{3}e \right) \end{aligned} \quad (\text{D.3.146})$$

In this case equation (D.3.144) on the preceding page becomes

$$\begin{aligned}\frac{16}{\gamma\Omega}\dot{\beta}_{1c} - n_1\beta_{1c} - S_\beta\beta_{1s} &= -n_2\theta_{1s} + \left(1 - \frac{4e}{3}\right)\frac{p}{\Omega} - \nu_\beta^2\frac{16}{\gamma}\frac{q}{\Omega} - 2x^2\mu\lambda \\ \frac{16}{\gamma\Omega}\dot{\beta}_{1s} - n_1\beta_{1s} + S_\beta\beta_{1c} &= n_2\theta_{1c} - \nu_\beta^2\frac{16}{\gamma}\frac{p}{\Omega} - \left(1 - \frac{4e}{3}\right)\frac{q}{\Omega}\end{aligned}\quad (\text{D.3.147})$$

D.3.7.4.2 Blade Equation of Motion: No-Flapping Hinge Offset and no Hub Precone

For a rotor that hinges at the hub the hinge offset is zero $e = 0$, $\varepsilon = 0$, with a hub spring K_β such that $\nu = K_\beta/I_\beta\Omega^2$ with no hub precone $\beta_P = 0$. Equation (D.3.145) becomes

$$\begin{aligned}\beta'' + \frac{\gamma}{8}\beta' + \left(1 + \frac{K_\beta}{\Omega^2 I_\beta}\right)\beta &= \frac{\gamma}{8}\theta - \frac{\gamma}{8}\lambda_i \\ + \frac{\gamma}{8}\left(\frac{p}{\Omega}\sin\psi + \frac{q}{\Omega}\cos\psi\right) + 2\left(\frac{p}{\Omega}\cos\psi - \frac{q}{\Omega}\sin\psi\right)\end{aligned}\quad (\text{D.3.148})$$

Substituting expression (D.3.133) in the above equation, and performing harmonic balancing results in the following coupled equations

$$\begin{aligned}\beta''_0 + \frac{\gamma}{8}\beta'_0 + \left(1 + \frac{K_\beta}{\Omega^2 I_\beta}\right)\beta_0 &= \frac{\gamma}{8}\theta_0 - \frac{\gamma}{8}\lambda_i \\ \beta''_{1c} + 2\beta'_{1s} + \frac{\gamma}{8}(\beta'_{1c} + \beta_{1s}) + \frac{K_\beta}{\Omega^2 I_\beta}\beta_{1c} &= \frac{\gamma}{8}\theta_{1c} - \frac{\gamma}{8}\frac{q}{\Omega} - 2\frac{p}{\Omega} \\ \beta''_{1s} - 2\beta'_{1c} + \frac{\gamma}{8}(\beta'_{1s} - \beta_{1c}) + \frac{K_\beta}{\Omega^2 I_\beta}\beta_{1s} &= \frac{\gamma}{8}\theta_{1s} - \frac{\gamma}{8}\frac{p}{\Omega} + 2\frac{q}{\Omega}\end{aligned}\quad (\text{D.3.149})$$

Discarding the rotor coning dynamics and transformation back to the rotating coordinate axis

$$\begin{aligned}\frac{8}{\gamma\Omega^2}\ddot{\beta}_{1c} + \frac{1}{\Omega}\dot{\beta}_{1c} + \frac{16}{\gamma\Omega}\dot{\beta}_{1s} + \beta_{1s} + \frac{8}{\gamma}\frac{K_\beta}{\Omega^2 I_\beta}\beta_{1c} &= \theta_{1c} - \frac{q}{\Omega} - \frac{16}{\gamma}\frac{p}{\Omega} \\ \frac{8}{\gamma\Omega^2}\ddot{\beta}_{1s} - \frac{16}{\gamma\Omega}\dot{\beta}_{1c} + \frac{1}{\Omega}\dot{\beta}_{1s} - \beta_{1c} + \frac{8}{\gamma}\frac{K_\beta}{\Omega^2 I_\beta}\beta_{1s} &= \theta_{1s} - \frac{p}{\Omega} + \frac{16}{\gamma}\frac{q}{\Omega}\end{aligned}\quad (\text{D.3.150})$$

In matrix form

$$\begin{aligned}
\frac{8}{\gamma\Omega^2} \begin{bmatrix} \ddot{\beta}_{1c} \\ \ddot{\beta}_{1s} \end{bmatrix} + \frac{1}{\Omega} \begin{bmatrix} 1 & 16/\gamma \\ -16/\gamma & 1 \end{bmatrix} \begin{bmatrix} \dot{\beta}_{1c} \\ \dot{\beta}_{1s} \end{bmatrix} \\
+ \frac{8}{\gamma} \begin{bmatrix} K_\beta/I_\beta\Omega^2 & \gamma/8 \\ -\gamma/8 & K_\beta/I_\beta\Omega^2 \end{bmatrix} \begin{bmatrix} \beta_{1c} \\ \beta_{1s} \end{bmatrix} \\
= \begin{bmatrix} 1 & \\ & 1 \end{bmatrix} \begin{bmatrix} \theta_{1c} \\ \theta_{1s} \end{bmatrix} + \frac{1}{\Omega} \begin{bmatrix} -16/\gamma & -1 \\ -1 & 16/\gamma \end{bmatrix} \begin{bmatrix} p \\ q \end{bmatrix}
\end{aligned} \tag{D.3.151}$$

As previously stated in equation (D.3.134) on page 303, the above equation has the form

$$[A]\ddot{\beta} + [D]\dot{\beta} + [K]\beta = [F] \tag{D.3.152}$$

Neglecting second order terms [22, 105], the equation (D.3.150) becomes

$$\begin{aligned}
\frac{16}{\gamma\Omega} \dot{\beta}_{1c} - \frac{1}{\Omega} \dot{\beta}_{1s} + \beta_{1c} - \frac{8}{\gamma} \frac{K_\beta}{\Omega^2 I_\beta} \beta_{1s} &= -\theta_{1s} + \frac{p}{\Omega} - \frac{16}{\gamma} \frac{q}{\Omega} \\
\frac{1}{\Omega} \dot{\beta}_{1c} + \frac{16}{\gamma\Omega} \dot{\beta}_{1s} + \beta_{1s} + \frac{8}{\gamma} \frac{K_\beta}{\Omega^2 I_\beta} \beta_{1c} &= \theta_{1c} - \frac{q}{\Omega} - \frac{16}{\gamma} \frac{p}{\Omega}
\end{aligned} \tag{D.3.153}$$

In matrix form

$$\begin{aligned}
\frac{1}{\Omega} \begin{bmatrix} 1 & 16/\gamma \\ 16/\gamma & -1 \end{bmatrix} \begin{bmatrix} \dot{\beta}_{1c} \\ \dot{\beta}_{1s} \end{bmatrix} + \frac{8}{\gamma} \begin{bmatrix} K_\beta/I_\beta\Omega^2 & \gamma/8 \\ \gamma/8 & -K_\beta/I_\beta\Omega^2 \end{bmatrix} \begin{bmatrix} \beta_{1c} \\ \beta_{1s} \end{bmatrix} \\
= \begin{bmatrix} 1 & \\ & -1 \end{bmatrix} \begin{bmatrix} \theta_{1c} \\ \theta_{1s} \end{bmatrix} + \frac{1}{\Omega} \begin{bmatrix} -16/\gamma & -1 \\ 1 & -16/\gamma \end{bmatrix} \begin{bmatrix} p \\ q \end{bmatrix}
\end{aligned} \tag{D.3.154}$$

Similar results were obtained by Chen [22] and utilized in practice by Mettler *et. all* [50, 105, 107, 108].

D.3.7.4.3 Simplified First Order Tip Path Plane Blade Flapping Equation of Motion

Discarding the cross coupling effects as suggested by equation (D.3.141) on page 305, the expanded form of equation (D.3.154) on the previous page is

$$\begin{aligned}\frac{16}{\gamma\Omega}\dot{\beta}_{1c} + \beta_{1c} - \frac{8}{\gamma}\frac{K_{\beta}}{\Omega^2 I_{\beta}}\beta_{1s} &= -\theta_{1s} + \frac{p}{\Omega} - \frac{16}{\gamma}\frac{q}{\Omega} \\ \frac{16}{\gamma\Omega}\dot{\beta}_{1s} + \beta_{1s} + \frac{8}{\gamma}\frac{K_{\beta}}{\Omega^2 I_{\beta}}\beta_{1c} &= \theta_{1c} - \frac{16}{\gamma}\frac{p}{\Omega} - \frac{q}{\Omega}\end{aligned}\tag{D.3.155}$$

Rearranging some terms

$$\begin{aligned}\frac{16}{\gamma\Omega}\dot{\beta}_{1c} &= -\beta_{1c} + \frac{p}{\Omega} - \frac{16}{\gamma}\frac{q}{\Omega} + \frac{8}{\gamma}\frac{K_{\beta}}{\Omega^2 I_{\beta}}\beta_{1s} - \theta_{1s} \\ \frac{16}{\gamma\Omega}\dot{\beta}_{1s} &= -\beta_{1s} - \frac{q}{\Omega} - \frac{16}{\gamma}\frac{p}{\Omega} - \frac{8}{\gamma}\frac{K_{\beta}}{\Omega^2 I_{\beta}}\beta_{1c} + \theta_{1c}\end{aligned}\tag{D.3.156}$$

In equation (D.3.156) above, the term

$$\tau_{MR} = \frac{16}{\gamma\Omega}\tag{D.3.157}$$

is the rotor time constant which depends on the rotor angular speed and corresponding Lock number. The same time constant applies to the longitudinal $\tau_{MR} q$ and lateral $\tau_{MR} p$ flapping produced by the body pitching rate q and rolling rate p respectively

$$\begin{aligned}q \tau_{MR} &= -\frac{16}{\gamma\Omega}q \\ p \tau_{MR} &= -\frac{16}{\gamma\Omega}p\end{aligned}\tag{D.3.158}$$

These terms above are important in that they are a source of rotor damping. The terms $-p/\Omega$ and $-q/\Omega$ are, respectively, the longitudinal and lateral blade flapping produced by aerodynamic cross coupling via the body roll p and pitch q rates. Finally, the term

$$\frac{8}{\gamma}\frac{K_{\beta}}{\Omega^2 I_{\beta}}\tag{D.3.159}$$

results from hinge offset and flapping restraint. It is a source of cross coupling and it is related to the blade natural flapping frequency defined in equation (D.3.101) on page 292

$$\frac{8}{\gamma} \frac{K_\beta}{I_\beta \Omega^2} = \frac{8}{\gamma} (\nu_\beta^2 - 1 - \varepsilon) \quad (\text{D.3.160})$$

Inasmuch as the term K_β relates to the flapping blade natural frequency ω_β^2/Ω^2 via equation (D.3.101), then K_β relates directly to the phasing of the flapping response [105, 119].

D.3.7.4.4 Blade Equation of Motion: Teetering Blade

In this case there is no restoring spring K_β and equation (D.3.148) becomes

$$\beta'' + \frac{\gamma}{8}\beta' + \beta = \frac{\gamma}{8}\theta - \frac{\gamma}{8}\lambda_i + \frac{\gamma}{8} \left(\frac{p}{\Omega} \sin \psi + \frac{q}{\Omega} \cos \psi \right) + 2 \left(\frac{p}{\Omega} \cos \psi - \frac{q}{\Omega} \sin \psi \right) \quad (\text{D.3.161})$$

In turn, the set of coupled equations (D.3.149) takes the form

$$\begin{aligned} \beta''_{1c} + 2\beta'_{1s} + \frac{\gamma}{8}(\beta'_{1c} + \beta'_{1s}) &= \frac{\gamma}{8}\theta_{1c} - \frac{\gamma}{8}\frac{q}{\Omega} - 2\frac{p}{\Omega} \\ \beta''_{1s} - 2\beta'_{1c} + \frac{\gamma}{8}(\beta'_{1s} - \beta'_{1c}) &= \frac{\gamma}{8}\theta_{1s} - \frac{\gamma}{8}\frac{p}{\Omega} + 2\frac{q}{\Omega} \end{aligned} \quad (\text{D.3.162})$$

After discarding the second order blade dynamics and transforming to the time domain

$$\begin{aligned} \frac{16}{\gamma\Omega}\dot{\beta}_{1c} - \frac{1}{\Omega}\dot{\beta}_{1s} + \beta_{1c} &= -\theta_{1s} + \frac{p}{\Omega} - \frac{16}{\gamma}\frac{q}{\Omega} \\ \frac{1}{\Omega}\dot{\beta}_{1c} + \frac{16}{\gamma\Omega}\dot{\beta}_{1s} + \beta_{1s} &= \theta_{1c} - \frac{q}{\Omega} - \frac{16}{\gamma}\frac{p}{\Omega} \end{aligned} \quad (\text{D.3.163})$$

Applying the simplifications suggested by equation (D.3.141) on page 305, the above expression becomes

$$\begin{aligned} \frac{16}{\gamma\Omega}\dot{\beta}_{1c} &= -\beta_{1c} + \frac{p}{\Omega} - \frac{16}{\gamma}\frac{q}{\Omega} - \theta_{1s} \\ \frac{16}{\gamma\Omega}\dot{\beta}_{1s} &= -\beta_{1s} - \frac{q}{\Omega} - \frac{16}{\gamma}\frac{p}{\Omega} + \theta_{1c} \end{aligned} \quad (\text{D.3.164})$$

Equations (D.3.156) and (D.3.164) differ by the term

$$\frac{8}{\gamma} \frac{K_\beta}{\Omega^2 I_\beta}$$

which is a cross-coupling term due to the presence of a flapping restraint, in this case a blade flap restoring device with spring constant K_β . A teetering rotor does not have a hinge offset and flaps about the main rotational axis, and therefore a teetering rotor cannot develop hub moments, in which case $K_\beta = 0$. Equation (D.3.163) describes the first order equation of motion for a teetering blade in the rotor hub reference frame. When steady state conditions apply ($\dot{\beta}_{1c} = 0$, $\dot{\beta}_{1s} = 0$) with no body angular motion ($q = 0$, $p = 0$), then

$$\begin{aligned} \beta_{1c} + \theta_{1s} &= \text{constant} \\ \beta_{1s} - \theta_{1c} &= \text{constant} \end{aligned} \tag{D.3.165}$$

The above is the same as equation (B.6.4) on page 200.

D.3.7.5 Blade Equation of Motion for Forward Flight: Constant Blade Flap Coefficients

The fundamental equation of motion for a flapping blade in forward flight is given by equation (D.3.117) on page 298, and is reproduced below for convenience

$$\begin{aligned} \beta'' + \frac{\gamma}{8} K_{\dot{\beta}} \beta' + \left(\nu^2 + \frac{\gamma}{8} K_{\beta\mu} \right) \beta &= \frac{\gamma}{8} K_\theta \theta - \frac{\gamma}{8} K_\lambda \lambda \\ &+ \left(\frac{\gamma}{8} K_{pq} \frac{p}{\Omega} - 2\nu_\beta^2 \left(\frac{q}{\Omega} \right) \right) \sin \psi \\ &+ \left(2\nu_\beta^2 \left(\frac{p}{\Omega} \right) + \frac{\gamma}{8} K_{pq} \frac{q}{\Omega} \right) \cos \psi + \nu_0^2 \beta_P \end{aligned} \tag{D.3.166}$$

where the transformation equation (D.3.13) on page 262 is used. Discard slow body rates of change dynamics ($\dot{q}, \dot{p} \rightarrow \text{small}$) and the hub precone β_P to obtain

$$\begin{aligned} \beta'' + \frac{\gamma}{8} K_{\dot{\beta}} \beta' + \left(\nu^2 + \frac{\gamma}{8} K_{\beta\mu} \right) \beta &= \frac{\gamma}{8} K_{\theta} \theta - \frac{\gamma}{8} K_{\lambda} \lambda \\ &+ \left(\frac{\gamma}{8} K_{pq} \frac{p}{\Omega} - 2\nu_{\beta}^2 \frac{q}{\Omega} \right) \sin \psi + \left(2\nu_{\beta}^2 \frac{p}{\Omega} + \frac{\gamma}{8} K_{pq} \frac{q}{\Omega} \right) \cos \psi \end{aligned} \quad (\text{D.3.167})$$

Substituting equation (D.3.114) and equation (D.3.116) on page 297 into (D.3.167), and after performing trigonometric reduction and harmonic balancing gives

$$\begin{aligned} \left(\frac{1}{3} - \frac{e}{2} \right) \left((\mu\theta_{1s} + \lambda) - \frac{p}{2\Omega} \mu \right) - \left(\frac{(e-1)^2 \mu^2}{4} + \left(\frac{1}{4} - \frac{e}{3} \right) \right) \theta_0 \\ + \left(e - \frac{1}{2} \right) \frac{e\mu}{2} \beta_{1c} + \frac{8\nu^2}{\gamma} \beta_0 = 0 \\ \left(\frac{(e-1)^2 \mu^2}{8} + \left(\frac{1}{4} - \frac{e}{3} \right) \right) \theta_{1c} - (\nu^2 - 1) \beta_{1c} + \left(\frac{1}{3} - \frac{e}{2} \right) \mu \beta_0 \\ - \left(\left(1 - \frac{8e}{3} + 2e^2 \right) + \frac{(e-1)^2 \mu^2}{2} \right) \frac{\beta_{1s}}{4} + \left(\frac{e}{3} - \frac{1}{4} \right) \frac{q}{\Omega} - \frac{16\nu_{\beta}^2 p}{\gamma \Omega} = 0 \quad (\text{D.3.168}) \\ \left(\frac{3(e-1)^2 \mu^2}{8} - \left(\frac{e}{3} - \frac{1}{4} \right) \right) \theta_{1s} + \left(e - \frac{2}{3} \right) \mu \theta_0 \\ + \frac{(e-1)^2 \mu}{2} \lambda - (\nu^2 - 1) \beta_{1s} + \left(\frac{e}{3} - \frac{1}{4} \right) \frac{p}{\Omega} \\ - \left(\frac{(e-1)^2 \mu^2}{2} - \left(1 - \frac{8e}{3} + 2e^2 \right) \right) \frac{\beta_{1c}}{4} + \frac{16\nu_{\beta}^2 q}{\gamma \Omega} = 0 \end{aligned}$$

In an effort to make the math tractable, the above expression discards higher powers of e and μ which restrict results to low advance ratio μ but with no loss of generality. Solving for the flap coefficients still results on very cumbersome and long expressions. To once again make the algebra tractable, the resulting flap coefficients are given for the case when the hinge offset is zero $e = 0$, and $\varepsilon = 0$, $\nu_{\beta} = 1$, $\nu^2 = 1 + K_{\beta} / I_{\beta} \Omega^2$ (see equation (D.3.116))

on page 297). Use the definition for stiffness number in equation (D.3.19) on page 263

$$\begin{aligned} S_\beta &= \frac{8}{\gamma} (\nu^2 - 1) \\ S_\mu &= \left(1 - \frac{\mu^4}{4}\right) + S_\beta^2 \end{aligned} \quad (\text{D.3.169})$$

The resulting flapping coefficients are then

$$\begin{aligned} \beta_0 &= \frac{\gamma}{8\nu^2} \left[\theta_0 (1 + \mu^2) - \frac{4}{3} (\mu\theta_{1s} + \lambda) + \frac{2\mu p}{3\Omega} \right] \\ \left(1 - \frac{\mu^4}{4} + S_\beta^2\right) \beta_{1s} &= \frac{8}{\gamma} \mu S_\beta \left(2\lambda - \frac{\gamma}{3} \theta_0\right) + \left(1 + \frac{3}{2} \mu^2\right) S_\beta \theta_{1s} \\ &\quad + \frac{4\mu}{3} \beta_0 + (S_\mu - S_\beta) \theta_{1c} \\ + \left(\frac{16}{\gamma} S_\beta + \frac{\mu^2}{2} - 1\right) \frac{q}{\Omega} - \left(S_\beta - \frac{16}{\gamma} \left(\frac{\mu^2}{2} - 1\right)\right) \frac{p}{\Omega} \end{aligned} \quad (\text{D.3.170})$$

$$\begin{aligned} \left(1 - \frac{\mu^4}{4} + S_\beta^2\right) \beta_{1c} &= 4 \left(1 + \frac{2}{3} \mu^2\right) \mu \theta_0 - (1 + 4\mu^2) \theta_{1s} \\ &\quad + \left(1 + \frac{\mu^2}{2}\right) S_\beta \theta_{1c} - \left(\frac{8}{\gamma}\right) \left(\frac{4\mu}{3}\right) \beta_0 - (4 + \mu^2) \mu \lambda \\ - \left(\frac{16}{\gamma} S_\beta + \frac{4}{3} \mu^2 - 1\right) \frac{p}{\Omega} - \left(S_\beta + \frac{16}{\gamma} \left(1 + \frac{\mu^2}{2}\right)\right) \frac{q}{\Omega} \end{aligned}$$

For the case when the advance ratio is zero $\mu = 0$ the flapping coefficients become

$$\begin{aligned} \beta_0 &= \frac{\gamma}{8\nu^2} \left[\theta_0 - \frac{4}{3} \lambda \right] \\ (1 + S_\beta^2) \beta_{1s} &= S_\beta \theta_{1s} + \theta_{1c} + \left(\frac{16}{\gamma} S_\beta - 1\right) \frac{q}{\Omega} - \left(S_\beta + \frac{16}{\gamma}\right) \frac{p}{\Omega} \\ (1 + S_\beta^2) \beta_{1c} &= S_\beta \theta_{1c} - \theta_{1s} - \left(\frac{16}{\gamma} S_\beta - 1\right) \frac{p}{\Omega} - \left(S_\beta + \frac{16}{\gamma}\right) \frac{q}{\Omega} \end{aligned} \quad (\text{D.3.171})$$

For a teetering rotor ($e = 0$) in forward flight ($\mu \neq 0$) when the hub or blade spring is zero ($K_\beta = 0$), then $\nu^2 = 1$ and the constant flapping coefficient solution to equation (D.3.167)

on page 312 becomes

$$\begin{aligned}
\beta_0 &= \frac{\gamma}{8} \left[(1 + \mu^2) \theta_0 - \frac{4}{3} (\mu\theta_{1s} + \lambda) + \frac{2\mu p}{3 \Omega} \right] \\
\left(1 - \frac{\mu^2}{2}\right) \beta_{1c} &= \frac{8}{3} \mu \theta_0 - 2\mu\lambda - \left(1 + \frac{3\mu^2}{2}\right) \theta_{1s} + \frac{p}{\Omega} - \frac{16 q}{\gamma \Omega} \\
\left(1 + \frac{\mu^2}{2}\right) \beta_{1s} &= \frac{4}{3} \mu \beta_0 + \left(1 + \frac{\mu^2}{2}\right) \theta_{1c} - \frac{q}{\Omega} - \frac{16 p}{\gamma \Omega}
\end{aligned} \tag{D.3.172}$$

For small advance ratio $\mu \ll 1$

$$\begin{aligned}
\beta_0 &= \frac{\gamma}{8} \left[\theta_0 - \frac{4}{3} (\mu\theta_{1s} + \lambda) + \frac{2\mu p}{3 \Omega} \right] \\
\beta_{1c} &= \frac{8}{3} \mu \theta_0 - 2\mu\lambda - \theta_{1s} + \frac{p}{\Omega} - \frac{16 q}{\gamma \Omega} \\
\beta_{1s} &= \frac{4}{3} \mu \beta_0 + \theta_{1c} - \frac{q}{\Omega} - \frac{16 p}{\gamma \Omega}
\end{aligned} \tag{D.3.173}$$

For hover flight the advance ratio is zero $\mu = 0$ and the above simplifies to

$$\begin{aligned}
\beta_0 &= \frac{\gamma}{8} \left(\theta_0 - \frac{4}{3} \lambda \right) \\
\beta_{1c} &= -\theta_{1s} + \frac{p}{\Omega} - \frac{16 q}{\gamma \Omega} \\
\beta_{1s} &= \theta_{1c} - \frac{q}{\Omega} - \frac{16 p}{\gamma \Omega}
\end{aligned} \tag{D.3.174}$$

D.4 Summary of Blade Equations of Motion

Table D.1: Summary of Blade Equations of Motion

Fundamental blade EOM	Equation (D.3.117) on page 298
thrust coefficient C_T in forward flight	Equation (D.3.122) on page 299
torque coefficient C_Q in forward flight	Equation (D.3.124) on page 300
teetering rotor $e = 0$	Equation (D.3.125) on page 300
symmetric flight	Equation (D.3.126) on page 301
$q, \dot{q}, p, \dot{p} \rightarrow small$	
Non-constant blade flap coefficients	Equation (D.3.134) on page 303
low frequency dynamics	Equation (D.3.142) on page 305
$\dot{q}, \dot{p} \rightarrow small$	
low translational speed $\mu \rightarrow small$	Equation (D.3.147) on page 307
$e = 0, \beta_P = 0$	Equation (D.3.149) on page 307
no hub precone	
discard conning dynamics	Equation (D.3.151) on page 308
discard higher order terms	Equation (D.3.154) on page 308
Simplified 1st order TPP	Equation (D.3.156) on page 309
teetering rotor	Equation (D.3.162) on page 310
simplified teetering EOM	Equation (D.3.164) on page 310
Constant blade flap coefficient	Equation (D.3.168) on page 312
discard higher order terms	Equation (D.3.170) on page 313
$e^2, \mu^2 \rightarrow small$	
no advance ratio $\mu = 0$	Equation (D.3.171) on page 313
teetering rotor $e = 0$	Equation (D.3.172) on the preceding page
small advanced ratio	Equation (D.3.173) on the previous page
$\mu \rightarrow small$	
hovering $\mu = 0$	Equation (D.3.174) on the preceding page

Appendix E

Helicopter Rotor Forces and Moments

Section B.6 on page 196 explores the relationship among the various reference frames for the helicopter rotor. Figure E.1 on page 318 and Figure D.10 on page 293 show the relevant parameters pertaining to the rotor forces and moments with the hub plane (HP) as a reference plane. Work related to rotor forces and moments are fundamental for the development of helicopter dynamic models and control laws. Early work by Glauert [54, 55, 57], Goldstein [58], and Lock [98] established a theoretical basis for the physics based modeling of the helicopter aerodynamic. More contemporary work resulted in the development and application of standard models for rotor forces and moments [21, 22, 23, 25, 68]. Modern references to the subject can be found in Johnson [82], Leishman [92], Padfield [119] and Prouty [124] which detail derivations of the rotor forces and moments.

E.1 Aerodynamic Rotor Forces and Moments

The advance ratio μ and the inflow ratio λ are defined in section §C.1.3 (page 217) by equations (C.1.48) and (C.1.49), and are reproduced below for convenience

$$\begin{aligned}\mu &= \frac{V \cos \alpha}{\Omega R} \\ \lambda &= \frac{v_i + V \sin \alpha}{\Omega R} = \mu \tan \alpha + \lambda_i\end{aligned}\tag{E.1.1}$$

where the above inflow value for the main (and tail) rotor result from momentum theory in equation (C.1.52) (page 219)

$$\lambda = \mu \tan \alpha + \frac{C_T}{2\sqrt{\mu^2 + \lambda^2}}\tag{E.1.2}$$

For small angle of attack $\alpha \rightarrow$ small, the advance ratio $\mu = V \cos \alpha / \Omega R \approx V / \Omega R$ is independent of the reference frame. Also, the thrust T_{MR} is an order of magnitude larger than the other rotor forces, and in this case, the rotor thrust T_{MR} is approximately independent of the reference plane. Based on the relations among the various rotor reference frames in equation (B.6.4), section §B.6.4 (page 200) the following holds [13, 92]

$$\begin{aligned}
\beta_{1c} + \theta_{1s} &= \text{constant} = [\beta_{1c}]_{NFP} = [\theta_{1s}]_{TPP} \\
\beta_{1s} - \theta_{1c} &= \text{constant} = [\beta_{1s}]_{NFP} = [\theta_{1c}]_{TPP} \\
[\mu]_{HP} &\approx [\mu]_{TPP} \approx [\mu]_{NFP} = \mu \\
[\lambda]_{HP} &= \lambda = [\lambda]_{TPP} + \mu \beta_{1c} = [\lambda]_{NFP} - \mu \theta_{1s} \\
[\alpha]_{TPP} &= [\alpha]_{NFP} - (\beta_{1c} + \theta_{1s}) \\
[\alpha]_{HP} &= \alpha = [\alpha]_{TPP} + \beta_{1c} = [\alpha]_{NFP} - \theta_{1s} \\
[C_T]_{HP} &\approx [C_T]_{TPP} \approx [C_T]_{NFP} = C_T \\
[C_H]_{HP} &= C_H = [C_H]_{NFP} - \theta_{1s} C_T = [C_H]_{TPP} + \beta_{1c} C_T \\
[C_Y]_{HP} &= C_Y = [C_Y]_{NFP} + \theta_{1c} C_T = [C_Y]_{TPP} + \beta_{1s} C_T
\end{aligned} \tag{E.1.3}$$

In section §C.2, Figure C.6 on page 223 illustrates the relationship between the various parameters associated with forces on rotor blades. A summary of results [82, 92] from equations (C.2.1) through (C.2.12) follows. Based on diagrams in Figure E.1 on the next page and Figure D.10 on page 293, and rearranging equations (C.2.6) and (C.2.8) results in the following set of equations [13, 11, 82, 92]:

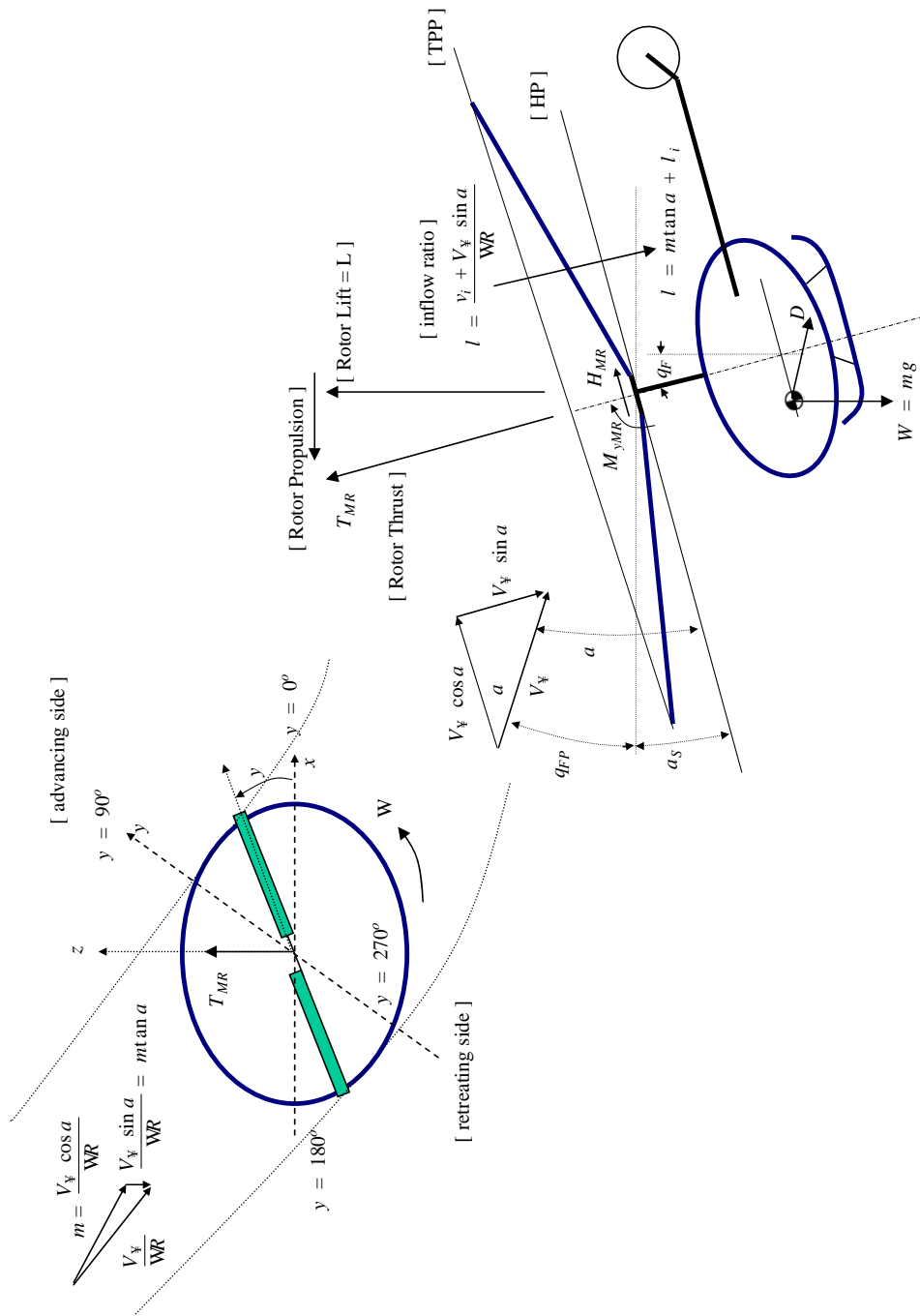


Figure E.1: Rotor Forces and Moments.

$$\begin{aligned}
dL &= \frac{1}{2}\rho U^2 c C_l dr = \frac{1}{2}\rho U_T^2 c C_{l_\alpha} \left(\theta - \frac{U_P}{U_T} \right) dr \\
&= \frac{1}{2}\rho c C_{l_\alpha} (\theta U_T^2 - U_T U_P) dr \\
dD &= \frac{1}{2}\rho U^2 c C_d dr = \frac{1}{2}\rho c C_d U_T^2 dr \\
dF_z &= dL \cos \phi - dD \sin \phi \approx dL \\
&\approx \frac{1}{2}\rho c C_{l_\alpha} (\theta U_T^2 - U_T U_P) dr \\
dF_x &= dL \sin \phi + dD \cos \phi \approx dL \phi - dD \\
&\approx \frac{1}{2}\rho c C_{l_\alpha} \left(\theta U_T U_P - U_P^2 + \frac{C_d}{C_{l_\alpha}} U_T^2 \right) dr \\
dF_r &= -dF_z \sin \beta + D_{radial} = [dL \cos \phi - dD \sin \phi] \sin \beta \\
&\approx -\frac{1}{2}\rho c \beta C_{l_\alpha} (\theta U_T^2 - U_T U_P) dr
\end{aligned} \tag{E.1.4}$$

Multiply times the number of blades to obtain loads on the entire rotor, and integrating from $0 \rightarrow 2\pi$ to find the average over one revolution to get [13, 92]

$$\begin{aligned}
T_{MR} &= \frac{b}{2\pi} \int_0^{2\pi} \int_0^{R(1-e)} dF_z d\psi \\
H_{MR} &= \frac{b}{2\pi} \int_0^{2\pi} \int_0^{R(1-e)} [dF_x \sin \psi + dF_r \cos \psi] d\psi \\
Y_{MR} &= \frac{b}{2\pi} \int_0^{2\pi} \int_0^{R(1-e)} [-dF_x \cos \psi + dF_r \sin \psi] d\psi \\
Q_{MR} &= \frac{b}{2\pi} \int_0^{2\pi} \int_0^{R(1-e)} (r + eR) dF_x d\psi \\
M_{xMR} &= \frac{b}{2\pi} \int_0^{2\pi} M_{MR} \sin \psi d\psi \\
M_{yMR} &= -\frac{b}{2\pi} \int_0^{2\pi} M_{MR} \cos \psi d\psi
\end{aligned} \tag{E.1.5}$$

where M_{MR} is the main rotor moment about the hub. A non dimensional version of equation (E.1.5) requires non-dimensional velocities such that

$$u_T = \frac{U_T}{\Omega R}, u_P = \frac{U_P}{\Omega R}, a = C_{l_\alpha}, \gamma = \rho a c R^4, \sigma = \frac{bc}{\pi R}, b = \# \text{ of blades}$$

The non-dimensional force equations become

$$\begin{aligned}
C_{T_{MR}} &= \frac{T_{MR}}{\rho (\pi R^2) (\Omega R)^2} \\
&= \frac{\rho abc}{2\rho (\pi R^2) (\Omega R)^2} \frac{R (\Omega R)^2}{2\pi} \int_0^{2\pi} \int_0^{(1-e)} (\theta u_T^2 - u_T u_P) dx d\psi \\
&= \frac{a\sigma}{4\pi} \int_0^{2\pi} \int_0^{(1-e)} (\theta u_T^2 - u_T u_P) dx d\psi \\
C_{H_{MR}} &= \frac{H_{MR}}{\rho (\pi R^2) (\Omega R)^2} \\
&= \frac{a\sigma}{4\pi} \int_0^{2\pi} \int_0^{(1-e)} \left[\begin{array}{l} \left(\theta u_T u_P - u_P^2 + \frac{C_d}{a} u_T^2 \right) \sin \psi \cdots \\ -\beta (\theta u_T^2 - u_T u_P) \cos \psi \end{array} \right] dx d\psi \\
C_{Y_{MR}} &= \frac{Y_{MR}}{\rho (\pi R^2) (\Omega R)^2} \\
&= -\frac{a\sigma}{4\pi} \int_0^{2\pi} \int_0^{(1-e)} \left[\begin{array}{l} \left(\theta u_T u_P - u_P^2 + \frac{C_d}{a} u_T^2 \right) \cos \psi \cdots \\ +\beta (\theta u_T^2 - u_T u_P) \sin \psi \end{array} \right] dx d\psi
\end{aligned} \tag{E.1.6}$$

The aerodynamic rotor torque takes the form

$$\begin{aligned}
Q_{MR} &= \frac{b}{2\pi} \int_0^{2\pi} \int_0^{R(1-e)} (eR + r) dF_x d\psi \\
&= \frac{\rho abc R^2 (\Omega R)^2}{2} \frac{1}{2\pi} \int_0^{2\pi} \int_0^{(1-e)} (e + x) \left(\theta u_T u_P - u_P^2 + \frac{C_d}{a} u_T^2 \right) dx d\psi \\
C_Q &= \frac{Q_{MR}}{\rho (\pi R^2) R (\Omega R)^2} \\
&= \frac{a\sigma}{4\pi} \int_0^{2\pi} \int_0^{(1-e)} (e + x) \left(\theta u_T u_P - u_P^2 + \frac{C_d}{a} u_T^2 \right) dx d\psi
\end{aligned} \tag{E.1.7}$$

A general expression for the velocities seen at each blade element is given by equation (D.3.107) on page 295 and reproduced below for convenience

$$\begin{aligned}
u_T &= \frac{U_T}{\Omega R} = (x + e) + \mu \sin \psi \\
u_P &= \frac{U_P}{\Omega R} = \lambda + x \frac{\dot{\beta}}{\Omega} + \mu \beta \cos \psi - (e + x) \left(\frac{p}{\Omega} \sin \psi + \frac{q}{\Omega} \cos \psi \right) \\
&\approx \lambda + x \frac{\dot{\beta}}{\Omega} + \beta \mu \cos \psi - x \left(\frac{p}{\Omega} \sin \psi + \frac{q}{\Omega} \cos \psi \right) \\
u_r &= \frac{U_R}{\Omega R} = \mu \cos \psi
\end{aligned} \tag{E.1.8}$$

E.2 Rotor Forces

After integration of equation (E.1.5) on page 319 and equation (E.1.6) on the preceding page with the velocity at each blade element given by equation (E.1.8), the following expressions give results for the average steady state forces. The thrust coefficient C_T is given by equation (D.3.121) on page 299 and is reproduced below for convenience

$$\begin{aligned}
\frac{2C_T}{\sigma a} &= \left(\frac{(1 - e^3)}{3} + \frac{(1 - e)}{2} \mu^2 \right) \theta_0 + \frac{(e^2 - 1)}{2} \lambda \\
&\quad + \left((e^2 - 1) \theta_{1s} + (1 - e) e \beta_{1c} + \frac{(1 - e^2) p}{2 \Omega} \right) \frac{\mu}{2}
\end{aligned} \tag{E.2.1}$$

The longitudinal force coefficient C_H takes the following form

$$\begin{aligned}
\frac{2C_H}{\sigma a} &= (1 - e^2) \frac{\mu C_D}{2} + \left((4 - 3e - e^3) \beta_{1c} + 2(e^3 - 1) \frac{p}{\Omega} \right) \frac{\theta_0}{12} \\
&\quad + \left((e - 3) \beta_{1c} + (e + 1) \left(2 \frac{p}{\Omega} - \theta_{1s} \right) + 2\mu \theta_0 \right) \frac{(1 - e) \lambda}{4} \\
&\quad + \frac{(e - 1) \mu \theta_{1s}}{4} \left(\frac{(e - 2)}{2} \beta_{1c} + \frac{3(e + 1) p}{4 \Omega} \right) \\
&\quad + \frac{(1 - e) \theta_{1c}}{4} \left(\frac{2(1 + e + e^2)}{3} \beta_0 - \frac{e\mu}{2} \beta_{1s} + \frac{(e + 1) \mu q}{4 \Omega} \right) \\
&\quad + \frac{(e^2 - 1) \mu \beta_{1c} p}{16 \Omega} + \left(\frac{2(e^3 - 1)}{3} \beta_0 + \frac{(e^2 - 1) \mu}{4} \beta_{1s} \right) \frac{q}{4\Omega} \\
&\quad - \frac{2 + 3e + e^2}{12} \beta_0 \beta_{1s} + \frac{(1 - e) \mu}{4} \left((e + 1) \beta_0^2 + \frac{(e + 2)}{2} \beta_{1c}^2 + \frac{e}{2} \beta_{1s}^2 \right)
\end{aligned} \tag{E.2.2}$$

For a teetering rotor the hinge offset is zero ($e = 0$) then

$$\begin{aligned} \frac{2C_H}{\sigma a} = & \frac{\mu C_D}{2} + \left(4\beta_{1c} - 2\frac{p}{\Omega}\right) \frac{\theta_0}{12} + \left(-3\beta_{1c} + 2\mu\theta_0 - \theta_{1s} + 2\frac{p}{\Omega}\right) \frac{\lambda}{4} \\ & + \frac{\mu\theta_{1s}}{4} \left(\frac{3p}{4\Omega} - \beta_{1c}\right) + \frac{\theta_{1c}}{4} \left(\frac{2}{3}\beta_0 + \frac{\mu q}{4\Omega}\right) \\ & - \frac{\mu\beta_{1c} p}{16\Omega} - \left(\frac{2}{3}\beta_0 + \frac{\mu}{4}\beta_{1s}\right) \frac{q}{4\Omega} - \frac{\beta_0\beta_{1s}}{6} + \frac{\mu}{4} (\beta_0^2 + \beta_{1c}^2) \end{aligned} \quad (\text{E.2.3})$$

For a teetering rotor in hover ($e = 0, \mu = 0$)

$$\frac{2C_H}{\sigma a} = \left(2\beta_{1c} - \frac{p}{\Omega}\right) \frac{\theta_0}{6} - \left(3\beta_{1c} + \theta_{1s} - 2\frac{p}{\Omega}\right) \frac{\lambda}{4} + \left(\theta_{1c} - \frac{q}{\Omega} - \beta_{1s}\right) \frac{\beta_0}{6} \quad (\text{E.2.4})$$

The corresponding average steady state lateral force coefficient C_Y takes the form

$$\begin{aligned} \frac{2C_Y}{\sigma a} = & \left((e-3)\beta_{1s} + 6\mu\beta_0 - 2(e+1)\frac{q}{\Omega}\right) \frac{(1-e^2)\lambda}{4} \\ & + \left(\frac{(4+e+e^2+6\mu^2)\beta_{1s}}{3} - 3(e+1)\mu\beta_0 + \frac{2(1+e+e^2)q}{3\Omega}\right) \frac{(1-e^2)\theta_0}{4} \\ & + \left((e+1)\lambda - \left(\frac{3e}{2} + 1\right)\mu\beta_{1c} - \frac{(e+1)\mu p}{4\Omega}\right) \frac{(1-e^2)\theta_{1c}}{4} \\ & + \left(\frac{2(1+e+e^2+3\mu^2)\beta_0}{3} - \frac{(4+3e)\mu\beta_{1s}}{2} - \frac{(e+1)\mu q}{4\Omega}\right) \frac{(1-e^2)\theta_{1s}}{4} \\ & + \left(\frac{2(e^3-1)}{3}\beta_0 + \frac{5(e^2-1)\mu}{4}\beta_{1s}\right) \frac{p}{4\Omega} - \frac{7(e^2-1)\mu\beta_{1c} q}{16\Omega} \\ & - \left(\frac{(e+e^2+12\mu^2-2)}{3}\beta_0 - \mu\beta_{1s}\right) \frac{(1-e^2)\beta_{1c}}{4} \end{aligned} \quad (\text{E.2.5})$$

For a teetering rotor the hinge offset is zero ($e = 0$) then

$$\begin{aligned} \frac{2C_Y}{\sigma a} = & \left(6\mu\beta_0 - 3\beta_{1s} - 2\frac{q}{\Omega}\right) \frac{\lambda}{4} + \left(\frac{(4+6\mu^2)}{3}\beta_{1s} - 3\mu\beta_0 + \frac{2q}{3\Omega}\right) \frac{\theta_0}{4} \\ & + \left(\lambda - \mu\beta_{1c} - \frac{\mu p}{4\Omega}\right) \frac{\theta_{1c}}{4} + \left(\frac{2(1+3\mu^2)\beta_0}{3} - 2\mu\beta_{1s} - \frac{\mu q}{4\Omega}\right) \frac{\theta_{1s}}{4} \\ & + \left(\frac{5\mu}{4}\beta_{1s} - \frac{2}{3}\beta_0\right) \frac{p}{4\Omega} - \frac{7\mu\beta_{1c} q}{16\Omega} + \left(\mu\beta_{1s} + \frac{(2-12\mu^2)}{3}\beta_0\right) \frac{\beta_{1c}}{4} \end{aligned} \quad (\text{E.2.6})$$

For a teetering rotor in hover ($e = 0, \mu = 0$)

$$\frac{2C_Y}{\sigma a} = \left(\theta_{1c} - 3\beta_{1s} - 2\frac{q}{\Omega} \right) \frac{\lambda}{4} + \left(\frac{4}{3}\beta_{1s} + \frac{2}{3}\frac{q}{\Omega} \right) \frac{\theta_0}{4} + \frac{\beta_0\theta_{1s}}{6} + \frac{\beta_0\beta_{1c}}{6} - \frac{\beta_0}{6} \frac{p}{\Omega} \quad (\text{E.2.7})$$

E.2.1 Simplified Rotor Forces

The disc incidence and blade flapping arrangement are given in Section §B.6.4 by Figure B.9 on page 199 and equation (B.6.4) on page 200. From these, the rotor hub forces are given by [82, 119]

$$\begin{aligned} \alpha &= \alpha_{HP} = \alpha_{NFP} - \theta_{1s} = \alpha_{TPP} + \beta_{1c} \\ H_{HP} &= H_{NFP} - T\theta_{1s} = H_{TPP} + T\beta_{1c} \\ Y_{HP} &= Y_{NFP} + T\theta_{1c} = Y_{TPP} + T\beta_{1s} \end{aligned} \quad (\text{E.2.8})$$

where the force $X = -H$ in which case an equivalent expression for the longitudinal force would be

$$X_{HP} = X_{NFP} + T\theta_{1s} = X_{TPP} - T\beta_{1c} \quad (\text{E.2.9})$$

The fundamental assumption is that the thrust vector has the same magnitude in all three rotor axis frames [119], and remains orthogonal to the TPP. This assumption usually holds true for hover and low speed flight [13, 105]. Under this assumption, the Tip Path Plane (TPP) forces in (E.2.8) and (E.2.9) are zero ($X_{TPP} = 0, Y_{TPP} = 0$) such that the projection of the thrust vector (in Figure E.2) onto the hub plane gives

$$\begin{aligned} X_{MR} &= -T \cos \beta_{1s} \sin \beta_{1c} \approx -T \beta_{1c} \\ Y_{MR} &= T \cos \beta_{1c} \sin \beta_{1s} \approx T \beta_{1s} \\ Z_{MR} &= -T \cos \beta_{1s} \cos \beta_{1c} \approx -T \end{aligned} \quad (\text{E.2.10})$$

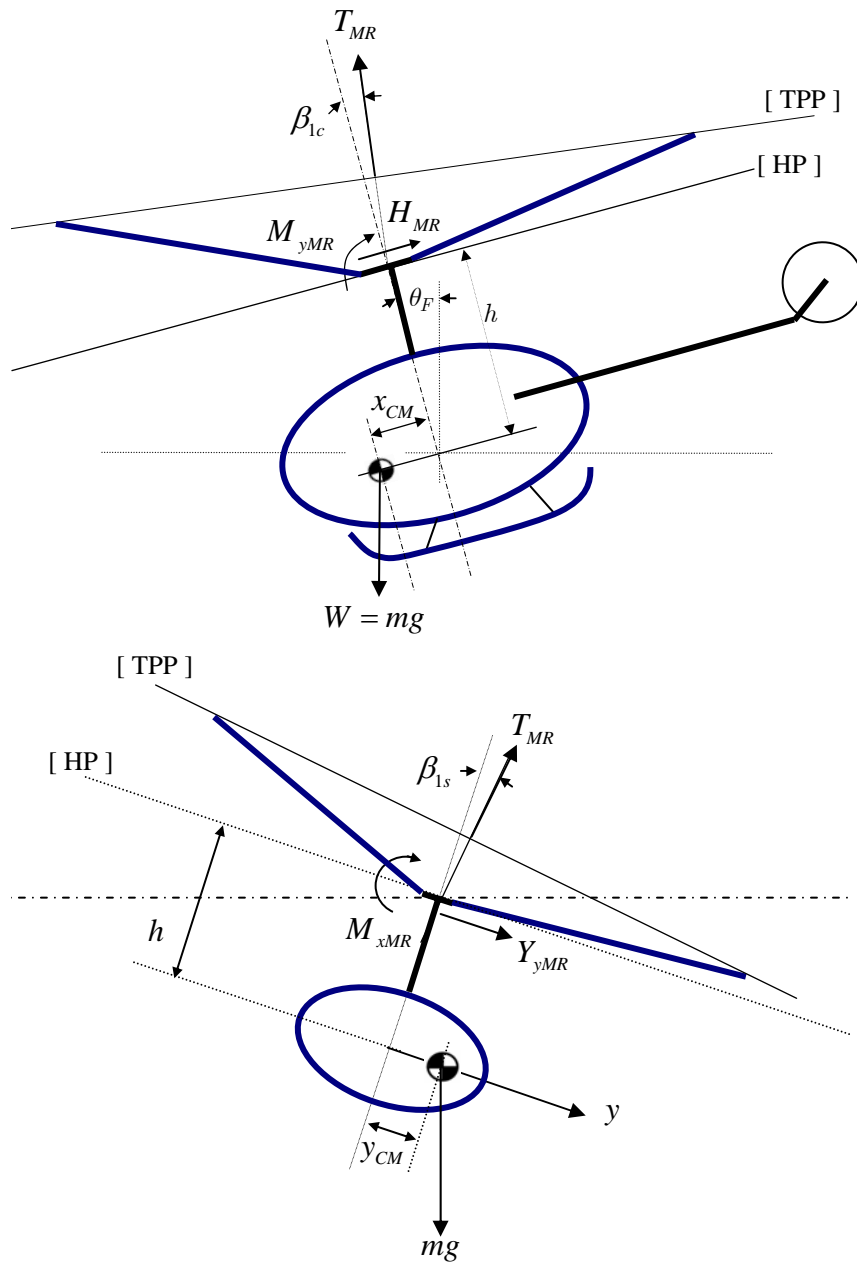


Figure E.2: Forces and Moments with Blade Flap Angles

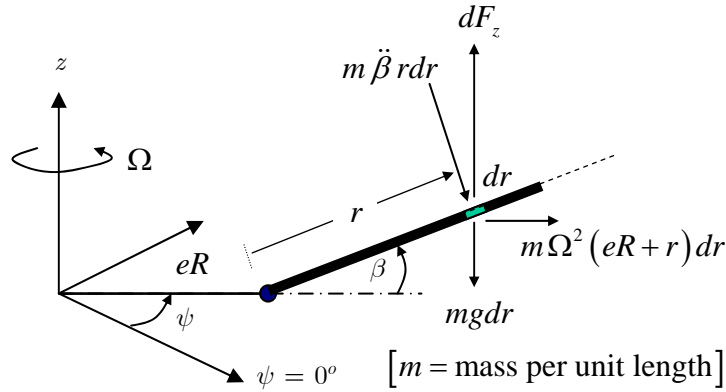


Figure E.3: Blade force equilibrium

E.3 Rotor Hub Moments

The main rotor moment M_{MR} about the hub center results from the sum of all forces acting on the blade element δm as shown in Figure E.3. The blade weight $r mg$ is usually very small compared to the other forces, and can be neglected. The forces acting on a blade element m and the moment arm associated with the relevant force are summarized in Table E.1 The moment about the hub center is given by

	force	moment arm
inertial:	$m \ddot{\beta} r dr$	$eR + r$
centrifugal:	$\Omega^2 (eR + r) m dr$	$r \beta$
aerodynamic:	F_z	$eR + r$

$$\begin{aligned}
 M_{hub} = & - \int_0^{R(1-e)} (eR + r) (m \ddot{\beta} r dr) - \int_0^{R(1-e)} [\Omega^2 m (eR + r) dr] (r \beta) \\
 & + \int_0^{R(1-e)} (eR + r) dF_z
 \end{aligned} \tag{E.3.1}$$

The terms $\ddot{\beta}$, β , Ω do not take part in the integration and can come outside the integral such that

$$M_{hub} = -\Omega^2 \left(\frac{\ddot{\beta}}{\Omega^2} + \beta \right) \left[\int_0^{R(1-e)} m(eR+r) r dr \right] + \int_0^{R(1-e)} (eR+r) dF_z \quad (\text{E.3.2})$$

In addition, the term $\ddot{\beta}$ is given by the fundamental flap equation (D.2.23) on page 243

$$\ddot{\beta} + \Omega^2 \nu^2 \beta = \frac{M_{aero}}{I_\beta} \quad (\text{E.3.3})$$

or in a more general case, the flap equation for a rigid rotor modeled as a rotor with hinge offset, hub precone and blade flap restoring spring as given by equation (D.3.115) on page 297

$$\begin{aligned} \ddot{\beta} + \Omega^2 \nu^2 \beta &= \frac{M_a}{I_\beta} + 2\Omega \nu_\beta^2 (p \cos \psi - q \sin \psi) + \nu_\beta^2 (\dot{p} \sin \psi + \dot{q} \cos \psi) + \nu_0^2 \beta_P \\ \frac{\ddot{\beta}}{\Omega^2} + \nu^2 \beta &= \frac{M_{aero}}{\Omega^2 I_\beta} + C_0 \\ C_0 &= 2\nu_\beta^2 \left(\frac{p}{\Omega} \cos \psi - \frac{q}{\Omega} \sin \psi \right) + \nu_\beta^2 \left(\frac{\dot{p}}{\Omega^2} \sin \psi + \frac{\dot{q}}{\Omega^2} \cos \psi \right) + \frac{\nu_0^2 \beta_P}{\Omega^2} \end{aligned} \quad (\text{E.3.4})$$

where ν^2 and ν_0^2 are given by equation (D.3.100) on page 292. Substituting equation (E.3.4) in equation (E.3.2) gives

$$\begin{aligned} M_{hub} &= -\Omega^2 \left[\int_0^{R(1-e)} m(eR+r) r dr \right] \left[(1 - \nu^2) \beta + \frac{M_{aero}}{I_\beta \Omega^2} + C_0 \right] \\ &\quad + \int_0^{R(1-e)} (eR+r) dF_z \end{aligned} \quad (\text{E.3.5})$$

where the blade mass moment of inertia about the hub center is

$$[I_b]_{Hub} = {}^H I_b = \int_0^{R(1-e)} m(eR+r) r dr \quad (\text{E.3.6})$$

and the blade aerodynamic moment about the hub center

$$M_{aero} = \int_0^{R(1-e)} (eR + r) dF_z \quad (\text{E.3.7})$$

The resultant moment about the hub center is [27, 82, 92, 110, 119, 120]

$$M_{hub} = I_b \Omega^2 (\nu^2 - 1) \beta - I_b \Omega^2 C_0 \quad (\text{E.3.8})$$

The average pitch and roll moment about the hub center are

$$\begin{aligned} M_{xMR} &= \frac{b}{2\pi} \int_0^{2\pi} M_{hub} \sin \psi d\psi \\ M_{yMR} &= -\frac{b}{2\pi} \int_0^{2\pi} M_{hub} \cos \psi d\psi \end{aligned} \quad (\text{E.3.9})$$

and the corresponding pitch and roll moment coefficients are

$$\begin{aligned} C_{xMR} &= \frac{M_{xMR}}{\rho (\pi R^2) R (\Omega R)^2} \\ &= \frac{I_b \Omega^2}{\rho (\pi R^2) R (\Omega R)^2} \frac{ac}{ac} \frac{b}{2\pi} \int_0^{2\pi} ((\nu^2 - 1) \beta - C_0) \sin \psi d\psi \\ &= \frac{a\sigma (\nu^2 - 1)}{\gamma} \frac{1}{2\pi} \int_0^{2\pi} \beta \sin \psi d\psi \\ C_{yMR} &= \frac{M_{yMR}}{\rho (\pi R^2) R (\Omega R)^2} \\ &= -\frac{a\sigma}{2\pi\gamma} \int_0^{2\pi} ((\nu^2 - 1) \beta - C_0) \cos \psi d\psi \end{aligned} \quad (\text{E.3.10})$$

Substituting the blade flap angle $\beta = \beta_0 - \beta_{1c} \cos \psi - \beta_{1s} \sin \psi$ in the above equation (E.3.10). Using the following integration formulas

$$\begin{aligned} \int_0^{2\pi} \sin \psi d\psi &= \int_0^{2\pi} \cos \psi d\psi = \int_0^{2\pi} \sin^2 \psi \cos \psi d\psi = 0 \\ \int_0^{2\pi} \sin \psi \cos \psi d\psi &= 0 \\ \int_0^{2\pi} \sin^2 \psi d\psi &= \int_0^{2\pi} \cos^2 \psi d\psi = \pi \end{aligned} \tag{E.3.11}$$

and integrating equation (E.3.10) gives [27, 82]

$$\begin{aligned} C_{HxMR} &= \frac{a\sigma}{2\gamma} \left((\nu^2 - 1) \beta_{1s} + 2\nu_\beta^2 \left(\frac{q}{\Omega} - \frac{\dot{p}}{2\Omega^2} \right) \right) \\ C_{HyMR} &= -\frac{a\sigma}{2\gamma} \left((\nu^2 - 1) \beta_{1c} - 2\nu_\beta^2 \left(\frac{p}{\Omega} + \frac{\dot{q}}{2\Omega^2} \right) \right) \end{aligned} \tag{E.3.12}$$

Equation (E.3.12) above says that the hub moment results from the tilt of the Tip Path Plane (TPP) relative to the Hub Plane (HP) [82]. The hub precone β_P has no effect on the hub moment, and the blade restoring spring K_β is part of the nondimensional rotating frequency ν^2 as given by equation (D.3.100) on page 292. The above equation indicates that as the TPP tilts, the rotor thrust vector tilts as well. This thrust vector tilt causes an offset of the thrust vector relative to the helicopter center of mass (CM) which results in additional moment about the body's CM (see Figure E.1 on page 318). Articulated rotors obtain half of the hub moment from hinge offset and half from rotor thrust tilt [82]. In contrast, a hingless or semirigid rotor obtains direct hub moment contributions from the blade centrifugal stiffness and a smaller portion from blade compliance under the presence of aerodynamic forces. The blade centrifugal stiffness can be modeled with a restoring spring, and the blade bending first harmonic mode can be modeled as a virtual hinge offset. Options for a model of a rigid rotor with no flap hinge range from a central hub spring [137], a virtual effective hinge offset and hub spring [159], and an effective flap hinge offset [12]. For a hingless rotor, the hub moment is 2 to 5 times the moment due to thrust tilt [13].

The various quantities in equation (E.1.5) would apply to the main rotor and the tail rotor correspondingly. The set of equations presented in this section can be solved via nonlinear computational methods. A number of strategies are available in the literature, most notably by Prouty [124] and Padfield [119] among others.

E.4 Coupled Fuselage-Rotor Forces and Moments

The in-plane longitudinal and lateral forces produced by the tilting of the rotor forces in equation (E.2.10) on page 323 as shown in Figure E.2 on page 324 induce a moment on the fuselage center of mass such that

$$\begin{aligned} L_T &= h Y_{MR} + y_{CM} (-Z_{MR}) = hT\beta_{1s} + y_{CM}T = (h\beta_{1s} + y_{CM})T \\ M_T &= h(-X_{MR}) + x_{CM}Z_{MR} = hT\beta_{1c} - x_{CM}T = (h\beta_{1c} - x_{CM})T \end{aligned} \quad (\text{E.4.1})$$

Using the result in equation (E.3.12) on the previous page, the resultant non-dimensional rotor moment coefficients acting on the fuselage are then

$$\begin{aligned} C_{xMR} &= \frac{L_T}{\rho(\pi R^2)(\Omega R)^2 R} + C_{HxMR} \\ &= (\bar{h}\beta_{1s} + \bar{y}_{CM}) C_T + \frac{a\sigma}{2\gamma} \left((\nu^2 - 1) \beta_{1s} + 2\nu_\beta^2 \left(\frac{q}{\Omega} - \frac{\dot{p}}{2\Omega^2} \right) \right) \\ C_{yMR} &= \frac{M_T}{\rho(\pi R^2)(\Omega R)^2 R} + C_{HyMR} \\ &= (\bar{h}\beta_{1c} - \bar{x}_{CM}) C_T - \frac{a\sigma}{2\gamma} \left((\nu^2 - 1) \beta_{1c} - 2\nu_\beta^2 \left(\frac{p}{\Omega} + \frac{\dot{q}}{2\Omega^2} \right) \right) \end{aligned} \quad (\text{E.4.2})$$

where $\bar{h} = h/R$, $\bar{x}_{CM} = x_{CM}/R$, $\bar{y}_{CM} = y_{CM}/R$, and the nondimensional rotating flap frequency ν^2 is given by equation (D.3.100) on page 292. In the case when $\bar{x}_{CM} \approx 0$, $\bar{y}_{CM} \approx 0$, and the body angular rate of change \dot{p} , \dot{q} are neglected, the above becomes

$$\begin{aligned} C_{xMR} &= \left(\bar{h}C_T + \frac{a\sigma}{16} S_\beta \right) \beta_{1s} + \nu_\beta^2 \frac{a\sigma}{\gamma} \frac{q}{\Omega} \\ C_{yMR} &= \left(\bar{h}C_T - \frac{a\sigma}{16} S_\beta \right) \beta_{1c} + \nu_\beta^2 \frac{a\sigma}{\gamma} \frac{p}{\Omega} \end{aligned} \quad (\text{E.4.3})$$

where the stiffness number $S_\beta = 8(\nu^2 - 1)/\gamma$ is given by equation (D.3.19) on page 263.

Appendix F

Helicopter Trim Equations

Steady helicopter flight requires equilibrium of forces and moments in all three axes of the helicopter. For a given flight condition, a helicopter trim solution converges on rotor and body orientation and corresponding control settings that archive equilibrium of all forces and moments. The collective and cyclic blade controls are necessary to impart the appropriate rotor and fuselage orientation for trim conditions. A number of solutions to the trim problem exist, and in essence, all trim solutions attempt to find the controls that are necessary to achieve a set of forces and moments that will achieve equilibrium. Figure F.1 on page 333 and Figure F.2 on page 333 show a simplified version of the forces and moments acting on a standard helicopter. Such a simplified approach is suitable for level 1 mathematical modeling and subsequent dynamic analysis [119]. Trim analysis is fundamental to the understanding of flight dynamics and control of aerospace systems, and as such, trim analysis is a basic tool for dynamic simulation and control synthesis and implementation. Many examples abound in the literature regarding trim equations of motion for the helicopter, more notably Prouty [124] examines the helicopter in trim and presents methods to determine the stability derivatives corresponding to the different helicopter components. Bramwell *et. all* [13], Cooke *et. all* [27] and Padfield [119] each provide fundamental analytical expressions for the trim equations. Leishman [92] sketches the helicopter trim solution as it relates to blade motion and associated collective and cyclic pitch of the blade.

Without loss of generality, the shaft incidence angle is set to zero in Figure F.1 on page 333 and Figure F.2 on page 333. These two figures show the longitudinal and lateral

trim forces and moments where

x_{cm} = distance from shaft to center of mass (CM).

Positive if x_{cg} is ahead of the shaft

h = distance from CM to the hub center along the shaft.

$\theta_F = \alpha_s$, is the shaft angle. Positive if shaft is tilted forward.

Note: assume zero shaft incidence angle with respect to the fuselage

α = angle of attack with respect to the fuselage or the hub plane

θ_{FP} = flight path angle such that ($\theta_{FP} = 0$ for straight and level flight) and

$$\alpha_s = \alpha - \theta_{FP}$$

y_{cg} = distance from shaft to center of mass (CM).

Positive if y_{cg} is ahead of the shaft

ϕ_F = shaft angle with respect to vertical. Positive if shaft is tilted forward.

Note: assume zero shaft incidence angle with respect to the fuselage

h_{TR} = distance from CM to the tail rotor hub center along the shaft $\bar{h} = h - h_{TR}$

F.1 Small Perturbation Theory and Trim Equations

The non-linear rigid body force equations of motion are given by equation (B.5.6) on page 193

$$\begin{aligned} \dot{u} &= rv - qw + -g \sin \theta + \frac{X}{m} \\ \dot{v} &= pw - ru + g \sin \phi \cos \theta + \frac{Y}{m} \\ \dot{w} &= qu - pv + g \cos \phi \cos \theta + \frac{Z}{m} \end{aligned} \tag{F.1.1}$$

The moment equations are given by equation (B.5.14) on page 196

$$\begin{aligned}
I_x \dot{p} &= L + I_{zx} (\dot{r} + pq) + (I_y - I_z) qr \\
I_y \dot{q} &= M + I_{zx} (r^2 - p^2) + (I_z - I_x) rp \\
I_z \dot{r} &= N + I_{zx} (\dot{p} - qr) + (I_x - I_y) pq
\end{aligned} \tag{F.1.2}$$

Solving for \dot{p} , \dot{q} , \dot{r} gives the following alternate expression

$$\begin{aligned}
\dot{p} &= \frac{I_z}{I_x I_z - I_{xz}^2} L + \frac{I_{zx}}{I_x I_z - I_{xz}^2} N \\
&\quad + \frac{(I_x - I_y + I_z) I_{zx}}{I_x I_z - I_{xz}^2} pq - \frac{(I_z - I_y) I_z + I_{xz}^2}{I_x I_z - I_{xz}^2} qr \\
\dot{q} &= \frac{M}{I_z} + \frac{I_{zx}}{I_z} (r^2 - p^2) + \frac{(I_z - I_x)}{I_z} pr \\
\dot{r} &= \frac{I_x}{I_x I_z - I_{xz}^2} N + \frac{I_{zx}}{I_x I_z - I_{xz}^2} L \\
&\quad - \frac{(I_y - I_x) I_x - I_{xz}^2}{I_x I_z - I_{xz}^2} pq - \frac{(I_x - I_y + I_z) I_{zx}}{I_x I_z - I_{xz}^2} qr
\end{aligned} \tag{F.1.3}$$

Define the following terms

$$\begin{aligned}
\bar{I}_{pL} &= \frac{I_z}{I_x I_z - I_{xz}^2} & \bar{I}_p &= \frac{(I_z - I_y) I_z + I_{xz}^2}{I_x I_z - I_{xz}^2} & \bar{I}_q &= \frac{(I_x - I_z)}{I_y} \\
\bar{I}_{rN} &= \frac{I_x}{I_x I_z - I_{xz}^2} & \bar{I}_r &= \frac{(I_y - I_x) I_x - I_{xz}^2}{I_x I_z - I_{xz}^2} & \bar{I}_{zx} &= \frac{I_{zx}}{I_y} \\
\bar{I}_{LN} &= \frac{I_{zx}}{I_x I_z - I_{xz}^2} & \bar{I}_{pr} &= \frac{(I_x - I_y + I_z) I_{zx}}{I_x I_z - I_{xz}^2} \\
\bar{L} &= \bar{I}_{pL} L + \bar{I}_{LN} N & \bar{M} &= \frac{M}{I_y} & \bar{N} &= \bar{I}_{rN} N + \bar{I}_{LN} L
\end{aligned} \tag{F.1.4}$$

Rewrite equation (F.1.3) as

$$\begin{aligned}
\dot{p} &= \bar{L} + \bar{I}_{pr} pq - \bar{I}_p qr \\
\dot{q} &= \bar{M} + \bar{I}_{zx} (r^2 - p^2) - \bar{I}_q pr \\
\dot{r} &= \bar{N} - \bar{I}_r pq - \bar{I}_{pr} qr
\end{aligned} \tag{F.1.5}$$

The kinematic rigid body motion is described by equation (B.4.6) on page 190

$$\begin{aligned}
\dot{\phi} &= p + q \sin \phi \tan \theta + r \cos \phi \tan \theta \\
\dot{\theta} &= q \cos \phi - r \sin \phi \\
\dot{\psi} &= q \sin \phi \sec \theta + r \cos \phi \sec \theta
\end{aligned}
\tag{F.1.6}$$

Equations (F.1.1), (F.1.5) and (F.1.6) are non-linear equations that describe the six degrees of freedom motion of a rigid body. Dynamic stability analysis and control design require the linearization of these non-linear equations about a trimmed flight condition. Once the aircraft is in a trimmed state, then the behavior of small disturbance forces and moments and the resulting motion should be linear. In this case, the forces involved in the deviation from trim can be described as a Taylor series expansion about the trimmed point [119].

$$\begin{aligned}
Z &= Z_0 + \frac{\partial Z}{\partial u} \delta u + \frac{\partial Z}{\partial w} \delta w + \dots + \frac{\partial Z}{\partial \theta} \delta \theta + \dots \\
M &= M_0 + \frac{\partial M}{\partial u} \delta u + \frac{\partial M}{\partial w} \delta w + \dots + \frac{\partial M}{\partial \theta} \delta \theta + \dots
\end{aligned}
\tag{F.1.7}$$

In general, the linearization consists of a first order variation addition δx to a trim state x_0 such that $x = x_0 + \delta x$. In like manner, the control inputs e are expressed such that

$$\begin{aligned}
x &= x_0 + \delta x \\
e &= e_0 + \delta e
\end{aligned}
\tag{F.1.8}$$

Substituting the trim plus variation in the non-linear equations yields a system of equations such that

$$\begin{aligned}
\delta \dot{u} &= (r_o + \delta r) (v_o + \delta v) - (q_o + \delta q) (w_o + \delta w) \\
&\quad -g \sin(\theta_o + \delta \theta) + X_0 + X_u \delta u + X_w \delta w + \dots + X_\theta \delta \theta + \dots
\end{aligned}
\tag{F.1.9}$$

Let the variation $\delta x = x$ in the above equations, then upon expansion

$$\begin{aligned}
0 &= r_o v_o - q_o w_o - g \sin \theta_o + X_0 \\
\dot{u} &= v r_o + r v_o - w q_o - q w_o \\
&\quad - g \theta \cos \theta_o + X_u \delta u + X_w \delta w + \cdots + X_\theta \delta \theta + \cdots
\end{aligned} \tag{F.1.10}$$

where the product of perturbation terms has been neglected and small angles assumption is implicit in the derivation. Also, the force derivatives are semi-normalized such that for the mass of the aircraft M_{heli} then

$$\frac{1}{M_{heli}} \frac{\partial Z}{\partial u} \delta u \equiv \frac{Z_u}{M_{heli}} u \equiv Z_u u \tag{F.1.11}$$

as is customary in aerospace literature [13, 119, 120, 124]. The context of the equation will tell whether Z_u is semi-normalized as in the above expression.

F.1.1 Symmetric Flight Equilibrium Equations

Expanding the non-linear equations as done in equation (F.1.10) and selecting the equilibrium equations yield

$$\begin{aligned}
0 &= r_0 v_0 - q_0 w_0 - g \sin \theta_0 + \frac{X_0}{m} \\
0 &= p_0 w_0 - r_0 u_0 + g \sin \phi_0 \cos \theta_0 + \frac{Y}{m} \\
0 &= q_0 u_0 - p_0 v_0 + g \cos \phi_0 \cos \theta_0 + \frac{Z}{m} \\
0 &= L_0 + I_{zx} p_0 q_0 + (I_y - I_z) q_0 r_0 \\
0 &= M_0 + I_{zx} (r_0^2 - p_0^2) + (I_z - I_x) r_0 p_0 \\
0 &= N_0 - I_{zx} q_0 r_0 + (I_x - I_y) p_0 q_0
\end{aligned} \tag{F.1.12}$$

where the subscript $)_0$ denotes the equilibrium condition in trim. The previous equation shows that the most general trim conditions require that the trim velocity vector (both linear and angular) be constant or equal to zero.

For the case of symmetric flight, the trim rates are set to zero. In this case, the summation of the equilibrium forces and moments for the longitudinal and lateral cases in Figure F.1 on page 333 and Figure F.2 on page 333 are set to zero for trim conditions:

$$\begin{aligned}
0 &= W - T_{MR} \cos \theta_F \cos \phi_F + D \sin \theta_{FP} \\
&\quad - H_{MR} \sin \theta_F + Y_{MR} \sin \phi_F + Y_{TR} \sin \phi_F \\
0 &= D \cos \theta_{FP} + H_{MR} \cos \theta_F - T_{MR} \sin \theta_F \cos \phi_F \\
0 &= Y_{MR} \cos \phi_F + T_{TR} \cos \phi_F + Y_F \cos \phi_F + T_{MR} \cos \theta_F \sin \phi_F \tag{F.1.13} \\
0 &= M_{yMR} + M_{yF} - W (x_{CM} \cos \theta_F - h \sin \theta_F) - D (h \cos \theta_F + x_{CM} \sin \theta_F) \\
0 &= M_{xMR} + M_{xF} + T_{TR} h_{TR} + W (h \sin \phi_F - y_{CM} \cos \phi_F) \\
0 &= Q_{MR} - Y_{TR} l_{TR}
\end{aligned}$$

where the aircraft weight is $W = mg$. Applying small angle approximations to the above set of equations (F.1.13) gives

$$\begin{aligned}
0 &= W - T_{MR} + D\theta_{FP} - H_{MR}\theta_F + (Y_{MR} + Y_{TR})\phi_F \\
0 &= D + H_{MR} - T_{MR}\theta_F \\
0 &= Y_{MR} + T_{TR} + Y_F + T_{MR}\phi_F \tag{F.1.14} \\
0 &= M_{yMR} + M_{yF} - W (x_{CM} - h\theta_F) - D (h + x_{CM}\theta_F) \\
0 &= M_{xMR} + M_{xF} + T_{TR}h_{TR} + W (h\phi_F - y_{CM}) \\
0 &= Q_{MR} - Y_{TR}l_{TR}
\end{aligned}$$

The terms $(Y_{MR}+Y_{TR})\phi_F$, $H_{MR}\theta_F$, $D\theta_{FP}$ are all much less than T_{MR} and weight $W = mg$.

Similar approximations with other terms result in the following simplified trim equations

$$\begin{aligned}
0 &= W - T_{MR} \\
0 &= D + H_{MR} - T_{MR} \theta_F \\
0 &= Y_{MR} + T_{TR} + Y_F + T_{MR} \phi_F \\
0 &= M_{yMR} + M_{yF} + W (h \theta_F - x_{CM}) - h D \\
0 &= M_{xMR} + M_{xF} + W (h \phi_F - y_{CM}) + T_{TR} h_{TR} \\
0 &= Q_{MR} - Y_{TR} l_{TR}
\end{aligned} \tag{F.1.15}$$

Equations (E.1.3) through (E.1.2) in section §E.1 contain the necessary expressions to solve the above set of equations (F.1.15). The equilibrium equations must be solved along with the inflow equation (E.1.2) which now takes the form below

$$\begin{aligned}
0 &= \left[\lambda - \mu \tan \alpha + \frac{C_T}{2\sqrt{\mu^2 + \lambda^2}} \right]_{MR} \\
0 &= \left[\lambda - \mu \tan \alpha + \frac{C_T}{2\sqrt{\mu^2 + \lambda^2}} \right]_{TR}
\end{aligned} \tag{F.1.16}$$

In the numerical solution, the trim process adjusts the main rotor blade pitch θ defined in equation (B.6.1) on page 198 as

$$\theta = \theta_0 - \theta_{1c} \cos \psi - \theta_{1s} \sin \psi \tag{F.1.17}$$

Bramwell's et. all [13], Johnson [82], Leishman [92], Padfield [119], and Prouty [124] are examples of literature that explore the helicopter trim solutions.

F.1.2 Linearized Equations of Motion about a Trim Condition

Expanding the non-linear equations as done in equation (F.1.10) and selecting the equations that describe the linear motion about the trim point yield

$$\begin{aligned} \dot{u} &= vr_o + rv_o - wq_o - qw_o \\ &\quad -g\theta \cos \theta_o + X_u\delta u + X_w\delta w + \dots + X_\theta\delta\theta + \dots \end{aligned} \quad (\text{F.1.18})$$

During trimmed symmetric flight conditions described in Figure F.1 and Figure F.2 on page 333 the body \mathcal{B} linear and angular velocity vector have the form

$$\begin{aligned} \vec{v} &= (u_o + u)\vec{b}_1 + v\vec{b}_2 + (w_o + w)\vec{b}_3 \\ \vec{\omega} &= p\vec{b}_1 + q\vec{b}_2 + r\vec{b}_3 \end{aligned} \quad (\text{F.1.19})$$

where $[b_1 \ b_2 \ b_3]^T$ are the body unit vectors as described in Section B.2 on page 184. Given that the perturbations from trim are small, then the second order quantities produced by squares and products are small also. Setting higher order terms to zero and substituting the above expressions in the equations of motion (F.1.1), (F.1.5) and (F.1.6) gives [13]

$$\begin{aligned} \dot{u} + q w_o &= \frac{X}{m} \\ \dot{v} + r u_o - p w_o &= \frac{Y}{m} \\ \dot{w} - q u_o &= \frac{Z}{m} \\ I_x \dot{p} - I_{zx} \dot{r} &= L \\ I_y \dot{q} &= M \\ I_z \dot{r} - I_{zx} \dot{q} &= N \end{aligned} \quad (\text{F.1.20})$$

An equivalent method for the linearization of the non-linear equations of motion yields a first order trim set of equations that can be represented as [119]

$$\dot{x} = Ax + Bu(t) + d(t) \quad (\text{F.1.21})$$

where $d(t)$ represents disturbances to the model. Let F represent the set of non-linear equations of motion (F.1.1), (F.1.5) and (F.1.6), then

$$A = \left(\frac{\partial F}{\partial x} \right)_{x=x_0} \quad B = \left(\frac{\partial F}{\partial u} \right)_{u=u_0} \quad (\text{F.1.22})$$

The stability matrix A can be divided in longitudinal and lateral dynamics such that

$$A = \begin{bmatrix} A_{lon} & A_{12} \\ A_{21} & A_{lat} \end{bmatrix} \quad (\text{F.1.23})$$

where the submatrix A_{12} is the coupling of lateral states into the longitudinal modes, and the submatrix A_{21} is the coupling of longitudinal states into the lateral modes. The state and control vector are

$$x = \begin{bmatrix} u & w & q & \theta & v & p & r & \phi \end{bmatrix}^T \quad (\text{F.1.24})$$

$$u = \begin{bmatrix} \theta_0 & \theta_{1s} & \theta_{1c} & \theta_{0TR} \end{bmatrix}^T$$

The control input vector u consists of the main rotor collective, longitudinal and lateral cyclic input, and the tail rotor collective inputs. The respective longitudinal and lateral stability matrices are

$$A_{lon} = \begin{bmatrix} X_u & X_w - q_0 & X_q - w_0 & -g \cos \theta_0 \\ Z_u + q_0 & Z_w & Z_q + u_0 & -g \cos \phi \sin \theta_0 \\ \bar{M}_u & \bar{M}_w & \bar{M}_q & 0 \\ 0 & 0 & \cos \phi_0 & 0 \end{bmatrix} \quad (\text{F.1.25})$$

$$A_{lat} = \begin{bmatrix} Y_v & Y_p + w_0 & Y_r - u_0 & g \cos \phi \cos \theta_0 \\ \bar{L}_v & \bar{L}_p + \bar{I}_{pr}q_0 & \bar{L}_r - \bar{I}_p q_0 & 0 \\ \bar{N}_v & \bar{N}_p - \bar{I}_r q_0 & \bar{N}_r - \bar{I}_{pr}q_0 & 0 \\ & 1 & \cos \phi_0 \tan \theta_0 & 0 \end{bmatrix}$$

The cross-coupling matrices are

$$\begin{aligned}
 A_{12} &= \begin{bmatrix} X_v + r_0 & X_p & X_r + v_0 & 0 \\ Z_v - p_0 & Z_p - v_0 & Z_r & -g \sin \phi \cos \theta_0 \\ \bar{M}_v & \bar{M}_p \cdots & \bar{M}_r \cdots & 0 \\ & -\bar{I}_q r_0 - 2\bar{I}_{zx} p_0 & -\bar{I}_q p_0 + 2\bar{I}_{zx} r_0 & \\ 0 & 0 & -\sin \phi_0 & \bar{K}_\phi \end{bmatrix} \\
 A_{21} &= \begin{bmatrix} Y_u - r_0 & Y_w + p_0 & Y_q & -g \sin \phi \sin \theta_0 \\ \bar{L}_u & \bar{L}_w & \bar{L}_q + \bar{I}_{pr} p_0 - \bar{I}_p r_0 & 0 \\ \bar{N}_u & \bar{N}_w & \bar{N}_q - \bar{I}_r p_0 - \bar{I}_{pr} r_0 & 0 \\ 0 & 0 & \sin \phi_0 \tan \theta_0 & \bar{K}_\theta \end{bmatrix}
 \end{aligned} \tag{F.1.26}$$

The control matrix is given as

$$B = \begin{bmatrix} B_{lon} \\ B_{lat} \end{bmatrix} \tag{F.1.27}$$

where the longitudinal and lateral control matrices are

$$B_{lon} = \begin{bmatrix} X_{\theta_0} & X_{\theta_{1s}} & X_{\theta_{1c}} & X_{\delta_T} \\ Z_{\theta_0} & Z_{\theta_{1s}} & Z_{\theta_{1c}} & Z_{\delta_T} \\ \bar{M}_{\theta_0} & \bar{M}_{\theta_{1s}} & \bar{M}_{\theta_{1c}} & \bar{M}_{\theta_{TR}} \\ 0 & 0 & 0 & 0 \end{bmatrix} \quad B_{lat} = \begin{bmatrix} Y_{\theta_0} & Y_{\theta_{1s}} & Y_{\theta_{1c}} & Y_{\delta_T} \\ \bar{L}_{\theta_0} & \bar{L}_{\theta_{1s}} & \bar{L}_{\theta_{1c}} & \bar{L}_{\delta_T} \\ \bar{N}_{\theta_0} & \bar{N}_{\theta_{1s}} & \bar{N}_{\theta_{1c}} & \bar{N}_{\delta_T} \\ 0 & 0 & 0 & 0 \end{bmatrix} \tag{F.1.28}$$

Appendix G

Helicopter Stability Derivatives

The goal in this section is to develop the stability derivatives that describe the motion of the helicopter due to a perturbation from a trim condition. The static stability derivatives describe the initial instantaneous reaction to a perturbation, and say something related to the direction of the actuation control. If the initial reaction opposes the disturbance, then the static stability is stable. The moments generated due to changes in the velocity components along the body axis are a metric for static stability. The most important terms that describe the helicopter static stability are

1. M_u , longitudinal static stability with respect to forward speed u .
2. M_w , longitudinal static stability with respect to angle of attack. Vertical velocity is used instead of rotor incidence angle α because $\alpha = 0$ in hover flight.
3. L_v , lateral static stability or dihedral effect.
4. N_v , directional static stability or Weathercock stability. N_v is used for a measure of the Weathercock stability because sideslip is not defined in hover. In fixed wing airplanes, this stability is given by $C_{L\beta}$.

The dynamic stability derivatives describe the subsequent behavior after a perturbation has taken place.

Bramwell [11, 13], Cooke *et. all* [27], Padfield [119], and Prouty [124] derive and develop analytical and experimental methods for obtaining the various helicopter stability derivatives. The work in this appendix is based on the previous mentioned literature and other references are noted where appropriate.

G.1 Main Rotor Stability Derivatives

The thrust coefficient in forward flight is given by equation (D.3.129) on page 302 for the case when the flap hinge offset $e \neq 0$,

$$C_T = \frac{a\sigma}{2} \left[\frac{\theta}{3} (1 - e) \left((e + 1)^2 - e + \frac{3}{2}\mu^2 \right) - \frac{(e^2 - 1)}{2}\lambda \right]. \quad (\text{G.1.1})$$

The rotor inflow is given by equation (C.1.49) on page 219,

$$\lambda = \frac{V \sin \alpha + v_i}{\Omega R} = \mu \tan \alpha + \lambda_i \quad (\text{G.1.2})$$

Use equation (C.1.51) on page 219 together with (C.1.49) to obtain

$$\lambda_i = \frac{C_T}{2(\mu^2 + \lambda^2)^{1/2}} = \frac{C_T}{2(\mu^2 + (\lambda_i + \mu_z)^2)^{1/2}} \quad (\text{G.1.3})$$

Consider the following approximation

$$\begin{aligned} &= V_\infty^2 \cos^2 \alpha + (V_\infty \sin \alpha + v_i)^2 \\ &= V_\infty^2 \cos^2 \alpha + V_\infty^2 \sin^2 \alpha + v_i (2V_\infty \sin \alpha + v_i) \end{aligned} \quad (\text{G.1.4})$$

$$(\Omega R)^2 \bar{V}^2 \approx V_\infty^2 + v_i^2$$

then equation (G.1.3) takes the form

$$\lambda_i \approx \frac{C_T}{2(\bar{V}^2 + \lambda_i^2)^{1/2}} \quad (\text{G.1.5})$$

where the hover induced hover velocity v_h is related to C_T by equation (C.1.18) on page 208 such that [13]

$$\begin{aligned} 2\lambda_h^2 = C_T &\quad \rightarrow \quad 2v_h^2 = (\Omega R)^2 C_T \\ \tilde{V} = \frac{\bar{V}}{\lambda_h} = \frac{V}{v_h} & \\ \tilde{v}_i = \frac{v_i}{v_h} & \end{aligned} \quad (\text{G.1.6})$$

Moreover, it follows that

$$\begin{aligned}
\lambda_h^2 &= \frac{C_T}{2} && \text{for } \mu = 0 \\
\lambda_i &= \frac{C_T}{2\mu} && \text{for } \mu > 0.08 \\
\tilde{v}_i &= \frac{v_i}{v_h} = \frac{\lambda_i}{\lambda_h} = \frac{C_T}{2\mu} \left(\frac{C_T}{2} \right)^{-1/2} \\
\frac{V}{v_h} &\approx \frac{\mu}{\lambda_h} = \mu \left(\frac{C_T}{2} \right)^{-1/2} \\
\left(\frac{V}{v_h} \right) \left(\frac{v_i}{v_h} \right)^3 &= \mu \left(\frac{C_T}{2\mu} \right)^3 \left(\frac{C_T}{2} \right)^{-2} = \frac{C_T}{2\mu^2}
\end{aligned} \tag{G.1.7}$$

G.1.1 Main Rotor Forward Velocity Stability Derivatives

Differentiation of thrust coefficient C_T with respect to the advance ratio μ in equation (G.1.1) gives

$$\frac{2}{a\sigma} \frac{\partial C_T}{\partial \mu} = (1 - e) \theta \mu^2 - \frac{(e^2 - 1)}{2} \frac{\partial \lambda}{\partial \mu} \tag{G.1.8}$$

The corresponding change of the rotor inflow λ with respect to the advance ratio μ as given by (G.1.2) is

$$\frac{\partial \lambda}{\partial \mu} \approx \alpha + \frac{\partial \lambda_i}{\partial \mu} \tag{G.1.9}$$

and from equation (G.1.5)

$$\begin{aligned}
\lambda_i &\approx \frac{C_T}{2(\bar{V}^2 + \lambda_i^2)^{1/2}} \quad \rightarrow \quad \left(\frac{2\lambda_i}{C_T} \right)^2 \approx \frac{1}{(\bar{V}^2 + \lambda_i^2)} \\
\frac{\partial \lambda_i}{\partial \mu} &= \frac{1}{2(\bar{V}^2 + \lambda_i^2)^{1/2}} \frac{\partial C_T}{\partial \mu} - \frac{C_T}{2(\bar{V}^2 + \lambda_i^2)^{3/2}} \left(\bar{V} + \lambda_i \frac{\partial \lambda_i}{\partial \mu} \right) \\
\frac{\partial \lambda_i}{\partial \mu} &= \frac{\lambda_i}{C_T} \frac{\partial C_T}{\partial \mu} - \frac{4\lambda_i^3}{C_T^2} \left(\bar{V} + \lambda_i \frac{\partial \lambda_i}{\partial \mu} \right)
\end{aligned} \tag{G.1.10}$$

Using the expressions in (G.1.6) yields

$$\frac{\partial \lambda_i}{\partial \mu} = \frac{\lambda_i}{C_T} \frac{\partial C_T}{\partial \mu} - \tilde{V} \tilde{v}_i^3 - \tilde{v}_i^4 \frac{\partial \lambda_i}{\partial \mu} \tag{G.1.11}$$

where the terms \tilde{v}_i and \tilde{V} are readily available or can be obtained from experimental data. Solving for $\partial\lambda_i/\partial\mu$ and substituting back into (G.1.9) and subsequently into (G.1.8) gives

$$\begin{aligned}\frac{\partial\lambda_i}{\partial\mu} &= \frac{2a\sigma(1-e)\theta\mu - a\sigma(e^2-1)\alpha - 4(C_T/\lambda_i)\tilde{V}\tilde{v}_i^3}{a\sigma(e^2-1) + 4(C_T/\lambda_i)(1+\tilde{v}_i^4)} \\ \frac{\partial C_T}{\partial\mu} &= \frac{2(1-e)\theta\mu a\sigma - a\sigma(e^2-1)\alpha - 2\tilde{V}\tilde{v}_i^3 a\sigma/(1+\tilde{v}_i^4)}{4 + a\sigma(e^2-1)(\lambda_i/C_T)/(1+\tilde{v}_i^4)}\end{aligned}\quad (\text{G.1.12})$$

An equivalent result can be found in [13, p. 151]. The above expression does not take into account aerodynamic augmentation to the rotor system such as a stabilizing bar [50]. Equation (C.1.46) on page 218 is valid in forward flight when $v_i \ll V_\infty$ then $\tilde{v}_i^4 \ll 1$, and $\lambda_i = C_T/2\mu$. In this case equation (G.1.12) becomes

$$\begin{aligned}\frac{\partial\lambda_i}{\partial\mu} &= \frac{2a\sigma(1-e)\theta\mu - a\sigma(e^2-1)\alpha - 4C_T/\mu}{a\sigma(e^2-1) + 8\mu} \\ \frac{\partial C_T}{\partial\mu} &= 2\mu a\sigma \left(\frac{2(1-e)\theta\mu - (e^2-1)\alpha - C_T/2\mu^2}{8\mu + a\sigma(e^2-1)} \right)\end{aligned}\quad (\text{G.1.13})$$

Bramwell [13, p. 151] gives equivalent results to equation (G.1.13) for the case when the hinge offset $e = 0$.

Equation (D.3.173) on page 314 represents a simplified expression for steady state blade dynamic coefficients for flight conditions with small advance ratio $\mu \ll 1$. The longitudinal blade flapping coefficient β_{1c} and its partial derivative with respect to advance ratio is given by

$$\begin{aligned}\beta_{1c} &\approx \frac{8}{3}\mu\theta_0 - 2\mu\lambda - \theta_{1s} + \frac{p}{\Omega} - \frac{16}{\gamma} \frac{q}{\Omega} \\ \frac{\partial\beta_{1c}}{\partial\mu} &\approx \frac{8}{3}\theta_0 - 2\lambda \frac{\partial\lambda}{\partial\mu}\end{aligned}\quad (\text{G.1.14})$$

where $\partial\lambda/\partial\mu$ is given by equation (G.1.9) and G.1.13 above. For cases when $\mu \ll 1$

$$\begin{aligned}\frac{\partial\lambda_i}{\partial\mu} &\approx K_\lambda\alpha \quad , \quad \mu \ll 1 \\ \frac{\partial\lambda}{\partial\mu} &\approx \alpha + \frac{\partial\lambda_i}{\partial\mu} \approx (1 + K_\lambda)\alpha \\ \frac{\partial\beta_{1c}}{\partial\mu} &\approx \frac{8}{3}\theta_0 - 2\lambda(1 + K_\lambda)\alpha\end{aligned}\tag{G.1.15}$$

The above is a first order approximation for a hingeless rotor with no restraining devices. The effects of advance ratio on α expressed in the term $2\lambda(1 + K_\lambda)\alpha$ can be lumped together with other un-modeled effects in the following simpler expression [50]

$$\frac{\partial\beta_{1c}}{\partial\mu} \approx K_\mu \left(\frac{8}{3}\theta_0 - 2\lambda \right)\tag{G.1.16}$$

To accomodate blade restraining mechanisms such as a hub spring and blade hinge offset, inspection of equation (D.3.170) on page 313 suggests the following modification to the above stability derivative

$$\frac{\partial\beta_{1c}}{\partial\mu} \approx \frac{S_\beta}{1 + S_\beta^2} K_\mu \left(\frac{8}{3}\theta_0 - 2\lambda \right)\tag{G.1.17}$$

Given rotor symmetry, the response to in-plane velocities is similar in magnitude and behavior regardless of the direction of the incoming wind [50, 105]. In this case

$$\frac{\partial\beta_{1c}}{\partial\mu} = \frac{\partial\beta_{1s}}{\partial\mu}\tag{G.1.18}$$

The above equation for the lateral dihedral derivatives indicates that the rotor flaps away from the incoming air. Whence

$$\begin{aligned}\frac{\partial\beta_{1c}}{\partial\mu} &= \frac{S_\beta}{1 + S_\beta^2} K_\mu \left(\frac{8}{3}\theta_0 - 2\lambda \right) \\ \frac{\partial\beta_{1s}}{\partial\mu} &= \frac{S_\beta}{1 + S_\beta^2} K_\mu \left(\frac{8}{3}\theta_0 - 2\lambda \right)\end{aligned}\tag{G.1.19}$$

The scaling factor K_μ can be estimated from steady state cyclic input in constant forward

flight [50].

G.1.2 Main Rotor Vertical Velocity Stability Derivatives

Consider the inflow through the rotor λ given by the following expression

$$\begin{aligned}\lambda &= \frac{V_\infty}{\Omega R} \sin \alpha + \lambda_i = \bar{V} \sin \alpha + \lambda_i = \bar{V} \sin \alpha + \lambda_i \\ \frac{\partial \lambda}{\partial \mu_z} &= \bar{V} \frac{\partial \alpha}{\partial \mu_z} \cos \alpha + \frac{\partial \lambda_i}{\partial \mu_z}\end{aligned}\tag{G.1.20}$$

The change of rotor angle α due to a disturbance $\delta\mu_z$ is

$$\begin{aligned}\delta\alpha &= \frac{\delta\mu_z}{\bar{V}} \\ \frac{\partial \alpha}{\partial \mu_z} &= \frac{1}{\bar{V}}\end{aligned}$$

and equation (G.1.20) is

$$\frac{\partial \lambda}{\partial \mu_z} = 1 + \frac{\partial \lambda_i}{\partial \mu_z}\tag{G.1.21}$$

Using the previous expression with equation (G.1.1) the following holds

$$\frac{4}{a\sigma} \frac{\partial C_T}{\partial \mu_z} = (e^2 - 1) \frac{\partial \lambda}{\partial \mu_z} = (e^2 - 1) \left(1 + \frac{\partial \lambda_i}{\partial \mu_z} \right)\tag{G.1.22}$$

Use (G.1.3) to obtain

$$\begin{aligned}\lambda_i &= \frac{C_T}{2(\mu^2 + (\lambda_i + \mu_z)^2)^{1/2}} \\ \frac{\partial \lambda_i}{\partial \mu_z} &= \frac{1}{2(\mu^2 + (\lambda_i + \mu_z)^2)^{1/2}} \frac{\partial C_T}{\partial \mu_z} - \frac{(\lambda_i + \mu_z) C_T}{2(\mu^2 + (\lambda_i + \mu_z)^2)^{3/2}} \left(1 + \frac{\partial \lambda_i}{\partial \mu_z} \right) \\ \frac{\partial \lambda_i}{\partial \mu_z} &= \frac{\lambda_i}{C_T} \frac{\partial C_T}{\partial \mu_z} - \frac{4\lambda_i^3}{C_T^2} (\lambda_i + \mu_z) \left(1 + \frac{\partial \lambda_i}{\partial \mu_z} \right)\end{aligned}\tag{G.1.23}$$

Let the vertical hub velocity μ_z be the result of a velocity variation in the vertical axis z such that $\delta\mu_z \rightarrow 0$, then the above expression for $\partial\lambda_i/\partial\mu_z$ becomes

$$\begin{aligned}
&\approx \frac{\lambda_i}{C_T} \frac{\partial C_T}{\partial \mu_z} - \frac{4\lambda_i^4}{C_T^2} \left(1 + \frac{\partial \lambda_i}{\partial \mu_z}\right) \\
&= \frac{\lambda_i}{C_T} \frac{\partial C_T}{\partial \mu_z} - \tilde{v}_i^4 \left(1 + \frac{\partial \lambda_i}{\partial \mu_z}\right) \\
\frac{\partial \lambda_i}{\partial \mu_z} &= \frac{\lambda_i}{C_T} \frac{a\sigma}{4} (e^2 - 1) \left(1 + \frac{\partial \lambda_i}{\partial \mu_z}\right) - \tilde{v}_i^4 \left(1 + \frac{\partial \lambda_i}{\partial \mu_z}\right)
\end{aligned} \tag{G.1.24}$$

where $4v_h^4 = (\Omega R)^4 C_T^2$ in (G.1.6) and

$$\frac{4\lambda_i^3}{C_T^2} = 4 \frac{(v_i/\Omega R)^4}{C_T^2} = 4 \frac{v_i^4}{(\Omega R)^4 C_T^2} = \frac{v_i^4}{v_h^4} = \tilde{v}_i^4$$

Solving for $\partial\lambda_i/\partial\mu_z$ in equation (G.1.24) and substituting in (G.1.20) and (G.1.22) gives

$$\begin{aligned}
\frac{\partial \lambda_i}{\partial \mu_z} &= \frac{(\lambda_i/C_T) a\sigma (e^2 - 1) - 4\tilde{v}_i^4}{4 - a\sigma (e^2 - 1) (\lambda_i/C_T) + 4\tilde{v}_i^4} \\
\frac{\partial \lambda}{\partial \mu_z} &= 1 + \frac{\partial \lambda_i}{\partial \mu_z} = \frac{4}{4 - a\sigma (e^2 - 1) (\lambda_i/C_T) + 4\tilde{v}_i^4} \\
\frac{\partial C_T}{\partial \mu_z} &= (e^2 - 1) \frac{\partial \lambda}{\partial \mu_z} = \frac{a\sigma (e^2 - 1)}{4 - a\sigma (e^2 - 1) (\lambda_i/C_T) + 4\tilde{v}_i^4}
\end{aligned} \tag{G.1.25}$$

In the hover case $\mu = 0$, $\tilde{v}_i = 1$, $C_T = 2\lambda_i^2$ then (G.1.25) becomes

$$\begin{aligned}
\frac{\partial \lambda_i}{\partial \mu_z} &= \frac{a\sigma (e^2 - 1) - 8\lambda_i}{16\lambda_i - a\sigma (e^2 - 1)} \\
\frac{\partial \lambda}{\partial \mu_z} &= \frac{8\lambda_i}{16\lambda_i - a\sigma (e^2 - 1)} \\
\frac{\partial C_T}{\partial \mu_z} &= \frac{2a\sigma (e^2 - 1) \lambda_i}{16\lambda_i - a\sigma (e^2 - 1)}
\end{aligned} \tag{G.1.26}$$

In the case when the advance ratio $\mu > 0.08$, $\tilde{v}_i^2 \ll 1$, $C_T = 2\mu\lambda_i$ then (G.1.25) becomes

$$\begin{aligned}\frac{\partial\lambda_i}{\partial\mu_z} &= \frac{a\sigma(e^2 - 1)}{8\mu - a\sigma(e^2 - 1)} \\ \frac{\partial\lambda}{\partial\mu_z} &= \frac{8\mu}{8\mu - a\sigma(e^2 - 1)} \\ \frac{\partial C_T}{\partial\mu_z} &= \frac{2a\sigma(e^2 - 1)\mu}{8\mu - a\sigma(e^2 - 1)}\end{aligned}\tag{G.1.27}$$

Bramwell [13, p. 154] and Padfield [119, p. 219] give similar results for the case when the hinge offset $e = 0$. The above results do not account for the cases when the rotor exhibits aerodynamic augmentation via a stabilizer bar. Finally, care must be taken when considering the sign convention as it relates with the direction of flow through the rotor and direction of the main rotor angular motion.

G.1.2.1 Main Rotor Heave Damping

The variation of vertical motion from equilibrium is given by

$$w_0 + \delta w$$

and the simplified variation of vertical acceleration due to changes in vertical force is given by equation (F.1.20) on page 339 as

$$M_{heli}(\dot{w}_0 + \delta\dot{w}) = Z_o + \frac{\partial Z}{\partial w}\delta w + \frac{\partial Z}{\partial\theta}\delta\theta + \dots\tag{G.1.28}$$

where M_{heli} is the mass of the helicopter. Following the convention in equation (F.1.11) on page 336, let the current context be such that $\delta w \rightarrow w$ be a small perturbation from equilibrium, then for the case when body rates are zero, the w component of equation (F.1.20) on page 339 takes the form

$$\begin{aligned}&= \frac{1}{M_{heli}} \left(\frac{\partial Z}{\partial w}\delta w + \frac{\partial Z}{\partial\theta}\delta\theta \right) = \frac{\partial Z}{\partial w}\delta w + \frac{\partial Z}{\partial\theta}\delta\theta \\ \dot{w} &= Z_w w + Z_\theta\theta\end{aligned}\tag{G.1.29}$$

The heave damping Z_w follows [119, p. 188]

$$\begin{aligned} &= \frac{\partial Z}{\partial w} \approx -\frac{\partial T_{MR}}{\partial w} = -\frac{\rho (\Omega R)^2 \pi R^2}{M_{heli}} \frac{\partial C_T}{(\Omega R) \partial \mu} \\ Z_w &= -\frac{\rho (\Omega R) \pi R^2}{M_{heli}} \frac{\partial C_T}{\partial \mu} \end{aligned} \quad (\text{G.1.30})$$

Using results from equation (G.1.26) and equation (G.1.27) on the preceding page gives for the hover case $\mu = 0$

$$\begin{aligned} &= \frac{\rho (\Omega R) \pi R^2}{M_{heli}} \frac{2a\sigma (e^2 - 1) \lambda_i}{16\lambda_i - a\sigma (e^2 - 1)} \\ Z_w &= \frac{2a\rho A_b(\Omega R) (e^2 - 1) \lambda_i}{M_{heli} [16\lambda_i - a\sigma (e^2 - 1)]} \end{aligned} \quad (\text{G.1.31})$$

For the forward speed case $\mu > 0.08$

$$\begin{aligned} &= \frac{\rho (\Omega R) \pi R^2}{M_{heli}} \frac{2a\sigma (e^2 - 1) \mu}{8\mu - a\sigma (e^2 - 1)} \\ Z_w &= \frac{2a\rho\mu A_b(\Omega R) (e^2 - 1)}{M_{heli} [8\mu - a\sigma (e^2 - 1)]} \end{aligned} \quad (\text{G.1.32})$$

where $A_b = b c R$ is the total blade area. The ratio of helicopter mass to total blade area M_{heli}/A_b is the rotor blade loading, and equations (G.1.31) and (G.1.32) show that it is an important parameter in the definition of heave damping [13, 119].

G.1.3 Main Rotor Control Derivatives

Differentiation of thrust coefficient C_T in equation (D.3.121) on page 299 with respect to collective blade pitch input θ_0 gives

$$\frac{2}{\sigma a} \frac{\partial C_T}{\partial \theta_0} = \left(\frac{(1 - e^3)}{3} + \frac{(1 - e)}{2} \mu^2 \right) + \frac{(e^2 - 1)}{2} \frac{\partial \lambda}{\partial \theta_0} \quad (\text{G.1.33})$$

The corresponding differentiation of the rotor inflow λ from equations (G.1.5) and equation (G.1.2) on page 343 is

$$\begin{aligned}
\frac{\partial \lambda}{\partial \theta_0} &= \frac{\partial \lambda_i}{\partial \theta_0} \\
\frac{\partial \lambda_i}{\partial \theta_0} &= \frac{1}{2(\bar{V}^2 + \lambda_i^2)^{1/2}} \frac{\partial C_T}{\partial \theta_0} - \frac{\lambda_i C_T}{2(\bar{V}^2 + \lambda_i^2)^{3/2}} \frac{\partial \lambda_i}{\partial \theta_0} \\
&= \frac{\lambda_i}{C_T} \frac{\partial C_T}{\partial \theta_0} - \tilde{v}_i^4 \frac{\partial \lambda_i}{\partial \theta_0} \\
(1 + \tilde{v}_i^4) \frac{\partial \lambda_i}{\partial \theta_0} &= \frac{\lambda_i}{C_T} \frac{\partial C_T}{\partial \theta_0}
\end{aligned} \tag{G.1.34}$$

where as before in previous sections

$$\begin{aligned}
&= \frac{\lambda_i^2}{(\bar{V}^2 + \lambda_i^2)} = \lambda_i^2 \left(\frac{2\lambda_i}{C_T} \right)^2 \\
\frac{\lambda_i C_T}{2(\bar{V}^2 + \lambda_i^2)^{3/2}} &= \frac{4\lambda_i^4}{C_T^2} = \frac{4v_i^4}{(\Omega R)^4 C_T^2} = 4v_h^4 = \frac{v_i^4}{v_h^4} = \tilde{v}_i^4
\end{aligned} \tag{G.1.35}$$

Solving for $\partial \lambda_i / \partial \theta_0$ and $\partial C_T / \partial \theta_0$ gives

$$\begin{aligned}
\frac{\partial \lambda_i}{\partial \theta_0} &= \frac{\sigma a}{6} \frac{(1 - e^3) + 3(1 - e)\mu^2/2}{(1 + \tilde{v}_i^4)(\lambda_i/C_T) - (e^2 - 1)\sigma a/4} \\
\frac{\partial C_T}{\partial \theta_0} &= \frac{\sigma a}{6} \frac{(1 - e^3) + 3(1 - e)\mu^2/2}{1 - \sigma a(\lambda_i/4C_T)(e^2 - 1)/(1 + \tilde{v}_i^4)}
\end{aligned} \tag{G.1.36}$$

For hover case $\mu = 0$, $\tilde{v}_i^4 = 1$ and $2\lambda_h^2 \approx C_T$

$$\begin{aligned}
\frac{\partial \lambda_i}{\partial \theta_0} &= \frac{2}{3} \frac{(1 - e^3)\sigma a \lambda_i}{4 - (e^2 - 1)\sigma a \lambda_i} \\
\frac{\partial C_T}{\partial \theta_0} &= \frac{8}{3} \frac{(1 - e^3)\sigma a \lambda_i}{16\lambda_i - \sigma a(e^2 - 1)}
\end{aligned} \tag{G.1.37}$$

For forward speed case when $\mu > 0.1$, $\tilde{v}_i^4 \ll 1$, and $C_T \approx 2\mu\lambda_i$

$$\begin{aligned}
\frac{\partial \lambda_i}{\partial \theta_0} &= \frac{2\sigma a \mu}{3} \frac{(1 - e^3) + 3(1 - e)\mu^2/2}{2 - (e^2 - 1)\mu\sigma a} \\
\frac{\partial C_T}{\partial \theta_0} &= \frac{4\sigma a \mu}{3} \frac{(1 - e^3) + 3(1 - e)\mu^2/2}{8\mu - \sigma a(e^2 - 1)}
\end{aligned} \tag{G.1.38}$$

As before, the vertical force derivative is given by

$$Z_{\theta_0} = -\frac{\rho (\Omega R)^2 \pi R^2}{M_{heli}} \frac{\partial C_T}{\partial \theta_0} \quad (\text{G.1.39})$$

where $\partial C_T \partial \theta_0$ takes the form in expression (G.1.37) and (G.1.38) resulting in the following expression

$$\begin{aligned} Z_{\theta} &= -\frac{8 A_{blade}}{3 M_{heli}} \frac{\rho a (\Omega R)^2 (1 - e^3) \lambda_i}{16 \lambda_i - \sigma a (e^2 - 1)} \quad (\mu = 0) \\ Z_{\theta} &= -\frac{4 A_{blade}}{3 M_{heli}} \left[\frac{(1 - e^3) + 3(1 - e) \mu^2 / 2}{8 \mu - \sigma a (e^2 - 1)} \right] \rho a (\Omega R)^2 \mu \quad (\mu > 0.1) \end{aligned} \quad (\text{G.1.40})$$

A similar development, this time with respect to θ_{1s} yields

$$\begin{aligned} \frac{2}{\sigma a} \frac{\partial C_T}{\partial \theta_{1s}} &= \frac{(e^2 - 1)}{2} \left(\mu + \frac{\partial \lambda_i}{\partial \theta_{1s}} \right) \\ (1 + \tilde{v}_i^4) \frac{\partial \lambda_i}{\partial \theta_{1s}} &= \frac{\lambda_i}{C_T} \frac{\partial C_T}{\partial \theta_{1s}} \end{aligned} \quad (\text{G.1.41})$$

From which the general solution is

$$\begin{aligned} \frac{\partial \lambda_i}{\partial \theta_{1s}} &= \frac{(e^2 - 1) \sigma a \mu}{4(1 + \tilde{v}_i^4) (C_T / \lambda_i) - (e^2 - 1) \sigma a} \\ \frac{\partial C_T}{\partial \theta_{1s}} &= \frac{(e^2 - 1) (1 + \tilde{v}_i^4) \sigma a \mu}{4(1 + \tilde{v}_i^4) - (e^2 - 1) \sigma a (\lambda_i / C_T)} \end{aligned} \quad (\text{G.1.42})$$

For the hover case $\mu = 0$, the above two derivatives are zero ($Z_{\theta_{1s}} = 0$), and for forward flight the following approximation applies

$$\begin{aligned} \frac{\partial \lambda_i}{\partial \theta_{1s}} &= \frac{(e^2 - 1) \sigma a \mu}{8(1 + \tilde{v}_i^4) 2\mu - (e^2 - 1) \sigma a} \\ \frac{\partial C_T}{\partial \theta_{1s}} &= \frac{2(e^2 - 1) \sigma a \mu^2}{8\mu - (e^2 - 1) \sigma a} \end{aligned} \quad (\text{G.1.43})$$

The corresponding control derivative is then

$$\begin{aligned}
&= -\frac{\rho (\Omega R)^2 \pi R^2}{M_{heli}} \frac{\partial C_T}{\partial \theta_{1s}} \\
Z_{\theta_{1s}} &= \frac{A_{blade}}{M_{heli}} \frac{2\rho a \mu^2 (\Omega R)^2}{\sigma a - 8\mu/(e^2 - 1)} \quad \mu > 0.1
\end{aligned} \tag{G.1.44}$$

In equations (G.1.40) and (G.1.44), the tip speed $(\Omega R)^2$ and the blade loading A_{blade}/M_{heli} are the dominant factors.

G.1.4 Main Rotor Blade Flapping Derivatives

Section §D.3.7.5 gives expressions for the flapping coefficients under several flight conditions. In particular, equation (D.3.170) and equation (D.3.171) on page 313 give the results for forward flight ($\mu > 0.1$) and for hover flight ($\mu = 0$) conditions. The following set of rotor control derivatives result directly from the previously mentioned equations.

The collective pitch longitudinal blade flapping derivatives are

$$\begin{aligned}
\frac{\partial \beta_0}{\partial \theta_0} &= \frac{\gamma (1 + \mu^2)}{8 \nu^2} & \frac{\partial \beta_0}{\partial \theta_{1s}} &= -\frac{\gamma \mu}{6 \nu^2} & \frac{\partial \beta_0}{\partial \theta_{1c}} &= 0 \\
\frac{\partial \beta_{1c}}{\partial \theta_0} &= \frac{(1 + 2\mu^2/3) - (1 + \mu^2)/3\nu^2}{1 + S_\beta^2 - \mu^4/4} (4\mu) \\
\frac{\partial \beta_{1s}}{\partial \theta_0} &= \frac{(\gamma/6\nu^2) (1 + \mu^2) - (8/3) S_\beta}{1 + S_\beta^2 - \mu^4/4} (\mu)
\end{aligned} \tag{G.1.45}$$

Change in the blade collective pitch setting influences the rotor thrust which results in a moment about the aircraft center of mass. In addition, any change in collective pitch setting changes the blade flapping angles, which induces a rotor hub moment proportional to the new flap angles [119]. The corresponding flapping blade behavior to cyclic control inputs is given by following direct $\partial \beta_{1c}/\partial \theta_{1c}$, $\partial \beta_{1s}/\partial \theta_{1s}$ and coupled $\partial \beta_{1c}/\partial \theta_{1s}$, $\partial \beta_{1s}/\partial \theta_{1c}$ responses

$$\begin{aligned}
\frac{\partial \beta_{1c}}{\partial \theta_{1c}} &= \frac{(1 + \mu^2/2) S_\beta}{1 + S_\beta^2 - \mu^4/4} & \frac{\partial \beta_{1s}}{\partial \theta_{1s}} &= \frac{(1 + 3\mu^2/2) S_\beta - 2\gamma\mu^2/9\nu^2}{1 + S_\beta^2 - \mu^4/4} \\
\frac{\partial \beta_{1c}}{\partial \theta_{1s}} &= \frac{16\mu^2/9\nu^2 - (1 + 4\mu^2)}{1 + S_\beta^2 - \mu^4/4} & \frac{\partial \beta_{1s}}{\partial \theta_{1c}} &= \frac{1 - \mu^4/4}{1 + S_\beta^2 - \mu^4/4}
\end{aligned} \tag{G.1.46}$$

In moderate forward flight when there is a finite but small advance ratio such that $\mu \ll 1$, then

$$\begin{aligned}
\frac{\partial \beta_0}{\partial \theta_0} &\approx \frac{\gamma}{8\nu^2} & \frac{\partial \beta_0}{\partial \theta_{1s}} &\approx -\frac{\gamma \mu}{6\nu^2} \\
\frac{\partial \beta_{1c}}{\partial \theta_0} &\approx \frac{(3\nu^2 - 1)4\mu}{3\nu^2} & \frac{\partial \beta_{1s}}{\partial \theta_0} &\approx -\frac{\partial \beta_0}{\partial \theta_{1s}} \approx \frac{\gamma \mu}{6\nu^2} \\
\frac{\partial \beta_{1c}}{\partial \theta_{1c}} &\approx \frac{\partial \beta_{1s}}{\partial \theta_{1s}} \approx \frac{S_\beta}{1 + S_\beta^2} \\
\frac{\partial \beta_{1c}}{\partial \theta_{1s}} &\approx -\frac{\partial \beta_{1s}}{\partial \theta_{1c}} \approx -\frac{1}{1 + S_\beta^2}
\end{aligned} \tag{G.1.47}$$

The direct and coupled blade flap derivatives due to cyclic control are almost independent of forward speed at low advance ratios, and are a function of stiffness number S_β . The above equations indicate that hingeless rotors with a low stiffness number flap in much the same way as teetering rotors [119]. The blade flap rate derivatives originate from the same set of equations (D.3.170) and (D.3.171) from which

$$\begin{aligned}
\frac{\partial \beta_0}{\partial p} &= \frac{\gamma}{8} \frac{2\mu}{3\Omega\nu^2}, & \frac{\partial \beta_0}{\partial q} &= 0 \\
\bar{C}_\beta \frac{\partial \beta_{1c}}{\partial p} &= -\left(\frac{16}{\gamma} \frac{S_\beta}{\Omega} + \frac{4}{3} \frac{\mu^2}{\Omega} - \frac{1}{\Omega} \right) - \frac{8\mu^2}{9\Omega\nu^2} \\
\bar{C}_\beta \frac{\partial \beta_{1s}}{\partial p} &= -\left(\frac{S_\beta}{\Omega} - \frac{16}{\gamma\Omega} \left(\frac{\mu^2}{2} - 1 \right) \right) + \frac{\gamma\mu^2}{9\Omega\nu^2} \\
\bar{C}_\beta \frac{\partial \beta_{1c}}{\partial q} &= -\left(\frac{S_\beta}{\Omega} + \frac{16}{\Omega} \left(1 + \frac{\mu^2}{2} \right) \right) \\
\bar{C}_\beta \frac{\partial \beta_{1s}}{\partial q} &= \left(\frac{16}{\gamma} \frac{S_\beta}{\Omega} + \frac{\mu^2}{2\Omega} - \frac{1}{\Omega} \right)
\end{aligned} \tag{G.1.48}$$

where $\bar{C}_\beta = 1 + S_\beta^2 - \mu^4/4$. As previously done, for moderate forward flight when the advance ratio is finite but small ($\mu \ll 1$), then

$$\begin{aligned}
\frac{\partial \beta_0}{\partial p} &= \frac{\gamma}{8} \frac{2\mu}{3\Omega\nu^2} & \frac{\partial \beta_0}{\partial q} &= 0 \\
\frac{\partial \beta_{1c}}{\partial p} &\approx -\frac{\partial \beta_{1s}}{\partial q} \approx \frac{1 - (16/\gamma) S_\beta}{\Omega (1 + S_\beta^2)} \\
\frac{\partial \beta_{1s}}{\partial p} &\approx \frac{\partial \beta_{1c}}{\partial q} \approx -\frac{S_\beta + 16/\gamma}{\Omega (1 + S_\beta^2)}
\end{aligned} \tag{G.1.49}$$

For a teetering rotor $K_\beta = 0$, $\nu = 1$, $S_\beta = 0$, then the above simplifies to the classical result shown in equation (D.3.43) on page 270, equation (D.3.65) on page 278 and equation (D.3.86) on page 287

$$\begin{aligned}\frac{\partial \beta_{1c}}{\partial p} &\approx -\frac{\partial \beta_{1s}}{\partial q} \approx \frac{1}{\Omega} \\ \frac{\partial \beta_{1s}}{\partial p} &\approx \frac{\partial \beta_{1c}}{\partial q} \approx -\frac{16}{\gamma \Omega}\end{aligned}\tag{G.1.50}$$

G.1.5 Main Rotor Force and Moment Derivatives

Equation (E.2.10) on page 323 presents the simplified rotor in-plane forces as

$$\begin{aligned}X_{MR} &= -T \cos \beta_{1s} \sin \beta_{1c} \approx -T \beta_{1c} \\ Y_{MR} &= T \cos \beta_{1c} \sin \beta_{1s} \approx T \beta_{1s}\end{aligned}\tag{G.1.51}$$

The derivatives follow directly [105]

$$\begin{aligned}\frac{1}{M_{heli}} \frac{\partial X}{\partial \beta_{1c}} &= X_{\beta_{1c}} = -\frac{T}{M_{heli}} \approx -\frac{W}{M_{heli}} = -g \\ \frac{1}{M_{heli}} \frac{\partial Y}{\partial \beta_{1s}} &= Y_{\beta_{1s}} = \frac{T}{M_{heli}} \approx \frac{W}{M_{heli}} = g\end{aligned}\tag{G.1.52}$$

Equation (E.4.3) on page 329 presents the simplified moment at the fuselage center of mass

$$\begin{aligned}C_{xMR} &= \left(\bar{h} C_T + \frac{a\sigma}{16} S_\beta \right) \beta_{1s} + \nu_\beta^2 \frac{a\sigma}{\gamma} \frac{q}{\Omega} \\ C_{yMR} &= \left(\bar{h} C_T - \frac{a\sigma}{16} S_\beta \right) \beta_{1c} + \nu_\beta^2 \frac{a\sigma}{\gamma} \frac{p}{\Omega}\end{aligned}\tag{G.1.53}$$

The corresponding derivatives follow

$$\begin{aligned}\frac{1}{I_x} \frac{\partial L}{\partial \beta_{1s}} &= L_{\beta_{1s}} = \frac{hT}{I_x} + \frac{b}{2} \frac{I_\beta}{I_x} (\Omega R)^2 (\nu^2 - 1) \\ \frac{1}{I_y} \frac{\partial M}{\partial \beta_{1c}} &= M_{\beta_{1sc}} = \frac{hT}{I_y} - \frac{b}{2} \frac{I_\beta}{I_y} (\Omega R)^2 (\nu^2 - 1)\end{aligned}\tag{G.1.54}$$

For the case when the hinge offset is zero $e = 0$, the above expression reduces to

$$\begin{aligned} L_{\beta_{1s}} &= \frac{h T}{I_x} + \frac{b K_\beta}{2 I_x} \\ M_{\beta_{1sc}} &= \frac{h T}{I_y} - \frac{b K_\beta}{2 I_y} \end{aligned} \tag{G.1.55}$$

where b is the number of blades, and K_β is the hub retaining spring.

Appendix H

Helicopter Model

Examples of work related to helicopter models abound in contemporary literature. For example, mathematical modeling R. T. Chen [21, 22], helicopter modeling and handling qualities Heffley *et al.* [66, 68], system identification Tomashofski and Tischler [148], Mettler *et al.* [108, 107, 106]. A number of research centers across the United States are actively engaged in modeling aspects for both full scale and scaled miniature helicopters.

The area of helicopter modeling is both wide and deep. Gavrilets *et al.* [50] explore the development of a low order dynamic model of a miniature helicopter that is suitable for dynamic simulation and control synthesis. Metter and other coauthors explore modeling and system identification of miniature helicopters [105, 106, 107, 108]. A small sample of work related to mathematical modeling and identification of miniature helicopters includes work by Cvetkovic *et al.* [30], Kim and Tilbury [87, 88], Kodak *et al.* [91], Perhinschi and Prasad [121].

H.1 Helicopter Model

Work by Gavrilets *et al.* [50], Mettler *et al.* [105, 108, 107] and Kondak *et al.* [91] have shown that the main rotor forces and moments dominate the dynamic response of small helicopters, and that the tail rotor can be considered a source of force. The main reason for such conclusions are due to characteristics unique to scaled model helicopters that fundamentally change the dynamic behavior of the helicopter system [50, 91]. In general, model helicopters have the following characteristics

- high ratio of the main rotor mass to the fuselage mass
- high thrust to weight ratio (2 to 3)

- very high main rotor angular speed with dominant inertial effects (gyroscopic effects).
- main rotor hubs are very stiff and have no flapping hinges. This allows for large rotor control moments.

The above characteristics of small scaled helicopters are very significant, and the body of literature related to the dynamics of full-scaled helicopters does not apply fully to scaled model helicopters [105]. Given that rotor dynamics are dominant in small scaled helicopters, the interaction between the tail rotor, fuselage and rotor wake, vortex sheet, and other physical characteristics of helicopter flight are of second and higher order. Therefore the primary flight conditions for first order small-scaled helicopters simulation are accurately modeled by

1. 6-DOF rigid body dynamics and 3D kinematics
2. first order main rotor and stabilizer bar dynamics
3. sensor and actuators modeling

Once a mathematical model is developed, model parameters need estimation. Model parameter estimation necessitates performing experiments that will yield best fits to unknown model parameters.

H.1.1 Rigid Body Equation of Motion

The six degrees of freedom (6-DOF) rigid body equation of motion (EOM) are given by equation (B.5.6) on page 193 and equation (B.5.14) on page 196 and are summarized below

$$\begin{aligned}
\dot{u} &= rv - qw + x(q^2 + r^2) + y(pq - \dot{r}) + z(pr + \dot{q}) - g \sin \theta + \frac{X}{m} \\
\dot{v} &= pw - ru + y(p^2 + r^2) + z(qr - \dot{p}) + x(pq + \dot{r}) + g \sin \phi \cos \theta + \frac{Y}{m} \\
\dot{w} &= qu - pv + z(p^2 + q^2) + x(pr - \dot{q}) + y(qr + \dot{p}) + g \cos \phi \cos \theta + \frac{Z}{m} \\
\dot{p} &= \frac{L}{I_x} + \frac{I_{yz}}{I_x} (q^2 - r^2) + \frac{I_{zx}}{I_x} (\dot{r} + pq) + \frac{I_{xy}}{I_x} (\dot{q} - rp) + \frac{(I_y - I_z)}{I_x} qr + \frac{{}^B H_x^i}{I_x} \\
\dot{q} &= \frac{M}{I_y} + \frac{I_{zx}}{I_y} (r^2 - p^2) + \frac{I_{xy}}{I_y} (\dot{p} + qr) + \frac{I_{yz}}{I_y} (\dot{r} - pq) + \frac{(I_z - I_x)}{I_y} rp + \frac{{}^B H_y^i}{I_y} \\
\dot{r} &= \frac{N}{I_z} + \frac{I_{xy}}{I_z} (p^2 - q^2) + \frac{I_{yz}}{I_z} (\dot{q} + rp) + \frac{I_{zx}}{I_z} (\dot{p} - qr) + \frac{(I_x - I_y)}{I_z} pq + \frac{{}^B H_z^i}{I_z}
\end{aligned} \tag{H.1.1}$$

The total force is itemized as

$$\begin{aligned}
X &= X_{MR} + X_F \\
Y &= Y_{MR} + Y_F + Y_{TR} + Y_{VT} \\
Z &= Z_{MR} + Z_F + Y_{TR} + Y_{HT}
\end{aligned} \tag{H.1.2}$$

The total moments acting on the helicopter are

$$\begin{aligned}
L &= L_{MR} + L_{TR} + L_{VT} + L_F \\
M &= M_{MR} + M_{HT} + M_F \\
N &= N_{MR} + N_{TR} + N_{HT} + N_F
\end{aligned} \tag{H.1.3}$$

The total moment contribution of the various rotating parts are

$$\begin{aligned}
{}^B H_x^i &= \sum_i {}^B \dot{h}_x^i + r \sum_i {}^B h_y^i - q \sum_i {}^B h_z^i \\
{}^B H_y^i &= \sum_i {}^B \dot{h}_y^i + p \sum_i {}^B h_z^i - r \sum_i {}^B h_x^i \\
{}^B H_z^i &= \sum_i {}^B \dot{h}_z^i + q \sum_i {}^B h_x^i - p \sum_i {}^B h_y^i
\end{aligned} \tag{H.1.4}$$

In the above expressions, the $)_{MR}$ subscript applies to the main rotor, $)_{TR}$ applies to the tail rotor, $)_{HT}$ applies to the horizontal tail, the $)_{VT}$ applies to the vertical tail, $)_F$ applies to the fuselage. Some simplifications are possible. If the helicopter does not have a vertical and horizontal tail, then the $)_{HT}$ and $)_{VT}$ components drop. Also, the fuselage moment contribution $M_F = 0, N_F = 0$ are zero when the fuselage center of pressure coincides with the vehicle's center of mass. All the rotating moment contributions are accounted for, and therefore the terms ${}^B H^i$ are zero. Moreover, by taking the moments about the center of mass, the x, y, z components of the moment arm are zero. In addition, the cross product moment of inertia can be neglected without loss of accuracy since the cross inertias are much smaller than the principal inertias [91]. The resultant 6-DOF EOM are now

$$\begin{aligned}
\dot{u} &= rv - qw + -g \sin \theta + \frac{X_{MR} + X_F}{m} \\
\dot{v} &= pw - ru + g \sin \phi \cos \theta + \frac{Y_{MR} + Y_F + Y_{TR}}{m} \\
\dot{w} &= qu - pv + g \cos \phi \cos \theta + \frac{Z_{MR} + Z_F + Z_{TR}}{m} \\
\dot{p} &= \frac{(I_y - I_z)}{I_x} qr + \frac{L_{MR} + L_{TR}}{I_x} \\
\dot{q} &= \frac{(I_z - I_x)}{I_y} rp + \frac{M_{MR}}{I_y} \\
\dot{r} &= \frac{(I_x - I_y)}{I_z} pq + \frac{N_{MR} + N_{TR}}{I_z}
\end{aligned} \tag{H.1.5}$$

The inertial velocities are given by a standard transformation expressed by equation (B.5.8) on page 194 from body \mathcal{B} reference frame to the inertial \mathcal{I} reference frame. In turn, the rotational kinematic equations are given by equation (B.4.6) on page 190 with the assumption of a non-rotating flat earth as the inertial reference frame (see Section B.1.8 on page 181). The three inertial velocity and three rotational kinematic equations are

summarized below in matrix form for convenience

$$\begin{aligned}
 \begin{bmatrix} \dot{\phi} \\ \dot{\theta} \\ \dot{\psi} \end{bmatrix} &= \begin{bmatrix} 1 & \sin \phi \tan \theta & \cos \phi \tan \theta \\ 0 & \cos \phi & -\sin \phi \\ 0 & \sin \phi \sec \theta & \cos \phi \sec \theta \end{bmatrix} \begin{bmatrix} p \\ q \\ r \end{bmatrix} \\
 \begin{bmatrix} \dot{x}_E \\ \dot{y}_E \\ \dot{z}_E \end{bmatrix} &= \begin{bmatrix} c\theta c\psi & s\phi s\theta c\psi - c\phi s\psi & c\phi s\theta c\psi + s\phi s\psi \\ c\theta s\psi & s\phi s\theta s\psi + c\phi c\psi & c\phi s\theta s\psi - s\phi c\psi \\ -s\theta & s\phi c\theta & c\phi c\theta \end{bmatrix} \begin{bmatrix} u \\ v \\ w \end{bmatrix}
 \end{aligned} \tag{H.1.6}$$

H.1.2 Main Rotor Forces and Moments

Wind tunnel tests by Harris [65] cited by Bramwell [13] and later used by Gavrillets *et al.* [50] have demonstrated that momentum theory (see section §C.1 on page 203) predictions are valid for steady state and over a wide range of advance ratio and blade collective pitch angles [50]. From Simple Momentum Theory (SMT) (section 'C.1') the trust coefficient C_T is defined by equation (C.1.17) on page 208, the normalized flow through the rotor or induced inflow λ_i is given by equation (C.1.49), and equation (C.1.52) on page 219 gives the rotor inflow λ for forward flight

$$\begin{aligned}
 &= \frac{V_\infty \sin \alpha + v_i}{\Omega R} = \mu \tan \alpha + \lambda_i \\
 \lambda &= \mu \tan \alpha + \frac{C_T}{2\sqrt{\mu^2 + \lambda^2}}
 \end{aligned} \tag{H.1.7}$$

From Blade Element Theory (BET) (Section C.2 on page 222), the thrust coefficient is given by equation (D.3.130) on page 302

$$C_T = \frac{1}{2} a \sigma \left[\frac{\theta}{3} \left(1 + \frac{3}{2} \mu^2 \right) - \frac{\lambda}{2} \right] \tag{H.1.8}$$

Equation (H.1.7) resulting from SMT says that the rotor inflow λ depends on the thrust, while equation (H.1.8) resulting from BET indicates that the thrust depends on the rotor induced velocity. The inflow rotor λ and associated induced velocity field across the rotor disk depend on knowledge of the individual blade tip vortices and consequent

rotor wake, which in turn depends on the rotor thrust, airload distribution and blade pitch and flapping dynamics [92]. From equation (H.1.8) above, the rotor inflow λ can be approximated in hover ($\mu = 0$) and in high speed forward flight ($\mu \ll V_\infty \cos \alpha / \Omega R$) as

$$\begin{aligned} \lambda_i &= \sqrt{\frac{C_T}{2}} & , \mu = 0 \\ \lambda &= \frac{C_T}{2\mu} & , 0.2 < \mu \end{aligned} \tag{H.1.9}$$

The above expression is valid for steady flight conditions when the rotor is trimmed and the flow is slowly varying [119]. For forward velocities between 0 and $\mu = 0.15$ ($-2 \leq \mu/\lambda_i \leq 0$), the inflow transients are nonuniform and non-linear. During this low speed regime and during slow descent flight ($-2 \leq V_C/v_h \leq 0$) when the vertical velocity approaches the rotor induced velocity, the slip stream breaks and becomes unsteady with the generation of toroidal vortex rings caused by blade tip vortices interacting with other blades [92, 119, 124]. To model these unsteady and non-linear effects, researchers use empirical results that accommodate both the causal physics and resulting dynamic effects of the vortex ring state portion of the flight envelope. Numerous experimental results have laid a rich body of literature related to the subject of rotor inflow modeling. Johnson [82], and Leishman [92] provide a good summary related to inflow models based on work and results by Brotherhood and Stewart [15], Heyson and Katsoff [69], Coleman *et. al.* [25], Drees [36], Mangler and Squire [99]. Bramwell [11], Stepniewski and Keys [142] and Payne [120] also summarize work on rotor inflow models. Other related literature includes early work by Lock [98], Goldstein [58], and Azuma [6], contemporary work by Castles and De Leeuw [84], R. T. Chen [23], and more recent work by Chen *et. al.* [19, 20], and Zhao *et. al.* [160]. Padfield [119] gives an iterative solution for the rotor inflow calculation, and Gavrillets [50] adapts this iterative solution to a scaled model helicopter. In this work, the thrust coefficient and inflow ratio are found given an airspeed, rotor angular speed and blade pitch collective setting. The modified Padfield [119, p. 123] iterative method

[50] augmented by [92, p. 66] includes the following fixed point algorithm

$$\begin{aligned}
\lambda_{n=0} &= \lambda_h = \sqrt{\frac{C_T}{2}} \\
\lambda_{n+1} &= \mu \tan \alpha + \frac{C_T}{2\eta_w \sqrt{\mu^2 + \lambda_n^2}} \\
C_{T,\max} &= \frac{T_{\max}}{\rho (\Omega R)^2 \pi R^2} \\
C_{T,BET} &= \frac{1}{2} a \sigma \left[\frac{\theta}{3} \left(1 + \frac{3}{2} \mu^2 \right) - \frac{\lambda}{2} \right] \\
C_T &= \begin{cases} -C_{T,\max} & C_{T,BET} < -C_{T,\max} \\ C_{T,BET} & -C_{T,\max} \leq C_{T,BET} \leq C_{T,\max} \\ C_{T,\max} & C_{T,\max} < C_{T,BET} \end{cases}
\end{aligned} \tag{H.1.10}$$

where

$$\begin{aligned}
\varepsilon &= \left\| \frac{\lambda_{n+1} - \lambda_n}{\lambda_{n+1}} \right\| \\
T_{\max} &= \left(\frac{T}{W} \right)_{\max} mg \\
\mu^2 &= \frac{(u - u_{wind})^2 + (v - v_{wind})^2}{(\Omega R)^2} \\
\mu_z &= \frac{w - w_{wind}}{\Omega R}
\end{aligned} \tag{H.1.11}$$

η_w – coefficient of non - ideal wake contraction

The term ε is the error estimator which indicates convergence when $\varepsilon < 0.05\%$. The term $(T/W)_{\max}$ is the maximum thrust to weight ratio for a particular helicopter, and the term $C_{T,BET}$ is the thrust coefficient result from BET in equation (H.1.8). The term η_w accounts for non-ideal slipstream and wake contraction and for power loss due to tip vortex and unsteady pressure distribution [50, 92, 119]. The above fixed point algorithm can be modified to use a Newton-Raphson iterative process such that from equation

(H.1.7)

$$\begin{aligned}
f(\lambda) &= \lambda - \mu \tan \alpha - \frac{C_T}{2\eta_w \sqrt{\mu^2 + \lambda_n^2}} = 0 \\
\frac{\partial f(\lambda)}{\partial \lambda} &= 1 + \frac{C_T}{2\eta_w} (\mu^2 + \lambda_n^2)^{-3/2} \\
\lambda_{n+1} &= \lambda_n - \left[\frac{\partial f(\lambda)}{\partial \lambda} \right]_n^{-1} f(\lambda_n)
\end{aligned} \tag{H.1.12}$$

Results from the above algorithms rely on momentum theory, but momentum theory does not apply in the vortex ring state during flight conditions when $(-2 \leq \mu/\lambda_i \leq 0)$. In this case, the fixed point algorithm will not converge when $\mu = 0$. In turn, the Newton-Raphson method will converge in this range of flight conditions, but the solution may be non-physical. Leishman [92, p. 58] proposes an empirical approximation to results obtained from various experiments given by

$$\frac{v_i}{v_h} = k_0 + k_1 \left(\frac{v_i}{v_h} \right) + k_2 \left(\frac{v_i}{v_h} \right)^2 + k_3 \left(\frac{v_i}{v_h} \right)^3 + k_4 \left(\frac{v_i}{v_h} \right)^4 \tag{H.1.13}$$

with

$$\begin{aligned}
k_0 &= \sqrt{\frac{C_T}{2}} \\
k_1 &= -1.125 & k_3 &= -1.718 \\
k_2 &= -1.372 & k_4 &= -0.655
\end{aligned} \tag{H.1.14}$$

The above empirical expression (H.1.13) is valid for the range $(-2 \leq V_C/v_h \leq 0)$. The rotor torque is given by equation (D.3.130) in section §D.3.7.1

$$C_Q = \lambda C_T + \frac{\sigma C_d}{8} (1 + \mu^2) \tag{H.1.15}$$

The full expression for the rotor in-plane forces C_H , C_Y are found in equation (E.2.2) and equation (E.2.5) on page 322. Using the fundamental assumption that the rotor thrust remains perpendicular to the rotor Tip Path Plane [13, 82, 119], then equation (E.2.10) on page 323 represents a simplified set of the in-plane forces X_{MR} , Y_{MR} . In turn, equation (E.3.12) on page 328 gives the rotor hub moments due to blade flapping, blade spring

restraint and flap hinge offset. The corresponding rotor moments at the fuselage center of mass are summarized in equation (E.4.3) on page 329. These equations are summarized below for convenience.

$$\begin{aligned}
 X_{MR} &= -T \cos \beta_{1s} \sin \beta_{1c} \approx -T \beta_{1c} \\
 Y_{MR} &= T \cos \beta_{1c} \sin \beta_{1s} \approx T \beta_{1s} \\
 Z_{MR} &= -T \cos \beta_{1s} \cos \beta_{1c} \approx -T \\
 C_{xMR} &= \left(\bar{h} C_T + \frac{a\sigma}{16} S_\beta \right) \beta_{1s} \\
 C_{yMR} &= \left(\bar{h} C_T - \frac{a\sigma}{16} S_\beta \right) \beta_{1c}
 \end{aligned} \tag{H.1.16}$$

H.2 Extended Linearized Rigid Body Equations for Motion

Equation (H.1.1) through equation (H.1.4) on page 359 represent the full six degrees of freedom (6-DOF) non-linear equations of motion (EOM) of a rigid body in atmospheric flight. Equation (F.1.1) through equation (F.1.6) on page 335 represent a simplified set of the 6-DOF rigid body EOM where it is assumed that the helicopter has a plane of symmetry, some of the rotating components have been dropped, and which also include three kinematic equations and three translational equations. Also the angular rate of change equations have been rearranged to make the set of equations suitable for linearization. The full linearized equations of motion are given by equation (F.1.21) through equation (F.1.28) on page 341. Table D.1 on page 315 presents a summary of the flapping blade equations of motion. Equation (D.3.144) on page 306 presents a first order approximation of the Tip Path Plane (TPP) blade dynamics while equation (D.3.147) on page 307 presents a simplified version of the same TPP blade dynamics for the case of low translational speed $\mu \rightarrow \textit{small}$. This first order TPP blade dynamic augments the 6-DOF rigid body equations of motion along with equation (G.1.52) and equation (G.1.54) on page 355.

The augmented linearized longitudinal EOM is

$$\begin{aligned}
 A_{lon} &= \begin{bmatrix} X_u & X_w - q_0 & X_q - w_0 & -g \cos \theta_0 & X_{\beta_{1c}} \\ Z_u + q_0 & Z_w & Z_q + u_0 & -g \cos \phi_0 \sin \theta_0 & \\ \bar{M}_u & \bar{M}_w & & & M_{\beta_{1c}} \\ & & \cos \phi_0 & & \\ & & -\nu_\beta^2 & & n_1 \gamma \Omega / 16 \end{bmatrix} \\
 A_{12} &= \begin{bmatrix} X_v + r_0 & X_p & X_r + v_0 & & \\ Z_v - p_0 & Z_p - v_0 & Z_r & -g s \phi_0 c \theta_0 & \\ \bar{M}_v & \bar{M}_p - \bar{I}_q r_0 - 2\bar{I}_{zx} p_0 & \bar{M}_r - \bar{I}_q p_0 + 2\bar{I}_{zx} r_0 & & \\ & & -\sin \phi_0 & \bar{K}_\phi & \\ & (1 - 4e/3) \gamma / 16 & & & \gamma \Omega / 16 S_\beta \end{bmatrix}
 \end{aligned} \tag{H.2.1}$$

The corresponding augmented linearized lateral EOM is

$$\begin{aligned}
 A_{21} &= \begin{bmatrix} Y_u - r_0 & Y_w + p_0 & Y_q & -g s \phi s \theta_0 & \\ \bar{L}_u & \bar{L}_w & \bar{L}_q + \bar{I}_{pr} p_0 - \bar{I}_p r_0 & & \\ \bar{N}_u & \bar{N}_w & \bar{N}_q - \bar{I}_r p_0 - \bar{I}_{pr} r_0 & & \\ & & \sin \phi_0 \tan \theta_0 & \bar{K}_\theta & \\ & & -(1 - 4e/3) \gamma / 16 & & -\gamma \Omega / 16 S_\beta \end{bmatrix} \\
 A_{lat} &= \begin{bmatrix} Y_v & Y_p + w_0 & Y_r - u_0 & g \cos \phi \cos \theta_0 & Y_{\beta_{1s}} \\ \bar{L}_v & \bar{I}_{pr} q_0 & \bar{L}_r - \bar{I}_p q_0 & & L_{\beta_{1s}} \\ \bar{N}_v & \bar{N}_p - \bar{I}_r q_0 & \bar{N}_r - \bar{I}_{pr} q_0 & & \\ & 1 & \cos \phi_0 \tan \theta_0 & & \\ & -\nu_\beta^2 & & & n_1 \gamma \Omega / 16 \end{bmatrix}
 \end{aligned} \tag{H.2.2}$$

The above A_{lon} , A_{lat} equations differ from equation (F.1.25) on page 340 in that the roll and pitch damping derivatives \bar{L}_p , \bar{M}_q are now captured by the rotor damping τ_p , τ_q

where $\tau = 16/\gamma\Omega$ is the main rotor time constant. In addition, the rotor forces and moments are represented by the rotor flapping derivatives $X_{\beta_{1c}}, Y_{\beta_{1s}}, L_{\beta_{1s}}, M_{\beta_{1c}}$ [104].

H.2.1 Flapping Motion for Semi-rigid Rotors with Stabilizer Bar

A model helicopter stabilizing bar and cyclic control mechanism is shown in Figure H.1 on page 369. The main rotor collective pitch results from the weighted sum of Bell cyclic input δ_{cyc} originating from pilot stick inputs and the indirect Hiller input contribution from the stabilizing bar flap angle β_{stab} such that

$$\begin{aligned}\delta_{cyc} &= -K_{lat}\delta_{lat}\cos\psi - K_{lon}\delta_{lon}\sin\psi \\ \delta_{stab} &= \delta_{cyc}\left(\psi + \frac{\pi}{2}\right) = -\bar{K}_{lat}\delta_{lat}\sin\psi + \bar{K}_{lon}\delta_{lon}\cos\psi \\ &= -\theta_{stab,1c}\cos\psi - \theta_{stab,1s}\sin\psi \\ \theta_{stab,1c} &= -\bar{K}_{lon}\delta_{lon} \\ \theta_{stab,1s} &= \bar{K}_{lat}\delta_{lat}\end{aligned}\tag{H.2.3}$$

where the constant $\bar{K}_{lat,lon}$ differs from the unbar version by some gear elements. Figure H.2 on page 370 illustrates the cyclic contributions by the pilot stick inputs δ_{cyc} and the augmented contributions by the stabilizer bar flapping angle β_{stab}

$$\begin{aligned}\theta_{cyc} &= \frac{L_2}{L_4}\delta_{cyc} + \frac{L_1L_3}{L_4(L_2 + L_3)}\beta_{stab} \\ \theta_{cyc} &= K_{cyc}\delta_{cyc} + K_{stab}\beta_{stab}\end{aligned}\tag{H.2.4}$$

Similar results are given by [87, 88]. The stabilizing bar is a teetering rotor that carries no thrust, and therefore has no coning angle. The paddle blade motion is then the same as the first order TPP equation of motion for a flapping rotor minus the coning angle [105]

$$\beta_{stab}(\psi) = -\beta_{stab,1c}\cos\psi - \beta_{stab,1s}\sin\psi\tag{H.2.5}$$

Equation (D.3.161) is an expression for the equation of motion for a flapping blade when neglecting effects due to advance ratio ($\mu \rightarrow$ small, i.e. ignore translational dynamics) and fast blade dynamics ($[\ddot{\beta}, \dot{p}, \dot{q}] \rightarrow$ small, fast). Moreover, in the case of the stabilizer bar there is no hinge offset ($e = 0, \varepsilon = 0$) and no blade restoring spring ($K_\beta = 0$). In this case equation (D.3.164) is an appropriate first order approximation of the teetering rotor.

$$\begin{aligned}\frac{16}{\gamma\Omega}\dot{\beta}_{stab,1s} &= -\beta_{stab,1s} + \frac{p}{\Omega} - \frac{16}{\gamma} \frac{q}{\Omega} + \theta_{stab,1c} \\ \frac{16}{\gamma\Omega}\dot{\beta}_{stab,1c} &= -\beta_{stab,1c} - \frac{q}{\Omega} - \frac{16}{\gamma} \frac{p}{\Omega} + \theta_{stab,1s}\end{aligned}\tag{H.2.6}$$

Let the stabilizer bar flapping time constant be $\tau_{stab} = 16/\gamma\Omega$

$$\begin{aligned}\tau_{stab}\dot{\beta}_{stab,1s} &= -\beta_{stab,1s} + \frac{p}{\Omega} - \tau_{stab}q - \bar{K}_{lon}\delta_{lon} \\ \tau_{stab}\dot{\beta}_{stab,1c} &= -\beta_{stab,1c} - \frac{q}{\Omega} - \tau_{stab}p + \bar{K}_{lat}\delta_{lat}\end{aligned}\tag{H.2.7}$$

The cyclic inputs to the main blade are now [105, 108]

$$\begin{aligned}\theta_{1s} &= K_{lon} (K_{cyc} \delta_{lon} + K_{stab} \beta_{stab,1s}) \\ \theta_{1c} &= K_{lat} (K_{cyc} \delta_{lat} + K_{stab} \beta_{stab,1c})\end{aligned}\tag{H.2.8}$$

Equation (D.3.147) on page 307 is the a general expression for the main blade flapping dynamics. After rearranging some terms

$$\begin{aligned}\tau_\beta\dot{\beta}_{1c} &= n_1\beta_{1c} + S_\beta\beta_{1s} - n_2\theta_{1s} + \left(1 - \frac{4e}{3}\right) \frac{p}{\Omega} - \nu_\beta^2\tau_\beta q - 2x^2\mu\lambda \\ \tau_\beta\dot{\beta}_{1s} &= n_1\beta_{1s} - S_\beta\beta_{1c} + n_2\theta_{1c} - \nu_\beta^2\tau_\beta p - \left(1 - \frac{4e}{3}\right) \frac{q}{\Omega}\end{aligned}\tag{H.2.9}$$

where the main blade flapping time constant $\tau_\beta = 16/\gamma\Omega$ and x, n_1, n_2 are defined in Equation (D.3.138) on page 304.. Equations (H.2.7), (H.2.8) and (H.2.9) comprise the first order Tip Path Plane (TPP) dynamics of the rotor-stabilizer bar system. Mettler and coworkers [50, 105, 108] have demonstrated that the rotor-stabilizer bar can be lumped to reduce the order of their model to only two states.

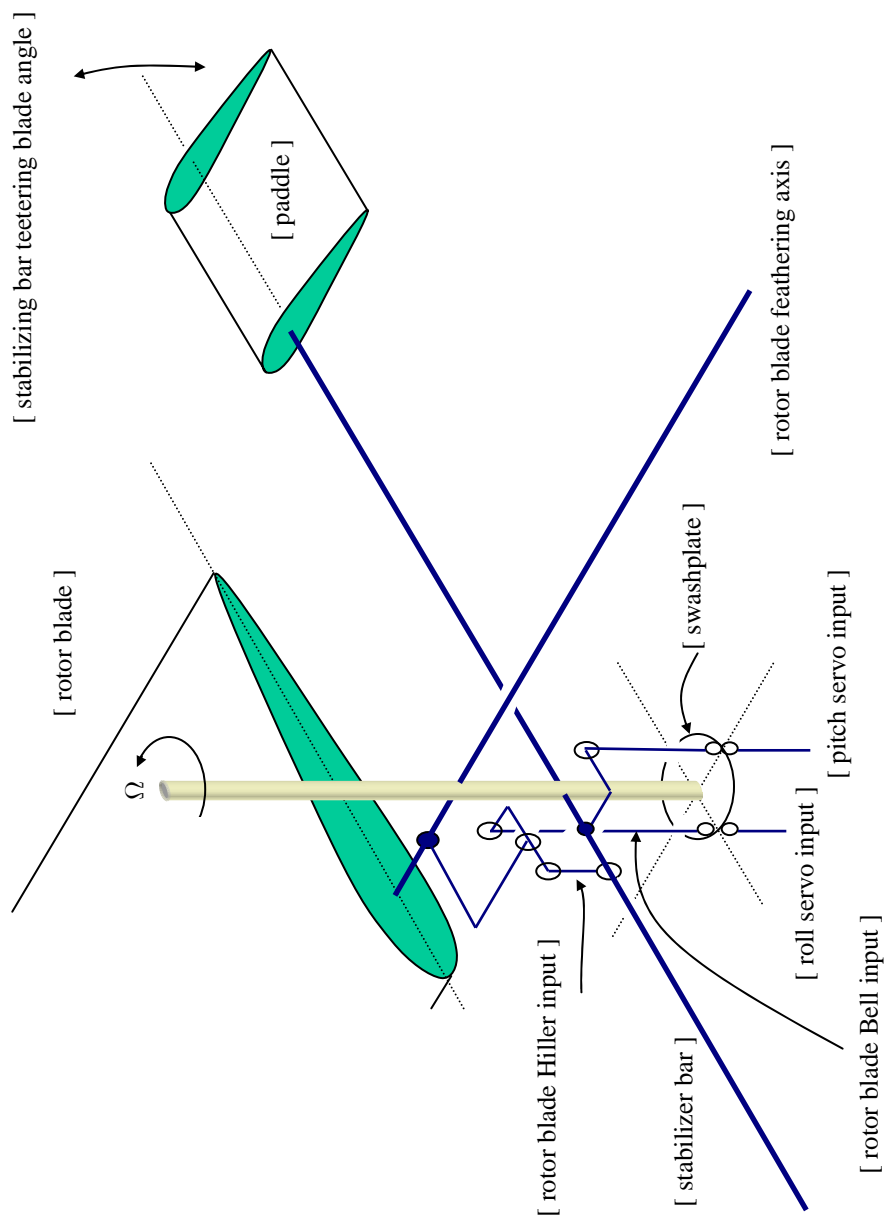


Figure H.1: Main Rotor Stabilizer Teetering Mechanism.

Appendix I

Hardware Parameters and Sensor Calibration

I.1 Helicopter Parameter Estimation

A number physical helicopter parameters listed below need estimation. To do so, physical principles along with work done by previous researchers are used extensively and are so noted where appropriate. Some parameters (such as the moment of inertia of the main rotor shaft) follow directly from applied physics and do not need explanation.

1. rotational inertia.
2. other.

I.1.1 Rotational Inertia

The helicopter rotational inertia I_{rot} can be estimated from the total kinetic energy $I_{rot}\Omega^2/2$ associated with the various helicopter rotating components

$$\begin{aligned} (I_{hub} + 2I_{MR}) \Omega^2 + I_{eng} (n_{MR}\Omega)^2 + 2I_{TR} (n_{TR}\Omega)^2 &= I_{rot}\Omega^2 \\ I_{MR} + I_{eng}n_{MR}^2 + I_{TR}n_{TR}^2 &= I_{rot} \end{aligned} \tag{I.1.1}$$

where I_{MR} is the main rotor blade inertia about the rotating axis, I_{TR} is the corresponding inertia for the tail rotor blades and tail rotor rotating parts, I_{eng} is the engine and other inertia components associated with the engine such as the ducted fan and transmission gears, I_{MR} is the shaft and hub inertia, and n_{MR} , n_{TR} are the engine-to-main rotor and engine-to-tail rotor transmission gear. Estimates for the engine and tail rotor inertias are borrowed from previous work done on similarly sized helicopters [50, 105]. These quantities are tabulated in Table I.1 on the following page.

I.1.2 Helicopter Testbed Platform Parameters

The helicopter inertial properties were determined using a two step approach:

1. torsional pendulum [32, 64] on the basic helicopter structure made up by
 - tail boom
 - main rotor
 - engine
2. itemized inertial contributions from the varioud components
 - CPU boards
 - GPS system and GPS antenna
 - wireless digital modem
 - IMU

Table Table I.2 on the next page shows the inertial characteristics of the helicopter, while Table I.3 on the following page shows the relevant helicopter dimensions as illustrated in figure F.1 and figure F.2 on page 333.

Table I.4 on the following page tabulates the main rotor components, Table I.5 on page 374 tabulates the stabilizer bar parameters and Table I.6 on page 374 tabulates the tail rotor parameters. Finally, Table I.7 on page 375 tabulates the various mass components for the Helicopter

Table I.1: Rotational Inertial Parameters

		unit	description
I_{rot}	0.117	$kg\ m^2$	rotating inertia
I_{MR}	0.0852	$kg\ m^2$	main rotor blade, shaft and hub inertia
I_{TR}	0.0044	$kg\ m^2$	tail rotor blade, hub and shaft inertia
I_{eng}	0.0003	$kg\ m^2$	engine-related rotating inertia
n_{MR}	9.29		engine-to-main rotor gear ratio
n_{TR}	4.667		main rotor-to-tail rotor gear ratio

Table I.2: Helicopter Mass and Inertial Parameters

		unit	description
M_{heli}	8.3	kg	helicopter mass
I_{xx}	0.074	kg m^2	roll moment of inertia
I_{yy}	0.34	kg m^2	pitch moment of inertia
I_{zz}	0.27	kg m^2	yaw moment of inertia

Table I.3: Helicopter Dimensions

		unit	description
l_{MR}	0.01	m	main rotor hub location behind the cm
h_{MR}	0.285	m	main rotor hub location above the cm
l_{TR}	0.932	m	tail rotor hub location behind the cm
y_{TR}	-0.057	m	tail rotor hub location sideways from the cm
h_{TR}	0.093	m	tail rotor hub location above the cm
$S_{x,fus}$	0.1	m^2	frontal fuselage drag area
$S_{y,fus}$	0.22	m^2	side fuselage drag area
$S_{z,fus}$	0.15	m^2	vertical fuselage drag area

Table I.4: Main Rotor Parameters

		unit	description
R	0.74	m	rotor radius
c	0.062	m	blade cord
e	0.083	m	geometrical hinge offset
b	2		number of blades
I_{MR}	0.0855	$kg m^2$	rotor hub inertia
I_{β}	0.0299	$kg m^2$	blade flapping inertia
Ω	157.1	rad/sec	nominal rotor speed (1500 <i>rpm</i>)
T_{MR}	106.7	N	nominal hover maximum thrust (24 <i>lbf</i>)
$C_{T,maxMR}$	0.0055		main rotor maximum thrust coefficient
ε	0.5		ratio of blade first to second moment of inertia
σ	0.0529		rotor solidity
γ	4.31		rotor Lock number
K_{β}	54.0	$N \cdot m/rad$	hub torsional stiffness
S_{β}	1.07		rotor stiffness number
n_{TR}	4.667		main rotor to tail rotor gear ratio
n_{MR}	9.29		engine to main rotor gear ratio
$C_{l_{\alpha}}$	5.7	rad^{-1}	blade lift curve slope
C_{D_0}	0.024		blade zero lift drag coefficient

Table I.5: Stabilizer Bar Parameters

		unit	description
R_{stab}	0.31	m	stabilizer bar radius
$R_{stab,i}$	0.23	m	inside stabilizer bar radius
c_{stab}	0.06	m	paddle cord
a_{stab}	2.67	rad^{-1}	paddle lift curve slope
m_{paddle}	0.028	kg	paddle mass
m_{rod}	0.048	kg	rod mass
l_{rod}	0.483	kg	rod length
$I_{\beta,stab}$	0.005	kgm^2	paddle and rod inertia
γ_{stab}	0.5		stabilizer Lock number

Table I.6: Tail Rotor

		unit	description
R_{TR}	0.13	m	tail rotor radius
c_{TR}	0.029	m	tail rotor cord
a_{TR}	5.0	rad^{-1}	tail rotor lift curve slope
C_{DTR}	0.024		tail rotor zero lift drag
δ_{trim}	0.1	rad	tail rotor trim offset
$C_{T,maxTR}$	0.05		tail rotor maximum thrust coefficient

Table I.7: Helicopter Mass (Weight) Parameters

		unit	description
M_{heli}	5.21	kg	basic (empty) helicopter mass (11.46 <i>lbf</i>)
M_{frame}	1.902	kg	main frame (4.2 <i>lbf</i>)
M_{engine}	0.600	kg	engine mass (1.32 <i>lbf</i>)
M_{tail}	0.464	kg	tail boom + tail rotor mass (1.02 <i>lbf</i>)
M_{mrgear}	0.26	kg	main rotor gear mass (9.12 <i>oz</i>)
M_{head}	0.236	kg	rotor hub mass (8.32 <i>oz</i>)
M_{blade}	0.202	kg	mass of one (1) blade (7.2 <i>oz</i>)
M_{shaft}	0.114	kg	main rotor shaft mass (4.0 <i>oz</i>)
M_{bar}	0.108	kg	fly-bar assembly mass (3.8 <i>oz</i>)
M_{egear}	0.096	kg	engine gear + pulleys mass (3.4 <i>oz</i>)
$M_{exhaust}$	0.080	kg	exhaust pipe mass (2.82 <i>oz</i>)
M_{mpak}	1.1	kg	MotionPak mass (2.43 <i>lbf</i>)
M_{batt}	0.652	kg	battery mass (1.44 <i>lbf</i>)
M_{GPS}	0.62	kg	GPS + FreeWave mass (1.37 <i>lbf</i>)
M_{cpu}	0.6	kg	main CPU mass (1.32 <i>lbf</i>)
M_{aux}	0.57	kg	auxiliary equipment mass (1.26 <i>lbf</i>)
M_{fuel}	0.494	kg	fuel mass (1.1 <i>lbf</i>)
M_{gpsant}	0.230	kg	GPS antenna mass (8.1 <i>oz</i>)
M_{total}	9.5	kg	total mass (21.0 <i>lbf</i>)

I.2 Sensors and Actuators

I.2.1 Systron Donner MotionPak

Figure I.1 shows the solid state Systron Donner MotionPak, a six degree of freedom (6dof) inertial sensing system used for measuring linear accelerations and angular rates in instrumentation and control applications. It is a highly reliable, compact, and fully self-contained motion measurement package. It uses three orthogonally-mounted solid-state micro-machined quartz angular rate sensors, and three high performance linear servo accelerometers mounted in a compact, rugged package, with internal power regulation and signal conditioning electronics [33, 34]. Table I.8 on the next page summarizes the mechanical and electronic specifications for the MotionPak. In addition, Table I.9 on the following page tabulates the MotionPak's specifications regarding angular measurements while Table I.10 on the next page tabulates similar information regarding linear measurements.



Figure I.1: Systron Donner MotionPak.

Table I.8: Mechanical and Electrical Specifications

Input Current (+15 Vdc):	+252 mA
Input Current (-15 Vdc):	-198 mA
Package Weight:	888 g
Temp. Sensor (AD590):	1 A/K

Table I.9: MotionPak Angular Measurements Specifications

	X-AXIS	Y-AXIS	Z-AXIS
Range	$\pm 200^\circ/\text{s}$	$\pm 200^\circ/\text{s}$	$\pm 500^\circ/\text{s}$
Scale Factor	12.469 mV/ $^\circ/\text{s}$	12.500 mV/ $^\circ/\text{s}$	5.014 mV/ $^\circ/\text{s}$
<i>Temp Performance</i>	$< \pm 0.03\% / ^\circ\text{C}$	$< \pm 0.03\% / ^\circ\text{C}$	$< \pm 0.03\% / ^\circ\text{C}$
Bias (@ +22°C)	+0.06 $^\circ/\text{s}$	+0.21 $^\circ/\text{s}$	-0.03 $^\circ/\text{s}$
<i>Temp Performance</i>	$< 3^\circ/\text{s}$ (\uparrow +22°C)	$< 3^\circ/\text{s}$ (\uparrow +22°C)	$< 3^\circ/\text{s}$ (\uparrow +22°C)
Alignment	0.83 $^\circ$	0.12 $^\circ$	0.09 $^\circ$
Bandwidth (-90°)	77 Hz	77 Hz	78 Hz
Damping	0.70	0.66	0.72
Noise (100-100Hz)	1.0 mVRMS	1.1 mVRMS	0.4 mVRMS

Table I.10: MotionPak Linear Measurements Specifications

	X-AXIS	Y-AXIS	Z-AXIS
Range	* (max) ± 15 g	* (max) ± 15 g	* (max) ± 15 g
Scale Factor	2.966 mA/g	2.961 mA/g	2.867 mA/g
<i>Temp Performance</i>	+0.001 $\% / ^\circ\text{C}$	+0.001 $\% / ^\circ\text{C}$	+0.001 $\% / ^\circ\text{C}$
Bias (@ +22°C)	+1.22 mg	+0.54 mg	+9.37 mg
<i>Temp Performance</i>	-14 $\mu\text{g} / ^\circ\text{C}$	-6 $\mu\text{g} / ^\circ\text{C}$	-46 $\mu\text{g} / ^\circ\text{C}$
Alignment	0.11 $^\circ$	0.11 $^\circ$	0.32 $^\circ$
Bandwidth (-90°)	1632 Hz	1496 Hz	1648 Hz
Damping	0.44	0.32	0.46
Noise (100-100Hz)	2.0 μARMS	2.3 μARMS	1.9 μARMS

I.2.2 NovAtel Global Positioning System

Figure I.2 on the following page shows the NovAtel [63] Global Positioning System (GPS) components. The NovAtel GPS system consists of a ground base waterproof unit called ProPack, on-board GPS card called MiLLennium GPScard, a ground reference antenna with multipath elimination technology, and an on-board active antenna. The ProPack ground station GPS unit knows its geological position very accurately, and as it receives updated GPS information, it forms a message which it passes on to the on-board GPS card. The ProPack and MiLLennium units work together to provide differential GPS information with an accuracy of 2cm Circle Error Probable (CEP). Figure I.3 on the next page shows a set of measurements taken with the differential GPS system from NovAtel, and Figure I.4 on page 380 shows the setup of the GPS reference antenna on top of the Sarkey Energy Center at the University of Oklahoma. Table I.11 tabulates relevant data related to the MiLLennium GPScard [75]. The ProPack card performance is equal to that of the MiLLennium card.

Table I.11: GPS MiLLennium GPScard Selected Performance Parameters

Frequency	1575.2 MHz & 1227.6 MHz (L2)
Codes Tracked	C/A and P codes
Channels	12 L1/L2 channel pair
Time to First Fix	70 sec typical (cold start)
Re-acquisition	L1: 3 sec, L2: 40 sec, typical
Computed Data Update Rate	4 solutions/sec
Measured Data Update Rate	4 data records/sec
Differential Pseudorange	$GDOP < 4, CEP < 0.75\text{m}, SEP < 1.00\text{m}$
Position Latency	175 msec
Differential Velocity Latency	0.03 m/sec
Acceleration	6g max.
Power	7.5 watts
Weight	0.175kg(6.2oz)



Figure I.2: NovAtel GPS Ground Station Receiver, On-Board Card, Antenna, and Reference Station Antenna.

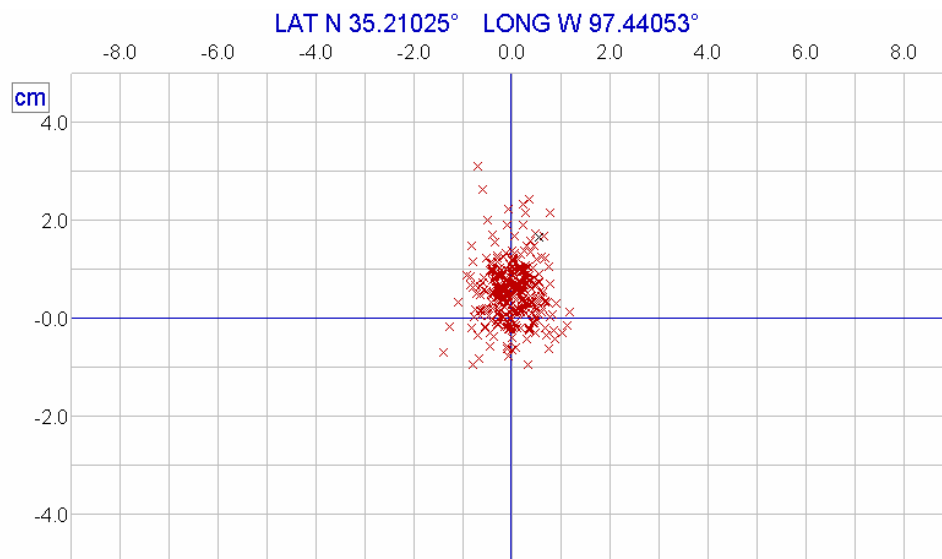


Figure I.3: Differential GPS measurements with 2.0cm Circle Error Probable (CEP) position accuracy at a location on the University of Oklahoma Campus.



Figure I.4: GPS Reference Antenna on top of the Sarkey Energy Center at the University of Oklahoma.

I.2.3 FreeWave Wireless Data Transceiver

Figure I.5 shows the on-board card and the ground station version of the FreeWave wireless digital data transceiver, and Table I.12 on the next page tabulates selected parameter pertaining to the device. The FreeWave transceiver sports the following features [47, 48]. The FreeWave performance has been robust and flawless at all times.

- Frequency Hopping
- High Speed - 115.2 Kbps true throughput.
- Long Range - 20 mile range with clear line of sight, ability to extend through repeaters
- Error Free Communications - 32 bit CRC with automatic retransmission
- Repeater and simultaneous Slave and Repeater function all in a single radio
- RS232 Interface
- Noise Immunity - Superior performance in noise congested environments
- UL Approved



Figure I.5: FreeWave Wireless Data Transceiver On-Board Card and Ground Station Unit.

Table I.12: FreeWave Selected Technical Specifications

Frequency	902 – 928 MHz
Range	20 miles
RS232 Data Throughput	1200 Baud - 115.2 KBaud
Modulation Type	Spread Spectrum, GFSK
Spreading Code	Frequency hopping
Hop Patterns	15 user selectable
Output Power	1 Watt
Error Detection	32 Bit CRC with packet retransmit
Power	180mA average
Weight	0.340kg(12oz)

I.2.4 SHARP GP2D02 Infrared Sensor

Figure I.6 shows a SHARP GP2D02 infrared distance sensor with a range of 10 – 80 cm. The sensor uses a digital interface to a microcontroller to provide measurements at 10 Hz. A number of calibration runs resulted in the general formula for distance estimation

$$L = \frac{1560}{dec - 47.7} - 0.5 \quad (\text{I.2.1})$$

where L is the range distance in cm and dec is the output of the infrared sensor [28, 29]. The infrared sensor provides complimentary range information for altitude estimation.

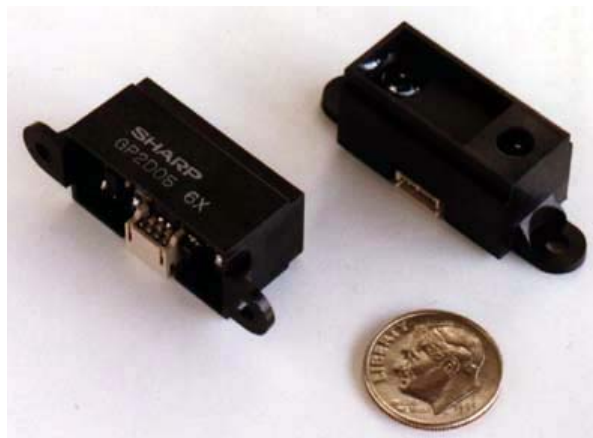


Figure I.6: SHARP GP2D02 Infrared Distance Sensor.

I.2.5 AccuStar II Dual Axis Clinometer

Figure I.7 shows the AccuStar II Clinometer. The AccuStar clinometer is a capacitance-based sensor with an output proportional to the tilt of two orthogonal axis. Table I.13 shows typical performance numbers for the AccuStar clinometer device.



Figure I.7: Dual Axis Clinometer AccuStar II.

Table I.13: AccuStar II Performance

Range	$\pm 20^\circ$
Threshold / Resolution	0.01
Linearity	
Null to 10°	$\pm 0.2^\circ$
10° to 12°	$\pm 2.5\%$
12° to 15°	$\pm 3.0\%$
15° to 20°	Monotonic
Null Repeatability	± 0.1
Frequency Response ($-3db$)	0.25 Hz

Figure I.8 on the next page shows the calibration curve for the AccuStar clinometer device. The clinometer is set to generate a pulse width modulated (PWM) output with a duty cycle given by

$$output = \frac{t_2}{t_2 - t_1}$$

where t_1 and t_2 varies from 0.2 to 0.7 msec. The simple calibration exercise consisted of

measuring the inclinometer output when subject to a known inclination. The calibration curves for the various clinometer devices are all consistently linear, and the small variations between the various curves amount to a master curve with a particular slope plus some small offset.

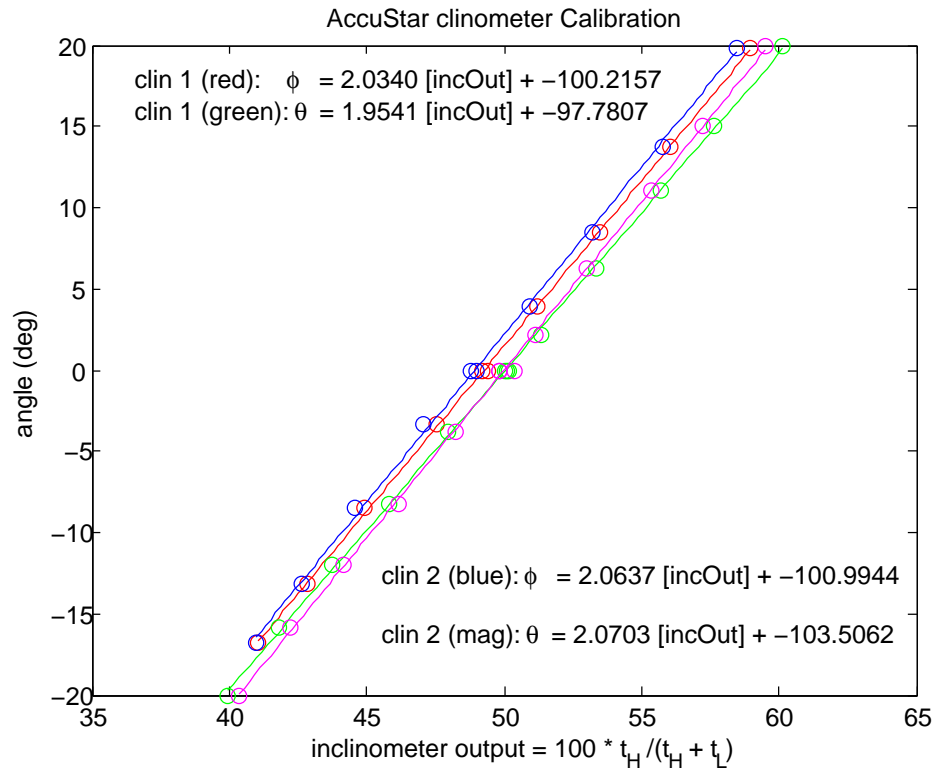


Figure I.8: Calibration Curve for the AccuStar II Dual Axis Clinometer.

I.2.6 Electronic Compass

Figure I.9 on the following page shows a picture of the Honeywell HMR3000 electronic compass module [72]. The compass provides heading, pitch and roll output for pitch and roll control, navigation and guidance. It is a solid state strapdown compass able to provide rate information up to 20 Hertz with accuracy of about 0.5° with 0.1° resolution. Table I.14 on page 386 and Table I.15 on page 387 tabulate the most relevant operational specifications related to the HMR3000.

The HMR3000 communicates with an external host via RS-232 or RS-485 electrical standard through simple ASCII character strings. ASCII characters are transmitted and

received using 1 Start bit, 8 Data bits, (LSB first, MSB always 0), no parity, and 1 Stop bit. Baud rate is user configurable to 1200, 2400, 4800, 9600, 19,200 or 38,400. HMR3000 responds to all valid inputs received with correct checksum value.

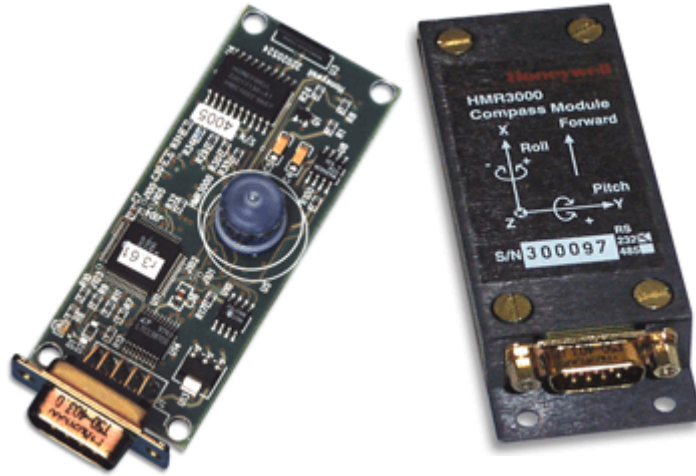


Figure I.9: Electronic Compass Honeywell HMR3000

I.2.7 O.S.61 Helicopter Engine

Figure I.10 shows an illustration of the O.S. 61 Max engine. In turn, Table I.16 on page 387 tabulates the engine specification along with basic performance numbers [8, 37].



Figure I.10: O.S.61 Helicopter Engine

Table I.14: Honeywell HMR3000 Specifications [72].

	<i>Heading</i>	
Accuracy (1)	< 0.5° RMS (2)	Dip <50°, Tilt <20° *
	< 1.5° RMS	Dip <75°, Tilt <20° *
Repeatability	±0.3°	
Resolution	0.1°	
Units	Degrees/mils	User Selectable
	<i>Pitch and Roll</i>	
Range	±40°	
Accuracy	±0.4°	Tilt <20°
	±0.6°	Tilt ≥20°
Repeatability	±0.2°	
Resolution	0.1°	
Units	Degrees/mils	User Selectable
	<i>Magnetic Field</i>	
Dynamic Range	±1.0 Gauss max	±0.5 Gauss Range
Resolution	1 mGauss	
	<i>Interface</i>	
Serial	RS-232	Half Duplex
	RS-485	
Baud Rate	1200 to 38400 bps	
Standard	NMEA 0183	
Update Modes	Continuous	≤ 20 Hz per Sentence
	Strobed	Selectable Averaging

Table I.15: Honeywell HMR3000 Physical Characteristics [72].

<i>Electrical</i>		
Supply Voltage	5.0 Vdc, 6-15 Vdc unregulated	
Power	35 mA @ 6 Vdc 13 mA 2.0 mA	Normal Operation STOP Mode SLEEP Mode
<i>Physical</i>		
Weight	0.75 oz (22g) 3.25 oz (92g)	Circuit Card Only Housed
Dimensions	1.2 x 2.95 x 0.760 1.5 x 4.2 x 0.88	Circuit Card Only Housed Compass
<i>Environment</i>		
Operating Temp	-20 to 70° C	
Storage Temperature	-35 to 100° C	
Shock	30 inch drop	MIL-STD-810E; TM 516.4
Vibration	20-2000 Hz Random 2 hrs/axis	MIL-STD-810E; TM 514.4
<i>Manufacturing</i>		
PCB	IPC 6012	
Assembly	IPC 610	Class II or Better

Table I.16: O.S.61 Helicopter Engine

Displacement	9.95 cc
Bore	24.0 mm
Stroke	22.0 mm
RPM	2,000 – 18,000
Output	2.2 hp @ 16,000 rpm
Torque	1.052 Nm @ 10,720 rpm
Weight	600 g

I.2.8 Ultrasound Altimeters

Figure I.11 is an ultrasound sensor used to find the range from the helicopter to the ground. This ultrasonic transducer has an approximate range of 3 – 24 inches that can be modified from software. A logic line triggers a pulse and the echo is returned on a second line. It is a compact, low weight sensor (86 grams) with minimal power requirements, and a self contained design. Figure I.12 shows the location of two of three ultrasound sensors in the helicopter.

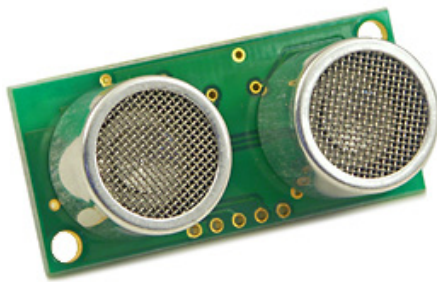


Figure I.11: Ultrasound Sensors



Figure I.12: Ultrasound Sensors Location in the Helicopter

I.3 Calibration

I.3.1 Helicopter Main Rotor Blade Pitch Angle Calibration

Calibration of the main rotor collective blade pitch angle θ_0 takes place by positioning the AccuStar II inclinometer device (see section Section I.2.5 on page 383) in lieu of the main rotor blades. Subsequent commands to the main rotor blade collective inputs generate the calibration curve seen in Figure I.13. After generating a number of similar calibration curves, the conversion from pulse width to main rotor blade pitch angle takes the form

$$\theta_0 = 0.0186 \delta_0 - 24.63 \quad (\text{I.3.1})$$

where the δ_0 is the command servo pulse width input.

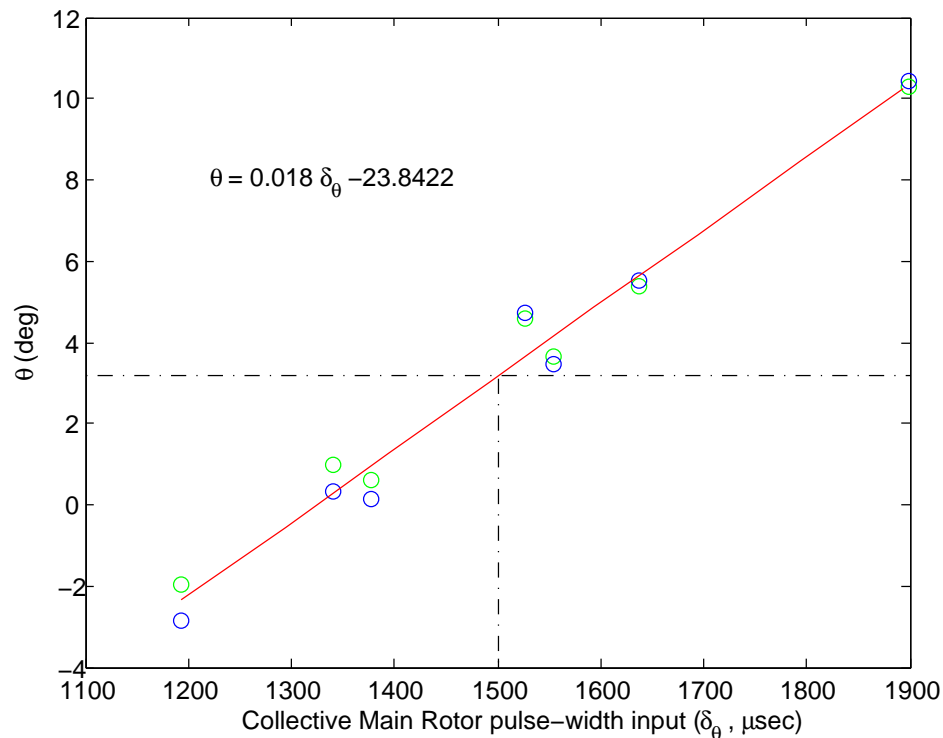


Figure I.13: Calibration curve for main rotor collective blade pitch θ from collective stick inputs δ_θ .

I.3.2 Helicopter Main Rotor Cyclic Angle Calibration

A similar process to the one described above in Section I.3.1 on the previous page generates the calibration curves for the cyclic inputs shown in Figure I.14. The resultant calibration equations take the form

$$\theta_{cyc} = 0.07 \delta_{cyc} - 103 \quad (I.3.2)$$

$$\delta_{cyc} = 14.2 \theta_{cyc} + 1482$$

where θ_{cyc} is the Bell cyclic input in degrees, δ_{cyc} is the cyclic stick input in pulse-width units (microseconds), and cyc is either *lat* for lateral inputs, or *lon* for longitudinal inputs. Figure I.15 on the next page shows the range and effect of the longitudinal and lateral cyclic stick inputs. Equation (H.2.4) on page 367 gives the final form to the main rotor cyclic inputs.

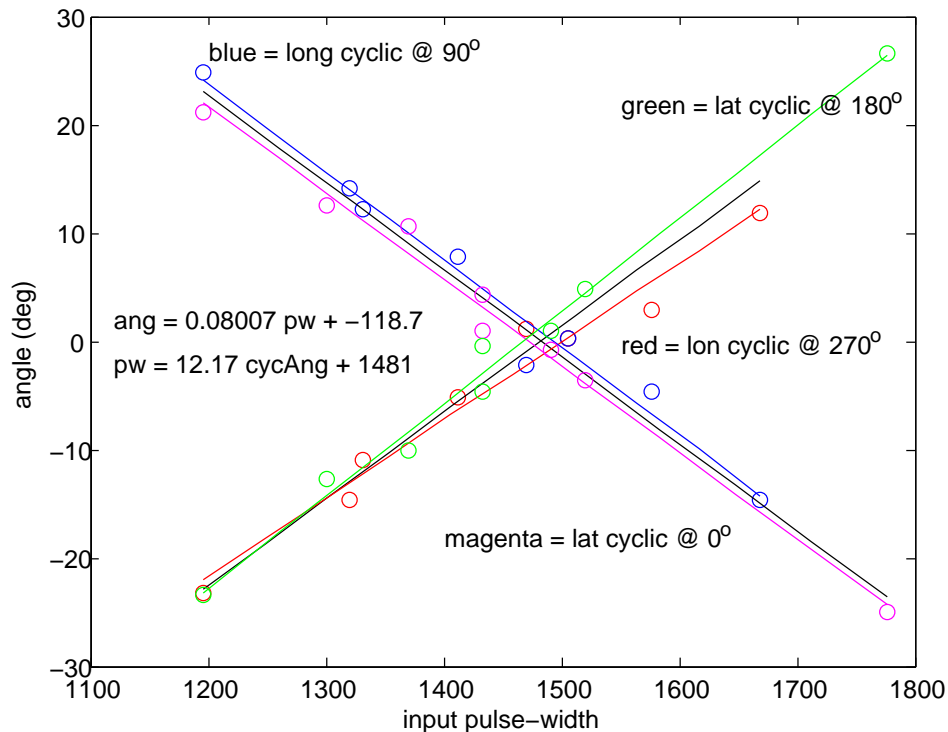


Figure I.14: Calibration Curve for longitudinal δ_{lon} and lateral δ_{lat} cyclic main rotor blade stick inputs.

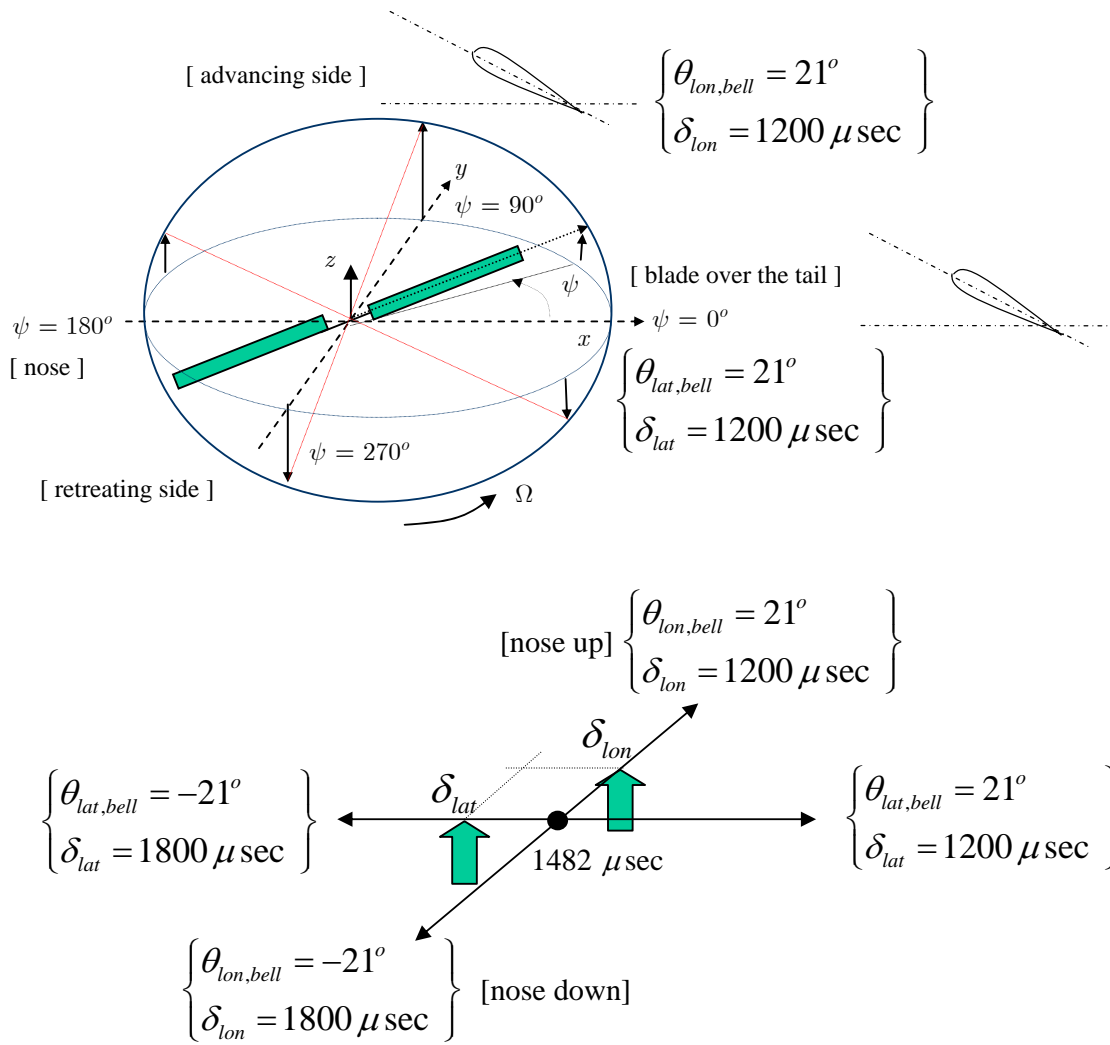


Figure I.15: Bell cyclic stick input range for longitudinal δ_{lon} and lateral δ_{lat} main rotor blade pitch angle.

I.3.3 Helicopter Tail Rotor Collective Angle Calibration

Figure I.16 on the next page records the calibration run for the tail rotor collective pitch angle θ_{TR} . The inclinometer described in Section I.2.5 on page 383 provides the measured angle data. The graph plots the inherent hysteresis present in the input mechanism for the tail rotor pitch angle $\theta_{TR} = f(\delta_{TR})$. The bottom graph in Figure I.16 plots the best estimate for the data (red curve) as a second order polynomial.

$$\begin{aligned}\theta_{TR} &= 0.0387 \delta_{TR} - 50.2917 \\ \delta_{TR} &= 24.3 \theta_{TR} - 1310\end{aligned}\tag{I.3.3}$$

I.3.4 OU Helicopter Throttle Fuel Flow Rate Calibration

The helicopter engine manufacturer (O.S. Engines) provides a set of instructions on how to operate the engine [37]. Figure I.17 on page 394 shows a map from throttle servo pulse-width command to throttle opening. Subsequent fuel and air mixing is a function of the throttle opening, carburetor inlet temperature, and fuel back-pressure generated by the engine.

I.3.5 Cantilever Beam Strain Gage Calibration

The cantilever beam in Figure I.18 on page 394 has a set of strain gages on each side of the beam surface set up in a Wheatstone Bridge configuration. The *strain* on the beam surface is the ratio of the change in length to the initial unstressed reference length. A strain gage senses the change in the beam's length by converting a variation in the strain gage resistance into a measurable voltage []. In the current setup, the details of the theory of elasticity are bypassed in favor of a simpler calibration setup. In this setup, a number of known masses are applied at carefully chosen locations in the cantilever beam. Then the voltage of the gage circuit is measured and correlated to the applied bending moment which include the mass and weight of the beam itself. Figure I.19 on page 395 shows the calibration curve for the cantilever beam. Subsequent use of this device as a bending beam load cell.

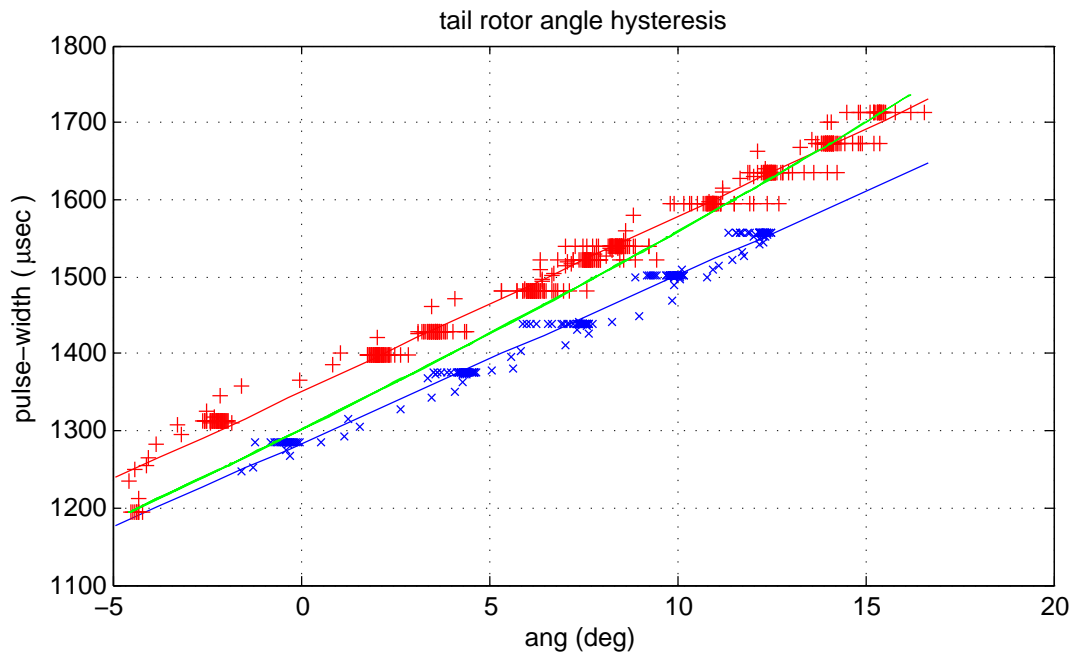
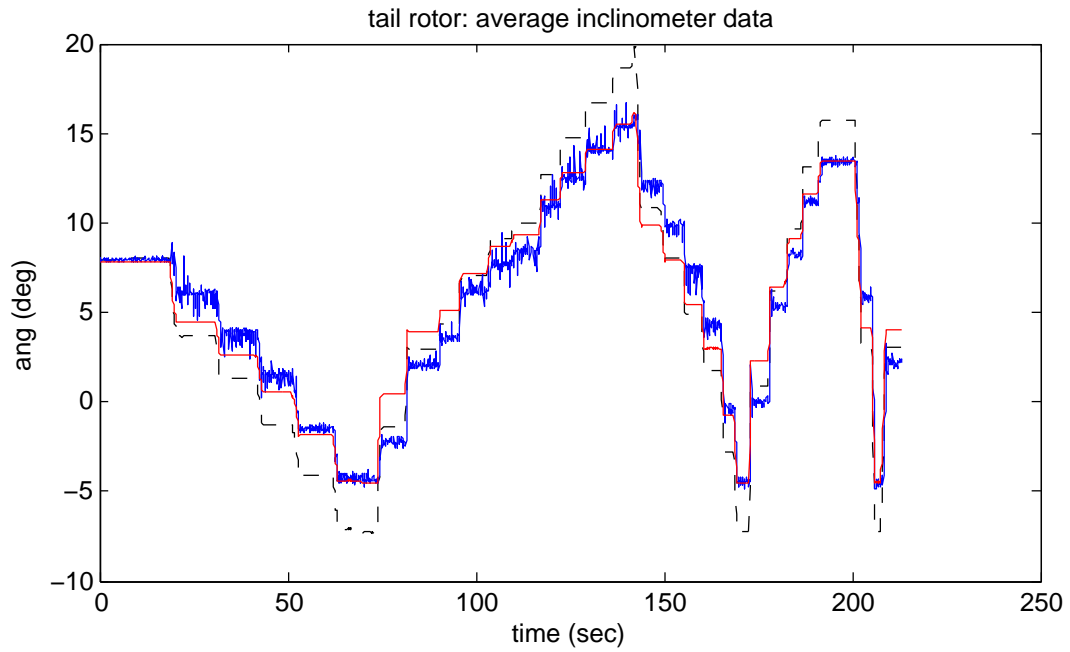


Figure I.16: Calibration curve for tail rotor collective pitch angle θ_{TR} . Top graph plots tail rotor servo input pulse-width δ_{TR} (μsec , dashed black curve) along with inclinometer data (deg , blue curve) and best-fit estimation curve (red curve). The bottom graph plots the measured tail rotor angle against the input pulse width. The data shows input hysteresis due to mechanical slop in the linkage.

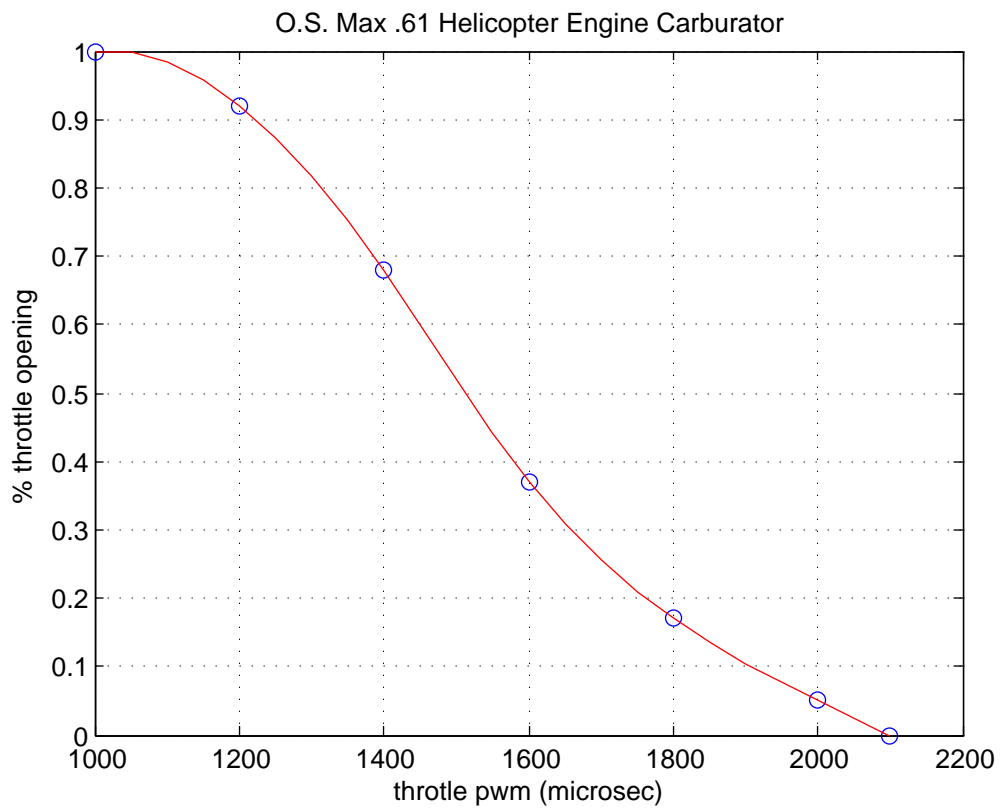


Figure I.17: Calibration Curve for throttle δ_{Th} servo pulse-width command to throttle opening.



Figure I.18: Cantilever Beam with strain gages.

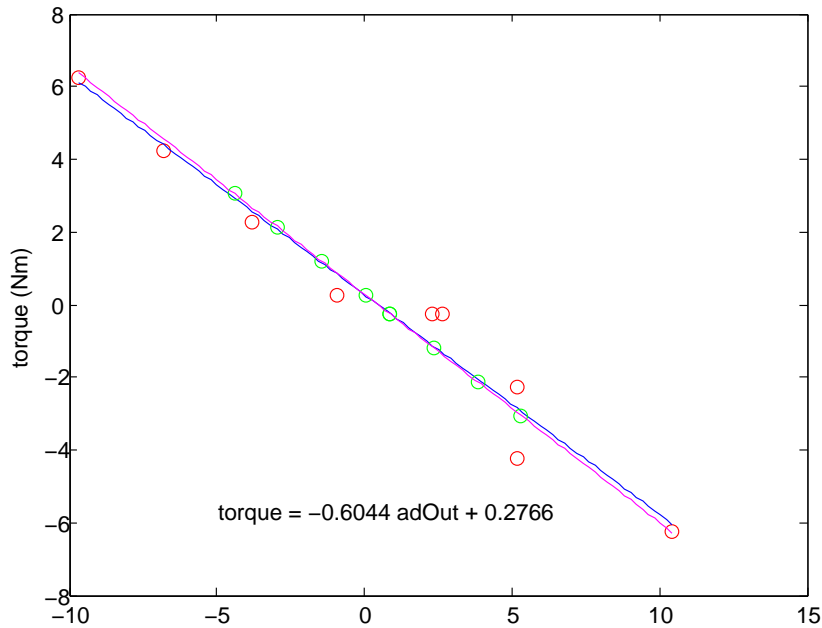


Figure I.19: Calibration Curve for cantilever beam with strain gages.

I.4 Helicopter Linear and Directional Test Platform

Figure I.20 on the following page shows a picture of the test Linear and Directional Test Stand (LDTS) or Helicopter Test Platform (HTP) with the helicopter on top. The LDTS is an apparatus conceived to aid in the development, testing and experimenting of the the various helicopter experiments. It is of particular importance for performing parameter estimation since it can operate in any combination of its two independent degrees of freedom at any one time. The first degree of freedom is along the vertical axis, while the second degree of freedom is rotation about the vertical axis or heading. The LDTS consists of a base supported by four shafts in which four springs sustain the weight of the helicopter. When the helicopter is placed in the LDTS, the springs deflect to an equilibrium position. When the helicopter lifts and raises, the force exerted by the helicopter can be computed with the help of the HFP calibration curve shown in Figure I.21 on page 397.



Figure I.20: Helicopter Test Platform.

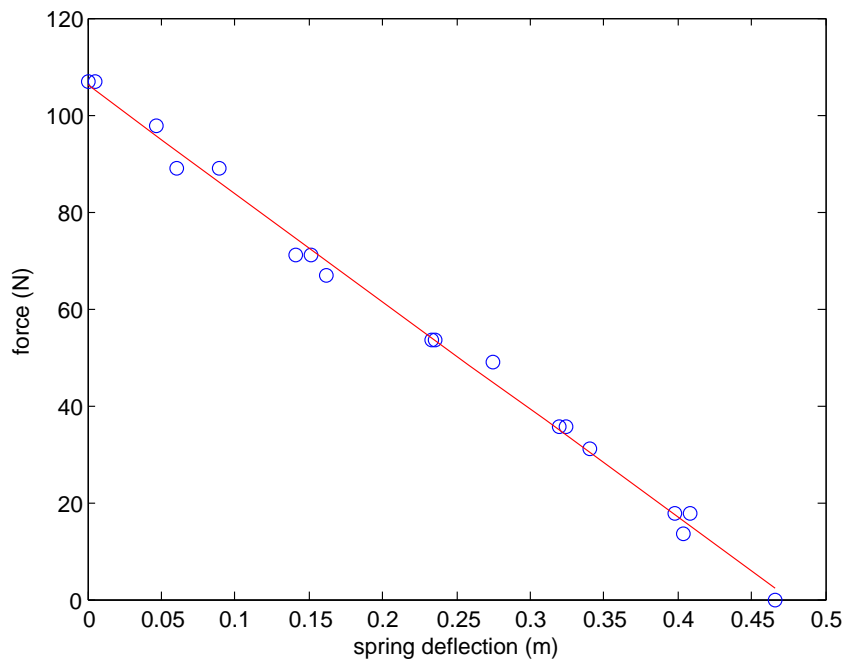


Figure I.21: Calibration curve for vertical force exerted by the HTF springs.

Appendix J

Helicopter Engine Controller

J.1 Introduction

Equation (J.1.1) below shows previous results from the combined Blade Element and Momentum and Theory (BEMT) presented in equation (C.2.14) on page 227.

$$C_T = \frac{a\sigma}{2} \left(\frac{\theta}{3} - \frac{1}{2} \sqrt{\frac{C_T}{2}} \right) \quad (\text{J.1.1})$$
$$C_P = C_Q = \frac{C_T^{3/2}}{\sqrt{2}} + \frac{1}{8} \rho C_D$$

The relevant control term in the thrust coefficient expression C_T is the main rotor blade pitch angle θ . The thrust and torque coefficients take the approximate form

$$C_T \simeq k_{C_T} \theta + C_{T_0} \quad (\text{J.1.2})$$
$$C_Q \simeq k_{C_Q} \theta^{3/2} + C_{Q_0}$$

Using the thrust and torque coefficient definition in equation (C.1.17) the corresponding main rotor thrust T_{MR} and torque Q_{MR} approximation are given by

$$T \simeq k_T \Omega^2 \theta + k_{T_0} \quad (\text{J.1.3})$$
$$Q \simeq k_Q \Omega^2 \theta^{3/2} + k_{Q_0}$$

Equation (J.1.3) says that when the main rotor angular velocity is constant, both the main rotor thrust and torque are simple functions of the blade pitch angle which is the main rotor primary control variable.

J.2 Main Rotor Characterization Experiment

This experiments has as it main goal the characterization of the coupled dynamics of the carburetor, engine, main rotor shaft and blade systems. The result of the experiment is a first order characterization of the aforementioned system that would lead to a preliminary design of the engine controller. Once a preliminary engine controller maintains a constant main rotor angular velocity Ω_{MR} , then the identification of the main rotor aerodynamic model follows via equations (J.1.1) through equation (J.1.3) on the previous page.

In this first experiment, the blade pitch angle remains constant while the main rotor angular velocity Ω_{MR} varies. The helicopter configuration is such that there is no yaw movement, and the helicopter is only allowed to move along the vertical axis. Figure J.1 on the following page illustrates one such run with main rotor blade pitch angle set at 8° . The green curve is the command input to the throttle servo, while the red curve is the measured main rotor RPM. The corresponding throttle opening and estimated fuel flow rate result from data presented in Figure I.17 on page 394. Similar experiments with the main rotor blade pitch angle set at 2, 3, 4, 5, 6 degrees yield the necessary data for first order system identification.

Data in Figure J.1 includes rotor dynamics, and carburetor dynamics, as well as losses incurred from fuel energy conversion to torque delivered to the main rotor. A first order estimate of the complete system dynamics is directly inferred from the step responses. Figure J.2 on page 401 is a snapshot of the data presented previously. These data sets yield approximate estimates for time to rise and time constant for the complete dynamic system. Figure J.3 on page 402 shows the time constant mean value from the experiments aforementioned. As expected, the time constant varies about a mean value which value is equal to 2.2 sec. Data in Figure J.1 indicates that the engine/carburetor-main rotor dynamic system could be expressed, in its most simple form as a first order lag transfer function of the form

$$\frac{\bar{\Omega}(s)}{\bar{\omega}_f(s)} = P(s) = \frac{K_{s1}}{\tau_{s1}s + 1} \quad (\text{J.2.1})$$

where ω_f is the fuel flow rate. Given that change in main rotor angular velocity is

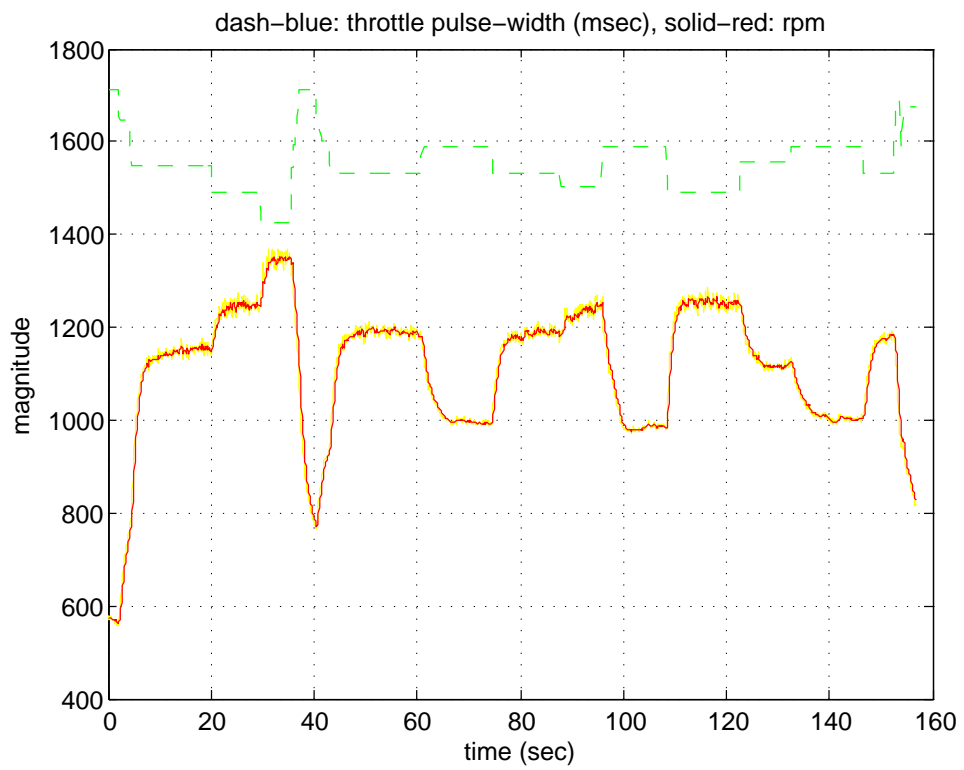


Figure J.1: Sample Main Rotor Angular Velocity Ω data resulting from varying throttle inputs and Main Rotor Blade Pitch Angle θ set at 8 degrees.

proportional to the total main rotor shaft torque, then

$$\dot{\Omega} - \dot{r} = \frac{1}{I_{rot}} (Q_e - Q_{MR} - n_{TR}Q_{TR}) \quad (J.2.2)$$

where I_{rot} given in Table I.1 on page 372 is the combined rotational inertia which includes the main rotor blades, hub and shaft, the tail rotor, engine and transmission rotational inertias [50, 119]. The term Q_e is the torque generated by the engine, Q_{MR} is the main rotor torque, n_{TR} is the main rotor-to-tail rotor gear in Table I.4 on page 373, and \dot{r} is the fuselage angular acceleration.

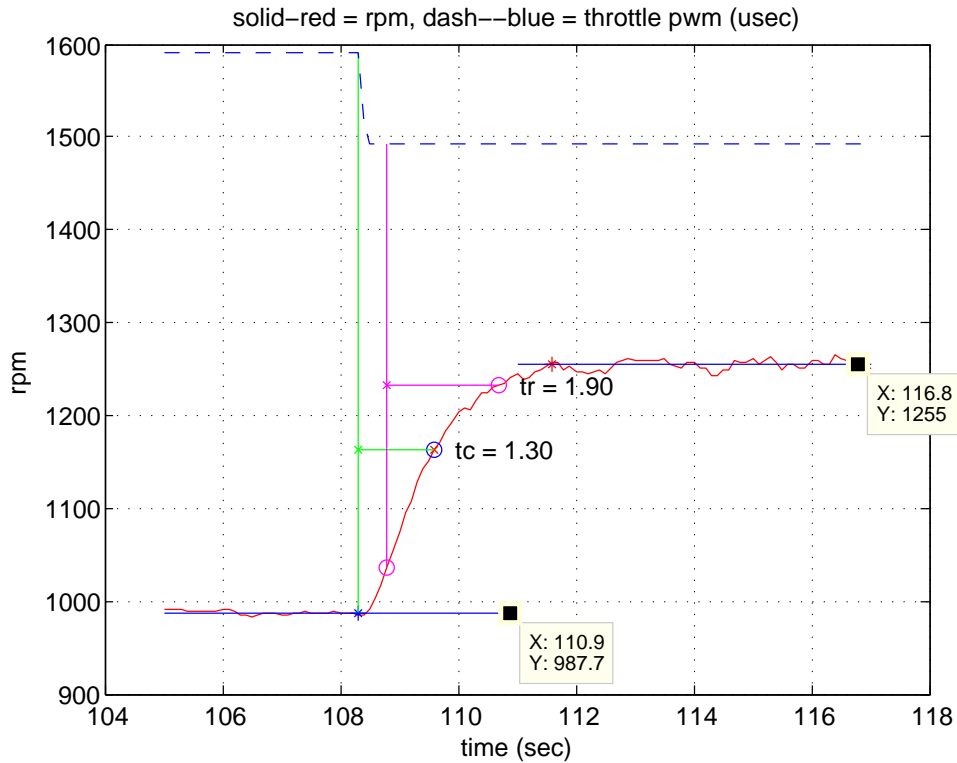


Figure J.2: Time to Rise and Time Constant estimates for Engine/Carburetor-Main Rotor dynamic system.

In the current experiments the fuselage remains stationary with motion along the vertical axis alone, in which case $\dot{r} = 0$. Substitute equation (J.1.3) on page 398 in place of $Q_{MR} + n_{TR}Q_{TR}$ to obtain

$$\dot{\Omega} = \frac{1}{I_{rot}} (Q_e - k_Q \Omega^2 \theta^{3/2} - k_{Q_0}) \quad (J.2.3)$$

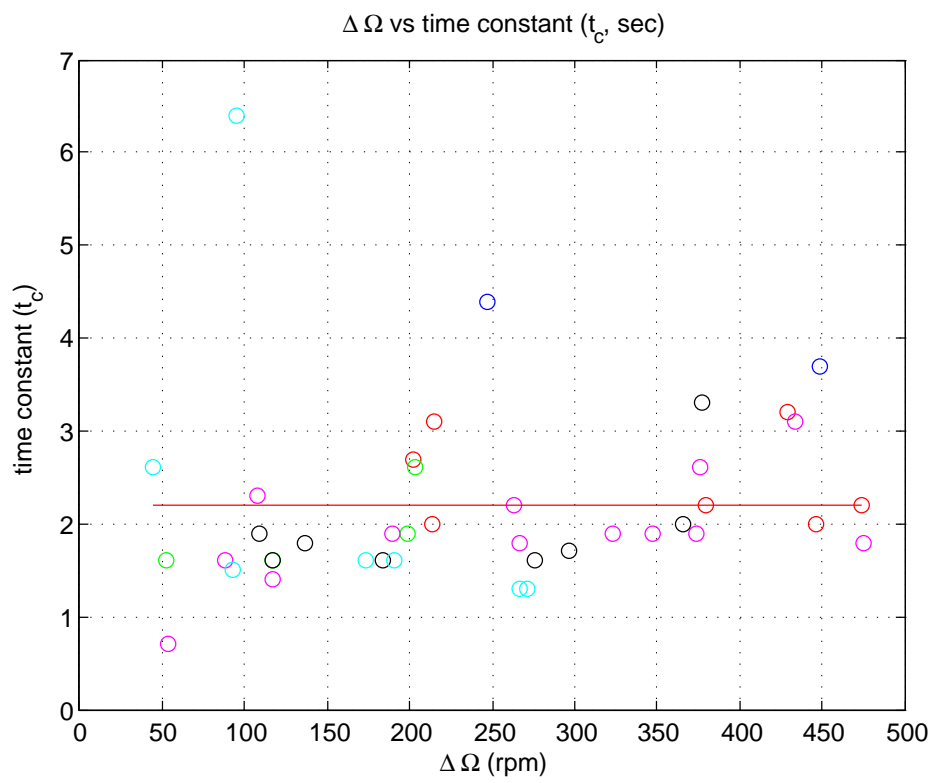


Figure J.3: Time Constant Estimation for Engine/Carburetor-Main Rotor dynamic system.

According to equation (J.1.3), the damping torque $\partial Q/\partial\Omega$ has the form

$$\frac{\partial Q}{\partial\Omega} = 2 k_Q \Omega \theta^{3/2} \quad (\text{J.2.4})$$

Substituting back in (J.2.3) and taking the Laplace transform of the resultant linearized equation yields

$$\begin{aligned} s\bar{\Omega}(s) + \frac{2k_Q\Omega_0\bar{\Omega}(s)\theta^{3/2}}{I_{rot}} &= \frac{1}{I_{rot}}\bar{Q}_e(s) \\ \left(s + \frac{2k_Q\Omega_0\theta^{3/2}}{I_{rot}}\right)\bar{\Omega}(s) &= \frac{1}{I_{rot}}\bar{Q}_e(s) \\ \bar{\Omega}(s) &= \frac{1/2k_Q\Omega_0\theta^{3/2}}{(I_{rot}/2k_Q\Omega_0\theta^{3/2})s + 1}\bar{Q}_e(s) \end{aligned} \quad (\text{J.2.5})$$

where k_{Q_0} is neglected momentarily. In the above equation (J.2.5) the term $\theta^{3/2}$ remains constant for any given data run. The term Ω^2 is substituted by a linearized equivalent $2\Omega_0\Omega$ where Ω_0 is *a priori* known rotor angular velocity about which Ω varies (as shown in Figure J.3 on the previous page). In a closed-loop system this term would correspond to the command (desired) angular velocity. In reality, for the current batch of experiments in which the rotor angular velocity varies, the term Ω_0 is not a constant. The penalty for setting $k_{Q_0} = 0$ and Ω_0 to a constant will result in open loop offset. Equating terms from equation (J.2.1) to the corresponding terms in the above equation (J.2.5) gives

$$\begin{aligned} K_{s1} &= \frac{1}{2 k_Q \Omega_0} \theta^{-3/2} \\ \tau_{s1} &= \frac{I_{rot}}{2 k_Q \Omega_0} \theta^{-3/2} \end{aligned} \quad (\text{J.2.6})$$

The above equation suggests that the time constant for the engine-carburetor and rotor system is a nonlinear function of main rotor angular velocity and main rotor blade pitch angle. In particular, the term k_Q is a function of both angular velocity and blade pitch angle:

$$k_Q = f(\Omega, \theta)$$

Therefore, any linear approximation to a time constant will only be true for the given

rotor angular velocity, main rotor blade pitch angle and corresponding main rotor torque. The transfer functions in equation (J.2.1) and equation (J.2.5) on the preceding page suggest a linear model as shown in Figure J.4.

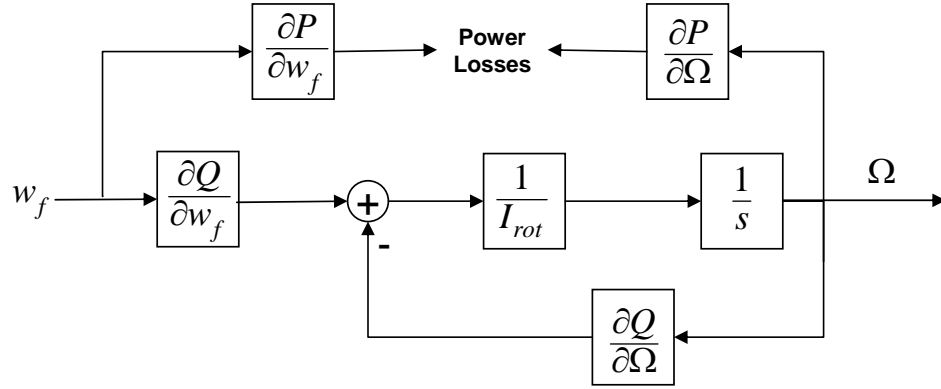


Figure J.4: Main Rotor Dynamics with Fixed Shaft Engine.

J.2.1 Estimation of Simple Engine-Rotor Dynamics from Experimental Data

The simplest approach for the estimation of the Engine-Rotor Coupled dynamics uses the transfer function in equation (J.2.1) on page 399. The estimated time constant is derived from results shown in Figure J.3 on page 402. The engine torque is a function of the fuel flow and maximum engine power such that [50]

$$\begin{aligned}
 P_e &= P_{e,\max} w_f \\
 Q_e &= \frac{P_e}{\Omega} = \frac{P_{e,\max}}{\Omega} w_f \\
 w_f &= f(\delta_{Th})
 \end{aligned}
 \tag{J.2.7}$$

where w_f is the fuel flow and δ_{Th} is the throttle opening in Figure I.17 on page 394. The estimation of the gain from fuel flow rate w_f to torque Q follows the following steps:

1. estimate total power P
2. estimate total torque Q

3. estimate the relation between the engine generated torque and available power

$$Q_e = \partial Q / \partial w_f \cdot w_f$$

J.2.1.1 Estimation of Available Power and Main Rotor Torque

Based on data presented in Figure J.1 on page 400 for a number of main rotor blade pitch angles, when the change in rotor angular velocity is zero ($\dot{\Omega} = 0$), the engine power available equals the total power required by the complete system. The total required power is given by equation (C.2.14) on page 227. Equation (C.3.5) on page 230 modifies the induced power coefficient by a factor k such that

$$C_{Pi} = \frac{k}{\sqrt{2}} C_T^{3/2}$$

and the resultant power coefficient is given by

$$C_P = \frac{k}{\sqrt{2}} C_T^{3/2} + \frac{\rho}{8} C_D \quad (\text{J.2.8})$$

The power loss factor k accounts for a number of non-linear effects which include tip losses and nonuniform rotor air inflow [92, 119]. The engine power available is in this case

$$P_e = \rho \pi R^2 (\Omega R)^3 C_P \quad (\text{J.2.9})$$

The main engine torque follows directly

$$C_Q = C_P \quad (\text{J.2.10})$$

$$Q_{MR} = \rho \pi R^3 (\Omega R)^2 C_P - n_{TR} Q_{TR}$$

where Q_{TR} is the tail rotor torque and n_{TR} is the main rotor to tail rotor gear presented in Table I.4 on page 373. In the experiments run to this point, the tail rotor is set to zero blade pitch angle, and therefore the data does not include any tail rotor effects other than parasite drag and transmission losses. This facilitates the engine-carburetor parameter identification in that the total power computed accounts for transmission and profile tail rotor power with no need for complex and error prone estimation of the tail rotor power

and torque components. Figure J.5 shows data for runs with 2 (red dots), 3, 4, 5, 6, and 8 (cyan dots) degrees of main rotor blade pitch angle and varying throttle settings. The torque and power are computed for places when the rotor angular velocity was stable and non-varying for which $\dot{\Omega} = 0$, $\dot{Q} = 0$ in equation (J.2.3) on page 401.

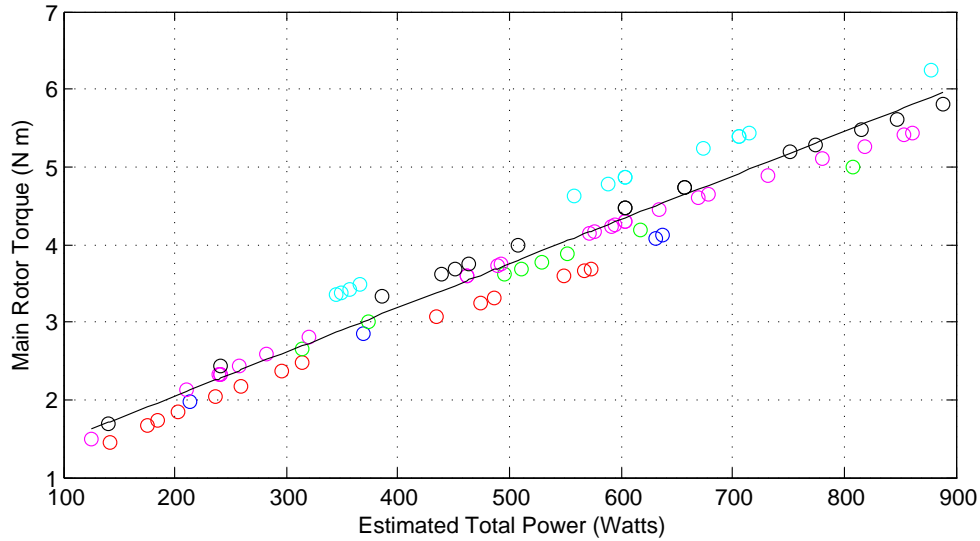


Figure J.5: Estimated engine power available for required main rotor torque.

J.2.1.2 Relationship between Available Power and Main Rotor Torque Required

Figure J.5 suggests a linear relationship between the total required power and corresponding torque for cases when changes in rotor angular velocity are small ($\Delta\Omega \approx \pm 500$, see Figure J.6 on the following page). This linear relationship between available power and required torque indicates that the simplest linear transfer function between throttle command input and the resulting torque delivered to the main rotor is linear for a variation of angular velocity and blade pitch angle settings about a trim point. In this case a linearized version of (J.2.7) would take the form

$$Q_e = \frac{\partial Q}{\partial w_f} w_f \quad (\text{J.2.11})$$

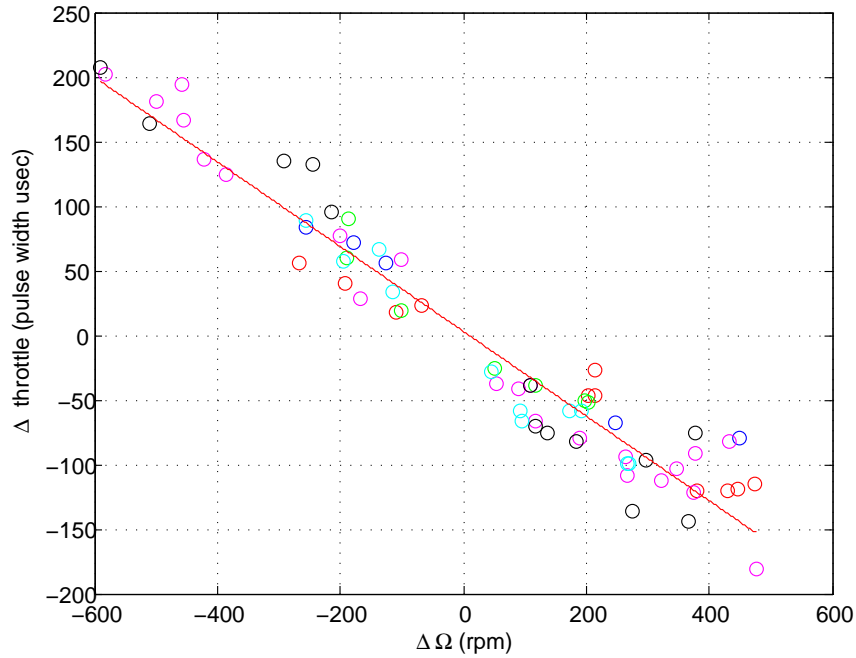


Figure J.6: Change in Main Rotor Angular Velocity Ω and related throttle inputs δ_{Th} to a Fixed-Shaft Engine.

Figure J.7 on the next page together with Figure J.6 plot experimental data that confirms equation (J.2.11) above for the case when the rotor angular velocity changes are small. The engine-carburetor mechanics can now be modeled as a lead/lag system with a transfer function of the following form [119]

$$\frac{\bar{Q}_e}{\bar{w}_f} = \frac{\partial Q}{\partial w_f} \left(\frac{1 + \tau_{ed}s}{1 + \tau_{en}s} \right) \quad (\text{J.2.12})$$

where the time constants are estimated from Figure J.2 and Figure J.3 on page 402. In turn, Figure J.7 on the following page shows data that allows for computation of an estimate for the engine torque control derivative $\partial Q/\partial w_f$. This graph of experimental data shows that the engine torque control derivative is non-linear, and tapers to a maximum as fuel flow increases. However, the control derivative $\partial Q/\partial w_f$ can still be estimated with a linear approximation of the data.

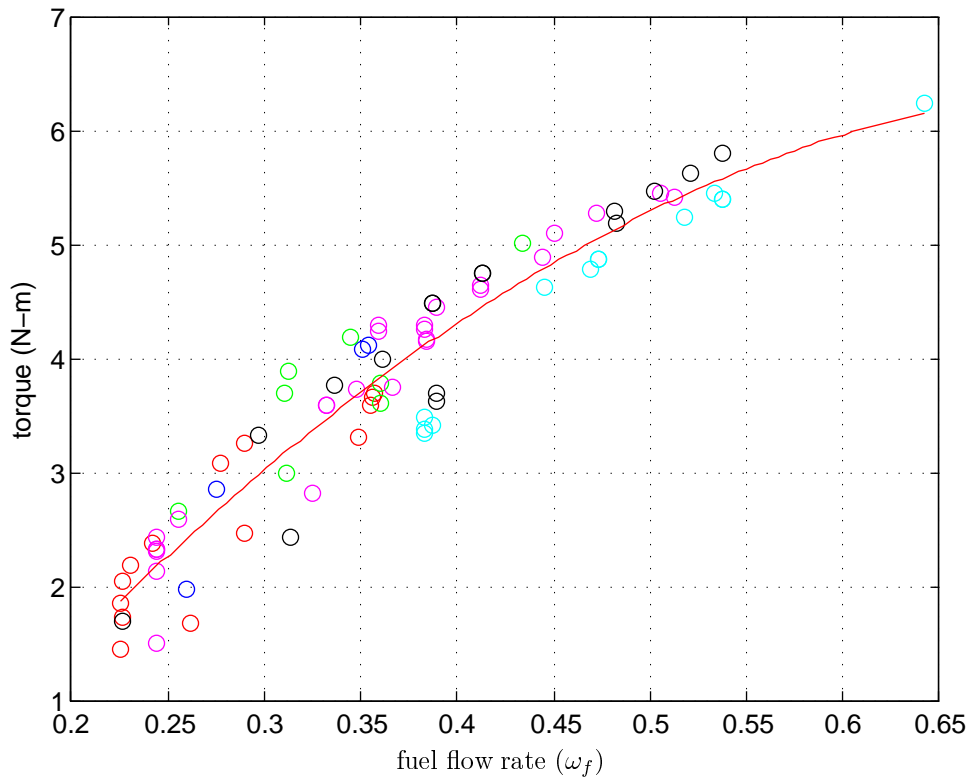


Figure J.7: Engine Torque Control Derivative $\partial Q/\partial w_f$ derived from estimated fuel flow rate.

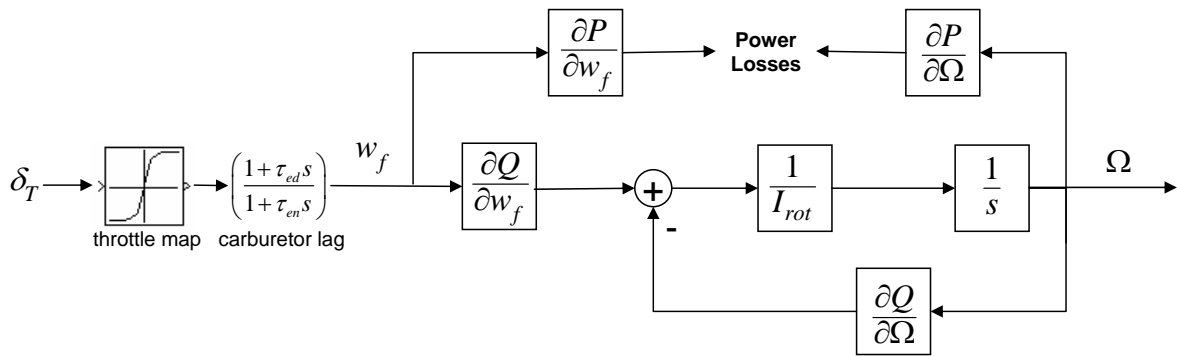


Figure J.8: Engine-Carburetor and Main Rotor Dynamics Model.

J.2.2 Engine-Carburetor and Coupled Main Rotor Dynamics

Open-Loop Modeling Results

Figure J.8 on the previous page shows the modified open loop engine-carburetor and main rotor coupled dynamic model. Illustrated in figure J.8 is the non-linear throttle command input mapping to fuel flow rate in Figure I.17 on page 394 with throttle input. The non-linear map generates estimated fuel flow rate ranging from 0 to 1. Subsequently, data in Figure J.7 on the previous page results in the carburetor mixing and chemical energy conversion to engine power and corresponding engine torque Q_e . Figure J.9 shows the result of the open loop simulation. In this graph, the rotor angular velocity Ω exhibits the same time constant and rise time as that of the real data. The estimated rotor damping is not sufficiently adequate for this run, but as a first approximation, the current results indicate that the model is adequate for subsequent engine-governor control design and synthesis.

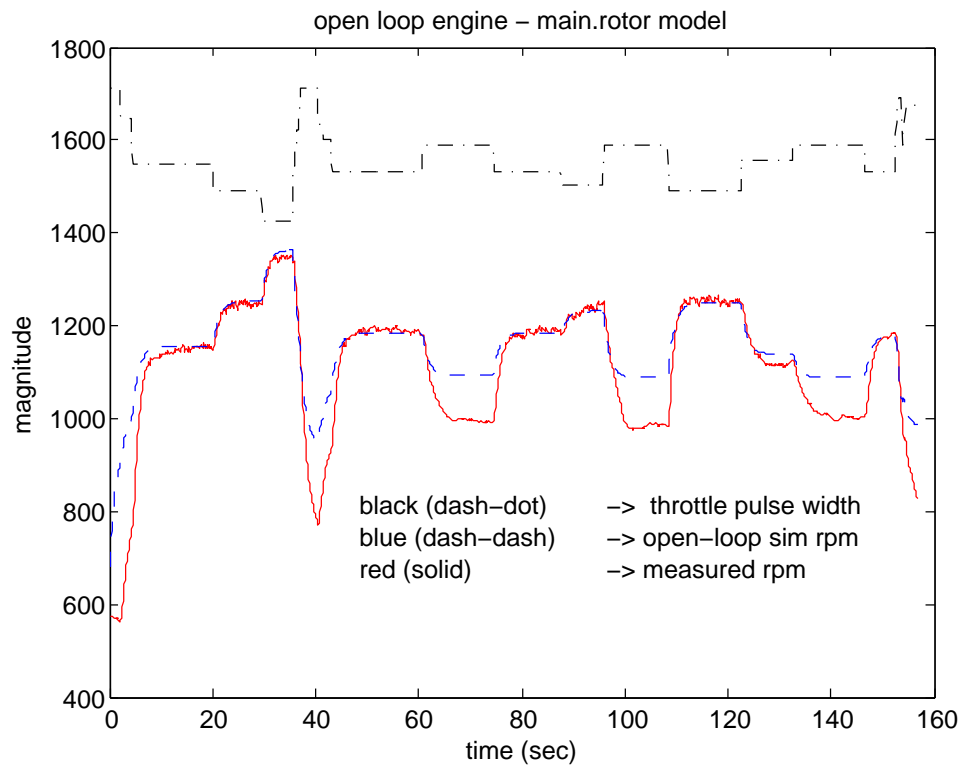


Figure J.9: Open Loop Simulation Result for Rotor Angular Velocity Ω .

J.2.3 Synthesis of the Engine Control Law Based on Experimental Data Parameter Estimation

The current set of experiments (of which Figure J.1 on page 400 is an example) provides the necessary data for the estimation of the various system derivatives. Figure J.10 on page 412 shows a linearized version of Figure J.8 on page 408 in which the nonlinear terms related to throttle δ_{Th} , fuel flow rate w_f , power losses and torque control derivative $\partial Q/\partial w_f$ have been dropped. The integral (k_i) plus proportional (k_p) control gains have replaced the non-linear open-loop dynamics instead. Standard manipulation of the single-input/single-output (SISO) system leads to the the loop transfer function \bar{L}

$$\begin{aligned} &= \left(\frac{k}{s + k k_\Omega} \right) \left(k_p + \frac{k_i}{s} \right) \\ \bar{L} &= \frac{k (k_p s + k_i)}{s (s + k k_\Omega)} \end{aligned} \quad (\text{J.2.13})$$

The standard closed loop form of the complimentary sensitivity transfer function $\bar{\Omega}(s)/\bar{\Omega}_c(s)$

$$\begin{aligned} &= \left(\frac{k}{s + k k_\Omega} \right) \left(k_p + \frac{k_i}{s} \right) (\bar{\Omega}_c(s) - \bar{\Omega}(s)) \\ &= \frac{k (s k_p + k_i)}{s (s + k k_\Omega) + k (k_i + s k_p)} \bar{\Omega}_c(s) \\ \bar{\Omega}(s) &= \frac{k (s k_p + k_i)}{s^2 + s k (k_\Omega + k_p) + k k_i} \bar{\Omega}_c(s) \end{aligned} \quad (\text{J.2.14})$$

where $k = 1/I_{rot}$ is the lumped rotational inertia of the engine-shaft-rotor system, and $k_\Omega = \partial Q/\partial \Omega$. The corresponding sensitivity transfer function $\bar{e}(s)/\bar{\Omega}_c(s)$ for the closed loop is given by

$$\begin{aligned} &= \bar{\Omega}_c(s) - \left(\frac{k}{s + k k_\Omega} \right) \left(k_p + \frac{k_i}{s} \right) \bar{e}(s) \\ \bar{e}(s) &= \frac{s (s + k k_\Omega)}{s^2 + s k (k_\Omega + k_p) + k k_i} \bar{\Omega}_c(s) \end{aligned} \quad (\text{J.2.15})$$

Application of the Final Value Theorem (FVT) [31, 111] to the complimentary $\bar{\Omega}(s)/\bar{\Omega}_c(s)$ and sensitivity $\bar{e}(s)/\bar{\Omega}_c(s)$ transfer functions (J.2.14) and (J.2.15) give

$$\begin{aligned}\lim_{t \rightarrow \infty} \Omega(t) &= \lim_{s \rightarrow 0} s \bar{\Omega}(s) = 1 \\ \lim_{t \rightarrow \infty} e(t) &= \lim_{s \rightarrow 0} s \bar{e}(s) = 0\end{aligned}\tag{J.2.16}$$

The above result indicates that, as expected, a simple proportional plus integral control design should deliver unity tracking and should reject disturbances adequately. The characteristic equation is given by

$$s^2 + s k (k_\Omega + k_p) + k k_i\tag{J.2.17}$$

Let

$$\begin{aligned}k (k_\Omega + k_p) &= 2 \zeta \omega_n \\ k k_i &= \omega_n^2\end{aligned}\tag{J.2.18}$$

where ζ is the damping ratio, and ω_n is the system's natural frequency. For good control quality, choose $\zeta = \sqrt{2}/2$ and $\omega_n = \pi$ where $\omega_n = \pi \ll \Omega/10$, and $\Omega = 157 \text{ rad/sec} \approx 25 \text{ Hz}$ is the main rotor natural frequency. Then

$$\begin{aligned}k_i &= \frac{\pi^2}{k} \\ k_p &= \frac{\pi \sqrt{2}}{k} - k_\Omega\end{aligned}\tag{J.2.19}$$

Substituting $k = 1/I_{rot}$, and $k_\Omega = \partial Q/\partial \Omega$ then the above equation (J.2.14) becomes

$$\frac{\bar{\Omega}(s)}{\bar{\Omega}_c(s)} = \frac{1}{I_{rot}} \frac{s (I_{rot} \pi \sqrt{2} - \partial Q/\partial \Omega) + I_{rot} \pi^2}{s^2 + s \pi \sqrt{2} + \pi^2}\tag{J.2.20}$$

This controller design is stable with poles at

$$s = \frac{\pi \sqrt{2}}{2} (-1 \pm i)\tag{J.2.21}$$

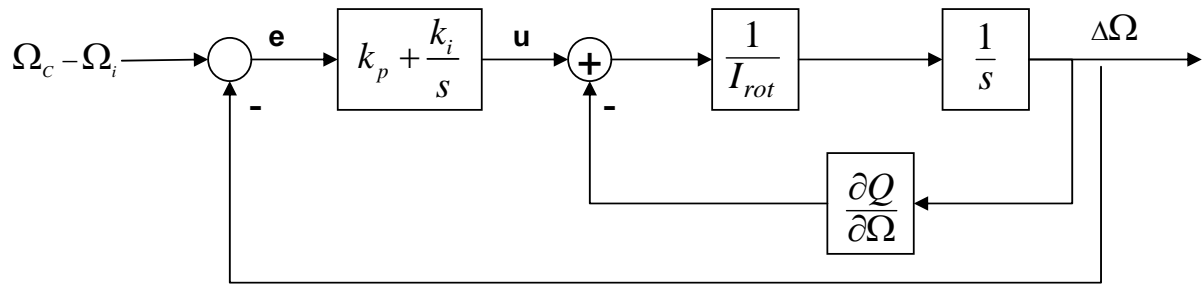


Figure J.10: Engine governor and main rotor angular velocity closed loop control design block diagram.

Figure J.11 on the following page plots the frequency domain characteristics of the loop transfer function \bar{L} in equation (J.2.13) on page 410. The infinite gain margin and the 60° phase margin give the control design sufficient margin for adequate stability and performance even in the presence of disturbances and parameter uncertainties. Figure J.12 on page 414 presents the data collected with the the helicopter running with the implementation of the above controller. The main rotor angular velocity Ω was commanded in steps of 1100, 1200, 1300, 1400, 1500 rpm, and during every step, the main rotor blade pitch angle was varied from 2 to 8 degrees. For each commanded step in rotor angular velocity, the controller kept a constant angular velocity even when in the presence of changing flight conditions due to the varying blade pitch angle.

Figure J.13 on page 414 shows the full linear engine-carburetor and main rotor simulation diagram. Figure J.14 on page 415 plots simulation data obtained using the actual command data utilized to run the real-time vehicle test presented in Figure J.12 on page 414 in the simulation scheme in Figure J.13. In these graphs, the simulation data overlays the experimental data. In the top graph, the throttle command input (in pulse-width) estimated from the simulation run (dashed blue line) closely matches the actual throttle used in the real-time run. Similarly, the main rotor angular velocity simulation data closely matches the actual real-time data.

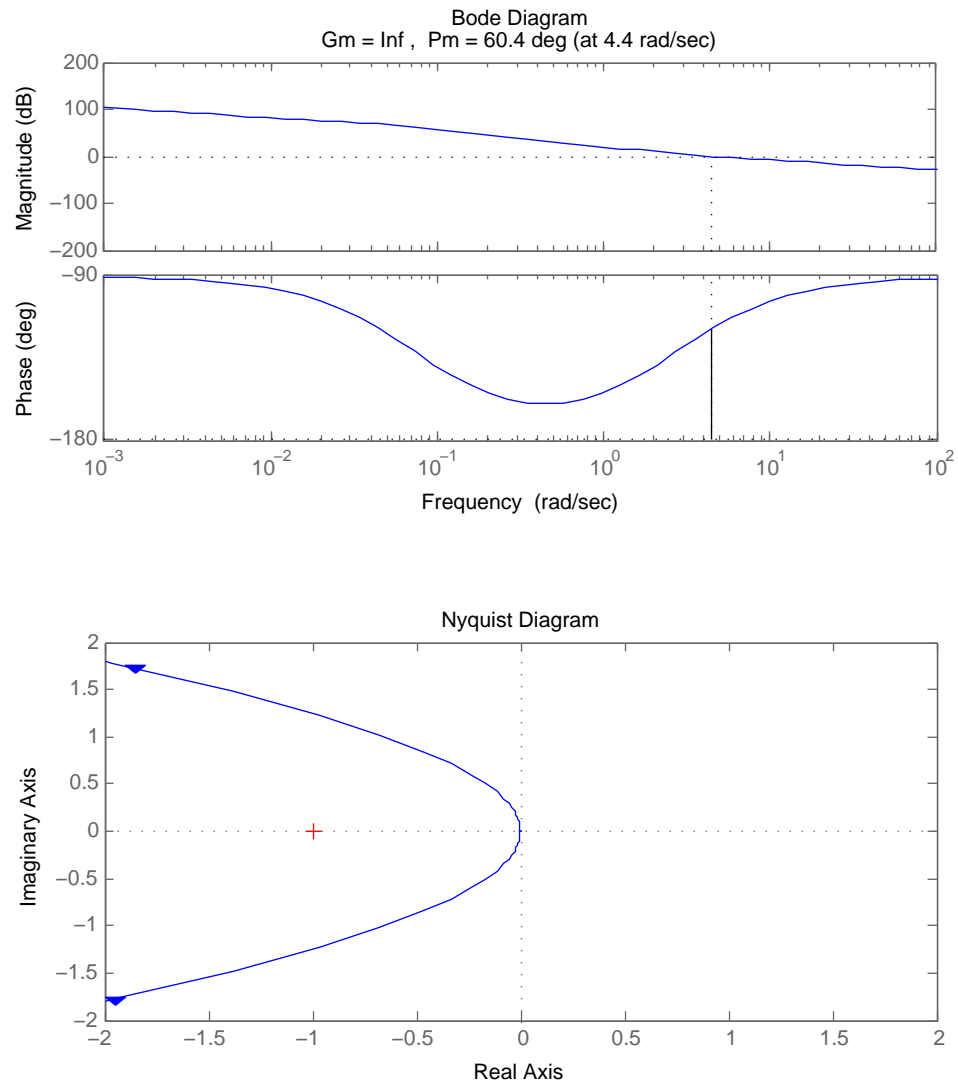


Figure J.11: Bode and Nyquist diagrams for the open-loop engine governor controller.

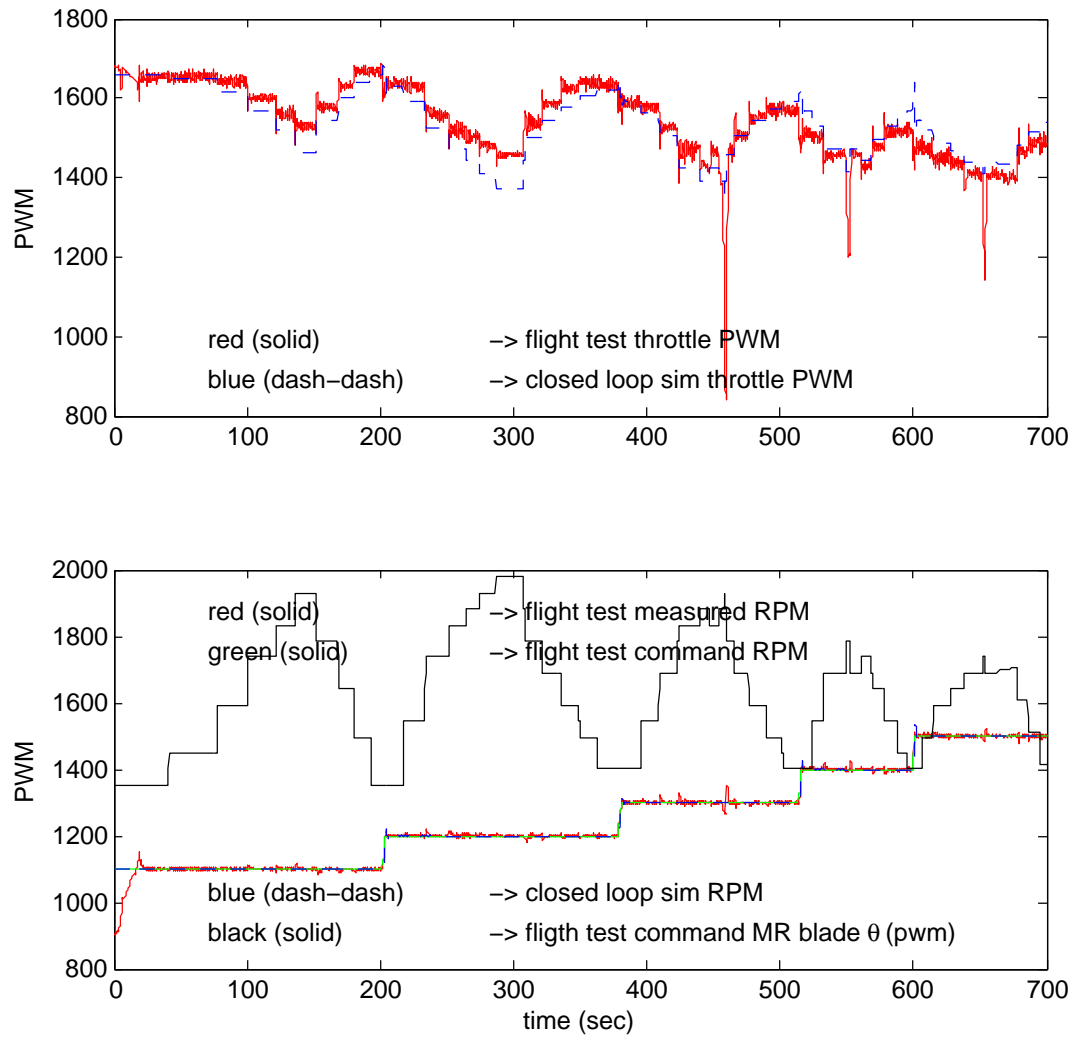


Figure J.14: Engine-Carburator model simulation results compared with real-time data.

J.3 Summary of Main Rotor Characterization Results

The main rotor characterization consists of two parts:

1. open loop characterization
2. closed loop control design and synthesis

The open loop characterization exercise uses a number of experiments such as the one presented in Figure J.1 on page 400. In these experiments a step command of main rotor angular velocity drives the dynamic of the coupled engine-carburetor and rotatory elements in the helicopter. Each step command experiment is set at a different constant setting for the main rotor blade pitch angle. A constant blade pitch angle allows for an estimate of the rotor damping derivative $\partial Q/\partial\Omega$ via the power absorbed and measured rotor speed. The real-time data collected generates the necessary information to estimate the system parameters listed in table J.1.

Table J.1: Engine-Carburetor and Main Rotor Rotational Dynamic Characteristics

rise time	2.5	sec
time constant	1.14	sec
carburetor control derivative $\partial Q/\partial w_f$	11.44	Nm
main rotor damping $\partial Q/\partial\Omega$	0.00037	Nm / rad/sec
throttle PWM to fuel flow (w_f)		see Figure I.10 on page 385

The original system was inherently stable, but with no engine governor control, the main rotor angular velocity would vary nonlinearly when the main rotor blade pitch angle changes due to command inputs necessary to maintain stability and deliver performance. The continuous time control design and loop transfer function characteristics are summarized in table J.2 on the next page.

Data collected in the real-time run of the engine in closed loop control presented in Figure J.11 on page 413, and subsequent simulation results presented in Figure J.14 on the previous page indicate that the initial first order engine governor control implementation is capable of maintaining a constant main rotor angular velocity Ω in the presence of varying flight conditions. Moreover, the simulation setup in Figure J.13 on page 414

Table J.2: Engine-Carburetor Control Characteristics

system damping ζ	$\sqrt{2}/2$
system natural frequency ω_n	π
proportional gain k_p	$I_{rot}\pi^2$, equation (J.2.19) on page 411
integral gain k_i	$I_{rot}\pi\sqrt{2} - \partial Q/\partial\Omega$
system poles	$s = \pi\sqrt{2}/2(-1 \pm i)$, equation (J.2.21) on page 411
gain margin	∞
phase margin	60 deg

models the behavior of the engine-carburetor and main rotor adequately, and can be used for subsequent simulation efforts.

Appendix K

Helicopter Aerodynamic Model Identification

K.1 Introduction

Equation (C.3.6) and equation (C.3.7) on page 231 are fundamental results from Combined Blade Element and Momentum Theory [92]. The equations are reproduced below for convenience

$$\begin{aligned}\lambda(r) &= \frac{\sigma a}{16} \left[\sqrt{1 + 32 \frac{\theta}{\sigma a} r} - 1 \right] \\ dC_T(r) &= \frac{\rho a}{2} (\theta r^2 - \lambda r) dr\end{aligned}\tag{K.1.1}$$

where r is a given blade station. The torque coefficient can be estimated from equation (C.2.14) on page 227

$$C_P = C_Q = \frac{k}{\sqrt{2}} C_T^{3/2} + \frac{1}{8} \rho C_D\tag{K.1.2}$$

where $k \approx 1.5$ is a power loss factor that accounts for non-uniform inflow, tip losses and other nonlinear effects. Empirical approximations for the thrust and torque are given by equation (J.1.3) on page 398

$$\begin{aligned}T &\simeq k_T \Omega^2 \theta + k_{T_0} \\ Q &\simeq k_Q \Omega^2 \theta^{3/2} + k_{Q_0}\end{aligned}\tag{K.1.3}$$

Equations (K.1.1) through (K.1.3) provide the bases for first order parameter identification of the helicopter aerodynamic terms. This time the main rotor angular velocity (and

therefore the angular velocity of all rotating elements) remains constant with the use of the engine controller in equation (J.2.19) on page 411 as implemented in Figure J.13 on page 414.

K.2 Helicopter Thrust Experimental Setup

The experimental setup uses the Helicopter Test Platform (HTP) shown in Figure I.20 on page 396. The helicopter thrust experiment setup allows for vertical motion only and locks the heading motion of the HTP. The tail rotor is disconnected from any control inputs and it is free to rotate in its equilibrium state. This in effect decouples any tail rotor effects on the thrust experiments. The ultrasonic range sensors shown in Figure I.12 on page 388 keep track of the height of the helicopter which can be correlated to the weight that the helicopter is lifting via the HTP calibration curve shown in Figure I.21 on page 397. Figure K.1 on the next page shows data from a real-time data collection run with the engine controller engaged to keep the rotor angular velocity constant. The solid red line is the altitude data, the dashed blue line is the main rotor blade pitch angle, and the green dash-dot line is the rotor angular velocity Ω . The altitude readings become noisier as the angular velocity increased. This is an artifact of the helicopter being constraint to the HTP with structural vibration feedback recorded in the ultrasound signal. Wavelet analysis and other signal filtering techniques allow for the estimation of the altitude in this portion of the data collected.

Figure K.2 on the following page plots the measured and computed force exerted by the helicopter. The computed force uses equation (K.1.1) on the previous page with the model parameters shown in Table K.1.

Table K.1: Aerodynamic Model Parameters for the Main Rotor

lift curve slope C_{l_α}	5.7	rad^{-1}
drag coefficient C_d	0.024	
zero-lift angle of attack α_0	-1.2	deg
maximum thrust coefficient C_T	0.0057	
air density ρ	1.1840	kg/m^2

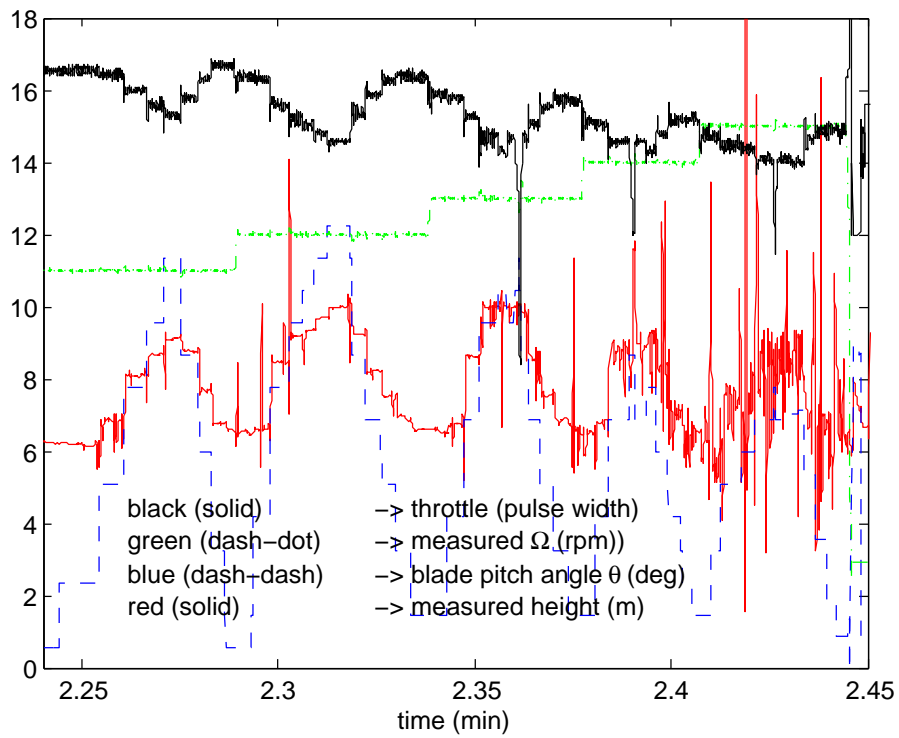


Figure K.1: Thrust Experiment with Helicopter on the HTF with vertical one-DOF enabled.

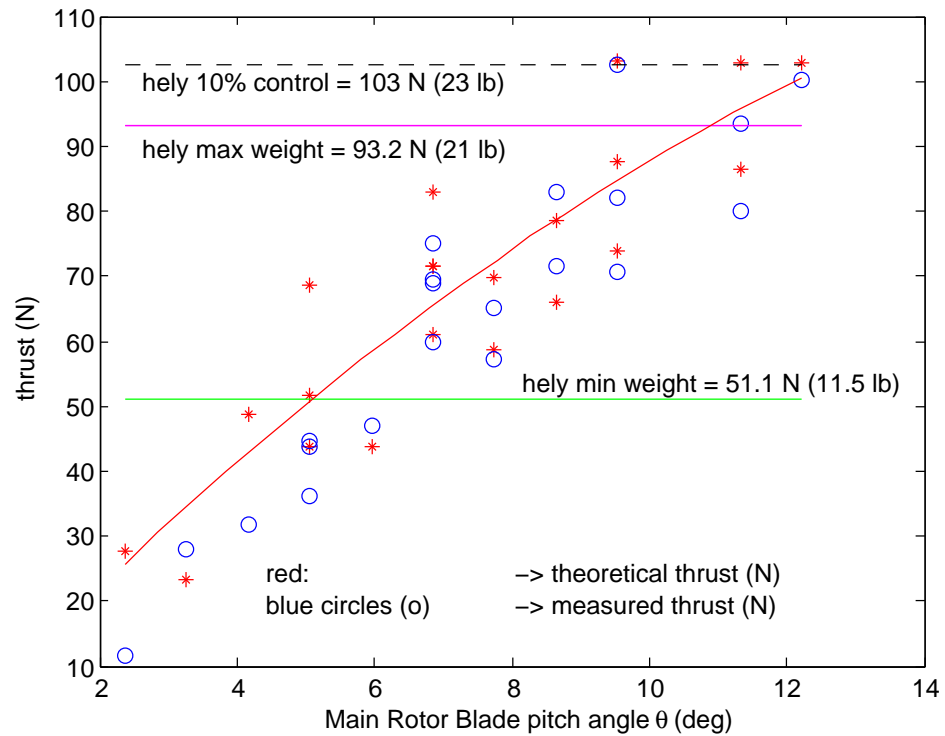


Figure K.2: Measured and Estimated Thrust. .

K.3 Helicopter Experimental Setup for Power and Torque Characterization

The power and torque experiment uses the Helicopter Test Platform (HTP) with the axial (altitude) and rotational (heading) enabled. The first portion of the experiment does not issue control commands to the tail rotor, and the tail rotor is free to rotate in its stick-free equilibrium trim setting. This portion of the experiment has as its main goal the identification of the main rotor induced power and rotatory profile power. The second part of the experiment engages the tail rotor, and the previous results are then utilized to estimate the tail rotor aerodynamic parameters.

In both cases, the experiment is set with a cantilever beam restraining the heading motion as shown in Figure K.3 on the next page. When the main rotor angular velocity increases, the resulting torque increases as per equation (K.1.2) on page 418. The cantilever beam, acting as a bending beam load cell, senses the strain in the device and records it as a voltage change. Figure I.19 on page 395 shows the calibration curve that correlates the sensed voltage to the applied bending moment.

K.3.1 Main Rotor Induced and Profile Power Experiment

The particulars related to this experiment are summarized below:

1. the tail rotor is free to rotate in its stick-free equilibrium state. This setup item decouples most of the tail rotor dynamics from the main rotor aerodynamics, with the notable exception of the associated profile power signature of the tail rotor and related transmission gear.
2. the helicopter is free to lift and sink along its vertical z-axis. This enables a coupled optimization of the thrust and torque aerodynamic parameters.

Figure K.4 on page 425 plots the results of a real-time run. The angular velocity Ω is constant for a short time while the blade pitch angle θ varies. Subsequent to this, the angular velocity increases, and the experiment repeats. Figure K.5 on page 426 shows a subset of this data for a run with constant rotor angular velocity $\Omega = 1400$. The top graph in this figure plots the recorded torque Q for various blade pitch angle θ plotted in



Figure K.3: Torque Experiment with Helicopter on the HTF with cantilever beam as a torque measuring device.

the bottom graph. Thus, the measured torque average for each step in blade pitch angle and rotor angular velocity becomes a point in Figure K.6 on page 427. The top graph in this figure plots the measured torque data (\circ) and the derived induced torque ($*$) from equation (C.2.16) on page 227 and equation (K.1.3) on page 418

$$C_{Q_i} = \frac{k}{\sqrt{2}} C_T^{3/2} \tag{K.3.1}$$

$$Q_i \simeq k_Q \Omega^2 \theta^{3/2}$$

The solid red line in this Figure K.6 is a best fit to the measured data, the x-axis corresponds to the term $\Omega^2 \cdot \theta^{3/2}$, and the term $k_Q = f(\Omega, \theta)$ in the above equation is a non-linear third order polynomial. The bottom graph in Figure K.6 plots the total torque from the previously mentioned equations (C.2.16) and (K.1.3)

$$C_P = C_Q = \frac{k}{\sqrt{2}} C_T^{3/2} + \frac{1}{8} \rho C_D \tag{K.3.2}$$

$$Q \simeq k_Q \Omega^2 \theta^{3/2} + k_{Q_0}$$

The circles (\circ) in the bottom graph correspond to the profile drag k_{Q_0} , and it is mostly constant for any tuple $(\Omega^2, \theta^{3/2})$. The asterisks ($*$) correspond to the computed torque Q in utilizing the above equation, and the solid blue line is a best fit to this data. The solid red line (below the solid blue) is the best fit to the measured data from the top graph in this Figure K.6. The bending beam load cell in Figure K.3 on the previous page is mostly sensitive to the induced torque since the constant profile torque serves to prime the spring that makes up the flexible cantilever beam setup. Figure K.7 on page 428 plots the blade pitch angle θ and estimated angle of attack α against measured torque. The torque is linear and then tapers off indicating that the torque available is less than the torque required. Equation (K.3.2) suggests that the torque should be linear to $\theta^{3/2}$ which can be seen in the bottom graph of Figure K.7. The top graph in Figure K.8 on page 429 plots the measured torque (solid red line), the computed induced torque (solid black line), and the computed total torque (dashed blue line). The bottom graph plots the input blade pitch angle (solid red line), the measured rotor angular velocity (dashed blue), and the input engine throttle (dash-dot line).

Figure K.9 on page 430 presents data related to engine torque as per equation (J.2.7) on page 404

$$\begin{aligned}
 P_e &= P_{e,\max} w_f \\
 Q_e &= \frac{P_e}{\Omega} = \frac{P_{e,\max}}{\Omega} w_f \\
 w_f &= f(\delta_{Th})
 \end{aligned}
 \tag{K.3.3}$$

where w_f is the fuel flow and δ_{Th} is the throttle opening in Figure I.17 on page 394, and the maximum engine power P_e is tabulated in Table I.16 on page 387.

Figure K.6 on page 427 shows that the compound main rotor and tail rotor torques could be modeled very accurately with a bias term plus a nonlinear term involving the product of RPM squared times the main rotor blade pitch angle raised to the three-halves power. This data corresponds well with the model in equation (J.2.5) on page 403. Moreover, Figure K.6 on page 427 indicates that the model in equation (J.2.5) is valid throughout the helicopter flight envelope. That is, equation (J.2.5) provides an accurate non-linear estimate of the trim throttle setting throughout the helicopter flight envelope as a function of both RPM and main rotor blade pitch angle. This is a fundamental result of this thesis work.

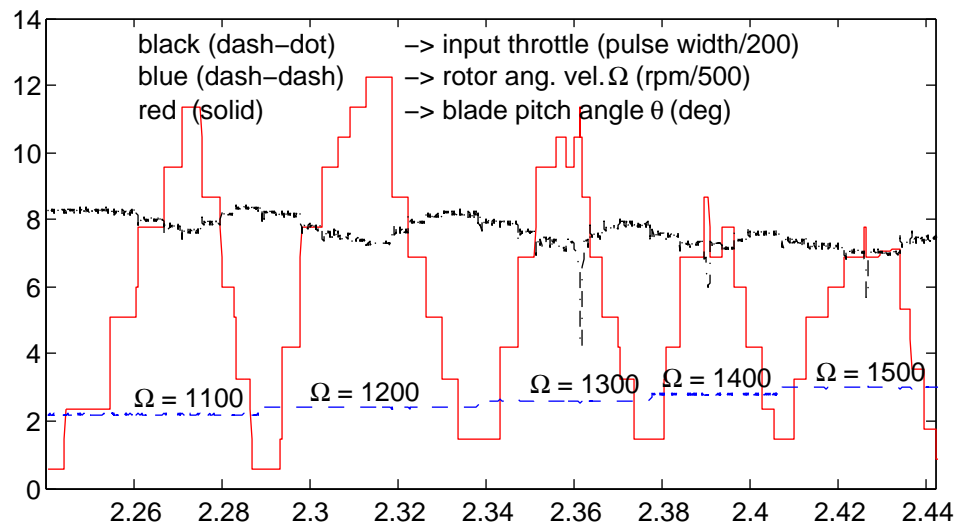
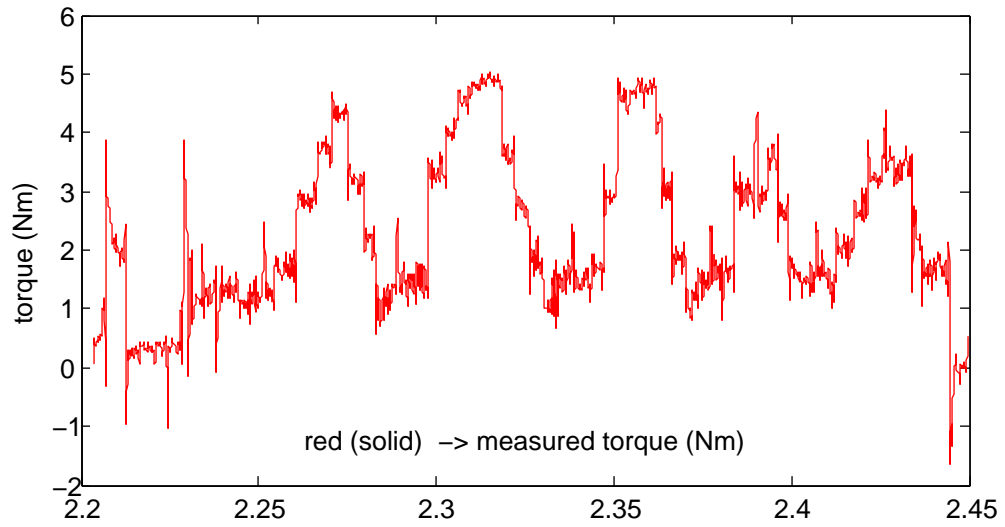


Figure K.4: Torque Experiment with no Tail Rotor Inputs.

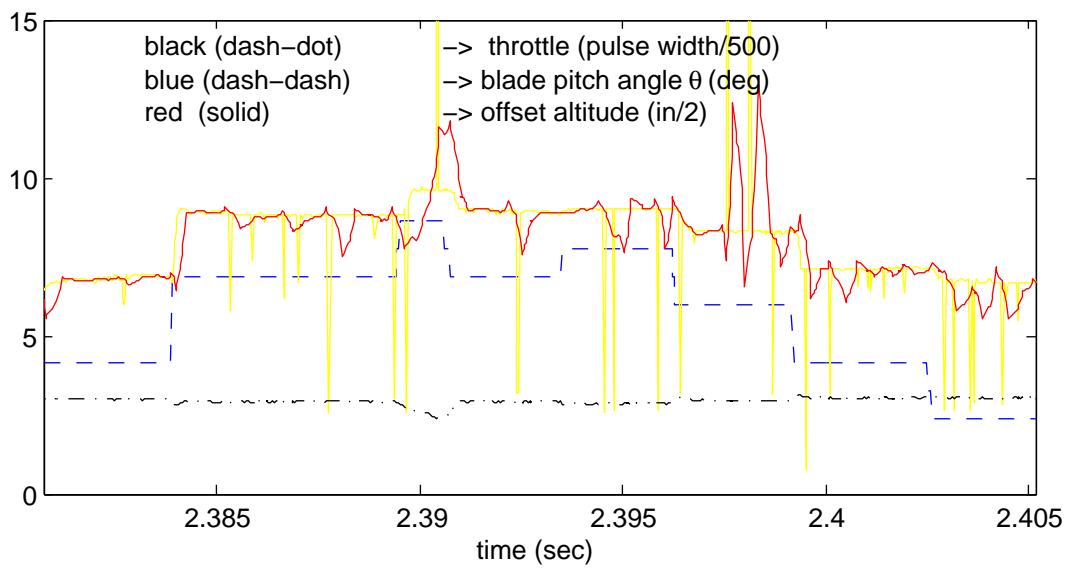
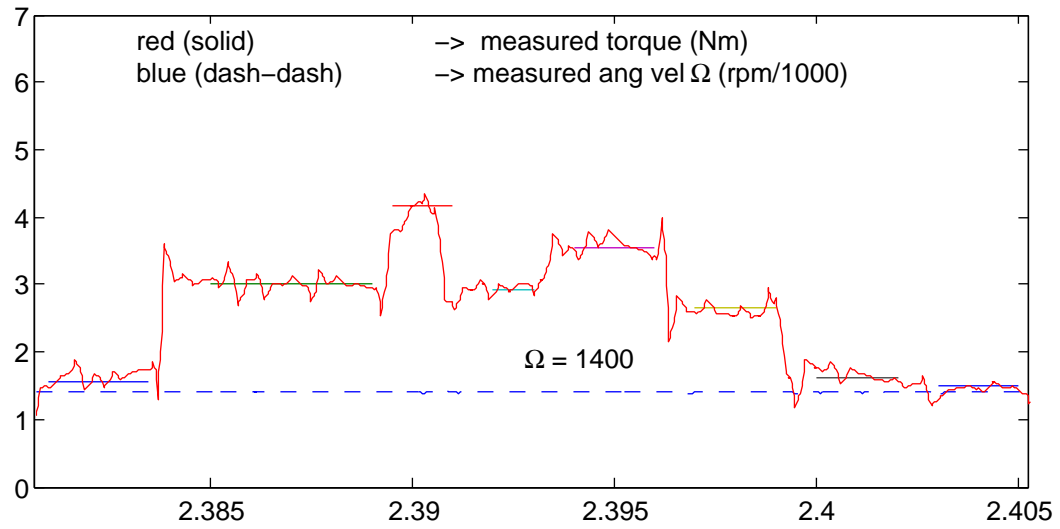


Figure K.5: Torque Experiment sample data $\Omega = 1400$ rpm.

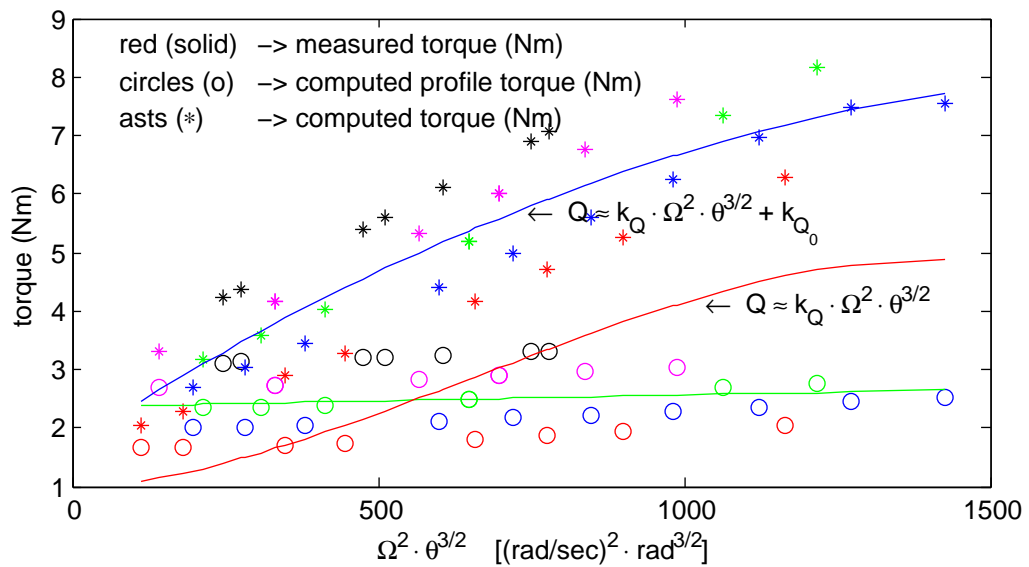
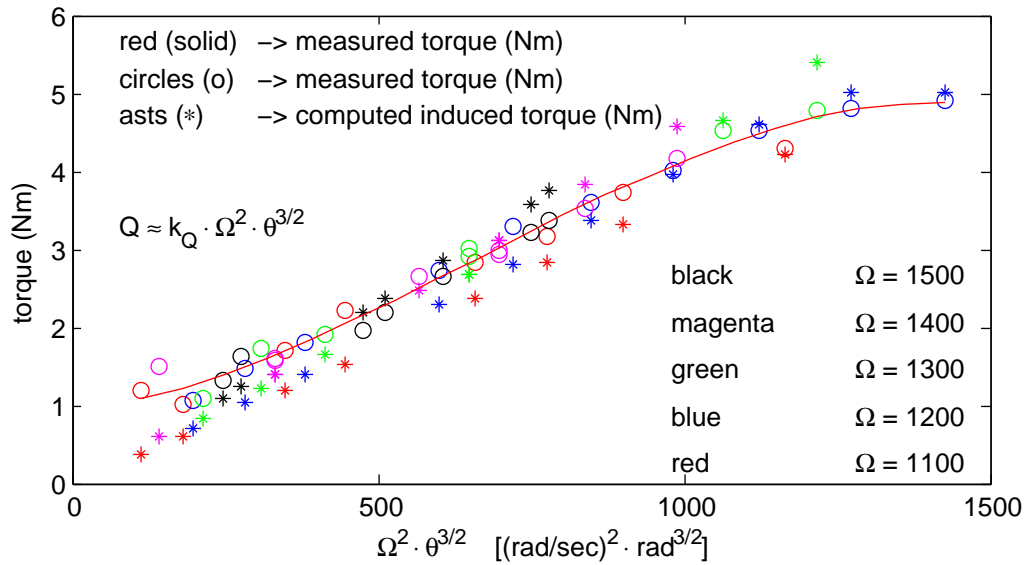


Figure K.6: Torque Measurements Experiment with free tail rotor inputs.

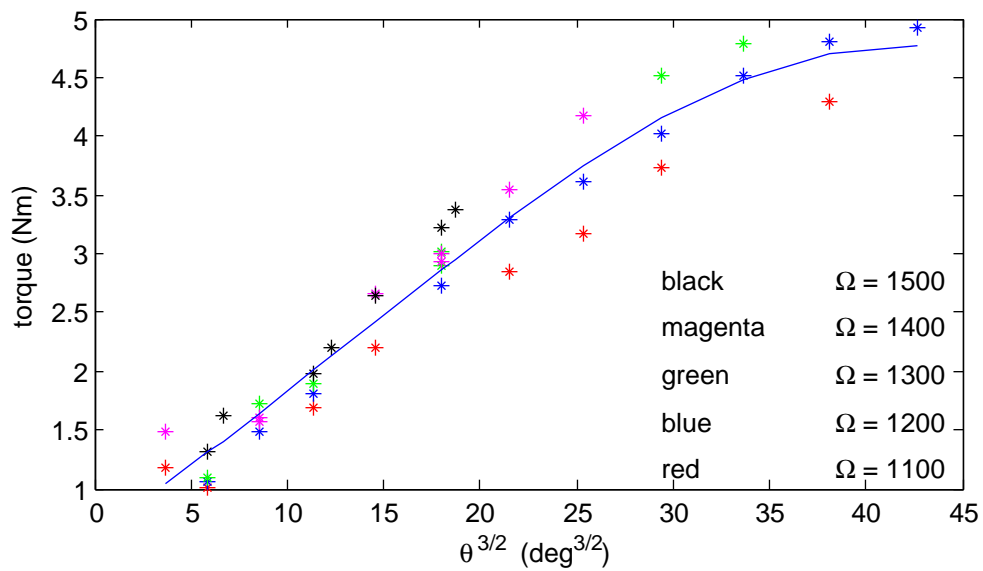
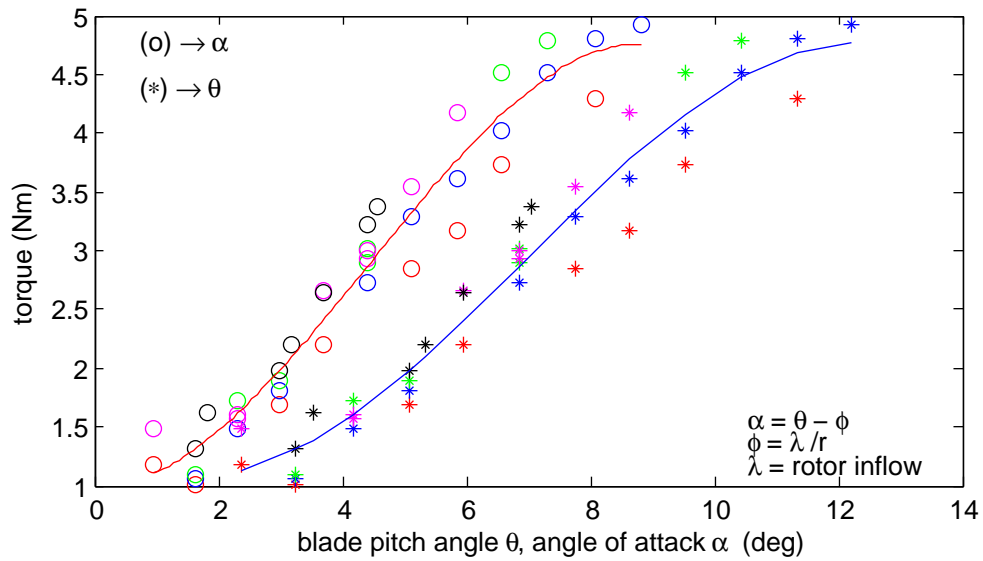


Figure K.7: Torque Measurements with blade pitch angle and angle of attack.

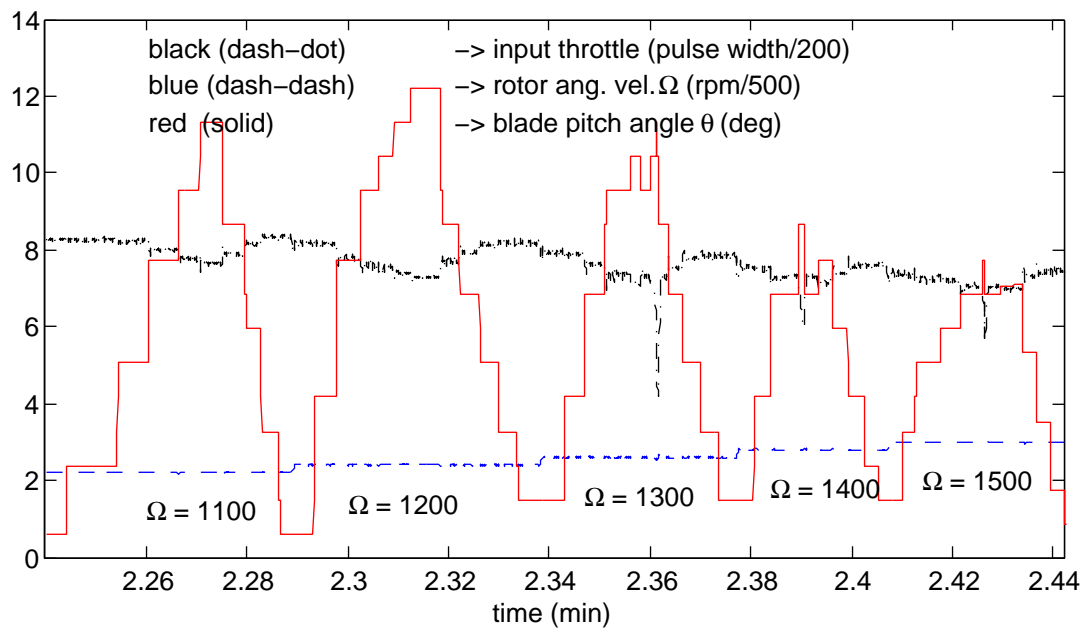
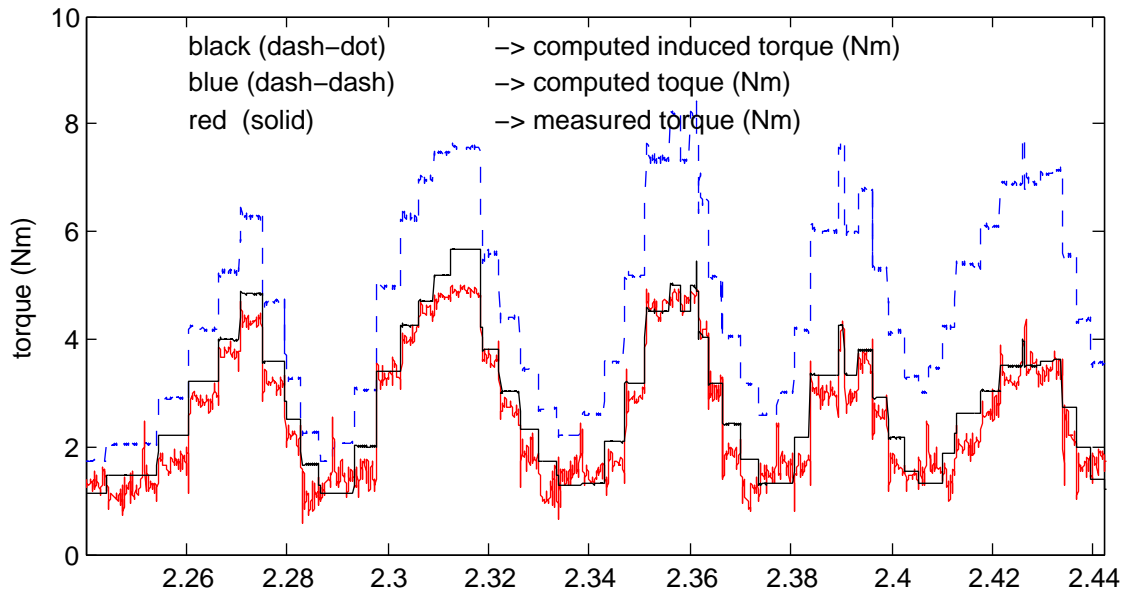


Figure K.8: Torque Measurements and Computed Torque.

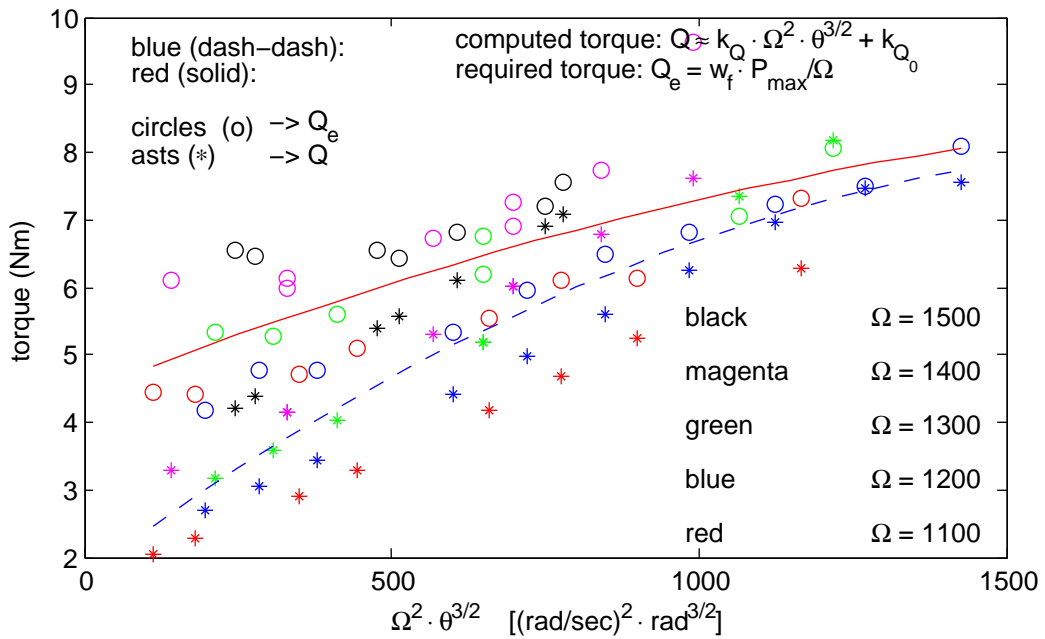
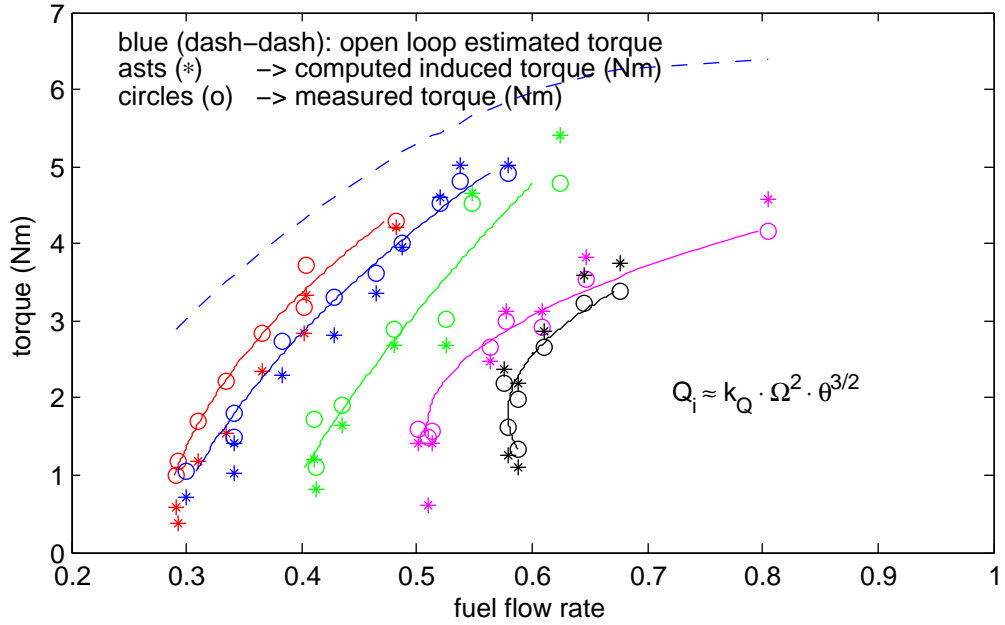


Figure K.9: Engine Torque Map.

K.3.2 Tail Rotor Aerodynamic Model Identification Experiment

Figure K.10 on the following page shows the data taken during a real-time experimental run. During this experiment the tail rotor was actively engaged and the helicopter was free to rotate about its z-axis. In the graph, the dashed blue curve is the rotor angular velocity $\Omega/100$ in rpm, the solid magenta curve is the throttle input pulse-width $\delta_{Th}/200$ in microseconds, the solid dark green curve is the blade pitch angle θ in degrees, the solid light green curve is the computed induced torque Q_i via equation (K.1.3) on page 418 in Nm , the solid yellow and red curve are, respectively, the raw and filtered measured torque Q_{mea} in Nm measured by the bending beam load cell, and the solid blue curve is a composite that contains the estimated tail rotor torque Q_{TR} and reaction torque for equilibrium points when $\dot{Q}_e = 0$

$$Q_i + n_{TR}Q_{TR} = l_{TR}T_{TR} \tag{K.3.4}$$

$$Q_i + n_{TR}Q_{TR} - l_{TR}T_{TR} = Q_{mea}$$

The measured torque Q_{mea} matches very well with the computed torque $Q_i + n_{TR}Q_{TR} - l_{TR}T_{TR}$ which indicates that the Tail Rotor aerodynamic model is adequate for the present first iteration. It can be seen that the bending beam load cell experiences a hysteresis, but for the most part, both the magnitude and the trend match to an acceptable degree. More detailed data requires the use of a torque load cell which is not available, and the trade off between the resources needed to acquire or manufacture such torque load cell is not commensurate to the small gain of obtaining slightly more accurate data. The tail rotor aerodynamic data is given in Table K.2

Table K.2: Aerodynamic Model Parameters for the Tail Rotor

lift curve slope C_{l_α}	5.0	rad^{-1}
drag coefficient C_d	0.024	
maximum thrust coefficient $C_{T_{TR}}$	0.05	
non linear torque factor k_{TR}	1.146	

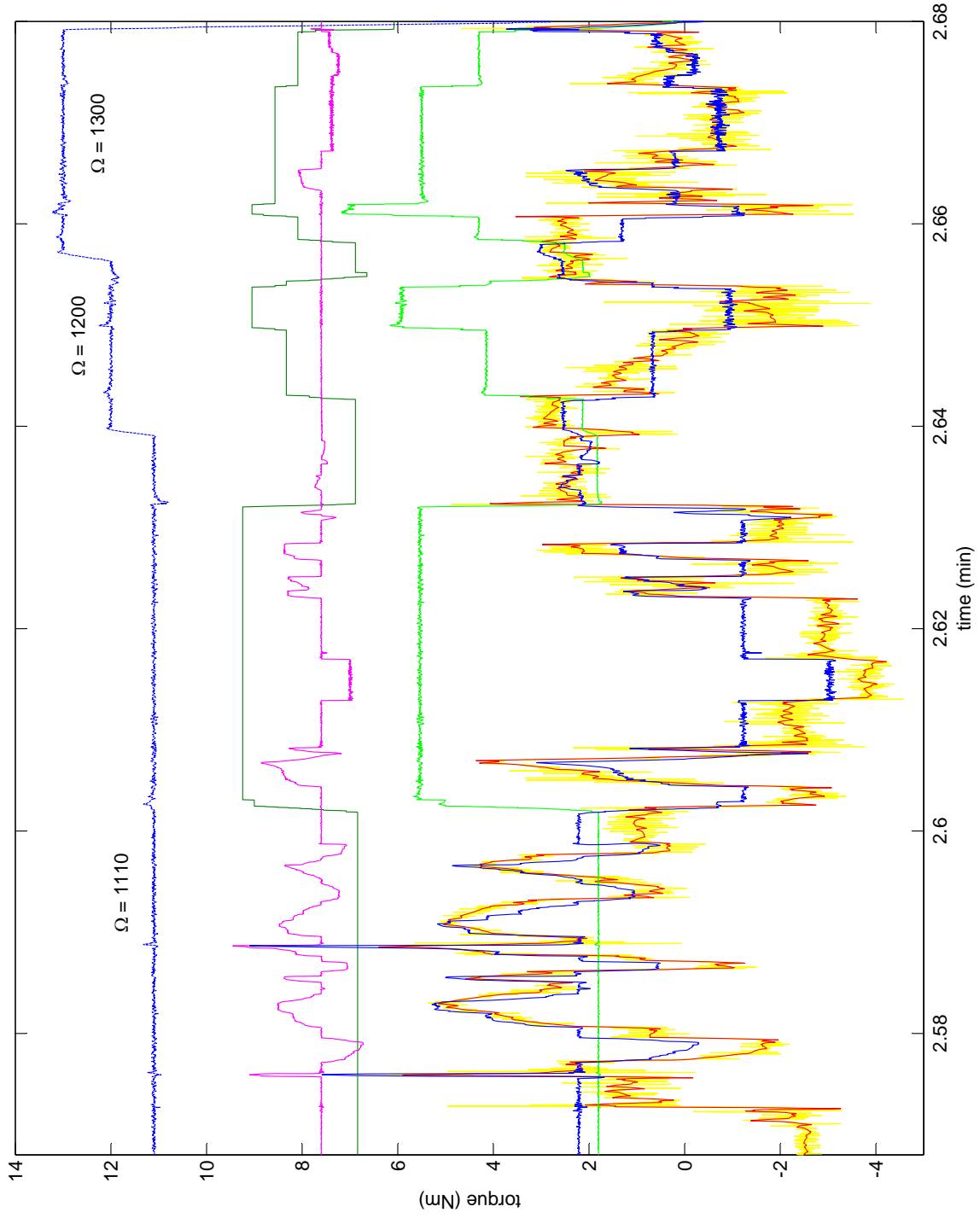


Figure K.10: Effects of Tail Rotor Torque on Bending Beam Load Cell Torque Measurements

Appendix L

Helicopter Stability and Control

L.1 Introduction

The result of Section §J is an engine governor that keeps a constant angular velocity in the presence of parameter uncertainty and environmental disturbances. The parameters in the aerodynamic models were identified in Section §K via a series of experiments in which the engine governor in equation (J.2.19) on page 411 maintained a constant main rotor angular velocity. The rotor angular velocity is prominent in all the fundamental aerodynamic terms such as thrust and torque and many stability derivatives, and it is therefore important to simplify the control laws of the helicopter by keeping the rotational dynamics at a constant angular speed.

The helicopter equations of motion (EOM) are summarized in equation (H.1.1) on page 359. Under the set of simplifying assumptions in Section H.1.1 on page 358, the governing rigid body EOM reduces to equation (H.1.5) on page 360:

$$\begin{aligned}\dot{u} &= rv - qw + -g \sin \theta + \frac{X_{MR} + X_F}{m} \\ \dot{v} &= pw - ru + g \sin \phi \cos \theta + \frac{Y_{MR} + Y_F + Y_{TR}}{m} \\ \dot{w} &= qu - pv + g \cos \phi \cos \theta + \frac{Z_{MR} + Z_F + Z_{TR}}{m} \\ \dot{p} &= \frac{(I_y - I_z)}{I_x} qr + \frac{L_{MR} + L_{TR}}{I_x} \\ \dot{q} &= \frac{(I_z - I_x)}{I_y} rp + \frac{M_{MR}}{I_y} \\ \dot{r} &= \frac{(I_x - I_y)}{I_z} pq + \frac{N_{MR} + N_{TR}}{I_z}\end{aligned}\tag{L.1.1}$$

For the sake of completion, the kinematic equations are presented in equation (H.1.6) on

page 361, and reproduced in equation (L.1.2) for convenience.

$$\begin{aligned}
 \begin{bmatrix} \dot{\phi} \\ \dot{\theta} \\ \dot{\psi} \end{bmatrix} &= \begin{bmatrix} 1 & \sin \phi \tan \theta & \cos \phi \tan \theta \\ 0 & \cos \phi & -\sin \phi \\ 0 & \sin \phi \sec \theta & \cos \phi \sec \theta \end{bmatrix} \begin{bmatrix} p \\ q \\ r \end{bmatrix} \\
 \begin{bmatrix} \dot{x}_E \\ \dot{y}_E \\ \dot{z}_E \end{bmatrix} &= \begin{bmatrix} c\theta c\psi & s\phi s\theta c\psi - c\phi s\psi & c\phi s\theta c\psi + s\phi s\psi \\ c\theta s\psi & s\phi s\theta s\psi + c\phi c\psi & c\phi s\theta s\psi - s\phi c\psi \\ -s\theta & s\phi c\theta & c\phi c\theta \end{bmatrix} \begin{bmatrix} u \\ v \\ w \end{bmatrix}
 \end{aligned} \tag{L.1.2}$$

L.2 Experiment: Yaw Stability and Heading Control

The Helicopter Test Platform (HTP) is described in Section I.4 on page 395. When the helicopter is mounted on the HTP, the ensuing linear motion of the helicopter is restricted along the vertical axis and the angular motion is restricted about the vertical axis. In this case, the governing EOM for the helicopter system becomes

$$\begin{aligned}
 \dot{w} &= g \cos \phi \cos \theta + \frac{Z_{MR} + Z_F + Z_{TR}}{m} \\
 \dot{r} &= \frac{N_{MR} + N_{TR}}{I_z}
 \end{aligned} \tag{L.2.1}$$

where the u, v, p, q and related terms are dropped from the equations. The tail rotor blade does not have cyclic pitch control, and the primary control of the tail rotor thrust is via the tail rotor blade pitch angle θ_{TR} . In this case, the fuselage force Z_F and tail rotor force Z_{TR} contribution to the vertical equation of motion (L.2.1) are small and can be ignored safely. In turn, the linear \dot{w} and angular \dot{r} equations are coupled through the main rotor torque Q_{MR} . The angular velocity controller developed in Section J.2.3 on page 410 decouples the rotor angular velocity Ω from the above equations, but the main rotor blade pitch angle θ_{MR} appears in both equations via the primary force Z_{MR} and moment N_{MR} components. The tail rotor torque $N_{TR} = l_{TR} \cdot T_{TR}$ is the primary control mechanism utilized to control body yaw attitude and maintain desired heading. Figure F.2 on page 333 shows the lateral forces and moments acting upon the helicopter. Figure L.1 on the following page presents an abstraction of the tail rotor hub as it relates

The tail rotor operates in a very complex flow field, and the velocities present at the tail rotor hub are equally complex. An estimation of the tail rotor thrust coefficient follows from direct application of the results obtained for the main rotor thrust and torque coefficients. The tail rotor has no flapping hinges and no cyclic inputs, and in this case equation (D.3.130) on page 302 holds such that

$$\begin{aligned} C_{T_{TR}} &= \frac{(a\sigma)_{TR}}{2} \left[\frac{\theta}{3} \left(1 + \frac{3}{2}\mu^2 \right) - \frac{\lambda - \mu_z}{2} \right]_{TR} \\ C_{Q_{TR}} &= \lambda C_{T_{TR}} + \left[\frac{\sigma C_d}{8} (1 + \mu^2) \right]_{TR} \end{aligned} \quad (\text{L.2.4})$$

Following development by Padfield [119], the tail rotor aerodynamic velocity and rotor inflow are approximated by

$$\begin{aligned} \mu_{TR} &= \frac{[u^2 + (w - k_{\lambda TR}\lambda_{TR} + ql_{TR})^2]^{1/2}}{(\Omega R)_{TR}} \\ \mu_{ZTR} &= \frac{(rl_{TR} - ph_{TR} - v)}{(\Omega R)_{TR}} \\ \lambda_{TR} &= \frac{C_{T_{TR}}}{2 [\mu_{TR}^2 + (\mu_{ZTR} - \lambda_{TR})^2]^{1/2}} \end{aligned} \quad (\text{L.2.5})$$

where $k_{\lambda TR}$ is a scaled factor of the main rotor inflow at the tail rotor [119]. For the helicopter test on the HTP, the above equation for the aerodynamic velocity reduces to

$$\begin{aligned} \mu_{TR} &= -\frac{k_{\lambda TR}\lambda_{TR}}{(\Omega R)_{TR}} \\ \mu_{ZTR} &= \frac{r l_{TR}}{(\Omega R)_{TR}} \end{aligned} \quad (\text{L.2.6})$$

Equation (C.3.7) on page 231 is a numerical approximation that uses results from momentum and blade element theory [92]. This discrete approximation sidesteps the iterative approach of equations (L.2.4) and (L.2.5). In this case, $\lambda_{c,TR} = \mu_{ZTR}$ together with

equation (D.3.129) on page 302 which results in

$$\begin{aligned}\lambda(x, \mu_{ZTR}) &= \frac{\sigma a}{16} \left[\sqrt{\left(1 - \frac{8}{\sigma a} \mu_{ZTR}\right)^2 + \frac{32}{\sigma a} \theta(x) x} - \left(1 - \frac{8}{\sigma a} \mu_{ZTR}\right) \right] \\ \Delta C_{T,TR} &= \frac{\sigma a}{2} \left[\theta \left(x^2 + \frac{\mu^2}{2}\right) - x\lambda \right] \Delta x\end{aligned}\quad (\text{L.2.7})$$

where all relevant variables apply to the tail rotor with the subscript $(\cdot)_{TR}$.

L.2.1 Trim Tail Rotor Blade Pitch Angle

Equation (L.2.1) on page 434 together with equation (L.2.2) indicates that a trim condition occurs when the yaw rate $\dot{r} = 0$. In this case

$$-N_{TR} = N_{MR} \quad \Rightarrow \quad Y_{TR} = \frac{Q_{MR}}{l_{TR}} \quad (\text{L.2.8})$$

Equation (L.2.4) on the preceding page together with equation (L.2.6) suggest that an important equilibrium case happens when the yaw angular rate $r = 0$. Then the case when $r \neq 0$ could be treated as a perturbation of the primary flight condition $r = 0$. Figure L.2 on the next page shows results from a real-time data run with open loop tail rotor inputs δ_{TR} in pulse width (dash-dash black curve). Multiple runs similar to the one in this figure allow for the selection of data points where the yaw rate $r = 0$ at different set points for the main rotor angular velocity Ω_{MR} and for different values of main rotor blade pitch angle θ_{MR} . Results are shown in Figure L.3 on page 439.

Given the empirical relation for main rotor torque Q_{MR} in equation (K.3.2) on page 423 along with equation (L.2.8), it is reasonable to expect that the trim value for the tail rotor blade pitch angle is a function of the main rotor angular velocity Ω_{MR} and the main rotor blade pitch angle θ_{MR} . This assumption matches the results in Figure L.3 and Figure L.4. This last Figure L.4 on page 440 presents the aforementioned trim equilibrium condition for the case when $\dot{r} = r = 0$

$$Y_{TR} = \left[\frac{Q_{MR} + n_{TR} Q_{TR}}{l_{TR}} \right]_{\dot{r}=r=0} \quad (\text{L.2.9})$$

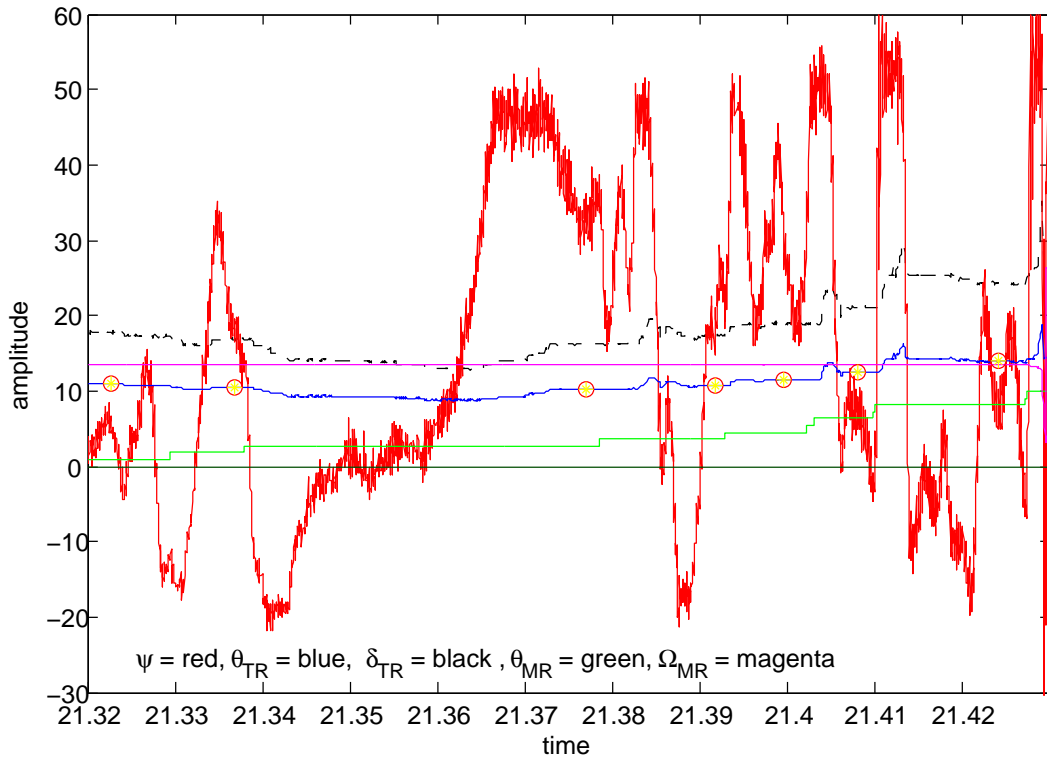


Figure L.2: Real Time Run with Tail Rotor Inputs.

Notice that the results presented in this section differ from those in Section K.3.2 on page 431 in that the helicopter is not constrained in the yaw axis as it was constrained by a torque measuring device in Section K.3.2. The total torque and the tail rotor trim torque presented in the bottom graph in Figure L.4 are those resulting from Section K.3.1 on page 421 and the previously mentioned Section K.3.2.

L.2.2 Helicopter Yaw Rate Control Design

Equation (L.2.1) on page 434 is the governing equation for the dynamic behavior of the helicopter sitting on top of the Helicopter Testing Platform (HTP). Coupling effects are accounted for by the engine governor derived in Section J.2.3 on page 410 and by the trim condition in equation (L.2.9) on the previous page. In this case, the perturbation yaw dynamics in the frequency domain can be simplified to

$$\frac{\dot{r}(s)}{r_c(s)} = \frac{1}{I_{zz}s} \quad (\text{L.2.10})$$

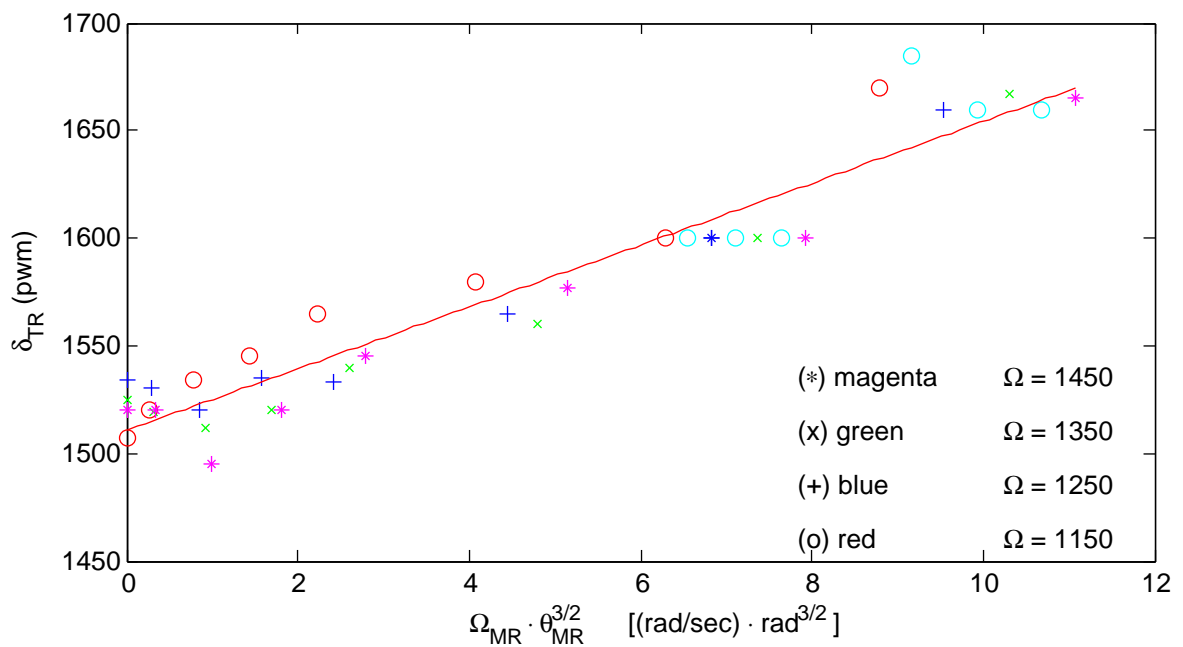
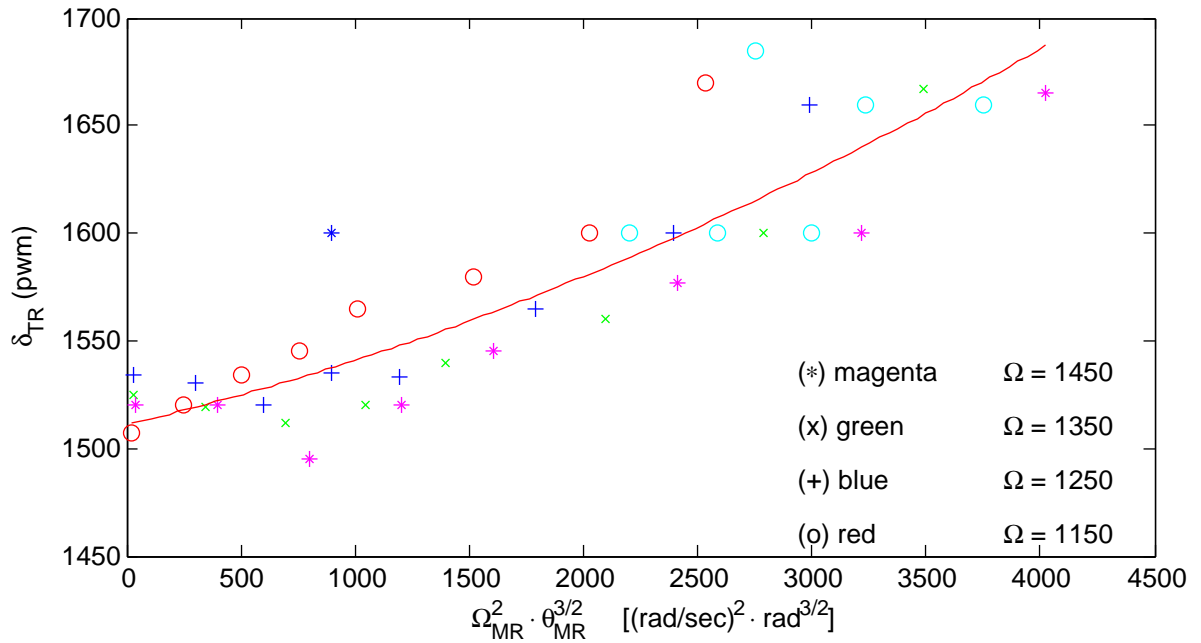


Figure L.3: Multiple Real Time Run with Tail Rotor Inputs.

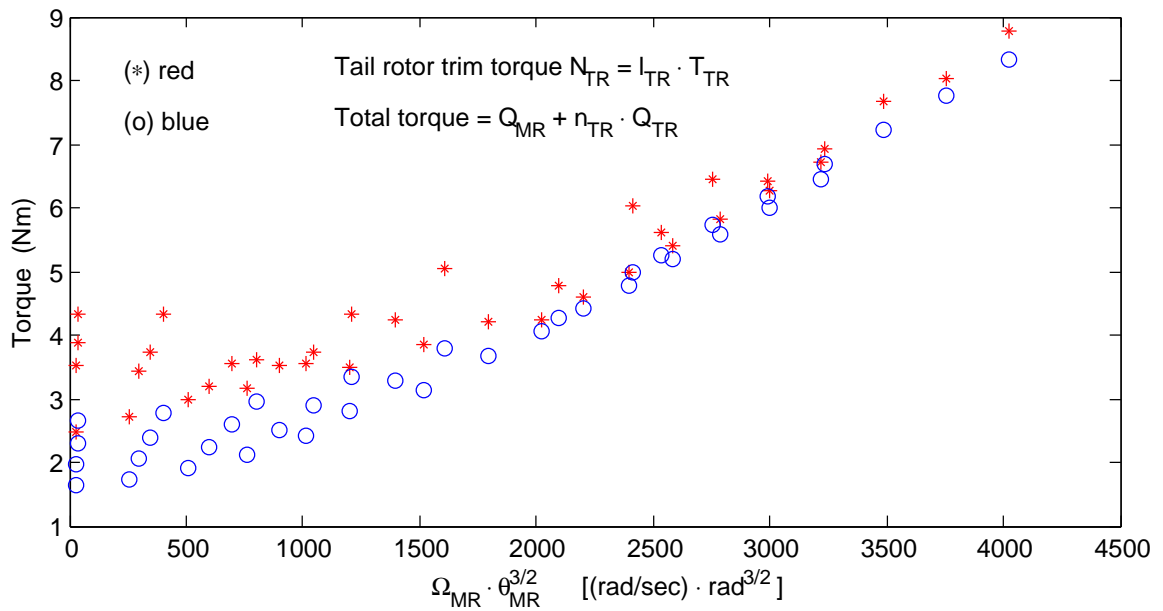
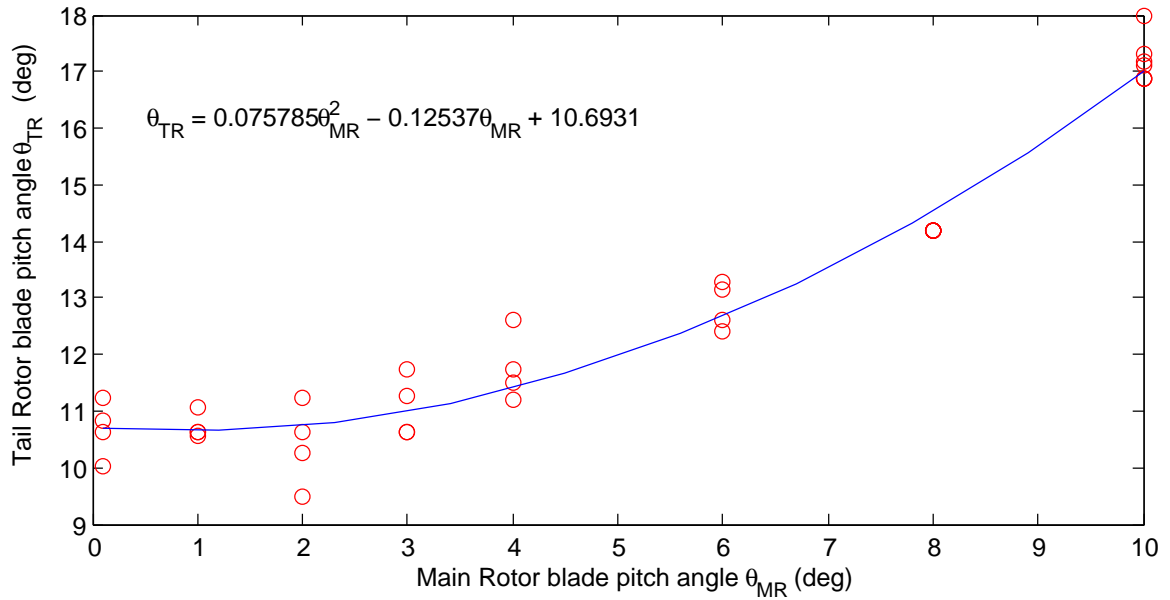


Figure L.4: Empirical Tail Rotor Blade Pitch Angle and resulting Equilibrium Torque N_{TR} .

A simple gain with unit feedback allows for a design of a first order feedback loop as shown in Figure L.5. In this case

$$\begin{aligned}
 r &= \frac{k_r}{I_{ZZ}} \frac{1}{s} (r_C - r) \\
 \frac{r}{r_C} &= \frac{k_r/I_{zz}}{s + k_r/I_{zz}} = \frac{1}{\tau_c s + 1} \\
 \tau_c &= \frac{I_{zz}}{k_r}
 \end{aligned}
 \tag{L.2.11}$$

where τ_c is the time constant for the augmented system, and k_r is the control gain that will provide acceptable performance. The final value theorem [44, 118] says that for a step command input

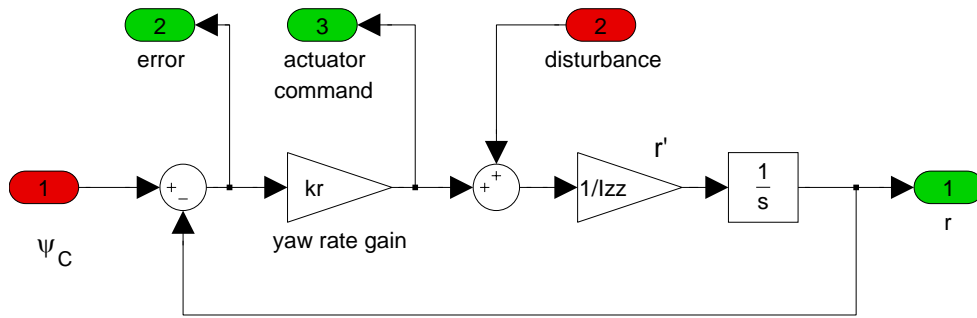


Figure L.5: Yaw Rate p Feedback Control Law.

$$\lim_{x \rightarrow \infty} r(t) = \lim_{s \rightarrow 0} s r(s) = s \frac{1/k_r}{\tau_c s + 1} \frac{1}{s} = 1
 \tag{L.2.12}$$

where $r(s) = \mathcal{L}\{r(t)\}$ is the Laplace transform of $r(t)$. The corresponding transfer functions from command input to error e/ψ_C , from disturbance r_d to error e/r_d , and from disturbance to yaw rate r/r_d are give by

$$\begin{aligned}
 \frac{e}{r_C} &= \frac{s/\tau_c}{\tau_c s + 1} \\
 \frac{r}{r_d} &= -\frac{e}{r_d} = \frac{1/k_r}{\tau_c s + 1}
 \end{aligned}
 \tag{L.2.13}$$

The steady state value of the above transfer functions are

$$\begin{aligned} \left[\frac{e}{r_C} \right]_{t \rightarrow \infty} &= 0 \\ \left[\frac{r}{r_d} = -\frac{e}{r_d} \right]_{t \rightarrow \infty} &= \frac{1}{k_r} \end{aligned} \quad (\text{L.2.14})$$

As expected, the constant gain for yaw rate feedback can not reject disturbances entirely, but yaw rate command is seldom used as a performance measure in its own right. Therefore, the non-zero steady error induced by a disturbance input to the plant (gust wind affecting the tail rotor and fuselage) is not as relevant for the current flight regime under consideration. The time constant is related to the rise time as given by

$$\begin{aligned} 1 - e^{-t_1/t_c} &= \frac{1}{10} & 1 - e^{-t_2/t_c} &= \frac{9}{10} \\ e^{-t_1/t_c} &= \frac{9}{10} & e^{-t_2/t_c} &= \frac{1}{10} \\ \frac{t_1}{t_c} &= \ln 10 - \ln 9 & \frac{t_2}{t_c} &= \ln 10 - \ln 1 \end{aligned} \quad (\text{L.2.15})$$

from which the time to rise t_r results in

$$t_r = t_c \ln 9 = t_2 - t_1 \quad (\text{L.2.16})$$

The time constant τ_c is related to the yaw rate gain k_r via equation (L.2.11) on the previous page as $\tau_c = I_{zz}/k_r$. In this case the yaw rate control gain k_r is then given by

$$\begin{aligned} t_r &= t_c \ln 9 = \frac{I_{zz}}{k_r} \ln 9 \\ k_r &= \frac{I_{zz}}{t_r} \ln 9 \end{aligned} \quad (\text{L.2.17})$$

For a desired rise time of $t_r = 1$ sec, then the time constant $t_c \approx 0.45$ seconds and the control gain is then $k_r = 0.593$. In contrast, a desired rise time one-tenth the previous one such that $t_r = 0.1$ sec will result in a control gain equal to $k_r = 5.93$. According to equation (L.2.14) the disturbance rejection improves by an order of magnitude as well. The final design choice takes into account other control design considerations that will

be presented momentarily.

L.2.3 Helicopter Heading Control Design

Figure L.6 shows the heading control loop which wraps the rate control loop shown in Figure L.5 on page 441. In turn, Figure L.7 shows the same loop with the stability yaw rate feedback control collapsed as given by the transfer function in equation (L.2.11) on page 441.

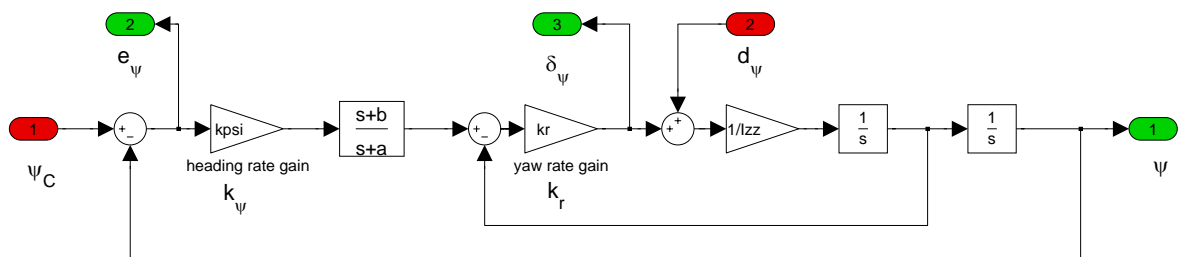


Figure L.6: Yaw Heading ψ Feedback Control Law.

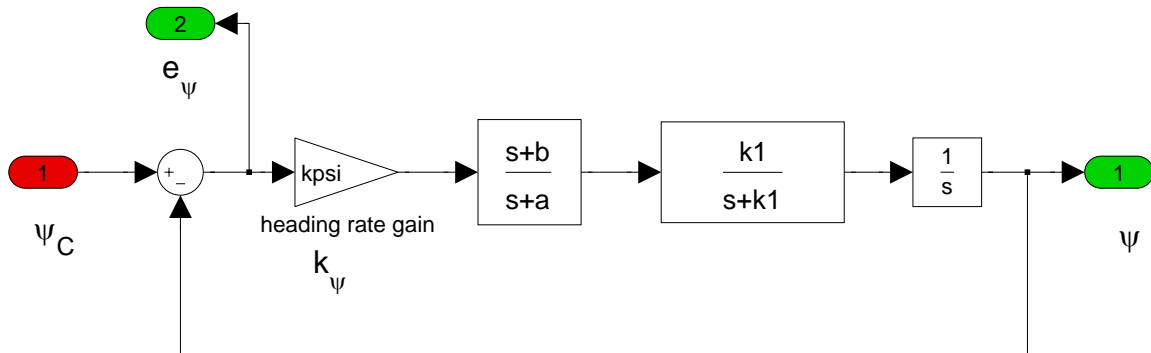


Figure L.7: Yaw Heading ψ Feedback Control Law with collapsed inner stability yaw rate loop. In this case, the constant $k_1 = k_r/I_{zz}$. The inner loops are equivalent to the transfer function equation (L.2.11) on page 441.

The compensator design for the heading loop follows a lead-lag formulation

$$\frac{u_\psi}{e_\psi} = k_\psi \frac{s+b}{s+a} \quad (\text{L.2.18})$$

where u_ψ is the output of the heading compensator, and e_ψ is the heading error signal. The first part of the compensator design follows by equating the numerator $s+b$ in the

lead-lag portion of the compensator (shown above) to the stable form of the denominator $s + k_r/I_{zz}$ of the augmented plant in (L.2.11). The zero in the lead-lag controller cancels the inner rate controller pole, and the loop transfer function $L(s)$ and the closed loop transfer function ψ/ψ_C become

$$\begin{aligned} L(s) &= \frac{\bar{k}k_\psi}{s(s+a)} \\ \frac{\psi}{\psi_C} &= \frac{\bar{k}k_\psi}{s(s+a) + \bar{k}k_\psi} = \frac{\bar{k}k_\psi}{s^2 + sa + \bar{k}k_\psi} \end{aligned} \quad (\text{L.2.19})$$

where $\bar{k} = k_r/I_{zz}$ for convenience. The characteristic equation $s^2 + sa + \bar{k}k_\psi$ in the above closed loop transfer function ψ/ψ_C has the standard form of $s^2 + 2\zeta\omega_n s + \omega_n^2$ where ω_n is the undamped natural frequency and ζ is the damping ratio of a second order system. Select $\zeta = \sqrt{2}/2$, $\omega_n = \pi$ or good flying qualities to obtain

$$\begin{aligned} s^2 + sa + \bar{K}k_\psi &= s^2 + 2\zeta\omega_n s + \omega_n^2 \\ \omega_n^2 &= \pi^2 \quad \zeta = \frac{\sqrt{2}}{2} \\ a &= 2\zeta\omega_n = \pi\sqrt{2} \\ \bar{k}k_\psi = \omega_n^2 &\rightarrow k_\psi = \frac{\pi^2 I_{zz}}{k_r} \end{aligned} \quad (\text{L.2.20})$$

This choice of controller yields a heading compensator design u_ψ/e_ψ with a transfer function as given in equation (L.2.18) on the previous page of the form

$$\frac{u}{e_\psi} = \frac{\pi^2 k_r}{I_{zz}} \frac{s + k_r/I_{zz}}{s + \pi\sqrt{2}} \quad (\text{L.2.21})$$

The choice of value for the yaw rate gain k_r in the above transfer function determines whether the heading compensator is a lead or a lag type. The choice for k_r is determined by performance considerations of the inner yaw rate loop since the heading performance is not sensitive to this factor. To illustrate this point, it is of benefit to realize that given the control choice in (L.2.20), then the performance transfer function ψ/ψ_C in (L.2.19) becomes

$$\frac{\psi}{\psi_C} = \frac{\omega_n^2}{s^2 + 2\zeta\omega_n s + \omega_n^2} \quad (\text{L.2.22})$$

L.2.4 Helicopter Yaw Rate and Heading Control Synthesis

The Helicopter mass properties are tabulated in Section I.1.2 in Table I.2 on page 373. Choose a yaw rate rise time of 0.2 seconds for good disturbance rejection, and the yaw rate time constant becomes $t_c = 0.09$ seconds with a feedback gain $k_r = 2.97$. According to equation (L.2.14) on page 442 this design gives good disturbance rejection with $1/kr = 0.337$. The resulting yaw rate and heading control gains are summarized in Table L.1.

Table L.1: Yaw Rate and Heading Control Design

vehicle inertia I_{zz}	0.27	kgm ²
design choice for rise time t_r	0.2	sec
yaw rate proportional control gain $k_r = \ln(9) \cdot I_{zz}/t_r$	2.97	
heading proportional control gain $k_\psi = \pi^2 I_{zz}/k_r$	0.897	
heading compensator zero k_r/I_{zz}	11.0	
heading compensator pole $\pi \cdot \sqrt{2}$	4.443	
phase margin PM	65.5	deg
gain margining GM	∞	
closed loop heading performance damping ratio $\zeta \approx \sqrt{2}/2$	0.707	
closed loop heading performance bandwidth $\omega_b \approx \pi$	3.14	rad

After the zero cancellation of the heading compensator with the pole of the augmented yaw rate stabilized plant, the loop transfer function $L(s)$ in Figure L.7 on page 443 becomes

$$L(s) = \frac{k_r k_\psi}{I_{zz}} \frac{1}{s(s + \pi\sqrt{2})} = \frac{\pi^2}{s(s + \pi\sqrt{2})} \quad (\text{L.2.23})$$

Figure L.8 on the following page presents the Bode and Nyquist plot for the control design summarized in Table L.1.

L.2.5 Test Results for Helicopter Yaw Rate and Heading Control

Figure L.9 on page 447 plots data measured during a real-time test run of the helicopter with the yaw rate r control loop enabled. The rate command loop from a run time of 250 seconds to 320 seconds was disabled and the helicopter was operating in open loop mode with Radio-Control (RC) inputs providing commands. Toward the end of the run at simulation time of 888 seconds, the main rotor angular velocity Ω was varied while the

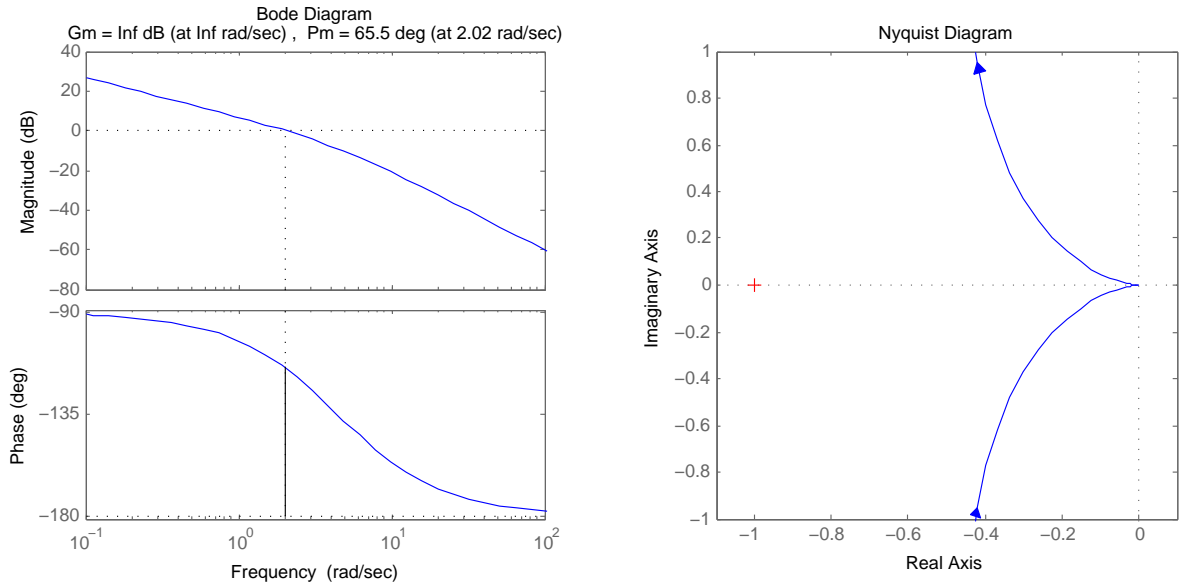


Figure L.8: Frequency plots for the heading compensator loop including inner yaw rate stability loop.

yaw rate controller maintained the commanded zero rate. From simulation time equal to zero to the simulation time of approximately 250 seconds, the commanded yaw rate is set to zero. During this time the helicopter heading drifted very slowly due to bias measurements. A similar behavior takes place from simulation time of 525 seconds to about 726 seconds. The heading (solid blue curve in the graph) wraps around 360^0 to zero. The heading control loop is disabled during runs in which the yaw rate command is enabled.

Figure L.10 on the next page plots data measured during a real-time test run of the helicopter with the heading control ψ loop enabled. The heading control loop was engaged at a simulation time of approximately 937 seconds. The controller is able to hold a heading in spite of large overshoot. This data is from an earlier data run presented with the intent to illustrate initial results. The large overshoot is due to inadequacies of early modeling efforts and subsequent initial heading control designs which were subsequently improved resulting in the heading control design presented in the previous section. Adequate control response to heading commands are shown later in the the appendix. It is important to note that had this controller been utilized in a free flying vehicle, it is probable that the loss of the aircraft would have taken place.

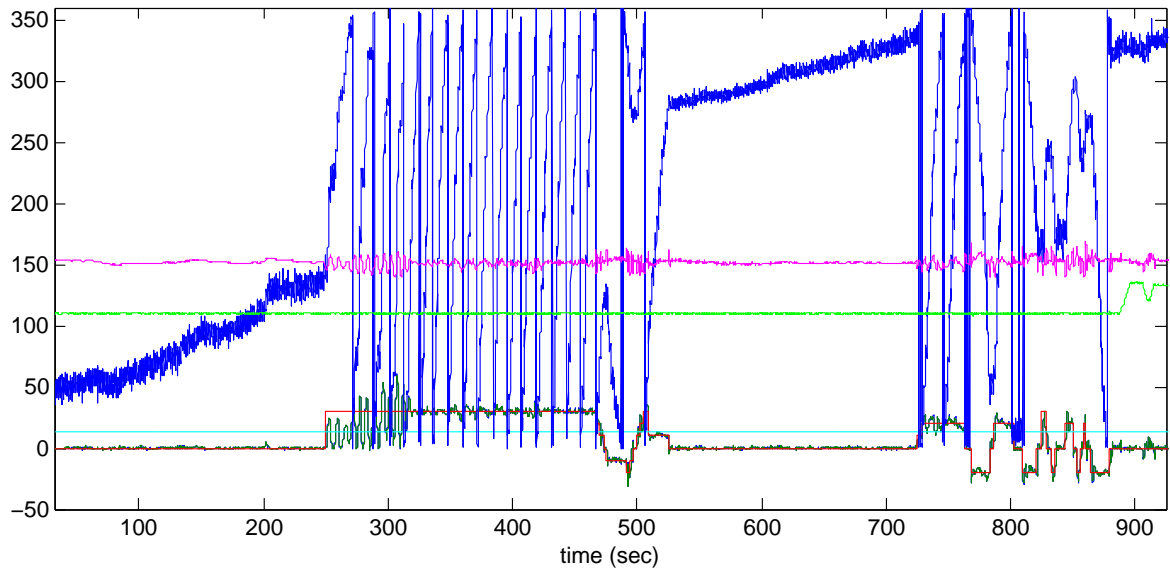


Figure L.9: Real-Time Data with Yaw Rate Command. The red solid curve is the yaw rate command r_C , dark green curve is the yaw rate r measured data. The solid blue curve is the helicopter heading ψ , and the magenta curve is the tail rotor blade pitch command δ_{TR} in pulse width (μ second). The light green curve is the scaled main rotor angular velocity $\Omega/100$. The outer loop for Heading performance is disabled.

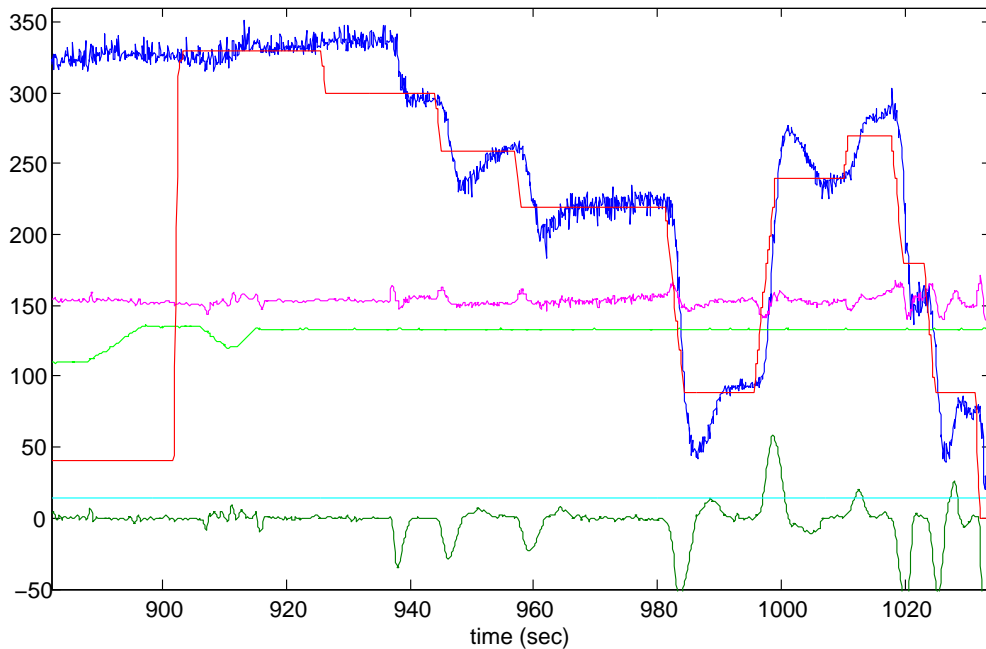


Figure L.10: Real-Time Data with Helicopter Heading Command. Red solid curve is the heading command ψ_C , dark green curve is the yaw rate r measured data. The solid blue curve is the helicopter measured heading ψ , and the magenta curve is the scaled tail rotor blade pitch command δ_{TR} in pulse width (μ second/100). The light green curve is the scaled main rotor angular velocity $\Omega/100$.

L.3 Experiment: Pitch Rate Stability and Pitch Attitude Hold Control

The experimental setup for the pitch control loop involves the use of the Rotational Dynamic Test Stand (RDTS) as shown in Figure L.11 on the following page. The RDTS is a three degrees of freedom test stand able to pitch, roll and yaw at the same time. The RDTS can be constrained to tilt in only one axis by setting stops on the second axis, and the yaw motion can also be constrained. The equations of motion for this setup involve the rotational dynamic equations Equation (F.1.5) on page 334 and the kinematic equations Equation (F.1.6) on page 335

$$\begin{aligned}
 \dot{p} &= \bar{L} + \bar{I}_{pr}pq - \bar{I}_pqr \\
 \dot{q} &= \bar{M} + \bar{I}_{zx}(r^2 - p^2) - \bar{I}_qpr \\
 \dot{r} &= \bar{N} - \bar{I}_r pq - \bar{I}_{pr}qr \\
 \dot{\phi} &= p + q \sin \phi \tan \theta + r \cos \phi \tan \theta \\
 \dot{\theta} &= q \cos \phi - r \sin \phi \\
 \dot{\psi} &= q \sin \phi \sec \theta + r \cos \phi \sec \theta
 \end{aligned} \tag{L.3.1}$$

For this particular experiment, the yaw axis and the roll axis are restrained, and motion is only allowed about the y-axis or pitch angles only. The above equation simplifies to

$$\begin{aligned}
 I_{yy} \dot{q} &= M \\
 \dot{\theta} &= q \cos \phi_0
 \end{aligned} \tag{L.3.2}$$

where $\phi_0 = 0$ is the flight condition of choice and therefore $\dot{\theta} = q$. Equation (E.4.1) on page 329 provides the coupled rotor moment equations

$$\begin{aligned}
 L_T &= (h\beta_{1s} + y_{CM})T \\
 M_T &= (h\beta_{1c} - x_{CM})T
 \end{aligned} \tag{L.3.3}$$

The resultant equations of motion for the helicopter mounted on the RDTS become

$$\begin{aligned} I_{yy} \dot{q} &= (h \beta_{1c} - x_{CM}) T \\ \dot{\theta} &= q \end{aligned} \tag{L.3.4}$$

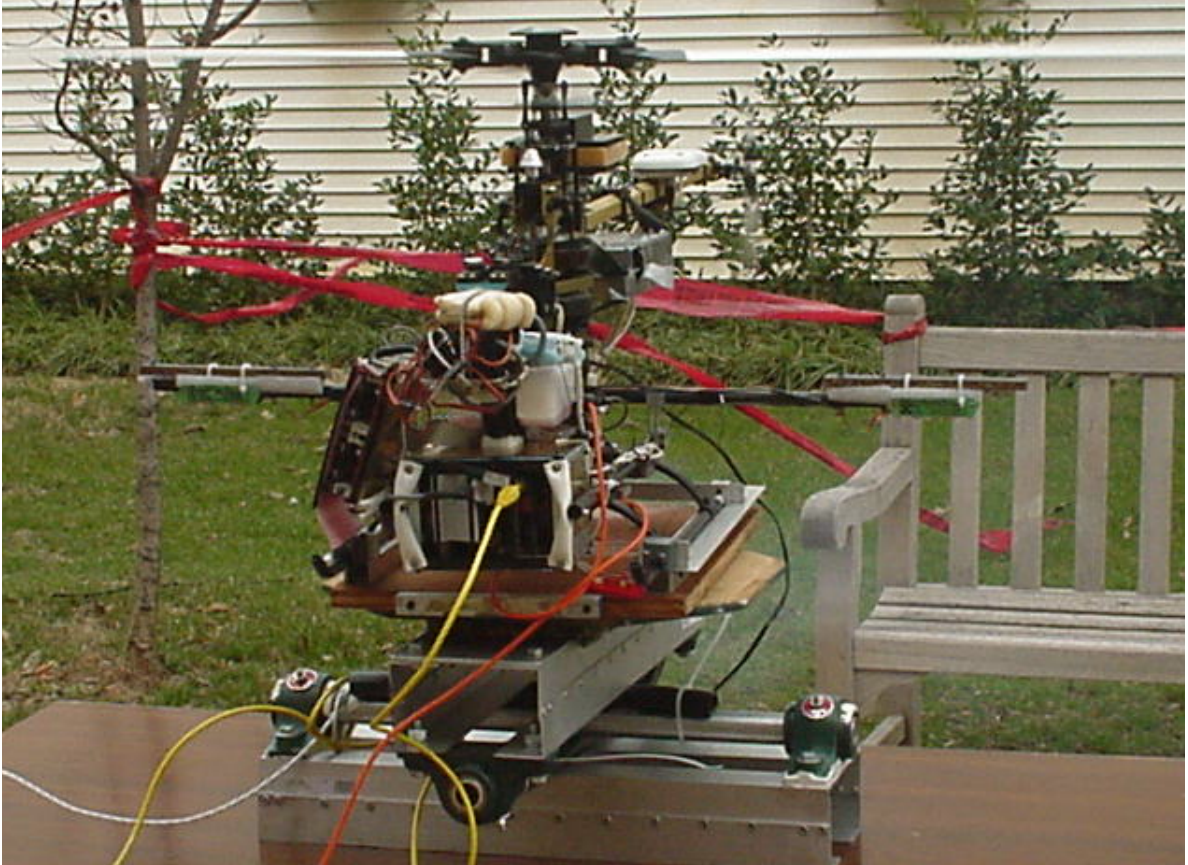


Figure L.11: Real-Time Run of the Helicopter on top of the Rotational Dynamic Test Stand (RDTS).

The main rotor longitudinal blade flapping β_{1c} is given by solving the coupled blade flapping equations of motion Equation (H.2.9) on page 368. Given the restrictions of the experiment, for simplicity, let the blade flapping angle be such that $\theta \approx \beta_{1c}$, then the equilibrium condition is simply

$$\beta_{1c} \approx \theta_0 = \frac{x_{CM}}{h} \tag{L.3.5}$$

which provides the trim pitch angle command. The approximation $\theta \approx \beta_{1c}$ yields the

perturbation equation

$$\begin{aligned} I_{yy} \dot{q} &\approx h T \theta \\ \dot{\theta} &= q \end{aligned} \tag{L.3.6}$$

Figure L.12 shows a model of the perturbation equations. Taking the term $h T \theta$ as a disturbance to the linear model, the yaw rate control loop follows directly as shown in Figure L.13 on the following page. The transfer function from input to pitch rate q takes the form

$$q = \frac{k_q/I_{yy}}{s + k_q/I_{yy}} u \tag{L.3.7}$$

The above equation suggests a value for the gain k_q as

$$\begin{aligned} \frac{I_{yy}}{k_q} &= \tau_c = \frac{16}{\gamma \Omega} \\ k_q &= \bar{k} \frac{\gamma \Omega}{16} I_{yy} \end{aligned} \tag{L.3.8}$$

where \bar{k} is a proportional design gain to be decided later in the process, the term $16/\gamma \Omega$ is the time constant of the flapping blades as given by equation (D.3.157) on page 309, and the main rotor Lock number is tabulated in Table I.4 on page 373.

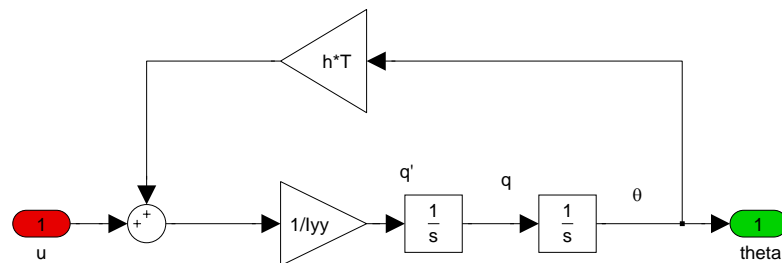


Figure L.12: Pitch Rate and Attitude Perturbation Model for the Helicopter on the Rotational Dynamic Test Stand (RDTS).

A simple compensator design for command pitch attitude θ_c follows in Figure L.14 on page 452. A direct design choice is to let

$$s + b = s + \frac{k_q}{I_{yy}} \tag{L.3.9}$$

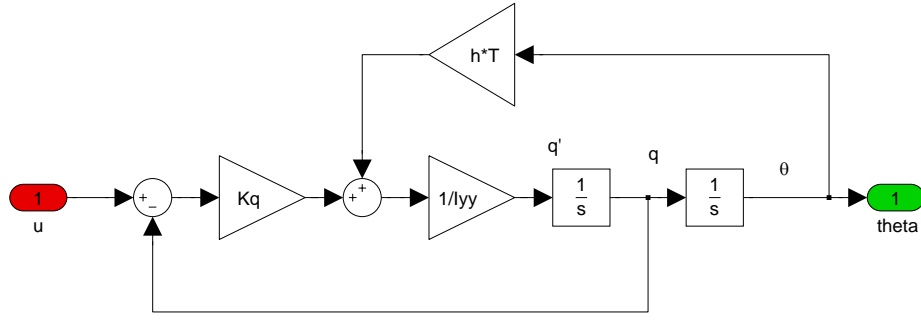


Figure L.13: Pitch Rate Feedback Control Loop for the Helicopter on the Rotational Dynamic Test Stand (RDTS).

The loop transfer function $L(s)$ and the transfer function from desired pitch angle θ_c to pitch attitude θ is then

$$L(s) = \frac{1}{I_{yy}} \frac{k_q k_\theta}{s(s+a)} \quad (L.3.10)$$

$$\frac{\theta}{\theta_C} = \frac{k_q k_\theta / I_{yy}}{s(s+a) + k_q k_\theta / I_{yy}} = \frac{k_q k_\theta / I_{yy}}{s^2 + sa + k_q k_\theta / I_{yy}}$$

The characteristic equation has the form

$$s^2 + sa + \bar{k} k_\theta = s^2 + 2\zeta\omega_n s + \omega_n^2 \quad (L.3.11)$$

Then it follows

$$\omega_n^2 = \pi^2$$

$$\zeta = \frac{\sqrt{2}}{2}$$

$$a = 2\zeta\omega_n = \pi\sqrt{2}$$

$$k_q k_\theta / I_{yy} = \omega_n^2 \rightarrow k_\theta = \frac{\pi^2 I_{yy}}{k_q} \quad (L.3.12)$$

Equation (L.3.8) on the preceding page and the previous equation (L.3.12) yield the design for the pitch rate feedback control loop. The choice of \bar{k} in (L.3.8) is done for stability and good flying qualities during the testing period. Figure L.15 on page 453 plots data collected during a real-time data run for pitch command tracking.

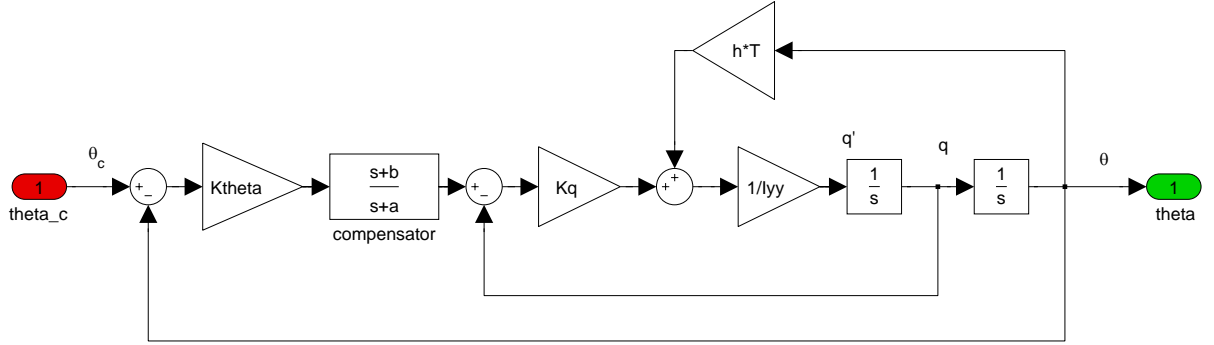


Figure L.14: Pitch rate and pitch attitude Feedback Control Loop for the Helicopter on the Rotational Dynamic Test Stand (RDTS).

L.4 Experiment: Roll Rate Stability and Roll Attitude Hold Control

The experimental setup for the pitch control follows the setup for pitch experiment very closely. The setup involves the use of the Rotational Dynamic Test Stand (RDTS) as shown in Figure L.11 on page 449. As before, the equations of motion for this setup involve the rotational dynamic Equation (F.1.5) on page 334 and the kinematic Equation (F.1.6) on page 335

$$\begin{aligned}
 \dot{p} &= \bar{L} + \bar{I}_{pr}pq - \bar{I}_pqr \\
 \dot{q} &= \bar{M} + \bar{I}_{zx}(r^2 - p^2) - \bar{I}_qpr \\
 \dot{r} &= \bar{N} - \bar{I}_r pq - \bar{I}_{pr}qr \\
 \dot{\phi} &= p + q \sin \phi \tan \theta + r \cos \phi \tan \theta \\
 \dot{\theta} &= q \cos \phi - r \sin \phi \\
 \dot{\psi} &= q \sin \phi \sec \theta + r \cos \phi \sec \theta
 \end{aligned} \tag{L.4.1}$$

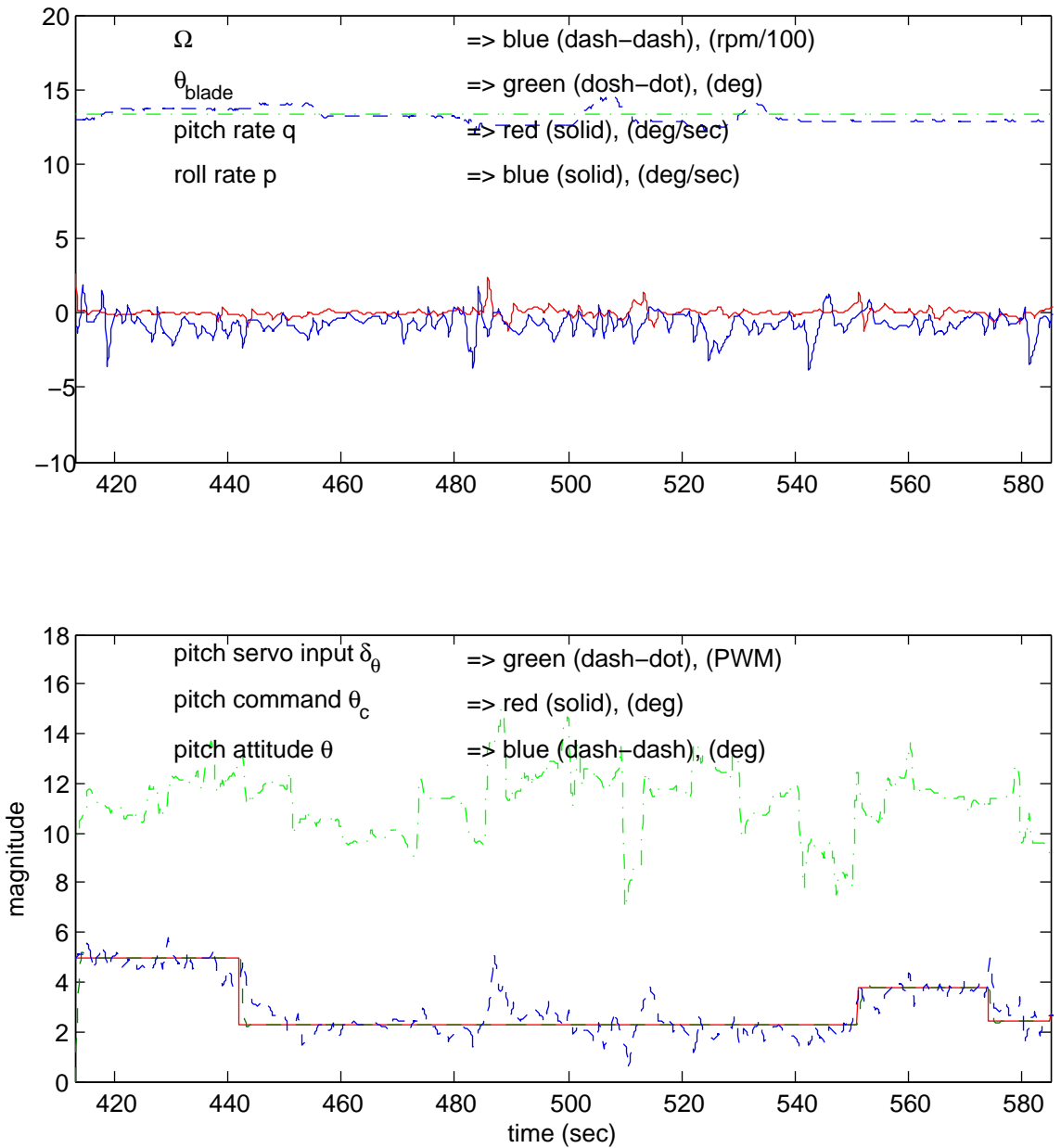


Figure L.15: Pitch command θ_c tracking with the helicopter on the Rotational Dynamic Test Stand (RDTS). In the figure, the top graph plots the roll p and pitch q rates and the main rotor angular velocity Ω .

For this particular experiment, the yaw axis and the pitch axis are restrained, and motion is only allowed about the x-axis or roll angle only. The above equation simplifies to

$$\begin{aligned} I_{xx} \dot{p} &= L \\ \dot{\phi} &= p \end{aligned} \tag{L.4.2}$$

Equation (E.4.1) on page 329 provides the coupled rotor moment equations

$$\begin{aligned} L_T &= (h\beta_{1s} + y_{CM}) T \\ M_T &= (h\beta_{1c} - x_{CM}) T \end{aligned} \tag{L.4.3}$$

The resultant equations of motion for the helicopter mounted on the RDTS with the roll loop enabled become

$$\begin{aligned} I_{xx} \dot{p} &= (h\beta_{1s} + y_{CM}) T \\ \dot{\phi} &= p \end{aligned} \tag{L.4.4}$$

Following the work done previously for the pitch loop, let the blade flapping angle be such that $\phi \approx \beta_{1s}$, then the equilibrium condition is simply

$$\beta_{1c} \approx \phi_0 = \frac{y_{CM}}{h} \tag{L.4.5}$$

which provides the trim pitch angle command. The approximation $\phi \approx \beta_{1s}$ yields the perturbation equation

$$\begin{aligned} I_{xx} \dot{p} &\approx h T \phi \\ \dot{\phi} &= p \end{aligned} \tag{L.4.6}$$

Figure L.16 on the next page shows the closed loop design for the roll rate. Following a

similar procedure as done before for the pitch loop yields

$$\begin{aligned}
 p &= \frac{k_p/I_{xx}}{s + k_p/I_{xx}} u \\
 L(s) &= \frac{1}{I_{xx}} \frac{k_p k_\phi}{s(s+a)} \\
 \frac{\phi}{\phi_C} &= \frac{k_p k_\phi/I_{xx}}{s(s+a) + k_p k_\phi/I_{xx}} = \frac{k_p k_\phi/I_{xx}}{s^2 + sa + k_p k_\phi/I_{xx}}
 \end{aligned}
 \tag{L.4.7}$$

The control design yields

$$\begin{aligned}
 k_p &= \frac{\gamma \Omega}{16} I_{xx} \\
 \omega_n^2 &= \pi^2 \\
 \zeta &= \frac{\sqrt{2}}{2} \\
 a &= 2\zeta\omega_n = \pi\sqrt{2} \\
 k_p k_\phi/I_{xx} &= \omega_n^2 \rightarrow k_\phi = \frac{\pi^2 I_{xx}}{k_p}
 \end{aligned}
 \tag{L.4.8}$$

Figure L.17 on the following page plots data collected during a test run with the roll attitude control loop engaged. The roll tracks the signal with a large time constant designed as such for tests with roll stability and performance. In general, the roll loop should react very slowly to commands to avoid becoming unstable. Later control designs improved upon roll performance (see Section L.5 on page 457)

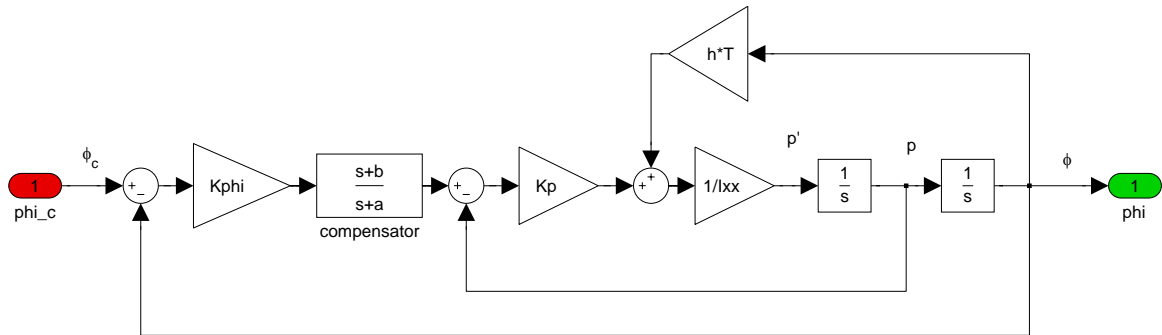


Figure L.16: Roll Rate Feedback Control Loop for the Helicopter on the Rotational Dynamic Test Stand (RDTS).

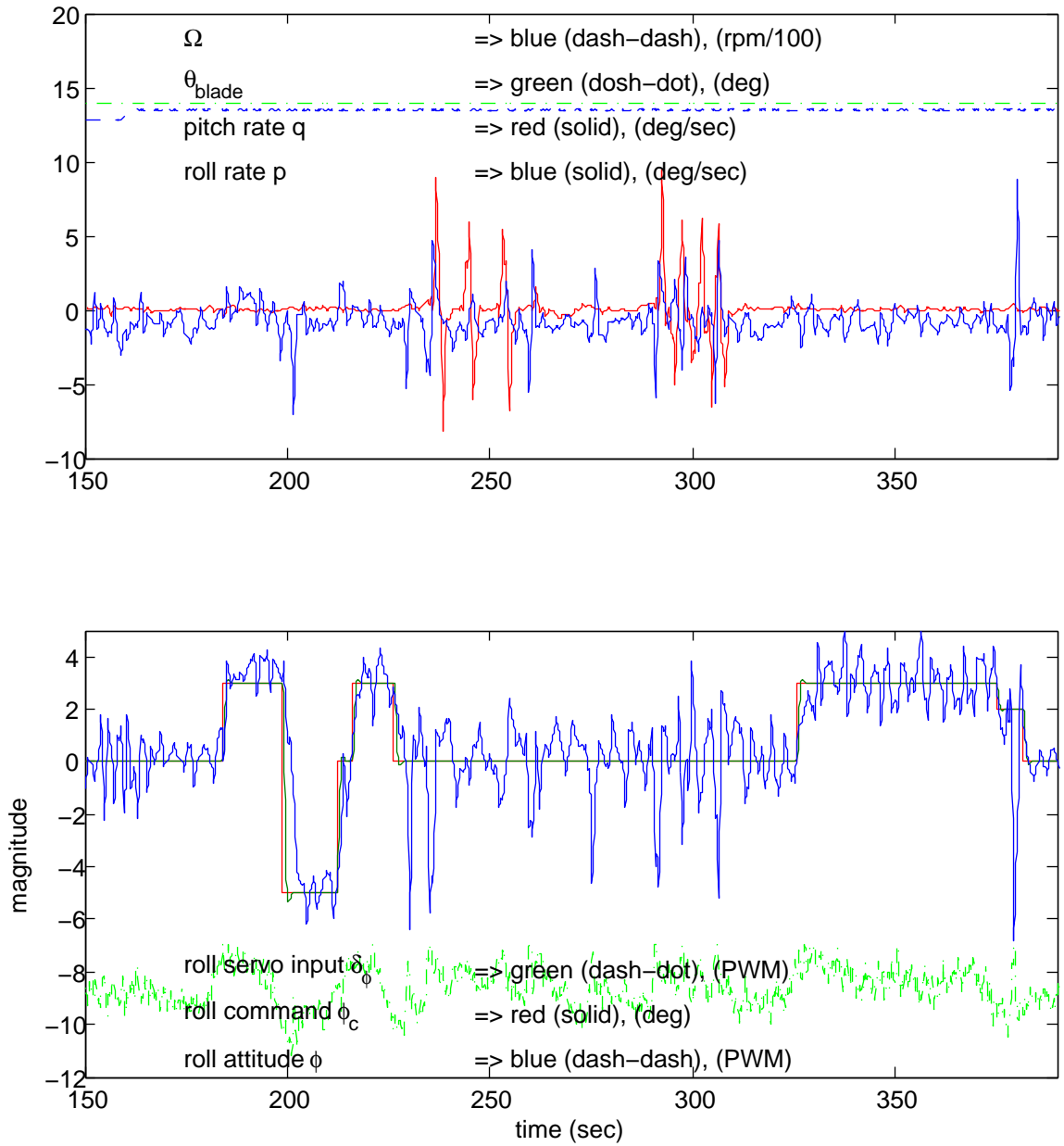


Figure L.17: Roll command ϕ_c tracking with the helicopter on the Rotational Dynamic Test Stand (RDTS). In the figure, the top graph plots the roll p and pitch q rates and the main rotor angular velocity Ω . Notice the large time constant of the feedback control loop during an experiment stability test.

L.5 Experiment: Roll and Pitch Stability with Yaw Rate and Heading Control

This last experiment tests all three axis roll ϕ , pitch θ and heading ψ under closed loop control with the main rotor angular velocity tracking its commanded setting. As previously done, the experimental setup involves the use of the Rotational Dynamic Test Stand (RDTS) as shown in Figure L.11 on page 449. Figure L.18 on the next page shows data collected during a real-time data run during which the three attitude loops were engaged simultaneously. In the top graph the heading ψ tracks and holds the command during the duration of the flight. The pitch attitude θ plotted in the third graph down tracks and holds a zero command during the heading maneuvers, and during the later part of the experiment the pitch attitude tracks and holds the commanded values. The roll attitude ϕ does likewise on the last graph. This experiment demonstrates a stable platform able to remain stable while holding performance commands.

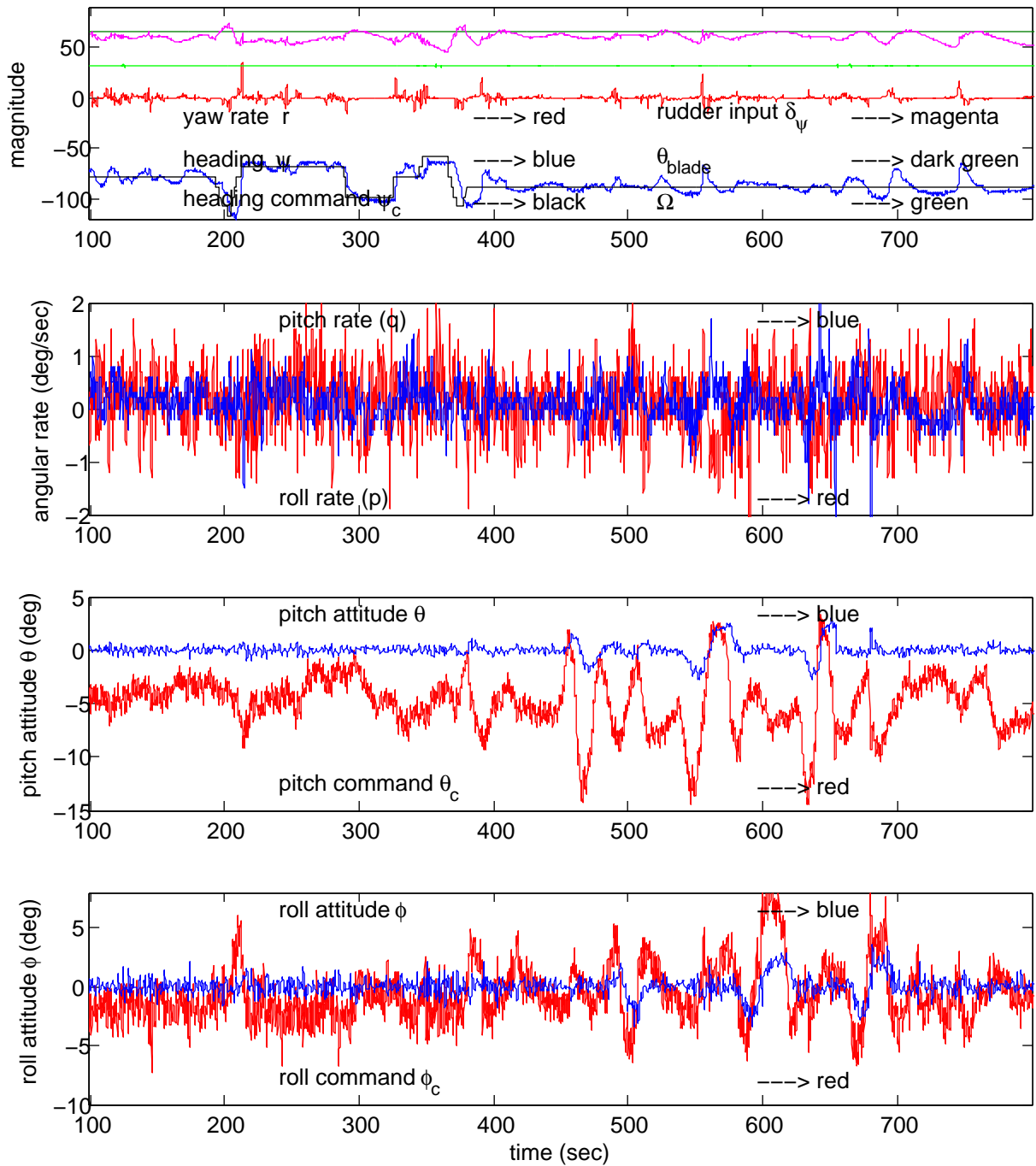


Figure L.18: Simultaneous attitude command tracking and hold for roll ϕ , pitch θ and heading ψ with constant angular velocity Ω . In the figure, the top-most graph presents the heading command tracking and hold, and the second graph shows the roll p and pitch rate q during the flight. The third graph shows the pitch attitude θ holding zero for the first part of the run, and tracking commands for the second part of the run. The same is true for the roll attitude ϕ in the fourth graph.

Appendix M

Helicopter Systems Design

M.1 Systems Engineering and Integration

Systems Engineering (SE) is an interdisciplinary framework suitable for the complete and accurate definition of systems requirements, analysis of the system as a whole with a top-down engineering approach with focus on the entire system Life Cycle, and design processes that focuses on system optimization and balance through the management and integration of multiple scientific and technical disciplines. Similarly, System Engineering and Integration (SE&I) is a mature engineering practice that brings together applied science with current or emerging interdisciplinary technologies within an integrated environment suitable for the creation and support of complex systems and related processes and products. Relevant SE&I processes include project management, quality assurance and hardware and software engineering. Relevant SE&I activities include system definition and design, manufacturing and production, operation and maintenance and other life-cycle support activities that include logistics, phaseout and disposal [41, 71, 122].

M.1.1 Systems Engineering Standards

The practice of Systems Engineering and Integration varies in form and practice among leading industries and research institutions. The United States Department of Defense (DoD) along with industry at large has established systems engineering standards since the 1960's. The first widely accepted SE standard MIL-STD-499A was released in May 1974, and the updated draft MIL-STD-499B was issued in 1994 [115]. Table M.1 on the following page tabulates various Systems Engineering standards that have been implemented throughout the years [41].

Table M.1: Systems Engineering (SE) Standards

standard	year	reference
MIL-STD-499	1969	
MIL-STD-499A	1974	
MIL-STD-499B (draft)	1994	[115]
· EIA/IS-632	1994	
ANSI/EIA-632	1999	[4]
· IEEE-1220 (trial)	1994	
IEEE-1220	1998	[138]
ECSS-E-10A	1994	[43]

M.1.2 Configuration Management Standards and Capability Maturity Models.

Configuration Management (CM) deals with the specification and coordination of the conceptual and preliminary systems design, follow on detailed design and development and overall system engineering management. Capability Maturity Models (CMM) compliment SE standards in that CMMs determine and rank how well the SE processes are defined and implemented [5, 41]. CMMs evaluate the SE processes with the objective of providing insight into improving the processes based on industry-wide best practices [24, 77, 78]. Table M.2 summarizes relevant CMM standards.

Table M.2: Configuration Management (CM) Standards

standard	year	reference
MIL-STD-973	1992	classic CM standard, [114]
SECMM-95-01	1995	[149]
ANSI/EIA-649-1998	1998	
EIA/IS - 731.1	1998	[5]
MIL-HDBK-61A(SE)	2001	[113]
CMU/SEI-2002-TR-011	2002	[78]
CMU/SEI-2002-TR-012	2002	[79]

Capability Maturity Models Integration (CMMI) encompasses current efforts to integrate several CMM products. CMMI attempts to put under one umbrella four engineering disciplines: System Engineering (SE), Software Engineering (SW), Integrated Product and Processes Development (IPPD), and Supplier Sourcing (SS) [24, 41, 86].

M.1.3 Systems Engineering Processes

SE encompasses the practice of both system engineering management and the system engineering processes. Three broad categories of SE tools allow for the implementation of the actual systems engineering processes [41].

1. Analysis Tools: tools that focus on formal and systematic ways of gathering system requirements. The practice of system requirements is essential to system engineering and product development, and is generally known as Requirements Engineering (RE). Examples of RE tools are Six-Sigma Techniques ($6-\sigma$) and Quality Function Deployment (QFD).
2. Synthesis Tools: these tools take the form of schematic tools (e.g. Unified Modeling Language (UML) tools), physical modeling tools (e.g. Computer Aided Design (CAD) tools), and physics based, mathematical modeling and simulation tools (e.g. Mathematica [126], Maple [100], Matlab [101] and other Finite Element Analysis (FEA) tools).
3. Evaluation Tools: decision-making aiding tools which include trade-off analysis tools for the evaluation and selection of alternative feasible solutions. QFD and $6-\sigma$ are examples of tools that provide for weighing criteria selection and identification of alternative solutions.

M.1.4 Definition of Integrated Product and Processes Development (IPPD)

According to Dr. William Perry, U. S. Secretary of Defense in 1995, IPPD is defined below [153]

IPPD is an expansion of concurrent engineering utilizing a systematic approach to the integrated, concurrent development of a product and its associated manufacturing and sustainment processes to satisfy customer needs. Integrated Product and Process Development (IPPD) is a management technique that simultaneously integrates all essential acquisition activities through the use of multidisciplinary teams to optimize the design, manufacturing and

supportability processes. IPPD facilitates meeting cost and performance objectives from product concept through production, including field support.

The key tenets of IPPD methodology are summarized below [153]

1. Customer Focus
2. Concurrent Development of Products and Processes
3. Early and Continuous Life Cycle Planning
4. Maximizing Flexibility for Optimization and Use of Contractor Unique Approaches
5. Encouraging Robust Design and Improved Process Capability
6. Event-Driven Scheduling
7. Multidisciplinary Teamwork
8. Empowerment
9. Seamless Management Tools
10. Proactive Identification and Management of Risk

One of the focuses of the IPPD methodology is the capture of systems requirements through the voice of the customer. The customer is an active participant in the SE process throughout the life-cycle of the system at large. This practice ensures that the customer needs are better satisfied within schedule and within budget. Various SE processing tools (Section M.1.3 on the preceding page) implement the IPPD tenets mentioned above [127].

1. The Seven Management and Planning Tools
 - (a) Affinity Diagram
 - (b) Tree Diagram
 - (c) Inter-Relationship Diagram
 - (d) Matrix Diagram
 - (e) Prioritization Matrices
 - (f) Process Decision Program Chart (PDPC)
 - (g) Activity Network Diagram
2. Quality Function Deployment (QFD)
3. Robust Design Simulation (RDS)
 - (a) Design of Experiments (DOE)
 - (b) Taguchi PDOM
 - (c) Response Surface Methodology (RSM)

4. Six Sigma Methods

M.1.5 IPPD Case Studies

Integrated Product and Processes Development (IPPD) is a SE&I practice recommended (and in some instances mandated) by the United States Department of Defense (U.S. DoD) [112]. IPPD is also one of the four multidisciplinary engineering disciplines of CMMI [41, 86]. Some case studies on the use of IPPD in the literature include the New Attack Submarine (NSSN) [158] and the McDonnell Douglas Corporation (MDC) design and subsequent procurement of the F/A-18E/F [139]. The Autonomous Scout Rotorcraft Testbed (ASRT) program at Georgia Tech was a pilot program for the testing of the IPPD practice from 1994 until 1997 [131, 150, 151].

M.2 Application of Integrated Product and Processes Development (IPPD) to the University of Oklahoma Helicopter Research Testbed

The University of Oklahoma Helicopter Research Testbed project is a small, focused and fixed-cost (\$50 K dollars) project sponsored by the Oklahoma Aeronautics Commission (OAC). The original customer requirements are listed below.

1. identify available custom off-the-shelf technology applicable to autonomous miniature helicopter flight
2. develop computer-based method for autonomous miniature helicopter flight
3. demonstrate autonomous hover flight

The development of a computer based method for autonomous flight with a miniature helicopter requires the simultaneous development of a product (autonomous miniature helicopter) and processes (method for autonomous flight). Application of the IPPD methodology allows for customer satisfaction by capturing the voice of the customer (VOC) and translating this established need into a set of design requirements that define the problem. To this effect, a subset of The Seven Management and Planning Tools and

the Quality Function Deployment (QFD) provide the means to translate the established need (customer requirements) into a defined problem (design requirements) [14, 59, 42, 130]. The combined autonomous miniature helicopter and the method for autonomous flight is collectively named the University of Oklahoma Helicopter Research Testbed (OU-HRT).

M.2.1 Voice of the Customer (VOC)

Systems requirements originate from the customer needs or from an established need. Capturing systems requirements is a fundamental step in systems engineering, and the collective efforts of capturing systems requirements is in the realm of Requirements Engineering.

M.2.1.1 VOC: Mission Profile Requirements

Figure M.1 illustrates the mission profile for the OU autonomous helicopter. The helicopter must climb to an altitude and maintain stable hover flight for a short time. Thereafter, the helicopter should navigate to a selected site a few feet away from the takeoff site, and loiter for a short time before landing at the site.

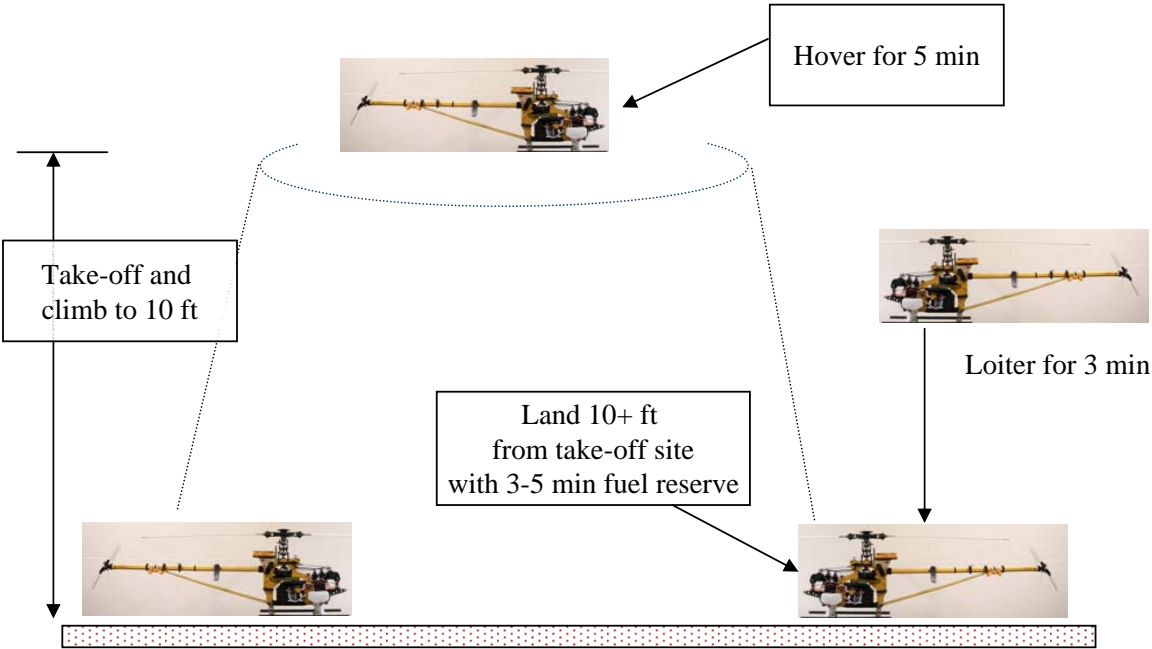


Figure M.1: Mission profile requirements for the OU autonomous miniature helicopter.

M.2.1.2 VOC: Affinity Diagram

The principal program objective is to identify enabling technologies suitable for miniature helicopter flight and to develop a method that automates the helicopter flight, all at a fixed cost to the customer. The affinity diagram organizes available data into natural groups that facilitate the identification of relationships among the various systems needs. Figure M.2 illustrates the affinity diagram for the University of Oklahoma Helicopter Research Testbed.

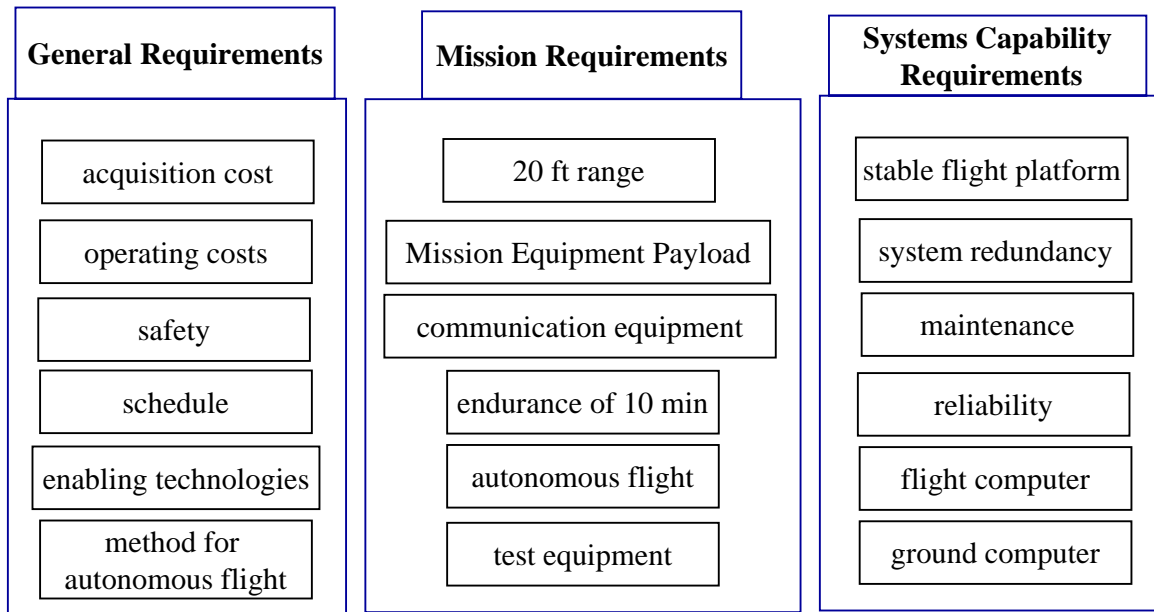


Figure M.2: The Affinity Diagram, Voice of the Customer (VOC).

M.2.1.3 VOC: Tree Diagram

Figure M.3 on the next page illustrates the tree diagram tool that refines the voice of the customer into finer levels of detail from the general to the more specific. In the figure, the cost breakdown portion of the tree diagram helps communicate to the customer the various sources of one-time and recurrent costs.

M.2.2 Voice of the Engineer (VOE)

Once the primary task of capturing the voice of the customer has been initiated, the engineer acts on the customer needs and further expands the set of requirements in an

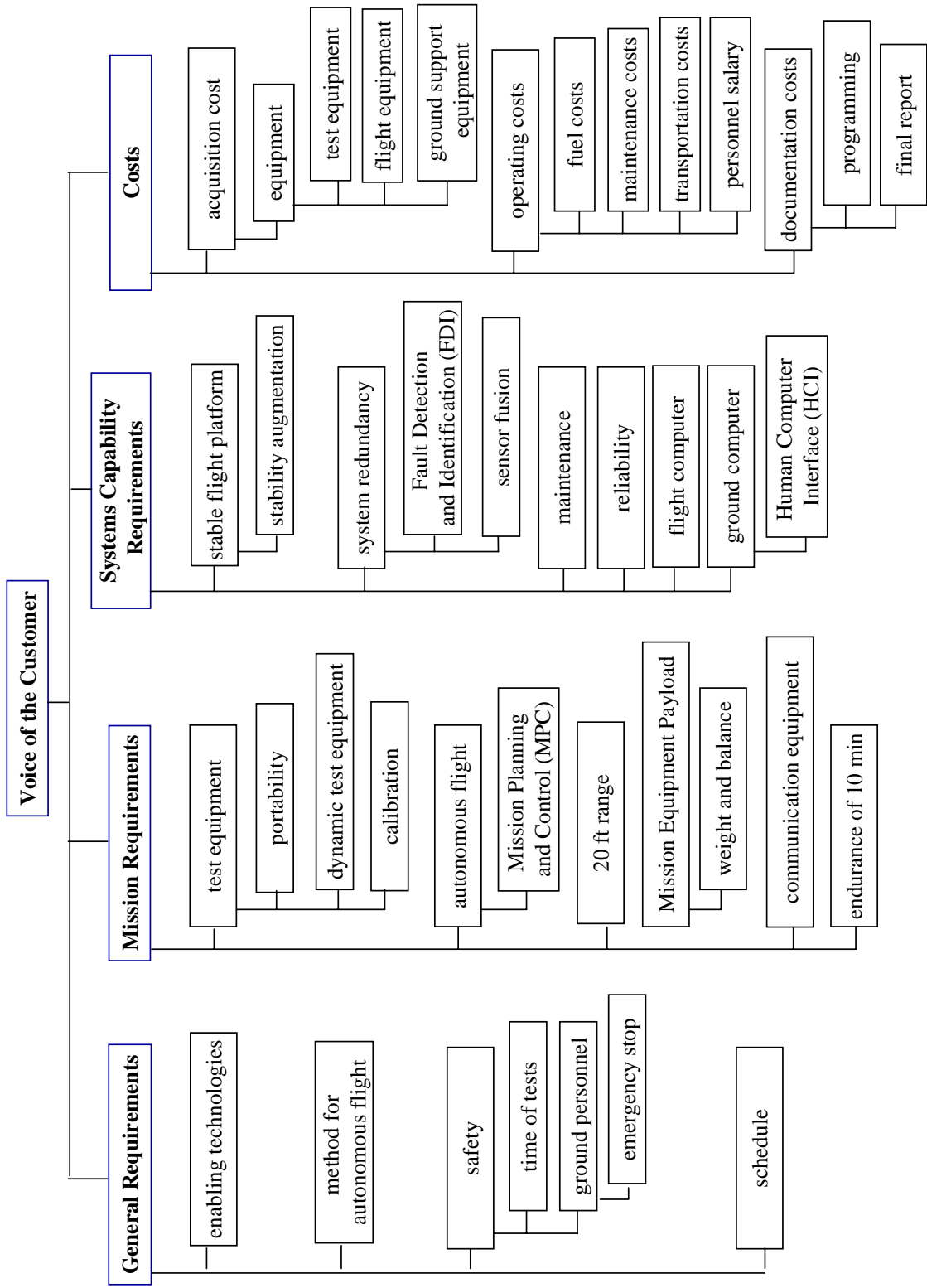


Figure M.3: Tree Diagram, Voice of the Customer.

iterative manner. In doing so, the engineer communicates back to the customer the engineering significance of the established need and related requirements. The voice of the engineer (VOE) uses the same tools that capture the customer requirements.

M.2.2.1 VOE: Affinity Diagram

Figure M.4 on the following page illustrates the voice of the engineer in an Affinity Diagram. The VOC drives the initial systems requirements process, and the VOE expands upon the requirements with engineering data that pertains to the system domain. This process is repeated interactively until the requirements converge.

M.2.2.2 VOE: Tree Diagram

Figure M.5 on page 469 illustrate the engineer's Affinity Diagram. As before, the VOC drives the initial systems requirements process. The VOE adds pertinent engineering details.

M.2.3 Quality Function Deployment (QFD)

Quality Function Deployment (QFD) focuses on identifying the products and services that best meet the customer needs and delivers the best value to the customer. Figure M.6 on page 470 shows the overall QFD design resulting from the analysis of the Voice of the Customer (VOC) (need) and the Voice of the Engineer (VOE) (design requirements) obtained from previous sections. Details for the different portions of the Quality Function Deployment (QFD) are shown in subsequent sections.

M.2.3.1 QFD: Functional Deployment Matrix

Figure M.7 on page 471 illustrates the actual QFD. Here, the VOC (the established need) is deployed onto the VOE (design requirements). In doing so, the process identifies the most relevant systems requirements and their correlation to the various engineering activities. This VOE for the University of Oklahoma Helicopter Research Testbed indicates that the development of a method for autonomous flight, actual autonomous flight and safety are the requirements that will deliver the best value to the customer. In turn, the

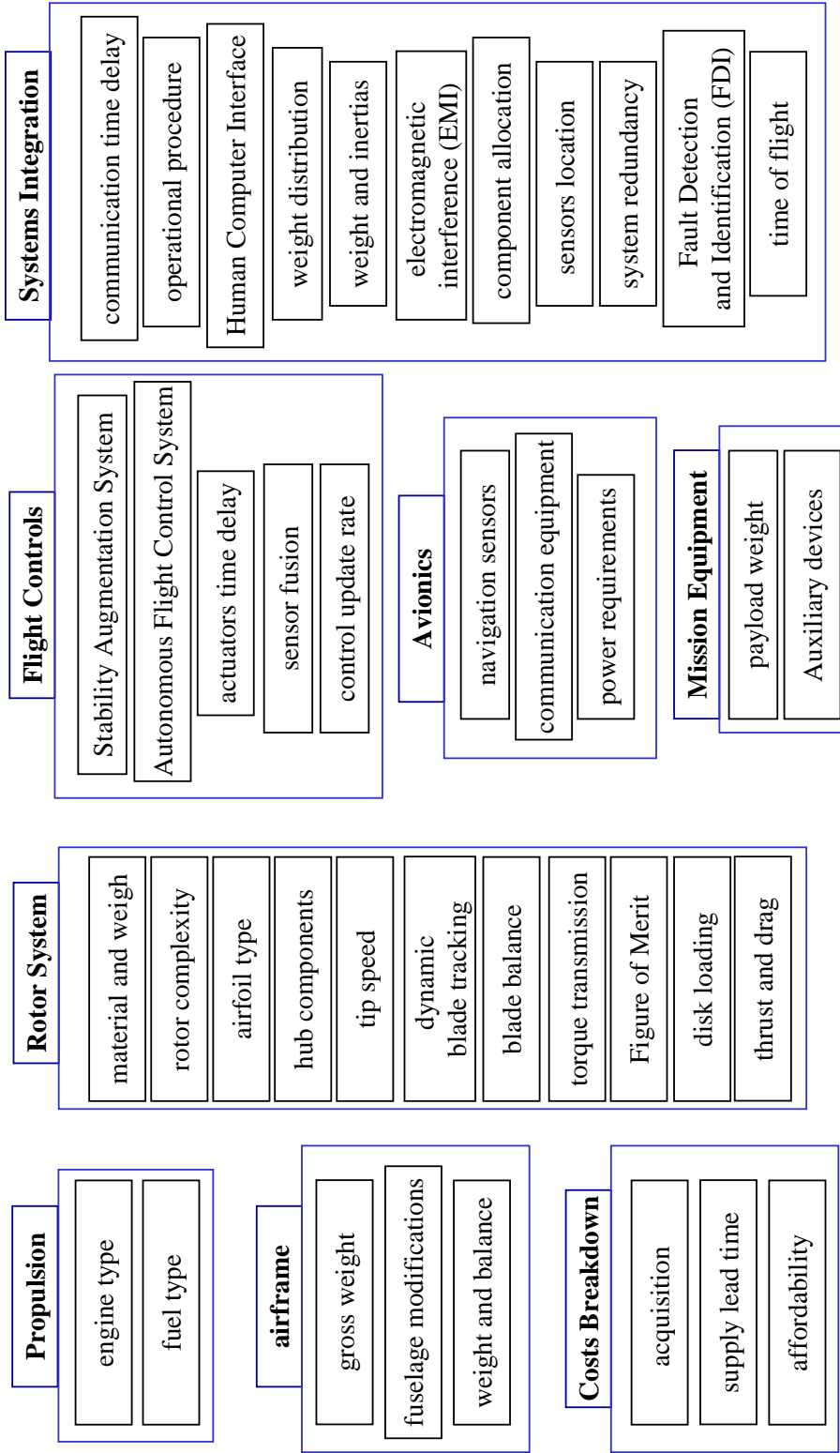


Figure M.4: Voice of the Engineer: Affinity Diagram.

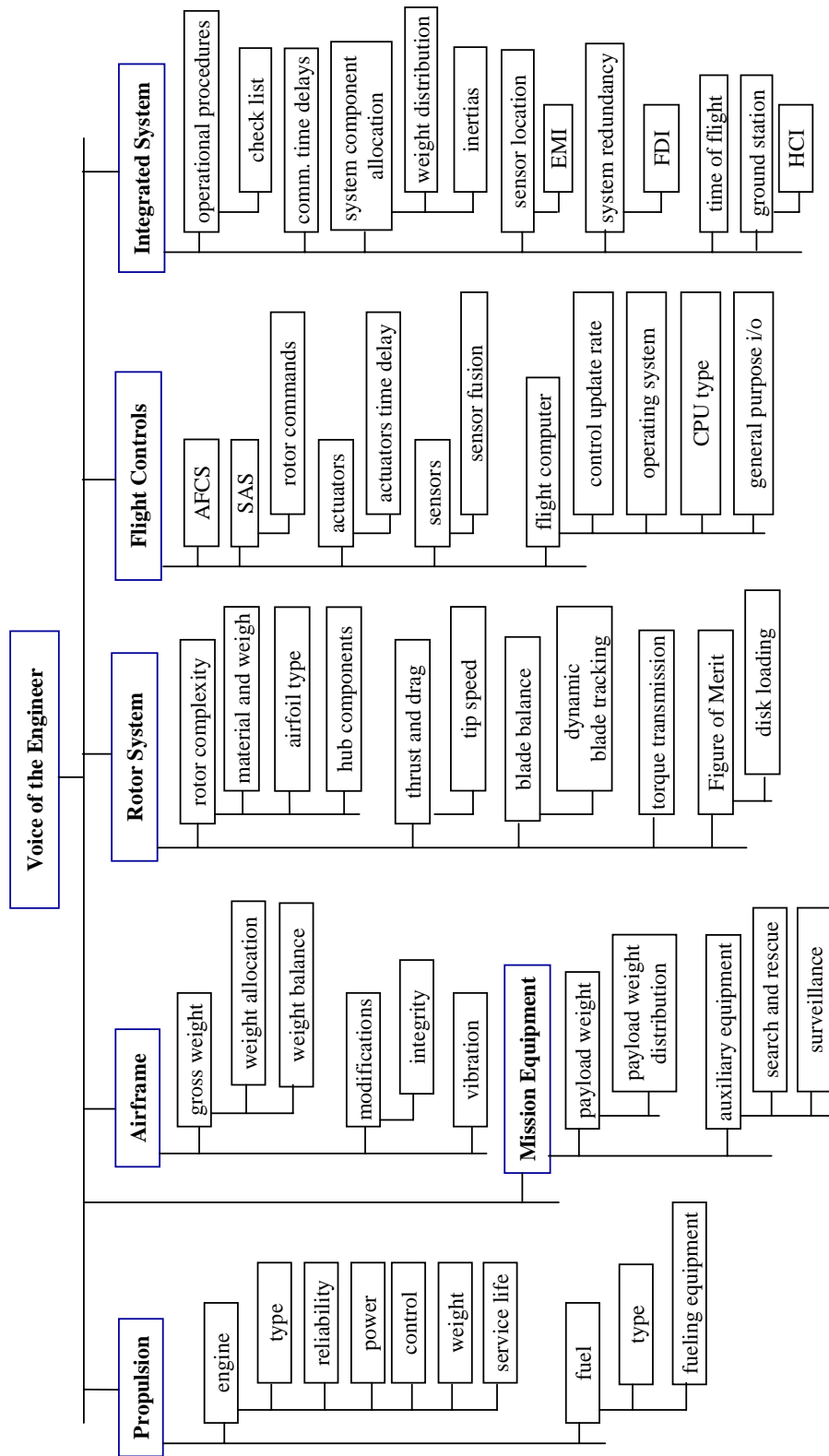


Figure M.5: Voice of the Engineer: Tree Diagram.

VOE matrix also identifies the helicopter gross weight, thrust and drag, and the development of flight control laws as the most relevant engineering activities that will best satisfy the customer needs.

QFD1	1 engine		2 airframe		3 rotor syst...			4 flight controls				5 integrated system				Number of significant relationships	
⊙ 9.00 strong correlation ○ 3.00 some correlation △ 1.00 possible correlation ...	1.1 power	1.2 control	2.1 gross weight	2.2 modifications	3.1 rotor complexity	3.2 thrust and drag	3.3 Figure of Merit	4.1 AFCS	4.2 SAS	4.3 actuators	4.4 sensors	4.5 flight computer	5.1 operational procedures	5.2 component location	5.3 sensor location		5.4 ground station
1 method for autonomous flight		△	△			○		⊙	⊙	⊙	⊙	⊙	⊙	△	○	⊙	7
2 enabling technologies	△		⊙	○		⊙		⊙	⊙	⊙	⊙	⊙	○			○	7
3 safety	○	○	○		△	⊙		○	⊙	○	○	○	⊙			⊙	3
4 autonomous flight	⊙	○	⊙	△	△	⊙	△	⊙	⊙	○	⊙	⊙	⊙	○	○	⊙	9
5 range	○	○	⊙			⊙	○	○	○	○	○	○	△			△	2
6 endurance	○	○	⊙			○	△	○	○	△	△	○	△			△	1
7 comm. equipment			○	△				⊙	⊙	○	△	⊙	⊙	○	△	⊙	4
8 acquisition costs	△		⊙	○	△	⊙		○	○	△	⊙	⊙				⊙	5
9 operation costs	⊙	△	⊙	○		⊙						○	○			○	3
10 test equipment	○	△	⊙			⊙		△	△	△	△	○	⊙	△	△	⊙	4
Significant relations	2		7			7		4	5	2	4	5	5			6	

Figure M.7: Quality Function Deployment matrix for the University of Oklahoma Helicopter Research Testbed.

M.2.3.2 QFD: Voice of the Customer Prioritization

Figure M.8 on the following page illustrates the customer prioritization of the system requirements. The development of a method for autonomous flight, autonomous flight and safety are the top selling points for the customer. The University of Oklahoma Helicopter Research Testbed is a fixed cost project, and therefore costs are not high on the requirements priority list. Demonstrating range and endurance are at the bottom of the customer requirements priority list.

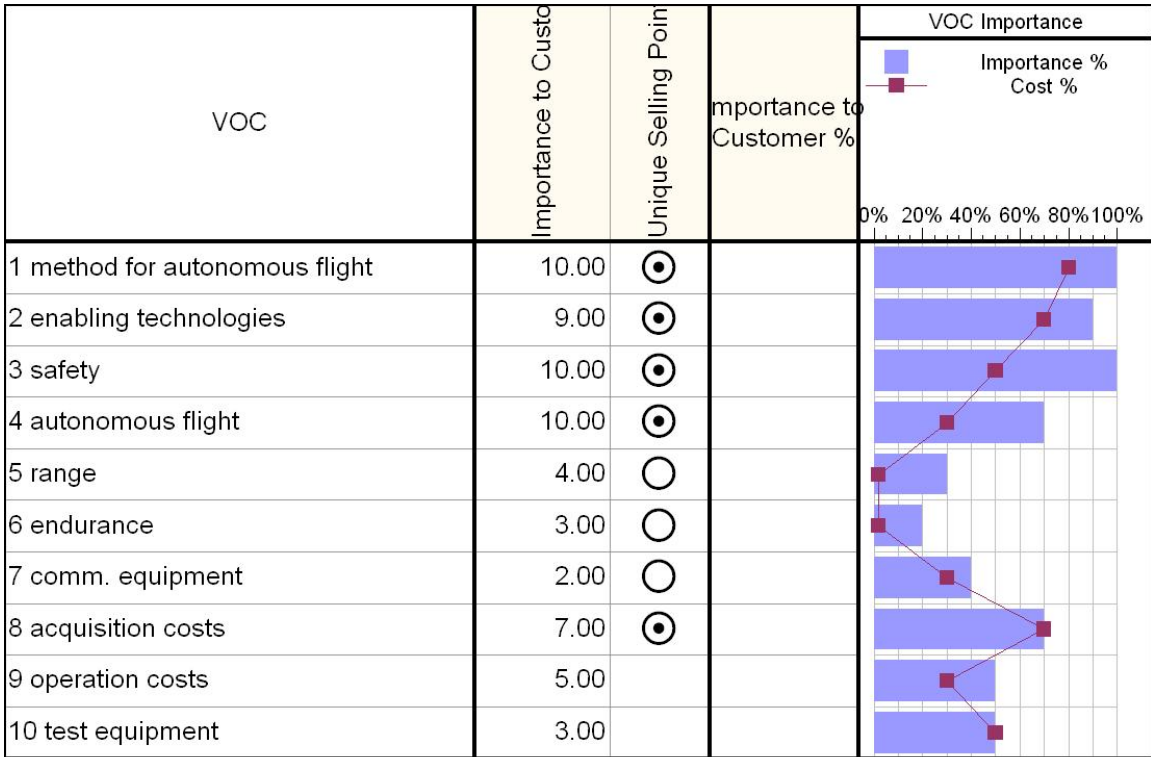


Figure M.8: Voice of the Customer Prioritization. In the graph, the symbol ⊙ is a strong selling point for the customer. The symbol ○ indicates some selling point for the customer.

M.2.3.3 Quality Function Deployment (QFD): Voice of the Customer Benchmark

Figure M.9 on the next page illustrates the benchmark results for the established need (VOC) and related design requirements (VOE) and engineering activities. The current solution for the University of Oklahoma Helicopter Research Testbed method for autonomous flight meets the customer needs in totality, and therefore this need displays total compliance in the benchmark. The safety record for the duration of all tests is 100%, and therefore this need is also fully met. The fixed cost for the project means that the enabling technologies and the operational costs are fully compliant. The helicopter gross-weight exceeds the thrust developed by the rotor, and the requirement for demonstrating autonomous flight remains unfulfilled. Similarly the range and endurance capabilities are also unfulfilled. The original acquisition costs are inadequate for a program of this magnitude, and therefore, the project did not meet the original budget. The communication equipment or digital remote communications between the flight platform and the groundstation outperforms the expectations. Finally, the test equipment used to achieve the various systems requirements outperformed the customer expectations.

M.2.3.4 QFD: Interaction Matrix for Design Requirements (VOE)

Figure M.10 on page 475 illustrates the interaction matrix for the various design requirements. This correlation matrix helps the engineers identify likely coupling among the various systems design requirements.

M.3 Modular Functional Decomposition

The affinity and tree diagrams have established the need (VOC) and the primary systems requirements (VOE). The QFD tool has helped identify the most important needs and related engineering requirements that will result in the best value for the customer. Engineering needs defined this way facilitate the functional decomposition of capabilities that the University of Oklahoma Helicopter Research Testbed needs to perform. Figure M.8 on the previous page illustrates the Voice of the Customer prioritization, and the development of a method for autonomous flight and a safe environment are the top-most

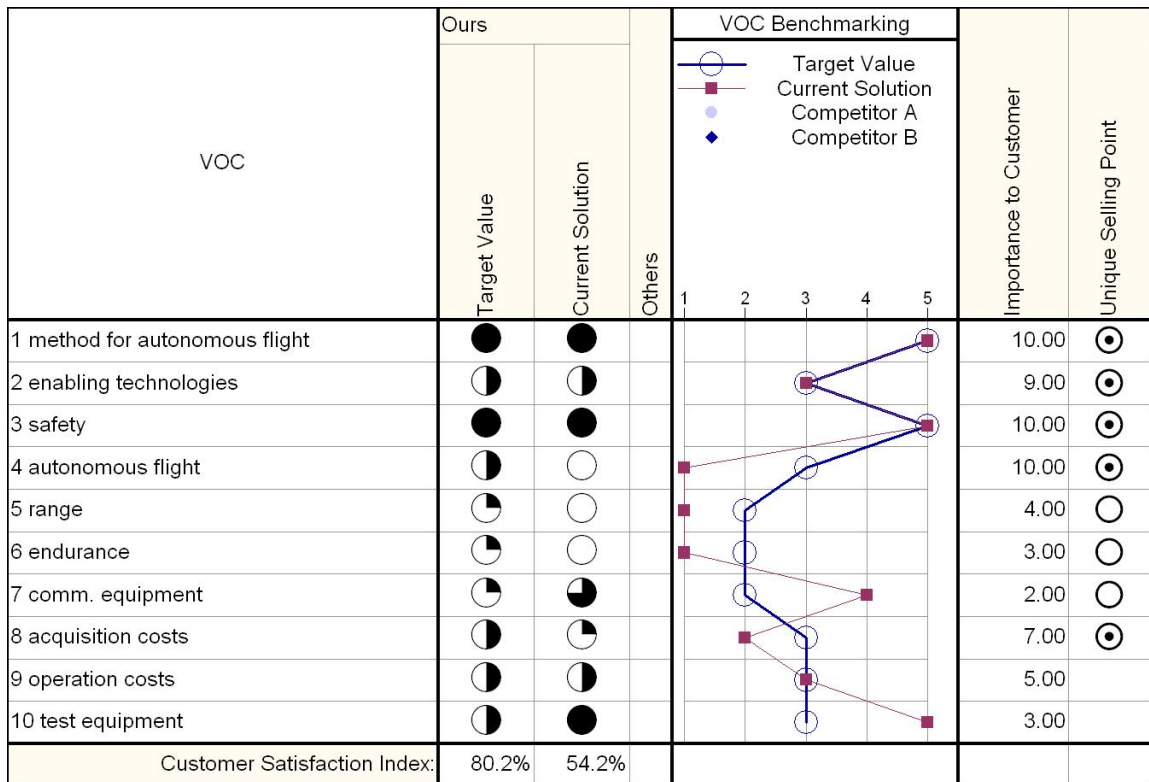


Figure M.9: Voice of the Customer Benchmarking. In the graph, the *VOC Benchmark* column follows the following convention: 1 = no compliance (empty circle), 2 = partial compliance, 3 = general compliance, 4 = full compliance, 5 = total compliance (full dark circle).

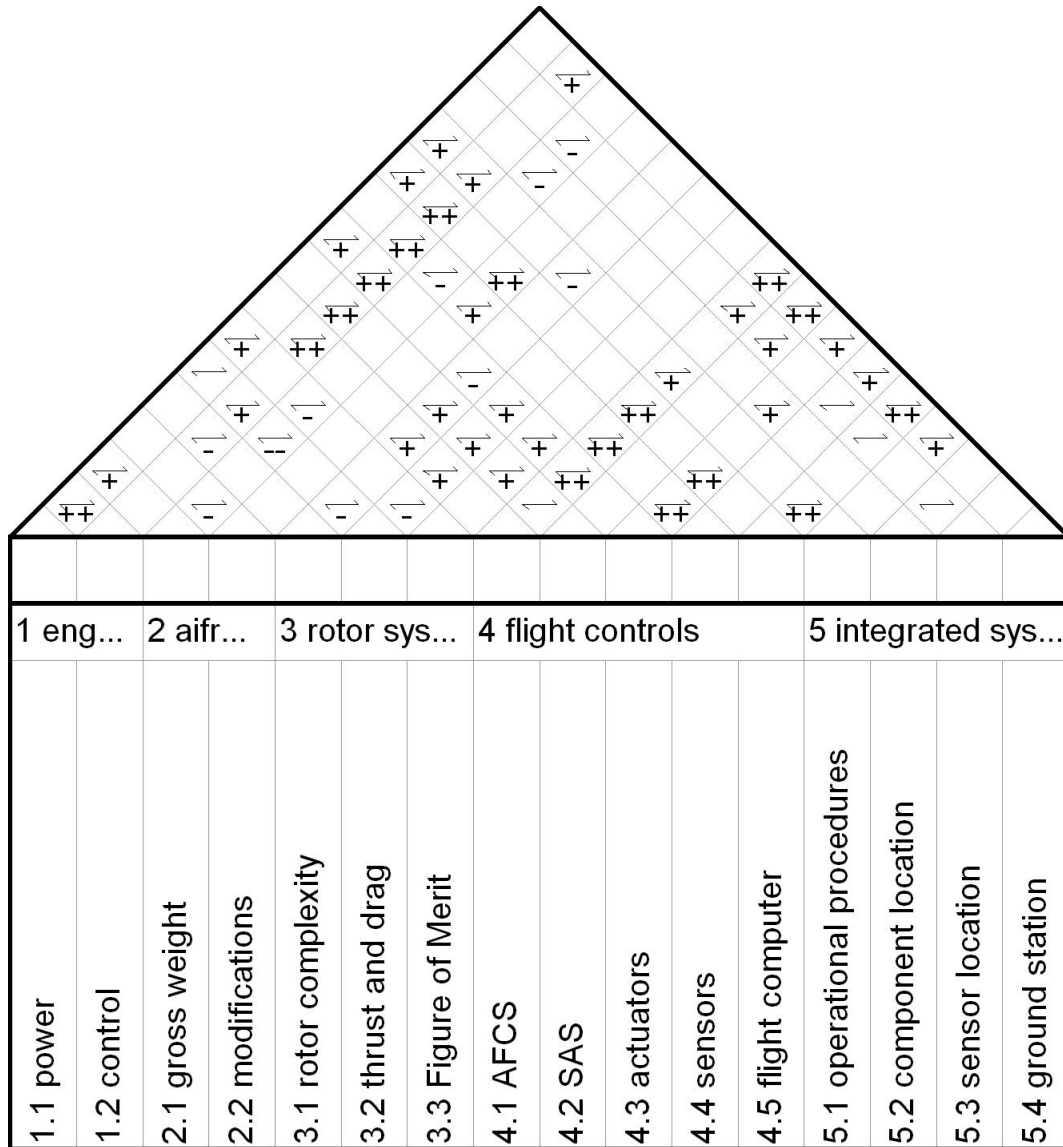


Figure M.10: Interaction Matrix for Design Requirements (VOC). In the figure, a lone horizontal bar indicates a primary correlation, a + sign indicates a possible positive effect among the two design requirements, a double ++ sign indicates a positive effect, a negative - sign indicates a possible negative effect, and a double negative sign -- indicates a negative effect.

priorities. Figure M.11 presents the result of the top level analysis in a functional decomposition breakdown. In turn, Figure M.12 on the next page illustrates the University of Oklahoma Helicopter Research Testbed work breakdown structure.

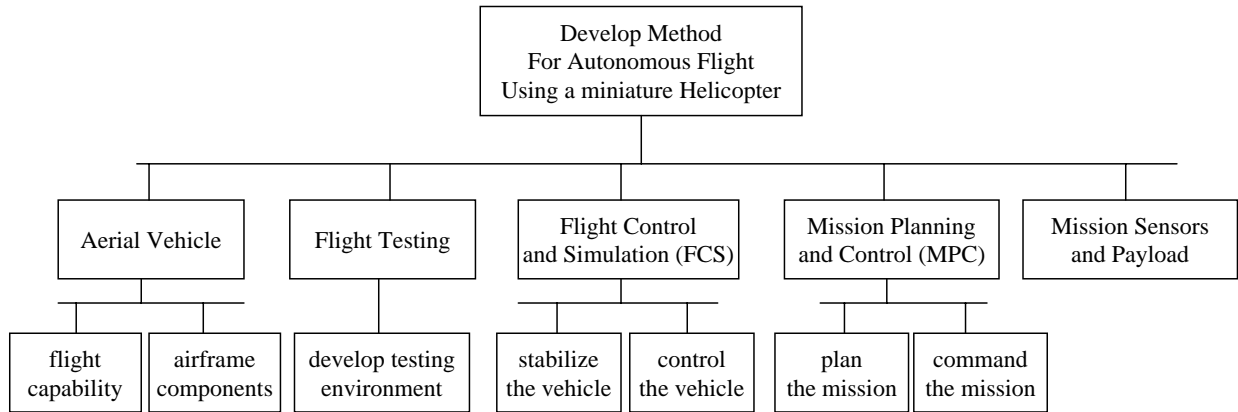


Figure M.11: First level functional decomposition.

M.4 System Architecture

The modular functional decomposition (Figure M.11) and related subsystems decomposition with a related work breakdown structure (Figure M.12 on the next page) helps with the definition of the various architectural modules that make up the system. This modular design facilitates identification and formalization of the interface between subsystems, and allows for clean maintenance and upgrade road of the various subsystems components. Figure M.13 on page 478 shows the full system architecture suitable for autonomous flight for the University of Oklahoma Helicopter Research Testbed. This system architecture is a modified version of work done by Thornhill et. all [38] and Gordon and Schrage et. all [59, 131].

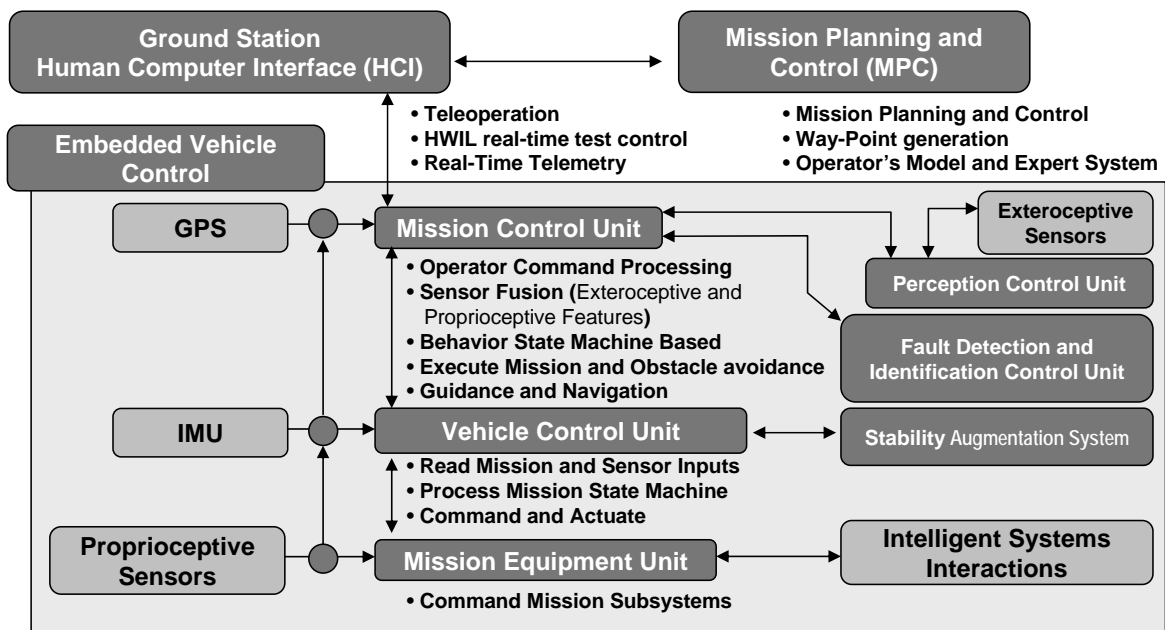


Figure M.13: System Architecture for the University of Oklahoma Helicopter Research Testbed for Autonomous Flight.

Appendix N

Nomenclature

ε	ratio of blade mass to inertial moments, $M_{blade} r_{CM} e R^2 / I_b = \frac{\text{static moment}}{\text{inertial moment}}$
γ	Lock number, $ca\rho R^4 / I_{blade}$
λ_i	normalized induced velocity, (positive downward through rotor disk), $(V_C + v_i) / \Omega R$
μ	advance ratio, $V_\infty \cos \alpha / \Omega R$
ν^2	nondimensional rotating flap frequency, $1 + \varepsilon + K_\beta / \Omega^2 I_\beta$
σ	blade solidity, $bc / \pi R$
A	rotor disk area, πR^2
b	number of blades
c	blade chord
C_P	dimensionless power coefficient, $P / \rho A (\Omega R)^3$
C_Q	dimensionless torque coefficient, $Q / \rho A (\Omega R)^2 R$
C_T	dimensionless thrust coefficient, $T / \rho A (\Omega R)^2$
S_β	stiffness number, $8(\nu^2 - 1) / \gamma$

Appendix O

Glossary

C

Computer Aided Design (CAD) Computer Aided Design tools, p. 461.

F

Finite Element Analysis (FEA) Mathematical modeling techniques used to study static, dynamic and thermal behavior of systems, p. 461.

Q

Quality Function Deployment (QFD) An organized, disciplined process for determining the product or service requirements necessary to achieve customer-perceived expressed or unexpressed quality., p. 461.

S

Six-Sigma Techniques ($6 - \sigma$) An approach to reduce process output variation so that six standard deviations lie between the mean and the nearest specification limit. This will allow no more than 3.4 defect Parts Per Million (PPM) opportunities, also known as Defects Per Million Opportunities (DPMO), to be produced., p. 461.

Systems Engineering (SE) Interdisciplinary framework suitable for the complete and accurate definition of systems requirements, analysis of the system as a whole

with a top-down engineering approach with a focus on the entire system Life Cycle, and with a design process that focuses on system optimization and balance through the management and integration of multiple scientific and technical disciplines., p. xv.

U

Unified Modeling Language (UML) Abstract, general-purpose object modeling specification language., p. 461.

Appendix P

Acronyms

6

six degree of freedom (6dof) , p. 376.

A

Autonomous Scout Rotorcraft Testbed (ASRT) Autonomous Scout Rotorcraft Testbed, Georgia Tech, p. 463.

B

Blade Element Momentum Theory (BEMT) , p. 15.

Blade Equation of Motion (BEOM) , p. 55.

Blade Element Theory (BET) , p. 15.

C

Comprehensive Identification from FrEQUENCY Responses (CIFER) , p. 50.

Configuration Management (CM) See Glossary, p. xv.

Capability Maturity Models (CMM) See Glossary, p. 460.

Capability Maturity Models Integration (CMMI) See Glossary, p. 460.

Control Plane (CP) , p. 198.

G

Global Positioning System (GPS) , p. 378.

H

Hub Plane (HP) , p. viii.

Hardware-in-the-Loop (HWIL) , p. xxiii.

I

Integrated Product and Processes Development (IPPD) See Glossary, p. xii.

L

Linear and Directional Test Stand (LDTS) , p. vi.

M

McDonnell Douglas Corporation (MDC) McDonnell Douglas Corporation, p. 463.

Mission Planning and Control (MPC) , p. 28.

Momentum Theory (MT) , p. 15.

N

Non Feathering Plane (NFP) , p. 198.

O

University of Oklahoma Helicopter Research Testbed (OU-HRT) , p. xii.

Q

Quality Function Deployment (QFD) , p. xii.

R

Remote Control (RC) , p. 12.

Rotational Dynamics Test Stand (RDTS) , p. vi.

Requirements Engineering (RE) See Glossary, p. 461.

Real-Time Operation System (RTOS) , p. 28.

S

System Engineering (SE) See Glossary, p. 10.

System Engineering and Integration (SE&I) See Glossary, p. 459.

Supplier Sourcing (SS) See Glossary, p. 460.

Software Engineering (SW) See Glossary, p. 460.

T

Tip Path Plane (TPP) , p. 52.

Time Processing Unit (TPU) , p. 30.

V

Voice of the Customer (VOC) , p. xii.

Voice of the Engineer (VOE) , p. xii.

Index

- S_β , *see* stiffness number
- ε , *see* inertia blade ratio
- λ , *see* rotor, inflow ratio
- λ_i , 208
- μ , *see* advance ratio
- ν , *see* flap frequency, *see* stiffness number
- σ , blade solidity, **226**
- Linear and Directional Test Stand (LDTS),
31
- Rotational Dynamics Test Stand (RDTS),
31
- Voice of the Customer (VOC), 464
- advance ratio, **219**, 316
- angular rates, *see* reference frames
- BEMT, *see* combined blade element theory
- BEOM, *see* rotor
- BET, *see* blade element theory
- blade element theory, 222
tip-loss factor, 228
- central processing unit, 26
- clinometer, *see* sensors
- coefficient
power, **208**
thrust, **208**
torque, **208**
- combined blade element theory, 229
- control servo
- main rotor
collective, 34
lateral, 36
longitudinal, 36
setting, 40
tail rotor collective, 39
throttle, 40
- dynamic stability, *see* stability
- dynamics
position, 193
rotational, 194
translation, 191
- electronic compass, *see* sensors
- embedded software, *see* systems integration
- experiments
main rotor
thrust, 419
torque, 100
pitch and roll, 123
pitch rate and pitch attitude hold, 119,
448
roll rate and roll attitude hold, 123,
452
pitch, roll and yaw hold, 457
tail rotor
aerodynamic identification, 107
trim collective, 437
yaw rate and heading hold, 116, 434

- heading hold, 443
 - yaw rate, 438
- feedback control loops
 - altitude hold, 86
 - pitch rate and pitch attitude hold, 82
 - position hold, 90
 - roll rate and roll attitude hold, 86
 - RPM and engine governor, 80
 - yaw rate and heading hold, 80
- flap frequency
 - rotating
 - nondimensional, ν^2 , **244**, 248, 268, 284, 292
- fluid equations, 169
 - conservation of energy, 176
 - conservation of mass, 172
 - conservation of momentum, 174
- Global Positioning System, 378
- helicopter
 - University of Oklahoma Helicopter Research Testbed (OU-HRT), **14**
 - calibration
 - bending beam load cell, 392
 - main rotor collective, 389
 - main rotor cyclic, 390
 - tail rotor collective, 392
 - test stand, 395
 - throttle fuel rate, 392
 - engine, 16, 385
 - equations of motion
 - linearized, 365
 - rigid body, 358
 - hardware interface, 20
 - main rotor, 14
 - torque and power models, 421
 - servos, 18
 - swashplate, 18
 - tail rotor, 15
 - aerodynamic model, 431
 - transmission gears, 17
- induced velocity, *see* rotor
- inertia
 - blade ratio, ϵ , **244**, 248, 268, 284, 292
- inflow ratio, *see* rotor
- infrared sensor, *see* sensors
- Lock number, **259**
- momentum
 - forward flight, 217
 - power, 220
 - hovering flight, 203
 - simple momentum theory, 202
 - vertical climb, 209
 - vertical descent, **213**
 - autorotation, 217
 - turbulent wake state, 217
 - vortex ring state, 216
 - windmill break state, 213
- MotionPak, *see* sensors
- nondimensional rotating flap frequency, **292**
- OU-HRT, *see* helicopter

power coefficient, **208**

rate table stand, 30

reference frames, 179

- atmosphere-fixed or wind , 181
- body-fixed, 181
- Earth-Centered , 180
- Earth-Surface , 180
- Euler angle rates, 189
- geocentric, 180
- heliocentric, 179
- inertial, 181
- main rotor, 196
 - hub plane, 198
 - non feathering plane, 199
 - tip path plane, 200
- vehicle-carried , 181

rotor

- Blade Equation of Motion (BEOM), 235
 - summary, 314
- forces and moments, 316, 361
 - coupled fuselage-rotor, 329
 - forces, 321
 - hub moments, 325
 - simplified, 323
- induced velocity, **208**
- λ , inflow ratio, **219**, 316
- rotational inertia, 371
- σ , blade solidity, **226**

sensors

- AccuStar II Dual Axis Clinometer, 383
- electronic compass, 384
- FreeWave wireless transceiver, 381
- GPS, 378
- Hall effect, 26
- MotionPak inertial measurement unit, 376
- SHARP GP2D02 infrared sensor, 382
- ultrasound altimeter, 388

SMT, *see* momentum

stability

- dynamic, **342**
- static, **342**

static stability, *see* stability

stiffness number, **263**, 313, 330

swashplate, 198, 201

systems engineering, 459

- CM & CMM, 460
- functional decomposition, 473
- IPPD, 461
- processes, 461
- QFD, 467
- standards, 459
- system architecture, 129, 476

systems integration

- embedded software, 136
- hardware and software, 138
- hardware interface, 131
- software interface, 134

test stand, 42

- Linear and Directional Test Stand (LDTS), 45

Rotational Dynamics Test Stand (RDTS),
47

Rate Table Stand (RTS), 48
survey, 44

thrust coefficient, **208**

torque coefficient, **208**

ultrasound altimeter, *see* sensors

wireless transceiver, *see* sensors